1968

TABLE OF CONTENTS

I. History and Future of the Program

1. Suomi, V. — Historical Background of ATS-I

II. Large Scale Phenomena

2. Kornfield, J. and K. Hanson — On the Double Structure of Cloud Distribution in the Equatorial Pacific

3. Charney, J. — Intertropical Convergence Zone and the Hadley Circulation of the Atmosphere

Never found 4. Lettau, H. — Cromwell Current Heat Transfer

III. Mesoscale Systems

5. Fujita, T., D. Bradbury, C. Murino, and L. Hull — A Study of Mesoscale Cloud Motions Computed From ATS-I and Terrestrial Photographs

6. Hanson, K. and T. Vonder Haar — Cloud Motion and Other Parameters From ATS-I Digital Data

IV. Reflections From the Earth's Surface and Clouds

Never found 7. Sekera, Z. — Atmospheric Glint

8. Levanon, N. — Determination of the Sea Surface Slopes Distribution and Wind Velocity From Sun Glitter Viewed From a Synchronous Satellite

9. Raschke, E. and W. Bandeen — Studies of Reflector Characteristics of the Planet Earth From a Synchronous Satellite - Preliminary Results

10. Peekna, S., R. Parent, and T. Vonder Haar — Possibilities for Quantitative Radiance Measurements in the 450-650nm Region From the ATS-I Satellite

V. Data Applications and Measurement Techniques

11.	Fritz, S., L. Hubert, and A. Timchalk	Relation Between Cloud Motions From ATS-I and Wind Direction
12.	Hasler, F., J. Kornfield, and L. Jensen	A Blink Measuring Technique for Quantitative Measurement of Cloud Motion From ATS-I Spin Scan Camera Pictures
13.	Hasler, F. and J. Kornfield	Display and Analysis of ATS-I Spin Scan Camera Pictures Through Time-Lapse Movie Technique
14.	Bristor, C., M. Frankel, and E. Kendall	Cloud Motion and Growth From Digitized ATS-I Picture Pairs
15.	Hubert, L. and E. Ramey	Analysis of ATS-I Pictures by Photogrametric Techniques
16.	Norman, T. and S. Venkateswaran	The Use of ATS Satellites for Ionospheric Studies

VI. Technical Description of Camera and Ground Equipment

17.	R. Thomsen, R. Parent and V. Suomi	ATS-I Camera
18.	Sunderlin, W. and J. Lahzun	Ground Display and Recording Equipment for the Spin Scan Camera System
19.	Holmes, D.	Wefax - A Weather Data Communications Experiment
20.	Suomi, V. and R. Parent	Calibration Procedure
21.	Parent, R. and J. Sitzman	Analog Recording System
22.	Hanson, K. and V. Suomi	The Inspace, Absolute Calibration of ATS-I Cloud Camera

VII. Data Registration, Processing and Cataloging

23.	Whitney, M., R. Doolittle, and B. Goddard	Processing and Display Experiments Using Digitized ATS-I Spin Scan Camera Data
24.	Lindstrom, J.	Processing, Archival and Documentation of the ATS-I Spin Scan Camera Photographic Data

25.	Hanson, K., T. Vonder Haar, and F. Nicholson	ATS-I Navigation
26.	Nicholson, F.	The Theoretical and Mathematical Justification for Navigation and Analysis From the ATS Satellites
27.	Smith, E. and T. Vonder Haar	Operational Display Techniques for ATS Digital Data Users

JUN 10 1968

1024 Regent Street
Madison, Wisconsin 53715

June 7, 1968

Miss Joan Krager
General Editor
Univ. of Wis. Press
Univ. of Wis.
Madison, Wis.

Dear Miss Krager:

Enclosed is a Title, Preface and Table of Contents for the ATS-I Volume. This is our best present attempt at defining these parts of the book. We would like the option of being able to change a few words of the Preface or Titles, etc., in the Table of Contents if this becomes necessary.

We have left open the question of Acknowledgements and Dedication. I would like to talk to you about these.

Sincerely,

KH:be

Kirby Hanson

Enclosure

cc/ Professor Suomi

WEATHER MOTIONS FROM SPACE

PREFACE

Weather is air in motion. A geostationary satellite such as the ATS-I spacecraft in a "hanging orbit" makes possible views of more than a third of the earth well enough to obtain cloud motions. The meteorologist is no longer forced to view the ever changing atmosphere as a series of static weather charts or snapshots from rapidly moving satellites. In a geostationary orbit the weather moves-not the satellite.

This volume treats three subject areas. First, while the ATS-I spin-scan camera experiment is conceptually rather simple, it is never-the-less a significant technological development. It is the first synchronous satellite camera system. It provides a large volume of high resolution cloud photographs having precise geometry and wide dynamic range. Description of the technical aspects of the spacecraft and camera system and the associated all important ground equipment have been included to provide the potential user with enough details to fully exploit the data. Secondly, these new views of the earth have aided a number of scientific studies. In our view these results which include weather motion and some causes are the main contribution of the volume, and are therefore presented first. Thirdly, a number of methods of treating the data have been worked out and we hope these techniques will be useful to others.

We wish to express our appreciation to the contributors. They withheld early publication of these papers so a complete description of the experiment and preliminary scientific results could be given as a single package reference. By combining the science and technology in this way we hope to show what is possible meteorologically and technologically using the synchronous satellite's

unique capability. If we succeed in accomplishing this, the efforts of the contributors and editors will have been justified.

Verner E. Suomi and
Kirby J. Hanson, Editors

Madison, Wisconsin
June 6, 1968

TABLE OF CONTENTS

I. History and Future of the Program

1. Suomi, V. — Historical Background of ATS-I

II. Large Scale Phenomena

2. Kornfield, J. and K. Hanson — On the Double Structure of Cloud Distribution in the Equatorial Pacific

3. Charney, J. — Intertropical Convergence Zone and the Hadley Circulation of the Atmosphere

4. Lettau, H. — Cromwell Current Heat Transfer

III. Mesoscale Systems

5. Fujita, T., D. Bradbury, C. Murino, and L. Hull — A Study of Mesoscale Cloud Motions Computed From ATS-I and Terrestrial Photographs

6. Hanson, K. and T. Vonder Haar — Cloud Motion and Other Parameters From ATS-I Digital Data

IV. Reflections From the Earth's Surface and Clouds

7. Sekera, Z. — Atmospheric Glint

8. Levanon, N. — Determination of the Sea Surface Slopes Distribution and Wind Velocity From Sun Glitter Viewed From a Synchronous Satellite

9. Raschke, E. and W. Bandeen — Studies of Reflector Characteristics of the Planet Earth From a Synchronous Satellite - Preliminary Results

10. Peekna, S., R. Parent, and T. Vonder Haar — Possibilities for Quantitative Radiance Measurements in the 450-650nm Region From the ATS-I Satellite

V. Data Applications and Measurement Techniques

11.	Fritz, S., L. Hubert, and A. Timchalk	Relation Between Cloud Motions From ATS-I and Wind Direction
12.	Hasler, F., J. Kornfield, and L. Jensen	A Blink Measuring Technique for Quantitative Measurement of Cloud Motion From ATS-I Spin Scan Camera Pictures
13.	Hasler, F. and J. Kornfield	Display and Analysis of ATS-I Spin Scan Camera Pictures Through Time-Lapse Movie Technique
14.	Bristor, C., M. Frankel, and E. Kendall	Cloud Motion and Growth From Digitized ATS-I Picture Pairs
15.	Hubert, L. and E. Ramey	Analysis of ATS-I Pictures by Photogrametric Techniques
16.	Norman, T. and S. Venkateswaran	The Use of ATS Satellites for Ionospheric Studies

VI. Technical Description of Camera and Ground Equipment

17.	R. Thomsen, R. Parent and V. Suomi	ATS-I Camera
18.	Sunderlin, W. and J. Lahzun	Ground Display and Recording Equipment for the Spin Scan Camera System
19.	Holmes, D.	Wefax - A Weather Data Communications Experiment
20.	Suomi, V. and R. Parent	Calibration Procedure
21.	Parent, R. and J. Sitzman	Analog Recording System
22.	Hanson, K. and V. Suomi	The Inspace, Absolute Calibration of ATS-I Cloud Camera

VII. Data Registration, Processing and Cataloging

23.	Whitney, M., R. Doolittle, and B. Goddard	Processing and Display Experiments Using Digitized ATS-I Spin Scan Camera Data
24.	Lindstrom, J.	Processing, Archival and Documentation of the ATS-I Spin Scan Camera Photographic Data

25.	Hanson, K., T. Vonder Haar, and F. Nicholson	ATS-I Navigation
26.	Nicholson, F.	The Theoretical and Mathematical Justification for Navigation and Analysis From the ATS Satellites
27.	Smith, E. and T. Vonder Haar	Operational Display Techniques for ATS Digital Data Users

MAY 20 1968

THE UNIVERSITY OF WISCONSIN PRESS

P.O. Box 1379, 807 West Dayton Street, Madison, Wisconsin 53701 Telephone 608/262-1116

OFFICE OF THE EDITOR

May 15, 1968

Professor Verner Suomi
Space Science and Engineering Center
601 East Main Street
Campus

Re: Suomi and Hanson, ATS Volume

Dear Mr. Suomi:

Tom Webb just sent down your latest print-out reporting progress in the collection of papers with the note:

"Put pressure on Suomi. Tell him I had told you to."

He is not alone in giving me this advice, as your colleagues will testify.

We now have almost two-thirds of the draft chapters, lacking the following:

1 Suomi	17 Norman & Venkateswaran	21 Suomi & Parent
4 Lettau	18 Thomsen, Parent & Suomi	22 Parent & Sitzman
7 Sekera	20 Hall & Holmes	28 Smith & Vander Haar

From the frequency with which the name Suomi crops up in the foregoing list, one wonders if some sort of bottleneck doesn't exist on East Main Street.

More seriously, we have enough papers to get a reasonably useful evaluation of the project if only we had some introductory materials describing the purpose and scope of the proposed volume. Our evaluation takes a little time, and we'd like to schedule it to correspond with the completion of the papers in the hope that the project could be proposed to our editorial board and accepted. We could then begin to edit papers as they were completed and lose no time in issuing a volume of immediate need and interest.

I shall look forward to writing you a minimum of tough notes.

Sincerely,

Joan M. Krager

Joan M. Krager
General Editor

cc - Mr. Kirby Hanson
Miss Martha Noerr

PREFACE

There are two reasons why this book was written. Neither reason, considered alone, would justify the effort. The first is that the ATS-1 Cloud Camera experiment was a large technological step forward and was the first synchronous satellite that was meteorologically useful. It is difficult and perhaps inappropriate to attempt to evaluate the effect of this new technology on meteorology. But whether it is appropriate or not, the interest and success of ATS-1 impels one to feel that this experiment has truely opened a new and sound vista for studies of the earth's atmosphere. This is indeed fortunate timing because it coincides with a revolutionary increase in the scientific capability in meteorology, made possible by the computer.

The second set of circumstances that gave rise to this volume is that in the past few years the ICSU/IUGG Committee on Atmospheric Sciences has taken an important step toward improved weather forecasting by establishing a global atmospheric research program (GARP). This program will add a great deal to our basic knowledge of the behavior of the atmosphere on a global scale. Thus, the new satellite technology is available at a time when it is most needed.

If the meteorological community is to benifit from and build on our present synchronous satellite capabilities, there is clearly a need to provide this existing knowledge in a readily accessible way. Over the years we have come to appreciate, how valuable

reference books like Smithsonian Meteorological Table and AFCRL Handbook of Geophysics can be to a researcher. With this in mind, we are attempting to provide a research ~~handbook that~~ reference book which will be useful for synchronous meteorological satellites in general and for ATS-1 in particular.

This volume is, in part, analogous to a ~~handbook~~ reference book in that it provides basic factual information on the camera, ground equiptment and resulting ATS-1 meteorological data. However, it goes beyond the usual ~~handbook~~ reference book in that it also presents the preliminary scientific results ~~from~~ of the ATS-1 experiment, by researchers in both universities and government agencies. By combining both, we hope to provide a volume which clearly shows the researcher what is possible, meteorologically and technologically, with ATS-1. If it succeeds in accomplishing this, the efforts of the contributors and editors will have been justified.

Why was it written at Wisconsin?

Verner E. Suomi
and
Kirby J. Hanson

Madison, Wisconsin
May 4, 1968

CLOUD IMAGES FROM SYNCHRONOUS ALTITUDE:

A PROSPECTIVE AND REVIEW

by

Verner E. Suomi

The key to weather is air motion.

The purpose of the spin scan camera experiment was to continuously monitor the weather motions over a large fraction of the earth's surface. Near earth weather satellites have provided an impressive array of visual and infrared observations of the earth's weather on a nearly operational basis, but the view from a near earth satellite is so fleeting that it is not possible to obtain any real measure of the weather motions. For example, in TIROS series of satellites, the life history of a model storm had to be derived from a number of different storms, at different times, at different places, and in different stages of development. A synchronous satellite allows one to measure the cloud motions rather than infer them because the earth's disc is under continuous surveillance. Under a synchronous satellite the weather moves—not the satellite!

In the tropics the weather motions have a much shorter time scale than the motions at higher latitudes. The tropics, between $\pm$ 30° latitude, covers half the earth's area which is 80% ocean. Here the surface observations are very sparse and polar orbiting satellites have the greatest gaps in their data.

The tropical region is the "boiler" of the giant atmospheric heat engine. Convective activity plays an all important role in the heat transfer process, yet its short time scale prevents its being observed adequately by near earth satellites.

The radiation balance of the earth as measured from Explorer VII, TIROS III, IV, and VII (House, 1965; Bandeen, et al., 1964), shows that the measured outgoing radiation is surprisingly close to previous estimates, while the albedo of tropical regions is significantly lower than these earlier estimates. Thus considerably greater poleward transfer of heat is required. For example, values 40% larger than London's estimates across latitude 20° have been obtained. The detailed mechanism whereby the atmosphere transfers the heat out of the tropics to higher latitudes is not adequately understood even though it is realized that latent heat transfer and large scale eddy circulations play a dominating role over meridional circulations.

Figure 1 shows the total heat content of the upper portion of the tropical troposphere is higher than the mid tropospheric portions even though the atmosphere is heated from the bottom. Riehl and Malkus (1962) proposed a "hot tower" mechanism for the transfer process (1962). In the "hot tower" process the number (or area) of upward convective thrusts is a key element in the quantitative evaluation of the heat transfer process. Not all clouds ascend through the entire troposphere so consideration of the <u>organization</u> of the cloud systems is also required.

The spin scan cloud camera on NASA's Applications's Technology Satellites ATS-I and ATS-III were developed to provide higher resolution spatial distribution information on cloud systems over a large fraction of the tropics and higher latitudes as well. Even more important, they provide key information on cloud system growth over time scales much

smaller than the diurnal interval. Finally, because the camera images are dimensionally accurate, it provides information on cloud displacement as well. The cloud displacements provide information on the large scale air motions which transport the heat out of the tropics to higher latitudes. The synchronous meteorological satellite turns out to be the key tool for study of the tropics.

In a synchronous orbit it is possible to take a "time exposure" of the earth about the subsatellite point. This feature allows a surprisingly simple optical and electronic system to generate a high resolution photograph. A two-mile resolution at the subsatellite point has been demonstrated.

While a number of schemes were considered for the camera system, the one actually used consisted of a "rocking telescope" which employs a 10" focial length Cassegrain telescope whose primary mirror is 5" in diameter.

REFERENCES

1. House, F., 1965. The Heat Budget of the Earth from a Satellite. Ph.D. Thesis, University of Wisconsin.

2. Bandeen, W., M. Malev and I. Strange, 1964. A Radiation Climatology in the Visible and Infrared from TIROS Meteorological Satellites. Paper presented at the International Radiation Symposium, Leningrad, August, 1964.

3. Riehl, H., and S. Malkus, 1962.

Science, 135:13.

(3)

ON THE DOUBLE STRUCTURE OF CLOUD DISTRIBUTION IN THE EQUATORIAL PACIFIC

by

Jack Kornfield

and

Kirby Hanson

#2

(mission copy)

INTRODUCTION

The circulation and cloud structure of the equatorial atmosphere have been studied because of their roles in the first stage of the atmospheric heat engine. Fletcher (1945), Palmer (1952), Riehl (1954), Flohn (1955) and others have provided the framework of knowledge by describing the general circulation of the equatorial atmosphere. Alpert (1945), Simpson (1947), Malkus, et al. (1961), among others, have added a great deal of information by describing the atmospheric behavior in regional studies of the Pacific. These early studies were based primarily on observations taken in the sparse network of Pacific Ocean weather stations, and on rawinsonde and aircraft observations. More recently, Sadler (1963a, b) has used TIROS satellite observations to reveal much about the local circulation and typhoon movement in the Eastern Pacific.

From seeing the first ATS-1 pictures it was apparent that some of the earlier concepts of cloud distribution in the tropics were not observed. There was a preference for cloudless conditions within a few degrees of the equator and deep convective cloudiness from 5 to 10 degrees latitude both north and south of the equator (but primarily north). This indeed is in sharp contrast to earlier ideas which had visualized rising motion and convective cloudiness over much of the broad equatorial region. How could one explain these new observations which seemed to show a reversed Hadley circulation in the region from 10° N to 10° S?

A very likely explanation is given by Professor Charney in an accompanying article in this volume. He shows that a zonally symmetric disturbance of a conditionally unstable tropical atmosphere could, by the instability process involving cooperation between the cumulus clouds and the large scale disturbance, give rise to two narrow regions of rapidly ascending motion more or less symmetrically placed about the equator and that, for dynamical reasons connected with the Coriolis control of the meridional mars transport in the planetary boundary layer, these zones would not coincide with the equator (Charney, 1966). It is now clear that cloud features observed in the tropical Pacific by ATS-1 and ESSA satellites in 1967 and 1968 occur in the same latitudinal zones as predicted by Charney's theory. This new observational evidence is the subject of our paper.

The exciting theoretical development of Professor Charney and ATS-1 pictures pose some important questions of the tropics. Is an anti-Hadley circulation present in the equatorial Pacific? If it is, what is the depth of the subsidence layer? Does wind and moisture convergence in the atmospheric boundary layer entirely determine the location of the ITCZ and underlying ocean currents, or do the ocean currents themselves play a roll in determining the position of the ITCZ?

None of these questions can be answered at this time but will undoubtedly be of great concern in the next few years as attention to the tropics is accelerated.

TWO METHODS OF CLOUD ANALYSIS

Our principal interest is to examine the cloud distribution over the Pacific Ocean averaged over specific time periods. To do this, we have used two completely independent techniques which are intended to approximate the monthly frequency of cloudiness.

One technique provides photographic averaging of a series of pictures. The individual pictures in the series are imaged, one at a time, on a single sheet of photographic film. The resulting picture represents an average of all the individual pictures of the series. Photographic averages of the ATS-1 pictures have been obtained in this way for monthly and half-monthly periods. A number of these mean monthly cloud pictures with latitude - longitude lines superimposed are shown in Figure 1. Each of these monthly average pictures is derived from about thirty pictures.

The second technique has been used to determine frequency of occurrence of band-type cloudiness which, for the purpose of this work, is defined as those clouds which appear to be organized into lines or bands having a width of about two degrees latitude or greater. One picture per day was used to determine the frequency of occurrence of this type of cloudiness for monthly periods. In order to accomplish this, each daily ATS-1 picture was overlain with a 5 by 5 degree latitude-longitude grid, and the presence or absence of line-type cloudiness in these boxes was determined. From this, the frequency of line-organized cloudiness was then determined for monthly periods and hand analysed. These are plotted in Figure 2.

Although the photo technique of Figure 1 and statistic technique of Figure 2 show the same general cloud structure in the Tropics, it is apparent that the hand nephanalysis of the statistical technique reveal the full structure of the cloud bands as does the photographic average. This is because the photographic technique can record clouds of smaller size and without a previously defined definite organization.

DISCUSSION OF TROPICAL PACIFIC CLOUD FEATURES

The convective cloud band located about 5 to 10 degrees north of the equator is a strikingly permanent cloud feature of the tropical Pacif, as shown in Figures 1 and 2, It is very apparent that this cloud band does not migrate across the equator, except perhaps in the eastern Pacific (east of 120° W. Long.) where there appears to be a slow southward migration during the latter part of winter in the northern hermsphere.

It appears to be an interesting fact that this cloud band, north of the equator, is most intense when the sun is either farthest north or farthest south, that is, in late December and late June. During the remainder of the year, the northern cloud band is less well developed and in March, April and May, there is a strong tendency to have convective cloud bands both north and south of the equator with a relatively clear zone between, as predicted by the theory of Charney, These are the essential features of the mean cloud condition we have observed over the tropical Pacific Ocean.

It is very tempting to think that Professor Charney's theory of moisture convergence in the boundary layer satisfactorily explains the symmetrical cloud doublet that we see in April (Figure 1 and Figure 2) when the sun is nearly directly over the equator. But what is the mechanism that causes

the intensification of the northern cloud band when the sun is in the northern hemisphere and again when it is in the opposite hemisphere? At present we cannot answer that question.

In Figure 3 (top right) we have superimposed the July streamlines of surface wind flow, as found by Mintz and Dean (1952) on the July mean cloud picture. It is clear that the northern cloud band coincides very well with the surface wind convergence line and verifies the mean position of the convergence line. However, it does not necessarily verify the streamlines which are shown to cross the equator as the cause of this convergence. It is equally possible that the observed convergence could be a result of an anti-Hadley circulation, as predicted by Charney, and the flow across the equator from south to north, as shown by Mintz and Dean, would not be required.

SUMMARY

A number of interesting cloud features have been observed in the tropical Pacific which tend to support the theory given by Charney in another paper in this volume. His theory predicts two cloud bands, one on each side of the equator with a clear zone between. This cloud distribution is observed during a few months near the vernal equinex. However, when the sun is either farther north or south, this double structure disappears and only the northern cloud band is present. It is not clear why this should occur,

From these photos it is not possible to determine whether the anti-Hadley circulation, which Charney has postulated, exists at the time when the cloud doublet is present and if it continues at other times when only the northern cloud band is present. It appears that the former is true, and it is mere speculation whether the latter is true. Others have suggested a link between ocean currents and these convergence cloud bands.

All of these possible causial factors will be receiving a great deal of attention in the next few years as more attention is focused on the tropics. Hopefully we will find more complete answers to the unknowns - of which Professor Charney has provided such an enlightening start.

REFERENCES

Alpert, A. C. 1945: The Intertropical Convergence Zone of the Eastern Pacific Region (I). Bull. Amer. Meteor. Soc., 26, 426 - 432.

Bjerknes, J., 1966: A Possible Response of the Atmosphere Hadley Circulation to Equatorial Anomalies of Ocean Temperature. Tellus, 18: p. 820 - 829.

Fletcher, R. D., 1945: The General Circulation of the Tropical and Equatorial Atmosphere, J. Meteor., 2, 167 - 174.

Flohn, H., 1955: Tropical Circulation Patterns. WMO Tech. Notes., 9.

Gentilli, J., 1958: A Geography of Climate, The University of Western Australia Press, Perth, Western Australia.

Malkus, J. S., H. Riehl, C. Ronne, and W. S. Gray, 1961: Cloud Structure and Distribution over the Tropical Pacific, Par II., Woods Hole Ocean. Inst. Ref. No. 61 - 24.

Mintz, Y., and G. Dean, 1952: The Observed Mean Field of Motion of the Atmosphere. Geophys. Res. P., 17., GRD, AFCRL, Cambridge, Mass.

Palmer, C. E. Tropical Meteorology, Quarterly Journal of the Royal Meteorological Society, Vol. 78, 1952, pp. 126 - 64.

Riehl, H., 1954: Tropical Meteorology, McGraw Hill, New York.

Sadler, J., 1963a: Utilization of Meteorological Satellite Cloud Data in Tropical Meteorology. Proceedings of First International Symposium on Rocket and Satellite Meteorology. Northland Publ. Co., Amsterdam, 335 - 356.

Sadler, J., 1963b: TIROS Observations of the Summer Circulation and Weather Patterns of the Eastern North Pacific. Symposium on Tropical Meteorology, Rotorus, New Zealand.

Simpson, R. H., 1947: Synoptical Aspects of the Intertropical Convergence Near Central and South America. Bull. Amer. Meteor. Soc., 28, 335 - 346.

Wyrtki, K. 1966: Oceanography of the Eastern Equatorial Pacific Ocean. Oceanogr. Mar. Biol. Ann. Rev., 4, 33 - 68.

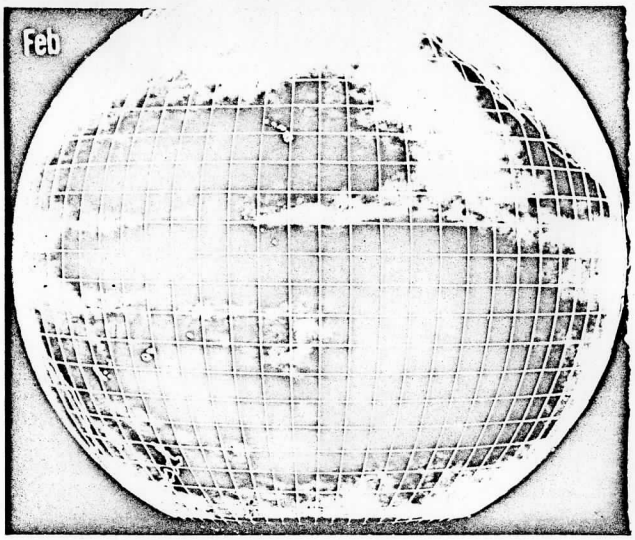

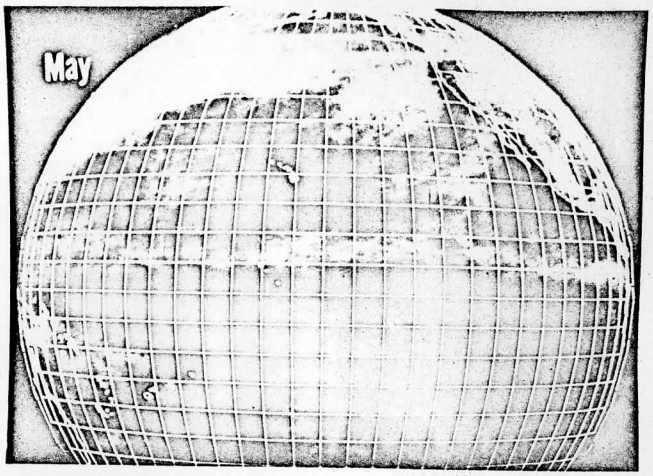

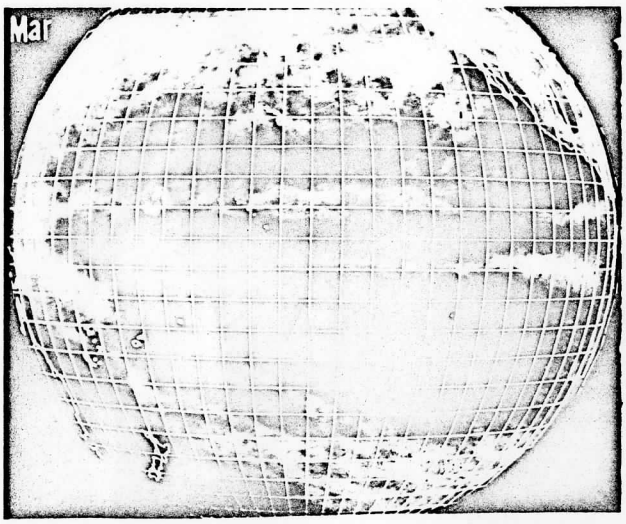

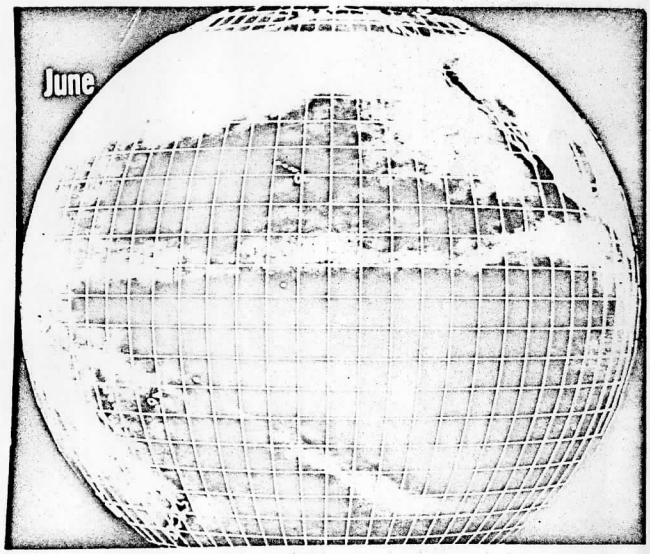

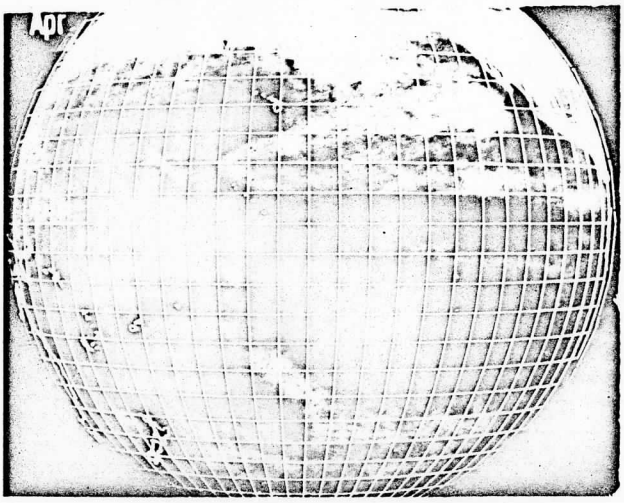

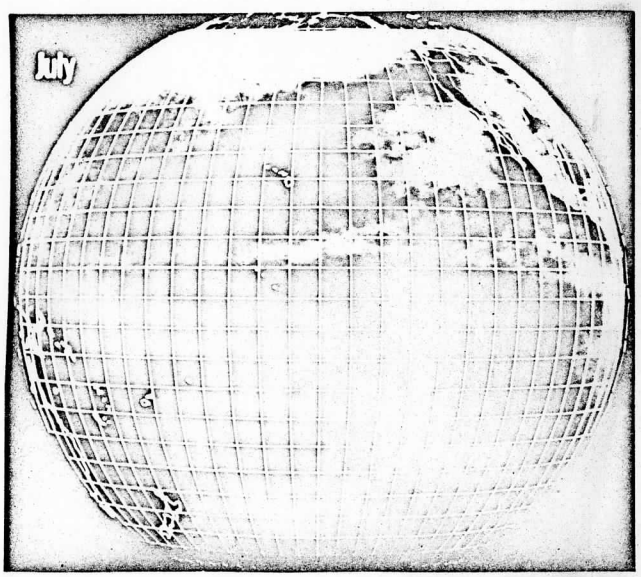

Fig. 1

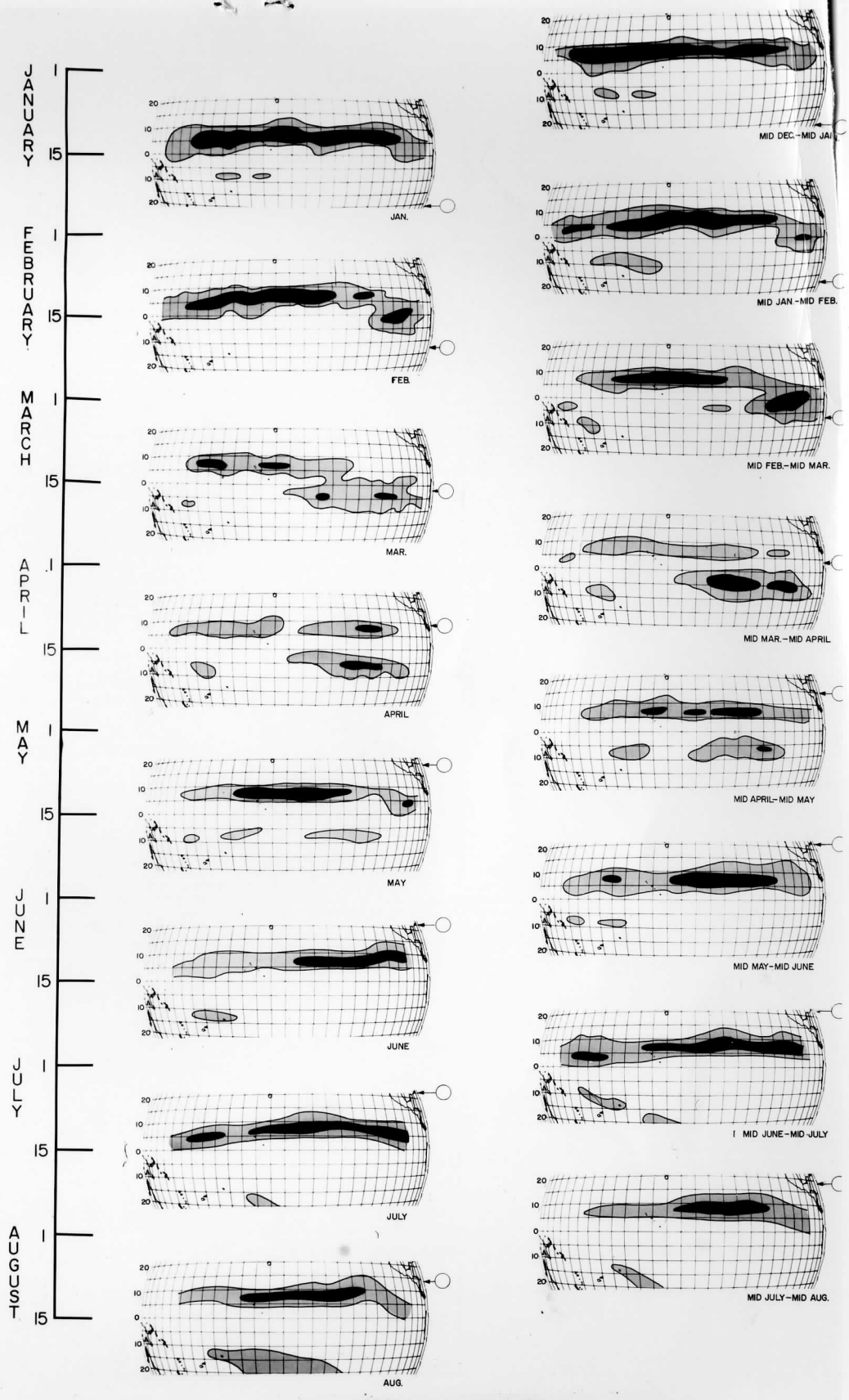
JANUARY
1
15
FEBRUARY
1
15
MARCH
1
15
APRIL
1
15
MAY
1
15
JUNE
1
15
JULY
1
15
AUGUST
1
15
JAN.
FEB.
MAR.
APRIL
MAY
JUNE
JULY
AUG.
MID DEC.-MID JAN.
MID JAN-MID FEB.
MID FEB.-MID MAR.
MID MAR.-MID APRIL
MID APRIL-MID MAY
MID MAY-MID JUNE
MID JUNE-MID JULY
MID JULY-MID AUG.
OCCURENCE OF BAND-TYPE CLOUDINESS
— < 20% OF TIME
— 20-40% OF TIME
— > 40% OF TIME

Fig. 2

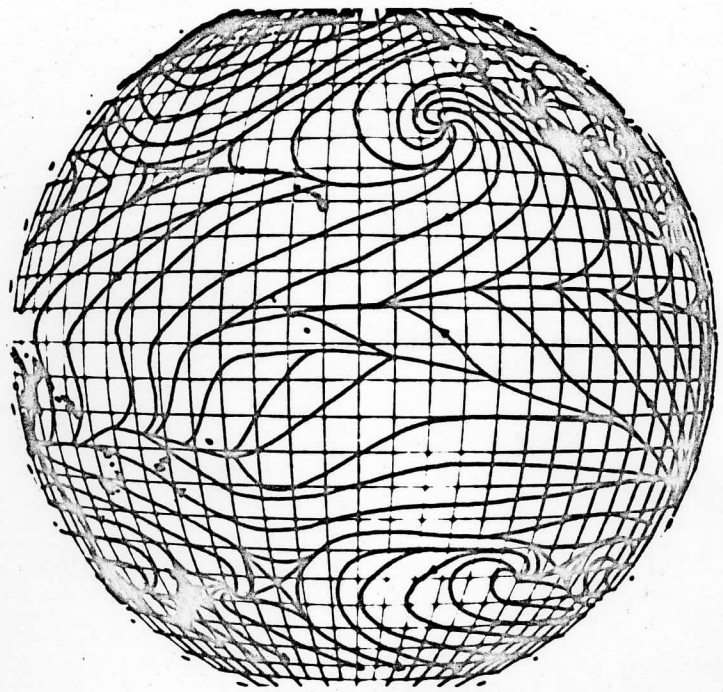

Jan. Surface Streamlines

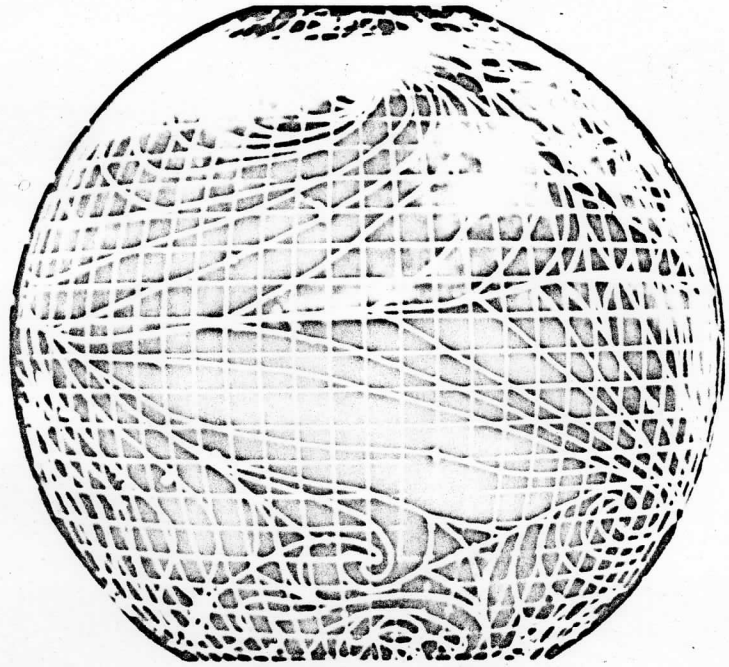

July Surface Streamlines

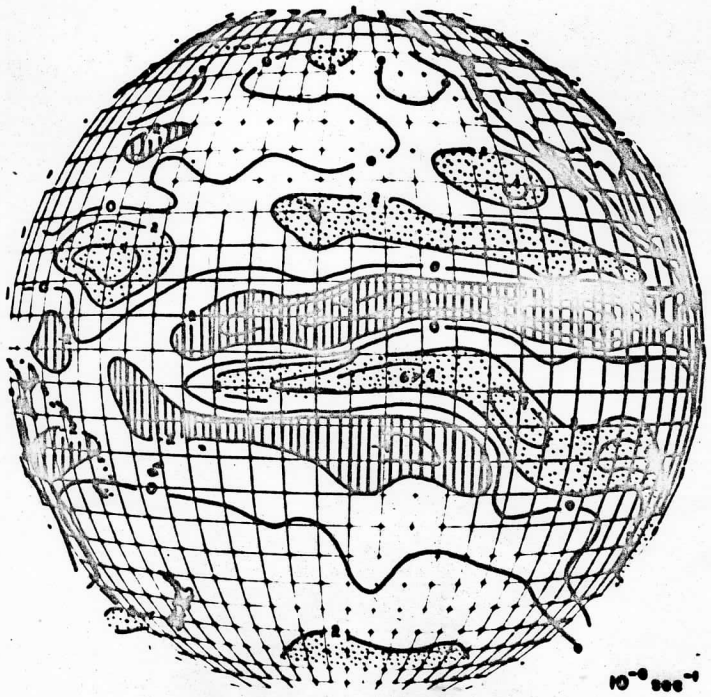

Jan. Surface Divergence

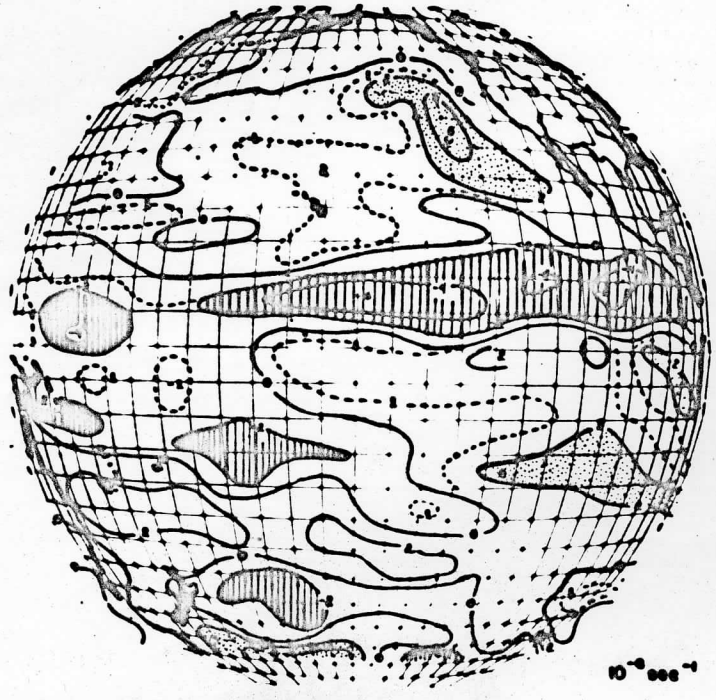

July Surface Divergence

Fig. 3

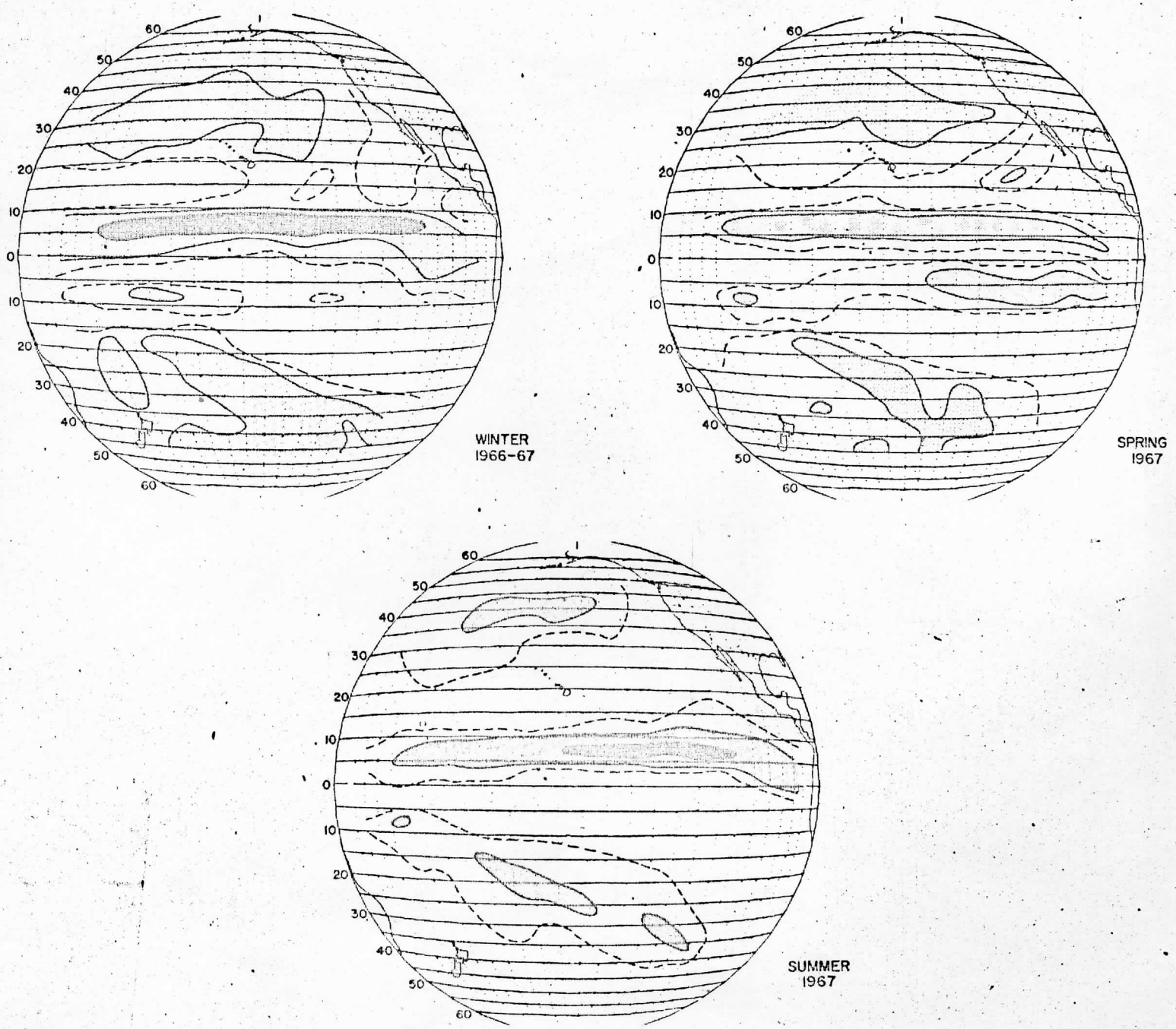

Fig. 4

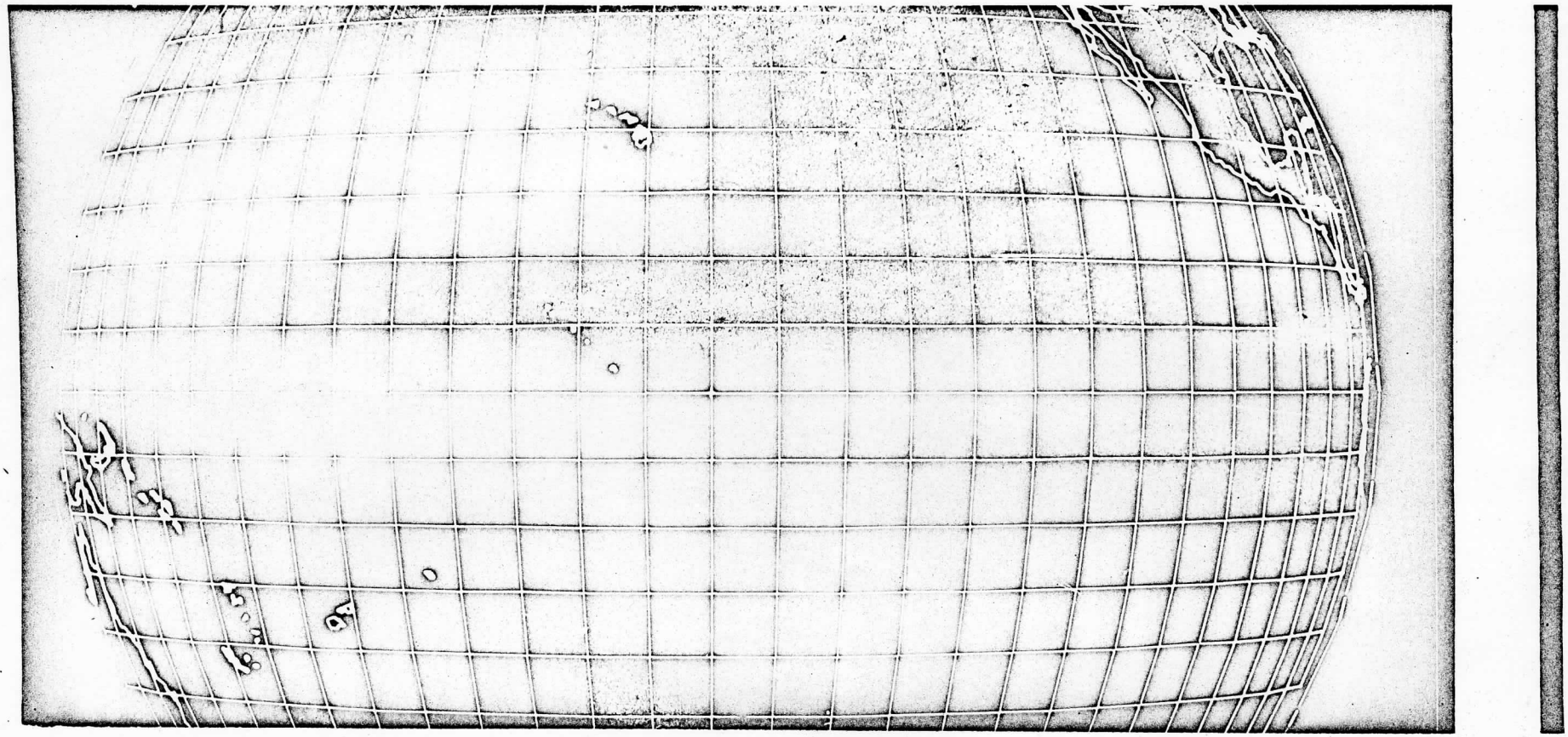

Fig. 5

(2)

THE INTERTROPICAL CONVERGENCE ZONE AND THE HADLEY CIRCULATION OF THE ATMOSPHERE

Jule G. Charney

Department of Meteorology
Massachusetts Institute of Technology
Cambridge, Massachusetts 02139

April, 1968

I. INTRODUCTION

In weather lore and in elementary textbooks the equator is pictured as wet. The view commonly held is that intense solar heating causes moisture-laden zonal rings of air at low levels to converge from both hemispheres towards the equator where they rise and release their moisture in copious quantities. We know that this picture is somewhat less than accurate, but just how inaccurate it is is revealed in a most striking manner by the spin-scan cloud photographs taken from the ATS-1 and ATS-3 synchronous satellites. The articles by Kornfield and Hasler (1968) and Kornfield and Hanson (1968) in this volume show that over the greater part of the tropical oceans convective activity is confined to narrow bands paralleling the equator but rarely crossing it. For example, over most of the Pacific the equator is in a clear, dry zone where the air is presumably sinking, not rising. This phenomenon is obscured in analyses of mean meridional circulations near the equator because of averaging with wet regions or because of lack of oceanic data. Thus Bjerknes and Venkateswaran (1957) find ascending air at the equator in winter, and Palmén (1964) finds ascending air in both winter and summer. However, in each case, the maximum ascent takes place away from the equator. Figure 1, taken from the former article, and Figures 2 and 3 from the latter, show a broad region of ascent rising to a maximum between 3 and 4°N in winter and 6 and 7°N in summer. These positions compare well with the observed mean cloud band structures over the Pacific given by Kornfield and Hanson (Figure 4 in their article).

The slightly more northward position of the bands in winter is probably due to inclusion in the averaging process of continental-monsoonal regions where a good deal of equatorial cloudiness and rainfall does occur.

Kornfield and Hanson point out that the convective cloud bands coincide with the so-called Intertropical Convergence Zone (ITCZ), the region of horizontal convergence in the Trades. This zone, in turn, is coincident, or nearly so, with the equatorial trough zone which has been established by Riehl and Malkus (1958) as the primary supplier of heat energy for the tropical circulation. Thus the bands are not mere curiosities; they are essential elements of the tropical circulation; and if one is to truly understand the circulation of the atmosphere, the following questions, directly posed by the satellite pictures, must be answered:

1. What determines the location of the cloud-convection zone away from the equator and why are there sometimes two such zones on opposite sides of the equator?
2. Why is there an associated equatorial dry zone?
3. Why is the cloud-convection zone so narrow, averaging less than five degrees of latitude in width?

These questions have occupied me from time to time in a study of tropical circulations I began some ten years ago. Indeed the first ATS-1 picture of the Pacific was released in the Boston Globe newspaper on December 11, 1966 while I was lecturing to my class at M.I.T. on a

theory I had recently published for the formation of the ITCZ (Charney 1966). I had been showing how the theory predicted that a zonally symmetric disturbance of a conditionally unstable atmosphere could, by an instability process involving cooperation between the cumulus clouds and the large-scale disturbance, give rise to two narrow regions of rapidly ascending motion more or less symmetrically placed about the equator, and that, for dynamical reasons connected with the Coriolis control of the meridional mass transport in the planetary boundary layer, these zones would not coincide with the equator. The ATS-1 picture showed two zones, a distinct one at about 6 or 7°N and a more diffuse one at about the same distance south. My calculations placed the zones at approximately 10° north and south. This qualitative agreement encouraged me to extend the theory to the problem of maintenance as well as generation of the ITCZ by completing some finite-amplitude calculations I had already begun. These calculations confirmed the stability analyses in some but not all respects. For example, a surprising degeneracy was discovered whereby the position and intensity of the steady-state ITCZ circulation depended not only on the physical parameters and external boundary conditions but also on how the circulation was started. Since the calculations clearly bring out the importance of the ITCZ in maintaining the temperature and wind structure of the entire region of the tropics and subtropics, and since the theory is directly relevant to an explanation of the cloud patterns observed from the ATS satellites, it will be presented here in outline form.

II. THE PHYSICAL MODEL

The principal idea of the theory is that organized cumulus convection is controlled through frictionally induced convergence of moisture in what is called the planetary boundary layer or the Ekman layer of the atmosphere. Roughly speaking, the vertical pumping of mass, and therefore of moisture, out of this layer is proportional to the vorticity of the surface geostrophic wind. Since the air at low levels holds the bulk of the moisture and has the greatest potential buoyancy for moist-adiabatic ascent in a conditionally unstable tropical atmosphere, cumulus convection and release of heat of condensation is largely determined by this vertical pumping and its associated boundary-layer convergence.* A local increase of vorticity in a zonally symmetric flow will give rise to the following sequence of events: (1) increased vertical flux of moisture, (2) increased cumulus convection with release of heat of condensation, (3) a temperature rise, (4) an accelerative pressure-density solenoidal field, (5) increased low-level convergence, (6) a bringing of high angular momentum air from the equatorward side of the disturbance into juxtaposition with low angular momentum air from the poleward side, (7) a still greater increase of positive vorticity. This is essentially the instability mechanism which would produce an ITCZ if one did not exist, or would maintain an ITCZ if it

---

*That the meridional transport of mass does in fact take place primarily in the planetary boundary layer is brought out in Figure 1 and also in Figure 4, taken from the article by Palmén (1964).

already existed. The same general process has been used to explain the formation of other synoptic scale circulations driven by heat of condensation. Thus Charney and Eliassen (1964) have used it to explain the formation of the pre-hurricane tropical depression, and Ooyama (1964) has used it to explain the formation and maintenance of the hurricane itself.

In all that follows it will be assumed that the model flow is zonally symmetric. This assumption is justified by the evidence presented by Bjerknes and Venkateswaran and by Palmén that the meridional transports of heat and angular momentum are dominated by the symmetric components of the flow at low latitudes. Additional evidence of this kind has been provided by a former student, ~~of mine,~~ Paul Janota, in an unpublished work. Using data gathered in the equatorial western North Pacific for May, 1956, he showed that the zonal pressure forces and the gradients of the zonal Reynolds stresses were small in comparison with the convective accelerations associated with the symmetric components of the flow. Finally, van de Boogaard (1964) has compared the meridional transports of water vapor by the symmetric component of the flow and by the eddies and has shown that the symmetric flow dominates from the equator to about 20°N.

Yet it is not the purpose of this article to prove that the flow must be symmetric, for one cannot escape the asymmetries due to the land-ocean distribution. It is rather to show that a tropical circulation of planetary scale in longitude must develop a narrow ITCZ

whose location, controlled largely by Coriolis effects, is at a small but finite distance from the equator and whose dynamics is essentially that of a circular vortex. This distance may vary slowly with longitude, and asymmetries may cause intensification or diminution of the ITCZ, but the overall effect is to produce a "Hadley" circulation in which the symmetric components of the flow dominate.

III. STABILITY ANALYSIS

The detailed stability analysis need not be given here. It is similar to that for the axially symmetric tropical depression presented in Charney and Eliassen (loc. cit.), the principal difference being that axial symmetry is replaced by line symmetry. The analysis depends critically on the calculation of the vertical mass flux from the Ekman layer, which, since it is also used in the finite-amplitude calculations, will not be given.

For lack of a complete theory of the surface Ekman layer, especially at low latitudes, the following semi-empirical approach is adopted. We assume that the time-scale of adjustment in the boundary layer is small in comparison to that of the flow under consideration, or else recognize that we are aiming at a steady-state theory; then the zonal momentum equation for the boundary layer on a sphere may be approximated by

$$-f\rho_s v = \tau_z \quad , \tag{1}$$

where ρ is the density, v is the meridional velocity component, $f = 2\Omega\sin\phi$ is the Coriolis parameter, τ is the zonal stress component, and the subscript "s" denotes a standard mean value dependent only on z. Integration of the above equation and the continuity equation

$$\frac{(\rho_s v \cos\phi)_\phi}{a\cos\phi} + (\rho_s w)_z = 0 \tag{2}$$

through the boundary layer then gives

$$(3) \qquad -fB = \tau_\ell - \tau_o \simeq -\tau_o \quad ,$$

and

$$(4) \qquad \frac{(B\cos\phi)_\phi}{a\cos\phi} + \rho_{s\ell} w_\ell = 0 \quad ,$$

where a is the radius of the earth, w is the vertical velocity component, τ_o is the zonal surface stress, $B = \int \rho_s v dz$ is the meridional mass transport in the boundary layer, and the subscripts "ℓ" denote quantities at the top of the boundary layer. In Ekman's theory, as modified by Taylor, it is assumed that the surface wind and surface stress are parallel, that the kinematic eddy coefficient of viscosity ν_e is constant, and that the surface wind makes an angle α with the surface geostrophic wind. We then find that

$$(5) \qquad \tau_o = (\nu_e \Omega \sin\phi)^{\frac{1}{2}} \rho_{so} u_{go} \sin 2\alpha \quad .$$

where u_{go} is the surface geostrophic zonal velocity component. In this theory the depth of the Ekman layer $D_E = (\nu_e/\Omega\sin\phi)^{\frac{1}{2}}$ becomes infinite as the latitude tends toward zero, and (5) becomes invalid. We therefore use instead the empirical relationship

$$(6) \qquad \tau_o = C_D \rho_{so} |u_{go}| u_{go}$$

in which C_D is the drag coefficient.

In performing the stability analysis one anticipates that the ITCZ will be a very narrow region, so that the physical parameters and the latitude may be assumed to vary only parametrically. Setting the dynamical variables proportional to $e^{\sigma t}$, one obtains the graph in Figure 5 showing the growth rate σ as a function of the width $\underline{b}$ of the convection zone. This width is plotted non-dimensionally as b/b_o, where b_o is the Rossby radius of deformation,

$$(7) \qquad b_o^2 = \frac{RT_{s2}}{f^2} \Delta \ell n \theta_s \quad .$$

Here R is the specific gas constant, T_{s2} the undisturbed mid-atmosphere temperature, and $\Delta\theta_s$ a vertical increment of the undisturbed potential temperature θ_s.

The growth rate is also plotted non-dimensionally as σ/σ_o, where σ_o is a frequency derived from the assumed character of the boundary layer. If the atmosphere is at rest, and the boundary layer is treated as an Ekman-Taylor layer, one obtains

$$(8) \qquad \frac{\sigma_o}{f} = \frac{D_E}{H} \sin 2\alpha \quad ,$$

where H is the mean scale-height RT_{s2}/g. If, on the other hand, a trade wind u_g has already been established and the more realistic determination, (3), (4) and (6), of the boundary layer pumping is used, one finds

that

$$\frac{\sigma_o}{f} = \frac{C_D|u_{go}|}{fH} \quad . \tag{9}$$

The conditional instability of the atmosphere is expressed by the parameter

$$\kappa = 1 - \frac{\Delta \ell n \theta_{es}}{\Delta \ell n \theta_s} \ ,$$

where $\Delta\theta_{es}$ represents the vertical increment in the mean equivalent potential temperature associated with the increment $\Delta\theta_s$. If the atmosphere is conditionally unstable, κ is greater than unity. In Figure 5 it is assumed that $\kappa = 1.1$, corresponding to a lapse rate of equivalent potential temperature of about 1°C per km, and also that $\alpha = 15°$.

The lower abscissa in Figure 5 is the dimensional width b for a latitude of 7.5°. We see that the growth rate remains nearly constant for b/b_o less than about 0.1, or b less than about 200 km, and then decreases rapidly. A width of this order is also obtained in the finite-amplitude, steady-state calculations. Zonal disturbances with greater width are stabilized by the earth's rotation; thus we see from (7) that an increase in latitude, and therefore of f, causes a decrease in the radius of deformation and, for a given κ, a decrease in the width of the ITCZ. It is difficult to compare the predicted with

the observed widths as revealed by satellite photographs because the region of active cumulonimbus convection is obscured by the cirrus shields spreading out from the Cb tops, but judging from brightness values and aircraft reports, a width of the order of ~~or~~ 300 km ~~200/km~~ would appear to be reasonable.

The maximum growth rate for a given latitude is found to be

$$\sigma_m = \frac{\frac{3}{2}\mu\kappa - 1}{1 - \mu\kappa}\sigma_o \quad , \tag{10}$$

where μ is the relative humidity and it is assumed that moisture may flow into a column at all elevations. If only the moisture flux from the boundary layer is considered, the maximum growth rate is

$$\sigma_m = (\kappa \frac{q_\ell}{\Delta q_s} - 1)\sigma_o \quad , \tag{11}$$

where q is the specific humidity and Δq_s is the vertical increment in q_s corresponding to $\Delta\theta_s$. In the Ekman-Taylor theory σ_o increases as $(\sin\phi)^{\frac{1}{2}}$, whereas the factor involving κ in the expression for σ_m decreases with κ and hence with latitude. Thus σ_m will have its maximum at some mid-latitude. The solid curve in Figure 6, showing σ_m as a function of latitude, is calculated from (10) for ~~with~~ μ = 75 percent, and is based upon the observed yearly average variation of κ with latitude in the Northern Hemisphere. We see that the maximum occurs at 15°N.

If the expression (9) for σ_o, together with the observed mean zonal surface geostrophic wind profile, is used instead of (8), one obtains the dashed curve in Figure 6. The maximum of σ_m is now at about 9°, and is closer to the mean position of the ITCZ in the cloud band pictures, but is still too far north. However, at this point it is unreasonable to expect any better agreement, since one cannot strictly apply stability considerations to wind profiles and temperature lapse-rates which have already been modified by the ITCZ circulation. It is perhaps more meaningful to calculate the dry Hadley circulation and study its stability for moist motions. This has been done, and with similar results; the ITCZ occurs at about 10°. For further progress one must proceed to a finite-amplitude theory in which stationary circulations may occur.

IV. THE MATHEMATICAL MODEL

For reasons given in the articles by Charney and Eliassen (1964) and Charney (1966) one may treat the flow as balanced. An approximate, energetically-consistent, set of momentum equations for such a flow is

$$u_t + \frac{v(u\cos\phi)_\phi}{a} + wu_z - fv \simeq \frac{\tau_z}{\rho_s},$$

$$fu + \frac{u^2\tan\phi}{a} \simeq \psi_\phi, \tag{12}$$

$$g(\ell n\theta - \ell n\theta_s) \simeq \psi_z,$$

where $\psi = (p - p_s)/\rho_s$. The corresponding energetically consistent statement of the first law of thermodynamics is

$$\psi_{zt} + w N_s^2 \simeq \frac{gQ}{c_p T_s}, \tag{13}$$

where Q is the rate of accession of heat per unit mass.

The principal approximations involved are the substitution of the gradient wind equation for the meridional momentum equation and the ignoring of the horizontal advection of entropy and the horizontal variation of static stability in the thermal equation. These approximations can be justified by scale analysis.

It is not sufficiently well-understood how moisture injected into a unit vertical column from the boundary layer and from its sides is converted to heat of condensation by cumulus convection, nor how this heat is distributed vertically. This is a major unsolved problem whose solution will require more observational study. We bypass it here at the expense of truncation error by treating a two-level model atmosphere in which only the integrated heating is required, and by assuming, with Ooyama (1964), that the flux of moisture into the sides of the column may be ignored altogether. The boundary layer character of the flow is taken into account explicitly only in the calculations of the vertical flux of moisture from the boundary layer.

The momentum, continuity and thermal equations are written in divergence form, and vertical derivatives are expressed as derivatives in the standard pressure $p_s(z)$ corresponding hydrostatically to the standard density $\rho_s(z)$. The standard surface pressure is 1000 mb, and the atmosphere is divided into quarters at the levels 0, 1, 2, 3 and 4 by the pressures 1000, 750, 500, 250 and 0 mb respectively. To obtain the two-level equations, one replaces vertical derivatives at levels 1, 2 and 3 by finite differences between levels 0 and 2, 1 and 3, and 2 and 4 respectively. Quantities at the level i are denoted by the subscript "i".

The heating function is divided into two parts. In view of the assumptions made, the part due to condensation may be written

$$Q_{2C} = \frac{g}{p_{s2}} \rho_{s\ell} w_\ell L q_{s\ell} \quad , \tag{14}$$

where L is the latent heat of condensation. In this expression the vertical mass flux $\rho_{s\ell} w_\ell$ is calculated from equations (3), (4) and (6). In the Ekman-Taylor theory the boundary layer depth behaves like $(\sin\phi)^{-\frac{1}{2}}$; in more sophisticated treatments (cf. Blackadar, 1962) it behaves like $(\sin\phi)^{-1}$, but neither of these treatments is valid at latitudes for which the Rossby number is no longer small. Obviously more observational and theoretical work is needed before an adequate theory can be formulated. For the present, we note that the dashed curve in Fig. 4, representing a $(\sin\phi)^{-\frac{1}{2}}$ variation, bounds the region of strong meridional transport reasonably well. This means that as the equator is approached the humidity, $q_{s\ell}$, which is injected vertically into the ITCZ comes from increasingly higher levels where it is increasingly smaller. If we assume a linear decrease of $q_{s\ell}$ with height (the decrease is actually more exponential) and a $(\sin\phi)^{-\frac{1}{2}}$ variation of the height of the boundary layer, we must multiply (14) by $(\sin\phi/\sin\phi_o)^{\frac{1}{2}}$, where $q_{s\ell}$ is normalized at the latitude ϕ_o. We may then continue the expression (3) for B all the way to the equator providing τ approaches zero with sufficient rapidity. This latter condition is insured in our model by equatorial symmetry and the absence of lateral viscosity.

In the vicinity of the ITCZ considerable evaporation must occur. The horizontal divergence of the Ekman transport of moisture does not by itself account for the mean precipitation. We must assume a continuity equation for moisture in the boundary layer which allows for surface evaporation. Since the effect of evaporation is to increase the humidity

of the air which is advected horizontally, we allow for it simply by increasing the specific humidity in the expression for the heating by condensation.

The second part of the heating function is due to long and short wave radiative exchange. Direct solar heating is small: the earth's atmosphere essentially looks down upon a warm ocean whose temperature $T_o(\phi)$ may be regarded as fixed on the time-scale of the development of an ITCZ circulation. In the present model this temperature is assumed to vary only with latitude. Since only the mean heating throughout an entire atmospheric column is needed, we may, for radiative purposes, regard the atmosphere as an isothermal "black" or "grey" body. Linearization of the Boltzman fourth-power law then gives a kind of Newtonian conduction according to which the heating is proportional to the difference between the actual mid-level temperature T_2 and a radiative equilibrium temperature $T_2^*(\phi)$ determined from the sea-surface temperature, i.e.,

$$T_2^*(\phi) = (2k)^{-\frac{1}{4}} T_o(\phi) \quad , \tag{14}$$

where k (≤ 1) is the coefficient of "grey" absorption of the atmosphere.

The foregoing approximations permit the thermal equation (13) to be written

$$(\psi_3 - \psi_1)_t + g' w_2 = g' \pi w_\ell + k_r[(\psi_3 - \psi_1)^* - (\psi_3 - \psi_1)] \quad , \tag{15}$$

where

$$(\psi_3 - \psi_1)^* = R(T_2^* - T_{s2}) \quad , \tag{16}$$

$$k_r = \frac{4R\sigma\, T_{s0}^4}{C_p \rho_{s0} g H^2} \simeq \frac{1}{14 \text{ days}} \quad , \tag{17}$$

$$\eta = \frac{Lq_{s\ell}}{C_p T_{s2} \Delta \ell n \theta_s} \simeq 1.4 \quad , \tag{18}$$

and σ is here the Boltzmann constant.

The circulation depends critically on the quantity η which relates the release of heat of condensation to the vertical mass flow from the boundary layer. This quantity cannot remain constant because heating by condensation causes (1) an increase in static stability and therefore a reduction in η, and (2) a stabilization of the atmosphere until finally no deep moist convection is possible. We express this constraint by multiplying η with the factor $[1 + \exp(\frac{T_2 - \bar{T}_2}{\Delta T})]^{-1}$, in which $\bar{T}_2$ represents the mid-level temperature corresponding to a moist-adiabatic lapse-rate between the sea-surface and level 2 at low latitudes, and ΔT is a small increment in temperature of the order of 2 or 3°C. This factor has the property that it is nearly unity for $T_2 < \bar{T}_2$ and nearly zero for $T_2 > \bar{T}_2$ but varies continuously between these limits. Another multiplicative factor, $[1 + \exp(\frac{\sin\phi - \sin\phi_o}{\Delta \sin\phi})]^{-1}$, allows for the variation of η with latitude — from nearly unity at $\phi < \phi_o$ to nearly zero

at $\phi > \phi_o$. Finally, to avoid the truncation error associated with a discontinuity in the heating function, we introduce a third multiplicative factor $[1 + \exp(-\frac{w_\ell}{\Delta w})]^{-1}$ in which Δw is a positive quantity which is small compared with the average value of $|w_\ell|$. This factor is nearly unity for positive w and nearly zero for negative w. Thus we have

$$\eta = \eta_o \left[(1 + e^{\frac{T_2 - \bar{T}_2}{\Delta T}})(1 + e^{\frac{\sin\phi - \sin\phi_o}{\Delta \sin\phi}})(1 + e^{-\frac{w_\ell}{\Delta w}}) \right]^{-1}, \tag{34}$$

which completes the specification of the heating.

A more general model containing finite-amplitude sinusoidal wave disturbances has been constructed. The waves are permitted to interact with the mean flow but not with themselves; they therefore contribute to the transport of heat and angular momentum while retaining their sinusoidal shape. Preliminary calculations with this model indicate that there is a significant interaction between the tropical Hadley regime and the mid-latitude Rossby (wave) regime but that the qualitative behavior of the Hadley circulation is not altered. A report on these calculations will be published elsewhere.

The general character of a symmetric circulation on a rotating sphere driven by differential heating is brought out by the analysis of the flow in simplified type models. Such an analysis has been carried out for an incompressible Boussinesq fluid with a free surface* which is heated differentially from below and cooled differentially from above

*The free surface is intended to simulate the effect of the stable stratosphere in reducing the eddy stress to zero, so that, in effect, there is a boundary layer at the tropopause, similar to that at a free surface, in which the stress, not the velocity, must go to zero.

To replace old page -19-

by conduction. Let U be a characteristic thermal wind and h the depth of the fluid. We define the Rossby number by $Ro = U/2\Omega a$ and the Ekman number by $E = \nu_e/2\Omega h^2$. It is assumed that $Ro = O(E^{\frac{1}{2}}) < O(1)$, as in the atmosphere, and that the ratio of the kinematic coefficient of viscosity to thermometric conductivity is order unity. The results of the analysis may be summarized as follows: The interior flow is zonal and geostrophic to order E, and the temperature is in conductive equilibrium to order $E^{\frac{1}{2}}$. The horizontal temperature gradient produced in the interior of the fluid by conduction from the boundaries gives rise to a non-vanishing vertical gradient of the zonal wind. Since the condition of zero stress at the upper free surface requires that this gradient by zero, a kind of Ekman layer arises in which there is an order E mass transport poleward. Since the interior transport vanishes to a higher order in the Ekman number, the Ekman layer at the lower rigid boundary adjusts itself to produce an equal equatorial mass transport. The upper and lower Ekman layers are divergent, and, except near the equator, there is a downward pumping of mass directly from one to the other which convects temperature and causes it to deviate from conductive equilibrium. The above properties appear to be in qualitative agreement with the analyses of the actual Hadley circulation of the atmosphere presented by Bjerknes and Venkateswaran and by Palmén, especially in winter.

In the present model the boundary-layer character of the flow is explicitly taken into account only in computing the heating by condensation. The nature of the truncation error caused by ignoring the boundary layer in

To replace old page -19a-

the momentum equation may be estimated by comparing the analytic solution for the above type model with the finite-difference numerical solution. It is found that the temperature at the mid level, and therefore also the wind difference between levels 1 and 3, is exact to zero order in E, but that the zero order zonal velocities are 25% too large at the upper level and 100% too large at the lower level.

V. RESULTS OF INTEGRATIONS

A large number of integrations have been performed with a thermal driving $T_2^*(\phi)$ symmetric about the equator. The driving and the initial conditions were varied, as were the parameters $\Delta\ell n\theta_s$, ν_e, C_D, k_r, η_o, $\overline{T}_2$ and ϕ_o, the first four specifying static stability, internal friction, surface friction and radiative exchange, respectively, and the last three condensational heating. The following general conclusions have been drawn from the results:

(a) The effect of condensation, while always present, manifests itself as an instability. When η_o is below a certain critical value (which varies with the other parameters but is roughly between 1 and 4) condensation has only a small effect, but when this threshold value is exceeded the effect becomes very large and decisively influences the entire circulation well into middle latitudes. The breakthrough occurs when the heating due to condensation in the ITCZ overcomes the cooling due to adiabatic expansion. In this sense the instability is analogous to conditional instability associated with small-scale cumulus convection, but here the dynamics are very different, since the instability pertains to large-scale, balanced flows, not to free convection, and for this reason Eliassen and the author (loc. cit.) have called it conditional instability of the second kind.

(b) The steady-state flow with strong condensation appears to be degenerate: several different steady states may be produced with the

same thermal driving and the same physical parameters by varying the initial conditions. The steady-state flow without condensation or with weak condensation does not appear to be degenerate.

(c) When η_0 is near its threshold value, both the strong and weak stationary condensational states can be produced with the same driving and the same parameters by varying initial conditions.

(d) By varying the initial conditions, an ITCZ can be produced at almost any location between the equator and about 15°, but never at the equator.

(e) The width of the ITCZ is of the order of 300 km or less in the model.

(f) There is some evidence that with condensation there can be a symmetric circulation which does not approach a steady or periodic state.

Insert e/1

(g) A small increase in the sea-surface temperature at a given latitude will influence the position and structure of the ITCZ, not so much because of the change in static stability but because of the large induced change in the thermal wind and the consequent increased transport of relative momentum, increased shear in the easterlies, and increased convergence in the boundary-layer moisture transport. 1/

Several examples of calculated circulations will now be presented. The radiative equilibrium temperature is assumed to be of the form

INSERT TO PAGE -21-

(g) The thermal balance in the narrow ITCZ is essentially between heating by condensation and cooling by adiabatic expansion in rising air. The radiative vooling is a small residual and could actually be ignored entirely.

(h) The absence of an ITCZ at the equator is directly associated with the absence of any boundary-layer pumping of moisture and therefore of condensation. Since the temperature is essentially that of the ITCZ, it is higher than the radiative equilibrium value, and sinking motion must take place to compensate for the radiative cooling.

$$T_2^*(\phi) = T_2^*(0) - T_m \sin^2\phi$$

where, in all that follows, $T_2^* = 0°C$ and $T_m = 66°C$. Since this thermal driving leads to a circulation which is symmetric about the equator, the circulation need only be calculated for a single hemisphere, and, of course, there will be two ITCZ's, one on either side of the equator. / The physical parameters are given the following values:

$$\Delta \ell n \theta_s = 0.11$$

$$H = RT_2/g = 7.75 \times 10^5 \text{cm}$$

$$\nu_e = 2.8 \times 10^5 \text{cm}^2\text{sec}^{-1}$$

$$C_D = 1.2 \times 10^{-3}$$

$$k_r = 0.47 \times 10^{-6} \text{sec}^{-1}$$

$$\bar{T}_2 = 10°C$$

$$\Delta T = 3°C$$

$$\Delta \sin\phi = 0.1$$

$$\Delta w = 0.03 \text{ cm sec}^{-1}$$

The curves in Figures 7, 8 and 9 show the zonal velocities, vertical velocities and temperatures, respectively, for the steady state circulation which is approached when the time-variable equations are integrated from an initial state of relative rest. The solid curves are for $\eta_o = 2.0$, the dashed curves for $\eta_o = 1.7$, and the dotted curves for the dry case, $\eta_o = 0$. The dash-dotted curve in Figure 9 represents the radiative equilibrium temperature $T_2^*(\phi)$. We note that there is a striking

difference between the two moist models. A small change of η_o brings about a radical change in the final circulation. Thus it is seen that the weak moist circulation resembles much more the dry than the strong moist circulation and that the strong circulation produces large temperature and zonal velocity increases that extend well into middle latitudes. It may be inferred from these computations that the temperature in the tropics and subtropics is maintained well above radiative equilibrium (essentially at a level corresponding to the saturated adiabatic lapse-rate) by the condensation occurring in the narrow ITCZ, and not, as has sometimes been supposed, by sporadic moist-convection occurring everywhere. Thus the high temperatures in the subtropics are due to a combination of the anchoring of the temperature in the region of the ITCZ and the dynamical control of its horizontal variation by the transport of the earth's momentum and the thermal wind constraint. The heat budget is, of course, a radiative loss balanced by an advective gain.

The absence of an ITCZ at the equator is directly associated with the absence of any boundary-layer pumping of moisture. Since the temperature is essentially that of the ITCZ, it is higher than the radiative equilibrium value, and sinking motion must take place to compensate for the radiative cooling.

Figures 10, 11 and 12 show the nature of the degeneracy for $\eta_o = 4$. The circulation represented in Figure 10 by a peak in w_2 at 4.5° was started from rest; those showing peaks at 10° and 13° were started from a steady, dry circulation in which u_1 and u_3 were given

negative perturbations at grid points coinciding with $\phi = 11.5°$ and $14.5°$, respectively. In each case the initial conditions determined the final steady state. The values of u at the lower level are shown in Figure 11. The strong cyclonic shear occurring just where w_2 is a maximum indicates that the vertical velocity is forced by the Ekman transport. The vertical velocities and temperatures shown in Figure 12 represent two different steady states, a strong and a weak moist circulation, occurring for the same physical parameters and thermal driving but for different initial conditions. The weak circulation was started from rest and the strong from an already developed circulation. In this particular case the linear expression for the Ekman transport, corresponding to equations (10) and (11), was used.

Many other numerical experiments similar to the preceding were performed. In some experiments a perturbation in T_2^*, corresponding to a perturbation in sea-surface temperature, was inserted. The effect was always appreciable, even for changes of sea-surface temperature of less than 0.5°C, and usually led to the formation of an ITCZ near the perturbation. If an ITCZ was already in existence, the effect was sometimes to create a second ITCZ. More experimentation with varied parameters will have to be performed before the nature of the sea-surface temperature influence can be precisely characterized. There is no doubt, however, that it exerts a strong control. A horizontal temperature gradient of 0.5°C per 1000 km will correspond to $u_3 - u_1 = 6$ m/sec at 10° latitude and $u_3 - u_1 = 12$ m/sec at 5° latitude, and it

may be seen from Figure 7 that these winds are considerably larger than those produced by the undisturbed strong moist circulation itself.

A rather coarse mesh size was used for most of the calculations, corresponding to about 300 km at low latitudes, but in some calculations this interval was reduced to ~~150~~ 60 km. The truncation error did not appear to affect the results greatly except for the width of the ITCZ itself. In most instances the width was one grid interval, but in some integrations with the smaller grid it was three grid intervals. It is not known yet whether a natural lower limit can be obtained in the present model without the introduction of horizontal viscosity or other effects.

What, it may be asked, would happen if, in the actual atmosphere, η_o were such that only the weak circulation could form? We see from Figure 9 that the temperature T_2 would ~~fall~~ be below radiative equilibrium and produce a statically unstable lapse-rate. But such a condition would be incompatible with the present model which presupposes a stable lapse-rate. An essential element lacking in ~~the~~ this model is a realistic coupling of the vertical temperature stratification with the motion, but in any case it is quite meaningless to try to imagine what the atmosphere was like before an organized circulation existed. If, in an organized circulation, η_o were to fall below its critical value, the air would cool radiatively until the static stablity fell low enough to bring η_o back up to the critical value. Hence, it would seem that the actual atmosphere is always in a state of conditional instability of the second kind, i.e., in a state of supercritical η_o.

One ~~would~~ can think that regional asymmetries, such as the effect of low-level divergence in the south-east quadrant of a semi-permanent oceanic high and low-level convergence in the south-west quadrant, would produce an asymmetry in the intensity of the ITCZ circulation. Thus the increase of static stability and decrease in the depth of the moist layer in the former region and the reverse in the latter would probably contribute to an increasing intensity of the ITCZ from the eastern to the western side of the Pacific. Further increase in intensity ~~may~~ could result from the synoptic-scale instabilities in the region of strong horizontal shear of the low level winds adding to the overall release of heat of condensation in the western Pacific.

The fact that two ITCZ's on either side of the equator are sometimes found despite the asymmetries must be attributed to the Coriolis control of the Ekman pumping coupled with some degree of symmetry in the thermal driving. The presence of two ITCZ's in the Pacific has already been noted, but what is more surprising is the existence of two distinct trough systems on either side of the equator in the Indian Ocean region, even during the occurrence of strong monsoonal circulations (Raman, 1965).

The degeneracies and instabilities that have been found present a strong temptation to speculate on the stability and predictability of the general circulation of the atmosphere and its control by small perturbations in sea-surface temperature. However, this temptation must be resisted until more definite results are obtained. We remark only

that the present results seem to accord with the view expressed by J. Bjerknes (1966) that the Hadley circulation in the tropics is very sensitive to small variations in sea-surface temperature near the equator, but that the sensitivity seems to apply primarily to the position rather than to the intensity or degree of influence of the ITCZ on the circulation in subtropical and middle latitudes.

ACKNOWLEDGMENTS

This paper had its beginning in an attempt to give a simple explanation of the general circulation of the atmosphere to a group of students in applied mathematics and physics at Harvard University in the spring of 1966. I wish to thank Harvard University for supplying the occasion to work out my ideas, and also to give thanks to my own students John R. Bates and Peter Webster for numerous discussions, to Peter Webster, Robert Gamill and Diana Lees for programming and operating assistance, and to Jutta Thorne for her skill and patience in preparing the manuscript for publication. The work was supported by NSF grants G-18985 and GA-402X.

REFERENCES

Bjerknes, J., and S. V. Venkateswaran, 1957: A model of the general circulation of the tropics in winter. Article III, Final Report, Large-Scale Synoptic Processes, AF 19(604)-1288. Department of Meteorology, University of California, Los Angeles, California.

Bjerknes, J., 1966: A possible response of the atmospheric Hadley circulation to equatorial anomalies of ocean temperature. Tellus, 18, 820-828.

Blackadar, A. K., 1962: The vertical distribution of wind and turbulent exchange in a neutral atmosphere. J. Geophys. Res., 67, 3095-3102.

Boogaard, H. M. E. van de, 1964: A preliminary investigation of the daily meridional transfer of atmospheric water vapour between the Equator and 40°N. Tellus, 16, 43-54.

Charney, J. G., and A. Eliassen, 1964: On the growth of the hurricane depression. J. Atmos. Sci., 21, 68-75.

Charney, J. G., 1966: Some remaining problems in numerical weather prediction. Advances in Numerical Weather Prediction, 1965-66 Seminar Series, The Travelers Research Center, Inc. Hartford, Connecticut, 61-70.

Kornfield, J., and K. Hanson, 1968: On the double structure of cloud distribution in the equatorial Pacific. This volume.

Kornfield, J., and A. F. Hasler, 1968: Photographic cloud averages. This volume.

Ooyama, K., 1964: A dynamical model for the study of tropical cyclone development. Geofisica Internacional, 4, 187-198.

Palmén, E., 1964: General circulation of the tropics. Proceedings of the Symposium on Tropical Meteorology, 1-30. New Zealand Meteor. Service, Wellington, New Zealand.

Raman, C. R. V., 1965: Cyclonic vortices on either side of the equator and their implications. Symposium on Meteorological Results of the Indian Ocean Expedition, International Meteorological Center, Bombay, India.

Riehl, H., and J. S. Malkus, 1958: On the heat balance in the equatorial trough zone. Geophysica, 6, 503-535.

FIGURE LEGENDS

Figure 1. Mean meridional mass circulation in the Northern winter (after Bjerknes and Venkateswaran).

Figure 2. Mean meridional mass circulation in the Northern winter (after Palmén). The transport capacity of every tube is 25×10^6 tons per second.

Figure 3. Mean meridional mass circulation in the Northern summer (after Palmén). The transport capacity of every tube is 25×10^6 tons per second.

Figure 4. Mean meridional wind averaged for December - February in the Northern Hemisphere (after Palmén). Isotachs in meters per second. The dashed line corresponds to a $(\sin\phi)^{-\frac{1}{2}}$ variation.

Figure 5. The growth-rate σ as a function of the width b of the zone of moist convection.

Figure 6. The maximum growth rate σ_m as a function of latitude.

Figure 7. The zonal velocities u_1 and u_3 as a function of latitude. The solid, dashed and dotted curves correspond to η_o = 2.0, 1.7 and 0 respectively.

Figure 8. The vertical velocity w_2 as a function of latitude. The continuous, dashed and dotted curves correspond to η_o = 2.0, 1.7 and 0 respectively.

Figure 9. The temperature T_2 as a function of latitude. The continuous dashed and dotted curves correspond to η_o = 2.0, 1.7 and 0 respectively. The dash-dotted curve corresponds to pure radiation equilibrium.

Figure 10. The vertical velocities w_2 for the same boundary conditions, physical parameters and thermal driving but different initial conditions.

Figure 11. The zonal velocities u_3 corresponding to the vertical velocities in Figure 10.

Figure 12. Temperature and vertical velocity for the strong and weak moist circulations corresponding to the same external conditions and physical parameters but different initial conditions.

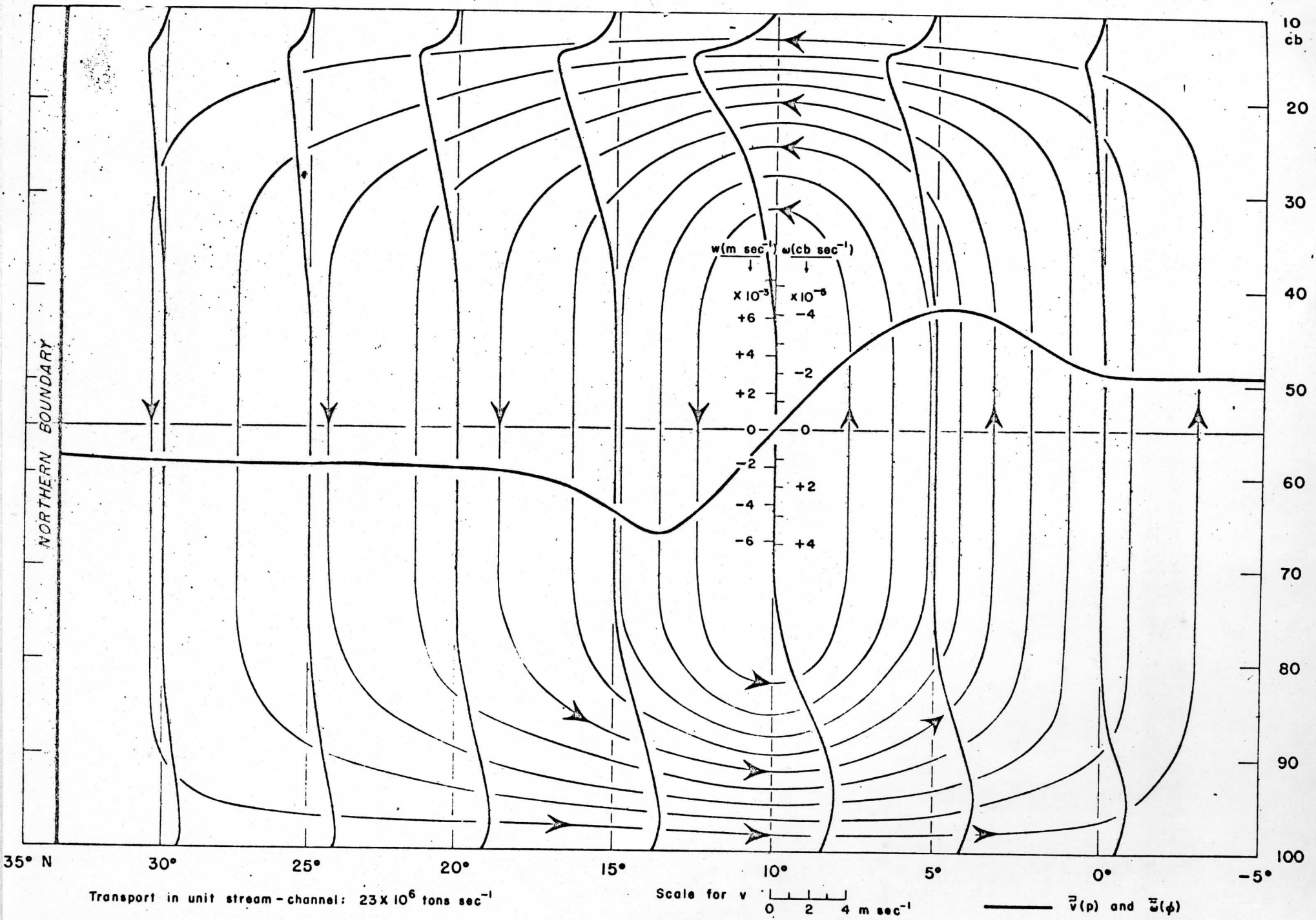
NORTHERN BOUNDARY
w(m sec⁻¹)
ω(cb sec⁻¹)
x 10⁻³
x 10⁻⁵
+6
+4
+2
0
−2
−4
−6
−4
−2
0
+2
+4
10 cb
20
30
40
50
60
70
80
90
100
35° N
30°
25°
20°
15°
10°
5°
0°
−5°
Transport in unit stream-channel: 23 X 10⁶ tons sec⁻¹
Scale for v
0 2 4 m sec⁻¹
v̄(p) and ω̄(φ)

FIGURE 1

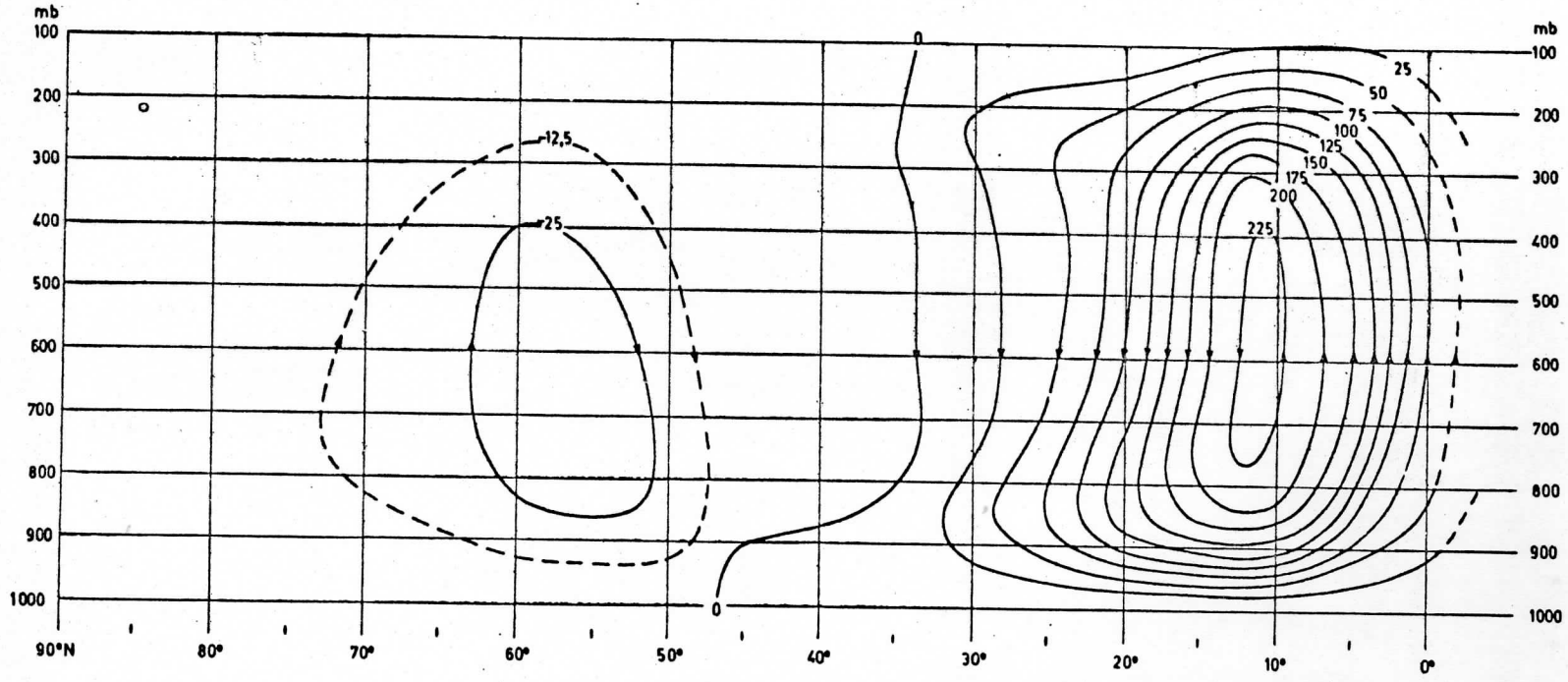
mb
100
200
300
400
500
600
700
800
900
1000
90°N
80°
70°
60°
50°
40°
30°
20°
10°
0°
0
12,5
25
0
25
50
75
100
125
150
175
200
225
0
mb
100
200
300
400
500
600
700
800
900
1000

FIGURE 2

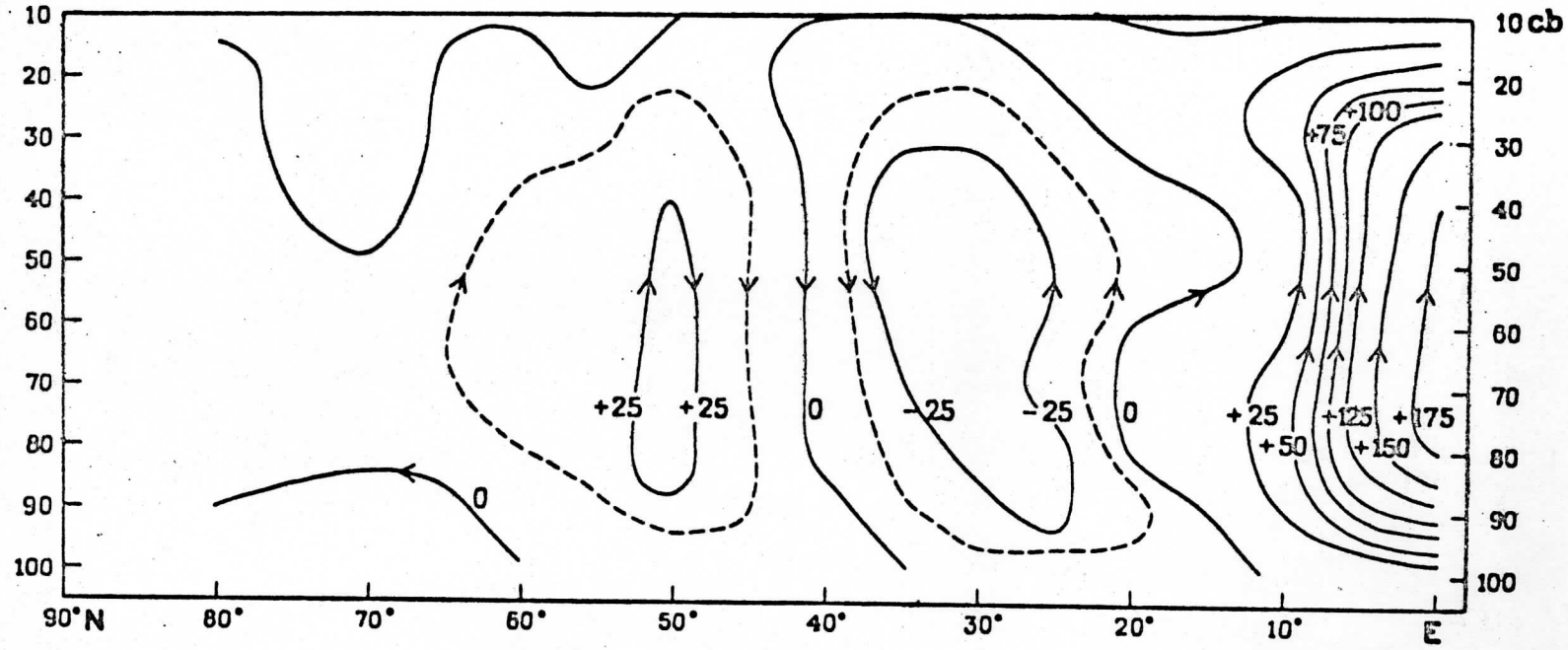
10
20
30
40
50
60
70
80
90
100
10 cb
20
30
40
50
60
70
80
90
100
+25
+25
0
-25
-25
0
+25
+50
+75
+100
+125
+150
+175
0
90°N
80°
70°
60°
50°
40°
30°
20°
10°
E

FIGURE 3

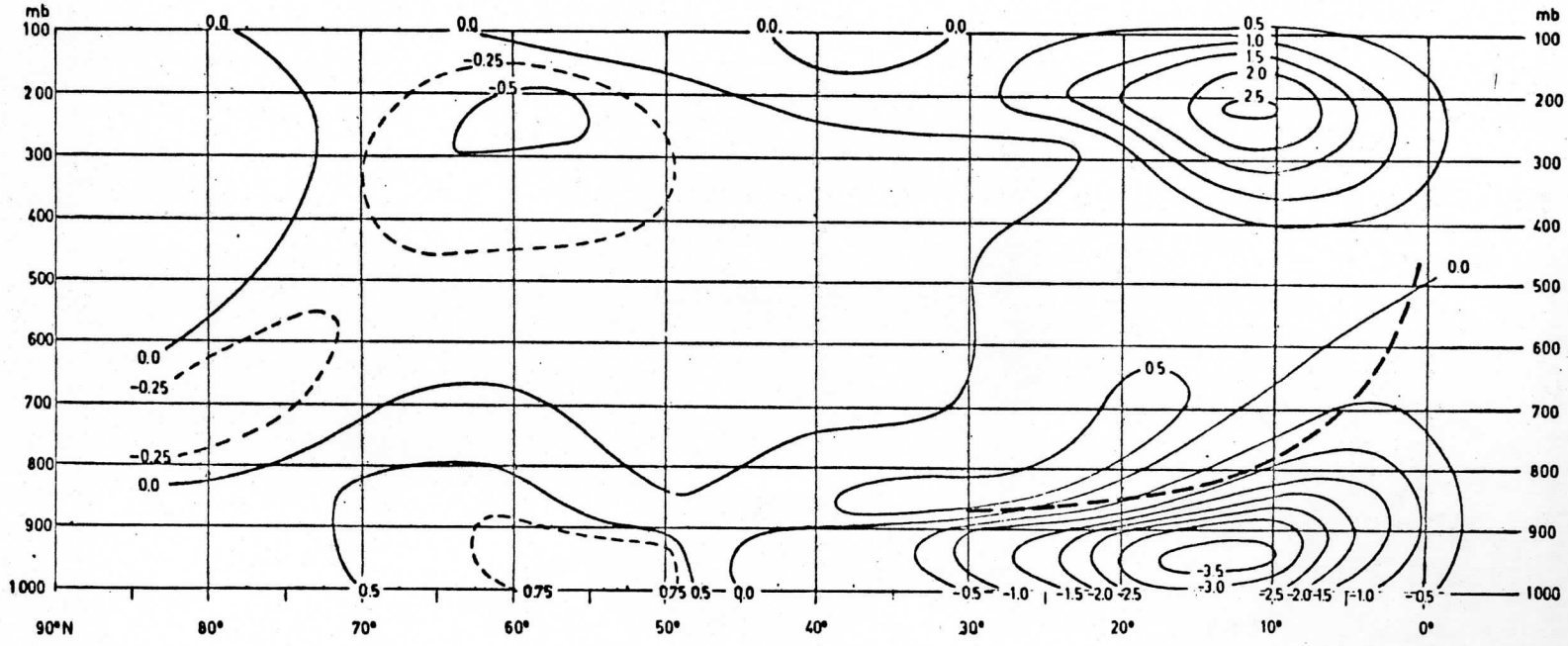
mb
100
200
300
400
500
600
700
800
900
1000
0.0
-0.25
-0.5
0.5
0.75
1.0
1.5
2.0
2.5
-1.0
-1.5
-2.0
-2.5
-3.0
90°N
80°
70°
60°
50°
40°
30°
20°
10°
0°

FIGURE 4

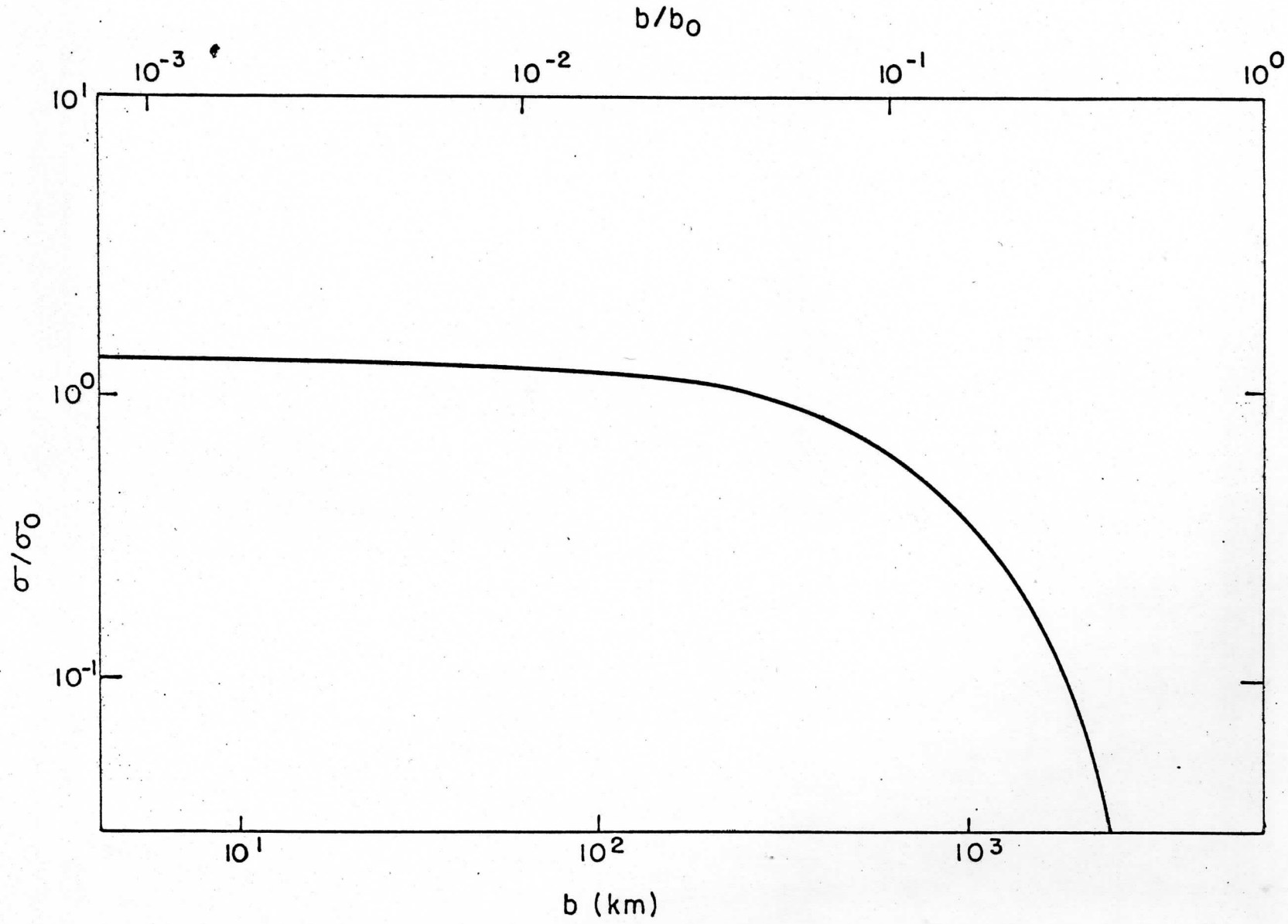

Figure 5

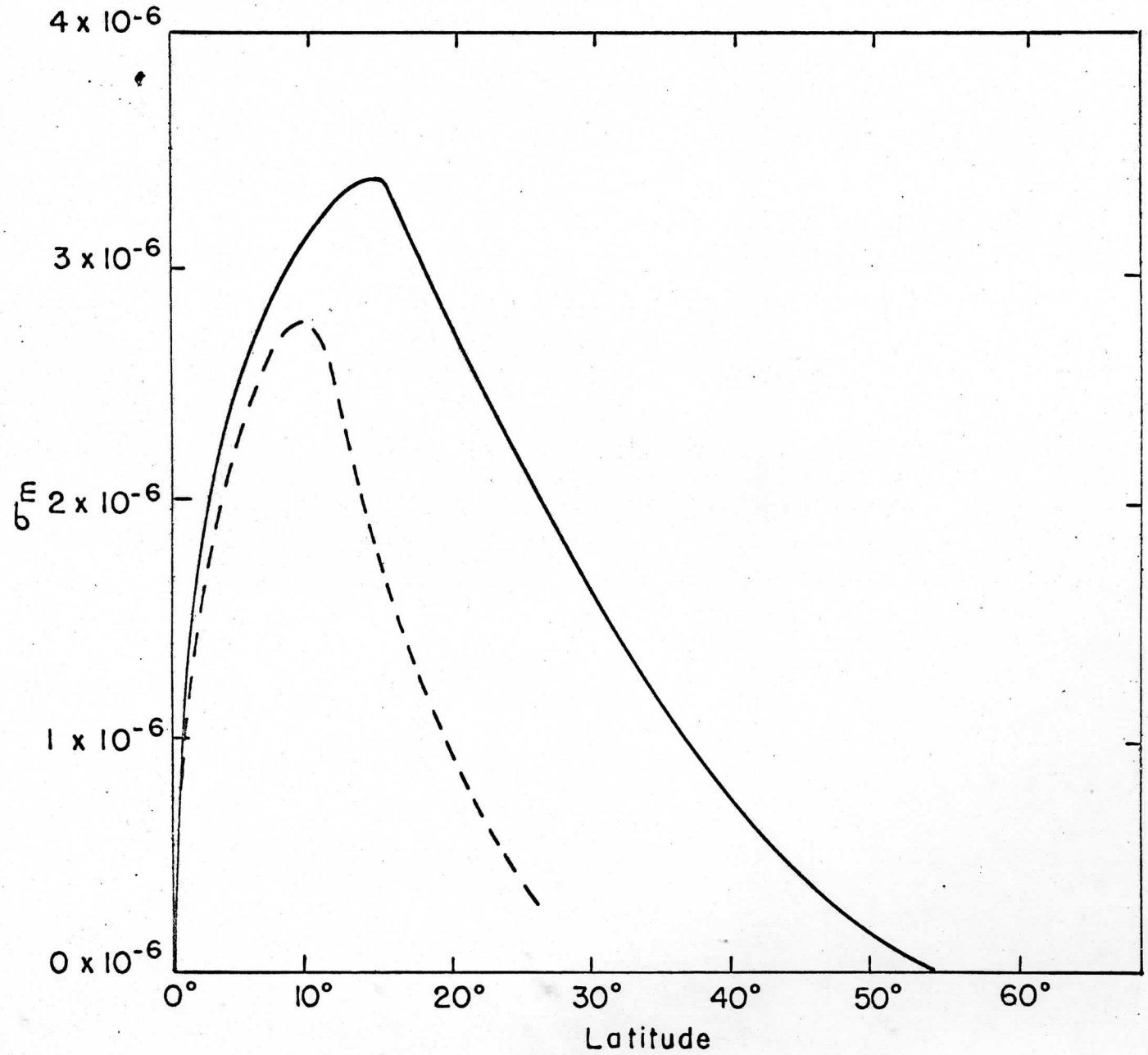
4 x 10-6
3 x 10-6
2 x 10-6
1 x 10-6
0 x 10-6
σ_E
0°
10°
20°
30°
40°
50°
60°
Latitude

FIGURE 6

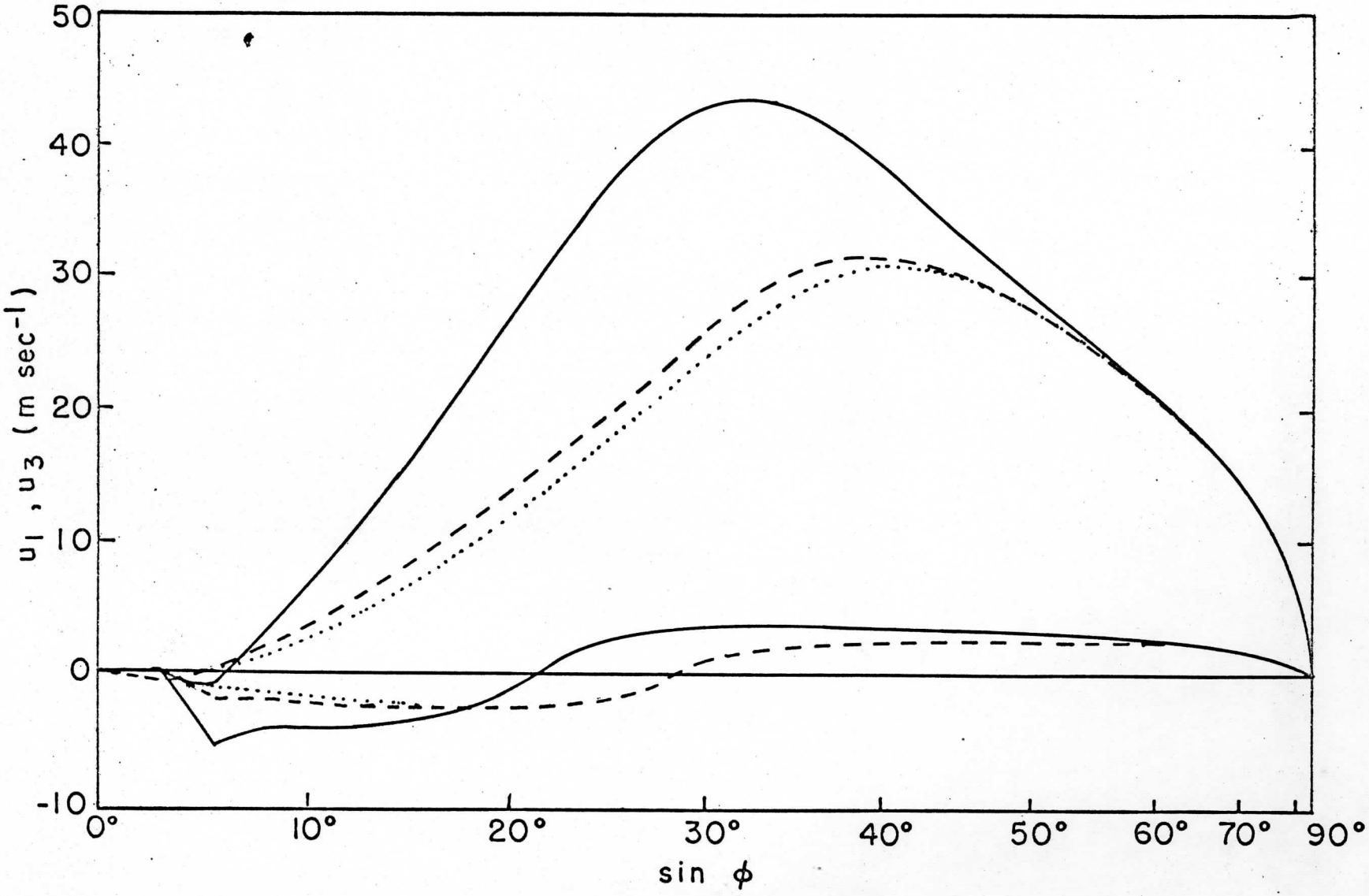

FIGURE 7

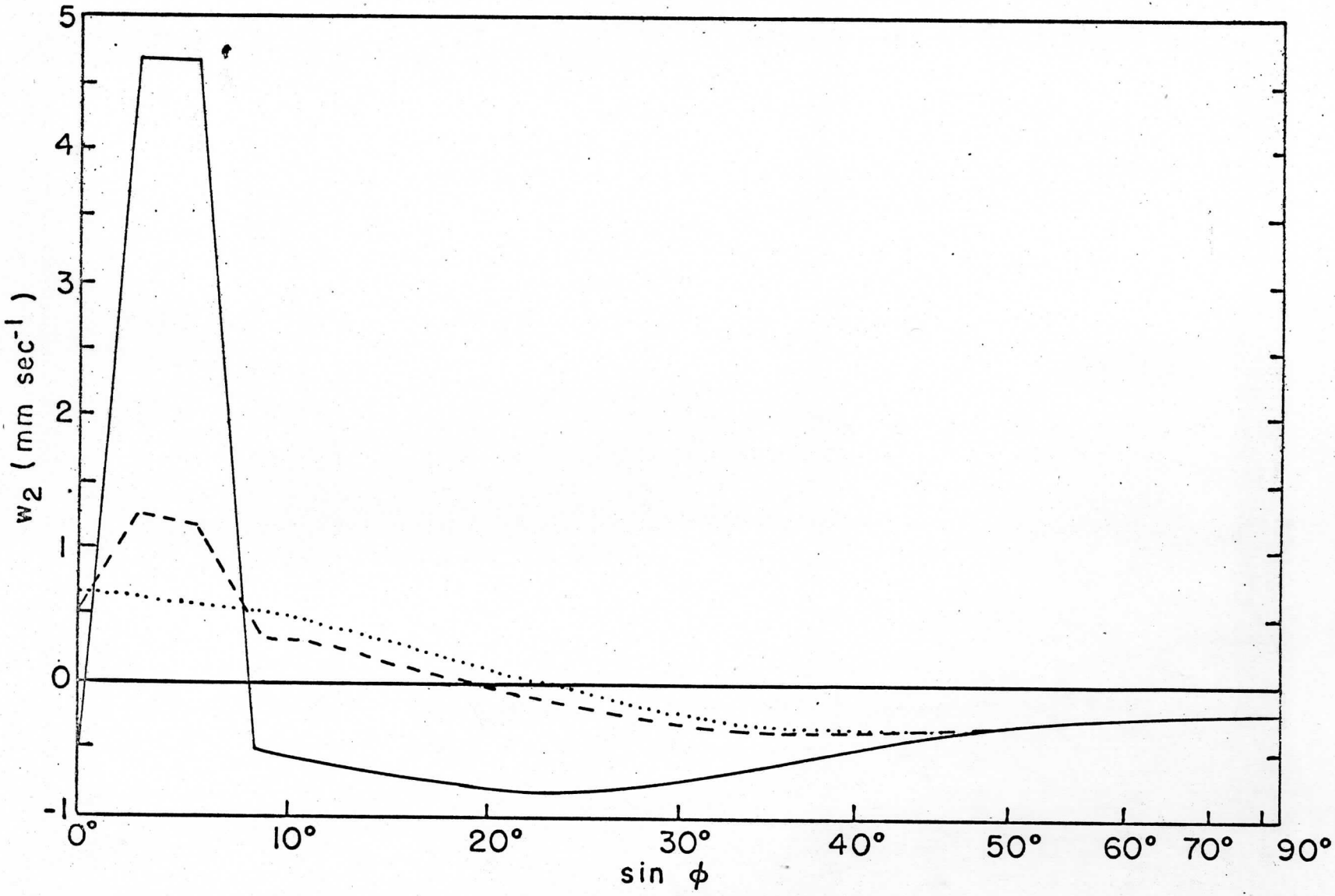

FIGURE 8

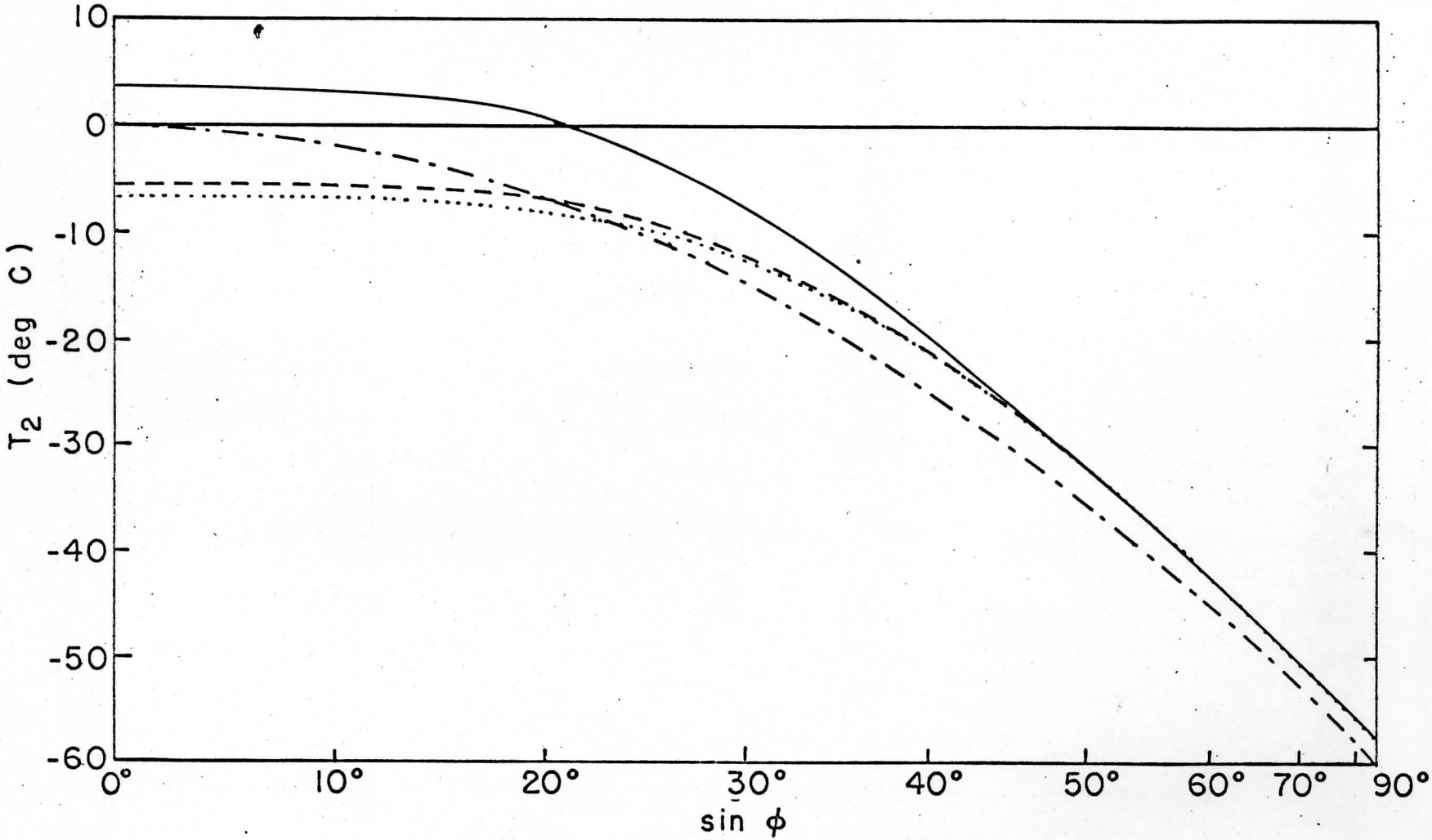

FIGURE 9

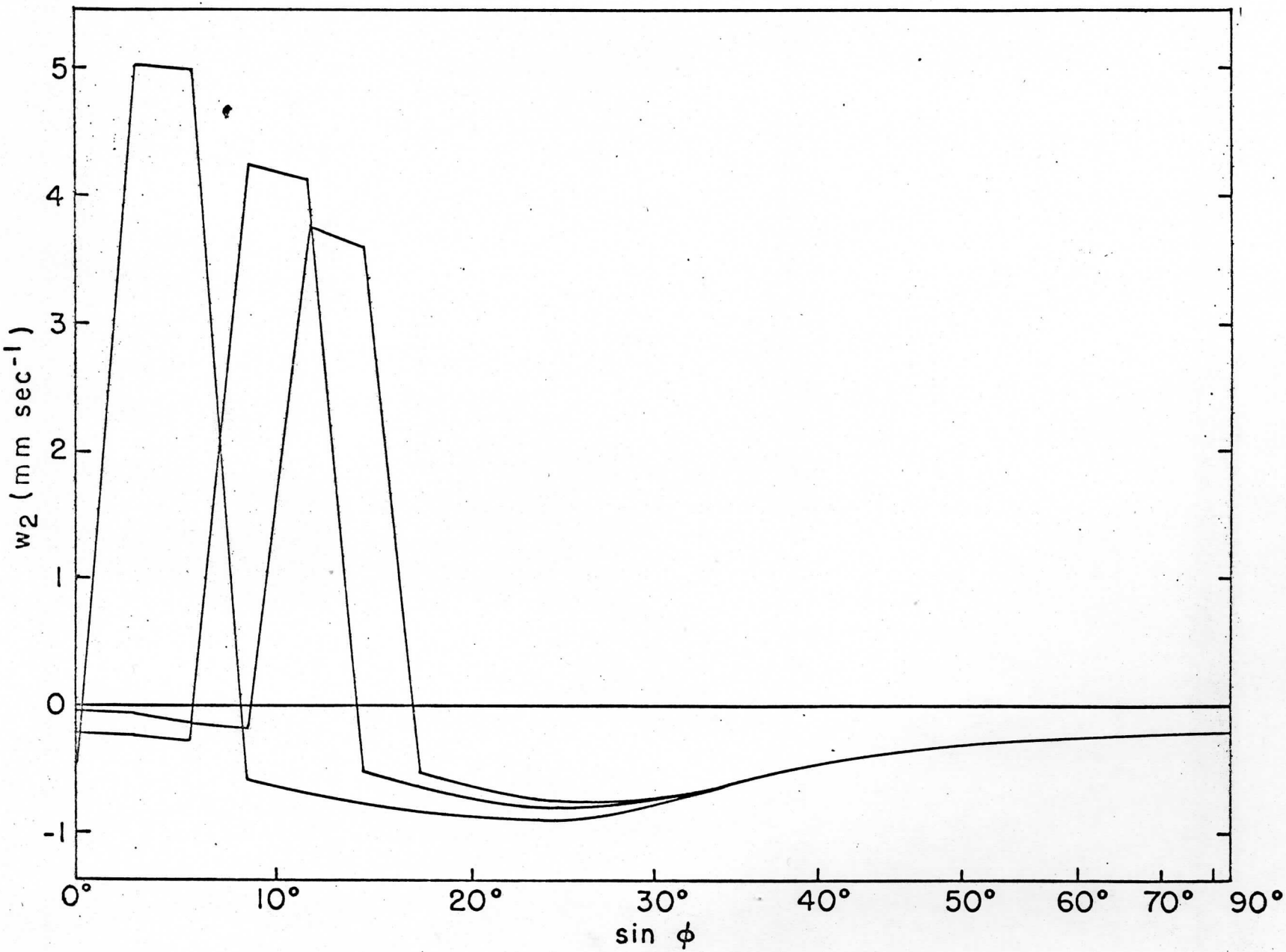

FIGURE 10

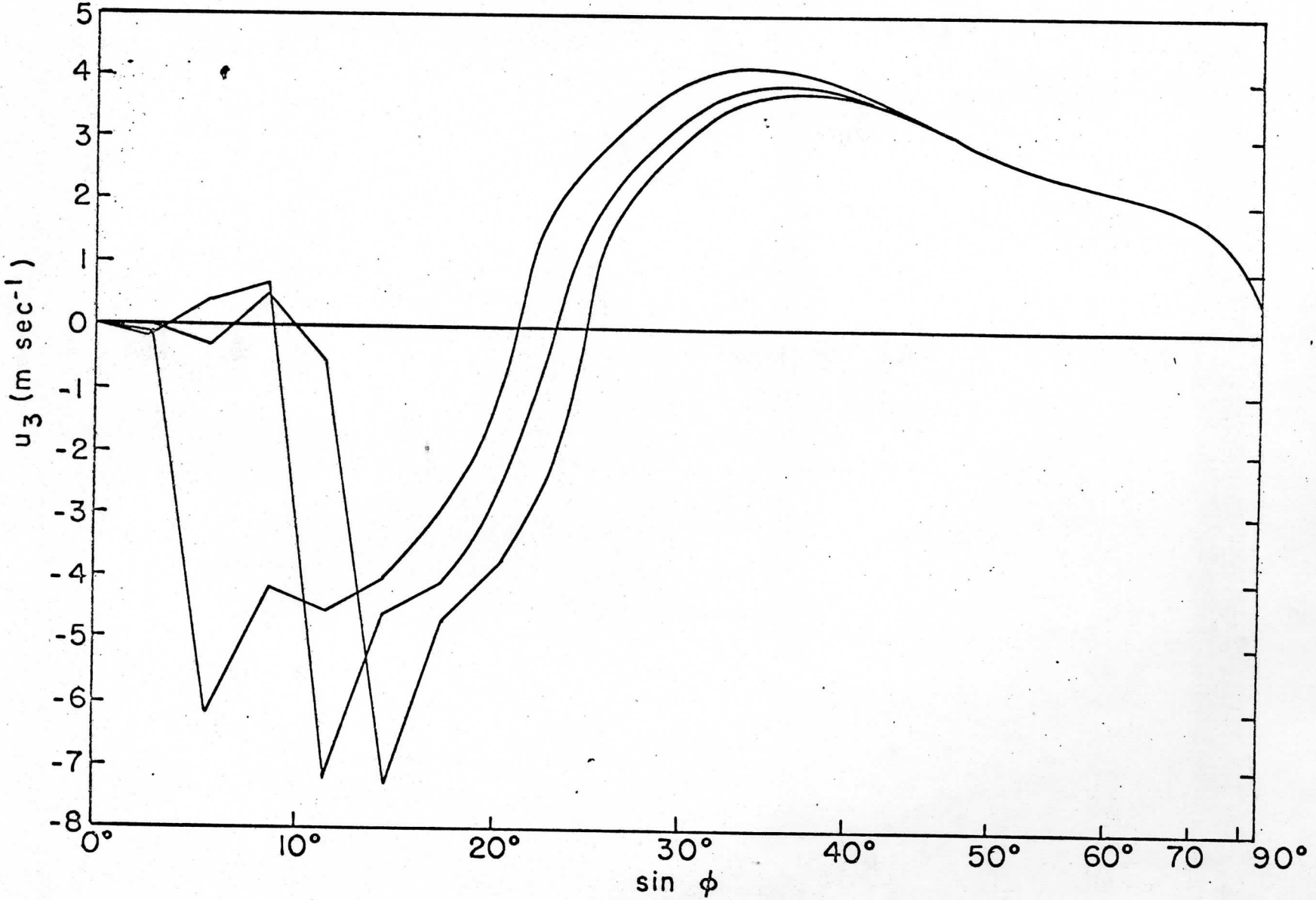

FIGURE 11

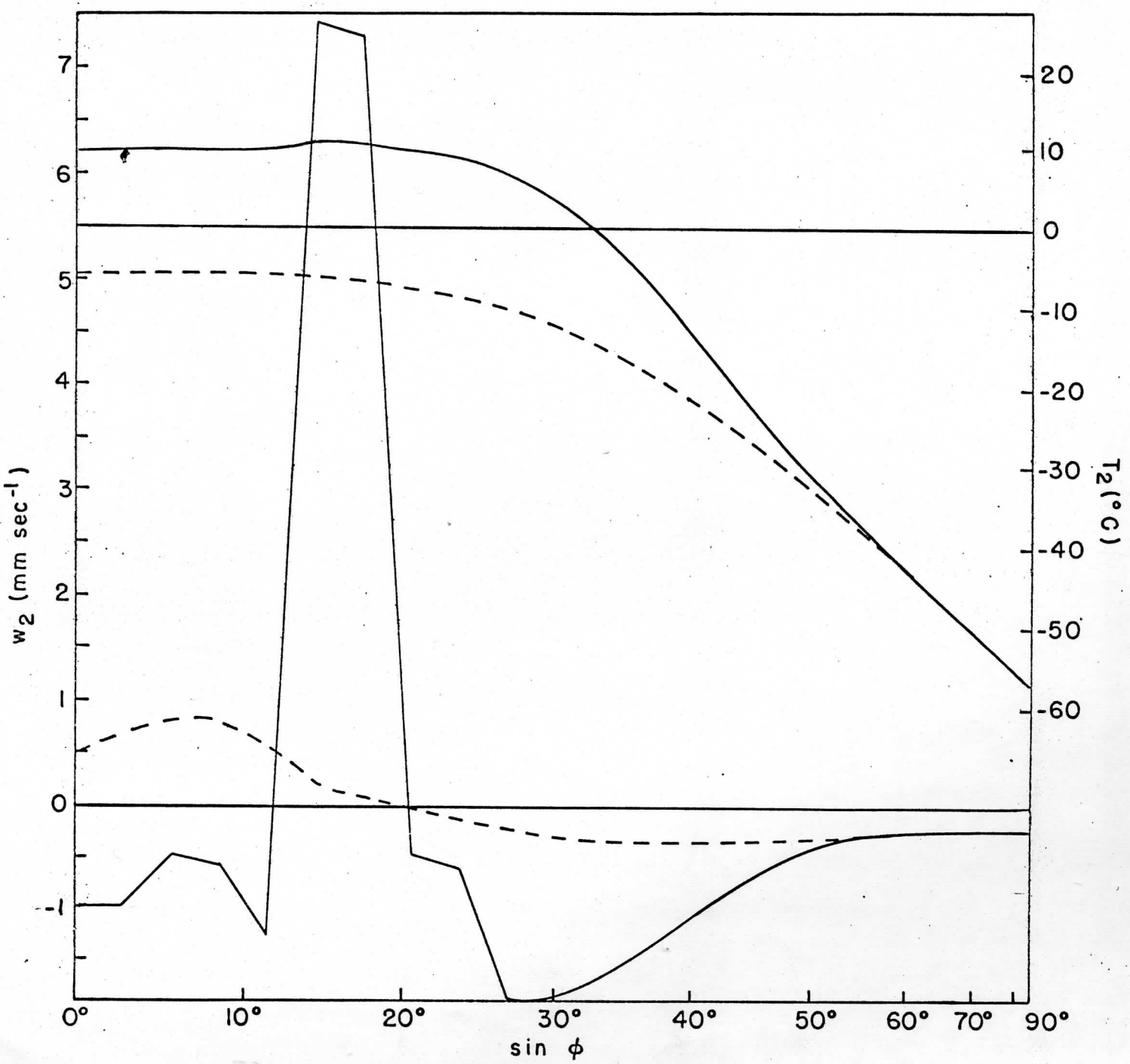
7
6
5
4
3
2
1
0
-1
w_2 (mm sec^{-1})
20
10
0
-10
-20
-30
-40
-50
-60
T_2 (°C)
0°
10°
20°
30°
40°
50°
60°
70°
90°
sin ϕ

FIGURE 12

SPACE
SCIENCE AND
ENGINEERING
CENTER

1225 West Dayton Street
Madison, Wisconsin 53706

THE UNIVERSITY OF WISCONSIN

February 10, 1969

MEMORANDUM

TO: Verner E. Suomi

FROM: Kirby J. Hanson KJH

SUBJECT: Preparing Weather Motions from Space to go to the U.W. Press

Enclosed is a copy of the paper "A Study of Mesoscale Cloud Motions Computed from ATS-I and Terrestrial Photographs", by which we have reviewed for publication in Weather Motions from Space.

If you have any further comments on this paper, please make them before February 20, 1969 . I plan on submitting this paper to the editors on that date.

KJH/mlk

enc.

A STUDY OF MESOSCALE CLOUD MOTIONS COMPUTED FROM ATS-I AND TERRESTRIAL PHOTOGRAPHS

by

Tetsuya Fujita and Dorothy L. Bradbury

The University of Chicago

and

Clifford Murino and Louis Hull

St. Louis University

1. Introduction

In conjunction with the Line Island Experiment operating near the subsatellite point of ATS-I, a terrestrial camera network was established by The University of Chicago and St. Louis University at the top of Haleakala volcano on Maui, Hawaii. The purpose of the operation was to identify and interpret the cloud elements appearing in a series of ATS-I pictures taken at 23-min intervals.

Meanwhile, several methods for determining the velocities of clouds from ATS picture sequences efficiently were explored at the Satellite and Mesometeorology Research Project, The University of Chicago, leading to the construction of a loop projector.

As a result, it is now feasible to compare cloud velocities computed independently from satellite and ground photogrammetry. Since the computation of cloud velocities from ATS pictures is carried out exclusively by filming ATS pictures in various modes, the computation method may be identified as the "cinegrammetric method" of cloud-velocity computation.

2. ATS-I Cloud Pictures in Relation to Upper-Air Flow over the North Pacific

In order to describe the large-scale cloud patterns over the central North Pacific, an ATS-I picture taken between 1354 and 1414 HST 15 March 1967 was gridded with 10-deg longitude and latitude intervals (see Fig. 1). Hawaii is situated to the southeast of a well-developed cyclone centered near 35N 170W. A long, anvil-like plume emanating from a large cellular cloud was passing over Hawaii, giving the impression that the plume was embedded in a strong jet stream passing over the island.

Both the 300- and 500-mb charts at 1400 HST on 15 March 1967 were analyzed as shown in Fig. 2. It is seen that a well-developed low to the northwest of Hawaii appears on

the 500-mb chart as a very small, closed circulation which did not extend to 300 mb. A blocking high, somewhat like that defined by Rex (1950), extended far to the north of Hawaii near 160W. The southern branch of the jet stream, split by the blocking high, extended from north of Hawaii toward the west coast of the United States. At 300 mb, the maximum wind speed along the jet axis was over 100 kt. At the 500-mb level the wind maximum was located between Hawaii and 120W. West of the blocking high, a jet stream was seen over Japan on both the 300- and 500-mb charts.

When these jet-stream patterns are compared closely with the ATS-I picture in Fig. 1, which was taken within 10 min of the 1400 HST map time, it will be found that there appears to be no jet-stream cirrus in the area of the jet stream extending eastward from Japan. Even a time-lapse movie made from an ATS-I picture sequence did not show any fast-moving, high clouds over the expected jet position. The ATS-I picture clearly shows a long plume-like band of clouds extending east-northeast from about 10N 175W to California, passing over Hawaii. Significant motion of cloud elements within this long band can be seen on an ATS-I time-lapse movie. The movie also shows that plumes from the tops of convective cells far to the south of the band converge toward the band, indicating confluent flow toward the area of the jet stream at 500 mb. The single frame ATS-I picture in Fig. 1 indicates such a confluent pattern made visible by the orientation of faint plumes.

The equatorial zone was generally cloud free, while the northern ITC was characterized by scattered convective cells with horizontal dimensions of up to about 300 km.

3. Computation of Cloud Motions from ATS Pictures using the SMRP Loop Projector

The first step to be taken before making a time-lapse movie of ATS-I pictures which are to be used in the determination of cloud motions is to grid the individual pictures as accurately as possible since gridding errors result in erratic cloud motions. It is not feasible in this paper to describe in describe in detail the gridding techniques used. However, it may be stated that, initially, geographic grid points at one-degree intervals were computed for undistorted ATS picture coordinates, assuming an ellipsoidal globe. Although these grid points for undistorted images are very accurate, final gridding errors result mainly from that distortion of the image which remains after the overall dimensions have been adjusted to a unique size. Thus the grid alignment on successive pictures requires not only satellite attitude data but also some geographic features appearing in each picture. Alignment accuracy of about one mile can be expected near well-defined landmarks and of a few miles if there are no landmarks in the vicinity. The gridding of the ATS-I pictures in the Hawaiian island area was done by referring to several islands, thus resulting in an accuracy of one to two miles.

After viewing a large number of time-lapse movies of ATS-I pictures, the authors became convinced that they are extremely useful in gaining knowledge of the development and motion of clouds. In many cases, the difference in the direction of cloud motions permits us to distinguish those clouds located at different levels. Three different directions of cloud motion were observed within a small area, suggesting that they could be used in determining the vertical distribution of winds if we could relate cloud and wind velocities.

In order to determine the cloud velocities on a movie screen it is necessary to follow a specific cloud element or cloud mass as it travels for a short distance during its life time or for the period of the daylight hours, whichever is shorter. Ususally the cloud life is much shorter than 12 hr, the average daylight period in lower latitudes. By filming two frames of every picture taken at 23-min intervals, changes in cloud during a 10 hr period, for instance, will be shown in about 60 frames and it appears on a movie screen in about three seconds. A cloud with a one- to two-hour lifetime would appear on only about 8 to 14 frames, which would not exceed one second of projection time.

In an attempt to prolong the projection time of specific cloud elements with about a one-hour lifetime, a cyclic filming technique was explored. This involves selecting a series of about five pictures and then filming them according to the schedule described in Table I.

Table I. An example of cyclic filming to produce various modes of reciprocal motion of a cloud. In this case, a series of five pictures, identified as numbers 1 through 5, were filmed in three filming modes.

Picture Number	1	2	3	4	5	4	3	2
Oscillation Mode	(16)	(3)	(3)	(3)	(16)	(3)	(3)	(3)
Quick-return Mode	(16)	(3)	(3)	(3)	(16)	(1)	(1)	(1)
Instant-return Mode	(16)	(3)	(3)	(3)	(16)	(0)	(0)	(0)

A cyclic filming in the oscillation mode is done by exposing picture No. 1 sixteen times, pictures No. 2, 3, and 4 three times each, picture No. 5 sixteen times; then by making three exposures each of No. 4, 3, and 2 to complete the first cycle consisting of 50 frames. In order to produce a 250-frame endless loop, for instance, five such cycles should be completed. When such a loop is projected at 16 frames sec^{-1}, the clouds on the first frame remain on the screen for one second; then they move very fast, taking only a fraction of a second, toward their positions on the fifth picture, which is shown for one second. Thereafter all clouds return to their positions on the first frame, taking only about half a second.

Shown in Fig. 3 is the loop projector designed and constructed at the Satellite and Mesometeorology Research Project (SMRP) at the University of Chicago. The loop projector takes a film loop with a total of between 200 and 300 frames. Such a loop may be projected for hours using a 500-watt bulb without damage to the film. The image is focused on the outer surface of a rectangular transparent glass plate with a 45 deg tilt. A sheet of tracing paper is taped on the outer surface of the glass and cloud motions are traced directly on the paper. To avoid the bending of the loop film because of the heat a push switch has been designed to turn on both the lamp and the fan simultaneously, but it will turn off only the lamp. The fan is shut off automatically by a pre-set timer after the projector cools. The film loop continues to run with the projection light off.

The dimension of the image area on the loop projector is 46 x 56 cm. By projecting an image about 30 degrees of longitude in width, for example, one degree or about 60 n mi near Hawaii will be blown up to about 190 mm. The magnification is, therefore, about 3 mm equal to one nautical mile. This means that the displacement of clouds moving at 1 kt and 10 kt are 1 mm and 10 mm, respectively, when two pictures taken at 20 min intervals are used. The corresponding displacements increase to 4 mm and 40 mm when five consecutive ATS pictures are used in the series. An added advantage of using several successive frames is that we are able to check the smoothness and continuity of the cloud motion.

Another important consideration is the duration or life of the clouds. The smallest cellular clouds in ATS pictures can be followed only for less than one hour while larger ones can be recognized for hours. To avoid the tracking of wrong clouds in velocity computations it is always preferable to use all pictures taken between the initial and last pictures in the series.

When a film loop is made in the quick-return mode, clouds stay in their positions on the first and fifth pictures for one second each. Unlike the oscillation-mode case, clouds move slowly from the first to the fifth picture, then they quickly return to their initial positions. In this mode, therefore, an analyst can tell immediately the direction of the cloud movement, which is more readily observed than in the oscillation mode.

By returning from the fifth to the first picture instantaneously, we produce a film in the instant-return mode. The projected image shows that all clouds simply move from the first to the fifth picture positions in repeated fashion. It was found that a film in this mode is also very useful in obtaining quickly a field of cloud velocities.

There are a large number of other filming modes that can be used for various purposes. We have also tested a three-color mode in which the first and fifth pictures are tinted in red and blue respectively, while the second, third, and fourth pictures remain black. It was found, however, that a rapid change in color within a short time does not create a comfortable feeling for our eyes. The use of identical color for all frames and the adoption of various filming modes seem to satisfy most of the necessities for the computation of cloud velocities with our loop projector.

We shall now discuss the continuity of cloud images appearing on successive ATS pictures taken at 23-min intervals. In order to identify easily the change in shape and position of the clouds on each picture, a set of six pictures, representing identical sections from enlarged prints, was pasted together in Fig. 4. The 8×10 inch negatives showing the global view used for making these prints were furnished by Prof. Suomi of the University of Wisconsin. The picture start time in Hawaiian Standard Time is indicated near the lower left corner of each picture.

As shown in the 1549 HST picture, the direction of the scan is very close to the east-west direction. The five major islands of Hawaii are indicated by arrows pointing toward the mostly cloud-covered islands. The largest and highest island, Hawaii, appears in all the pictures as a large white area with an elongated hole near the western edge of the cloud-covered area. This hole represents that part of the island above the top of the clouds including Mauna Loa and Mauna Kea.

The large convective cloud west of Hawaii shows some rotational characteristics. The rotation center is apparent in the pictures for 1526 and 1549 HST and was located near the west end of the cloud mass with horizontal dimensions of about 200 km. A long plume of middle cloud extended eastward from the large convective cloud and passed over the islands of Maui and Hawaii practically the entire day.

In order to make a test analysis of the cloud motion in the vicinity of Hawaii, an area shown in Fig. 5 was selected from the ATS-I picture, for which scanning started at 1223 HST. The area of individual clouds is outlined by thin lines inside of which the areas of bright clouds are stippled. As indicated in the figure, some 200 points

were selected in order to determine their displacement on the image plane of the loop projector. Five pictures, with scan starting times of 1223, 1246, 1309, 1332, and 1354 HST, were filmed in the quick-return mode defined in Table I. The film thus produced was projected continuously until the cloud velocities shown in Fig. 6 were obtai ned. These velocity vectors were then grouped together into low, middle, and unknown cloud motions which were plotted, respectively, with solid arrows, shafts and barbs, and open arrows. These cloud heights are, more or less, the speculated heights except for those over the island of Maui where a ground network of cameras was operated. Despite the fact that the ATS-I pictures do not tell us the cloud height, the patterns of cloud motion give definite indication of the differences in the cloud height when the clouds move in different directions and at different speeds from one another. The grouping of clouds in Fig. 6 into low, middle, and unknown was made tentatively, according to their movement only.

4. Photogrammetric Determination of Cloud Motion and Height from Whole-Sky and Panoramic Pictures from Maui, Hawaii

The Satellite and Mesometeorology Research Project of the University of Chicago and St. Louis University established a camera network of stations atop the northern rim of Mt. Haleakala on Maui during the early part of March 1967, and it was in operation from 13 March through 3 April. The purpose of the network was to gather photographic cloud data during the period of the Line Island Experiment and the ATS-I picture acquisition in order to study the time changes in mesoscale nephsystems and to compute the motions of clouds in the region of the Hawaiian Islands. A comparison was made between the values of cloud motions determined in this manner and those computed from ATS-I pictures using the SMRP loop projector described in the previous section.

Three different camera systems were used to gather the photographic data, namely, whole-sky cameras, panoramic cameras, and stationary wide-angle movie cameras. The whole-sky cameras were set to take 16-mm color movies at intervals of 20 sec during the daylight hours, and the wide-angle time-lapse movie cameras were set to take 16-mm time-lapse movies at 15-sec intervals during daylight hours. The

panoramic cameras were manually operated 35-mm cameras using IR film and were equipped with 35-mm lenses. Eight consecutive pictures were taken, each centered on an octant beginning with N, then NE, etc. This allowed about a 7-deg overlap of the coverage of adjacent frames. Panoramic pictures were taken at 20-min intervals and as near as possible to the ATS picture acquisition schedule.

Figure 7 shows the photographic network established at three sites on Mt. Haleakala. The two wide-angle time-lapse cameras were mounted on the roof of a building at the Kolekole site (elevation of about 9990 ft) with one camera pointing toward the island of Hawaii and the other toward the island of Lanai. At the Red Hill site (elevation 10,010 ft), a whole-sky and a panoramic camera were placed about 25 ft apart and were designated "Station A". At 3.6 km north-northeast of this station, the second whole-sky camera station was erected at the Kalahaku site, or "Station B". In order to get the best available view in all octants, the panoramic IR stand was erected on a peak approximately 0.3 km south-southwest of the whole-sky site.

A stereo-pair of the whole-sky pictures is shown in Fig. 8. It was impossible to have the two cameras synchronized perfectly, but two pictures taken within a few seconds of each other are acceptable as a stereo-pair. Selecting such a pair was accomplished by making a plot of frame number vs. time for each camera and then choosing the frames most closely simultaneous. A large number of detached clouds or cloud elements can be identified on each picture of the stereo pair. Only six from a large number of clouds chosen from these two pictures used for computation of height and motion are labeled.

Before cloud height and cloud motion can be computed, the whole-sky parabolic mirrors must first be calibrated in order to determine the horizon and elevation angles. This can be done by different techniques. One method is to compute the angles theoretically by using the dimensions of the parabola. This assumes that the mirrors are perfect and that the principal point was exactly at the center of the circular image. The most practical method was to select a picture-taking day when the sky had been mostly clear and to plot a composite of the sun's images during the day. Then using the Fujita technique and a Transverse Equidistant Cylindrical Projection overlay (1963) the zenith angles of the solar image, ζ, were determined. Labeling the parallels as $(90-\zeta)$, the elevation angles of cloud images could then be read.

The distance of a specific cloud or cloud element is determined by the intersection of the azimuth-angle rays from the two cameras at a known base-line distance apart. Figure 9 shows a result of determining the position and height of six different clouds, numbered 1 to 6, which are indicated in the picture in Fig. 8. The heights of these clouds were determined by using the computed distances and the elevation angles. Table II lists the various parameters thus obtained. All 28 clouds in the list were chosen from the same stereo-pair of whole sky pictures. Since the maximum computed distance of the cloud from the camera stations was 22 km and the highest percentage of the cases were found to be between 5 and 10 km, it is obvious that these clouds were passing over the island of Maui or in its near vicinity. The ten cases of cloud motion computation represent one minute averages and agree quite well with the wind speed values reported at 1400 HST from Kahalui and Hilo of 22 and 36 kt, respectively, at the 4 km level; of 38 and 46 kt, respectively, at the 5 km level; and of 48 and 56 kt, respectively, at the 6 km level. Since the two observation times are approximately one and one-half hours apart one cannot expect perfect correlation. These values are also within range of the cloud velocities of middle clouds over Maui as computed with the loop projector (Fig. 16). The values computed from the loop projector were average motions for larger cloud masses for a period of approximately 90 minutes. More details on computation techniques are described in a paper by Bradbury and Fujita (1967).

Since infrared more or less penetrates atmospheric haze, clouds with tops at 5 km could be photographed up to about 440 km from the station. Shown in Fig. 10 are an enlarged view of the ATS-I picture started at 1526 HST (top), and the three sections of the panoramic view taken at 1520 HST. As can be seen in both pictures, the only clouds in the northerly direction are those surrounding the island of Maui at low elevations. They do not reach to the height of the camera station. To the northeast, at a range of about 100 km, two cloud lines can be observed on the ATS photograph. With the use of the nomogram shown in Fig. 11, the intersection of the 100-km distance line with the zero elevation angle would give a 0.75-km height, indicating that these are probably low cumuli. To the southwest of Maui in the ATS-I picture, a line of clouds extending toward the island can be observed. These can be identified in the SW panoramic view as the line of altocumulus passing directly over the station. In the southeasterly direction, the top of Mauna Loa and Mauna Kea can be seen protruding above the top of the low-level stratocumulus. The area between Maui and Hawaii appears to be cloud-free on the ATS-I photograph as well as on the panoramic view. But a W-E line of clouds about 75 km south of Maui on the ATS-I picture appears as a line about 3 deg above the horizon on the panoramic view (middle strip). Using Fig. 11, this would give a cloud height of approximately 5 km, which agrees with the cloud height computed for those clouds from the same streamer passing over Maui.

Table II. Computed range of clouds from whole-sky camera stations, their height (MSL) and cloud motion for clouds shown in the stereo-pair of Fig. 8. Cloud motion was computed as a 1-min average. Clouds numbered 1 to 6 are shown in Fig. 8.

Cloud No.	Distance from A (km)	Distance from B (km)	Elev. ∠ A (deg)	Elev. ∠ B (deg)	Height A (km)	Height B (km)	Mean Cloud Motion (kt)
1	17.0	13.5	8.5	11.0	5.5	5.5	
2	7.1	5.0	21.0	30.0	5.5	5.4	
3	7.1	6.6	19.0	20.0	5.3	5.2	31.9
4	5.1	6.6	24.0	19.4	5.1	5.1	38.4
5	5.9	9.1	27.2	17.0	5.7	5.6	45.3
6	8.4	7.7	19.5	24.4	5.8	6.1	57.4
7	11.3	8.2	10.0	15.0	5.0	5.0	
8	11.4	8.8	12.0	16.3	5.4	5.4	
9	7.4	5.1	18.0	25.0	5.3	5.1	
10	9.9	7.8	8.5	11.0	4.5	4.4	
11	10.0	8.4	7.5	10.7	4.3	4.5	
12	9.6	8.1	7.2	11.2	4.2	4.5	
13	6.6	5.3	20.0	25.3	5.2	5.2	
14	5.0	4.7	28.0	29.7	5.3	5.2	
15	3.6	4.7	34.3	29.0	5.0	5.2	
16	7.4	7.9	16.8	16.5	5.1	5.2	33.5
17	7.8	8.9	17.0	13.7	5.3	5.0	39.9
18	10.3	11.5	11.3	11.0	5.0	5.1	39.9
19	7.3	9.0	18.0	15.0	5.3	5.2	
20	4.0	6.4	29.5	20.0	5.0	5.1	
21	3.4	6.2	29.8	20.0	4.7	5.1	31.9
22	5.9	8.3	20.0	15.2	5.0	5.1	
23	6.8	10.0	13.5	10.2	4.6	4.7	31.9
24	3.6	7.1	20.0	13.0	4.2	4.5	
25	2.2	5.6	39.0	20.0	4.4	4.8	
26	22.3	22.2	10.0	10.0	6.9	6.8	
27	5.4	5.8	25.4	27.8	5.3	5.6	50.0
28	8.0	9.2	20.0	19.0	5.7	5.9	

TABLE II - corrections

Cloud No.	Height A (km)	Height B (km)
1	5.5	5.5
2	5.7	5.7
3	5.4	5.3
4	5.2	5.2
5	5.9	5.7
6	6.0	6.3
7	5.0	5.0
8	5.4	5.4
9	5.4	5.2
10	4.5	4.4
11	4.3	4.4
12	4.2	4.4
13	5.4	5.3
14	5.6	5.5
15	5.5	5.5
16	5.2	5.2
17	5.3	5.0
18	5.1	5.1
19	5.4	5.2
20	5.3	5.2
21	5.0	5.1
22	5.2	5.1
23	4.7	4.7
24	4.3	4.5
25	4.8	4.9
26	6.9	6.8
27	5.6	5.9
28	5.9	5.9

Any number of such cloud masses within a 400 km range from Maui can easily be matched with those appearing on the ATS-I picture providing there is nothing obstructing the view. Thus, if the range can be determined from the ATS-I view and elevation angle from the panoramic view, the cloud height is easily computed.

It was found that a comparison of the velocities derived from the stereo-pair whole sky camera system and those of the panoramic system could not be made since cloud masses or cloud elements at elevation angles between 20 and 60 degrees give best results for the whole sky system while the panoramic picture includes the range of +20 and -20 degrees of elevation angle. However, the cloud heights computed independently by the two techniques can be compared since in this case the cloud elements chosen for the computations were in general of the same cloud band or layer.

5. Analysis of Soundings

Photogrammetric determination of cloud heights and velocities in Section 4 revealed that the plume-like clouds that extended from a large convective cloud west of Hawaii were mostly of the altocumulus type with heights ranging between about 4.5 and 6.5 km MSL. Their speed varied from 30 to 50 kt.

Since the large convective cloud was located half-way between Johnston Island and Hilo, some 1400 km apart in a WSW-ENE direction, we shall attempt a detailed analysis of the soundings at 1400 HST from these stations. As shown in Figs. 12 and 13, the atmosphere above 700 mb over Johnston Is. was very dry, suggesting that the subsidence in the subtropical high reached down to about 700 mb. On the other hand, there was a marked moist layer over Hilo between the 520- and 600-mb surfaces. The heights of these pressure surfaces correspond to the cloud heights measured by the Maui camera network. From these moisture distributions we may postulate that most of the outflow from the convective cloud passed over Hawaii at about 5 km MSL.

Winds over Johnston Is. between the 500- and 600-mb surfaces were very light, increasing from 20 to 25 kt. Over Hilo, however, the winds at corresponding heights increased from 38 to 53 kt, indicating that the wind velocity inside the moist layer was about 45 kt from the west. It is of interest to note that the velocity of the plume-like clouds in the vicinity of Hilo was about 40 kt. This means that the motion of the altocumulus over Hawaii computed from ATS-I pictures represents the winds at the cloud level. The horizontal dimensions of the altocumulus used in the velocity computation were kept below about 50 km.

At higher levels, the wind speed increased upward, reaching a maximum of 63 kt at about 200 mb over Johnston Is. and 103 kt at 250 mb over Hilo. None of the cloud velocities computed from ATS-I pictures indicated such high velocities. Furthermore, no cirrus-type clouds drifting from the west were observed from the Maui network stations. It is therefore very likely that the top of the large convective cloud west of

Hawaii was not as high as the clouds of the average midwestern thunderstorm. If the cloud top reached the 300 mb level, for instance, more plume-like cirriform clouds should have been seen over Hawaii and they should have moved at the rate of about 100 kt.

6. Synoptic Interpretation of Cloud Motion

In the preceding sections it was found that the velocities of plume-like middle clouds over Hawaii computed from both ATS-I pictures and terrestrial stereo-pictures were ~~identical to~~ in close agreement with the wind velocities at the cloud level. This would mean that these middle clouds simply drifted away from their source region. An attempt was made, therefore, to plot the cloud velocities on upper-air charts close to these cloud heights.

A sectional surface chart at 1400 HST was constructed in Fig. 14 with all available ship and land station reports. Note that the cloud covers are indicated and low clouds are separated from middle and high clouds. Both cloud types and station temperatures are shown near each station. It is seen that the large convective cloud was located ahead of an advancing cold front followed by a weak surge of cold air. The region of Hawaii and the convective cloud was under the influence of weak, easterly trade winds with their tops located between the 800- and 870-mb surfaces.

Without verifying the height of cellular clouds which are likely to be of the low cloud type, all cloud velocities obtained by tracking these cellular clouds were plotted on an 850-mb chart for 1400 HST (see Fig. 15). Of extreme interest is the velocity of the clouds to the southeast of the convective cloud, all of which are about 12 kt from the southeast. Due to the warm tropospheric temperature over Johnston Is. as compared with that over Hilo (see Fig. 13), the height of the 850-mb surface over Johnston Is. was much higher than that over Hilo. This resulted in drawing a trough or a convergence line, as shown in Fig. 15, in order to construct height contours which would fit both the cloud motions and the 850-mb height over Johnston Island. It appears that the large convective cloud under consideration was located on this convergence line.

The 850-mb chart in Fig. 15 was constructed by taking the computed low cloud velocities and the 850-mb heights and winds into consideration. The cloud motions inside the region behind the cold front northwest of Hawaii were all from the west-

southwest, suggesting that the cold air was very shallow. A convergence line far to the northeast of Hawaii was characterized by a significant horizontal shear in the cloud motion. It seems that this convergence line and the weak, warm front on the surface chart are closely related. The slope of the warm frontal surface appears to be extremely small when it is computed by combining the surface and the 850-mb charts. Such a result would be realistic in view of the errors involved in the surface chart analysis and of the transient stage of the warm front formed at the tail end of a dissipating cold front.

The cloud motions from the southeast in the vicinity of the islands of Hawaii and Maui are not consistent with the westerly to southwesterly 850 mb winds. This may be due to the fact that the winds at cloud level were very light and variable and in some way may reflect some island effect. Coastal stations reported cloud bases ranging from 2,000 to 3,000 feet.

Figure 16 is a 500-mb chart for 1400 HST, including the middle-cloud velocities computed from the ATS-I pictures taken between 1223 and 1354 HST. Although we were not able to verify the cloud types and the height of the clouds, except those over Maui, we assume that there was no variation in the height of the plume-like clouds as they drifted eastward from their source. The cloud speeds increased significantly from 22 kt, just east of the convective cloud, to 88 kt as they crossed the 148W meridian. A similar increase in the wind speed from 34 kt over the island of Kauai to 53 kt over the island of Hawaii is seen.

Isotachs at 10 kt intervals were drawn to describe the velocity field of the cloud motions. The resulting isotach pattern turned out to be very similar to that of the entrance regions of jet streams. Note that those isotachs drawn for cloud velocities fit reasonably well with the observed winds on the 500-mb surface over the Hawaiian island area. The direction of cloud motion was used to determine the orientation of height contours, and they showed definite directional convergence toward the core region of the 500-mb jet stream.

Using the streamline and isotach analyses at 500 mb as shown in Fig. 16, both the divergence and relative vorticity of middle-cloud velocities were computed by reading off the direction and the speed at grid points. Figure 17 shows that most of the jet-stream region was characterized by less than 2×10^{-5} sec^{-1} divergence. The field was more or less non-divergent despite the speed increase toward the east-northeast. The direction convergence actually cancelled out the speed increase. This shows that both north and south of the 500-mb jet stream in the entrance area the cloud motion vectors result in divergence. Convergence north of the jet position would have helped to explain why the clouds remained south of the jet. One explanation may be that these divergence fields represent conditions in the cloud layer and not that above this level; the jet maximum does after all lie at a higher level so that convergence is possible north of the jet and increased divergence south of the jet just above the cloud level. In this case the cloudiness could be largely the result of advection from the bright cloud mass upstream from Hawaii rather than vertical motions about the jet. Also the cloud motions may not be completely representative of the true wind field.

The relative vorticity was divided into cyclonic to the north and anticyclonic to the south by the jet axis, showing patterns very similar to those of high-level jet streams studied by Palmen and Newton (1948). The Coriolis parameter over the area of the

analysis is approximately $2\Omega \sin\phi = 5.0\times10^{-5}\text{sec}^{-1}$. Therefore, the absolute vorticity of the cloud velocities to the south of the jet axis turned out to be slightly anticyclonic.

According to Palmen and Newton (1948), the absolute vorticity to the south of a polar jet stream is nearly zero. Riehl, Berry, and Maynard (1955) also verified this evidence by using aircraft traverse data. A negative absolute vorticity, however, was reported by Reiter (1961), suggesting the existence of anticyclonic absolute vorticity to the south of the jet axis.

The authors do not intend to justify the computed anticyclonic absolute vorticity values, since the 500-mb surface is too low to expect anticyclonic absolute vorticity. Furthermore, the cloud velocities may not represent the air motion throughout the entire region. Nonetheless, cloud velocities of such density as was utilized in computing divergence and vorticity would be of great value in estimating the field of air motion where no data are otherwise available.

7. Summary and Conclusions

Presented in this paper are the results of the computation of cloud velocities from a series of ATS-I pictures. A local area near Hawaii was selected for such computation because a stereo-camera network was operated on top of Haleakala on Maui. Independent computation of cloud velocities from terrestrial photogrammetry revealed that the velocities of middle clouds computed from both ATS-I and terrestrial photographs are very close to each other. These cloud velocities were found to represent approximately the wind velocities at the cloud levels.

An attempt was made to improve local upper-air analyses by adding the cloud velocities on corresponding upper-air charts even though the heights of the clouds were not known accurately. It was found that cloud velocities are very useful in determining the mesoscale field of air motions which affect the cloud motions.

Also computed were the divergence and vorticity of the cloud velocities determined from ATS-I pictures. Despite the fact that it is uncertain that a group of clouds which moves with similar velocities is located at a unique height, the computed fields are found to be quite meaningful.

Through this study of cloud motions by using ATS-I and terrestrial pictures, the authors recommend that (1) it is necessary to develop an accurate and quick method for computing cloud velocities from ATS picture sequences, (2) terrestrial photogrammetric studies of cloud heights and velocities should be performed simultaneously and independently, and (3) the relationship between the air motion and the velocity of various clouds must be established through observational and theoretical studies. After solving these problems, it will become feasible to add a large number of wind velocities at several levels by computing cloud velocities from ATS pictures.

Acknowledgements: The authors are very grateful to Professor Verner E. Suomi, who made ATS-I pictures available to the authors study. This study was performed at Maui, Hawaii and at the University of Chicago. The research contributed by the University of Chicago group was sponsored by NSF under grant No. GA-864 and ESSA under Cwb WBG-34, while those from St. Louis University by NSF under grant No. GA-410.

REFERENCES

Bradbury, Dorothy L. and T. Fujita, 1967: Computation of height and velocity of clouds from dual, whole-sky, time-lapse picture sequences. Satellite and Mesometeorology Research Project Research Paper No. 70, The University of Chicago.

Fujita, T., 1963: A technique for precise analysis of satellite data; Volume I, Photogrammetry. U.S. Dept. of Commerce, Meteorological Satellite Laboratory Report No. 14, 106 pp.

Palmen, E. and C.W. Newton, 1948: A study of the mean wind and temperature distribution in the vicinity of the polar front in winter, J. Meteor. 5, 220-226.

Reiter, E.R., 1961: The detailed structure of the wind field near the jet stream. J. Meteor., 18, 9-30.

Riehl, H., F.A. Berry, and H. Maynard, 1955: Exploration of the jet stream by aircraft during the 1952-53 winter, J. Meteor. 12, 26-35.

FIGURES

Fig. 1. An ATS-I picture started at 1354 HST 15 March 1967 showing plumes and streamers drifting eastward from a couple of large convective cloud systems. Longitudes and latitudes are drawn at 10-deg intervals.

Fig. 2. Constant pressure charts at 300 and 500 mb for 1400 HST 15 March 1967. Areas with wind speed in excess of 75 kt are stippled.

Fig. 3. A loop projector constructed by SMRP for use in cinegrammetric study of ATS cloud motions.

Fig. 4. A series of ATS-I pictures started at 1417, 1440, 1503, 1526, 1549, and 1612 HST 15 March 1967. These pictures were enlarged from 8 x10 inch high-resolution negatives produced by Prof. Suomi, the University of Wisconsin.

Fig. 5. Cloud patterns and cloud elements selected for computation of cloud velocities. Initial positions at 1223 HST are represented by black circles (low clouds), double circles (middle clouds), and encircled dots (unknown clouds).

Fig. 6. Computed velocities of all cloud elements shown in Fig. 5. The velocities were computed from the cloud displacements during the 1 min period between 1223 and 1354 HST.

Fig. 7. The Haleakala camera network of March-April 1967. A stereo-pair of whole-sky and panoramic cameras were operated at the Kalahaku site (9320-9410 ft) and the Red Hill Site (10,010 ft) on the north rim of Haleakala volcano on Maui. Two wide-angle time-lapse cameras were operated at the Kolekole site (9990 ft); one to monitor clouds in the direction of the islands of Hawaii and the other in the direction of Lanai.

Fig. 8. An example of a stereo-pair of whole-sky pictures taken within 2 sec of each other. The degrees on concentric circles in each picture denote the elevation angles. Selected cloud elements for velocity computation are identified by number 1 through 6.

Fig. 9. An example of the plan-position determination by using the pair of pictures shown in Fig. 8. The base line distance was 3.6 km. The height given in parenthesis denotes the mean cloud height (MSL) computed from the range and the elevation angles from both sites A and B.

Fig. 10. Comparison of an ATS-I picture started at 1526 HST and a panoramic picture taken at 1520 HST. Boundaries of the islands are added to the ATS-I picture. The Haleakala camera network is shown by a small triangle on Maui. The panoramic view is reproduced in three sections. The apparent horizon is about 200 km which is about the distance to Oahu. The plume-like cloud extending eastward from the large convective cloud appears as altocumulus with practically no vertical development. A standing wave cloud is visible between NE and SE directions.

Fig.11. A nomogram constructed to be used for relating the cloud heights with the distance from Haleakala and the elevation angle measured from the apparent horizon. Note that the horizontal scale was decreased at the range of 250 km. This nomogram can be used to obtain the cloud height from known range and elevation angle. If the height and the elevation angle are known the range can be obtained immediately and verification can be made on the cloud position on an ATS picture. For instance, cirrus at 10 km height will be seen 0.5 deg above the apparent horizon even though its range is as far as 500 km.

Fig. 12. Sounding from Hilo, Hawaii at 1400 HST 15 March 1967. The moist layer between 600 and 530 mb agrees with the computed height of the altocumulus cloud.

Fig. 13. Sounding from Johnston Island at 1400 HST 15 March 1967.

Fig. 14. Surface chart at 1400 HST 15 March 1967 with isobars drawn at 1-mb intervals.

Fig. 15. 850-mb chart with low-cloud velocities. The height contours are drawn for every 10 m. Numbers beside each cloud velocity vector denotes the cloud speed in kt.

Fig. 16. 500-mb chart with contours drawn for every 20 m. Middle-cloud velocities are plotted and isotachs are drawn for every 10 kt.

Fig. 17. Divergence and relative vorticity of middle-cloud velocities as shown in Fig. 16. Numbers at grid points are the values in units of 10^{-5} sec^{-1}. Thin irregular lines enclose areas with clouds. Stippled areas denote estimated middle clouds.

1354 HST MAR 15, 1967

FIG-2

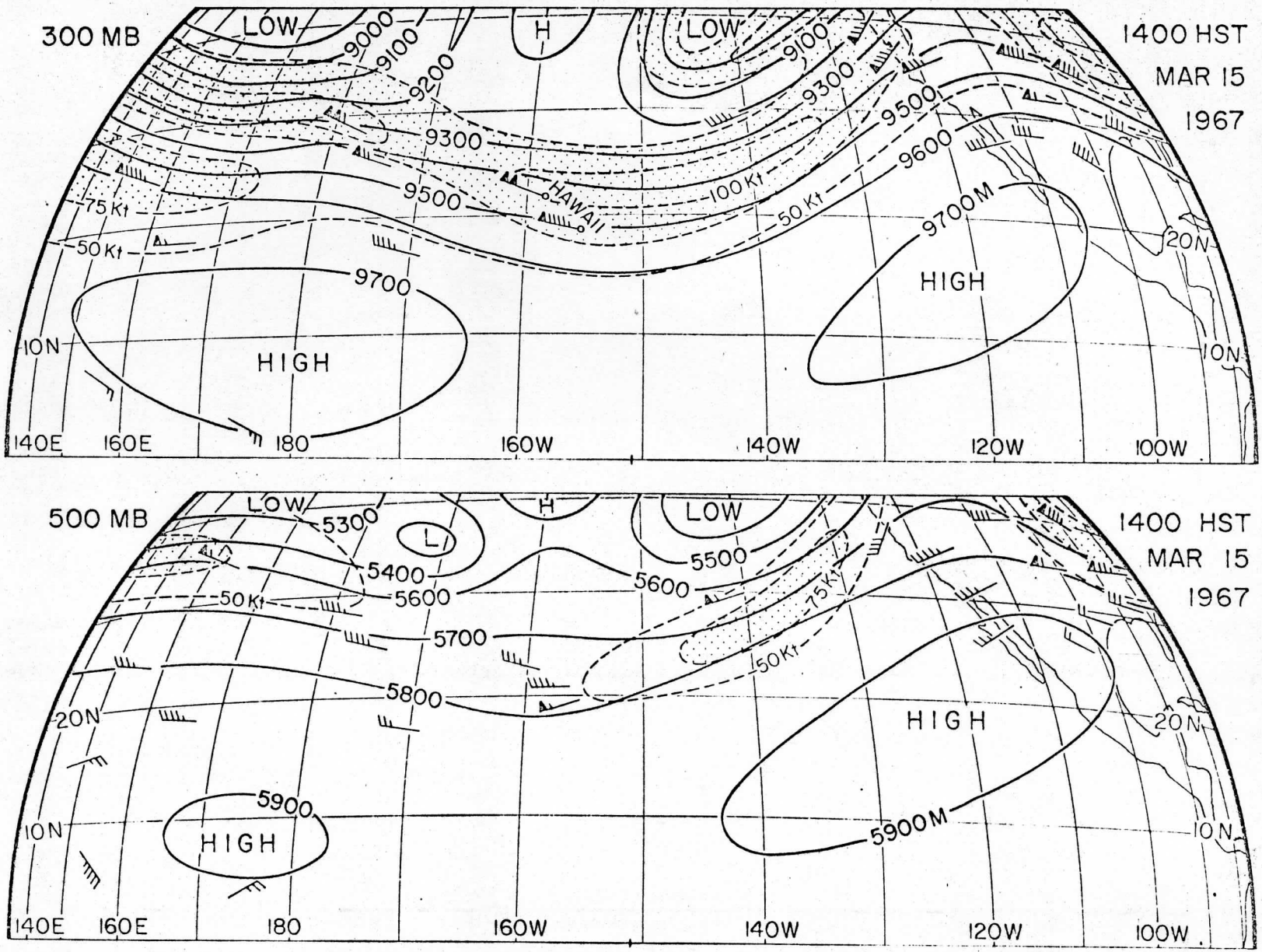
300 MB
1400 HST
MAR 15
1967
LOW
H
LOW
9000
9100
9200
9300
9500
9600
9700M
9700
100 Kt
75 Kt
50 Kt
HAWAII
HIGH
HIGH
20N
10N
140E
160E
180
160W
140W
120W
100W
500 MB
1400 HST
MAR 15
1967
LOW
H
LOW
L
5300
5400
5500
5600
5700
5800
5900
5900M
75 Kt
50 Kt
HIGH
HIGH
20N
10N
140E
160E
180
160W
140W
120W
100W

Fig. 3

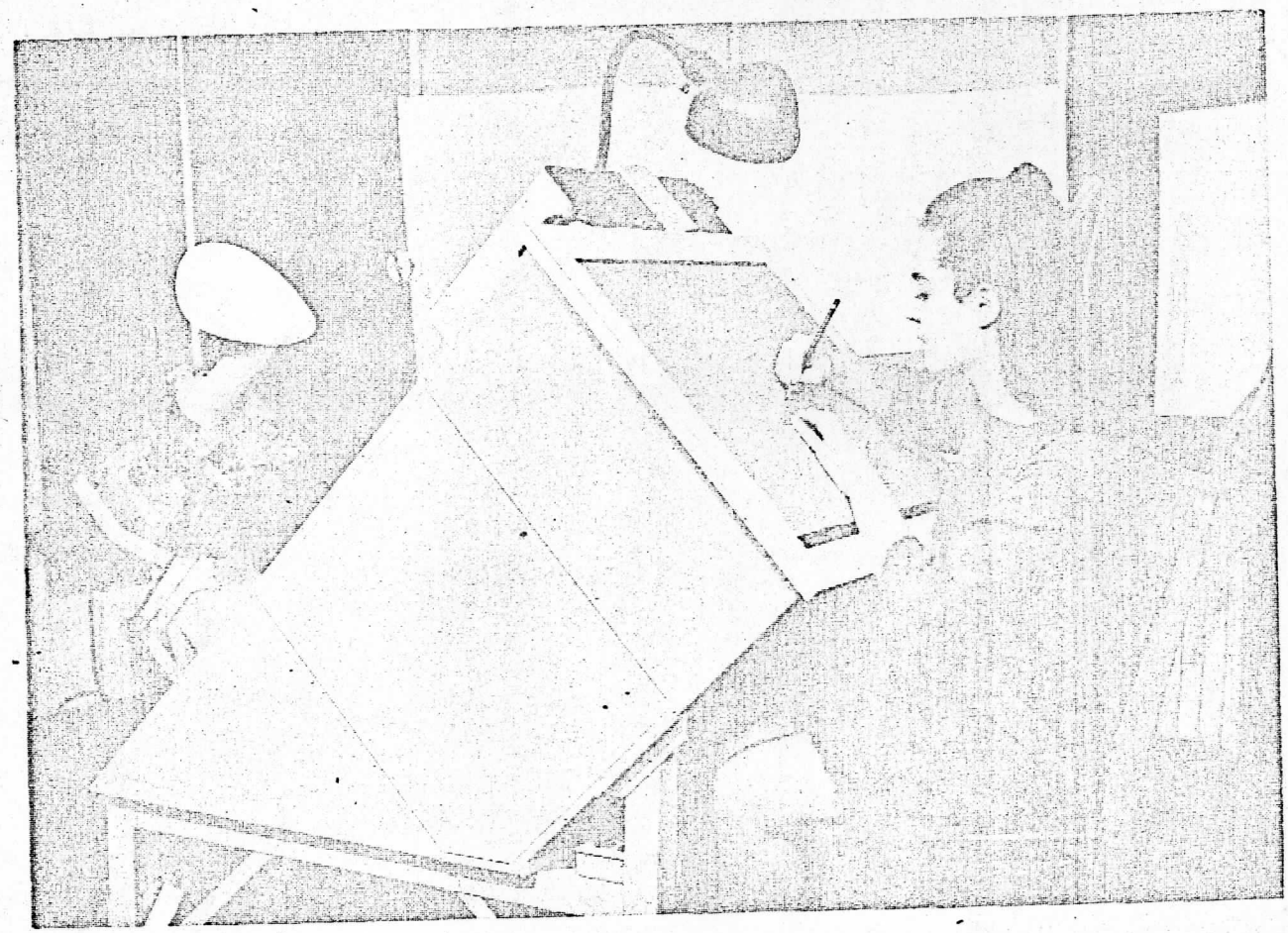

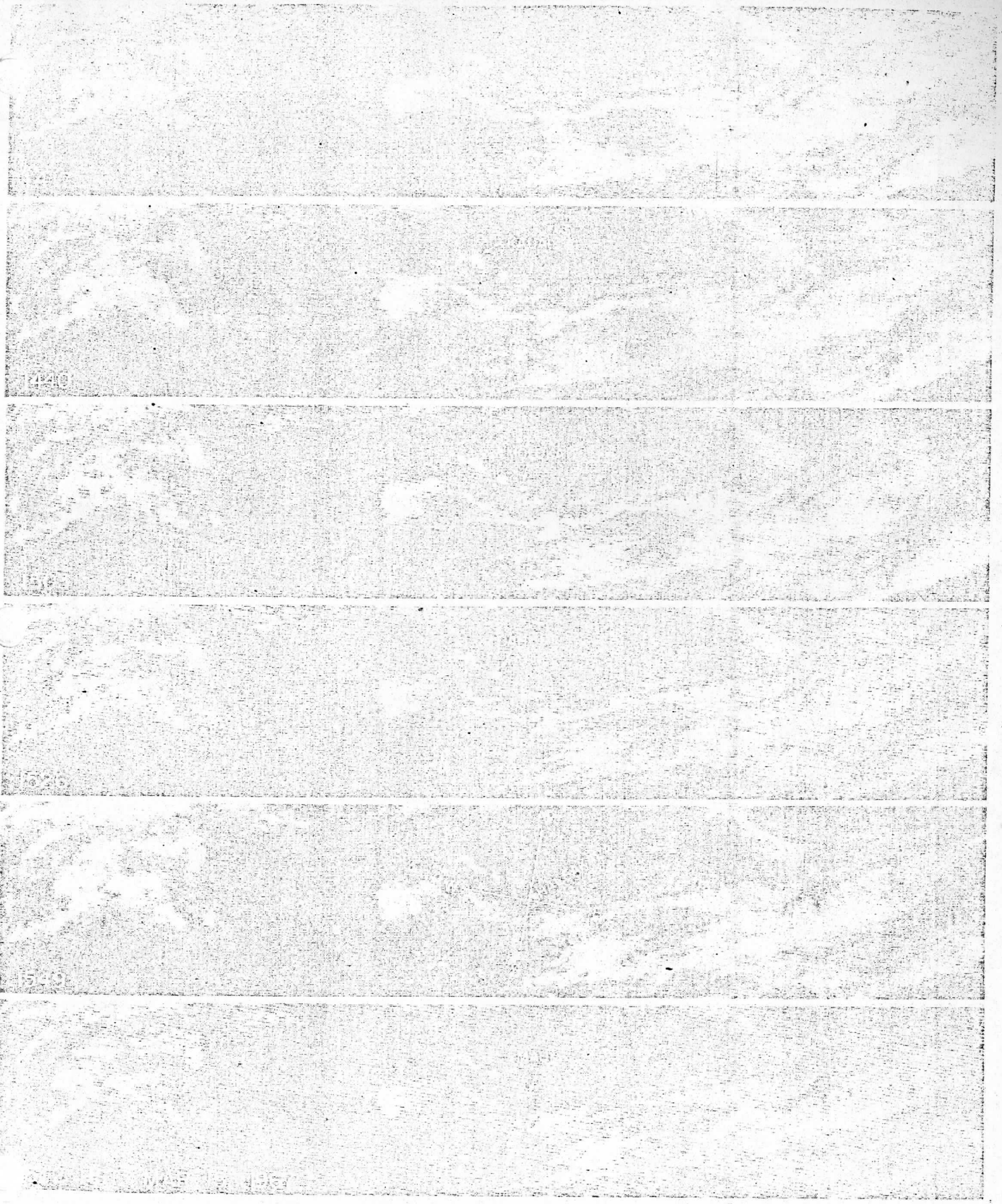

Fig 5

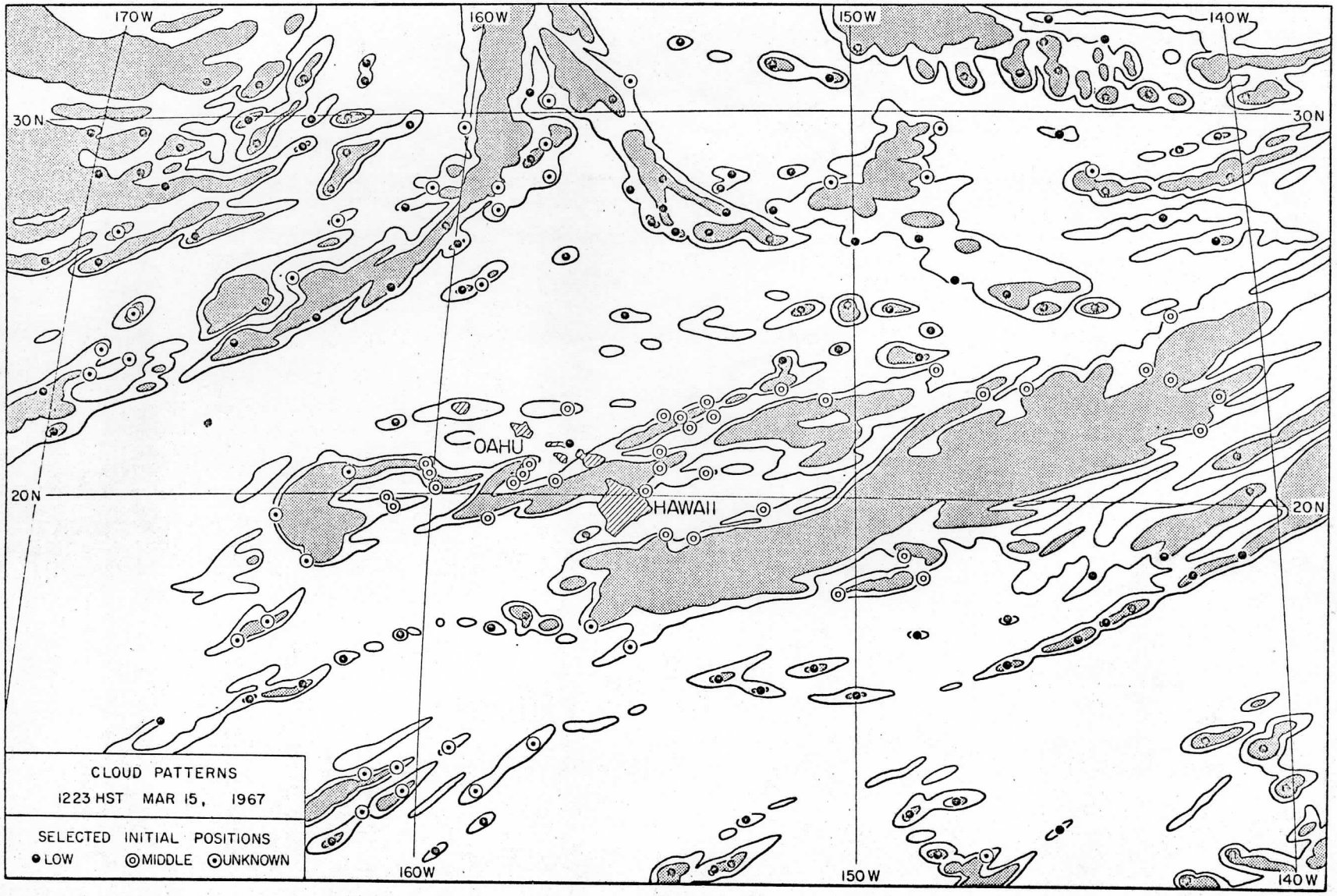
170W
160W
150W
140W
30N
20N
OAHU
HAWAII
CLOUD PATTERNS
1223 HST MAR 15, 1967
SELECTED INITIAL POSITIONS
LOW
MIDDLE
UNKNOWN
160W
150W
140W

Fig. 6.

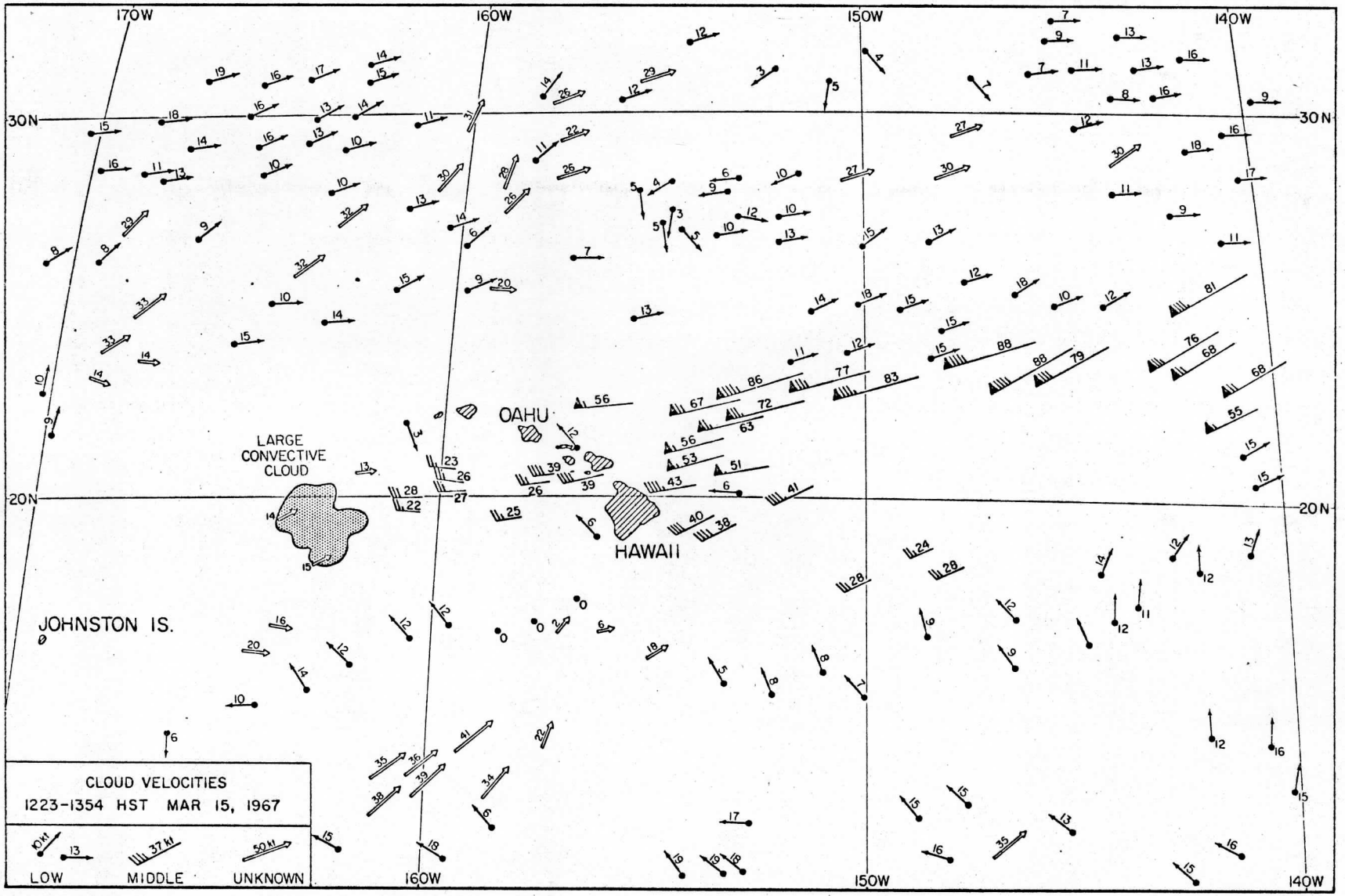
170W
160W
150W
140W
30N
20N
OAHU
HAWAII
LARGE
CONVECTIVE
CLOUD
JOHNSTON IS.
CLOUD VELOCITIES
1223-1354 HST MAR 15, 1967
10 KT
37 KT
50 KT
LOW
MIDDLE
UNKNOWN

FIG-7

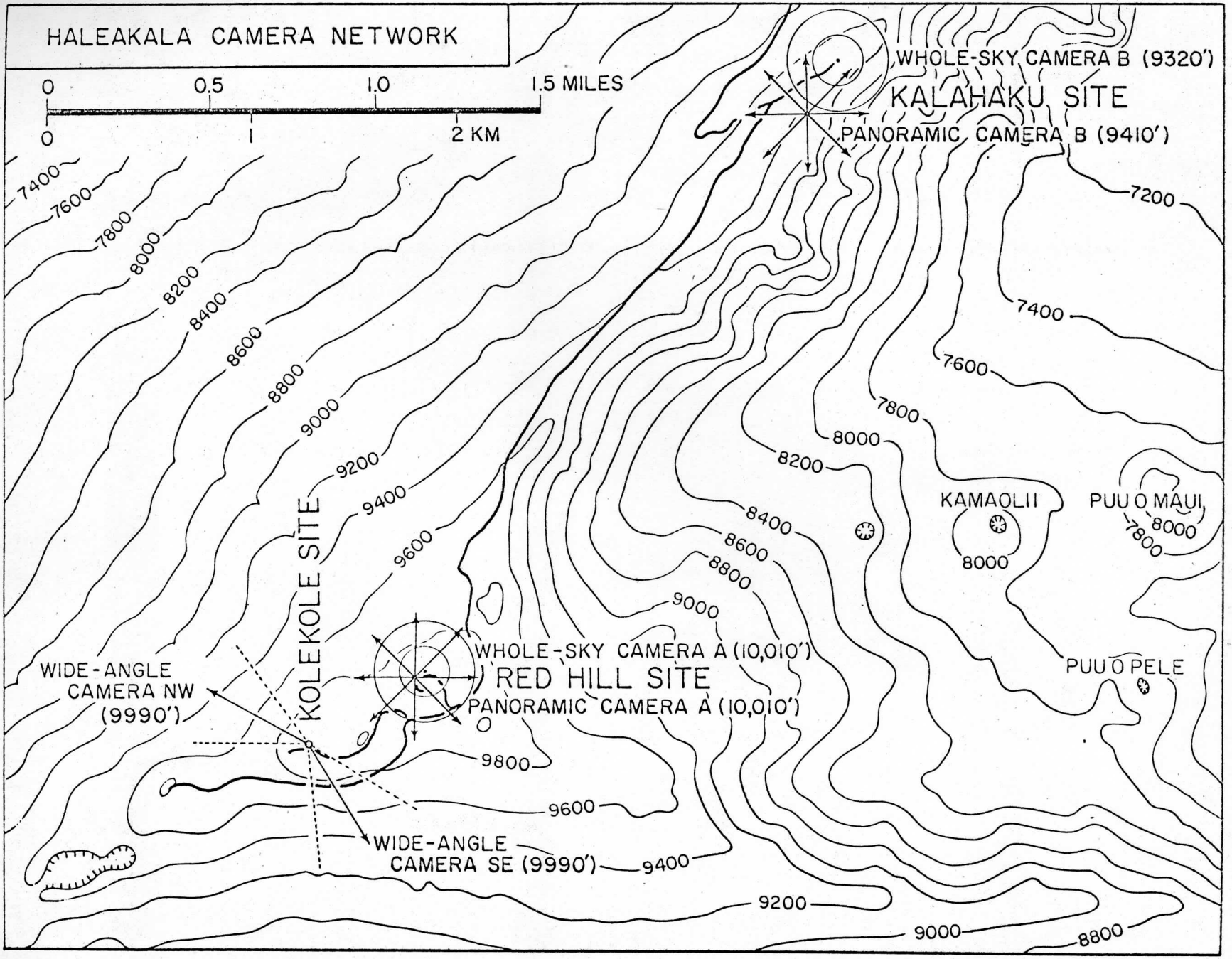
HALEAKALA CAMERA NETWORK
0
0.5
1.0
1.5 MILES
0
1
2 KM
WHOLE-SKY CAMERA B (9320')
KALAHAKU SITE
PANORAMIC CAMERA B (9410')
KOLEKOLE SITE
WHOLE-SKY CAMERA A (10,010')
RED HILL SITE
PANORAMIC CAMERA A (10,010')
WIDE-ANGLE CAMERA NW (9990')
WIDE-ANGLE CAMERA SE (9990')
KAMAOLII
PUU O MAUI
PUU O PELE
7400
7600
7800
8000
8200
8400
8600
8800
9000
9200
9400
9600
9800

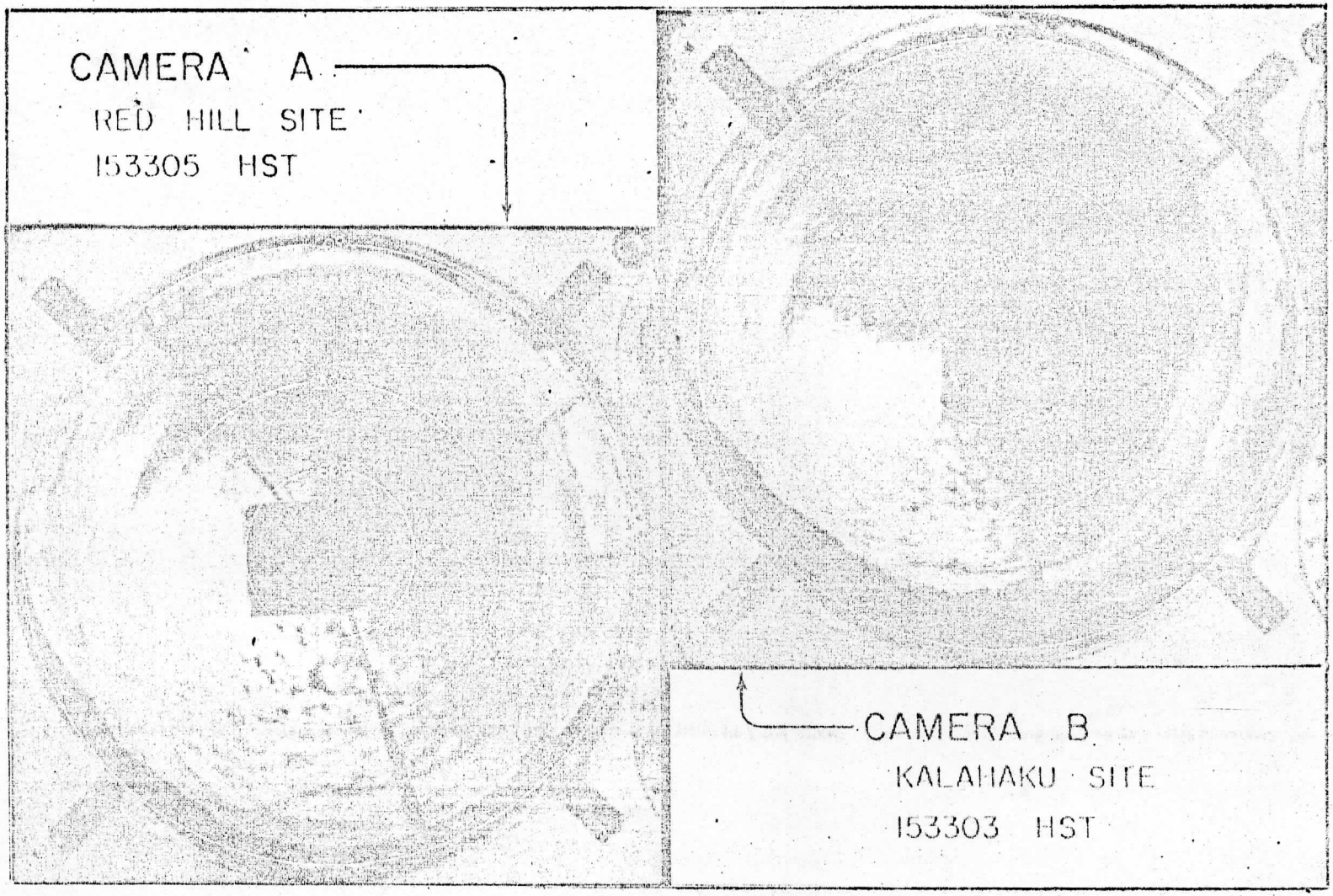
CAMERA A
RED HILL SITE
153305 HST
CAMERA B
KALAHAKU SITE
153303 HST

Fig 9

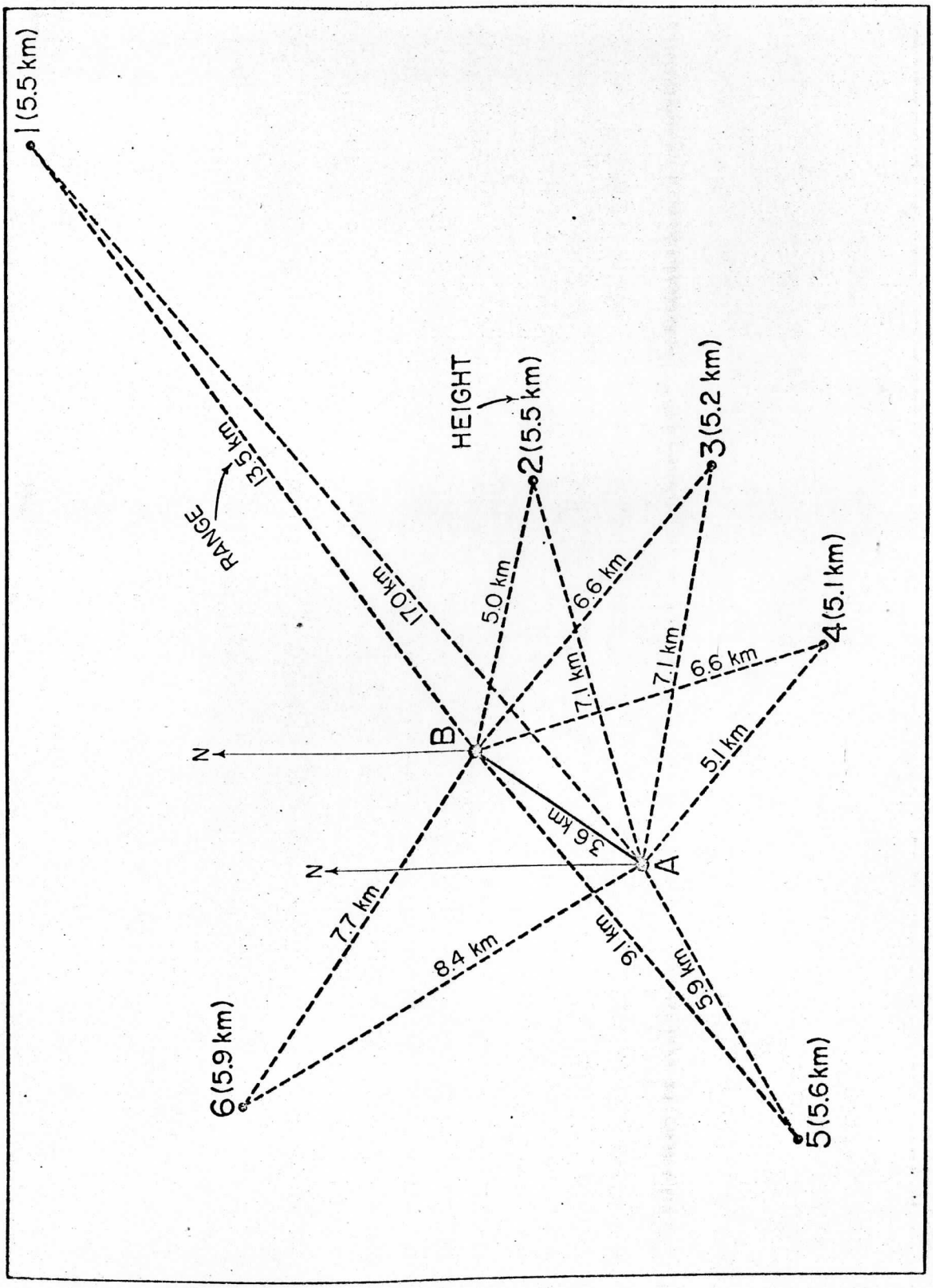
1 (5.5 km)
2 (5.5 km)
3 (5.2 km)
4 (5.1 km)
5 (5.6 km)
6 (5.9 km)
HEIGHT
RANGE
13.5 km
17.0 km
5.0 km
6.6 km
7.1 km
6.6 km
5.1 km
3.6 km
7.7 km
8.4 km
9.1 km
9.5 km
A
B
N
N

Fig 9

Fig. 10

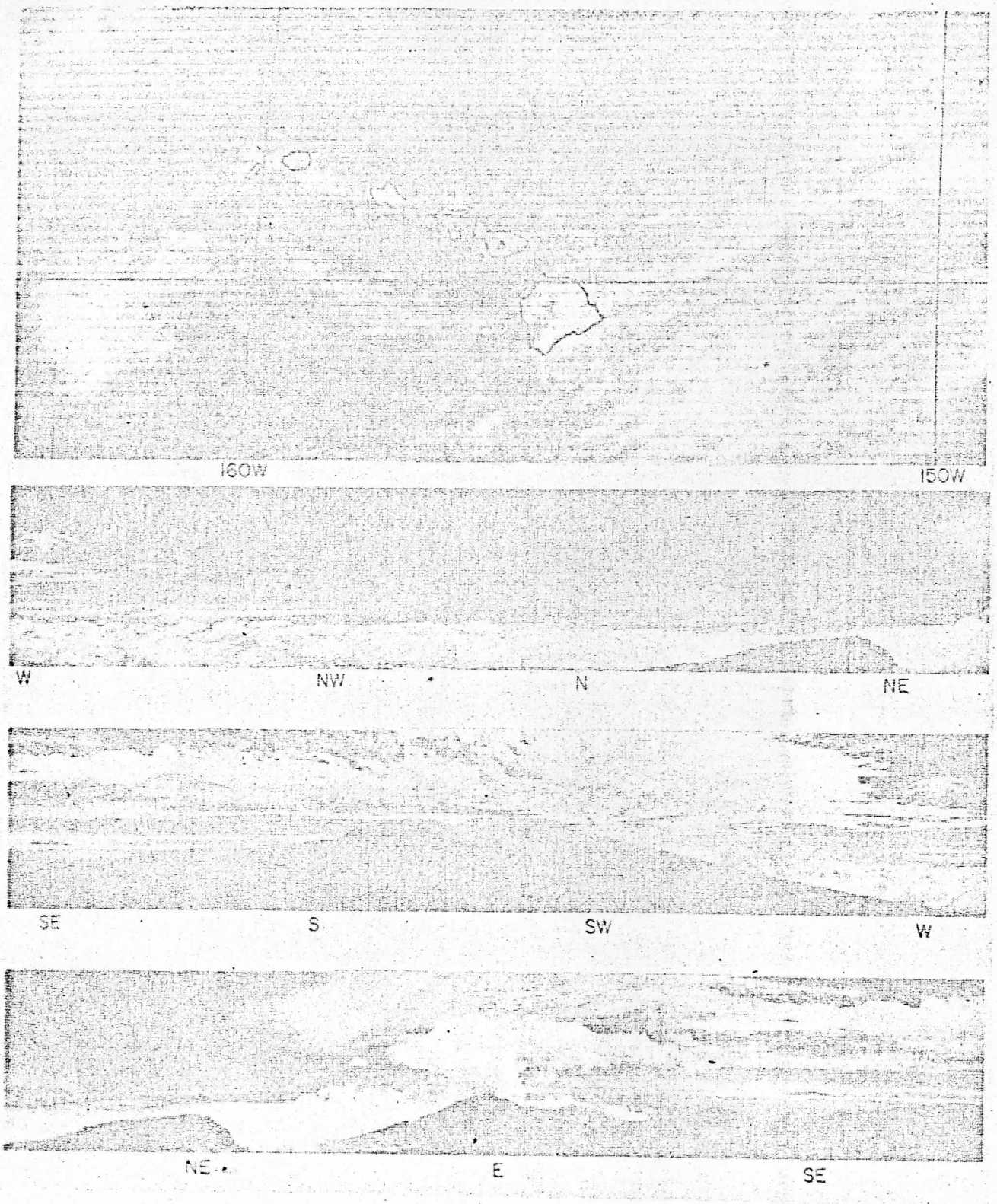

Fig-11

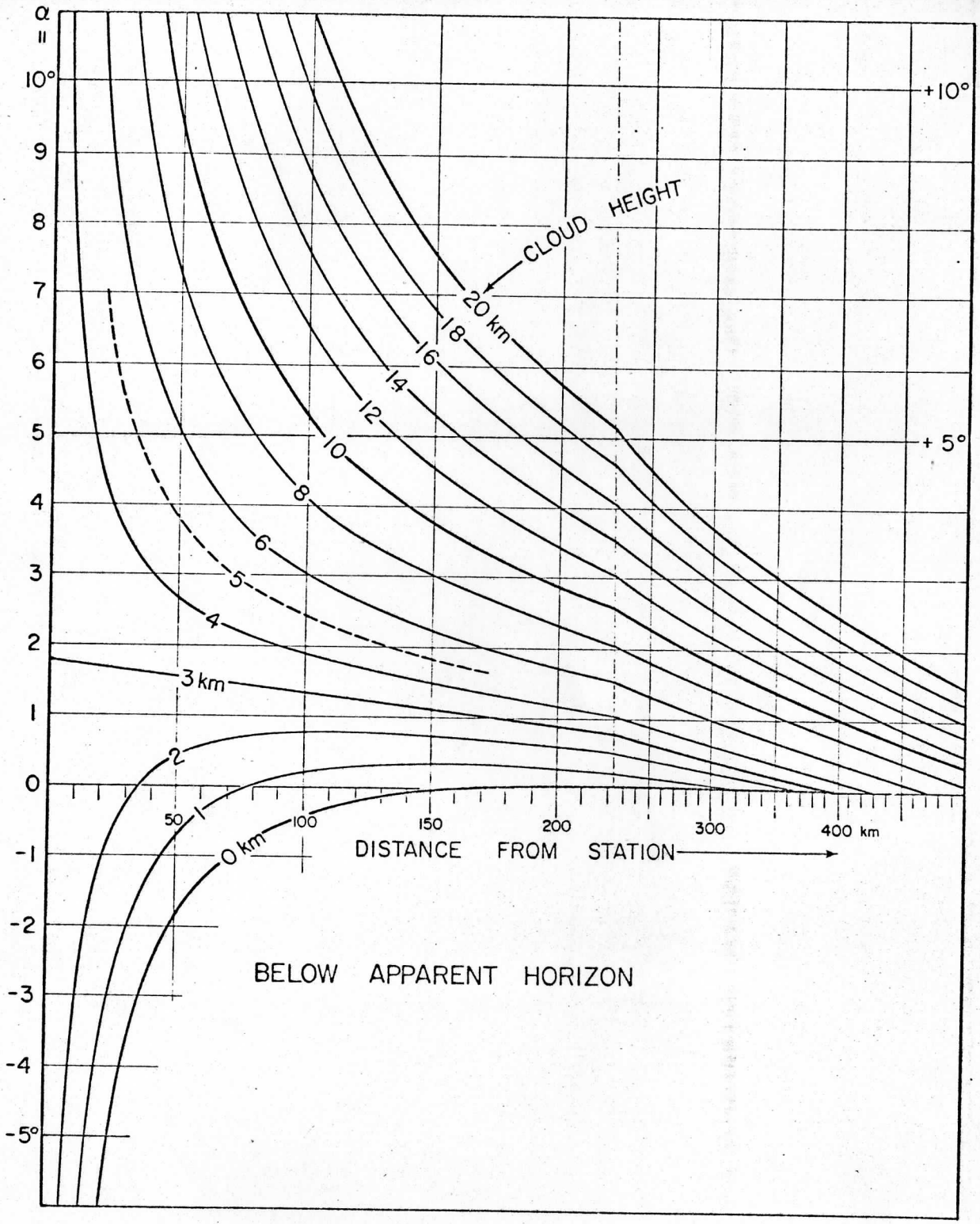
α
=
10°
9
8
7
6
5
4
3
2
1
0
-1
-2
-3
-4
-5°
+10°
+ 5°
CLOUD HEIGHT
20 km
18
16
14
12
10
8
6
5
4
3 km
2
1
0 km
50
100
150
200
300
400 km
DISTANCE FROM STATION
BELOW APPARENT HORIZON

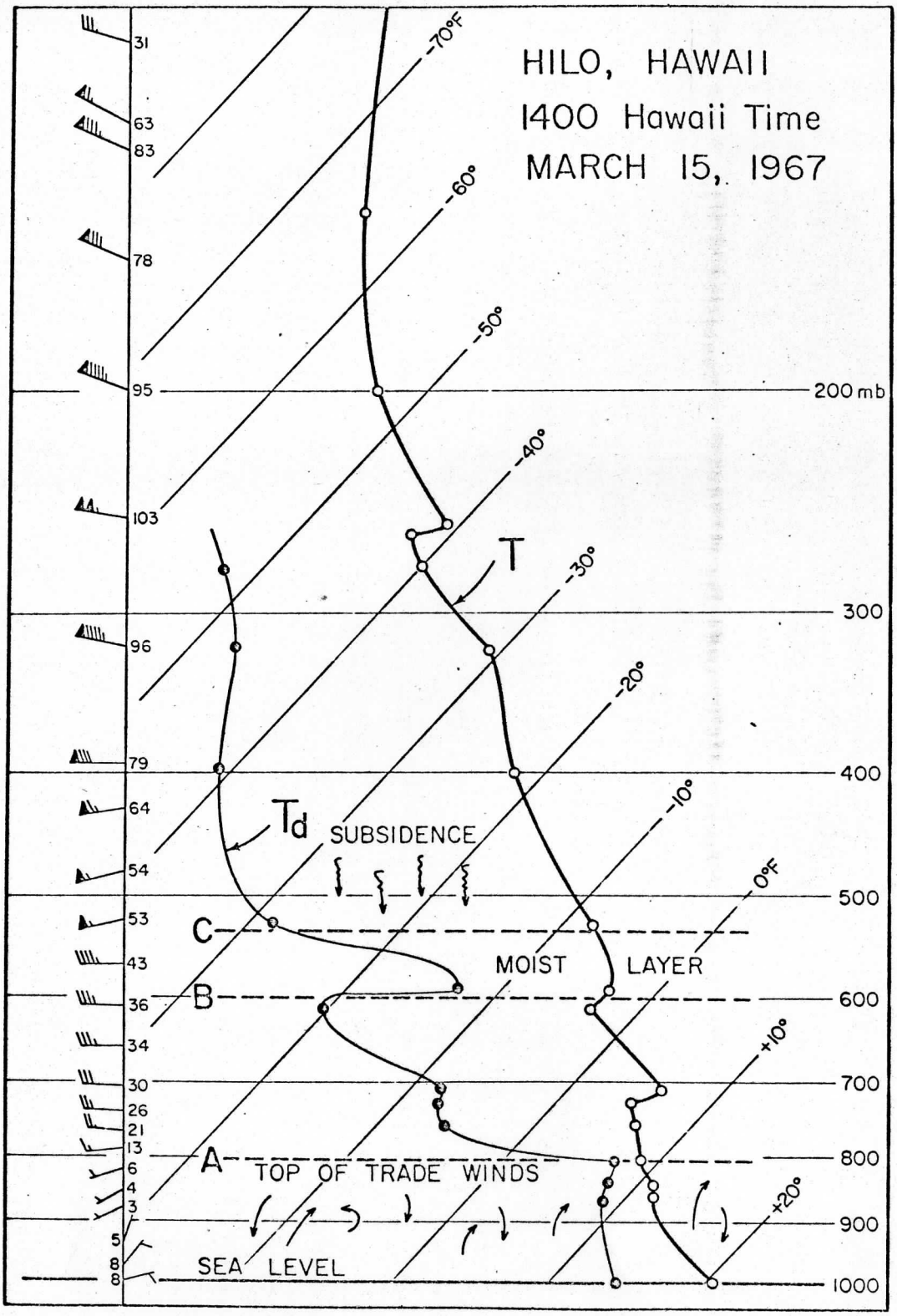
HILO, HAWAII
1400 Hawaii Time
MARCH 15, 1967
-70°F
-60°
-50°
-40°
-30°
-20°
-10°
0°F
+10°
+20°
200 mb
300
400
500
600
700
800
900
1000
31
63
83
78
95
103
96
79
64
54
53
43
36
34
30
26
21
13
6
4
3
5
8
8
T
Td
SUBSIDENCE
C
MOIST
LAYER
B
A
TOP OF TRADE WINDS
SEA LEVEL

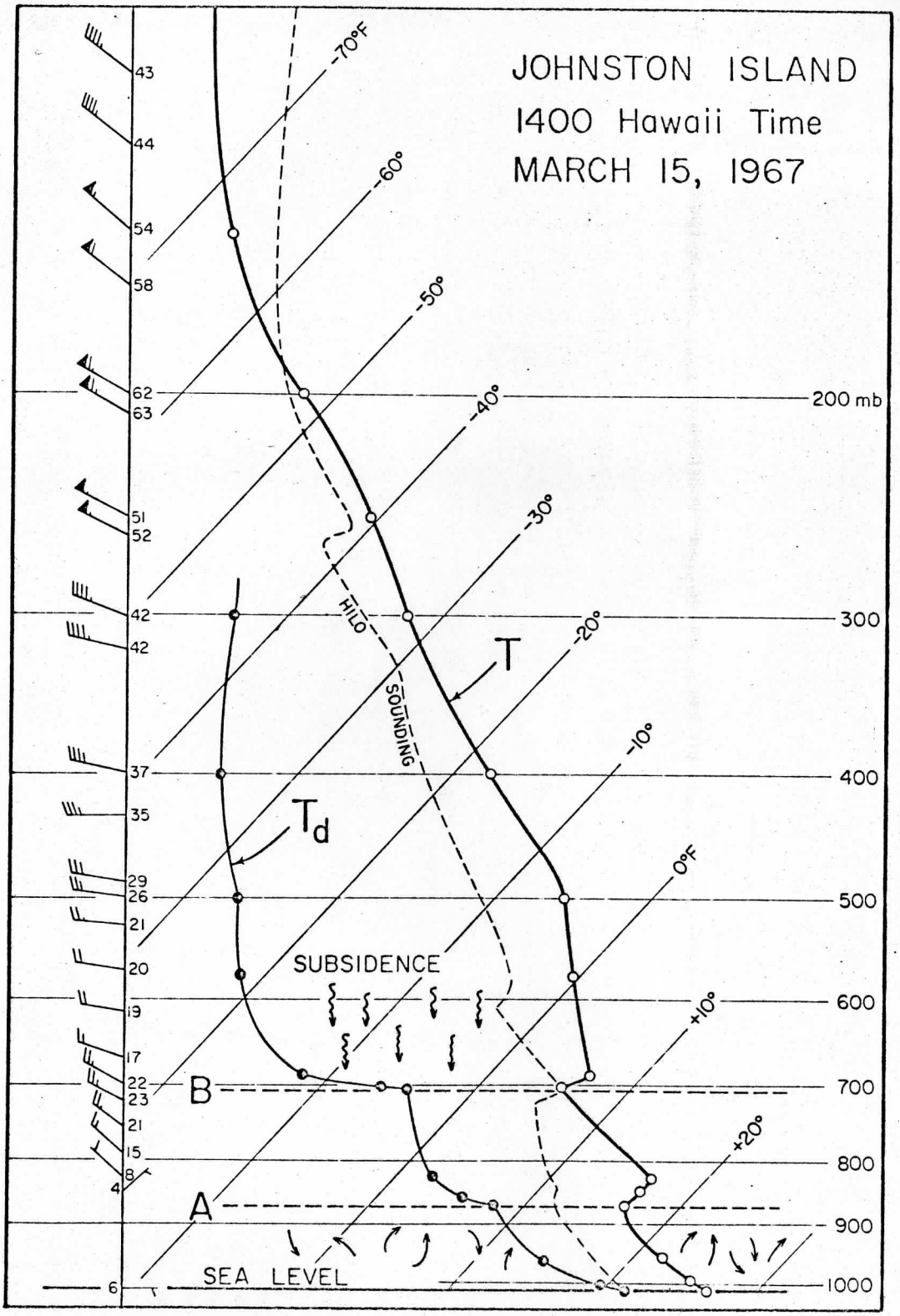
JOHNSTON ISLAND
1400 Hawaii Time
MARCH 15, 1967
-70°F
-60°
-50°
-40°
-30°
-20°
-10°
0°F
+10°
+20°
200 mb
300
400
500
600
700
800
900
1000
43
44
54
58
62
63
51
52
42
42
37
35
29
26
21
20
19
17
22
23
21
15
8
4
6
HILO
SOUNDING
T
Td
SUBSIDENCE
B
A
SEA LEVEL

Fig 14

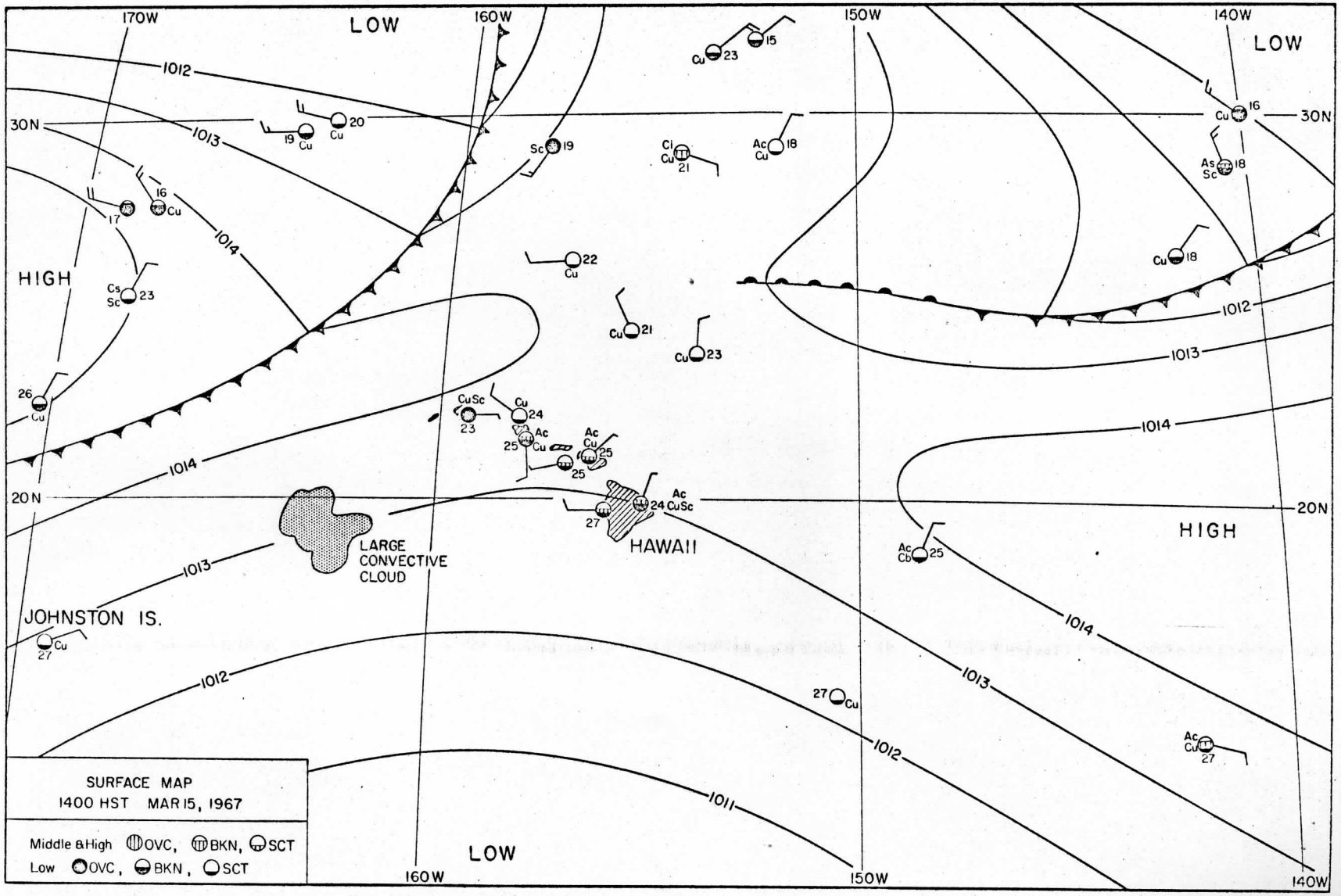
170W
160W
150W
140W
LOW
LOW
LOW
HIGH
HIGH
30N
20N
1012
1013
1014
1011
LARGE CONVECTIVE CLOUD
HAWAII
JOHNSTON IS.
SURFACE MAP
1400 HST MAR 15, 1967
Middle & High OVC, BKN, SCT
Low OVC, BKN, SCT

Fig 15

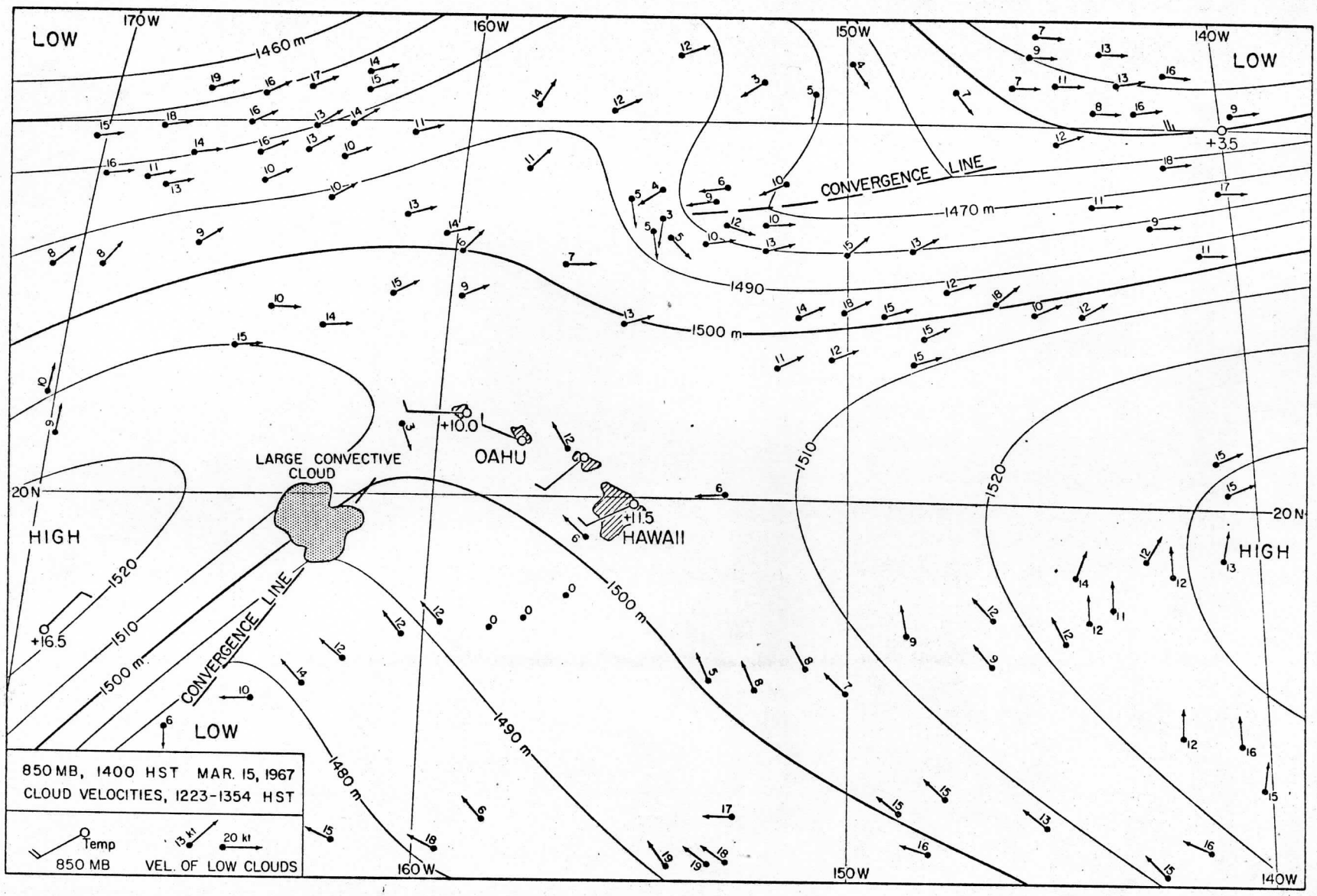
LOW
170W
160W
150W
140W
LOW
1460 m
1470 m
1490
1500 m
1510
1520
CONVERGENCE LINE
+3.5
+10.0
OAHU
LARGE CONVECTIVE CLOUD
+11.5
HAWAII
20N
HIGH
+16.5
CONVERGENCE LINE
1500 m
1490 m
1480 m
LOW
850 MB, 1400 HST MAR. 15, 1967
CLOUD VELOCITIES, 1223-1354 HST
Temp
850 MB
VEL. OF LOW CLOUDS

Fig. 16

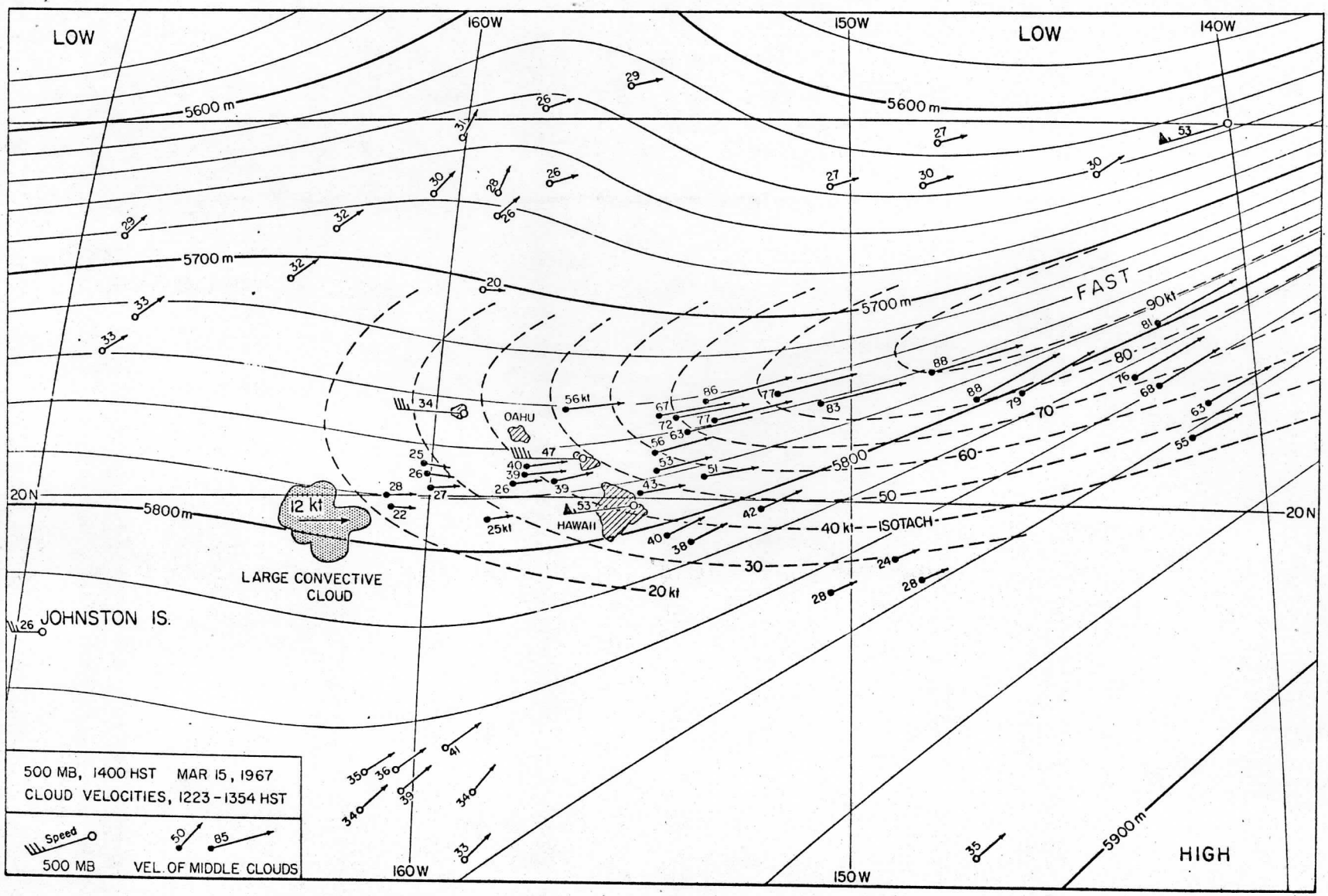
LOW
160W
150W
LOW
140W
5600 m
5600 m
5700 m
5700 m
FAST
90 kt
80
70
60
50
40 kt
ISOTACH
30
20 kt
5800
5800m
20N
20N
OAHU
HAWAII
56 kt
25 kt
12 kt
LARGE CONVECTIVE CLOUD
JOHNSTON IS.
5900m
HIGH
160W
150W
500 MB, 1400 HST MAR 15, 1967
CLOUD VELOCITIES, 1223 - 1354 HST
Speed
500 MB
VEL. OF MIDDLE CLOUDS

Fig 17

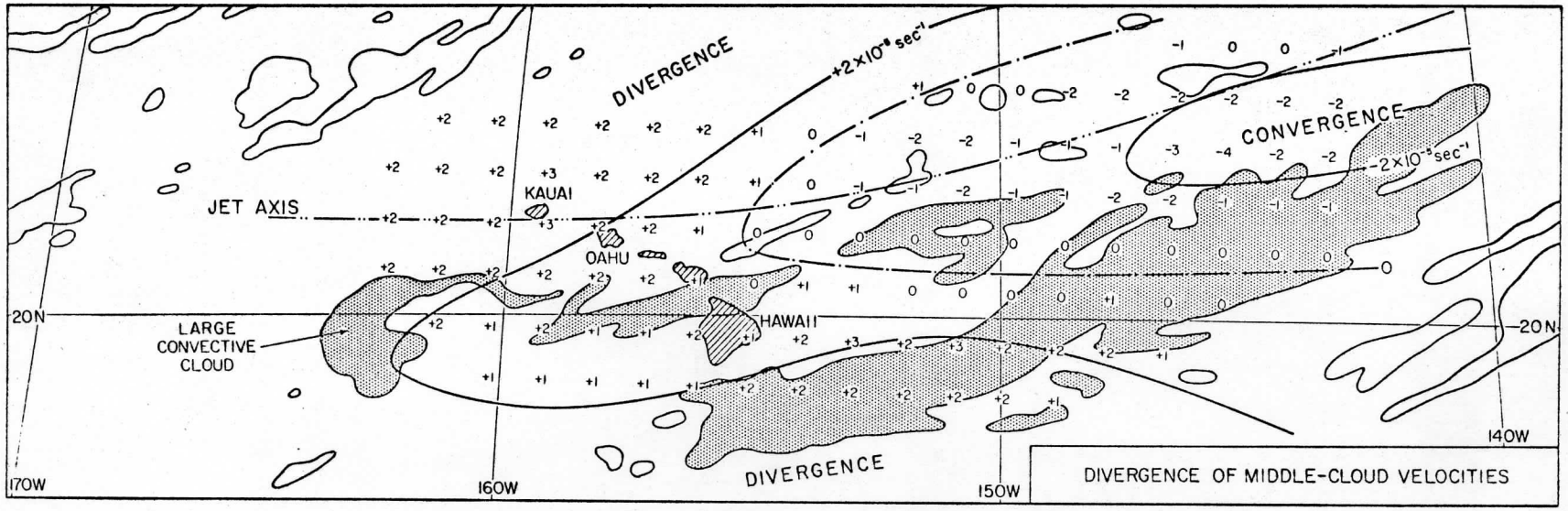

DIVERGENCE OF MIDDLE-CLOUD VELOCITIES

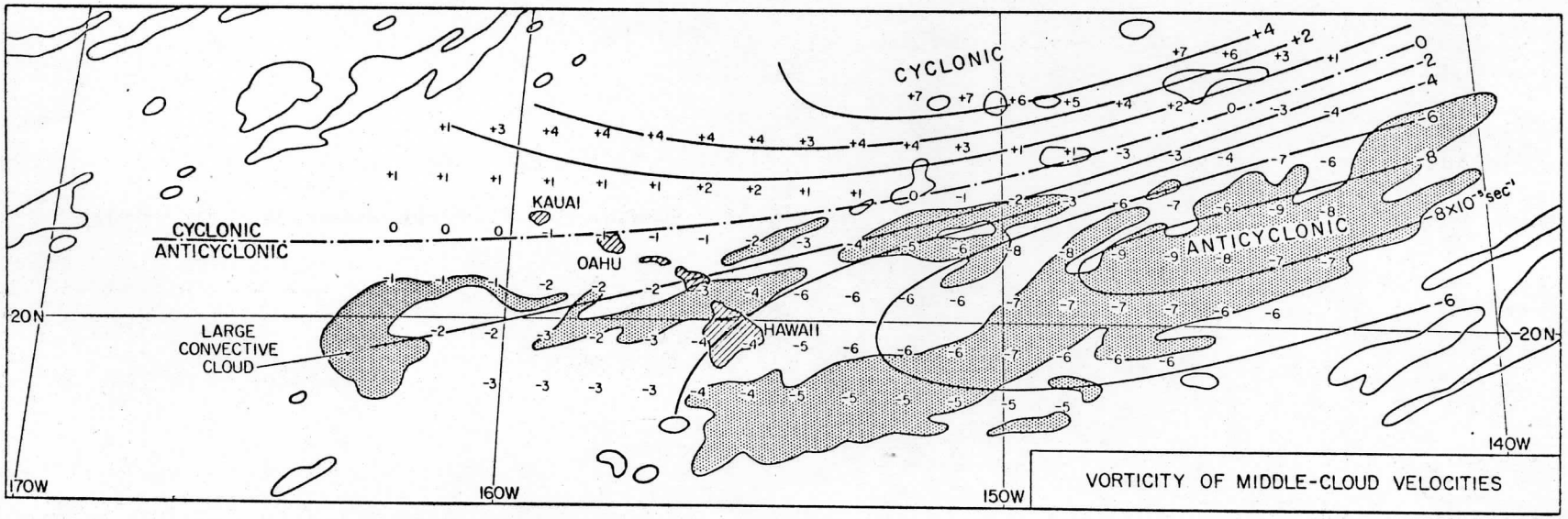

VORTICITY OF MIDDLE-CLOUD VELOCITIES

NOAA
(7)

CLOUD MOTION AND OTHER PARAMETERS FROM ATS - I DIGITAL DATA

by

Kirby J. Hanson
and
Thomas H. Vonder Haar

CONTENTS

1. Introduction
2. Tropical Cloud Motion and Divergence
3. Tropical Cloud Structure
   a. Polygon Shaped Cloud Ensembles
   b. Typhoon Sarah
4. Summary
5. Acknowledgment

1. INTRODUCTION

The ATS-I digital data recording system is designed to provide the maximum amount of quantitative brightness information from the ATS-I cloud camera. This is accomplished by storing cloud brightness data in a matrix which has the dimensions of approximately 2018 scan lines by 8196 picture elements. At each picture element in this matrix the cloud brightness is digitized on a scale from 0-255. Clearly, there is considerably more information on the ATS digital data than we are accustomed to seeing in the usual ATS pictures which are produced in real time at the NASA ground station and are intended to serve as a signal monitor.

In other papers in this volume, Whitney, et. al. have used the digital data to show the quality of cloud brightness data stored in this form, and have demonstrated the capability of discriminating clouds at various brightness thresholds. Also in this volume, Bristor, et. al. have examined the possibility of determining cloud displacement and growth using picture pairs of ATS digital data.

The purpose of our contribution to the volume is to give meteorologists a better idea of information in the digital data that may be useful to them in discriminating cloud motion and parameterizing cloud features. We have done this by treating examples of familiar clouds.

The first section of the paper treats low level cumulus embedded in the tropical easterlies. The cloud boundaries are discriminated using the digital data; cloud velocity and divergence fields are determined from a picture pair. The second section of the paper examines cloud ensembles in the tropics which are much brighter than low-level cumulus, and apparently are composed of deep convection. The cloud ensembles appear as rings or polygons, connected somewhat

as a chain. The horizontal dimensions of a typical polygon shaped cloud ensemble are given, assuming a certain cloud model. The last section of the paper illustrates the brightness contours of typhoon Sarah in the mid-Pacific on September 11, 1967.

Throughtout this paper the ATS-I digital data have been displayed using techniques developed at the Space Science and Engineering Center, University of Wisconsin. These programs are discussed in detail in this volume by Smith and Vonder Haar.

2. TROPICAL CLOUD MOTION AND DIVERGENCE

ATS-I digital data have been used to derive the wind field from cloud motions over a region of the equatorial Pacific. An area near the Line Islands on April 19, 1967 was chosen in order to compare the computed winds with observed winds from the same period. Two cloud maps of the same area were prepared from ATS-I pictures obtained at 2124 and 2148Z. These maps were constructed from digitized ATS-I measurements using a character display technique for computer output. On both maps the brightness threshold used to define cloud from no-cloud areas was set at 50 digital counts which are proportional to brightness. This relationship is discussed in other papers in this volume by Peekna et al. and by Hanson and Suomi.

In this test case the wind direction and speed were inferred from the movement of clouds. However, because of slight changes in satellite attitude relative to the earth, ATS-I pictures obtained only minutes apart do not view precisely the same areas. This causes an alignment problem between any two pictures which can significantly effect computed winds by adding an unreal component to cloud

displacements. In another paper in this volume, Hanson, et. al. have shown the ATS-I measurements can be correctly positioned without the aid of a land feature and that near the subsatellite point attitude changes cause primarily a north-south shift in the observed features. Using their technique, the two cloud maps were properly superimposed. Christmas Island is recognized on both maps and serves as an additional alignment check.

On the ATS-I photo in Fig. 1 the area (2-6°N; 157-163°W) in which the wind field was derived is shown in the small rectanglar area. Figure 2 illustrates the cloud patterns and Christmas Island as seen on the digital maps of this area. Solid lines mark the cloud boundaries on the 2124Z picture and dashed lines indicate the boundaries 24 minutes later. Differences between the two patterns can be caused by any combination of:

a) cloud motion

b) changing cloud size

c) changing cloud brigthness

An overall movement of the clouds toward the west is apparent in Fig. 2. In order to remove the random effects of (b) and (c), mean cloud displacements within each 1 X 1 degree latitude area were derived from many hand measurements of the apparent movement of cloud centers and edges. These displacements were converted into normal components of the wind within each 60 n. mi. square area. For this test case, it is assumed that these values represent the average wind direction and speed within the cloud layer.

Figure 3 shows the computed winds and the divergence field derived from the $\underline{u}$ and $\underline{v}$ wind components. Of course, no winds are obtained from cloud-free areas. On the same illustration, a sketch of the major cloud regions is shown. Although the cloud systems are probably better related to convergence patterns in the

sub-cloud layer, the general alignment of clouds and features of the wind field is good. Together they depict a weak wave embedded in the easterly flow. Subsequent ATS pictures show that the cloud pattern retained its shape and intensified west of the test area during the next 24 hours. Computed winds ranged from 15 to 25 knots and from 60 to 110 degrees. These values together with others derived near the border of the area shown were used to compute divergence magnitudes of $\pm$ 3 X 10^{-5} sec^{-1}.

Normally, very few standard meteorological observations are available for this region. On April 19, 1967, however, the Line Island Experiment (LIE) was still in progress and some surface, upper air and aircraft data were obtained at various locations within our test area. (A data summary of the LIE is given in the Appendix of this volume). Thus, it was possible to assess the computed winds against observed.

Synoptic data obtained within three hours of the picture times are available and at some locations aircraft wind measurements are available for more than one level. Both surface and aircraft (B-47) observations reported only cumulus clouds over the area with bases at 2000-2500 feet. Aircraft data at points X, Y and P on Figure 3 placed the top of the primary cloud layer near 6000 feet. At Y scattered cumulonimbus towers reaching 22,000 feet were also reported.

Because these data indicate measured cloud displacements pertain to the lower troposphere, wind observations below 6000 feet near P, F and C were used to check the computed winds. The comparison in Table 1 contains both windspeed in knots (VV) and direction in degrees (DDD). Computed and observed winds are in close agreement considering the uncertainty in altitude determination.

Since the above comparison is limited by the representativeness of the observed data, perhaps a better test of the computed winds is the overall

meteorological situation they depict. Figure 3 shows a weak wave embedded in moderate easterly flow with cloud regions lying along the wave axis and greatest vertical development found at the location of maximum low level convergence. Neither the scattered meteorological observations, nor individual cloud pictures could provide such a complete description of the typical tropical conditions which are evident from displacement and divergence patterns which two pictures allow. This test case demonstrates the usefulness of wind and divergence fields computed from the ATS digital data for the study of meso-scale weather patterns. It also suggests that a more automated technique using digital data cloud yield realistic winds on an operational basis.

The latter application is currently under investigation and tests not reported here but similar to that described in this study have shown that:

a) strong vertical wind shear can be detected from the ATS digital data,

b) changing cloud brightness or size may obscure cloud motions when the time period between two view of the same area exceeds one and one-half hours,

c) optimum cloud brightness thresholds or gradients must be derived to adequately represent the presence or absence of clouds.

Further work in these areas and on operationally registering the digital pictures will allow us to make maximum use of these high resolution, quantitative digital data for remote wind measurements.

3. TROPICAL CLOUD STRUCTURE

a. Polygon Shaped Cloud Ensembles

In looking at cloudiness of the tropical Pacific on ATS-I pictures, one is struck by the great amount of organization to the clouds. In one of the lower

scales of organization discernable in the ATS pictures, we notice a great deal of the cloudiness forms into polygons of various shapes and distortions. Typical examples of polygon shaped cloud ensembles are seen in Figure 4. In that picture one can see that not only clouds within the white bordered area are organized in this way but many of the remaining clouds as well. In the present study, however, we have considered only clouds in the enclosed area of Figure 4. These clouds are depicted by computer display of the digital data and are shown in Figure 5. In that illustration, clouds appear as the whitest areas. The lower brightness contour which outlines the cloud has a value of 54 digital counts and the higher contour 63 digital counts. The various cloud ensembles in Figure 5 have been designated 1, 2 and 3 to facilitate discussing them.

Cloud ensemble 1 is a relatively large cloud group in which the northern section of the cloud ring is absent. Perhaps this shape results from moderate vertical wind shear which tends to form such U-shaped cloud cells (Rogers, 1965). The horizontal brightness gradient is very steep along the edges of the cloud band. This is evident in Figure 6, for example, which shows the brightness cross section of scan line 970. It is clear that brightness values within the polygon are about 25 but increase to over 100 at the cloud edge. In Figure 7 we have contoured the brightness of this cloud ensemble from a lowest contour of 50, which outlines the cloud, to a highest contour of 175 which appears as the smallest closed contours within the "tic" marked areas. The contour with "tic" marks is 125. From this illustration it is clear that such ensembles are made up of organized deep convection and that there is continuity of brightness associated with this convection. Clearly, it is possible to identify the brightest areas in such polygon shaped cloud ensembles and thereby identify the deepest

convective elements that make up the polygon.

Two other cloud groups, ensembles 2 and 3 of Figure 5, are contoured in greater detail in Figure 8. These ensembles appear to have somewhat smaller horizontal dimensions than ensemble 1.

If much of the convection in the tropics is organized into polygons, as it appears to be in ATS pictures, then it is important to determine the feasibility of obtaining the dimensions of such polygons using the digital data. These dimensions provide necessary input to cloud models where such parameterization is required. We have picked ensemble 2 to study this feasility.

In order to study ensemble 2, let us assume two cloud Models, A and B, as shown in Figure 9. Cloud Model A is similar to that suggested by Kuo (1961), and Asai (1967), among others. In this model the boundary is taken through the center of the cloud bands; thus vertical motion is upward along the boundary. Model B differs from Model A in that it includes all of the cloud ensemble within the model boundary. In this model the boundary is through the cloudless areas; therefore the vertical motion along the boundardy is downward.

When Model A is applied to cloud ensemble 2 and average values of a and b are computed, we find there are two distinct domains of cloudiness. As shown in the top of Figure 10, the small gradient of brightness from radius 0 to 21 miles indicates one cloud domain within the polygon, and the greater brightness gradient from 21 to 31 miles radius indicates another. The second apparently is deep convection in the polygon cloud ring. The calculated values of a and b do not depend, to any significant extent, on a precise selection of the polygon "center", providing the central point is located somewhere near the visual center of the polygon.

When Model B is applied to ensemble 2, we are able to observe the average

brightness cross section for the entire ensemble; this is shown in the top of Figure 11. It is apparent that the horizontal brightness slope on the inside ($\bar{a}$) and outside ($\bar{a}'$) of the polygon are very similar. Furthermore, there appear to be discernable domains of cloudiness outside the polygon, as well as inside. Thus, parameters r_1 and r_2 in Figure 11 are useful for defining the horizontal dimensions of such cloud ensembles. These parameters can be determined from brightness gradient alone; absolute values of brightness are not required.

For certain cloud models, such as that given by Asai (1967), it is useful to determine the parameters a and b, as defined in Model A. We have obtained these constants by planimetering the "clear" area of ensemble 2 in Figure 10 corresponding to brightness values less than that associated with the cloud domain boundary, r_1, and also by planimetering the total area within the model boundary. The results, given in Table 2, show the inner "clear" area covers 48 percent and the outer cloud area 52 percent of the total area. This is in general agreement with the areas covered by clouds in cellular cloud patterns, reported by Krueger and Fritz (1961). They observed cellular patterns with horizontal diameters as large as 30-50 miles and with "clear" centers bounded by cloud elements about 10-15 miles wide. Such cellular patterns would have cloud areas which average about 53 percent of the total area. Both these observations of polygon shaped cloud ensembles indicate considerably more cloudiness than suggested by theoretical considerations for maximum heat transport (3 to 16 percent) by Asai (1967). However, Asai's Model has the opposite circulation to that reported here, and by Krueger and Fritz.

The data in Figure 10 and 11 indicate that ATS digital data can be used to determine a variety of descriptive parameters for defining the horizontal dimen-

sions of tropical cloud ensembles. In addition, brightness values may also give the clouds' vertical dimensions. Perhaps the most important capability of the ATS-I data is that growth and decay of clouds can be studied in great detail using pictures at 20 minute intervals.

b. Typhoon Sarah

Typhoon Sarah was a mature tropical disturbance in 1818GMT on September 11, 1967, several days before she struck Wake Island. The ATS picture of Typhoon Sarah at the time is shown in Figure 12. The enclosed area is also illustrated in the computer produced digital data display of Figure 13. The lowest brightness contour there is 16 and the highest is 48. The structure of cloud bands in the typhoon is clearly discernable. Brightness cross sections of Typhoon Sarah are given in Figure 14. The cloud band structure of the storm is also evident in these cross sections. For example, scan line 675 shows three distinct bands within the typhoon. Scan line 660 is through the eye of the typhoon and shows a minumum brightness in the eye and also a brightness peak corresponding to the illuminated west wall of the eye.

Obviously, there is considerable information in the digital data on band structure of the typhoon in spite of the fact that the storm was near the terminator at the time of the picture.

4. SUMMARY

The ATS digital data have been used to determine cloud displacement and divergence of low-level convection in the tropics. Both the speed and direction of the winds agree quite well with wind measurements below and within the cloud layer. The digital data have also been used to determine parameters for de-

fining the horizontal dimensions of cloud ensembles which are made up of deep tropical convection. It was found that such ensembles can be parameterized by examining the horizontal brightness gradient and integration of cloud area. Parameters for a typical polygon shaped cloud ensemble have been determined and are presented. Typhoon Sarah is illustrated with the digital data, and the detailed band structure of the typhoon is clearly evident.

These three applications of ATS-I digital data show that quantitative, high-resolution measurements from a geosynchronous satellite provide a data resource that promises to be of value for operational wind calculations and for studies of cloud physics and dynamics.

5. ACKNOWLEDGMENTS

This research was supported by grants from ESSA and NASA. The computer programs used to display the ATS data were written by Mr. Eric Smith and Mrs. Marilyn Mantei.

TABLE 1

COMPUTED AND OBSERVED WIND SPEEDS AND DIRECTIONS

Lat. (deg. N)	Long. (deg. W)	Observed Speed (VV)	Observed Direction (DDD)	Computed Speed (VV)	Computed Direction (DDD)
5.5	162.0	15	080	22	075
3.5	160.0	15	095	15	080
2.0	158.5	Missing	110	35	100

TABLE 2

Parameters		Values
$(a/b)^2$	-	0.48
(a/b)	-	0.69

REFERENCES

1. Asai, T., 1967: On the Characteristics of Cellular Cumulus Convection. J. Meteor. Soc. Japan, 45, 251-260.

2. Krueger, A., and S. Fritz, 1961: Cellular Cloud Patterns Revealted by TIROS I. Tellus, 13, 1-7.

3. Kuo, H., 1961: Convection in Conditionally Unstable Atmosphere. Tellus, 13, 441-459.

4. Rogers, C., 1965: A Technique for estimating Low Level Wind Velocity from Satellite Photographs of Cellular Convection. J. Appl. Meteor., 4, 387-393.

ILLUSTRATIONS

TABLES

1. Computed and Observed Wind Speeds and Directions.

2. Model A applied to cloud ensemble 2. The ratio $(a/b)^2$ is the "clear" area relative to the total. The ratio (a/b) is the radius of the "clear" area.

FIGURES

1. ATS-I picture for 2148GMT, April 19, 1967.

2. Cloudiness in the Line Island Region (Fig. 1). Solid cloud boundaries are for 2124GMT and dashed boundaries for 2148GMT, April 19, 1967.

3. Clouds, winds and divergence pattern based on cloud motion of Figure 2. Divergence units are 10^{-5} sec^{-1}.

4. ATS-I picture for 202700GMT, April 26, 1967.

5. ATS digital data depiction of cloud structure in enclosed area of Fig. 4. Heavy horizontal lines correspond to the scan lines in Fig. 6. The three cloud ensembles noted in this illustration are shown in greater detail in other illustrations.

6. Brightness plots for scan lines in Figure 5.

7. Brightness contours for cloud ensemble 1 shown in Fig. 5. Scan lines 954 and 970 in Fig. 6 show a brightness crossection of this cloud ensemble. Minimum brightness contour is 50. Maximum contour is 175 digital counts.

8. Brightness contours for cloud ensembles 2 and 3 in Figure 5. Scan line 970 in Figure 6 shows the brightness crossection through cloud ensemble 2. Minimum brightness contour is 54. Maximum brightness contour is 150 digital counts.

9. Definition of cloud modeling parameters for two models. Light areas indicate cloud bands.

10. Upper graph indicates cloud parameters a and b determined for Model A on cloud ensemble 2, shown in the lower illustration.

11. Upper graph indicates cloud parameters a, and b determined for Model B on cloud ensemble 2, shown in the lower illustration.

12.- ATS-I picture for 1818GMT, September 11, 1967. Typhoon Sarah is visible in the enclosed area located about 100 miles southwest of Honolulu, Hawaii, near 18° North, 165° West.

13. Typhoon Sarah at 1818GMT, September 11, 1967. The dark horizontal lines are scan lines which in Figure 14 show brightness cross sections of Typhoon Sarah.

14. Brightness cross sections of Typhoon Sarah in Figure 13.

Fig 1

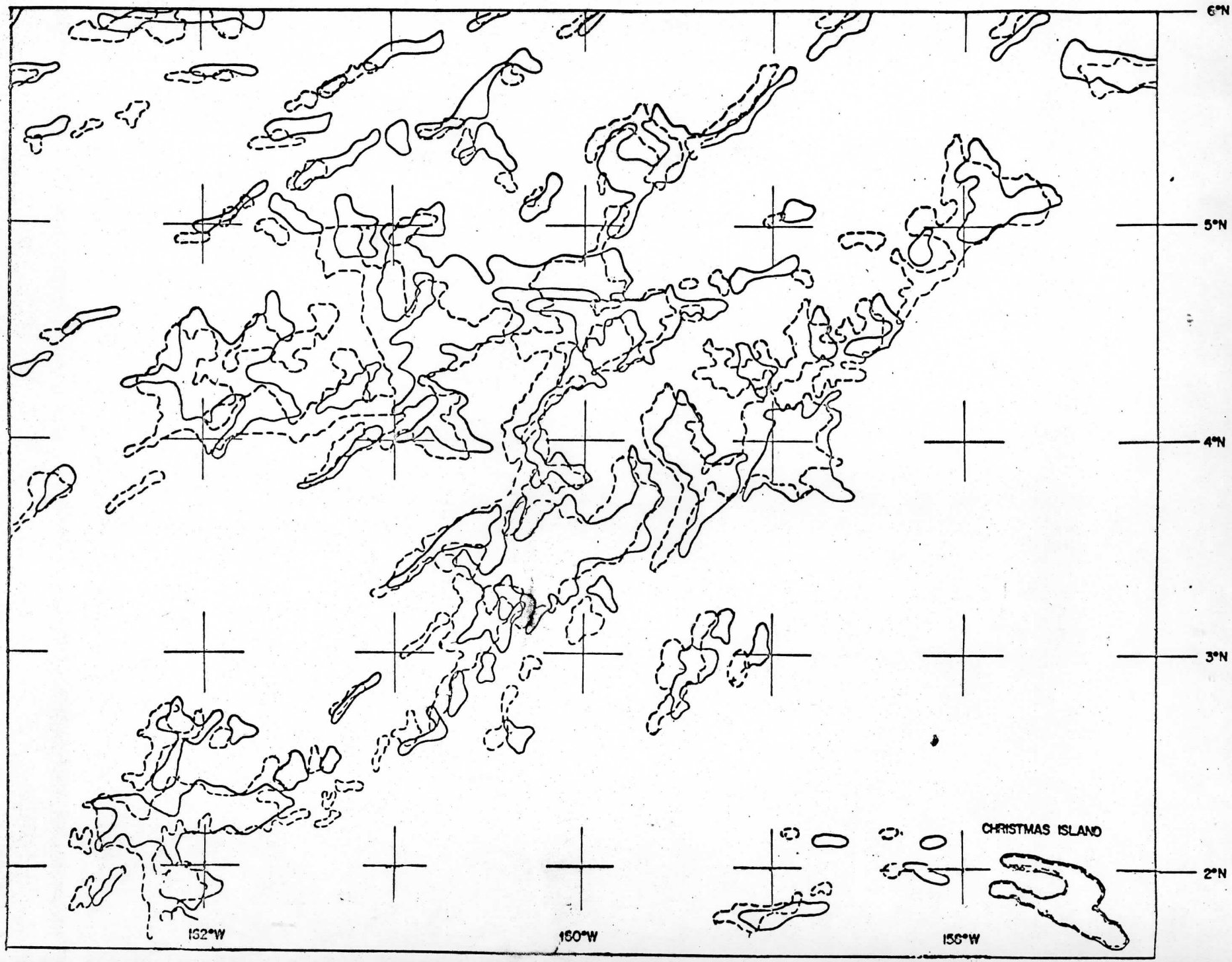

Fig 2

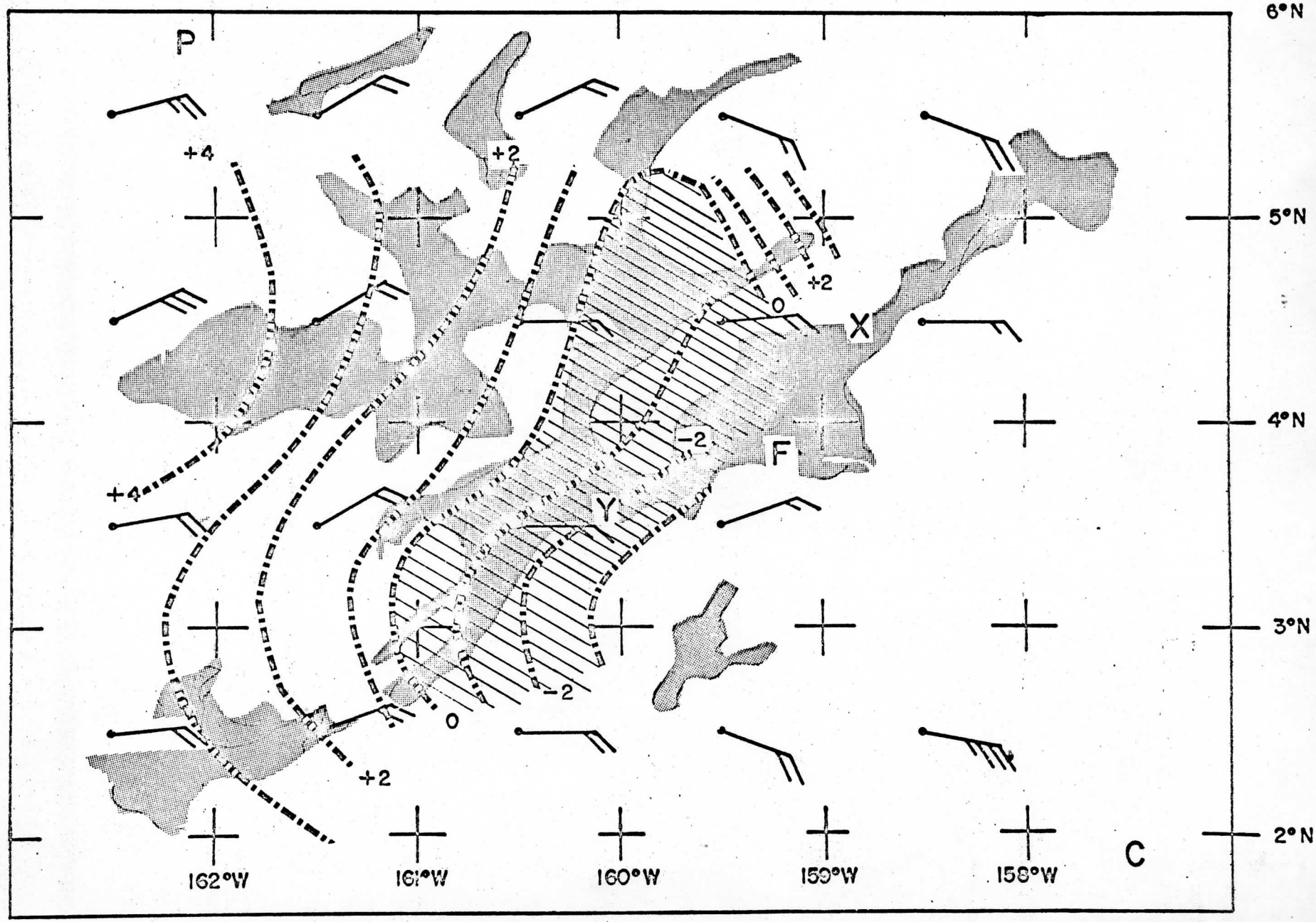

Fig 3

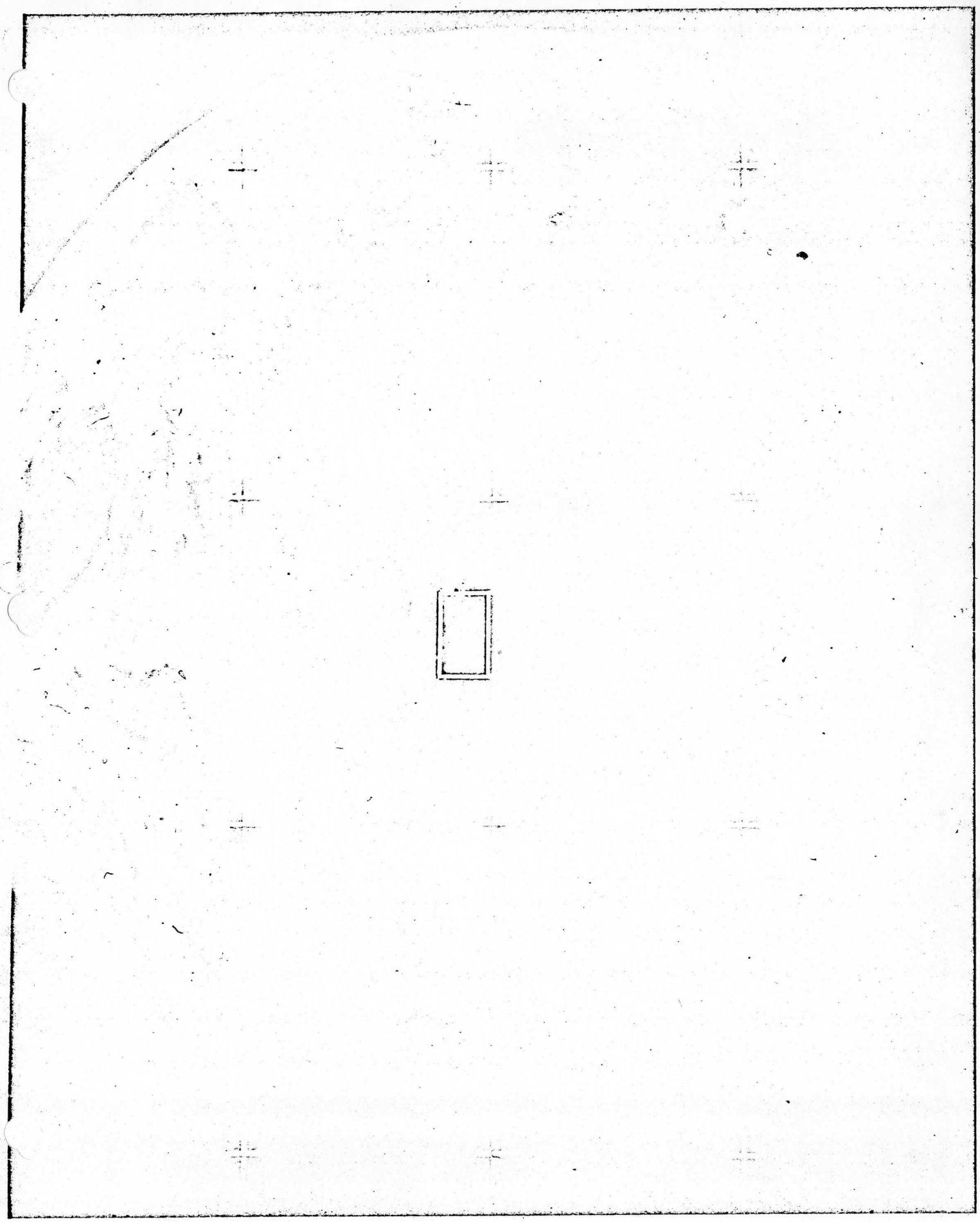

Fig 4

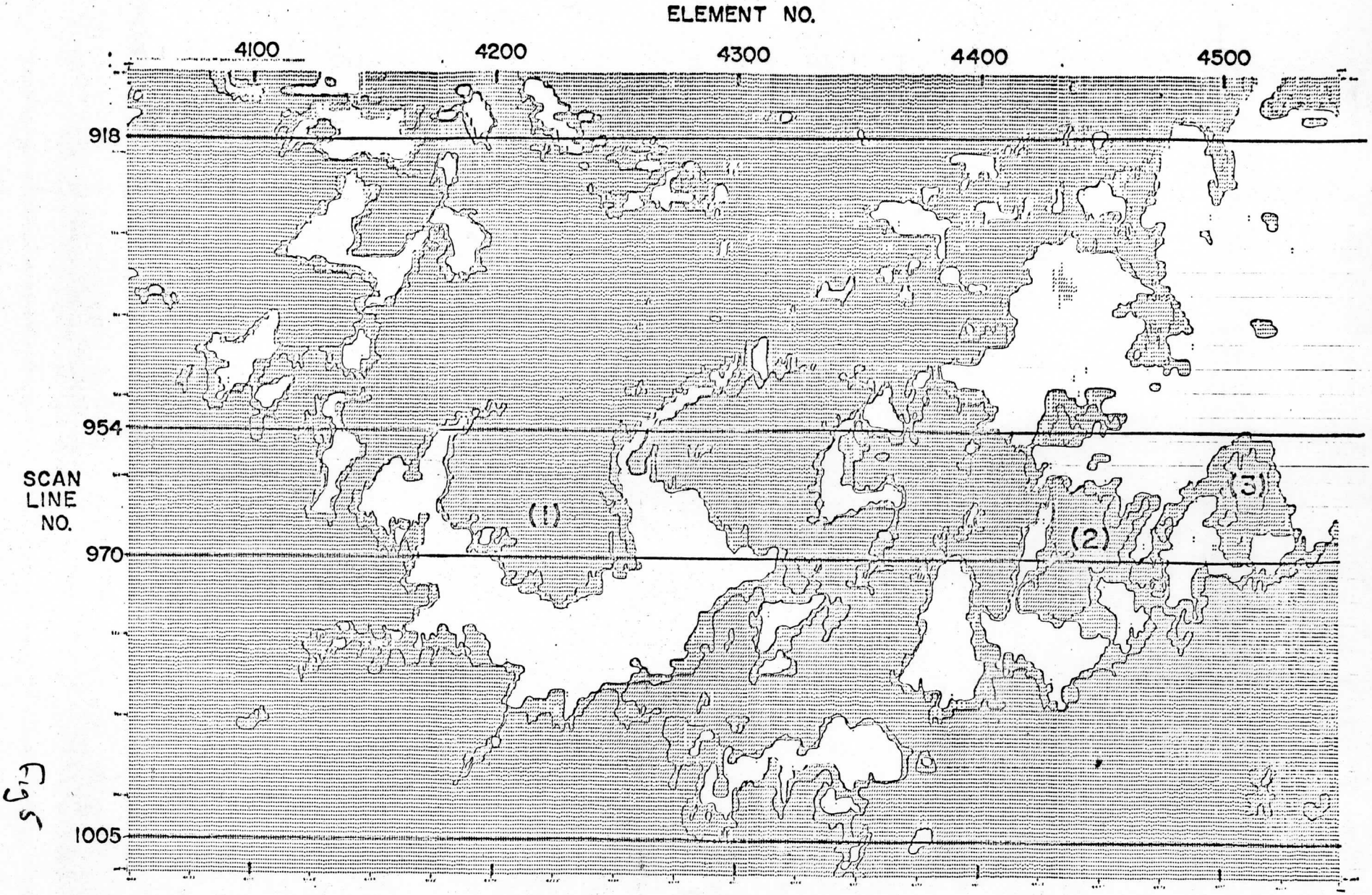
ELEMENT NO.
4100
4200
4300
4400
4500
SCAN LINE NO.
918
954
970
1005
(1)
(2)
(3)

Fig 5

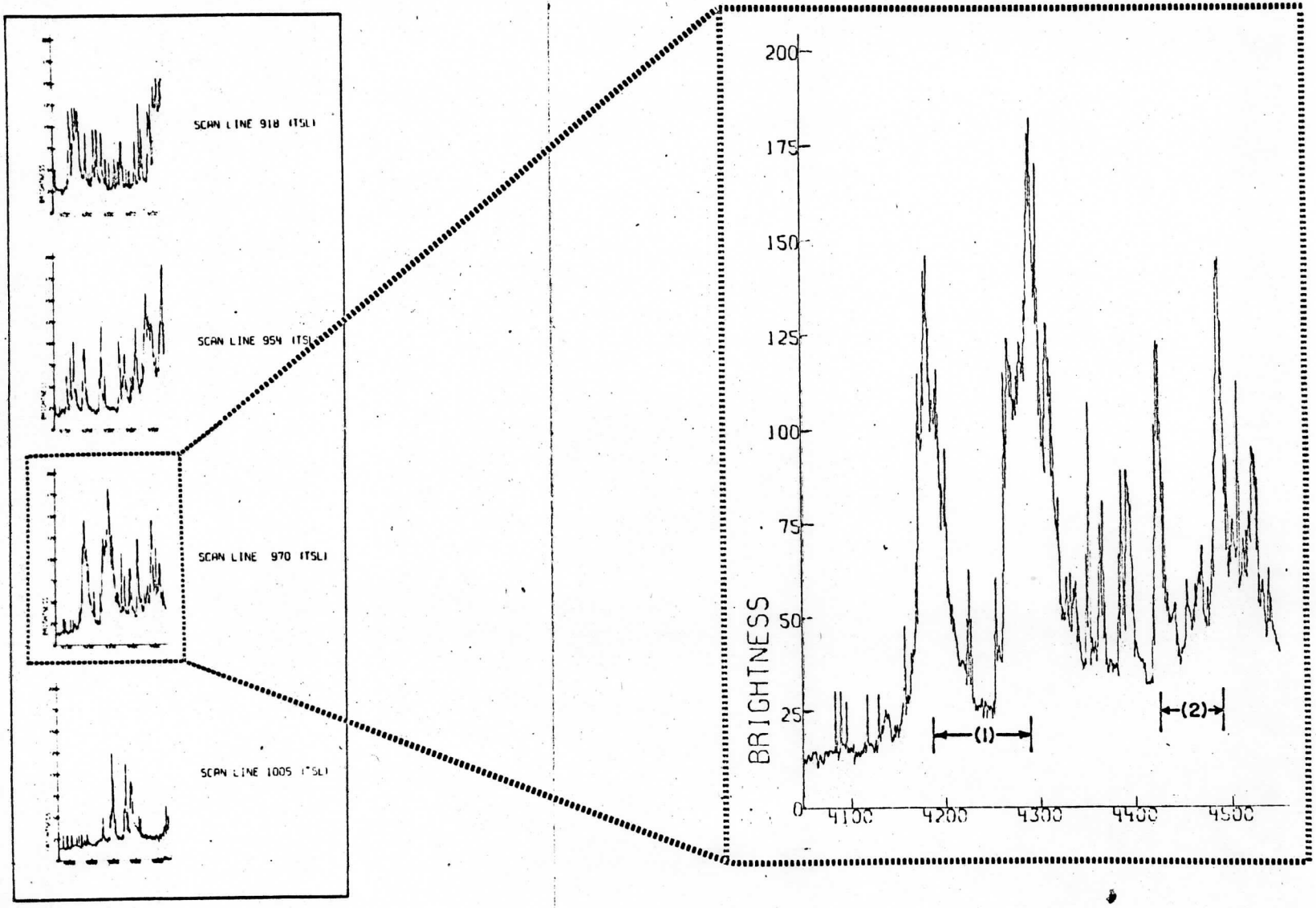
SCAN LINE 918 (TSL)
SCAN LINE 954 (TSL)
SCAN LINE 970 (TSL)
SCAN LINE 1005 (TSL)
BRIGHTNESS
200
175
150
125
100
75
50
25
0
4100
4200
4300
4400
4500
(1)
(2)

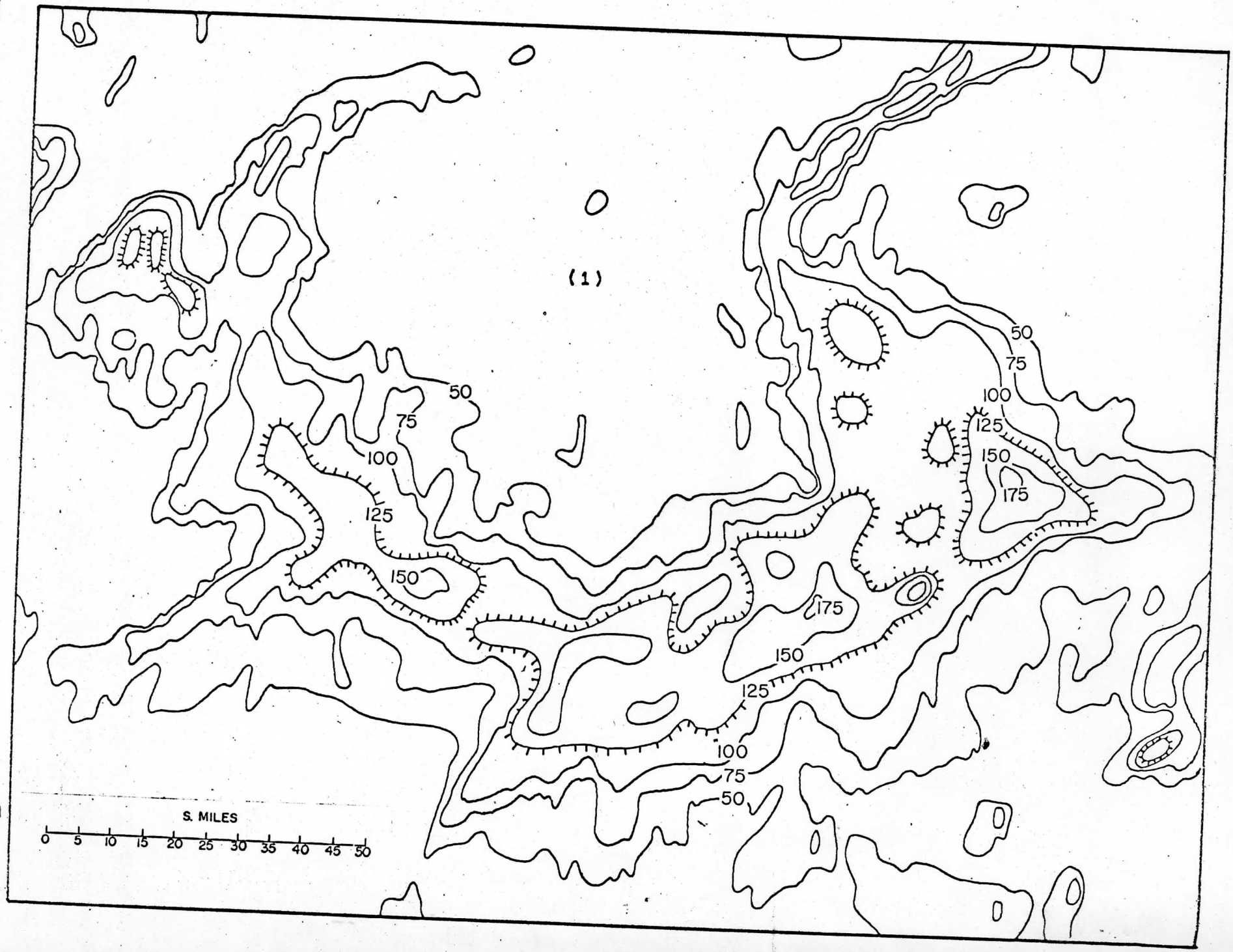

Fig 1

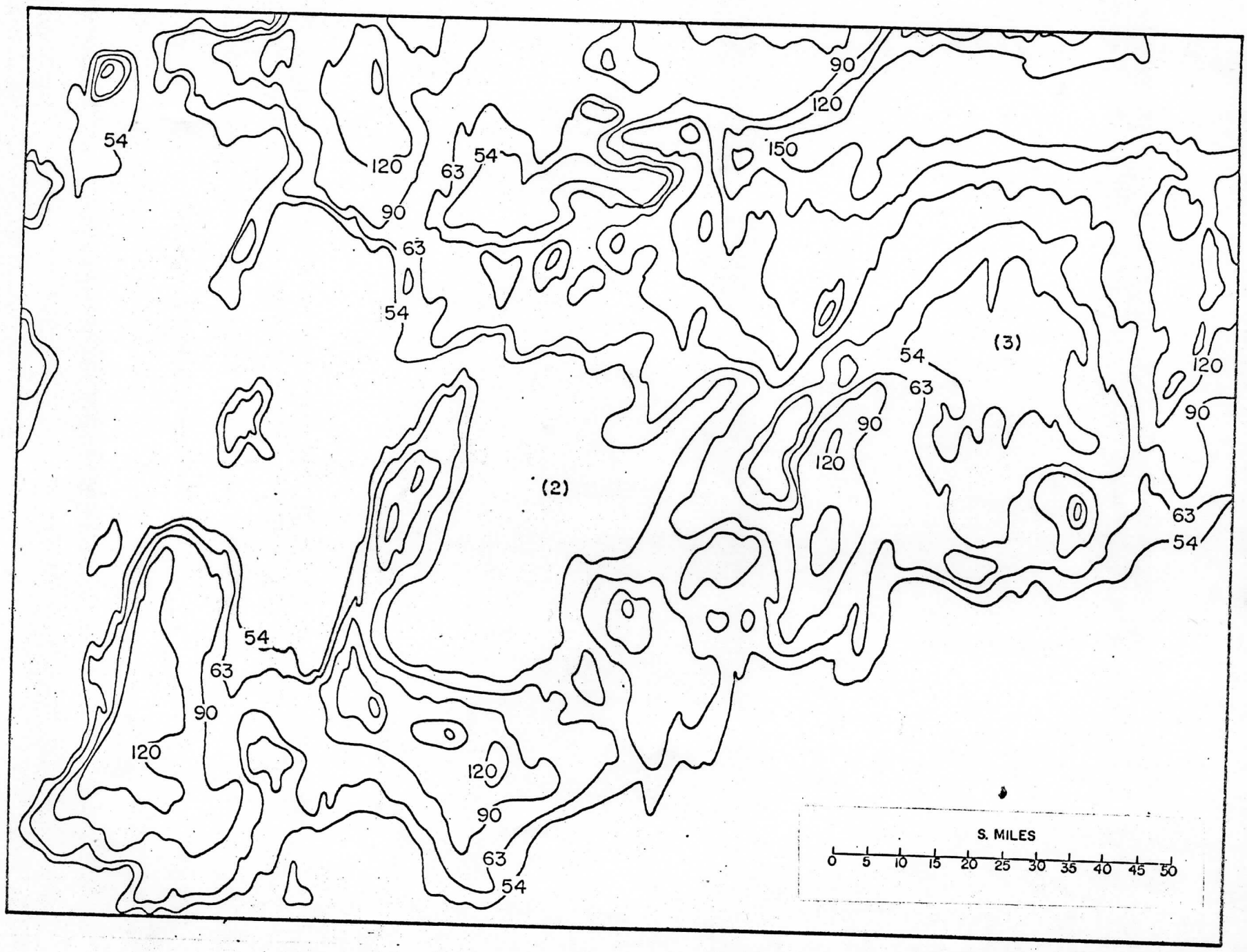
54
120
63
54
90
120
150
90
63
54
(3)
54
63
90
120
120
90
(2)
63
54
54
63
90
120
120
90
63
54
S. MILES
0 5 10 15 20 25 30 35 40 45 50

Fig 8

BASIC CLOUD PATTERN	MODEL A APPLIED TO CLOUD PATTERN	MODEL B APPLIED TO CLOUD PATTERN
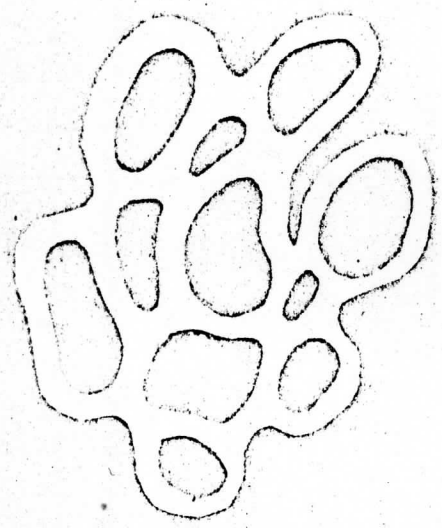	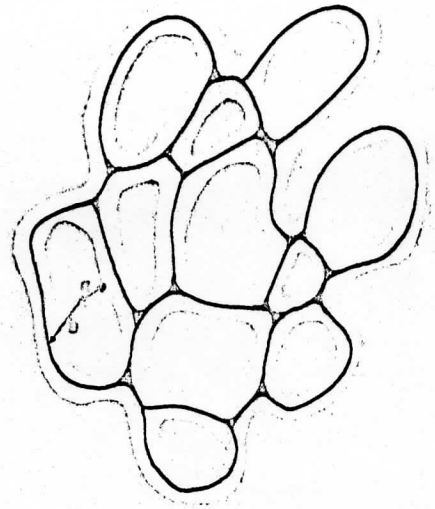	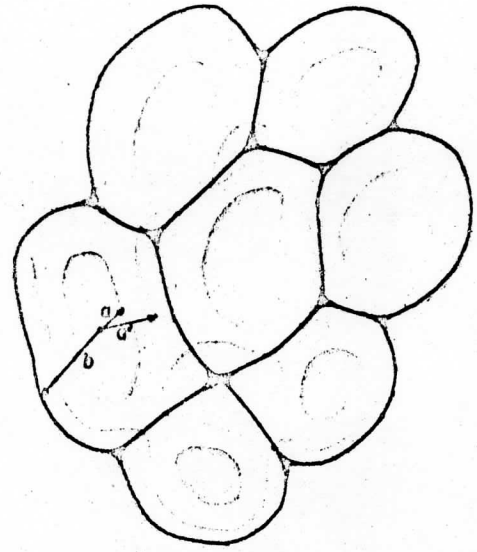

Fig 1

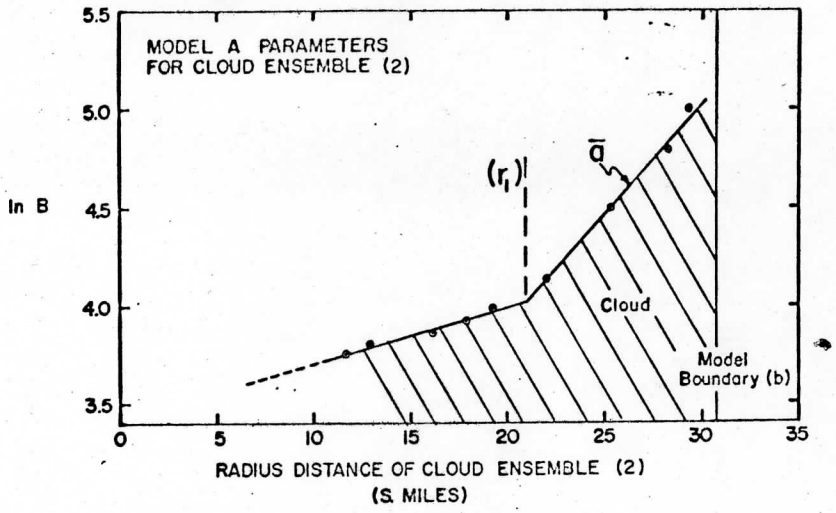
MODEL A PARAMETERS
FOR CLOUD ENSEMBLE (2)
ln B
5.5
5.0
4.5
4.0
3.5
(r_1)
$\bar{a}$
Cloud
Model
Boundary (b)
0
5
10
15
20
25
30
35
RADIUS DISTANCE OF CLOUD ENSEMBLE (2)
(S. MILES)

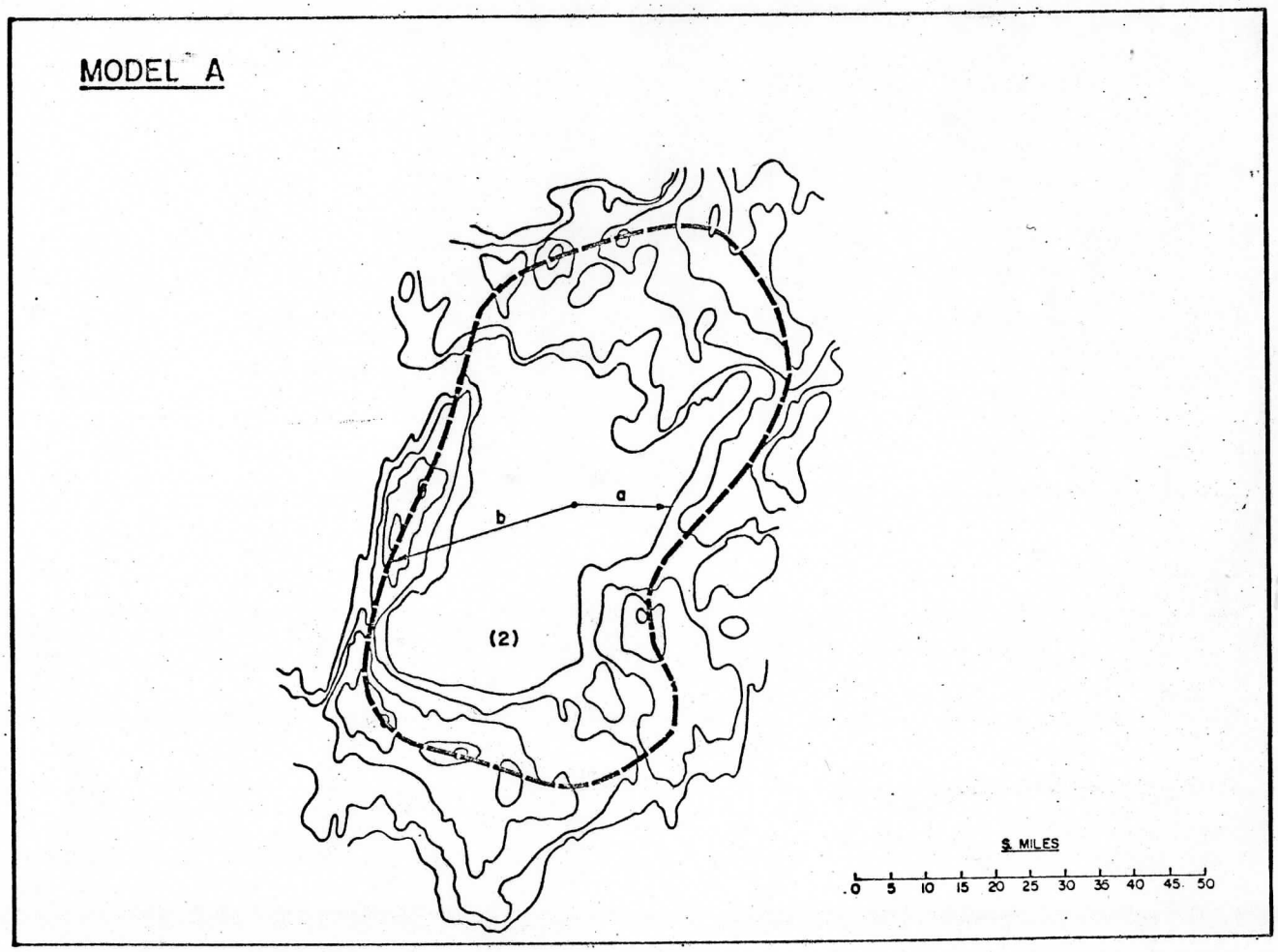
MODEL A
a
b
(2)
S. MILES
0
5
10
15
20
25
30
35
40
45
50

Fig 10

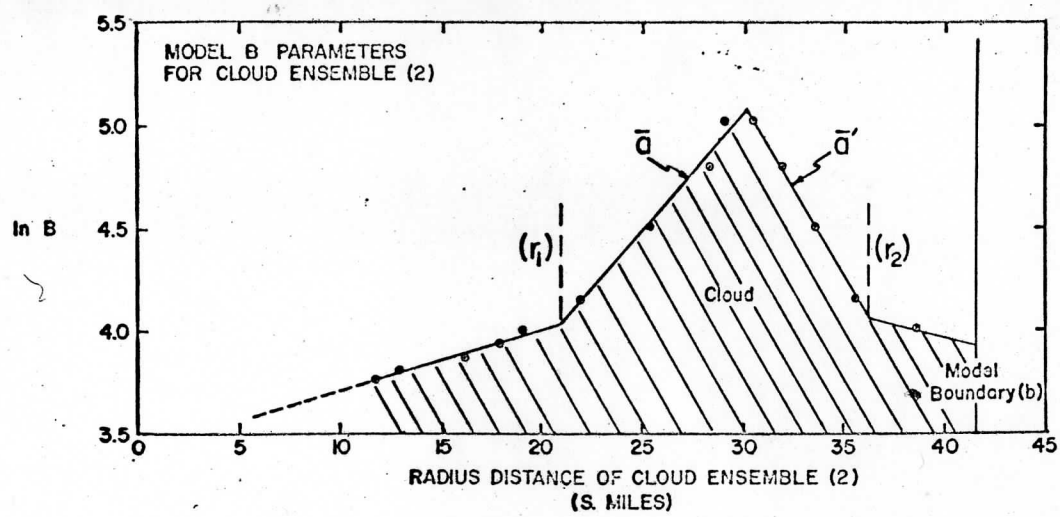
MODEL B PARAMETERS
FOR CLOUD ENSEMBLE (2)
ln B
5.5
5.0
4.5
4.0
3.5
0
5
10
15
20
25
30
35
40
45
$\bar{a}$
$\bar{a}'$
(r_1)
(r_2)
Cloud
Model
Boundary (b)
RADIUS DISTANCE OF CLOUD ENSEMBLE (2)
(S. MILES)

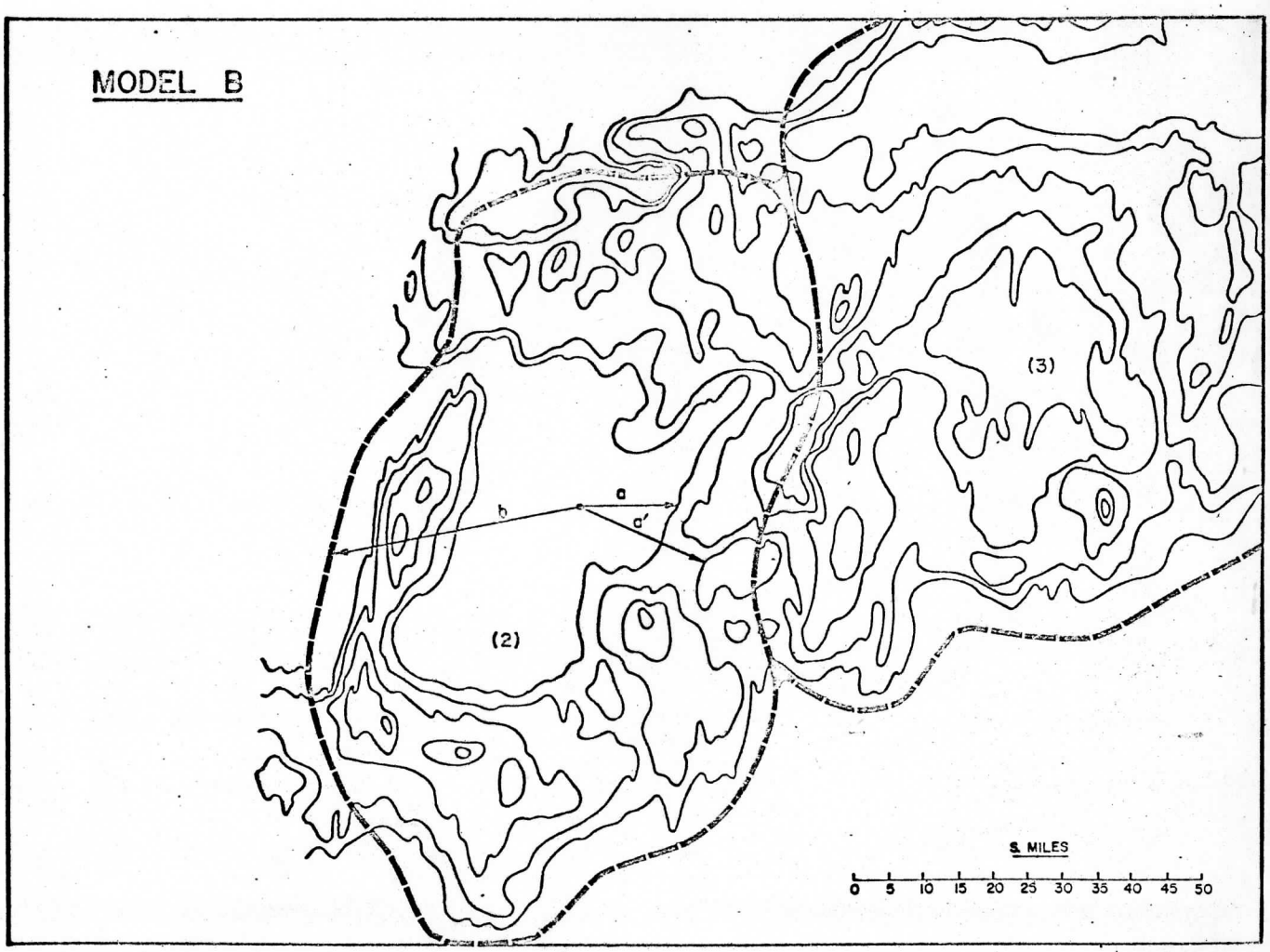
MODEL B
(3)
(2)
a
b
a'
S. MILES
0 5 10 15 20 25 30 35 40 45 50

Fig 11

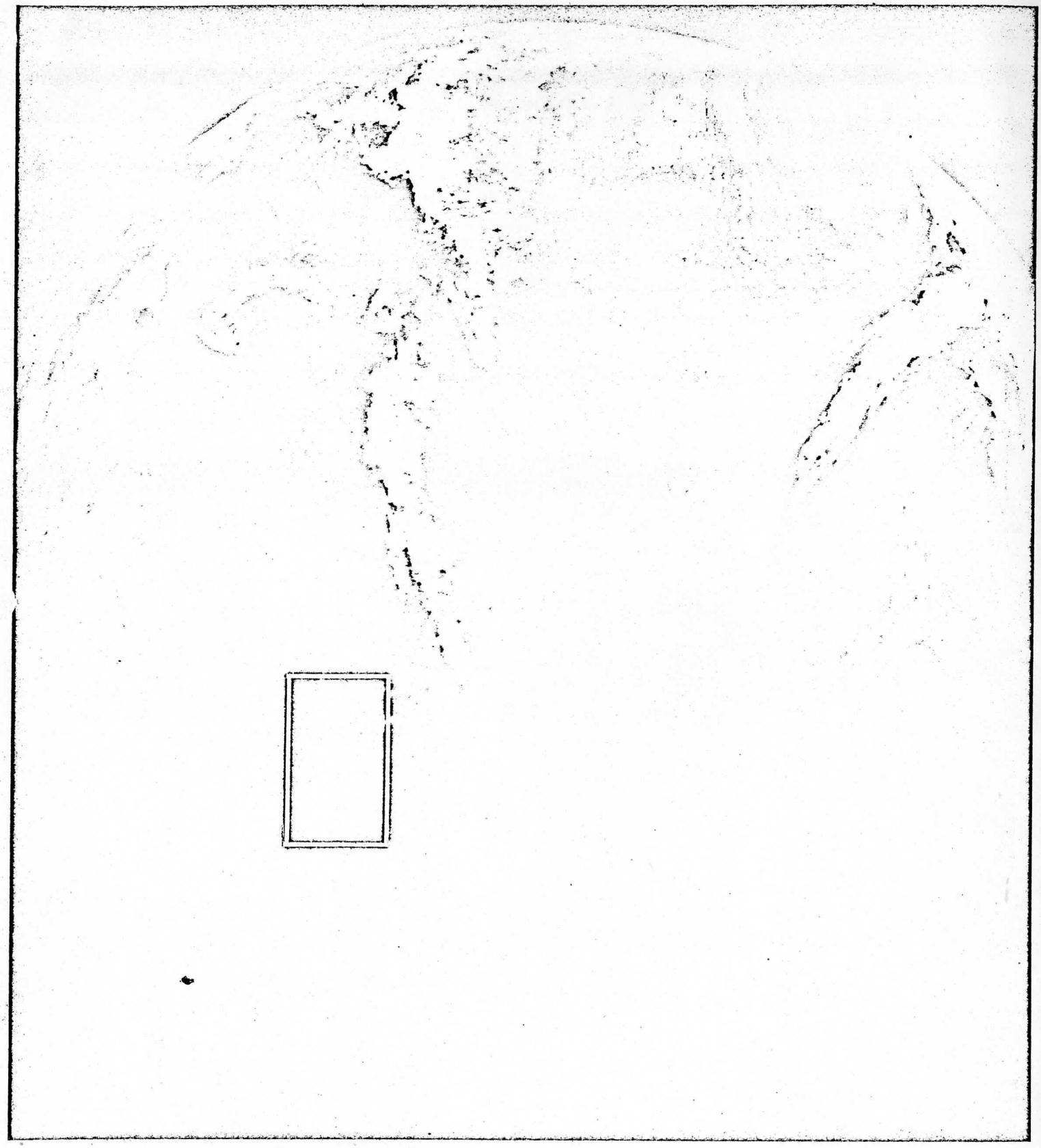

Fig 12

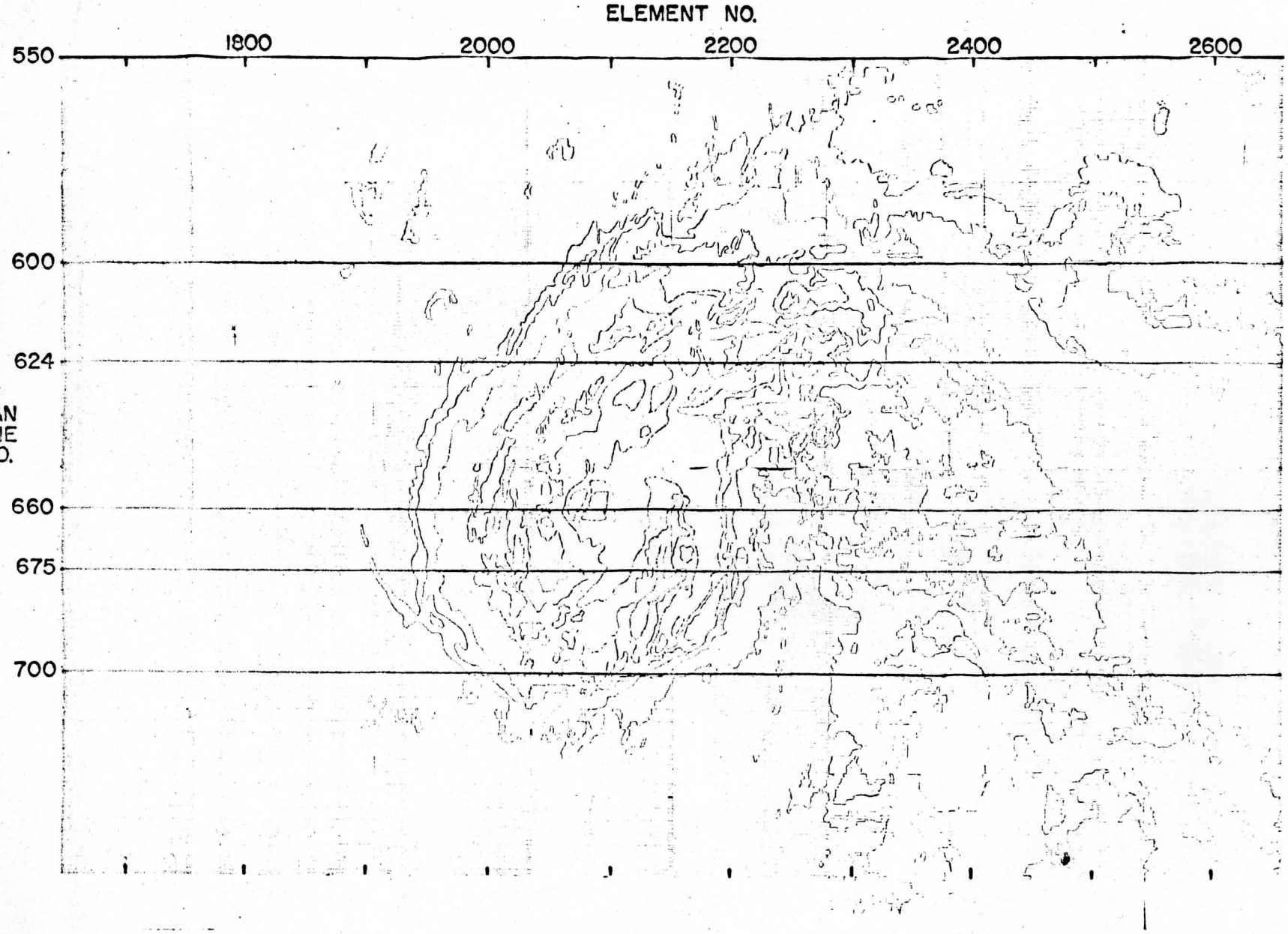
ELEMENT NO.
1800
2000
2200
2400
2600
550
600
624
660
675
700
SCAN
LINE
NO.

Fig 13

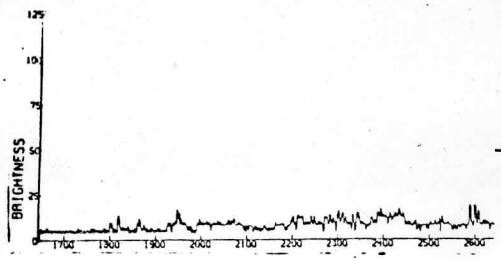

254-7-181826 *** SCAN LINE 550 (TSL)

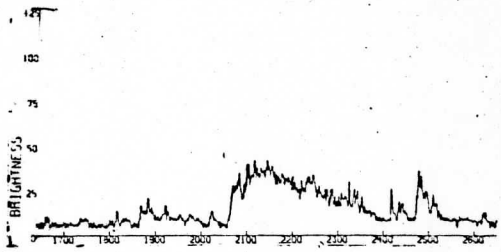

254-7-181826 *** SCAN LINE 600 (TSL)

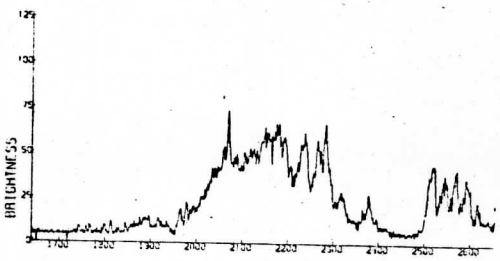

254-7-181826 *** SCAN LINE 624 (TSL)

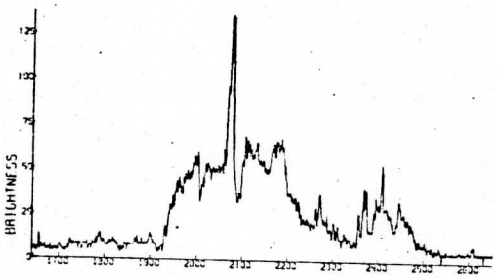

254-7-181826 *** SCAN LINE 660 (TSL)

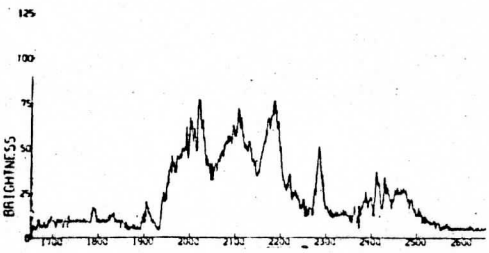

254-7-181826 *** SCAN LINE 675 (TSL)

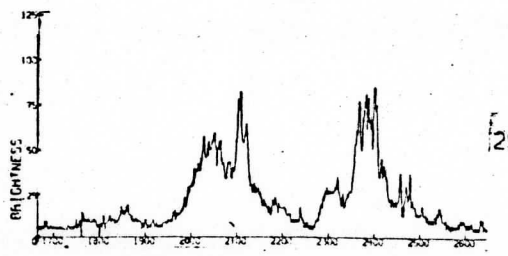

254-7-181826 *** SCAN LINE 700 (TSL)

Fig 14

DETERMINATION OF THE SEA SURFACE SLOPES DISTRIBUTION AND WIND VELOCITY USING SUN GLITTER VIEWED FROM A SYNCHRONOUS SATELLITE

by

Nadav Levanon

Space Science and Engineering Center
The University of Wisconsin
1225 West Dayton Street
Madison, Wisconsin 53706

March 21, 1969

TABLE OF CONTENTS

1. INTRODUCTION 1

2. THE SYNCHRONOUS SATELLITE AS THE OBSERVER 3

3. THE SATELLITE, THE POINTS OF REFLECTION AND THE SUN SUBPOINT 5

4. THE GEOMETRY OF REFLECTION 6

5. SLOPE PROBABILITY AND LIGHT INTENSITY 9

6. BACKGROUND LIGHT 10

7. THE SLOPE DISTRIBUTION 12

8. RESULTS 15

9. CONCLUSIONS 17

10. REFERENCES 18

11. THE FIGURES 20

INTRODUCTION

The use of sun glitter to study the slope statistics of the sea was suggested and explored by Cox and Munk[1,2]. Their basic idea can be summarized as follows. If the sea surface were entirely calm, then an overhead observer would see a single, mirror-like reflection of the sun at the horizontal specular point. The sea, of course, is never mirror flat, but due to the short wavelength of light, can be considered as constructed from many small facets, each with its own inclination. The farther a facet is from the horizontal specular point, the greater is the inclination required to reflect light toward the observer. The location of the reflected light source can therefore be interpreted as a certain sea slope, and the average intensity of the light coming from this location can be interpreted as the frequency with which this particular slope occurs.

Cox and Munk estimated sea-slope distributions using sun glitter photographs taken from an aircraft. They also suggested an empirical relation between the variance of the slopes and the surface wind velocity.

With the advent of the ATS-1 synchronous satellite, the sun glitter has appeared as a major phenomenon on the photographs received daily from the spin-scan camera.

The purpose of the present work is to adapt the Cox - Munk technique to pictures taken from a much higher altitude, by a synchronous satellite. The main modification involves the use of a sequence of photographs of a limited area (taken over a time period) rather than a single photograph of the whole sun glitter area.

Such data from the satellite were used to calculate the slope distribution, and from it the wind velocity, for the locations of Palmyra, Fanning and Christmas Island, on the 16th and 19th of April, 1967. The calculated values were compared to direct wind measurements obtained at these locations during the "Line Island Experiment"[3].

Utilizing the ATS-1 data stored on magnetic tape in digital form, it was possible to by-pass the highly degrading photographic and photometric processes and to work quantitatively on the received video signal.

THE SYNCHRONOUS SATELLITE AS THE OBSERVER

In their work, Cox and Munk photographed the sun glitter from aircraft altitudes, and studied the slope distribution from a single photograph. This was done by identifying each location within the glitter with the specific sea slope which would cause reflection at that location.

The basic assumption involved in using different locations within a single glitter is that the statistical characteristics of the sea surface are essentially constant over the whole area of the sun glitter. When the photograph is taken from an aircraft this assumption is true. However, when the photograph is taken from synchronous altitude (35,783 km), the sun glitter covers a circle whose diameter can exceed 3000 km, and with regard to such a large area the above basic assumption is no longer plausible.

This point is brought out in Figure 1, which shows a sequence of 6 photographs of the same portion of the ocean (5°N-15°N and 160°W-230°W), taken at intervals of about 23 minutes. The sun glitter is apparent in all the frames, and its shift to the west can be clearly seen. Note the calm area of the ocean which appears as a dark area in the midst of the sun glitter in the second frame. In the third frame this area already includes the horizontal specular point of reflection, and the light intensity reflected from part of it is greater than the light scattered from the clouds. In the last frame the specular point of reflection has moved outside the calm area and the sun glitter ends sharply at its edge. Thus, Figure 1 shows that the sea roughness may vary considerably over the glitter large area. But we also note that the shape of the calm area did not change appreciably in the two hour period between the first and the last frame. This leads to an alternative assumption, viz., that the statistical

characteristics of the sea surface in the open ocean at a fixed point does not vary appreciably over a period of several hours.

Recalling that the synchronous satellite is in a fixed position relative to the earth while the horizontal specular point of reflection shifts with time from east to west, we see that this assumption allows us to adapt the Cox - Munk technique to the case of observation from a synchronous satellite. Specfically, the values of light intensity reflected towards the satellite from a fixed point at different times, can be interpreted in terms of the sea slope distribution around that point.

THE SATELLITE, THE POINTS OF REFLECTION AND THE SUN SUBPOINT

The ATS-1 Satellite is positioned over the equator at about 150° West Longitude. From a height of 35,783 km, its spin scan camera usually observes the portion of the earth bounded by 70°W to 130°E, and by 52.5°N to 52.5°S. This area is scanned by 2018 horizontal (west to east) lines. The optical resolution is approximately 2.0 nautical miles when the telescope is pointed toward the subsatellite point. The normal down scan takes 20 minutes and the retrace, an additional 2 minutes. The optical system bandpass is 4750A to 6300A. The camera video output is linear within ± 2%, up to the intensity of 10,000 foot lamberts. Camera characteristics are described in detail in other sections of this volume.

The data at the ground station was available in three forms: as photographs; on analog tape; and on digital tape. On the digital tape, the camera output is digitized from 0 to 255 units. Each scan line has 8196 picture elements, of which the limb distance of an equatorial line occupies 7128 picture elements.

The present work utilized the simple navigation method of identifying two landmarks, Baja-California and Hawaii, which were not overcast on the specific days used for analysis. The accuracy achieved with this method was better than 50 miles.

The points of reflection in our study, corresponded to Palmyra Island (50°53'N 162°05'W), Fanning Island (3°54'N 159°23'W) and Christmas Island (1°55'N 157°20'W). Actual wind measurements were obtained on these three islands during the Line Island Experiment.

On the 16th of April, 1967, the sun subpoint traveled along the 10°N latitude, and on the 19th of April, along the 11°N. The exact longitude and latitude of the sun subpoint as function of time, were obtained from the Air Almanac[7]

THE GEOMETRY OF REFLECTION

To apply the method, we need an answer to the following geometrical question: given the longitude and latitude of the sun and the synchronous satellite subpoints, and of the point of reflection, what is the tilt magnitude and direction and the angle of incidence, at that point of reflection?

To derive the necessary formulae we shall use the following notation (Fig. 2):

O - The center of the earth

S - The sun subpoint

A - The synchronous satellite

P - The point of reflection

i - An index taking values S,R, or P

Q_i - The point created by the surface and a vector parallel to $\underset{\sim}{i}$ and starting at O

θ_i - Latitude of i (or of Q_i)

ϕ_i - Longitude of A - longitude of i (or of Q_i)

r - The radius of Earth

h - The synchronous altitude

$\underset{\sim}{\ell}$ - Vector between the satellite and the point of reflection

$\underset{\sim}{n}$ - The normal required for reflection from P

θ - The northward tilt at P

ϕ - The eastward tilt at P

β - The magnitude of the total tilt at P

ω - The angle of incidence

An elementary manipulation of rectangular and spherical coordinates yields the formulae:

$$\phi_\ell = \tan^{-1} \frac{-r \cos\theta_p \, \mathrm{Sin}\, \phi_p}{h + r\,(1-\cos\theta_p \cos\phi_p)} \tag{3}$$

$$\theta_\ell = \tan^{-1} \frac{-r \, \mathrm{Sin}\, \theta_p}{[(h+r)^2 - 2r(h+r) \cos\theta_p \cos\phi_p + r^2 \cos^2\theta_p]^{1/2}} \tag{4}$$

and

$$\phi_n = \tan^{-1} \frac{\cos\theta_\ell \, \mathrm{Sin}\phi_\ell + \cos\theta_s \, \mathrm{Sin}\phi_s}{\cos\theta_\ell \cos\phi_\ell + \cos\theta_s \cos\phi_s} \tag{5}$$

$$\theta_n = \tan^{-1} \frac{\mathrm{Sin}\theta_\ell + \mathrm{Sin}\theta_s}{[\cos^2\theta_\ell + \cos^2\theta_s + 2 \cos\theta_\ell \cos\theta_s \cos(\phi_\ell - \phi_s)]^{1/2}} \tag{6}$$

At the point of reflection the tilt in the east (or ϕ) direction is given by

$$\phi = \phi_n - \phi_p \tag{7}$$

and the tilt in the north (or θ) direction by

$$\theta = \theta_n - \theta_p \tag{8}$$

Recalling that ϕ and θ are orthagonal, we get for the total tilt magnitude

$$\beta = \tan^{-1} \left[\tan^2 \theta + \tan^2 \phi\right]^{1/2} \tag{9}$$

and the angle of incidence is given by

$$\omega = \tan^{-1} \left[\tan^2(\theta_n - \theta_s) + \tan^2(\phi_n - \phi_s)\right]^{1/2} \tag{10}$$

If both the point of reflection and the sun subpoint are near the satellite subpoint, i.e., if all θ and ϕ values are small, the above equations can be approximated by the simplified formulae:

$$\phi \simeq \frac{\phi_s}{2} - \left(1 + \frac{r}{2h}\right) \phi_p \tag{11}$$

$$\theta \simeq \frac{\theta s}{2} - \left(1 + \frac{r}{2h}\right) \theta p \tag{12}$$

$$\beta^2 \simeq \theta^2 + \phi^2 \tag{13}$$

$$\omega^2 \simeq \frac{1}{4} \left(\theta_s + \frac{r}{h} \theta_p\right)^2 + \frac{1}{4} \left(\phi_s + \frac{r}{h} \phi_p\right)^2 \tag{14}$$

SLOPE PROBABILITY AND LIGHT INTENSITY

Cox and Munk[1,2] and Cox[8] have shown that the probability density P of the slope (determined by the location) is related to the received intensity J, from this location, in the following manner:

$$P = (4H^{-1}\ \rho^{-1}(\omega)\ A^{-1}\ \cos\mu)J\cos^{4}\beta \qquad (15)$$

where: H - the solar energy flux per unit area of beam

ω - the angle of incidence

$\rho(\omega)$ - the reflection coefficient

β - the slope magnitude

A - the telescope effective area

μ - the telescope tilt from nadir

They have calculated $\rho(\omega)$ for sea water to be: $\rho(\omega) = 0.020, 0.021, 0.060$ and 1.00 for (respectively) $\omega = 0°, 30°, 60°$ and 90°.

In our system (fixed satellite and single point of reflection), the angle μ is constant. For the case of small angles, ω is less than 30 degrees and therefore $\rho(\omega)$ is also essentially constant. Therefore, the term in brackets in (15) does not vary with time, and the only variable correction is $\cos^{4}\beta$.

BACKGROUND LIGHT

In additon to the sun glitter two other sources of radiation have to be considered.[8] Cox and Munk pointed out two of them, (1) the skylight reflected at the sea surface, and (2) the sunlight scattered by particles beneath the sea surface. Rozenberg and Mullamaa[9] pointed out another source, (3) the scattered light in the air column separating the satellite from the water surface. Undoubtedly there are more contributors to the background light.

The sources (1) and (2) were studied by Cox and Munk, who found that their contribution depends mainly on the angle between the vertical and the vector from the point under analysis to the observer. In the case of an observer on a synchronous satellite this angle is fixed.

Some idea on the contribution of the scattered light in the atmosphere (3) can be received from the maps of Sekera and Viezee[10] even though they assume the satellites at infinity. We will use the maps calculated for the case of a planetary surface that absorbs all the incident radiation (A = 0); i.e., when the only return is from scattering in the atmosphere. Those maps indicate only slight variations in the intensity of the scattered light in the vicinity of the satellite subpoint, as the sun subpoint shifts away, as long as the angular distance between the sun and the satellite is smaller than about 40 degrees. For our small angles case, we can therefore assume this contribution to be constant.

The above indicates that the background light can be estimated by measuring the radiation received from the point when it is outside the sun glitter limits.

The camera on the ATS-3 Satellite has three channels: Blue (.38-.48 micron), Green (.48-.58) and Red (.55-.63), the respective background intensities were related to each other as 5:6:2, when calibrated for equal reflection from cloud tops. Thus, for reducing the background light, the red channel data is the best choice.

There is of course no way to study the sun glitter in the case of overcast. However, in the case of scattered clouds, our method (since it is based on measurements at a single point) can be used to study the wind velocity in any neighborhood within which a clear area of the size of the telescope resolution can be found.

THE SLOPE DISTRIBUTION

Cox and Munk found that the slope distribution is "almost" like a two-dimensional Gaussian (normal) distribution, the "almost" standing for peakedness at the probabilities of the small slopes, and skewness toward the upwind directed slopes. To simplify our discussion we will assume the slope distribution to be Gaussian and with zero mean. Thus if c is the slope toward the crosswind direction and u toward the upwind direction, their probability density is given by

$$f(c,u) = \frac{1}{2\pi\ \sigma_c\ \sigma_u \left(1 - r^2\right)^{1/2}} \exp\left[- \frac{1}{2(1-r^2)} \left(\frac{c^2}{\sigma_c^{\,2}} - \frac{2rcu}{\sigma_c\ \sigma_u} + \frac{u^2}{\sigma_u^{\,2}} \right) \right] \tag{16}$$

where σ_c σ_u are the standard deviations of c and u, and r is their correlation coefficient.

Cox and Munk found that r is close to zero, i.e., c and u are approximately independent. In this case the c and u axes are the principal axes of the ellipses of constant density (fig. 3). However, they will not in general coincide with the north (θ) and east (ϕ) axes, i.e., θ and ϕ will be jointly normal but correlated.

The sun glitter scan over a fixed point in the ocean may be considered equivalent to traversing the slope probability plane along a certain path. Note that in equations (11) and (12) the only variable (with time) is the longitude of the sun subpoint ϕ_s. For the small angles case, we see that only ϕ varies with time while θ remains constant. Our path in the slope probability plane is therefore a line θ = const. and the density P measured using (15) is (up to a constant) the conditional probability density

$$f(\phi \,|\, \theta = \text{const.}) \tag{17}$$

This density is also normal, with the mean

$$E(\phi|\theta) = \frac{r\sigma_\phi}{\sigma_\theta}\,\theta \tag{18}$$

and the standard deviation

$$\sigma_{\phi|\theta} = \sigma_\phi \left(1-r^2\right)^{1/2} \tag{19}$$

where r is the correlation coefficient of ϕ and θ.

Cox and Munk found linear relations between the wind velocity W and the variances as follows:

$$\sigma_c^2 = 0.003 + 1.92 \times 10^{-3} W \pm 0.002 \quad ; \tag{20}$$

$$\sigma_u^2 = 0.000 + 3.16 \times 10^{-3} W \pm 0.004 \quad ; \tag{21}$$

$$\sigma_c^2 + \sigma_u^2 = 0.003 + 5.12 \times 10^{-3} W \pm 0.004 \quad ; \tag{22}$$

where σ is in radians and W is the mean wind in meters per seconds (measured 41 feet above the sea surface). Other relations of this type by Cox and Munk for sea covered by slicks, have received support from other works.[12]

It can be shown (ignoring the anomaly of $\sigma_c \neq \sigma_u$ at no wind) that

$$|r| < \frac{\sigma_u^2 - \sigma_c^2}{2\sigma_c^2} \tag{23}$$

Using (20), (21) and (23) we get that $r<0.2$ up to average winds of 10 m/sec., (This was the case 99.67% of the time, on the three islands during

March and April). This and the small θ, rules out any chance to use (18) as a clue for the wind direction. It also means that (19) will reduce to:

$$\sigma_{\phi|\theta} \simeq \sigma_{\phi} \tag{24}$$

Eq. (24) indicates that as could be seen intuitively at the beginning of this section, our method estimates the distribution of slopes in the East West direction. We do not usually know whether this direction coincides with the upwind or cross wind direction, or with any other direction between the two. We, therefore, can not use only one of Cox and Munk's linear relations between the wind velocity and the variance (eq. 20,21), but we must use the two of them together. This is done in fig. 4 where the lines represent the two linear relations and their uncertainty boundaries. The lack of knowledge about the wind direction expands the range of possible wind velocities for each value of the slopes variance.

RESULTS

The comparison between calculated scalar winds and actual wind measurements, were made on two dates (the 16th and 19th of April, 1967) for each of the three islands (Palmyra, Fanning and Christmas).

The process of calculating the scalar wind involved the following steps:

(1) Plotting those scan lines which include the sun glitter, from a sequence of consecutive pictures.

(2) Navigating on each picture to find which line and picture element represent each island location. (There were apparent variations in the line number, between consecutive pictures, because of the spacecraft variable pitch.)

(3) Plotting the intensity J as a function of time.

(4) Converting time to corresponding East directed tilt ϕ, using equation (11).

(5) Subtracting the background light.

(6) Finding β from (13), and applying the corrections $\cos^4\beta$ (15), to get values of the probability P (up to a constant). (This correction was significant only in cases where the latitude of the reflecting point was far from the latitude of the horizontal specular line of reflection).

(7) Finding the standard deviation of the probability curve.

(8) Finding the range of possible wind velocities from fig. 4.

In figure 5 some of these steps are illustrated for two cases: Palmyra and Fanning, 16 April 1967. The records on the right side of figure 5 are 8 scan lines over the latitude of Fanning Island, taken in intervals of 23 minutes, the

longitude of the island is marked by the vertical line. These 8 intensities yield the normal curve shown in the middle. Similar procedure is shown also for Palymyra Island.

The calculated standard deviation results are plotted against actual wind measurements, as points, in fig. 4. The numbers in brackets near those points indicate the measured wind direction relative to the east west direction.

Except for one of the c points which is only 5 degrees from the E-W direction and therefore should have been closer to the σ_u^2 line, all other points are within the limits suggested by Cox and Munk.

CONCLUSION

Our work shows the feasibility of studying the east west component of the waves' slope distribution from a synchronous satellite by using the sun as the radiation source with its movement, relative to the earth, as a scanning mechanism.

Using Cox and Munk's [1,2] linear relation between the variance of the waves' slope and the wind velocity, it was possible to calculate scalar wind velocities in the area of the sun glitter and to compare them to actual wind measurement taken on the ocean. These comparisons revealed that the enormous height of the observer did not degrade the accuracy of the observation. When the wind direction is given, the accuracy of the calculated wind velocity is as good as if the sun glitter is studied from aircraft altitude, i.e., $\pm$ 1 m/sec.

In the course of this work, it became more and more evident that the sun glitter is a strong and reliable source of radiation that should be studied instead of being avoided.

References

1. Cox C. and W. Munk 1954: Measurement of the Roughness of the Sea Surface from Photographs of the Sun's Glitter. Jour. Optical Soc. Am. 44 (11) 838-850.

2. Cox C. and W. Munk 1954: Statistics of the Sea Surface Derived from Sun Glitter. Jour. Marine Res. 13 (2) 198-227.

3. Zipser E. J. and R.C. Taylor 1968: A Catalogue of Meteorological Data Obtained During the Line Islands Experiment February - April 1967. NCAR-TN-35

4. Santa Barbara Research Center and University of Wisconsin 1967: ATS Spin-Scan Cloud Camera and Prelaunch Calibration Procedure. Ann. Report 1966, Dept. of Meteorology, the University of Wisconsin, Madison, Wisconsin.

7. United States Naval Observatory and Her Majesty's Stationery Office 1966: The Air Almanac 1967 January - April.

8. Cox C. 1965: The Relation of Backscattered Radiation to Wind - Stress at the Sea Surface. Presented at the AGU - AMS International Symposium on Electromagnetic Sensing of the Earth from Satellites. Miami 1965.

9. Rozenberg G. V. and Yu. A.R. Mullamaa 1965: Some Possibilities of Determining Wind Speed Over an Ocean Surface Using Observations from Artificial Earth Satellites. Izv. Atmospheric and Oceanic Series, Vol. 1 No. 3, pp. 282-290, translated by P. A. Keehn.

10. Sekera z. and W. Viezee 1961: Distribution of the Intensity and Polarization of the Diffusely Reflected Light Over a Planetary Disk. The RAND Corporation Report R - 389 - PR November 1961.

12. Kinsman B. 1965: Wind Waves, Their Generation and Propagation on the Ocean Surface. Prentic-Hall, Inc. (See chapters 7 and 8).

THE FIGURES

Figure 1: The sun glitter shifts toward west over a calm area in the midst of a rough ocean.

Figure 2: The geometry of reflection.

Figure 3: The probability space of the two dimensional normal distribution of the waves slope.

C - slope in the cross wind direction

u - slope in the upwind direction

ϕ - slope in the East direction

θ - slope in the North direction

Figure 4: The linear relation between the waves slope variance and the wind velocity (after Cox and Munk), compared to six points represented by variance calculated from the satellite data, and actual wind measurements.

Figure 5: Some of the steps involved in reducing the satellite data, to the standard deviation of the waves slope.

17 APRIL 1967
G.M.T.

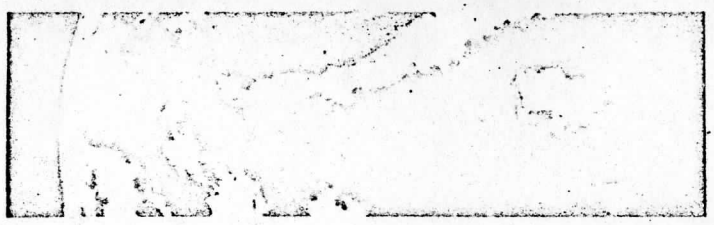

01:14:51

01:38:05

02:01:21

02:24:34

02:47:52

03:11:05

FIGURE 1

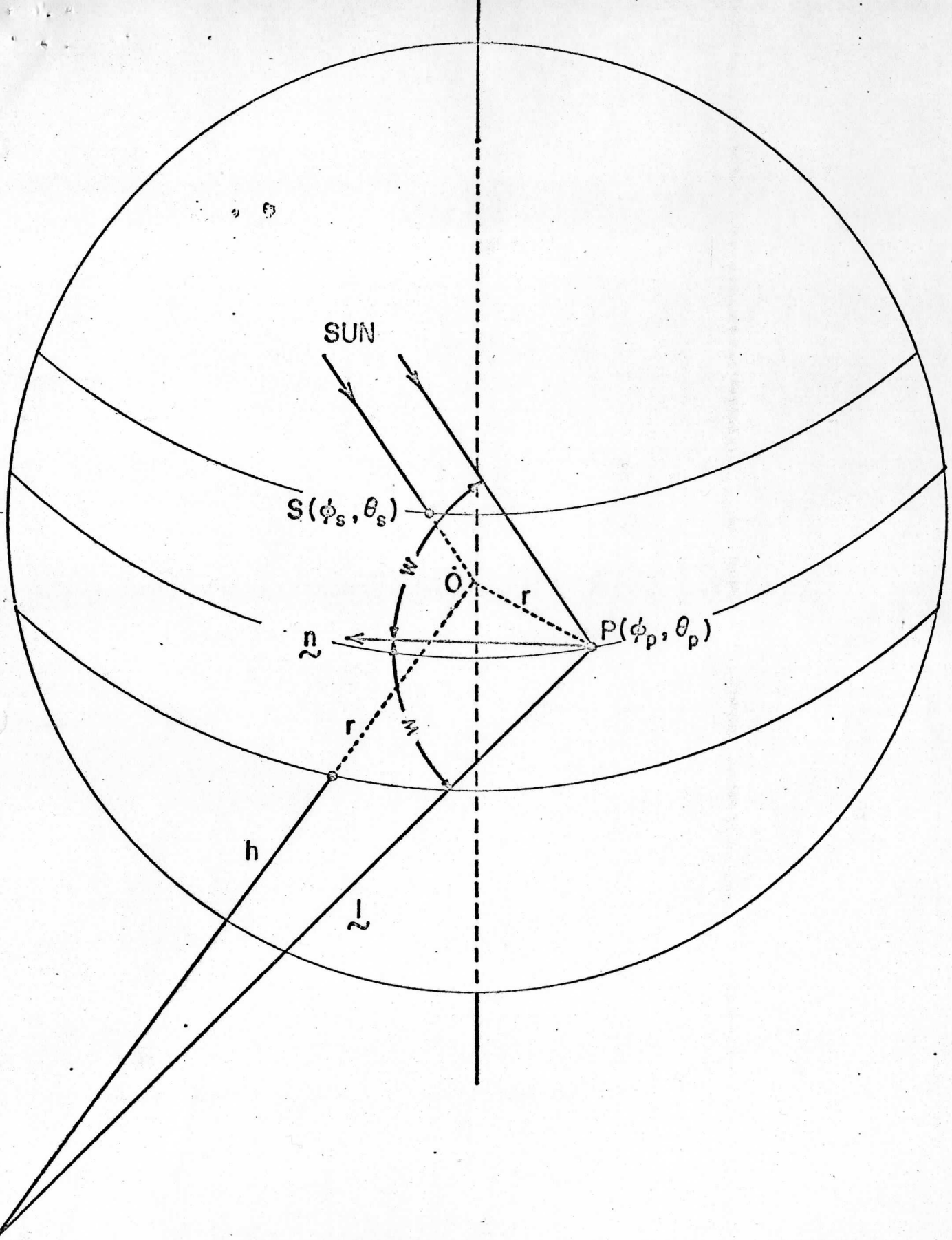
SUN
S(ϕ_s, θ_s)
W
O
r
P(ϕ_p, θ_p)
n
r
W
h
A
tellite (ϕ_A=0, θ_A=0)

FIGURE 2

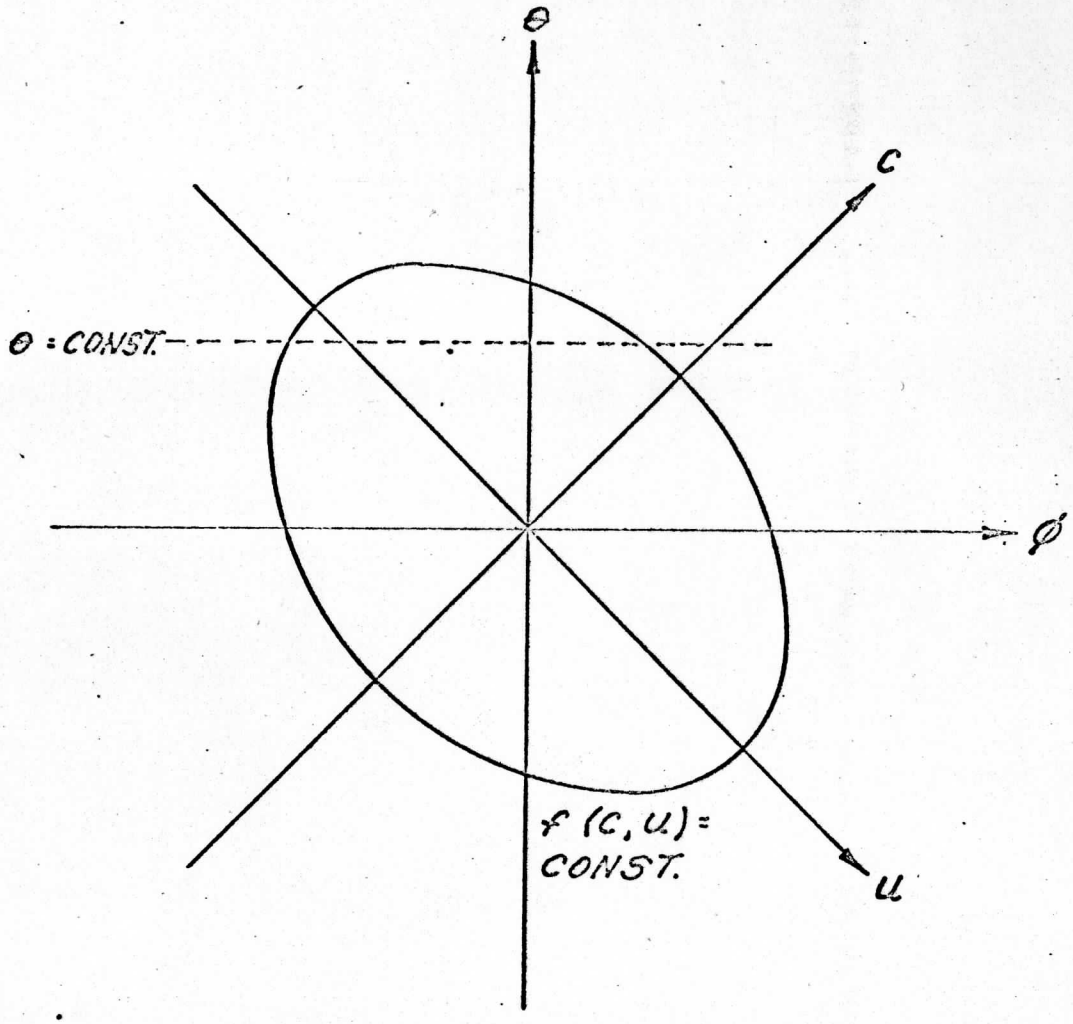

FIGURE 3

PALMYRA ISLAND

FANNING ISLAND

APR. 16, 1967

LOCAL TIME

11:31

11:54

12:17

12:40

13:04

13:27

13:50

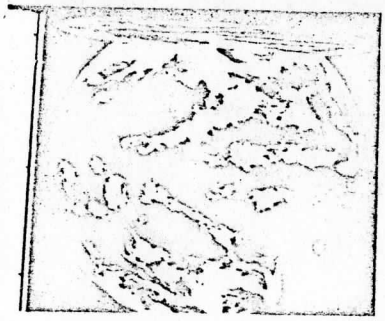

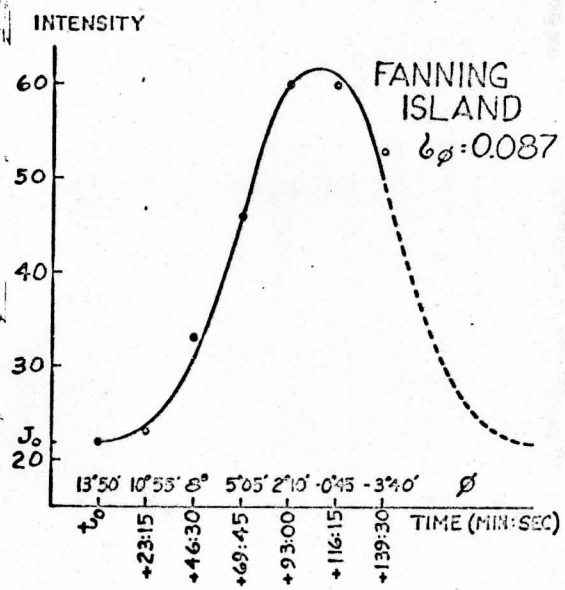

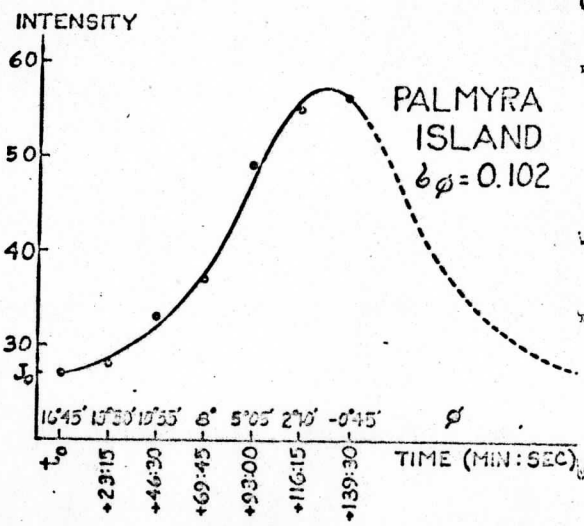

FIGURE 5

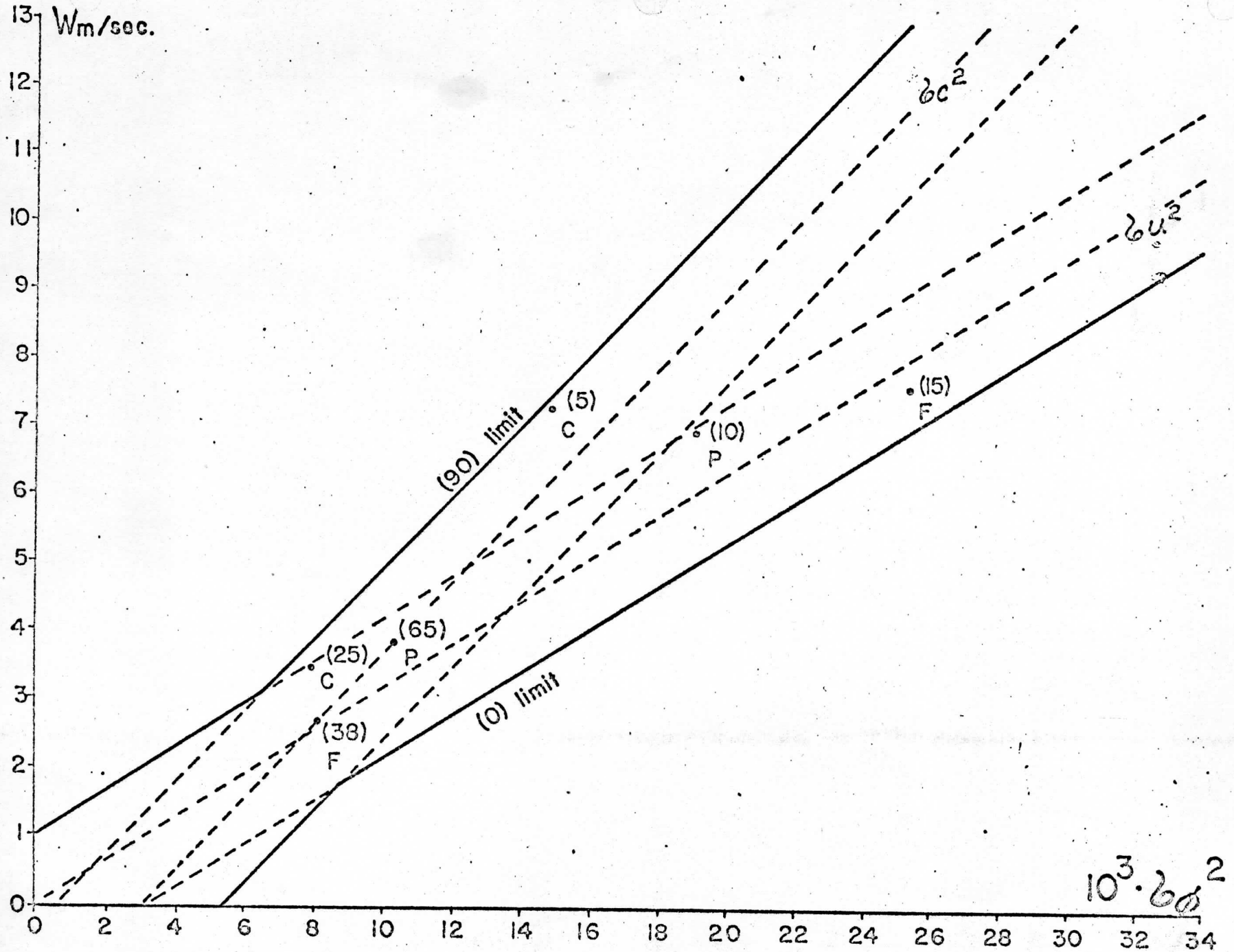

P= Palmyra F = Far g C= Christmas

( ) deviation of the wind direction from the east west direction (in degrees)

FIGURE 4

CORRECTED COPY

STUDIES OF REFLECTION CHARACTERISTICS OF THE PLANET EARTH FROM A SYNCHRONOUS SATELLITE

- PRELIMINARY RESULTS -

Ehrhard Raschke*
and
William R. Bandeen
Laboratory for Atmospheric and Biological Sciences

GODDARD SPACE FLIGHT CENTER
Greenbelt, Maryland

*On leave from the University of Munich, Germany, as a Postdoctoral Resident Research Associate of the National Academy of Sciences, Washington, D. C.

STUDIES OF REFLECTION CHARACTERISTICS OF THE PLANET EARTH FROM A SYNCHRONOUS SATELLITE - PRELIMINARY RESULTS-

Ehrhard Raschke
and
William R. Bandeen
Laboratory for Atmospheric and Biological Sciences

ABSTRACT

Digitized data of nine ATS-1 photographs taken on 21 and 22 April 1967 were used to study statistically the dependence of reflection properties of the earth-atmosphere system on the zenith and azimuthal angles of measurement and on the zenith angle of incident solar radiation. Four states of the sky were defined for this study: "complete overcast," "cloudy-overcast," "cloudless atmosphere," and "minimal reflection." The limited quantity of data analyzed so far provides sufficiently accurate results only for small solar zenith angles ($0.0° \leq \zeta \leq 25.8°$). A remarkably high reflection was found in all conditions in a small angular range around the specular point of the sun on the earth's surface. The horizon appeared to be brighter than other areas for "cloudless atmosphere" conditions only. A maximum of reflected solar radiation due to direct backscattering was not found ~~in these preliminary results~~.

INTRODUCTION

Scattering processes in the atmosphere and reflection from ground and cloud surfaces cause part of the incident solar electromagnetic radiation to be lost to space without exchanging its energy with the scatterers and reflectors. These processes have been studied in the past by many researchers, both theoretically and experimentally. All of their results showed that these processes cause an anisotropic field of solar radiation reflected from the planet earth back to space.** This anisotropy, for instance, may be important for calculations of the reflected flux of solar radiation from satellite measurements of the reflected radiance (Ref. 3).

Several authors (see e.g. RUFF et al., 1967) have previously studied statistically the dependence of satellite beam measurements of reflected solar radiation on the angles of measurement and on the zenith angle of incident solar radiation. Their results generally confirmed the angular reflection characteristics which have previously been predicted theoretically. But a basic limitation existed in the data available to these workers, caused by the rather wide aperture angle ($\sim$ 70 mrad) of the scanning radiometers flown on the TIROS and Nimbus satellites, which did not permit accurate studies of reflected radiation close to the earth's horizon.

In the preliminary investigations reported here, the reflection characteristics of the earth-atmosphere system are studied with digitized records of nine photographs which were obtained at about 1.5-hour intervals on 21 and 22 April 1967 with the ATS-I Spin Scan Cloud Camera System (Ref. 6). This camera has a field of view of only 0.1 mrad at the 50% response level. Thus it allows in principle very detailed studies of solar radiation reflected from various surfaces even very close to the limb of the earth. Observations of the illuminated part of the disc of the earth are possible every 25 minutes. Therefore, statistical studies are possible for a very great variety of zenith angles of the sun and of combinations of the zenith and azimuthal angles of measurement.

** References to these earlier investigations are available in many textbooks on radiative transfer in atmospheres. See, for example, Calculation of the Brightness of Light in the Case of Anisotropic Scattering, Part 1 (1960) by E. M. Feigelson, et al., and Part 2 (1963) by V. S. Atroshenko, et al. Consultants Bureau, New York (Translations from the original Russian).

The photographs used here cover nearly a full daylight period over that part of the earth observable from ATS-1. Further studies with data of other photographs are underway to extend these preliminary results.

ANALYSIS OF DATA

A radiometer or a camera aboard a satellite, having a narrow field of view and observing an illuminated area on the earth's surface, measures only the radiance N_f of solar radiation reflected in the direction of the satellite. The bidirectional reflectance ρ'_f of this area may be obtained from N_f by

$$\rho'_f(\theta,\psi,\zeta;\text{sfc}) = \frac{N_f(\theta,\psi,\zeta;\text{sfc})}{\cos\zeta \cdot S_f} \quad [\text{sr}^{-1}] \qquad (1)$$

where S_f is the incident solar irradiance in the filter range f of the ATS-I camera system which is located between 0.46 and 0.65 microns. This narrow spectral region is located in the visible. Thus, the results obtained in this study do not necessarily represent mean angular characteristics required for calculations of the total flux of reflected solar radiation in the rather wide range from 0.3 to 4.0 microns.

The angles θ and ψ designate the zenith angle and the azimuthal angle (relative to the sun's ray) of measurement on the observed surface, while ζ is the sun's zenith angle as seen from the observed area. All observed areas were assumed to be located on the earth's surface. The abbreviation "sfc" characterizes the type of surface associated with a particular measurement.

At the time of our analysis, a conversion of the ATS-I signals from digital numbers D, which are available on tape, to values of the outgoing radiance was not possible due to the lack of a reliable calibration in radiometric units. Prelaunch laboratory calibrations (Ref. 6), however, showed a nearly linear relationship between the luminance of a quartz iodide light source (in foot-lamberts) and the camera output in (millivolts). The latter was digitized linearly into 255 intervals. Thus, it was assumed that a linear relationship existed between the radiance viewed by the camera and the corresponding digital value D on the magnetic tape. From Eq. (1), then, ρ'_f is linearily proportional to $D/\cos\zeta$. Therefore, in this study the angular dependence of D' given by

$$D'(\theta,\psi,\zeta;\text{sfc}) = \frac{D(\theta,\psi,\zeta;\text{sfc})}{\cos\zeta} \qquad (2)$$

is investigated instead of ρ'_f.

The ATS-1 satellite is positioned over the Equatorial Pacific. The mean geographic coordinates of its subpoint on 21 and 22 April 1967 were 150.5°W longitude and 0.05°N latitude. Slight changes in these coordinates of about $\pm$ 0.3 degrees during this period were not taken into account. From a position 35,787 km above this point, that portion of the earth can be observed which is bounded by about 70°W and 230°W and about 70°N and 70°S. This area consists almost entirely of the Pacific Ocean. Only a few small fractions of the observable disc show the land surfaces of North and Central America and, at very large zenith angles θ , New Zealand and parts of Australia. Therefore, the results of these investigations apply only to an ocean-atmosphere system.

The investigation of the dependence of D' on the angles θ , ψ and ζ requires an accurate determination of the geographic coordinates of the area from which each signal was obtained. In determining these positions, it was assumed that each area was located on the surface of a spherical earth having a radius of 6371 km.

The only known coordinates of the original ATS-1 camera signals in a coordinate system with respect to the spin axis of ATS-1 are the increments of the camera step angle $\Delta\nu$ = 27.06" arc (Ref. 6) and of the angular distance between two digital values on a scan line $\Delta\mu$ = 8.7891" arc. The latter is obtained from digitizing the analog signals of a 20-degree scan into 2^{13} = 8192 equidistant digital steps. From facsimile prints* of the digital data D, the number of the scan line which coincides with the earth's equator was determined, assuming that the satellite spin axis is parallel to the earth's rotation axis. This particular scan line was used as the initial value for locating all other scan lines of a given photograph.

These calculations could be performed very easily if the attitude of the satellite were known very accurately. But slight oscillations and motions of the spin axis of ATS-1, which are not recorded on the ground, as well as errors of synchronization of all recording equipment cause perturbations in the pictures. On the original photographs some of them can be observed as irregularities in the shape of the illuminated limb of the earth. Thus, many empirical adjustments were necessary, such as the defining of an "effective" step angle and the shifting of scan lines in order to effect a geographic registration using available landmarks or cloud features whose positions were known. In this regard, a valuable source of information were photographs of the ESSA 3-satellite from

*These facsimile prints were obtained through the courtesy of Mr. C. L. Bristor, Chief of the Data Processing and Analysis Division of the National Environmental Satellite Center, ESSA, Suitland, Md.

which approximate positions of typical cloud features were taken. The only clear observable landmarks were the western coastlines of the United States and Mexico.

The above-mentioned errors in the satellite attitude do not allow an absolute location of the data by an operational computer procedure of better than 1 - 2 degrees of longitude and latitude, even over areas close to the subsatellite point. But an even higher spatial resolution of 0.5 degrees of longitude and latitude was chosen for an analysis grid, expecting that later geostationary satellites would allow this accuracy. Mean values D'' were computed for each grid element from all individual values D' falling within that element. The angular dependence of these averages D'', then, was the subject of these investigations.

The increments of the angles θ, ψ and ζ were chosen to be: $\Delta\psi$ = 5 degrees, $\Delta \sin\theta = 0.1$, and $\Delta \cos\zeta = 0.1$.

In addition four types of atmospheric states were categorized assuming, generally, that each increase of the cloudiness or turbidity of atmosphere results in an increase of the brightness of a viewed area. Evidence for this assumption is shown in theoretical investigations of the field of solar radiation reflected to space from different atmospheric models (see e.g. KORB, et. al., 1957). In fact, areas of clear atmosphere over ocean surfaces, except when viewing near the specular point of the sun, are the darkest areas in all photographs. Increments of D'' were chosen by experience to categorize the following conditions of atmospheric state:

complete overcast	:	$171 \leq D''$
cloudy - overcast	:	$41 \leq D'' \leq 170$
cloudless	:	$8 \leq D'' \leq 40$

Additionally the smallest values of D'' falling within each combination of the increments of all three angles of measurement were sought. These lowest values of D'', designated herein "minimal reflection", were assumed to represent all cases of a least cloudy atmosphere over the ocean surface.

Values of $D'' \leq 8$ were not found over all parts of the illuminated disc of the earth except over areas where the sun's zenith angle was larger than 88.85° ($\cos\zeta < 0.02$). These areas were excluded from our investigations.

These numbers in particular are only valid for the photographs which were here analyzed. It was found in further studies, that the response of the entire system (camera + ground equipment) is not constant over longer periods.

Uncertainties in the A/D converter caused considerable additional noise in the data, usually in the form of single noise peaks. A simple "data filter" was designed to reject these noise peaks and to replace them by the arithmetic averages of the adjacent data points. This filter was invoked when increments of the digital value D between two adjacent digital numbers exceeded $\Delta D = 10$ for $D \leq 100$ and $\Delta D = 20$ for $D > 100$. It also checked the "trend" of the data along a scan line, in order to retain such large changes, if they persisted for more than one sample indicating that they were really caused by sharp cloud boundaries rather than by noise. These increments ΔD were chosen by experience.

Fig. 1 shows two parts of a scan line. Symbols + designate unfiltered data, while the data points * are considered to be noise. The filter replaced them by the new data ⊕. This example, shown in Fig. 1, demonstrates one of the worst cases observed so far.

This simple operationally used filter, indeed, might "smooth out" very small, but very bright single clouds over the dark ocean surface. But there was no other possibility to omit the noise from the useful data records. To test for any possible dramatic and artificial effect introduced into the analysis by means of the filter, a comparison of computed map averages (over a latitude-longitude grid having a 0.5 X 0.5-degree mesh size) of "filtered" and "unfiltered" data of the same photograph was made. No significant changes in the patterns were observed.

The response of the camera system and the amplification of all systems involved in producing the digital numbers were assumed to be constant during the entire period of 17 hours spanned by the nine pictures included in this analysis.

PRELIMINARY RESULTS:

The limited number of data obtained so far from only nine photographs did not produce statistically representative averages of D" for each increment of all three angles θ, ψ and ζ. Especially at larger solar zenith angles ($\cos \zeta \leq 0.8$) there were wide gaps in the fields of $D''(\theta, \psi, \zeta; sfc)$. Therefore, in this report only results which were obtained for very small solar zenith angles ($0.9 \leq \cos\zeta \leq 1.0$) are shown.

Figs. 2 and 3 show in polar coordinates the results for the conditions "complete overcast" and "cloudy-overcast". In both distributions a marked increase in the brightness of the earth-atmosphere system occurs within a small range of angles close to the specular point of the sun ($\psi = 0°$; $0° \leq \theta \leq 25.8°$). This might be caused either by specular reflection from the ocean surface in gaps between the clouds and/or possibly from the clouds themselves.

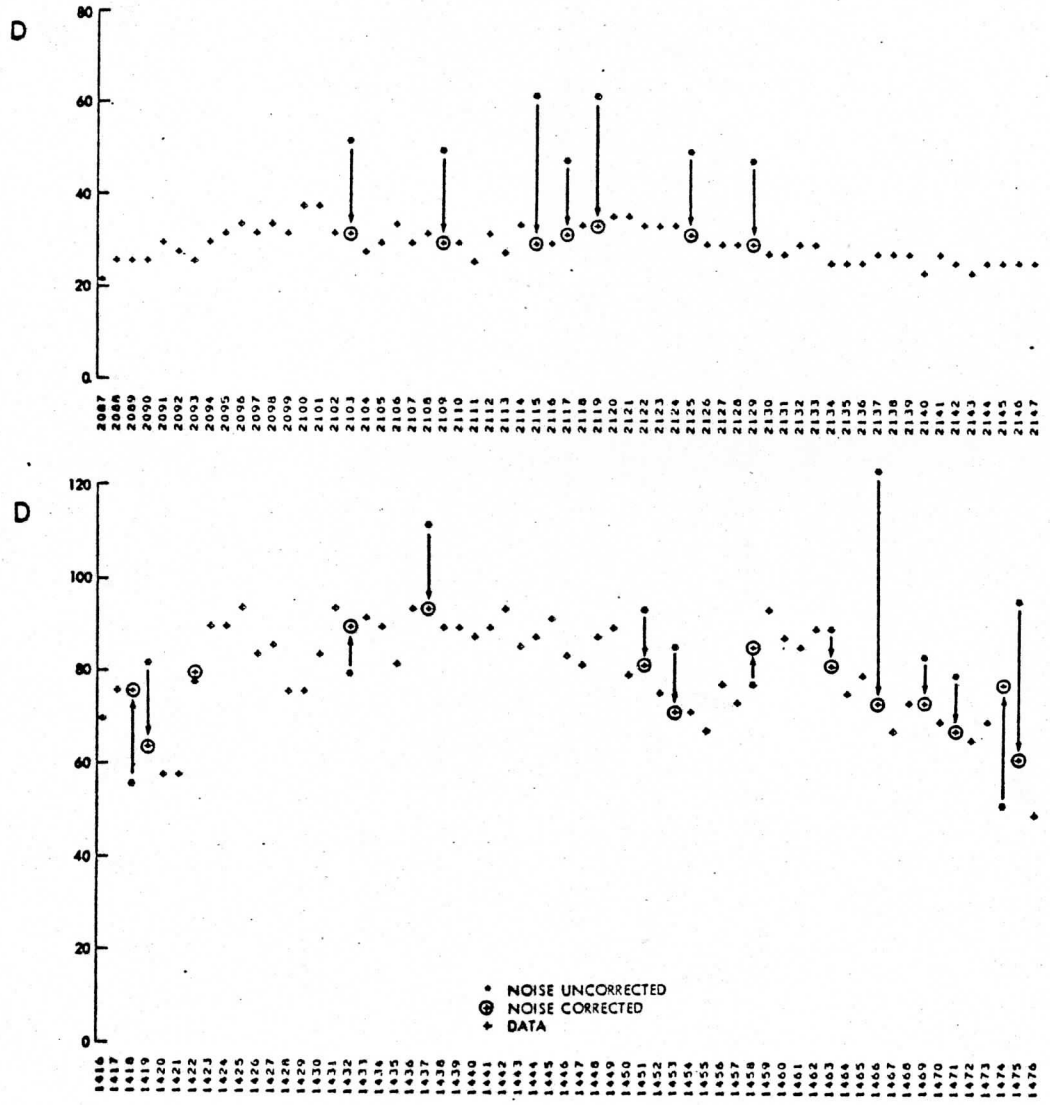

Figure 1. Digital Values D vs. Arbitrarily-numbered Increments of Scan Angle ($\Delta\mu$= 8.7891" Arc), Showing Two Particularly Noisy Sections of One Scan Line. The Results of Applying the "Data Filter" are Illustrated.

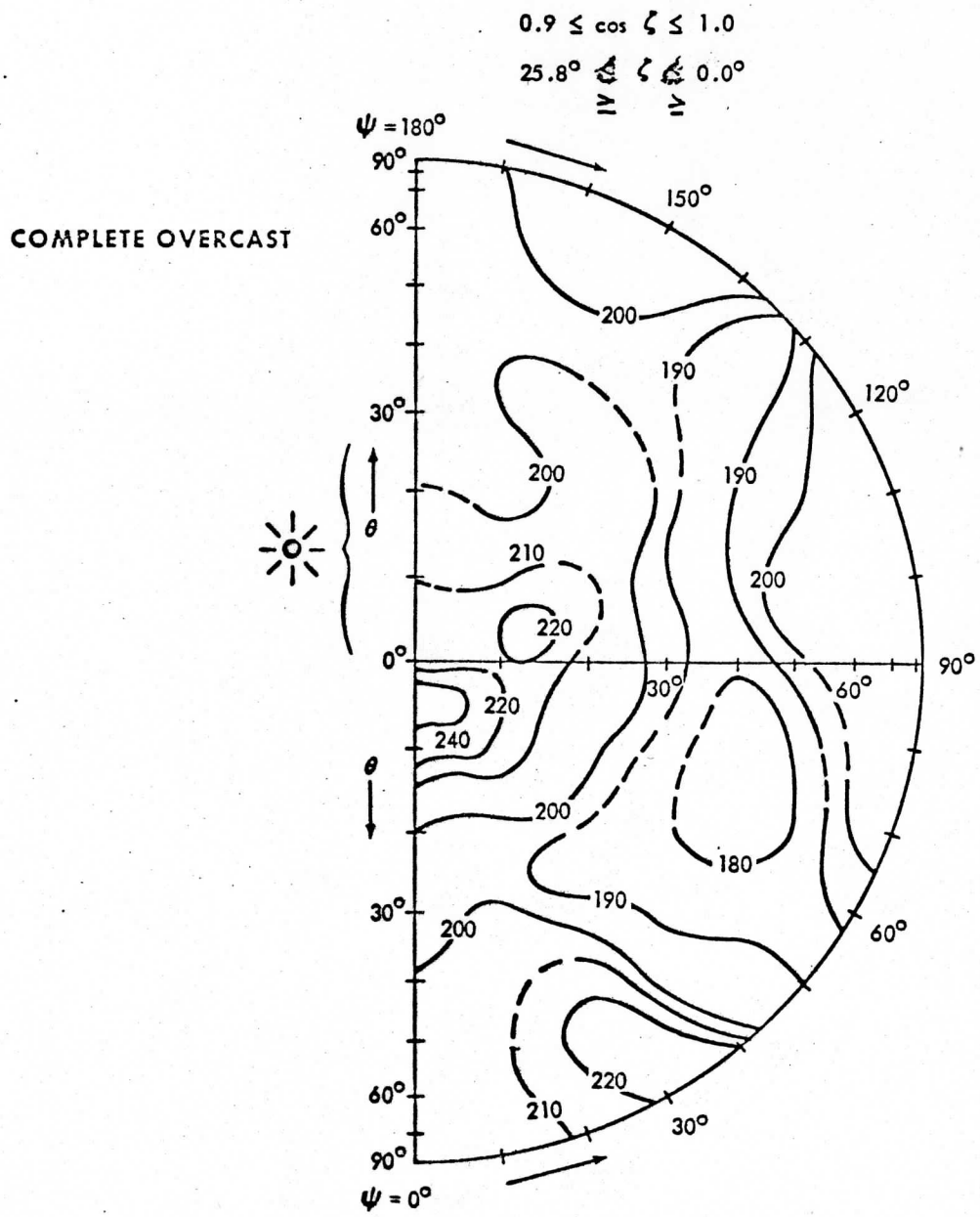

Figure 2. Angular Distribution of the Digital Values D'' (= D/cos ζ) for "Complete Overcast" Conditions

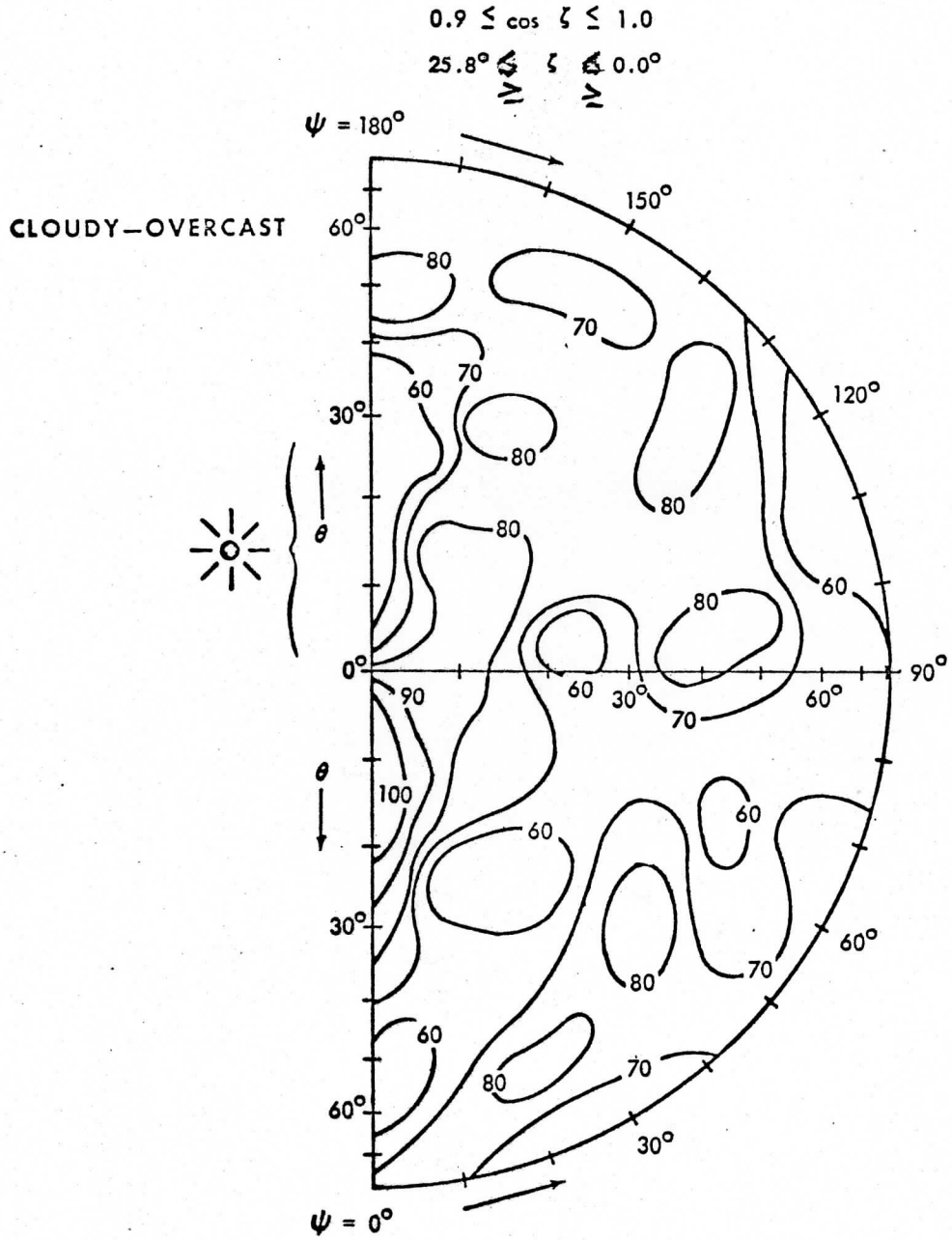

Figure 3. Angular Distribution of the Digital Values D'' (= D/cos ζ) for the Conditions "Cloudy-Overcast"

In Fig. 2 the brightness seems to increase slightly toward the horizon. In both figures there is no definite indication of a maximum caused by direct backscattering, which was found by SALOMONSON (1966) over a strato-cumulus cloud layer.

Evidence of specular reflection and of an increase in brightness toward the horizon is more pronounced in Figs. 4 and 5 which show the angular distribution of D'' for "cloudless atmosphere" and "minimal reflection" conditions. But, here as in Figs. 2 and 3 the bright area around the specular point of the sun extends over a small angular range only. Thus the specular contribution to the directional reflectance (i.e., the total reflectance from a surface into the upward hemisphere for a given value of ζ) is comparatively small.

No special attention is given in this report to the occurrence of other minima and maxima of D'' in Figs. 2 through 5. They might be caused by an accidental arrangement of bright and dark areas in the photographs analyzed so far.

Table 1 lists the total averages of D'', which were obtained by integration of D'' over the two angles of observation, expressed by

$$\bar{D}''(\zeta = \text{const; sfc}) = \frac{2}{\pi}\int_0^{\pi}\int_0^{\frac{\pi}{2}} D''(\theta, \psi, \zeta = \text{const; sfc}) \sin\theta \cos\theta \, d\theta \, d\psi \qquad (3)$$

The total averages $\bar{D}''$ in Table 1 correspond to $(1/\pi) \times$ the directional reflectances of surfaces having the characteristics shown in Figs. 2 through 5. Therefore, one should expect to obtain at least relative information about the directional reflectance (BARTMAN, 1967) of the earth-atmosphere system from these values. If it is assumed that the directional reflectance over very thick clouds (as assumed under "complete overcast" conditions) is about 75%, then the directional reflectance over an extremely clear ocean surface would be only about 8% (Table 1). The slightly higher value of 11% obtained for "cloudless atmosphere" conditions might be due to some cloudiness included in this statistical analysis.

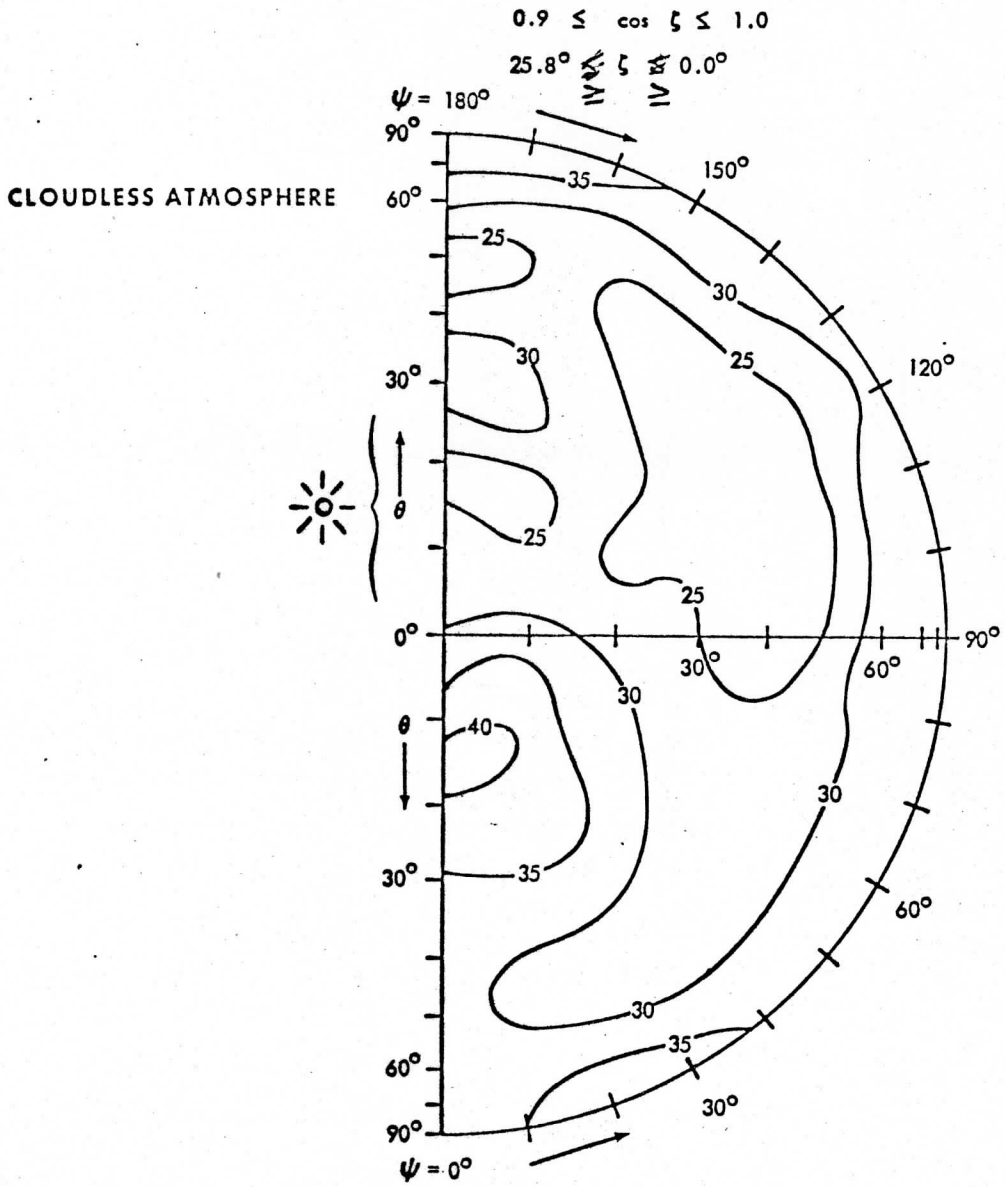

Figure 4. Angular Distribution of the Digital Values D'' (= D/cos ζ) for the Conditions "Cloudless Atmosphere"

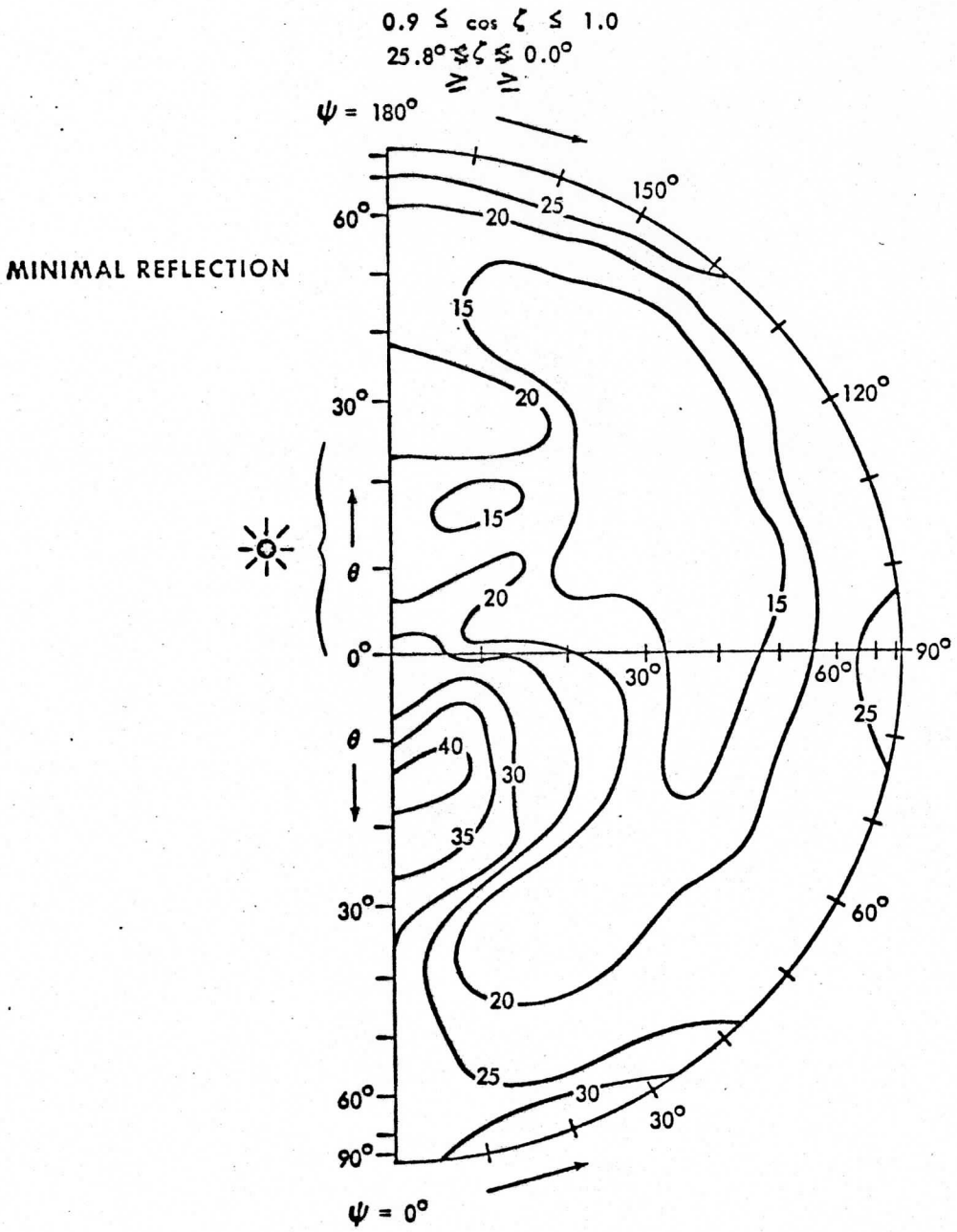

Figure 5. Angular Distribution of the Smallest Values of D″ (=D/cos ζ) Which Are Assumed to Represent Conditions of a Least Turbid Atmosphere Over the Ocean Surface

Table 1

Total Averages $\bar{D}''$, Obtained by Integration of the Angluar Distributions of D'', Shown in Figs. 2 Through 5, Over the Upward Hemisphere

Condition	$\bar{D}''$	Directional Reflectance
complete overcast	197	75% (assumed)
cloudy - overcast	71	27%
cloudless	29	11%
minimal reflection	21	8%

CONCLUSIONS

INSERT FROM PAGE 12a

The preliminary results presented here of the angular dependence of reflected solar radiation in the spectral range 0.46-0.65 microns, obtained from nine photographs of the ATS-1 spin scan camera, indicate that a specular component exists but that it is of little importance to the total directional reflectance for small solar zenith angles. Unfortunately the quantity of data was not statistically representative for all angular increments and, hence, no general conclusions can be drawn. However, the results are encouraging and illustrate the potential of more comprehensive studies of this type, using a more representative sample of data having improved signal-to-noise characteristics.

ACKNOWLEDGMENT:

The authors would like to thank Mr. R. T. Hite and Mr. E. Merill for their extensive efforts in the computer processing of the vast amount of data utilized in this study.

CONCLUSIONS

Preliminary results of the angular dependence of reflected solar radiation in the spectral range 0.46 - 0.65 microns have been presented. These results were obtained by a statistical analysis of data from nine photographs of the ATS-1 Spin Scan Cloud Camera System. Differentiation among different categories of cloud cover was based only upon one quantity, viz., the brightness of an observed area.

Unfortunately the quantity of data which was available to us was not statistically representative for all angular increments or for all "surface" categories. Even if one were to consider only the cases of a complete overcast and a cloudless atmosphere, it would be highly desirable to have complete data samples from several daylight periods at different declination angles of the sun. But the use of such large amounts of data, necessarily obtained over many months of the year, would require some means of continually monitoring the sensitivity of the camera and the calibration of all recording and processing equipment on the ground, and of making corrections as needed to maintain a high degree of accuracy in the measurements throughout. To accomplish this goal under the existing system, would appear to be very difficult. Further, the method of differentiating among different cloud cover categories, based only upon the observed brightness, does not appear to be entirely satisfactory. Perhaps simultaneous measurements in other spectral regions, such as the 11-micron atmospheric window in the infrared, would permit a better categorization of cloud cover. (It is appropriate to note at this point that radiometers to obtain such measurements from geosynchronous satellites are now in an advanced stage of development.)

However, in spite of these difficulties, we believe our results are encouraging. They illustrate in principle the potential of more comprehensive studies of this type for the future when more representative data become available.

REFERENCES

1. Bartman, F. L., 1967: The Reflectance and Scattering of Solar Radiation by the Earth. Contr. NASr-54(03), Dept. of Engineering, The University of Michigan.

2. Korb, G., J. Michalowsky, F. Möller, 1957: Die Absorption der Sonnenstrahlung in der wolkenfreien und bewölkten Atmosphäre. Beitr. Phys. Atm., 30, 63-77.

3. Raschke, E., and M. Pasternak, 1967: The Global Radiation Balance of the Earth Atmosphere System Obtained from Radiation Data of the Meteorological Satellite Nimbus II. NASA-X-622-67-383 (to be published in "Space Research VIII").

4. Ruff, I., R. Koffler, S. Fritz, J. S. Winston, and P. K. Rao, 1967: Angular Distribution of Solar Radiation Reflected from Clouds as Determined from TIROS IV Radiometer Measurements. ESSA Technical Report NESC-38.

5. Salomonson, V. V., 1966: Anisotropy of Reflected Solar Radiation from Various Surfaces as Measured with an Aircraft-Mounted Radiometer. Contr. NASr-147, Dept. of Meteorology, Col. State Univ., Fort Collins, Colo.

6. Santa Barbara Research Center and University of Wisconsin, 1967: ATS Spin-Scan Cloud Camera and Prelaunch Calibration Procedure. Ann. Report 1966, Dept. of Meteorology, The University of Wisconsin, Madison, Wis.

C.29

revised

POSSIBILITIES FOR QUANTITATIVE RADIANCE MEASUREMENTS IN THE 450–650 nm REGION FROM THE ATS-1 SATELLITE

by

Susan K. Peekna
Robert J. Parent
and
Thomas H. Vonder Haar

The University of Wisconsin

LIST OF SYMBOLS

A_c : Area camera entrance aperture, m^2

A_s : Area of source radiation, m^2

$A_{s\perp}$: Source area projected perpendicular to r_s, m^2

$H'(\delta)$: Effective irradiance on A_s from a zenith angle δ

m : Optical air mass

$N_{\lambda s}$: Spectral radiance from a source, watts m^{-2} $ster^{-1}$ nm^{-1}

$N_s'(\gamma)$: Effective radiance from A_s in direction γ, watts $. m^{-2} . ster^{-1}$

$N_r'(\delta)$: Effective radiance on A_s from direction δ, watts $. m^{-2} . ster^{-1}$

P' : Effective power input to camera, watts

$P_{\lambda r}$: Power of wavelength λ received at camera entrance, watts nm^{-1}

r_s : Distance from camera to A_s, m

r' : Effective directional reflectance

r : Total directional reflectance of Kodak white paper

R_λ : Normalized spectral transmission of the camera optics

V_0 : Voltage output from the camera system, millivolts, volts

ϕ : Azimuth angle in plane of A_s

γ : Zenith angle of satellite from A_s, degrees, radians

δ : Zenith angle of sun from A_s, degrees, radians

λ : Wavelength, millimicrons (nanometers)

ρ' : Effective bi-directional reflectance ($ster^{-1}$)

α : Angular field of view of camera, radians

ω_c : Solid angle field of view of camera, steradians

A_c :

ω_s : Solid angle subtended by the camera entrance aperture

A_s : at the source

$d\Omega$: Elemental solid angle

$\Omega_\odot$: Solid angle subtended by the Sun at A_s

E : C

$N_{\lambda s}$: S

$N_s''(\gamma)$: E

$N_r(\epsilon)$: E

P' : E

E

E

E

E

E

W

E : E

1. INTRODUCTION

The Spin-Scan Camera experiment flown on ATS-1 consists essentially of a photomultiplier tube and associated optics that respond to variations in a selected portion of solar energy reflected and scattered from the earth and its atmosphere. Other papers in this Volume discuss the details of camera construction (Thomsen, et al. (1968)), and the pre-launch (Suomi and Parent (1968)). They show that the spectral bandpass of the camera is from 450 to 650 mμ.

The purpose of this paper is to develop the equations that could be used in prelaunch calibration of satellite cameras such as that flown on ATS-1. We have used the prelaunch calibration that was done on ATS-1 only as an example of how such a calibration might be performed, because these particular measurements were obtained under less-than-optimum conditions and were intended merely to make necessary prelaunch adjustments to the camera gain level setting. An absolute calibration of ATS-1 cloud camera has carried out after launch and is discussed in another paper in this volume by Hanson and Suomi.

Effective radiance values can be used to investigate the radiation budget of the earth-atmosphere system and, together with surface observations, the absorption of solar energy in the atmosphere. They can also provide new information about the spectral and bi-directional reflectance characteristics of different surfaces. Variations of cloud thickness can be inferred from radiance values and the type and amount

of cloudiness over a region can be related to the reflected energy. Among the other possible uses of these quantitative values are studies of the diurnal variation of cloudiness, background brightness of various regions and work oriented toward passive thermal control of spacecraft.

The advantages of applying ATS-1 data to these problems stem from the high spatial resolution and large dynamic range of the sensors and the nearly continuous time sampling of the experiment. For many studies only relative brightness measurements are required. This paper will present information about this type of application of the ATS-1 data and will also discuss the procedure for obtaining absolute values of reflected spectral radiance. At the present time the most accessible quantitative values of ATS-1 measurements are stored in digital form on magnetic tape. Thus, the following sections will consider the necessary steps required to convert these digital count values to the effective radiance of the source as viewed by the camera.

2. TOTAL POWER INPUT TO THE CAMERA IN TERMS OF EARTH RADIANCE

The total power incident on the camera entrance aperture within the field of view of the camera can be related to the radiance of the source. The geometry for this calculation is shown in figure 1, which depicts the instantaneous view of the camera of an area on the surface

of the earth. Assuming the field of view is a cone of angle α with a uniform response (i.e., the response is uniform within the cone of view and zero elsewhere), the spectral power $P_{\lambda r}$ received is from an area A_s on the earth defined by the intersection of the cone and the earth. $P_{\lambda s}$ can be calculated under these conditions in terms of the radiance of A_s, $N_{\lambda s}$, following the definition of N_λ used by Nicodemus.* Assuming the radiating surface to be the top of the atmosphere and thus neglecting atmospheric absorption, we have,

$$P_{\lambda r} = A_s \omega_s N_{\lambda s}(\gamma)\cos\gamma \quad [\text{watts nm}^{-1}] \tag{1}$$

Where ω_s is the solid angle subtended at the center of A_s by the camera entrance aperture A_c. Using a small angle approximation,

$$\omega_s = \frac{A_c}{r_s^2} \quad [\text{sr.}] \tag{2}$$

Now let $A_{s\perp}$ be the source area projected perpendicular to r_s. Then

$$A_{s\perp} = A_s \cos\gamma$$

$$A_s = \frac{A_{s\perp}}{\cos\gamma} \tag{3}$$

The area $A_{s\perp}$ is a circle, and its radius $a_{s\perp}$ is given by small angle approximation, when α is expressed in radians, as,

---

*Radiance is the radiant power (P) per unit solid angle (Ω) in the direction of a ray per unit projected area ($A \cos\theta$) perpendicular to the ray.

$$a_{s\perp} = r_s \frac{\alpha}{2} \tag{4}$$

Substituting,

$$A_{s\perp} = \pi a_s^2 = \frac{\pi r_s^2 \alpha^2}{4} \tag{5}$$

Then:

$$A_s = \frac{\pi r_s^2 \alpha^2}{4 \cos \gamma} \tag{6}$$

Substituting (6) and (2) into (1),

$$P_{\lambda r} = N_{s\lambda}(\gamma) A_c \pi \frac{\alpha^2}{4} \tag{7}$$

which is the desired relationship between $P_{\lambda r}$ and $N_{\lambda s}(\gamma)$.

3. RADIANT INPUT MEASURED BY THE CAMERA

In order to interpret the output of the camera as a measurement of radiant input, it is important to note that it is not the total power input that is being measured, but only that part which lies within the spectral band width (450 - 650 nm) of the ATS-1 camera. With this in mind, the "effective" power input, P', to the camera is defined as:

$$P' = \int_{\lambda_1}^{\lambda_2} P_{\lambda r} R_\lambda \, d\lambda \tag{8}$$

Where R_λ is the normalized spectral transmission of the camera optics, which includes the effects of the mirrors, lens, filter, and photocathode surface, and λ_1 and λ_2 are the limits of the spectral bandwidth of the camera. (Fig. 2)

A thorough examination of the camera response to a known source is essential in providing a reliable relationship between P' and camera output. This information will be provided by the inflight calibration. Substituting (7) into (8) gives the effective power received from the source as:

$$P_r' = \frac{A_c \pi \alpha^2}{4} \int_{\lambda_1}^{\lambda_2} N_{\lambda s}(\gamma) P_\lambda d\lambda \qquad (9)$$

The integral in this equation can be defined as the effective radiance from the source A_s in the direction γ, or $N_s'(\gamma)$. Using this definition,

$$P_r' = \frac{A_c \pi \alpha^2}{4} N_s'(\gamma) \qquad (10)$$

Since for small angles, $\omega_c = \frac{\pi \alpha^2}{4}$, Eq. (10) can be expressed as:

$$P_r' = A_c \omega_c N_s'(\gamma) \qquad (11)$$

This last equation is true in general only under the condition stated, i.e., the field of view is a cone with a uniform response, and the source viewed is radiating uniformly over the area A_s.

4. BI-DIRECTIONAL REFLECTANCE MEASUREMENTS

Additional information can be derived from the ATS measurements of $N_s'(\gamma)$, when they are used to infer the effective bi-directional reflectance $\rho' = \rho(\delta, \phi_1, \gamma, \phi_2)$ of the region viewed by the camera (Fig. 3).

The general expression for this relation (Nicodemus (1965)), is:

$$N_s'(\phi_2, \gamma) = \int \rho' \, N_r'(\phi_1, \delta) \cos \delta \, d\Omega_\delta \tag{12}$$

Where the effective incoming radiance $N_r'(\phi_1, \delta)$ as well as $N_s'(\phi_2, \gamma)$ depends on an azimuth angle, ϕ, in the plane of A_s; and $d\Omega_\delta$ is an elemental solid angle subtended by the radiation source at A_s. The integration is taken over all such solid angles.

For the special case when the incident radiation is only direct solar energy (no "sky" radiation) we may assume that ρ' and $N_r'(\phi_1, \delta)$ are constant over Ω_δ, which is the solid angle subtended by the sun. Now δ is the zenith angle of the sun and the subscript r is replaced by $\odot$ for the sun. Then (12) becomes

$$N_s'(\phi_2, \gamma) = \rho' \, N_\odot'(\phi_1, \delta) \cos \delta \, \Omega_\odot \tag{13}$$

and since $H_\odot' = N_\odot'(\phi_1, \delta)\Omega_\odot$, we have

$$N_s'(\phi_2, \gamma) = \rho' \cos \delta \, H_\odot' \tag{14}$$

or,

$$\rho' = \frac{N_s(\gamma, \phi_2)}{H_\odot' \cos \delta} \tag{15}$$

and from Eq. (11)

$$\rho' = \frac{P'}{A_c \, \omega_c \, H_\odot' \cos \delta} \tag{16}$$

Note also that the effective directional reflectance, $r' = r'(\phi_1, \delta)$ is

defined as the ratio of radiation incident on A_s from the direction δ, ϕ_1, to that reflected (or scattered) in all directions and is related to ρ' by:

$$r' = \int_0^{2\pi} \int_0^{\pi/2} \rho'(\delta, \phi_1, \gamma, \phi_2) \cos\gamma \sin\gamma \, d\gamma d\phi_2 \tag{17}$$

and only for a Lambert reflector, where ρ' is constant over all directions, it is possible to integrate (17), so

$$r' = \pi \rho' \tag{18}$$

and Eq. (15) becomes

$$r' = \frac{\pi N_s'(\phi_2 \ \gamma)}{H_\odot' \cos\delta} \tag{19}$$

Since many natural surfaces and clouds are known to be non-Lambert reflectors, measurements of ρ' from the ATS data can only be used to compute effective "albedo" values if a bi-directional reflectance pattern is known or assumed (see Bartman (1967)). In addition, some knowledge of the spectral reflectance properties of the regions viewed is required before the measurements in the 450-650 nanometer region can be used to infer the "total" shortwave albedo.

5. PRE-LAUNCH CALIBRATION TESTS

In order to relate P' to camera output, a reliable calibration must be made. This is provided in another paper in this volume by K. Hanson.

However, it is possible to use the pre-launch calibration tests as a basis for understanding the requirements for determining earth radiance values, and as an estimate of the relationship between P' and camera output.

The primary result of the pre-launch calibration tests was the determination of the required gain of the photomultiplier and the video amplifier such that the brightest clouds would not saturate the system while allowing a good dynamic range. A second important result was the determination of the slope of the input-output curve of the camera, and establishing the fact that below the saturation level, this relationship is nearly linear (Fig. 4). To accomplish this, two kinds of measurements were made. In one, the camera and a spot photometer with a spectral response close to that of the camera (Fig. 2) viewed a light box with a variable quartz iodine source. Plots of the photometer output against the camera output on a log-log scale showed that below the saturation level, the response of the camera was linear. Another set of measurements was made outdoors with the camera and the photometer viewing a piece of Kodak white paper illuminated by sunlight at normal incidence at various times of day. (Fig. 5) From a knowledge of the solar zenith angle at the time of each measurement, the number of optical air masses, (m), was calculated. Plots of camera output v. s. m. extrapolated to the top of the atmosphere, give the photomultiplier output when viewing non-attenuated sunlight incident normal to a highly reflecting

surface. This was assumed to be near the maximum input to the camera from clouds. Combined with the results of the previous test, this information was used to set the photomultiplier supply voltage and the video amplification such that this maximum value occurred at the top of the linear portion of the curve.

6. RELATIONSHIP BETWEEN CAMERA OUTPUT AND P'

The results of the pre-launch (solar) tests can also be used to illustrate a method for determining the relationship between P' and camera output if the solar spectral distribution at the time of the tests is assumed to be known. Since any linear relationship when plotted on a log-log plot has a slope of one, only one point on the slope need be calculated to establish the P' vs. camera output relationship.

The following calculation of P' is based on the spectral distribution of solar radiation for m = 0 from the Handbook of Geophysics and Space Environments (1965).

The geometry for the test set-up was as shown in Fig. 5. As can be seen, the source in this case is a piece of Kodak white paper (average total directional reflectance, r = 0.88), at a distance of only 49 inches from the camera. Considering Eq. (11) from section 2, it can be seen that P', however, is independent of the distance from the source. Thus, the radiance of the paper can be substituted into this equation to get the effective power.

The tests were made with the paper kept nearly perpendicular to the sun's rays and the camera axis nearly perpendicular to the paper, the deviation from the normal being just enough so that the camera did not cast a shadow on the paper.

The effective spectral radiance of the paper is then given by:

$$N_s' = \int_{\lambda_1}^{\lambda_2} \frac{H_{\lambda\odot}}{\pi} R_\lambda \, r \, d\lambda \qquad (20)$$

where $H_{\lambda\odot}$ is the solar spectral irradiance on the paper, and $H_{\lambda\odot} r/\pi$ is the normal component of the radiance from a Lambert surface of reflectivity r.

Equation 20 has been evaluated numerically using the distribution for $H_{\lambda\odot}$ at m = 0 and the spectral response of the camera R_λ shown in Fig. 2.* The result of this calculation is

$$P' = 4.55 \times 10^{-9} \text{ [watts]} \qquad (21)$$

From Fig. 6, the camera output for this input was 700 millivolts (mv). This, then, established the point which was used to plot the curve shown in Fig. 7. As shown in Fig. 4, this value would actually saturate the camera, and so is shown on the curve on an extension of the linear portion.

It should be mentioned that this curve is only an estimate based on prelaunch calibration tests which were intended to assist in making necessary adjustments to the camera gain level setting, in order that the camera would respond favorably to viewed conditions on earth.

*See paper in this volume by Thomson, Parent and Suomi for a tabulation of R_λ and a more detailed plot.

7. FIELD OF VIEW CONSIDERATIONS

The real field of view does not have a uniform response. Its probable response was determined during the pre-launch calibration tests (Thomsen, et al.). The angular field of view was estimated to be 0.1 m.r. at the half power points, tailing off to zero at 0.35 mr. From the response curve in the above reference, it can be seen that about 26% of the detected input is from beyond the 0.1 mr field.

In practice, the way to deal with this situation is influenced by the fact that both the ground calibration and the inflight calibration were done with sources that completely fill the field of view. Thus, in order to use these calibration curves the data used must represent a source which also entirely fills the field of view.

This is especially important to note for those who wish to measure the radiance from small clouds. The following examples, shown in Figures 8 and 9, are intended to demonstrate ambiguities and other difficulties which arise when one attempts to obtain a measurement of a source smaller than the field of view from the digital ATS data.

In the first set (Fig. 8), a uniform field of view is assumed. The signals from clouds of equal radiances larger than or equal to the field of view have equal amplitude. However, a cloud of the same radiance smaller than the field of view does not produce the same amplitude, because the signal is integrated over the whole field. The signal from a cloud which does not have as large a radiance, but fills more of the field

could have the same amplitude as the smaller brighter cloud, but a different duration. In addition, the duration of the signal produced by clouds of the same size but smaller than the field of view is different depending on their location within the field of view in the direction perpendicular to the scan direction.

In the second set, a field of view more like the real case is assumed. In this case the same difficulties arise as for the step function field of view, with added ambiguities. Here, a cloud seen by the "outer edge" of the detector which is less sensitive could have the same amplitude as a less bright cloud seen by the center of the detector.

From these examples, it is clear that the only time one can make unambiguous measurements of the radiation from a cloud is when it fills the whole field of view (i.e., beyond 0.35 mr). To get an idea of how large a cloud has to be to get a measurement of its effective radiance by the camera, consider the plot shown in Figure 10. Here the major and minor axes and the area of the ellipse formed by the intersection of a 0.1 mr. cone, vertex at the satellite, and a plane tangent to the earth at the intersection of the earth and the axis of the cone is plotted against the nadir angle of the camera.

Clouds having these areas at these distances would fill the field of view defined by the half power points, i.e., the amplitudes of the signals from then would be approximately 70% of the amplitude for clouds of the same effective radiance filling a 0.35 mr. field of view.

If one were using the digital data, one would have to average the number of digital samples in the field of view. The signal is digitized linearly with respect to the scan angle, and there are 8192 samples within a 20° scan. This means a sampling rate of about 2.35 samples per 0.1 milliradian, or about 8.23 samples per .35 milliradians. Thus, measurements from areas smaller than 10 samples wide (8 n. mi. sq. at the subpoint and 15 n. mi. sq. near the limb) must be interpreted with care when using the calibration curves.

8. USING THE DIGITAL DATA

When using the digital data with the calibration curve in Fig. 4, the digital count (or average digital count) must be converted to millivolts out of the camera.

The video amplifier on board the satellite has two gain modes which can be commanded from the ground; mode 2, or normal mode, and mode 1, or high gain mode, which is 10 db* (3.161 times) higher than mode 2. In addition to this, there is the capability of increasing the gain on the ground up to 12 db higher (3.98 times) in steps of 2 db (1.26 times).** Table 1 lists these various gain steps and their corresponding amplification factors.

---

*The notation db means decibels. The number of decibels is equal to 20 log V2/V1, where V2/V1 is the ratio of the voltage outputs.
**This gain information is recorded on the digital tapes as part of the documentation code.

As a result of the pre-launch test, the gains were set so that the maximum anticipated output of the camera video amplifier, when viewing bright clouds, would be approximately 500 millivolts in normal gain mode, zero ground gain. The telemetry link from the satellite through the ground station analog to digital (A/D) converter, is set so that the maximum digital number, D = 255, occurs for a 500 millivolt signal from the satellite video amplifier when in mode 2, zero ground gain.

Thus if the camera is in the high gain mode and/or the ground gain is other than zero, the voltage represented by the digital value must be adjusted to give the equivalent reading for mode 2, zero ground gain, in order to use the calibration curve done in this gain.

For example, assume the camera is in high gain mode, the ground gain is 2 db, and the digital number for a certain camera reading is 100. Then:

$$\frac{\text{millivolts}}{\text{count}} = \frac{500}{255} = 1.96$$

$$1.96 \times 100 = 196 \text{ m.v.}$$

The high gain mode is 3.161 times higher than the normal mode, so:

$$\frac{196}{3.16} = 62 \text{ m.v.}$$

is the corresponding reading for normal mode, ground gain 2 db. To convert to ground gain zero, this must be divided by 1.26 (2 db), which gives

$$\frac{62}{1.26} = 49.2 \text{ m.v.}$$

as the millivolt output of the camera referred to mode 2, zero ground gain. Hanson and Suomi have referenced their inflight calibration to mode 2, ground gain 0.

9. SUMMARY

Measurements of $N_s'(\gamma)$ can be derived from the ATS-1 observations, and the relationship between these reflected radiance values and the camera voltage output or digital counts has been shown. Even with the camera inflight calibration, the digitized ATS data must always be considered in terms of the following:

a) the camera measures only the effective radiance, $N_s'(\gamma)$ between 450 and 650 mμ reflected and scattered through the "top of the atmosphere" in a given direction.

b) the camera has a non-uniform response across its nominal field of view and thus measurements over areas of nonhomogeneous radiance must be interpreted with care.

c) the relation between the digital count values and the camera output voltage depends on two gain settings and must be considered before calibration curves are used to obtain absolute values of N_s'.

In addition, the ATS-1 data can be used to measure the effective bidirectional reflectance of the region viewed by the camera. However, the conversion of this measurement into an albedo value, even for the instant of observation, requires supporting information on the bi-directional and spectral reflectance pattern of the area in view.

TABLE 1

Spacecraft Gain	Ground Station Gain	Amplification Factor Relative to Lowest Setting
(Mode 2) 0 db	0 db	1.00
"	2 db	1.26
"	4 db	1.58
"	6 db	1.99
"	8 db	2.51
"	10 db	3.16
"	12 db	3.98
(Mode 1) 10 db	0 db	3.16
"	2 db	3.98
"	4 db	5.01
"	6 db	6.31
"	8 db	7.94
"	10 db	10.00
"	12 db	12.59

REFERENCES

1. Bartman, F. L., 1967: The Reflectance and Scattering of Solar Radiation by the Earth, Technical Report 05863 - 11 - T, The University of Michigan, College of Engineering, 257 pp.

2. Handbook of Geophysics and Space Environments, Valley, S. L. (Editor), 1965: McGraw Hill, N.Y., 16-4, 16-6.

3. Hanson, K. J. and V. E. Suomi, 1968: In-Flight Calibration of the ATS-1 Camera. ATS-1 Volume, University of Wisconsin Press ( ) - ( ).

4. Nicodemus, F. E., 1965: Directional Reflectance and Emissivity of an Opaque Surface, Appl. Optics, 4, 767-773.

5. Suomi, V. and R. Parent, 1968: Calibration Procedure for ATS-1 Spin-Scan Camera. ATS-1 Volume, University of Wisconsin Press ( ) - ( ).

6. Thomsen, R., R. Parent and V. Suomi, 1968: The ATS-1 Camera. ATS-1 Volume, University of Wisconsin Press ( ) - ( ).

LIST OF FIGURES:

Figure 1. Satellite - earth geometry.

Figure 2. Normalized spectral response of camera and photometer; normalized spectral solar irradiance on a surface perpendicular to the sun's rays for m = 0 at mean earth-sun distance.

Figure 3. Geometry of incident and reflected radiation used in bi-directional reflectance discussion.

Figure 4. Spot photometer output vs. camera output for two sources. Data taken during pre-launch tests.

Figure 5. Geometry of pre-launch solar test.

Figure 6. Camera output viewing sunlight vs. number of optical air masses.

Figure 7. Camera output vs. effective power input.

Figure 8. Schematic representation of signals from various sources as seen by an aperature having a uniform field of view.

Figure 9. Schematic representation of signals from various sources as seen by an aperature having a non-uniform field of view.

Figure 10. Camera nadir angle vs. area, major axis, and minor axis of projected ellipse.

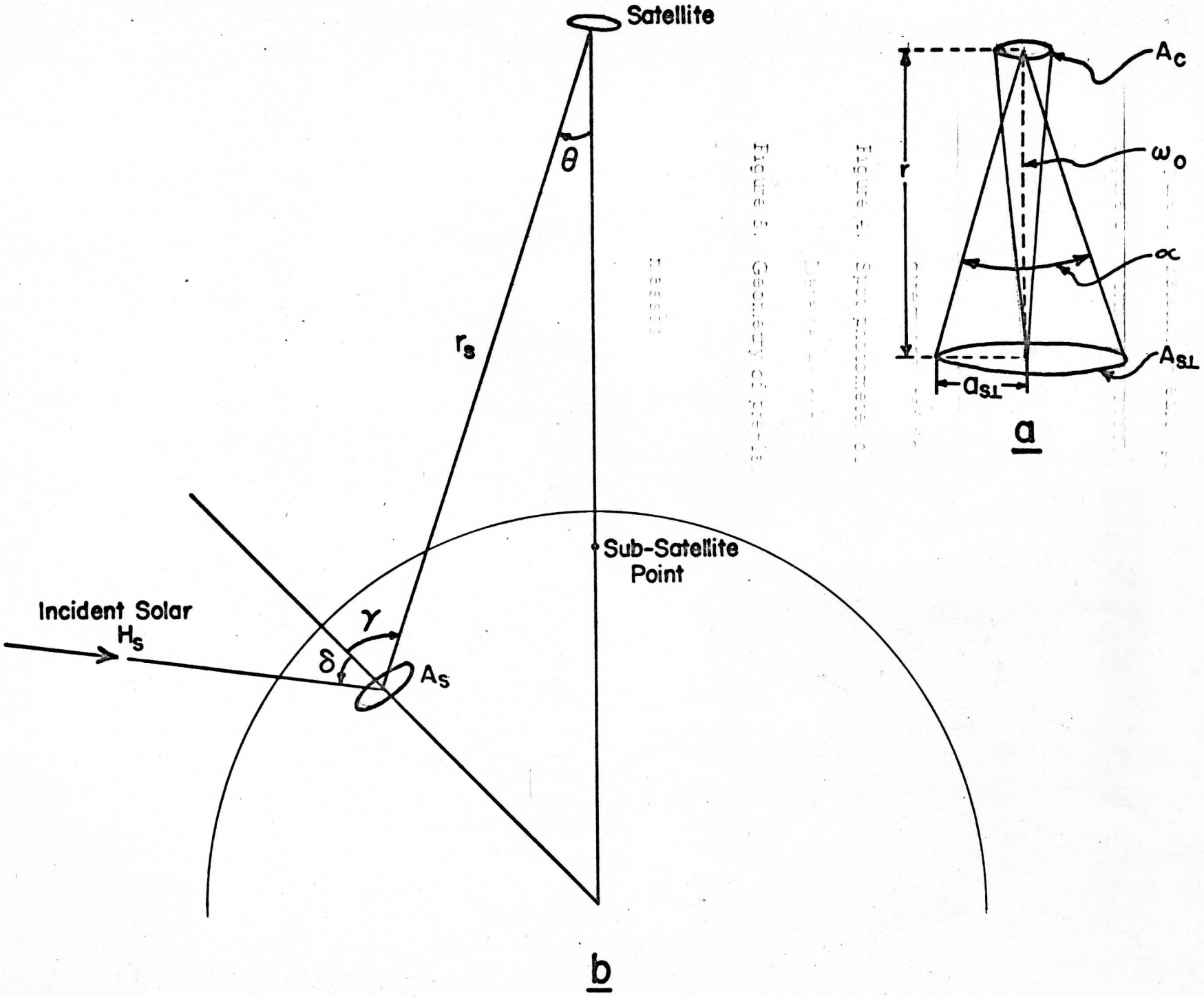
Satellite
θ
r_s
Sub-Satellite
Point
Incident Solar
H_s
γ
δ
A_s
b
A_c
ω_o
r
α
A_{SL}
a_{SL}
a

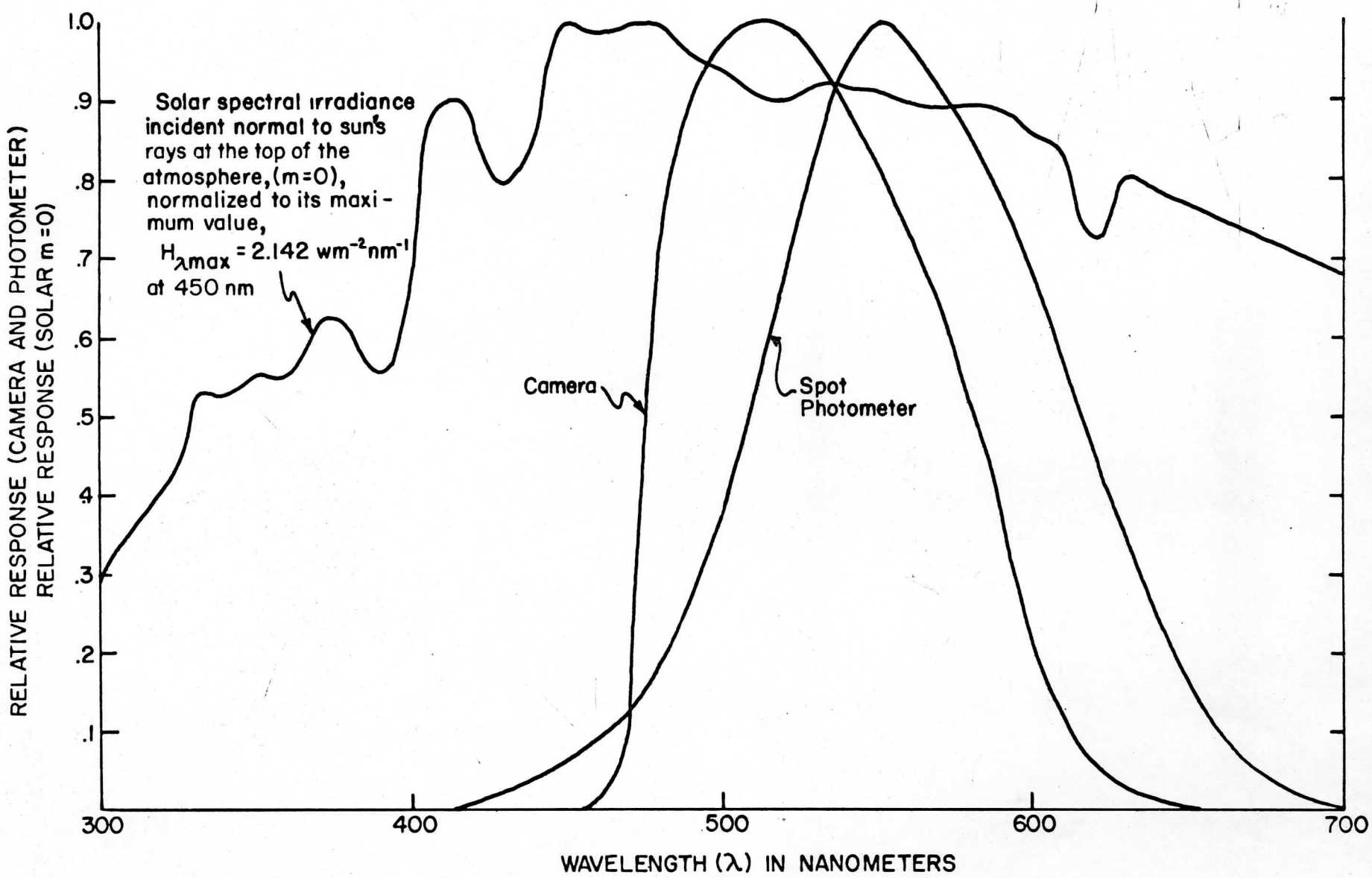
RELATIVE RESPONSE (CAMERA AND PHOTOMETER)
RELATIVE RESPONSE (SOLAR m=0)
1.0
.9
.8
.7
.6
.5
.4
.3
.2
.1
Solar spectral irradiance incident normal to sun's rays at the top of the atmosphere, (m=0), normalized to its maximum value,
$H_{\lambda max} = 2.142\ wm^{-2}nm^{-1}$
at 450 nm
Camera
Spot Photometer
300
400
500
600
700
WAVELENGTH (λ) IN NANOMETERS

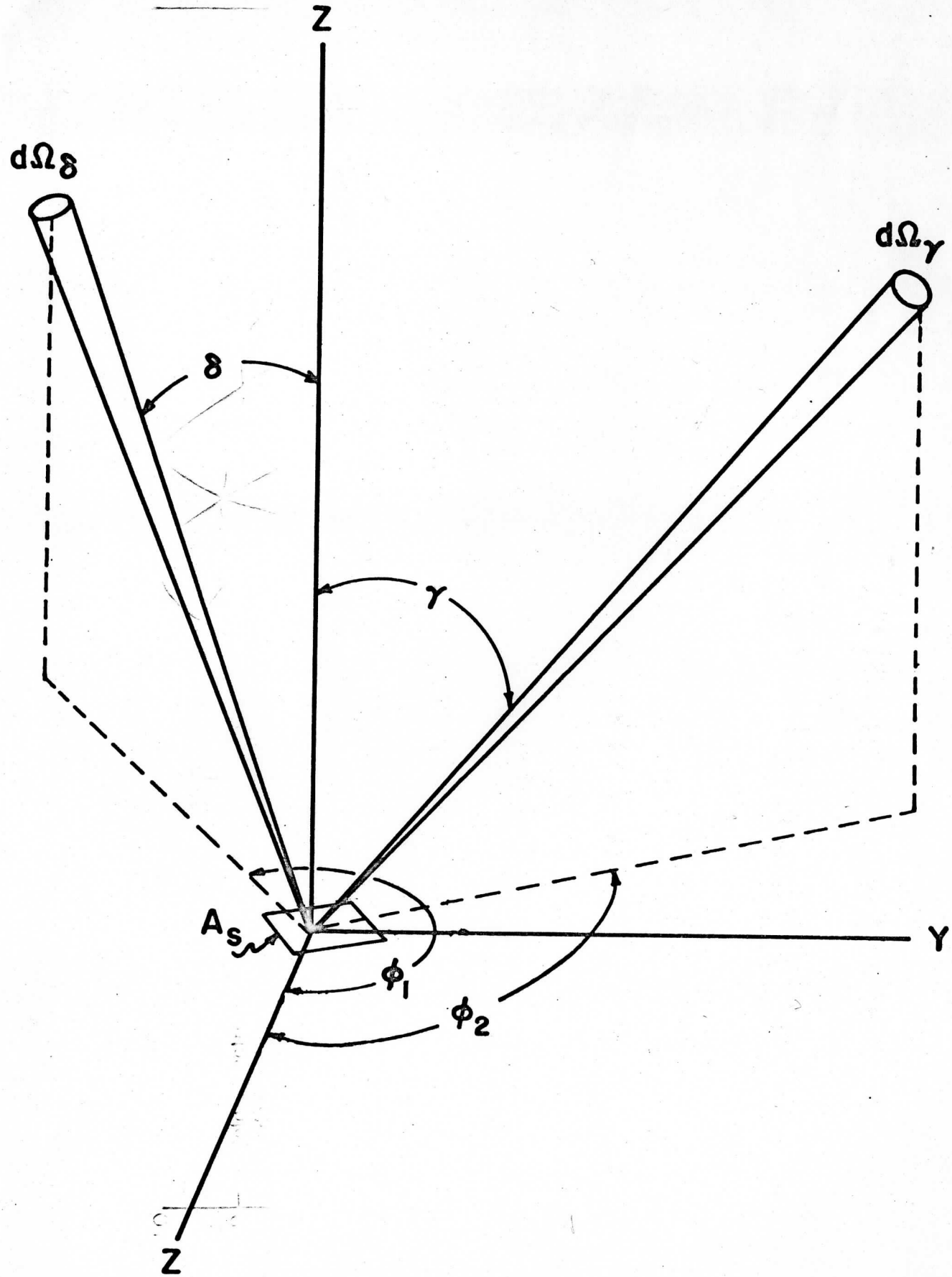

Fig 3

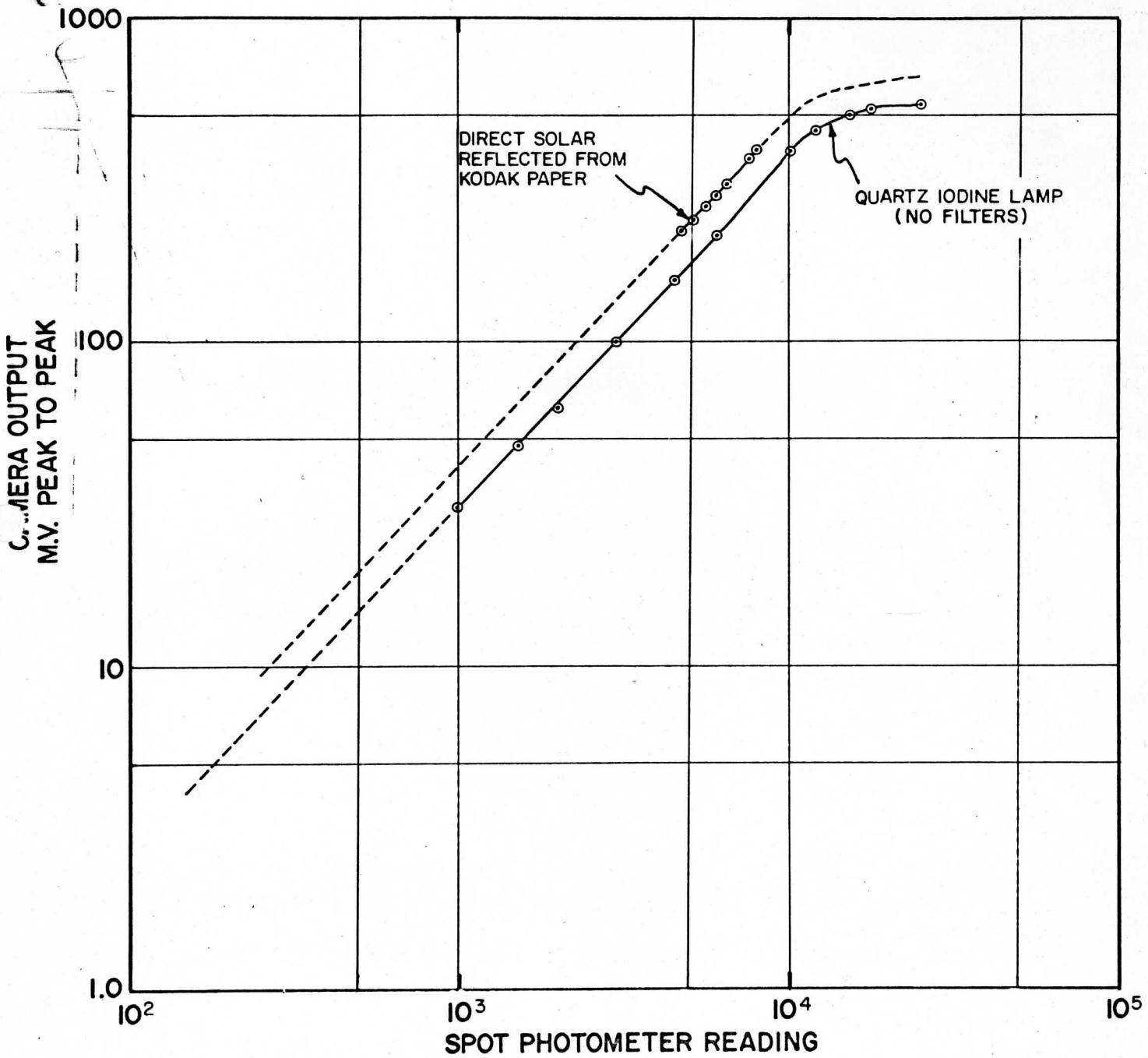
1000
100
10
1.0
CAMERA OUTPUT
M.V. PEAK TO PEAK
DIRECT SOLAR
REFLECTED FROM
KODAK PAPER
QUARTZ IODINE LAMP
(NO FILTERS)
10^2
10^3
10^4
10^5
SPOT PHOTOMETER READING

Fig 4.

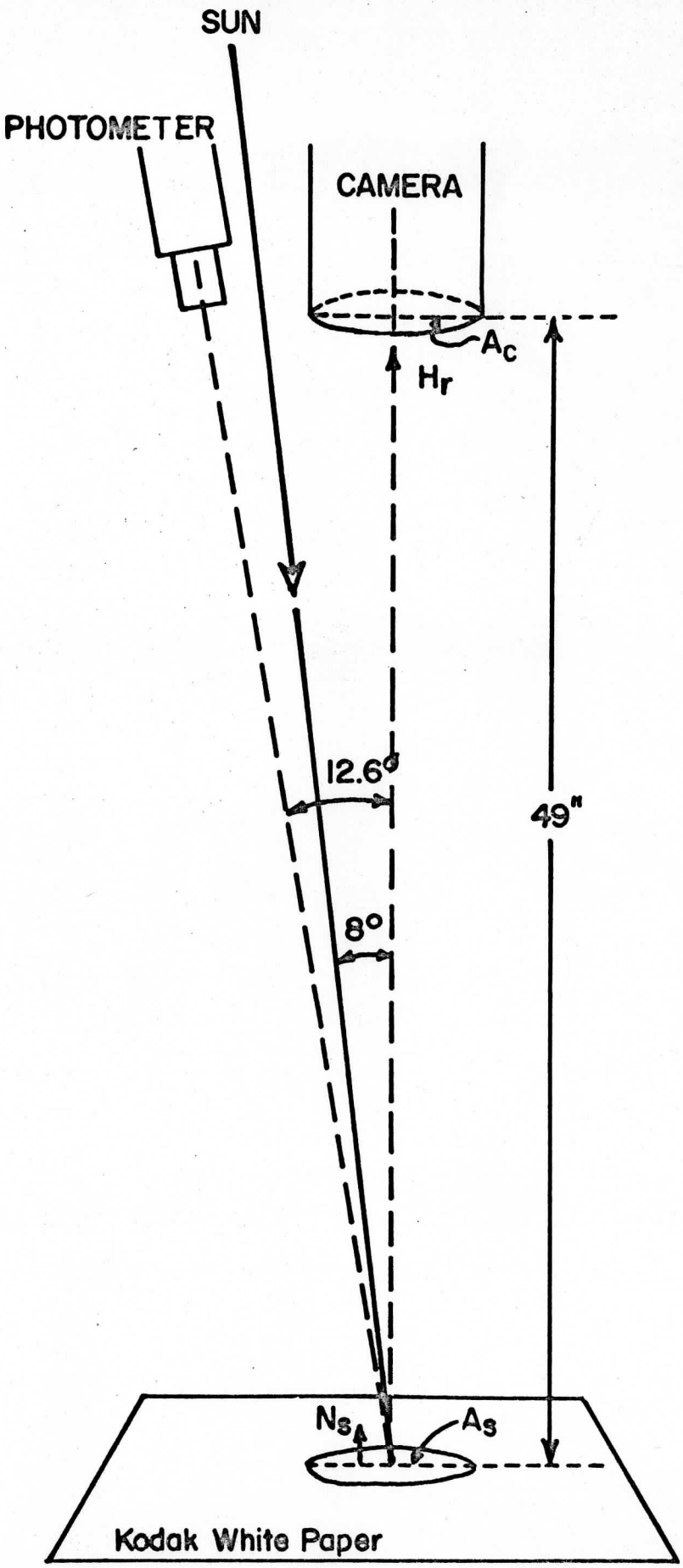

Fig 5

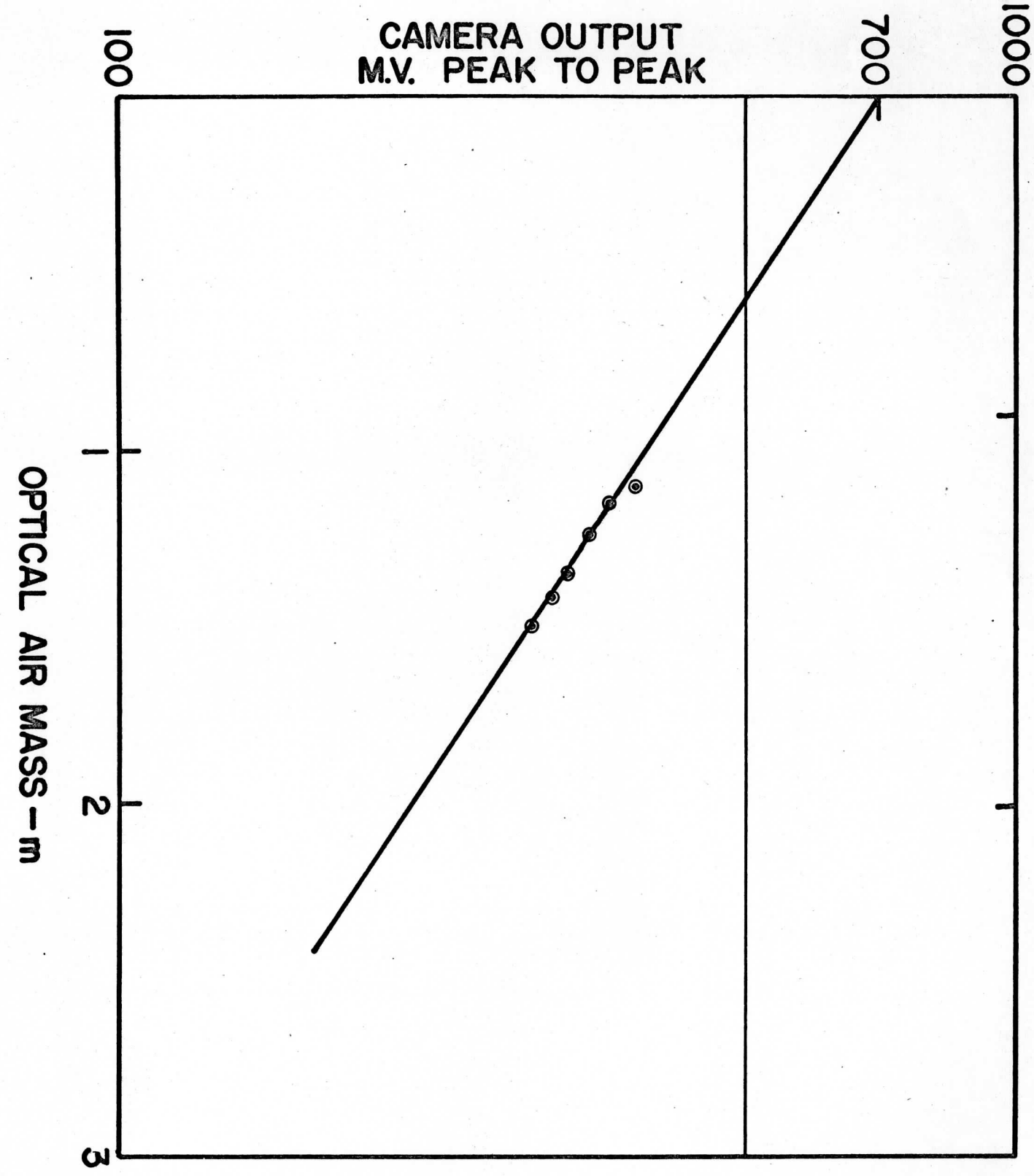
CAMERA OUTPUT
M.V. PEAK TO PEAK
100
700
1000
OPTICAL AIR MASS - m
1
2
3

Fig 6

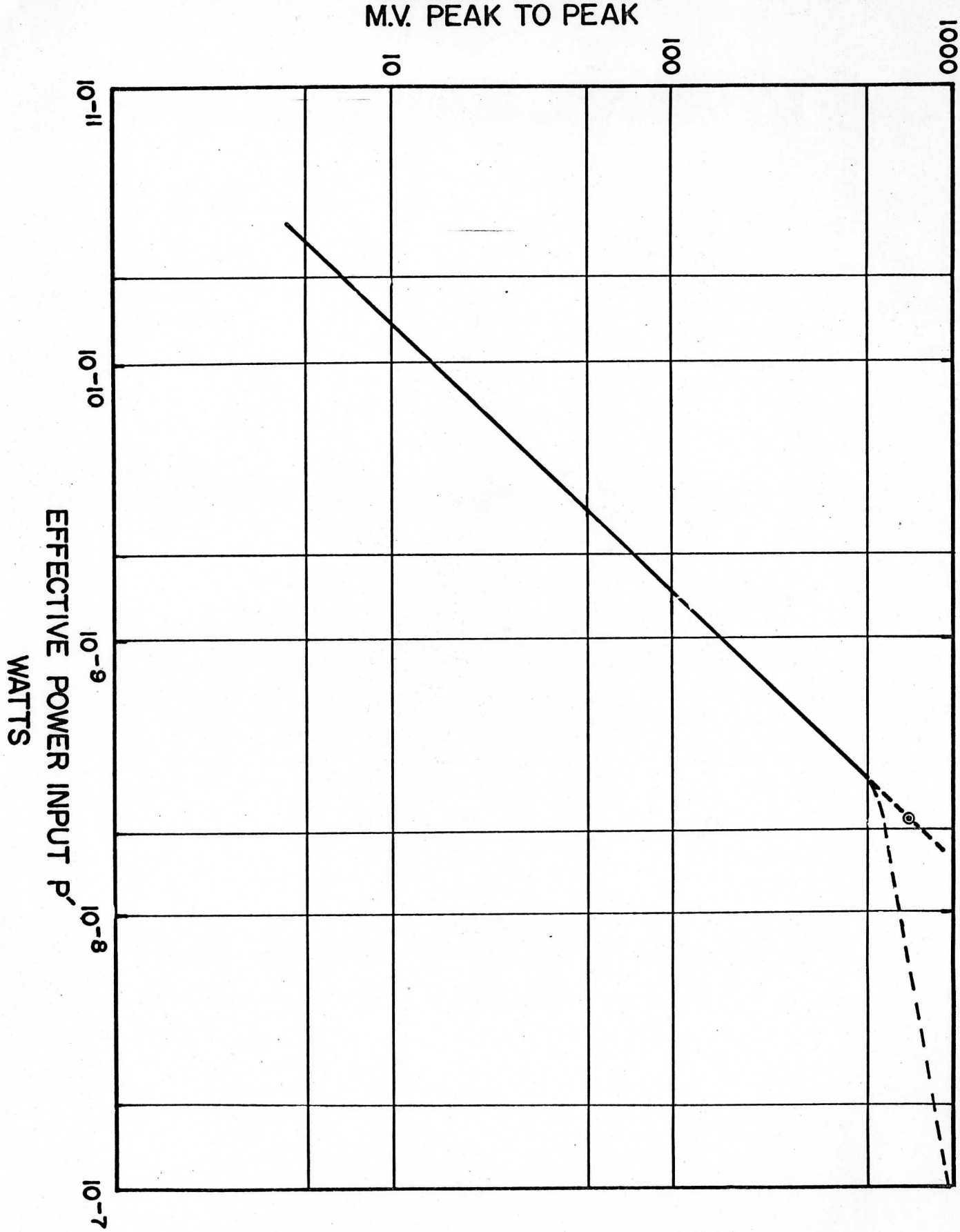
CAMERA OUTPUT V_o
M.V. PEAK TO PEAK
10
100
1000
10^{-11}
10^{-10}
10^{-9}
10^{-8}
10^{-7}
EFFECTIVE POWER INPUT P'
WATTS

Fig 7.

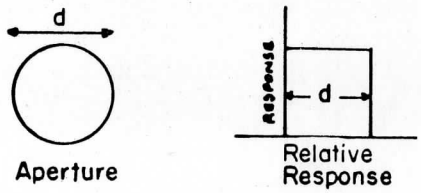

APERTURE SCANNING FROM LEFT TO RIGHT, VIEWING

A Cloud larger than field of view, effective radiance N_1

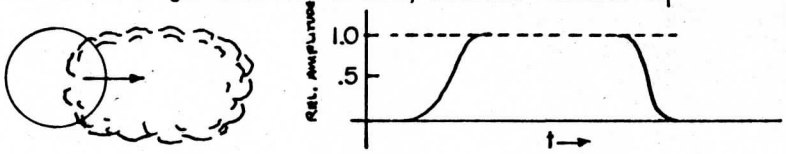

Physical Configuration

Signal Shape

B Cloud which exacty fills field of view, effective radiance N_1

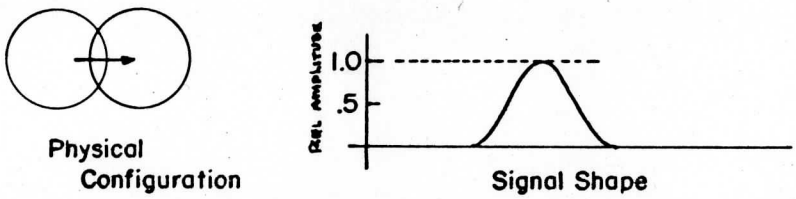

Physical Configuration

Signal Shape

C Cloud which fills 50% field of view, effective radiance N_1

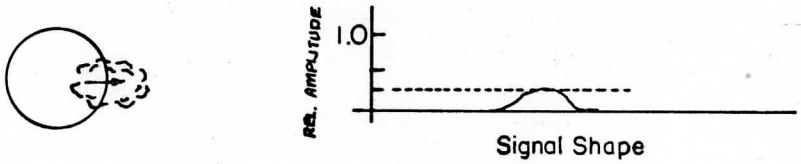

Signal Shape

D Cloud which fills 70% field of view, effective radiance $N_2 < N_1$

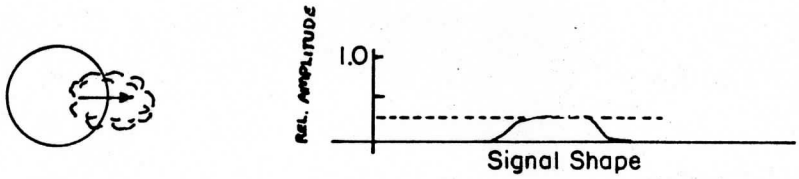

Signal Shape

E Cloud which fills 50% field of view, effective radiance N_1, detected by upper part of field of view

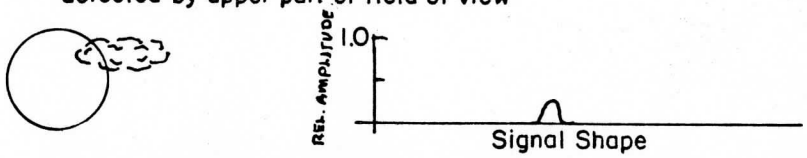

Signal Shape

Fig 8

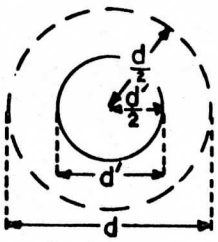

Aperture
d' = half power point

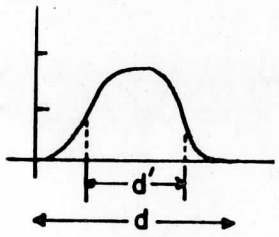

Relative
Response

APERTURE SCANNING FROM LEFT TO RIGHT, VIEWING

A) cloud extending beyond field of view, effective radiance N_1

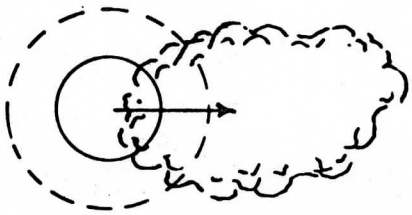

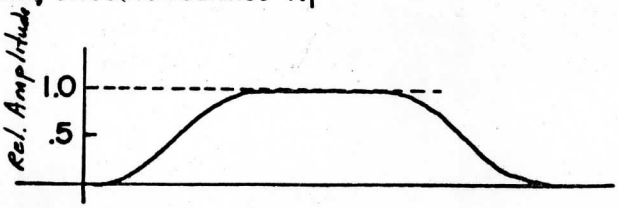

B) cloud filling field defined by half power points;
effective radiance N_1, scanned through center of cloud

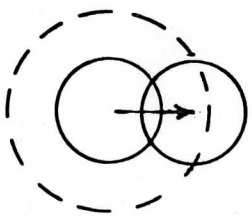

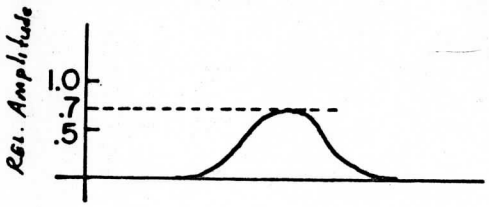

C) cloud filling field defined by half power points;
effective radiance N_1, scanned through one edge of cloud

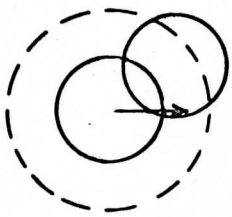

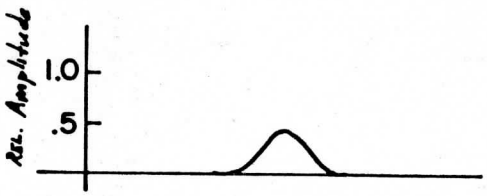

Fig 9

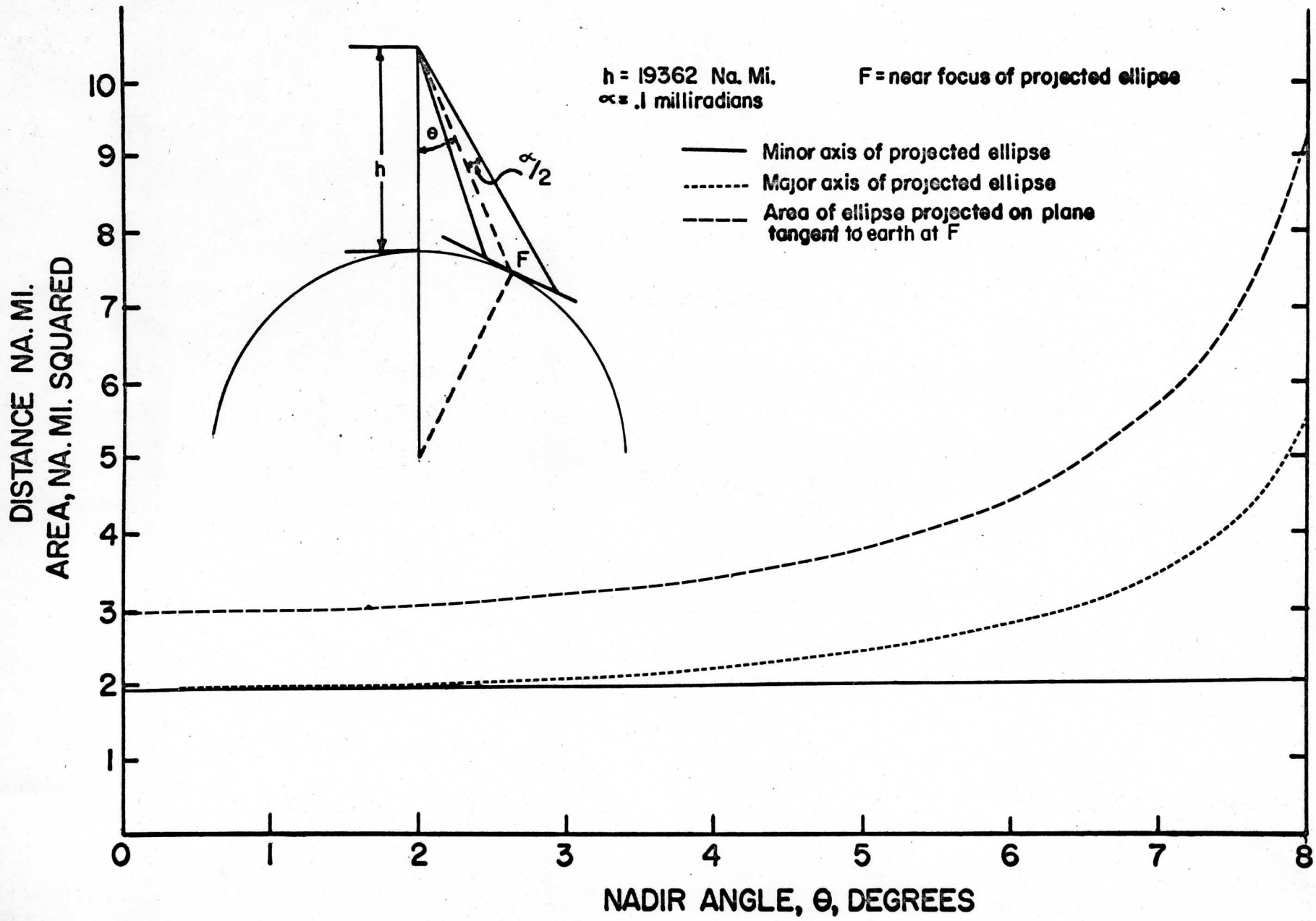
h = 19362 Na. Mi.
∝ = .1 milliradians
F = near focus of projected ellipse
Minor axis of projected ellipse
Major axis of projected ellipse
Area of ellipse projected on plane tangent to earth at F
h
θ
∝/2
F
DISTANCE NA. MI.
AREA, NA. MI. SQUARED
NADIR ANGLE, θ, DEGREES
0
1
2
3
4
5
6
7
8
9
10

Fig 10

Border line paper (13)

Not clear about you assume cannot cloud motion, or analyses

RELATION BETWEEN CLOUD MOTIONS FROM ATS-1 AND WIND DIRECTION

by

S. Fritz, L. F. Hubert, A. Timchalk

National Environmental Satellite Center
Washington, D. C.

September 1967

Final Version:
Revised per Reviewers suggestions 5/15/68
L.H.

Copy # 2

Fritz, S., L. Hubert + A. Twinchalk

RELATION BETWEEN CLOUD MOTIONS FROM ATS-1 AND WIND DIRECTION

1. Introduction

Cloud pictures covering the whole world have been available from ESSA satellites once a day for some time. But the synchronous satellite, ATS-1, introduced a new dimension into the observations of clouds, namely the dimension of time, which makes possible the study of cloud motions and cloud developments over short intervals. Cloud motions appear dramatically when pictures taken at 23-minute intervals are projected in a movie sequence at about 8 pictures per second.

It is a simple matter to observe and to measure the directions of the cloud motions and speeds can be catagorized on a qualitative scale such as slow, moderate, and fast. A simple method is to produce a movie loop for continuous, repeated projection. While the pictures are being projected on a sheet of paper, arrows that parallel the cloud motions can be drawn.

This paper reports only preliminary results obtained from the first ATS movie available. Quantitative displacement measurements, similar to those reported elsewhere in this book, are also being made, but are not reported here.

An important question is whether or not the cloud motions really represent wind directions and wind speeds. If the clouds that are observed to move during a movie sequence are small cloud elements that are neither being formed nor destroyed, they would act essentially like balloons and would represent the wind direction at their level. However, if either cloud formation or dissipation occurred in a systematic manner, the cloud speeds would not be representative of the actual wind speeds. If the cloud form changed along some direction, for example, perpendicular to the wind direction, then the inferred wind direction would also be incorrect. This paper presents comparisons of ATS-1 cloud motions with the actual wind field, where balloon or airplane measurements were available.

2. Data

The cloud motions to be described occurred within ± 6 hours of 2200 GMT 19 February 1967 (local noon at the satellite subpoint). The cloud field "seen" by the satellite is shown in Fig. 1. Here we see frontal cloud systems in the Northern and Southern Hemispheres on the western side of the picture near latitudes 30° to 40° and the cloudiness associated with the Intertropical Convergence Zone (ITCZ). A bright cloud mass near 10°S 170°W is of interest since it is the source of high clouds which are advected northeastward across the equator. Many less-organized clouds, apparently mainly at the lower levels, are located near 20°S 120°W, and in a broad zone generally south of Hawaii. These are mainly associated with the large oceanic anticyclones.

RELATION BETWEEN CLOUD MOTIONS FROM ATS-1 AND WIND DIRECTION

1. Introduction

Cloud pictures covering the whole world have been available from ESSA satellites once a day for some time. But the synchronous satellite, ATS-1, introduced a new dimension into the observations of clouds, namely the dimension of time, which makes possible the study of cloud motions and cloud developments over short intervals. Cloud motions appear dramatically when pictures taken at 23-minute intervals are projected in a movie sequence at about 8 pictures per second.

It is a simple matter to observe and to measure the directions of the cloud motions and speeds can be catagorized on a qualitative scale such as slow, moderate, and fast. A simple method is to produce a movie loop for continuous, repeated projection. While the pictures are being projected on a sheet of paper, arrows that parallel the cloud motions can be drawn.

This paper reports only preliminary results obtained from the first ATS movie available. Quantitative displacement measurements, similar to those reported elsewhere in this book, are also being made, but are not reported here.

An important question is whether or not the cloud motions really represent wind directions and wind speeds. If the clouds that are observed to move during a movie sequence are small cloud elements that are neither being formed nor destroyed, they would act essentially like balloons and would represent the wind direction at their level. However, if either cloud formation or dissipation occurred in a systematic manner, the cloud speeds would not be representative of the actual wind speeds. If the cloud form changed along some direction, for example, perpendicular to the wind direction, then the inferred wind direction would also be incorrect. This paper presents comparisons of ATS-1 cloud motions with the actual wind field, where balloon or airplane measurements were available.

2. Data

The cloud motions to be described occurred within ± 6 hours of 2200 GMT 19 February 1967 (local noon at the satellite subpoint). The cloud field "seen" by the satellite is shown in Fig. 1. Here we see frontal cloud systems in the Northern and Southern Hemispheres on the western side of the picture near latitudes 30° to 40° and the cloudiness associated with the Intertropical Convergence Zone (ITCZ). A bright cloud mass near 10°S 170°W is of interest since it is the source of high clouds which are advected northeastward across the equator. Many less-organized clouds, apparently mainly at the lower levels, are located near 20°S 120°W, and in a broad zone generally south of Hawaii. These are mainly associated with the large oceanic anticyclones.

Certain cloud fields consist predominantly of middle and higher clouds. Thus the frontal systems, with their clouds of fairly uniform texture and sometimes with edges of decreasing brightness, indicate the presence of cirrus clouds. The more broken-up clouds, characteristic of cumulus and stratocumulus fields, probably lay at low levels, except that cumulus congestus clouds also reach into middle levels. There are also many thin, wispy clouds, noticeable only after careful inspection, above the cumulus-appearing cloud forms. These wispy clouds are more prominent when viewed in the movie sequence mode, for they move across the scene at levels above the lower clouds. They are probably at high levels or middle levels; the exact cloud heights, of course, are somewhat uncertain.

An attempt was made to separate the higher clouds from the lower clouds with the aid of the appearance criteria mentioned above. The motions for the higher clouds are shown in Fig. 2 whereas the motions for the lower clouds are shown in Fig. 3. In each case the Honolulu Weather Bureau analysis has been superimposed on the ATS-1 cloud motion chart.

It is also useful to compare the cloud motion vectors with actual balloon wind measurements. Such a comparison shows to what extent the cloud motions can be identified with wind motions at particular levels. Fig. 4 shows the actual wind data at upper air stations where "cloud motions" could be observed in ATS films. These stations are identified by circles in Figs. 2 and 3. In Fig. 4 the cloud direction is shown by a heavy vertical line; the direction envelope $\pm$ 20° and $\pm$ 40° from the cloud direction are

shown by thinner vertical lines. Only qualitative cloud speeds were assigned; long arrows were designated "fast," short arrows were designated "slow," intermediate length arrows were designated "moderate."

3. High Clouds

In Fig. 4a, which applies to high clouds, it is evident that in almost every case a level exists where the cloud direction and wind direction are the same; and in every case a level exists where the cloud direction differs from the wind direction by no more than 20°. Table 1a summarizes these results. Table 1a also contains a column showing the winds reported at 40,000 ft. (about 200 mb). This was included for the following reason: If one were to use the cloud motions in drawing streamline analyses, it would be necessary to assign a height to the clouds, even when the exact height is not known. For the purpose of aiding analyses we could assume that the clouds identified as high clouds are cirrus clouds, which are often found near the 200 mb level.

How would the cloud motions agree with the wind motions under such an assumption? Although the data sample is small, Table 1a suggests that the agreement would be fairly good. At most stations the difference between the cloud direction and the 40,000 ft. wind direction is 20° or less. At two stations it was 30° and at Noumea it was 40°.

In studying these data, three facts need to be considered. At some stations, such as Noumea, the wind direction changed appreciably near the 40,000 ft level, so that closer agreement between cloud and wind direction might be found at a level near, but not at, 40,000 ft.

Thus in Fig. 4a it is seen that at Noumea the 33,000 ft wind direction and cloud direction would agree exactly. Secondly, in some places the cloud directions changed significantly over relatively short distances near the upper-air station. Therefore, valid comparisons between cloud motion and balloon sounding can be made only where cloud motion is measured in the immediate vicinity of the station. Finally, since the cloud motions are, perforce, obtained from pictures taken over an interval of several hours, the wind field can change with time especially in areas where the horizontal change of direction is large.

If we accept the results of Table 1a viz. that "high" cloud direction does indicate the wind direction near 200 mb, especially when the cloud displacements are large ("fast" and "moderate" in Fig. 4a), then it is valid to compare the ATS "winds" with the Honolulu 200-mb analysis in Fig. 2.*

Along the major frontal systems the most rapid cloud displacements occur from the southwest in the Northern Hemisphere and from the northwest in the Southern Hemisphere. These motions suggest the presence of a jet stream in those areas. The strong wind fields in the Honolulu analysis 30N, 160E to 45N, 160W agree well with ATS cloud motion.

However, in some areas the agreement is ~~not as good~~ less satisfactory. For example, the strong southwest cloud motions at 7N, 162W suggest that the low center located there on the Honolulu maps should have been placed somewhat further west; and the trough, associated with

---

* The Honolulu analysis is actually made on data from the layer 200 mb to 300 mb.

that low center, should have been extended with appreciable amplitude to at least about 10S, 175W. The clockwise circulation associated with the low near 10S, 140W should have been extended across the equator with somewhat greater amplitude than the Honolulu analysis shows. The ridge near 20S, 160W does not seem to have existed at the cloud level.

An interesting feature is the area of confluence and difluence of the cloud motions at high levels. At about 10°S, 165°W high clouds moved northeastward across the equator into the ITCZ cloud at about 5N and then formed a large clockwise whirl with a southbound leg beginning near 5°N, 140°W. At that location the cloud motions also continue along the ITCZ northeastwards toward Mexico. Thus judging from the cloud motions, an area of difluence was present in the vicinity of longitude 5°N, 140°W; this agrees with the Honolulu analysis.

The broad southwesterly current flowing from the ITCZ towards Mexico was joined by another stream of rather wispy clouds moving from the west and northwest near 20°N, 140°W, forming a region of confluence.

In the Southern Hemisphere the area south of 20°S and east of New Zealand contains very sparse or nonexistent wind data. In areas such as these, the cloud displacements could certainly be helpful in filling such data gaps.

4. Low Levels (approximately 850-700 mb)

We now consider those clouds that, because of their broken-up form, are interpreted to be cumulus and stratocumulus clusters. The motion of these clouds should, therefore, be compared with winds in the lower levels of the troposphere.

Figure 4b and Table 1b contains a comparison of cloud motions, for low clouds, with wind measurements from balloons. The stations for which comparisons were made are shown as dark circles in Fig. 3.

Here again levels exists for which the cloud direction and wind direction closely agree. These data show that the 5000 ft winds agree well with the cloud directions for the stations as a group. However, as might be expected, at individual stations other levels give better agreement.

Table 1b includes the comparison between cloud direction and 5000 ft winds. Again at most stations the agreement is within 20°. At Wake the deviation is 60° but at 7000 feet the deviation is reduced to 30°. The low clouds always had small displacements suggesting "slow" winds. This sometimes made the cloud direction difficult to determine.

It would have been desirable to compare the cloud direction field with an 850-mb chart, but no 850-mb chart was available from Honolulu. Therefore, in Fig. 3, a comparison is made with the 700-mb chart from Honolulu. The main synoptic feature is the anticyclone near 25°N, 170°W; where the cloud motion field and the conventional analysis agree.

Some discrepancies are noted. At the equator from 155°W to 170°E the cloud displacements suggest east winds but the Honolulu analyses indicates a counterclockwise circulation near 162°W and a clockwise circulation of appreciable amplitude further west. The reason for this discrepancy is not obvious, although differences in height between the cloud "level" and the height of the 700-mb surface might be one factor. Another difference appears near 35°N,

150°W. Here the clouds suggest a closed circulation but the Honolulu analysis contains only an open trough near that area. Perhaps height is a factor again, for the surface map did show a closed low.

As with high level clouds, in data sparse areas the cloud displacements could be helpful in streamline analysis. Such an area occurs near 30°S, 155°W, where a closed vortex is suggested by the cloud motions. East of 130°W, no conventional data appear on the maps, but the cloud motions suggest generally east winds between 15°S and 20°S and west or southwest winds near 35°S, 105°W.

5. Summary

Comparisons made between cloud motion direction on ATS-1 time-lapse movies and actual wind measurements by balloons indicate that cloud motion can be used as supplementary wind directions near the 40,000 ft level for high clouds and near the 5000 ft level for low clouds. In data-sparse areas cloud motions would enable useful streamline analysis that otherwise would be impossible.

TABLE 1a

Station Name & Number	Height(s) of Closest Wind-Direction Agreement (thsds of ft)	Deviation (degrees)	High Cloud Direction/ Speed (degrees)	Wind at 40,000 ft. (Deg/Kts)	High Cloud Direction Minus 40,000 ft. Wind Direction (degrees)
Oakland 72-493	07-08 20-30	0 0	320/Moderate	310/59	+ 10
San Diego 72-290	07-53	0-30	310/Moderate	290/46	+ 20
Ship 4YN	02-04 19-45	0-30 0-30	230/Moderate	200/35	+ 30
Ship 4YV	10-45	0-20	230/Fast	240/151	- 10
Marcus Island 91-131	10-35	20-30	230/Fast	250/130	- 20
Wake Island 91-245	18-54	0-30	230/Moderate	250/28	- 20
Noumea 91-592	33-47	0-30	320/Slow	280/29	+ 40
Lord Howe 94-995	15-50	0-30	320/Moderate	340/72	- 20
Norfolk 94-996	17-46	0-20	300/Moderate	320/63	- 20
Whenaupai 93-112	10-40	0-20	260/Moderate	260/70	0
Christ Church 93-780	17-50	20-30	260/Moderate	230/76	+ 30
Pago Pago 91-765	29-46	0-20	260/Slow	270/34	- 10
Takaroa 91-943	37-50	0-40	180/Slow	160/32	+ 20
Rikitea 91-948	36-40	0-40	(240-260) /Slow	260/12	- 10 to 0

TABLE 1b

Station Name & Number	Height(s) of Closest Wind-Direction Agreement (thsds of ft)	Deviation (degrees)	Low Cloud Direction/ Speed (degrees)	Wind at 5000 ft (Deg/Kts)	Low Cloud Direction Minus 5000 ft Wind Direction (degrees)
Ship 4YN	01-06 19-45	0-20 40	180/Slow	190/16	- 10
Kauai 91-165	Sfc-14	0-30	020/Slow	040/20	- 20
Kahului 91-190	Sfc-14	0-40	020/Slow	060/12	- 40
Lyman 91-285	Sfc-09	0-30	030/Slow	030/10	0
Johnston Island 91-275	Sfc-6 08-22	0-30 0-30	090/Slow	120/20	- 30
Wake Island 91-245	06-08 15-25	30-40 0-40	180/Slow	120/15	+ 60
Nandi 91-680	04-35	0-30	090/Slow	070/18	+ 20
Canton Island 91-700	Sfc-07	10-30	090/Slow	070/31	+ 20
Atuona 90-925	Sfc-10	0-20	100/Slow	090/12	+ 10
Takaroa 91-943	01-34	0-20	090/Slow	080/28	+ 10

FIGURE LEGENDS

Figure 1. ATS-1 photograph (050-7-Seq. 43) for 2209 GMT 19 February 1967, from the sequence that comprised the movie.

Figure 2. High cloud motion directions (heavy arrows) from movie mid-time 22 GMT 19 February 1967; Honolulu streamline analysis for the layer 200 mb to 300 mb (thin lines), 00 GMT 20 February 1967; and upper wind data. Aircraft winds identified by underlined height digit, all others are balloon soundings. Large digits are identification numbers for the circled stations.

Figure 3. Low cloud motion directions (heavy arrows) from movie mid-time 22 GMT 19 February 1967; Honolulu 700-mb streamline analysis (thin lines), 00 GMT 20 February 1967; and upper wind data. Aircraft winds are identified by underlined height digit, all others are balloon soundings. Large digits are identification numbers for circled stations.

Figure 4a. Wind soundings for 00 GMT 20 February 1967 (circles on broken line) and high cloud motion from ATS-1 movie (heavy vertical line) with envelopes $\pm$ 20° and $\pm$ 40° (thin vertical lines).

Figure 4b. Wind soundings for 00 GMT 20 February 1967 (circles on broken line) and low cloud motion from ATS-1 movie (heavy vertical line) with envelopes $\pm$ 20° and $\pm$ 40° (thin vertical lines).

fig1

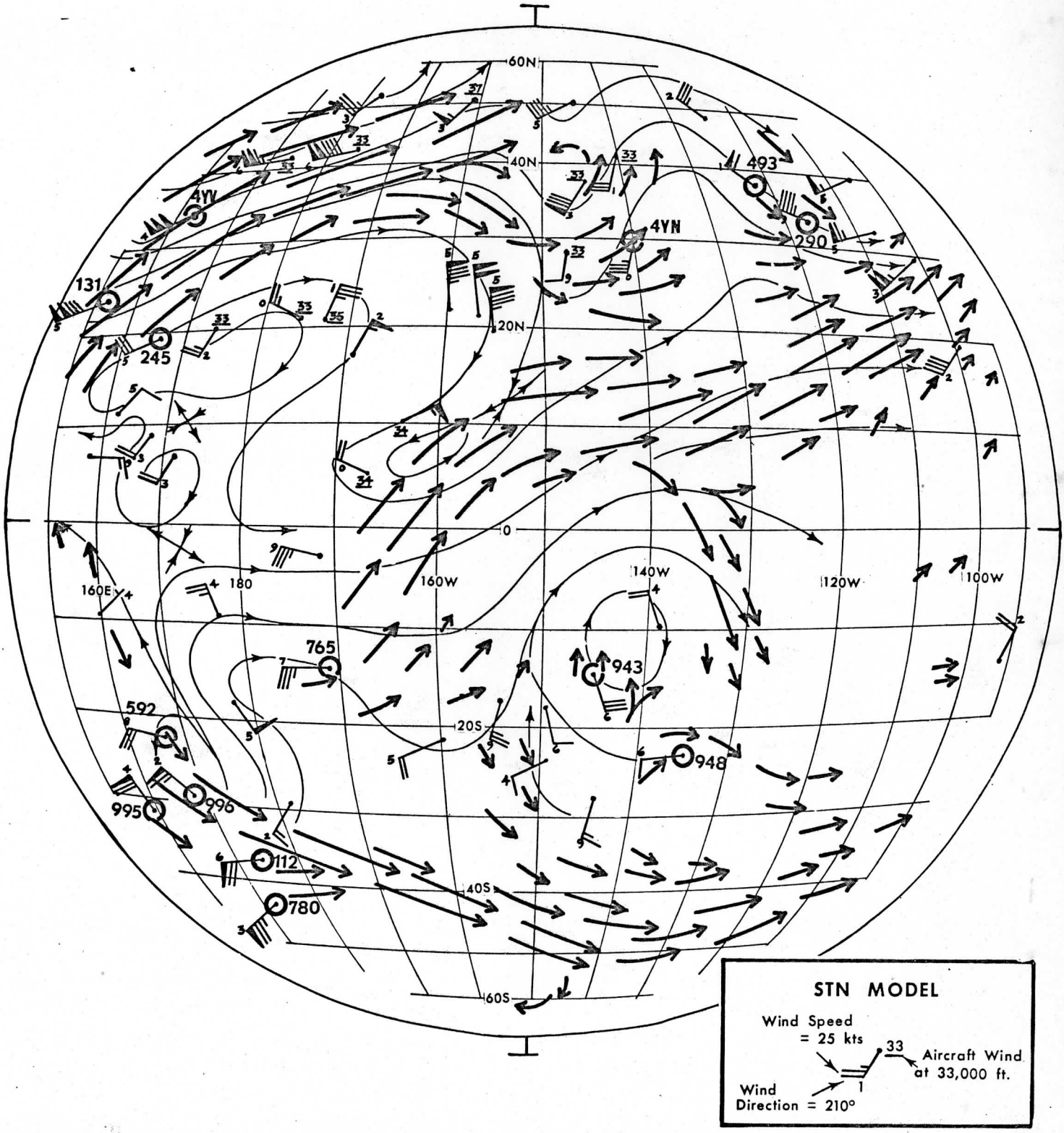
60N
40N
20N
0
20S
40S
60S
160E
180
160W
140W
120W
100W
4YY
4YN
493
290
131
245
765
943
592
948
995
996
112
780
STN MODEL
Wind Speed
= 25 kts
33
Aircraft Wind
at 33,000 ft.
1
Wind
Direction = 210°

Fig 2

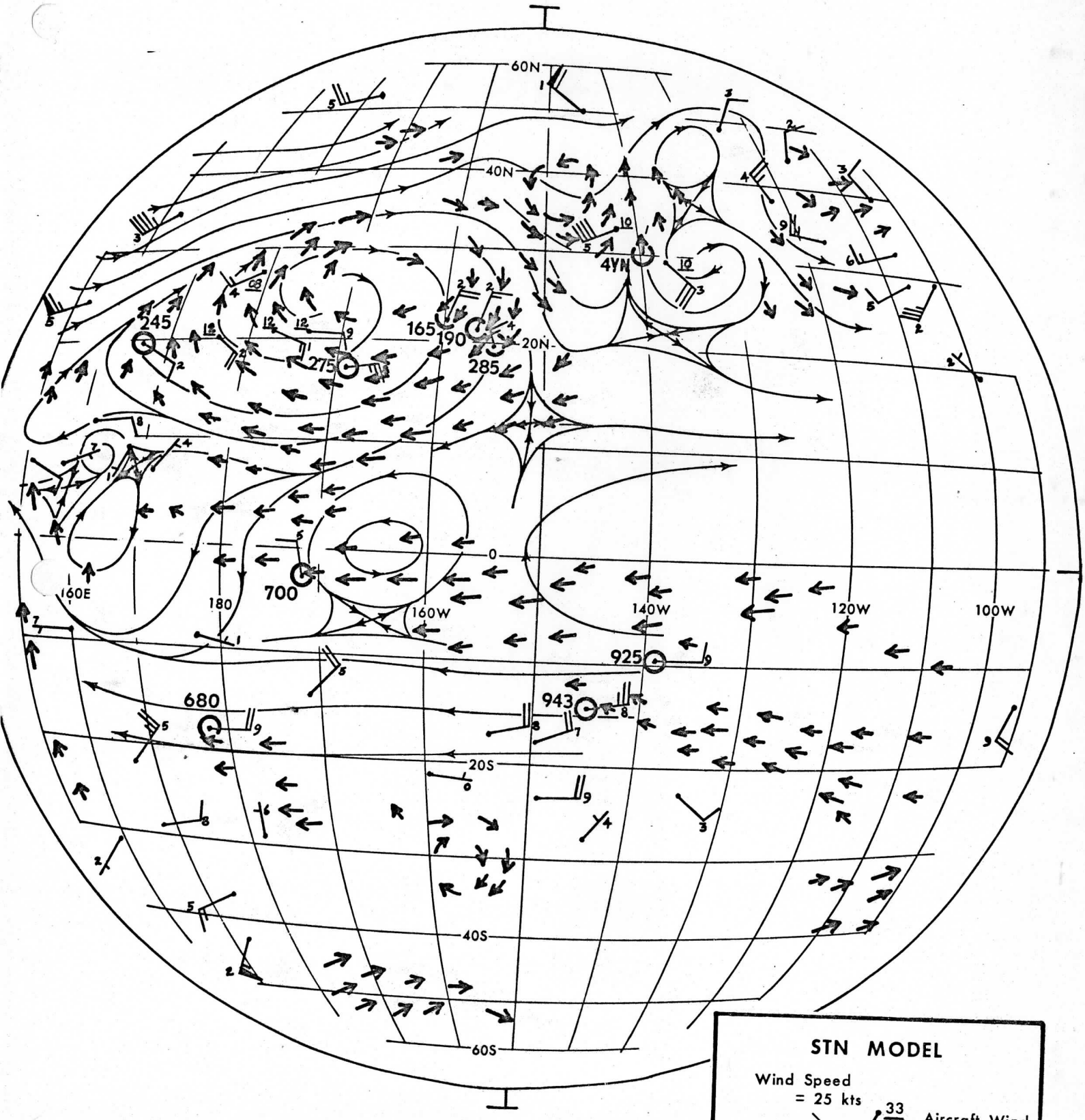
60N
40N
20N
0
20S
40S
60S
160E
180
160W
140W
120W
100W
245
275
165
190
285
4YN
700
680
925
943
STN MODEL
Wind Speed
= 25 kts
33
Aircraft Wind
at 33,000 ft.
Wind
Direction = 210°

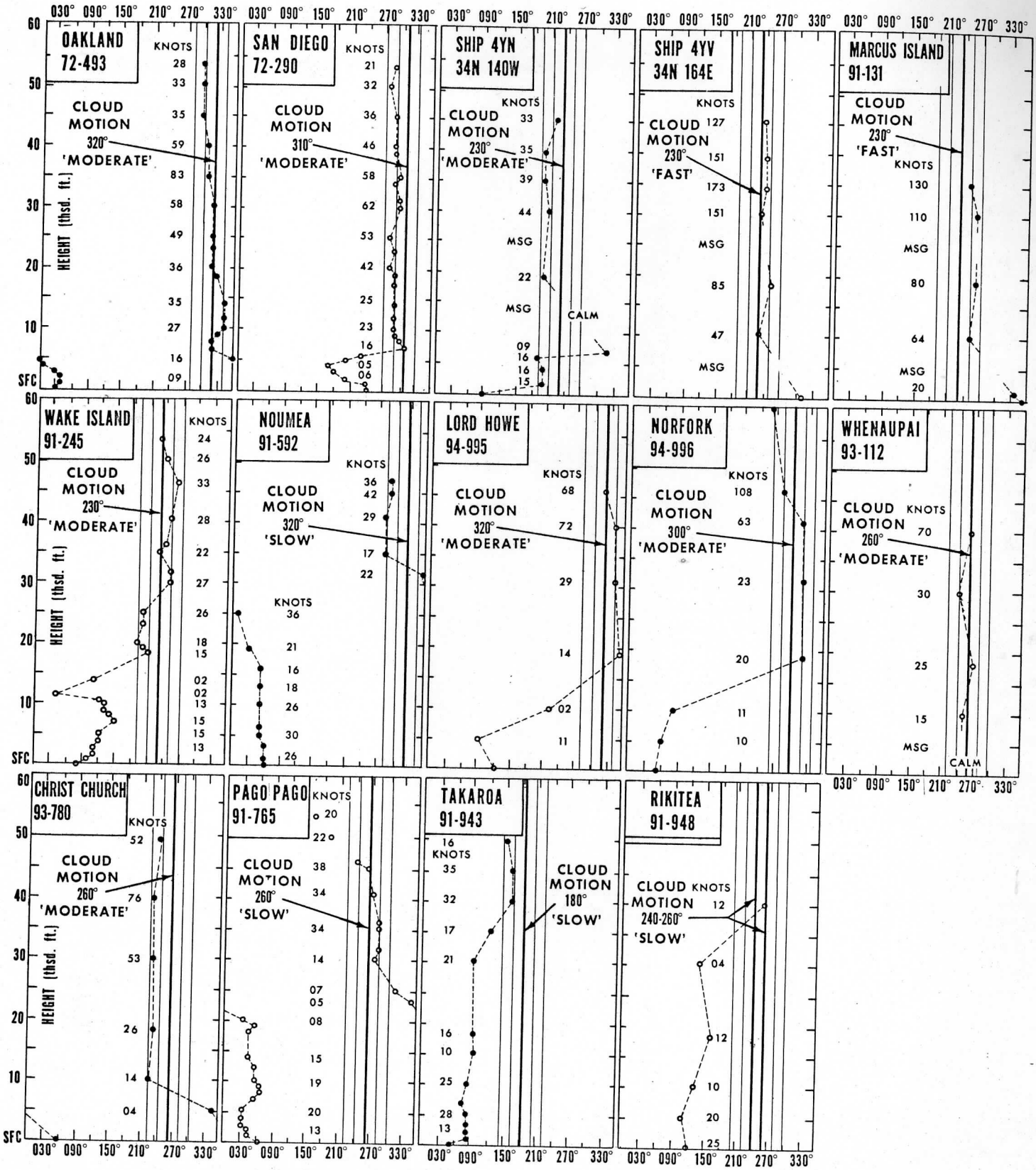
OAKLAND
72-493
CLOUD MOTION
320°
'MODERATE'
SAN DIEGO
72-290
CLOUD MOTION
310°
'MODERATE'
SHIP 4YN
34N 140W
CLOUD MOTION
230°
'MODERATE'
CALM
SHIP 4YV
34N 164E
CLOUD MOTION
230°
'FAST'
MARCUS ISLAND
91-131
CLOUD MOTION
230°
'FAST'
WAKE ISLAND
91-245
CLOUD MOTION
230°
'MODERATE'
NOUMEA
91-592
CLOUD MOTION
320°
'SLOW'
LORD HOWE
94-995
CLOUD MOTION
320°
'MODERATE'
NORFORK
94-996
CLOUD MOTION
300°
'MODERATE'
WHENAUPAI
93-112
CLOUD MOTION
260°
'MODERATE'
CALM
CHRIST CHURCH
93-780
CLOUD MOTION
260°
'MODERATE'
PAGO PAGO
91-765
CLOUD MOTION
260°
'SLOW'
TAKAROA
91-943
CLOUD MOTION
180°
'SLOW'
RIKITEA
91-948
CLOUD MOTION
240-260°
'SLOW'
KNOTS
HEIGHT (thsd. ft.)
SFC
030° 090° 150° 210° 270° 330°

Fig 4a

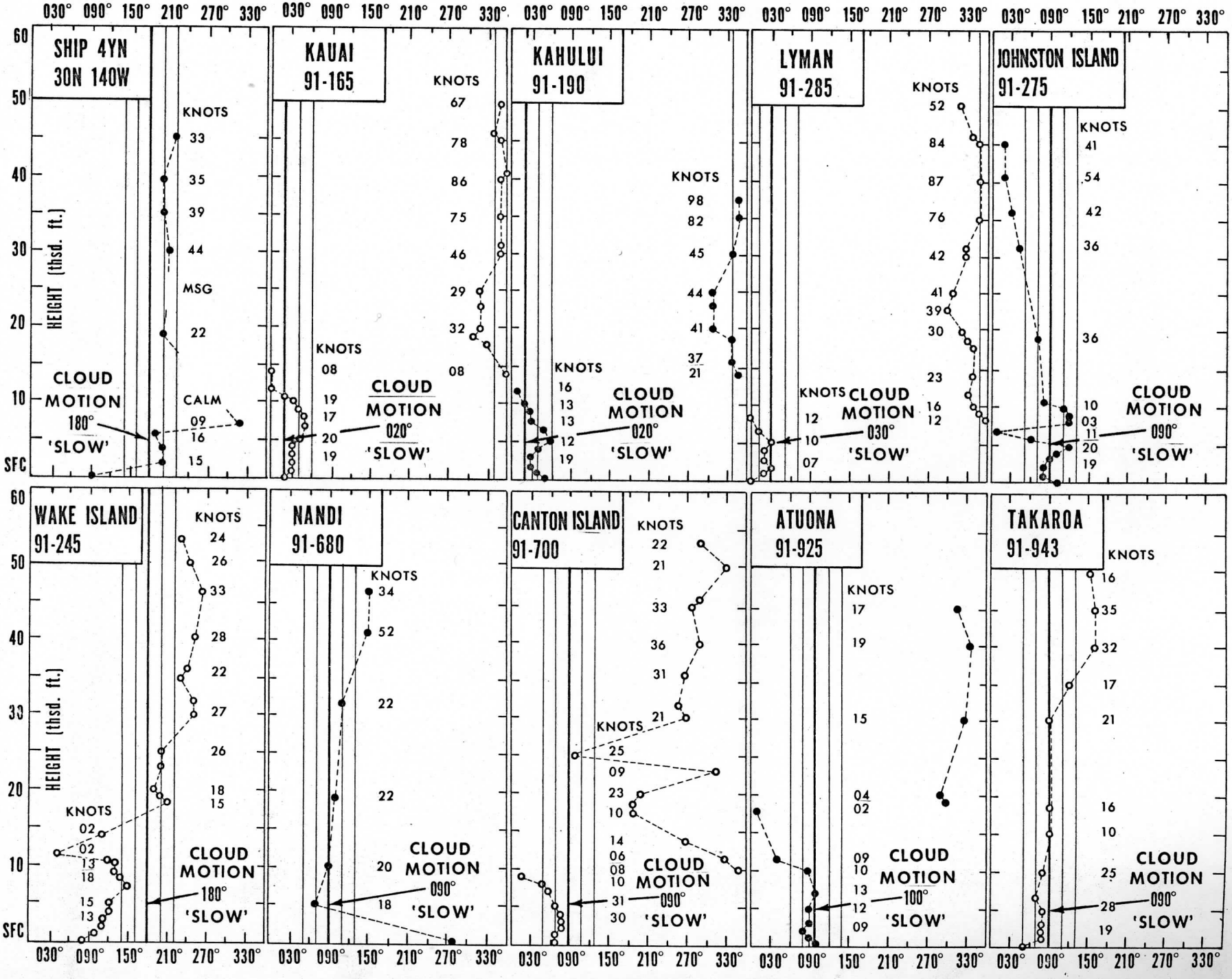
030° 090° 150° 210° 270° 330°
60
50
40
30
20
10
SFC
HEIGHT (thsd. ft.)
SHIP 4YN
30N 140W
KNOTS
33
35
39
44
MSG
22
CALM
09
16
15
CLOUD MOTION
180°
'SLOW'
KAUAI
91-165
KNOTS
67
78
86
75
46
29
32
08
KNOTS
08
19
17
20
19
CLOUD MOTION
020°
'SLOW'
KAHULUI
91-190
KNOTS
98
82
45
44
41
37
21
KNOTS
16
13
13
12
19
CLOUD MOTION
020°
'SLOW'
LYMAN
91-285
KNOTS
52
84
87
76
42
41
39
30
23
16
12
KNOTS
12
10
07
CLOUD MOTION
030°
'SLOW'
JOHNSTON ISLAND
91-275
KNOTS
41
54
42
36
36
10
03
11
20
19
CLOUD MOTION
090°
'SLOW'
WAKE ISLAND
91-245
KNOTS
24
26
33
28
22
27
26
18
15
KNOTS
02
02
13
18
15
13
CLOUD MOTION
180°
'SLOW'
NANDI
91-680
KNOTS
34
52
22
22
20
18
CLOUD MOTION
090°
'SLOW'
CANTON ISLAND
91-700
KNOTS
22
21
33
36
31
21
KNOTS
25
09
23
10
14
06
08
10
31
30
CLOUD MOTION
090°
'SLOW'
ATUONA
91-925
KNOTS
17
19
15
04
02
09
10
13
12
09
CLOUD MOTION
100°
'SLOW'
TAKAROA
91-943
KNOTS
16
35
32
17
21
16
10
25
28
19
CLOUD MOTION
090°
'SLOW'

Fig 46

Persson

Shirley Hansen

SECTION
8.1.6

III B. 4.

A "BLINK" MEASURING TECHNIQUE FOR QUANTITATIVE MEASUREMENT OF CLOUD MOTION FROM ATS-I SPIN SCAN CAMERA PICTURES

Prepared by

A. F. Hasler
J. Kornfield
L. Jensen
Space Science and Engineering Center

November 1969

THE UNIVERSITY OF WISCONSIN
Madison, Wisconsin

A "BLINK" MEASURING TECHNIQUE FOR QUANTITATIVE MEASUREMENT OF CLOUD MOTION FROM ATS-I SPIN SCAN CAMERA PICTURES

A. F. Hasler
J. Kornfield
L. Jensen
Department of Meteorology
The University of Wisconsin, Madison

ABSTRACT

A "blink" measuring technique for making quantitative geometric measurements of cloud displacements from a series of ATS-I pictures is explained. This technique requires two or more ATS-I pictures which are reasonably well superimposed by projectors on an electronic digitizing table. All geometric calculations, that is, distortion correction, superimposition and rectification, are done analytically through a computer program. The mathematical assumptions and operations involved are discussed in detail in the Appendix. A systematic testing program was devised to evaluate the technique first with an ideal grid and finally with real ATS-I pictures. Some possible applications of the technique include measurement of cloud trajectories (i.e., velocities), measurement of area change in clouds and cloud systems and measurement of location and orientation of cloud features. The best cloud displacement accuracy to date has been approximately 9 nautical miles which provides cloud speeds within approximately 3 knots for clouds that can be observed for 3 hours. Preliminary comparisons of cloud trajectories with standard wind observations are presented.

TABLE OF CONTENTS

Section		Page
ABSTRACT		iii
8.1.6.3	A "BLINK" MEASURING TECHNIQUE FOR QUANTITATIVE MEASUREMENT OF CLOUD MOTION FROM ATS-I SPIN SCAN CAMERA PICTURES	1
	3.1 Description of the Technique	1
	3.2 Test Results	3
	3.3 Preliminary Comparison of Cloud Trajectories with Standard Wind Observations	4
	3.4 Conclusion	7
ACKNOWLEDGMENTS		10
REFERENCES		10
APPENDIX		A-1

LIST OF ILLUSTRATIONS

Figure		
1	Projection System and Electronic Digitizing Table	2
2	ATS-I SSCC Picture Printed from a Duplicate EIS Negative	5
3	ATS-I Cloud Trajectories Compared with Surface and High-Level Winds	6
4	ATS Negative Printed from Negatives Made from ATS-I Analog Tape	8
5	ATS Cloud Trajectories Compared with Surface and High-Level Winds	9
A-1	ATS SSCC Coordinate System	A-2
A-2	Process of Distortion Correction and Superimposition of ATS-I SSCC Pictures	A-4
A-3	Spherical Triangle Used to Calculate the Displacement on the Surface of the Earth	A-7
A-4	Geometrical Relationships Used to Rectify ATS SSCC Pictures	A-8
A-5	Cross-Section of Figure A-4.	A-9

8.1.6.3 A "BLINK" MEASURING TECHNIQUE FOR QUANTITATIVE MEASUREMENT OF CLOUD MOTION FROM ATS-I SPIN SCAN CAMERA PICTURES

3.1 Description of the Technique

At first thought, an excellent method for making quantitative measurements of cloud motions would be to project a time-lapse movie [1] made from ATS Spin Scan Cloud Camera (ATS-(SSCC) pictures onto an electronic measuring table and to trace the motion of the clouds with a measuring head. Unfortunately, this method has the following limitations:

1. It is very difficult and time-consuming to superimpose the pictures accurately for the movie.

2. A registration error is introduced by the movie camera and the movie projector.

3. The resolution of presently available 16-mm film is inadequate to preserve the picture quality over the full earth disk.

4. It is difficult to correct for variable distortion and size changes from picture to to picture.

A "blink" measuring system has been developed which, to a large extent, overcomes these problems. Two or three projectors are used to superimpose ATS SSCC pictures on an electronic measuring table (Figure 1). The projectors allow adjustment of the picture in the film gates such that reasonably good superimposition of images on the table is achieved. Once the images are approximately superimposed, the film remains fixed. The projection lamps are easily controlled so that it is possible to blink rapidly from one picture to another giving a "movie" effect. The electronic measuring table is a 36-in. × 36-in. projection table with a measuring head on it. The head consists of a platin with inscribed cross-hairs, which is linked to a pair of rotary digital encoders. The encoders are interfaced directly to an on-line computer. This system enables one to record the x and y coordinates of any point on any picture.

The advantages of this system are as follows: It is in fact a 2- or 3-frame time-lapse movie with very high resolution because of the large 70-mm film size used. The fixed registration of the film allows the following mathematical operations: distortion correction, superimposition, rectification and all other geometric calculations to be performed on each picture individually in the computer.

Each image is located on the measuring table by determining the x and y coordinates of many points on the Earth's limb and the location of at least one landmark. The mathematical operations (discussed in detail in Part I of the Appendix) are then performed in the

Figure 1. Projection System and Electronic Digitizing Table Used for Blink Measuring Technique. (Images from three overhead projectors are deflected onto the measuring table by a 45°-angle mirror. Projection lamp controls are on the operator's left. Operator positions measuring head by hand. The measuring head is linked to two rotary digital encoders which are interfaced through the teletype on the right to an on-line computer. X and Y coordinates of the measuring head are recorded when a foot switch is activated. The measuring system shown belongs to the High Energy Physics Group, Department of Physics, University of Wisconsin.)

'lowing manner:

1. Distortion Correction: An ellipse is fitted to the limb points by a least-squares technique and the parameters of the ellipse are computed. The Earth is then restored to a circle, correcting for any linear distortion in the picture. The pictures are scaled using the apparent Earth radii for any size variability.

2. Superimposition: The center of each circle is transposed to the origin of the measuring table coordinate system and the pictures are rotated until the landmarks coincide.

3. Rectification: The picture is regarded as that made by a conventional camera so that a tangent plane approximation can be used. Distances between any two points on one or more pictures are calculated by spherical geometry.

3.2 Test Results

A systematic testing program was devised to evaluate the technique. The measuring system and the computer programs were tested first on an ideal grid[1] and finally on real ATS-I pictures.

1. The tangent plane approximation was evaluated theoretically.[2] The error introduced by using it was found to be less than 6 nm and was therefore neglected.

2. The distance-measuring calculations were carefully scrutinized for error and tested on the ideal grid by measuring distances on the measuring table. The average error in the distance between several pairs of points was only 3 nm, so the distance calculations were considered to be absolute and were used for all further evaluation.

3. The best possible accuracy with which landmarks can be located was tested by repeated measurement of the same landmark or cloud. The distance in nautical miles between successive measurements was used to give the relocation or repeatability error. For the highest quality ATS-I negatives,[3] the average error in relocating both clouds and landmarks was 3 nautical miles (nm), where 95 percent of the data points were within 6 nm. For the lower quality EIS negatives,[4] an average error of 6 nm was found with 95 percent of the data points within 11 nm. When the actual measure-

---

[1] Computer-produced ATS-I grid supplied by NASA.

[2] A detailed evaluation of the tangent plane approximation is contained in Part I of the Appendix.

[3] Produced at The University of Wisconsin from an analog tape record of the ATS-I SSCC signal.

[4] Negatives made by the EIS (Electronic Image Systems Corporation, Boston, Massachusetts) display system at the ground station as test pictures.

ments were made, each cloud or landmark was measured three times and the average coordinates were taken to minimize the repeatability error.

4. Next, the accuracy with which two pictures can be superimposed by the technique was tested. This was done by carrying out the superimposition routine and then measuring the apparent displacement of stationary landmarks caused by errors in the superimposition. Location errors and any distortion errors which have been neglected are also included here so that the superimposition error gives a good estimate of the total error of the technique.

For the ideal grid, grid points near the subsatellite point were found to be superimposed with an average accuracy of 3 nm, which approaches the resolution limit (about 2 nm) of the ATS-I camera. For two different ATS-I pictures, the best superimposition achieved for points on Baja California and the Hawaiian Islands had an average error of 9 nm. These represent the best results achieved to date for real data. It has been found that clouds can often be traced for over 3 hours. If we use a total error of 9 nm, average cloud speeds over a 3-hour period can be determined within approximately 3 knots. According to a COSPAR [2] report, one of the global observation data requirements for prediction with diabatic numerical models is the knowledge of the horizontal wind within 4 to 6 knots. Therefore, if it can be established that cloud speeds can be accurately related to wind speeds, we are approaching the recommended accuracy.

3 Preliminary Comparison of Cloud Trajectories with Standard Wind Observations

The measuring procedure is thus: In the tropics, one selects the smallest persistent fair-weather cumulus clouds resolved by the ATS-I camera. Small cumulus clouds are used if possible because they most nearly resemble an ideal marker (i.e., a passive, infinitely small marker). Large clouds or cloud systems and large cloud decks are avoided if possible because they are more likely to affect the ambient wind field and are more likely to be propagated by wave phenomena than the smaller clouds. Distances are measured from cloud center to cloud center, as the operator determines by eye. For larger clouds whose centers cannot easily be determined, such as large convective cloud groups, bright spots or distinctive edge features are used. Cirrus clouds are less well defined and are therefore more difficult to locate accurately. However, since their velocities are usually higher, the error in location is still a small part of the distance traveled.

The first comparison of cloud trajectories with wind observations was done with data from 19 February 1967. The ATS-I SSCC pictures, taken at 2040 Universal Time (U), 2208 (U) and 2317 (U) on 19 February 1967, were selected. The ATS-I picture nearest local noon for the subsatellite point is 2208 (U). It is shown in Figure 2. Trajectories of fair-weather cumulus clouds, assumed to be low-level clouds, were compared with the surface wind observations from the U.S. Weather Bureau's Hawaiian analysis for 0000 (U) 20 February 1967. Trajectories of higher speed clouds, usually cirrus (assumed to be high-level clouds), were compared with the 200-250-300 millibar (mb) wind observations from rawinsondes and aircraft ppler radar, again from the Hawaiian analysis at 0000 (U) 20 February 1967. The comparison of these data is illustrated in Figure 3. For this case, the average superimposition error was 9.3 nm and, since the period of observation was 3 hours, cloud speeds can be found within approximately 3 knots. Of 30 cumulus trajectories and 10 cirrus trajectories selected

Figure 2. ATS-I SSCC Picture from 2208 (U) 19 February 1967. (Printed from a duplicate EIS negative.)

Figure 3. ATS-I Cloud Trajectories Compared with Surface and High-Level Winds. (19-20 February 1967 (U).)

to cover the tropics as uniformly as possible, only four cases of cumulus trajectories and no cases of cirrus trajectories were found near enough (i.e., less than 200 nm) to be compared with the standard observations. This points up the difficulty of making this type of comparison. While a more complete selection of cumulus trajectories would have given a better comparison, there were virtually no upper air wind observations near enough to the cirrus clouds visible in this picture to make any comparisons. In the four cases of cumulus trajectories, the average speed difference between cloud and surface wind was 3 knots or 10 percent of the wind speed, while the average direction departure was 10°. Transequatorial cirrus flow from north to south at approximately 145° was measured at 32 knots, while a "cloud jet" over Baja California and Southwestern United States, flowing to the northeast, was measured at up to 52 knots. (See Figure 3.)

Two high-resolution negatives produced at The University of Wisconsin from analog tapes recorded at 2215 (U) on 21 June 1967 and at 0013 (U) on 22 June 1967 (see Figure 4) were used for a second comparison. These negatives are much better than the duplicate EIS negatives used for the 19 February case. In fact, they preserve nearly the full resolution of the ATS SSCC. An improved comparison procedure was used for this case. First, the locations of all surface and upper air wind observations were plotted on the measuring table. The actual wind data were omitted to prevent bias on the part of the operator. Cloud trajectories were selected which coincided as nearly as possible with the wind observation locations and times. When the cloud trajectories had been measured and plotted, the wind observations were then plotted and compared, as shown in Figure 5. In this case, the average superimposition error was 18 nm and, since the period of observation was only 2 hours (negatives were not available for a longer period), cloud speeds can be found to within about 9 knots. For 12 cases of tropical cumulus trajectories compared with surface wind observations, the difference between surface wind speed and cloud speed was an average of 8 knots or 38 percent of the cloud speed, while the departure in direction averaged 15°. For four cases of cirrus trajectories compared with the 200-250-300 mb winds, the speed departure averaged 20 knots or 46 percent of the cloud speed, while the direction departure averaged 30°. These are only limited preliminary results and, while some of the departure may of course be attributed to actual differences between cloud and wind speed, because of relatively large differences in location and unknown differences in height of the compared data, there is fairly good agreement.

3.4 Conclusion

A practical technique for making quantitative measurements of cloud displacement from ATS-I pictures has been explained. Two ATS-I pictures were superimposed by two projectors on an electronic digitizing table. Distortion correction, superimposition and rectification were done analytically through a computer program. An estimate of the accuracy of the best results to date gave cloud speeds to within approximately 3 knots. A preliminary comparison of cloud trajectories with standard wind observations has been presented. Fairly good agreement was found in spite of relatively large differences in location of the compared data. Improved comparisons are planned in which cloud heights and complete wind profiles will be known.

Figure 4. ATS-I SSCC Picture from 2215 (U) 21 June 1967. (Printed from negatives made at the University of Wisconsin from ATS-I analog tape.)

Figure 5. ATS-I Cloud Trajectories Compared with Surface and High-Level Winds. (21-22 June 1967 (U).)

ACKNOWLEDGMENTS

This project was supported by grants from the National Aeronautics and Space Administration and Environmental Science Services Administration. The authors would like to thank Professor V. E. Suomi, principal investigator on the ATS-I Spin Scan Camera project, for his help and NASA for providing us with the Spin Scan Camera negatives. The assistance of Ken Moss and the use of The University of Wisconsin Physics Department equipment has also been indispensable.

REFERENCES

1. Hasler, A. F.; and Kornfield, J.: Display and Analysis of ATS-I Spin Scan Camera Pictures Through Time-Lapse Movie Techniques. Weather in Motion, University of Wisconsin Press, in press.

2. COSPAR Working Group IV: Status Report on the Application of Space Technology to the World Weather Watch. Committee on Space Research, Paris, June 1967.

APPENDIX

I. Tangent Plane Approximation

A box camera looking directly down on the subsatellite point would produce a circular image of the Earth. An ATS picture looks the same as one taken by an ordinary box camera; however, the Spin Scan Camera picture is a display of the intensities observed by its telescope as a function of the telescope's stepping and rotation angles. In order to find how much the two pictures actually differ, we first set up a coordinate system as follows.

Let the origin of the coordinate system be at the satellite as shown in Figure A-1. The x-axis is directly along the line connecting the satellite's center and the Earth's center. The z-axis is parallel to the Earth's axis of rotation with the positive direction northward. The y-axis is perpendicular to both the x- and z- axes so as to form a right-handed coordinate system.

Angular variations in the x-z plane are designated θ and measured from the x-axis. θ is the stepping angle of the ATS camera. In the x-y plane the angular variations are designated by ϕ and are also measured from the x-axis. ϕ is the rotational angle of the satellite about its nominal spin axis z.

When viewed by an ordinary box camera, the Earth's disk would appear as a perfect circle formed by the rays tangent to the planet. To find the equation for the Earth's limb in spin scan [illegible]ure coordinates we refer to Figure A-1, in which the circle is formed by the tangents and lies in plane P'. Plane P' is described by the equation

$$x = \text{Constant} \tag{A-1}$$

If we express x in spherical coordinates, $x = R \cos\theta \cos\phi$. When R is fixed as the distance from the Earth's limbs to the satellite, one obtains the equation of the circle:

$$R \cos\theta \cos\phi = R \cos M \tag{A-2}$$

where 2M is the angle subtended by the Earth as seen from the satellite.

When the satellite's spin axis is tilted away from z by an angle, τ, we have merely a rotation about the y-axis so that equation (A-2) becomes

$$\cos\theta \cos\phi \cos\tau + \sin\phi \sin\tau = \cos M \tag{A-3}$$

Since the Earth's limb looks quite circular on an ATS picture, we approximate equation (A-3) as

$$(\theta - \tau)^2 + \theta^2 - M^2 = 0 \tag{A-4}$$

To test the approximation, values of θ, ϕ, τ and M were chosen that satisfied equation (A-3). The same values were used in equation (A-4). The amount by which equation (A-4) differed from zero was used to estimate the error in θ or ϕ. For a large tilt angle of

Figure A-1. ATS SSCC Coordinate System. (The origin of the coordinate system, 0, is at the center of the satellite. The x-axis is directed along the line connecting the satellite's center and the Earth's center and passes through the subsatellite point T. The z-axis is parallel to the Earth's axis of rotation. The y-axis is mutually perpendicular to the x- and z-axes. θ is the stepping angle of the SSCC telescope. ϕ is the rotational angle of the satellite about its nominal spin axis z. τ is the deviation or tilt of the satellite spin axis with respect to z. If a line is constructed which passes through 0 and is tangent to the Earth's surface, R is the distance from 0 to the tangent point. The circle defined by all of these tangent points lies in the plane P'. M is the angle between the tangent line and the x-axis.)

$\tau = 2°$, the greatest error in θ and ϕ was less than 3×10^{-4} radians, or an error of about m at the limb of the Earth. Since τ is normally much less than $2°$ in the pictures used and the largest error occurs only in limited areas near the limb, the error is considered to be less than 6 nm and has been neglected.

II. Distortion Correction and Superimposition

A step-by-step description of the distortion correction and superimposition process is given below and illustrated in Figure A-2. A detailed discussion of each step follows the list.

1. Fit an ellipse to the limb of the Earth (Figure A-2, Part 1).

2. Determine the angle between the major axis of the ellipse and the x-axis of the measuring table coordinate system (MTCS) (Figure A-2, Part 2).

3. Rotate the MTCS through this angle so that the x-axis is parallel to the major axis of the ellipse (Figure A-2, Part 3).

4. Determine the semi-major and semi-minor axes of the ellipse.

5. Translate the origin of the MTCS to the center of the ellipse (Figure A-2, Part 4).

6. Transform the ellipse into a circle (Figure A-2, Part 5).

Each of the pictures is processed separately as above. Then a final step with both pictures produces the final superimposed image.

7. Rotate one picture relative to another so that vectors to a landmark $\vec{L}_1$ and $\vec{L}_2$ are superimposed (Figure A-2, Part 6).

Each of these steps will now be taken up in more detail. The major distortion correction involves transforming the distorted Earth into a circle. The elliptical distortion is introduced when the SSCC scan lines are not reproduced with the proper line spacing or when linear stretching of the photographic material occurs. To determine the shape of the ellipse a least-squares fit to the limb of the Earth is made using the general equation for a conic section:

$$z^2 + T_1 yz + T_2 y^2 + T_3 z + T_4 y + T_5 = 0 \qquad \text{(A-5)}$$

where $T_1 \ldots T_5$ are fitted coefficients and y, z are the measuring table coordinates.

A rotation of the MTCS gives the elliptical equation

$$z^2 + (\frac{S}{P})z + (\frac{Q}{P})y^2 + (\frac{T}{P})y + (\frac{T_5}{P}) = 0 \qquad \text{(A-6)}$$

ere

$$P = \cos^2\theta + T_1 \cos\theta \sin\theta + T_2 \sin^2\theta$$

Figure A-2. Step-by-Step Process of Distortion Correction and Superimposition of ATS-I SSCC Pictures. (1. The elliptically distorted Earth arbitrarily positioned on the MTCS. 2. Determination of the angle between the major axis of the ellipse and the x-axis of the MTCS. 3. Rotation of the MTCS so that the x-axis is parallel to the major axis of the ellipse. 4. Translation of the origin of the MTCS to the center of the ellipse. 5. Transformation of the ellipse into a circle of radius a. 6. Rotation of one picture relative to another such that the vectors to a landmark, $\vec{L}_1$ and $\vec{L}_2$, are superimposed.

$$Q = \sin^2\theta - T_1 \cos\theta \sin\theta + T_2 \cos^2\theta$$

$$S = T_3 \cos\theta + T_4 \sin\theta$$

$$T = -T_3 \sin\theta + T_4 \cos\theta$$

The angle θ is the smallest angle obtained from

$$\tan 2\theta = \frac{T_1}{1 - T_2} \qquad \text{(A-7)}$$

Finding equation (A-6) is equivalent to the rotation discussed in steps 2 and 3. This equation can be modified further by completing the square and rearranging terms:

$$\frac{(x - x_0)^2}{a^2} + \frac{(y - y_0)^2}{b^2} = 1 \qquad \text{(A-8)}$$

where

$$x_0 = -\frac{S}{2P} \qquad a^2 = \left(\frac{S}{2P}\right)^2 + \frac{T^2}{4PQ} - \frac{T_5}{P}$$

$$y_0 = -\frac{T}{2Q} \qquad b^2 = a^2 \frac{P}{Q}$$

The semi-major and semi-minor axes are a and b, respectively. The center of the ellipse is at (x_0, y_0). Translation of the origin is accomplished by subtracting x_0 from every measured x and subtracting y_0 from every y. Transformation of the ellipse into a circle is accomplished by multiplying the translated y coordinate by the ratio a/b. The variation of the Earth's radius from its mean value is approximately 6 nm, so we can regard the Earth to be a circle. The circle then has radius a. Every time a distance is measured on the picture, it is divided by a. This normalizes every circle so that they are equivalent.

The final rotation is accomplished using vectors $\vec{L}_1$ and $\vec{L}_2$ on pictures 1 and 2, respectively. $\vec{L}$ is a vector from the origin to a particular landmark. The angle, ζ, between $\vec{L}_1$ and $\vec{L}_2$ is given by the dot product

$$\vec{L}_1 \cdot \vec{L}_2 = |\vec{L}_1||\vec{L}_2| \cos\zeta \qquad \text{(A-9)}$$

One picture is then rotated with respect to another through the angle ζ. The procedure by which this is accomplished is discussed in Part III.

The process of superimposition is complete once the above is carried out. Displacements of clouds between the two pictures may now be computed since the two pictures can be regarded as one picture.

Rectification

The last problem is one of rectification or one of relating geometric distances on the photograph to actual distances on the Earth's surface. For the case of finding cloud trajectories the cloud displacement D is desired.

On a spherical Earth, the subsatellite point (SSP) and the positions of two clouds can be used to locate a spherical triangle. If we know two arcs, σ_1 and σ_2, and one angle, β, the third arc, ξ (or $D = R\xi$, where R is the Earth radius and D the displacement), can be found. See Figure A-3. This situation is analogous to looking down upon the North Pole, where β is the longitude separation between two arcs of the triangle and each σ is 90° minus the latitude. D is the great circle distance between two clouds (or, in the case of one cloud, the displacement). Let us find the angles σ_1 and σ_2 first.

Using the same coordinate system as in Figure A-1, position a plane P perpendicular to x at the SSP. The arc length for σ_1 projects onto P as a straight line ℓ_1, with endpoints (H, 0, 0) and (H, y_1, z_1). H is the height of the satellite above the Earth's surface. See Figure A-4.

The line r_1, from the origin through (H, y_1, z_1), intersects the Earth as shown in Figure A-5. Figure A-5 is just a cross-section from Figure A-4.

The equation of the circle with center at E is:

$$[x - (R+H)]^2 + \rho^2 = R^2 \qquad H \leq x \leq 2R + H \tag{A-10}$$

The line r_1 has equation

$$\rho = x \tan \alpha \tag{A-11}$$

where

$$\cos \alpha = \cos \theta \cos \phi \tag{A-12}$$

Substituting (A-11) into (A-10) and solving for x allows us to find σ_1 from

$$\tan \sigma = \frac{x \tan \alpha}{(R+H) - x} \tag{A-13}$$

The process is repeated for σ_2. Thus, we have two sides of the triangle.

To find the remaining angle, β, we define the vector $\vec{\ell_1}$ as the vector of length ℓ_1 from the SSP (H, 0, 0) to (H, y_1, z_1). Vector $\vec{\ell_2}$ is similarly defined. Thus, by the dot product of two vectors

$$\beta = \cos^{-1}\left(\frac{\vec{\ell_1} \cdot \vec{\ell_2}}{|\vec{\ell_1}||\vec{\ell_2}|}\right) \tag{A-14}$$

Figure A-3. Spherical Triangle Used to Calculate a Displacement, D, on the Surface of the Earth Which is Part of the Rectification Process for ATS SSCC Pictures. (If we know two arcs, σ_1 and σ_2, and one angle, β, the third side, ξ (or $D = R\xi$, where R is the Earth radius and D is the displacement), can be found.)

Figure A-4. Geometrical Relationships Used to Rectify ATS SSCC Pictures. (r_1 = distance from origin to surface of Earth; α_1 = angle between r_1 and the x-axis; P = plane tangent to the Earth at the subsatellite point; σ_1 = great circle angle (see Figure A-3); ℓ_1 = projection of arc length corresponding to σ_1 onto plane P; β = angle between ℓ_1 and ℓ_2, also angle between great circle segments $R\sigma_1$ and $R\sigma_2$, where R is the radius of the Earth. See Figure A-3.)

The final side of our triangle follows directly from the spherical trigonometric relation

$$\cos \xi = \cos \sigma_1 \cos \sigma_2 + \sin \sigma_1 \sin \sigma_2 \cos \beta \qquad \text{(A-15)}$$

whence the displacement, D, is

$$D = R\xi \qquad \text{(A-16)}$$

where R = Earth's radius.

Note: The last step of superimposition (rotation through the angle ζ as defined in equation (A-9)) is accomplished by subtracting ζ from β each time β is calculated.

Figure A-5. Cross-Section of Figure A-4. (H = height of the satellite above Earth; ρ = half chord length; X = distance from origin to the intersection of ρ with the x-axis; R = radius of the Earth; E = center of the Earth; T = subsatellite point; P = plane tangent to Earth at subsatellite point.)

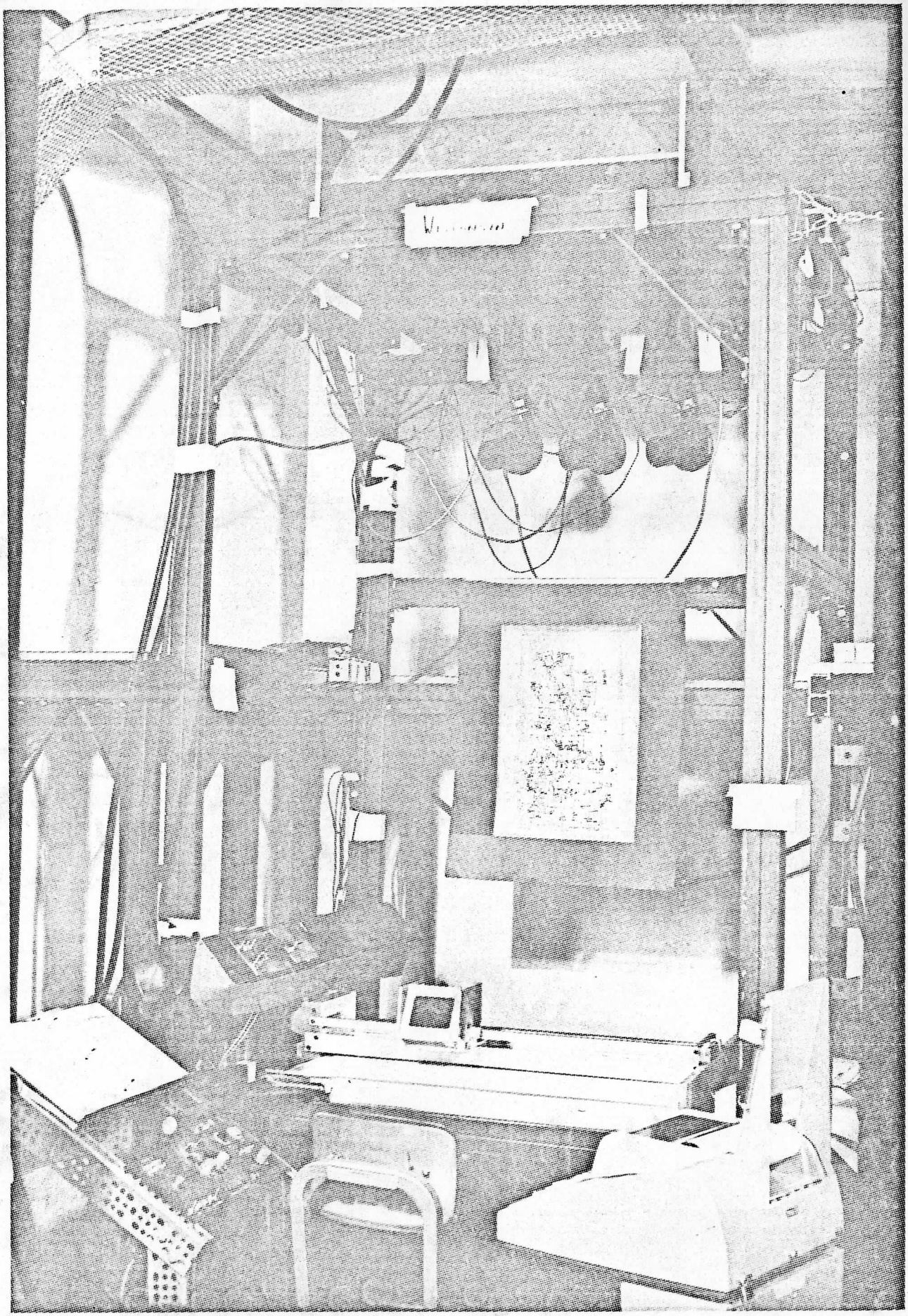

FIG 1

FIG 2

ATS-I CLOUD TRAJECTORIES COMPARED WITH SURFACE AND HIGH LEVEL WINDS

FEBRUARY 19-20, 1967 (U)

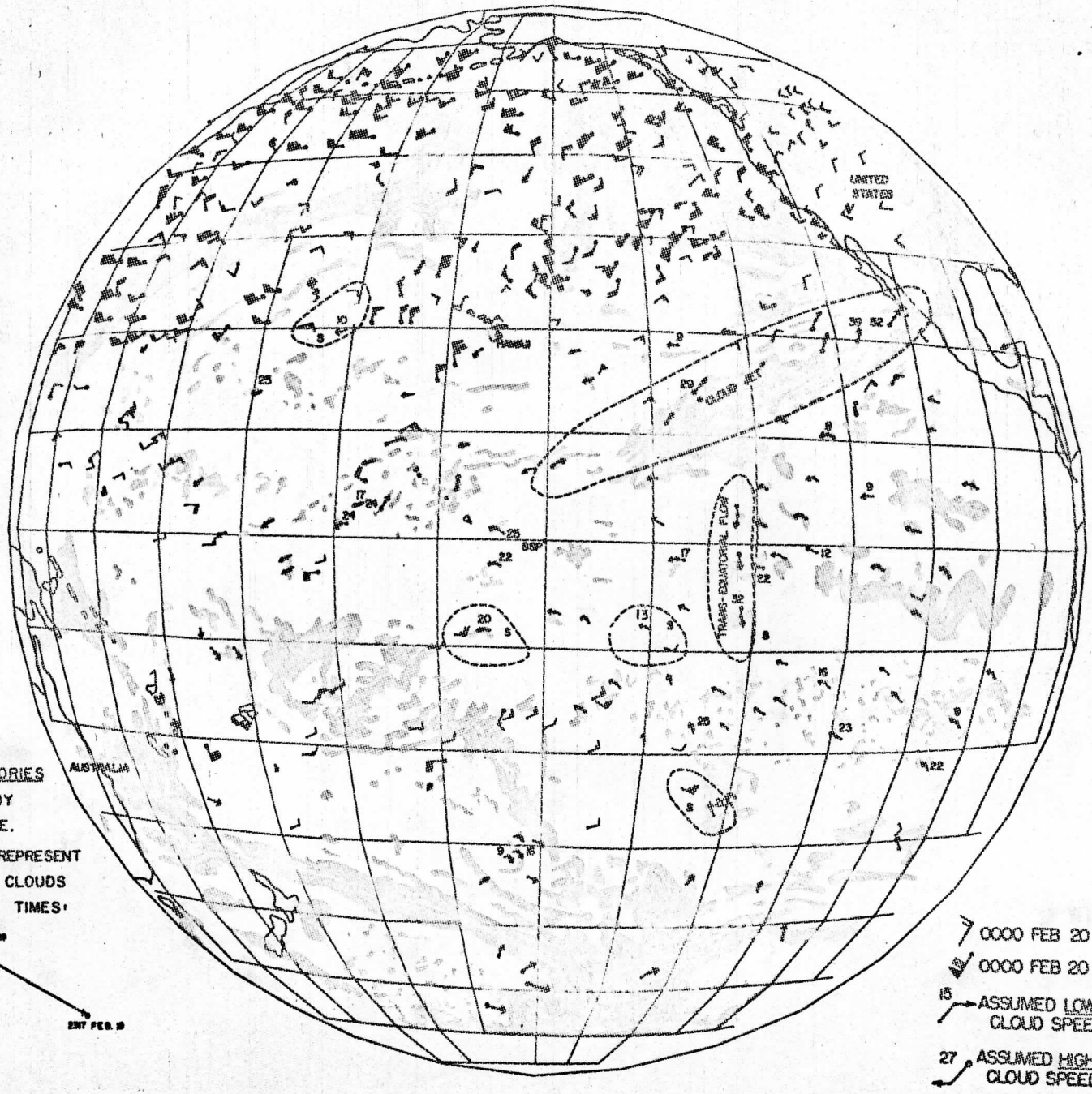

FIG 3

CLOUD TRAJECTORIES ARE DETERMINED BY "BLINK" TECHNIQUE.

DOTS ON ARROWS REPRESENT THE POSITION OF CLOUDS AT THE FOLLOWING TIMES:

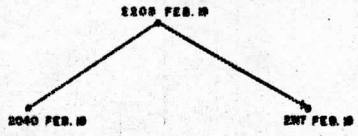

0000 FEB 20 SURFACE

0000 FEB 20 200-250-300 MB

15 → ASSUMED LOW LEVEL CLOUD TRAJECTORY
CLOUD SPEED = 15 KNOTS

27 → ASSUMED HIGH LEVEL CLOUD TRAJECTORY
CLOUD SPEED = 27 KNOTS

FIG 4

ATS-1 CLOUD TRAJECTORIES COMPARED WITH SURFACE AND HIGH LEVEL WINDS
JUNE 21-22, 1967 (u)

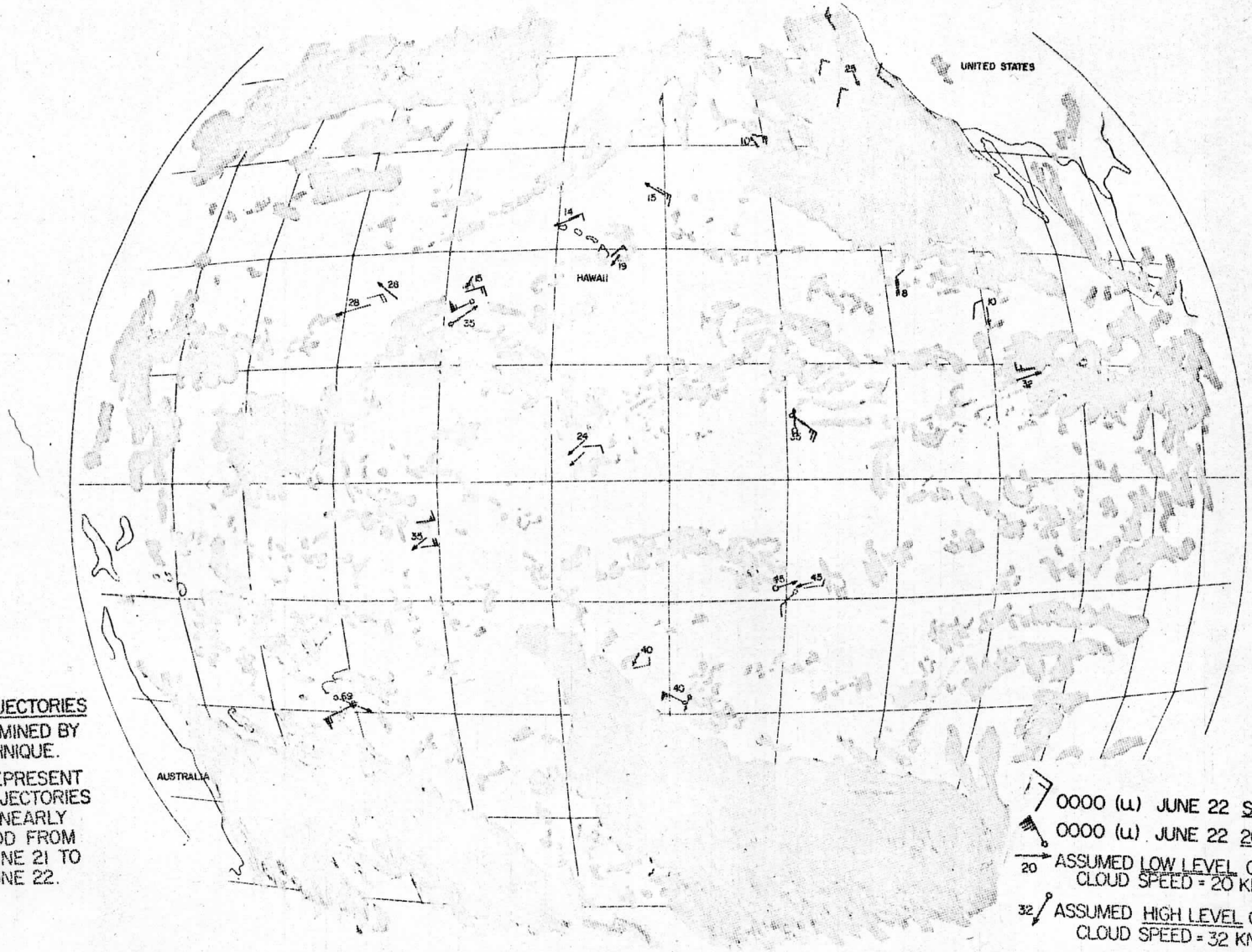

CLOUD TRAJECTORIES ARE DETERMINED BY "BLINK" TECHNIQUE.

ARROWS REPRESENT CLOUD TRAJECTORIES OVER THE NEARLY 2 HR. PERIOD FROM 2215 (u) JUNE 21 TO 0013 (u) JUNE 22.

0000 (u) JUNE 22 SURFACE

0000 (u) JUNE 22 200-250-300 MB

20 ASSUMED LOW LEVEL CLOUD TRAJECTORY CLOUD SPEED = 20 KNOTS

32 ASSUMED HIGH LEVEL CLOUD TRAJECTORY CLOUD SPEED = 32 KNOTS

NOTE: LENGTH OF CLOUD TRAJECTORIES IS MULTIPLIED BY 3 TO IMPROVE LEGIBILITY

FIG 5

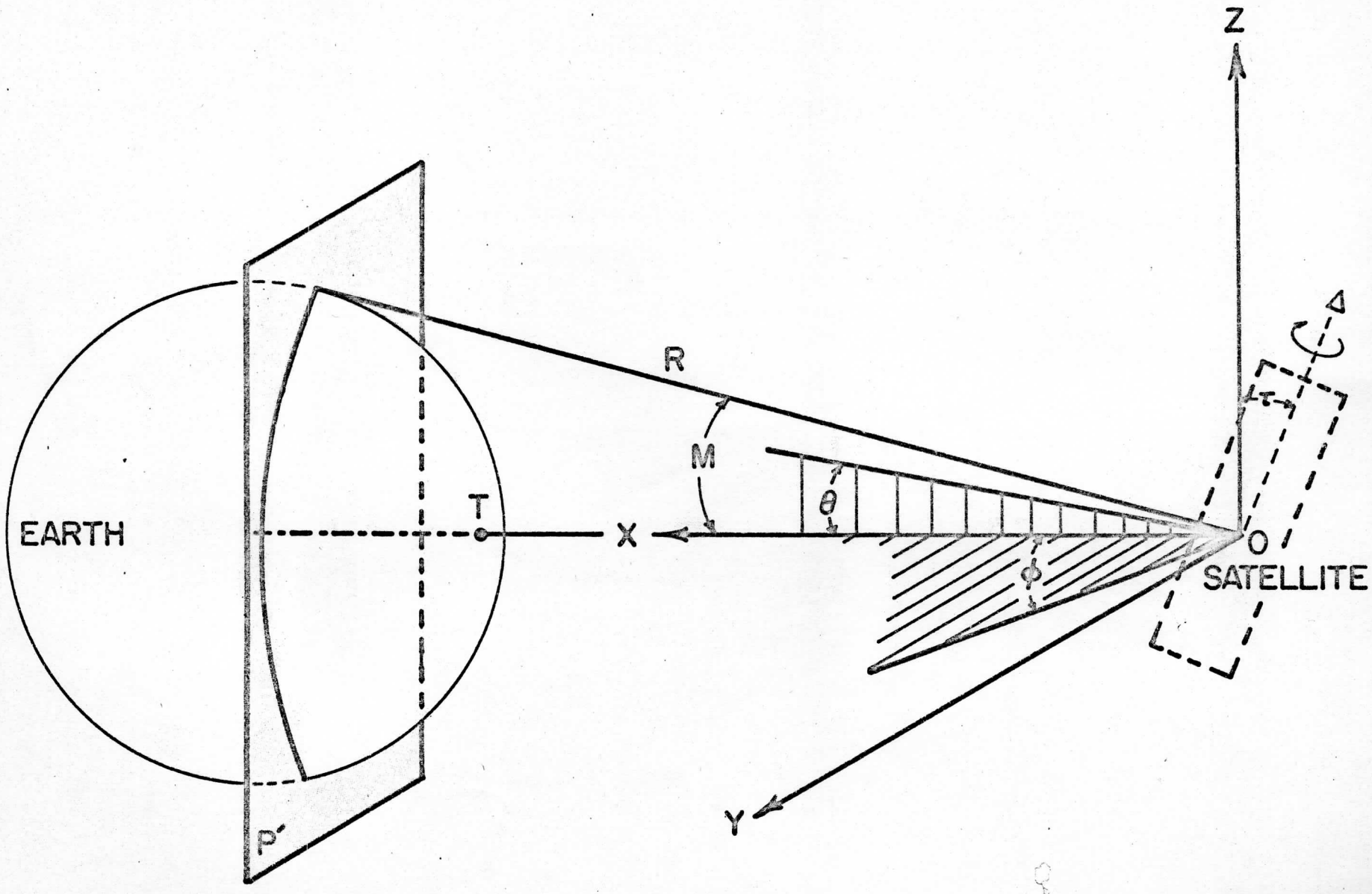

FIG A-1

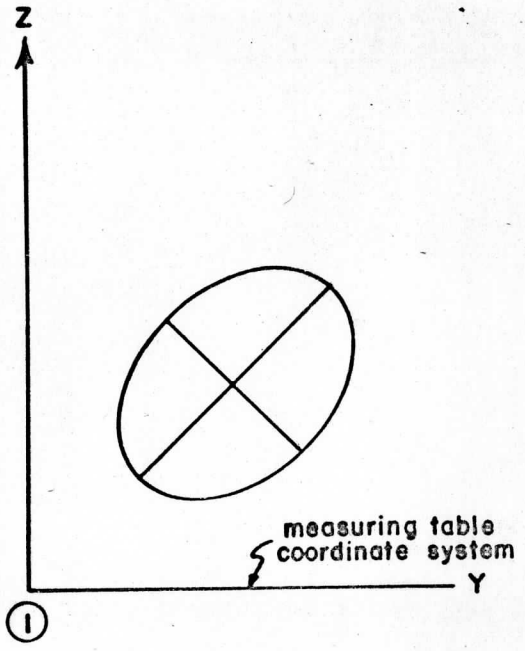
Z
Y
measuring table
coordinate system
1

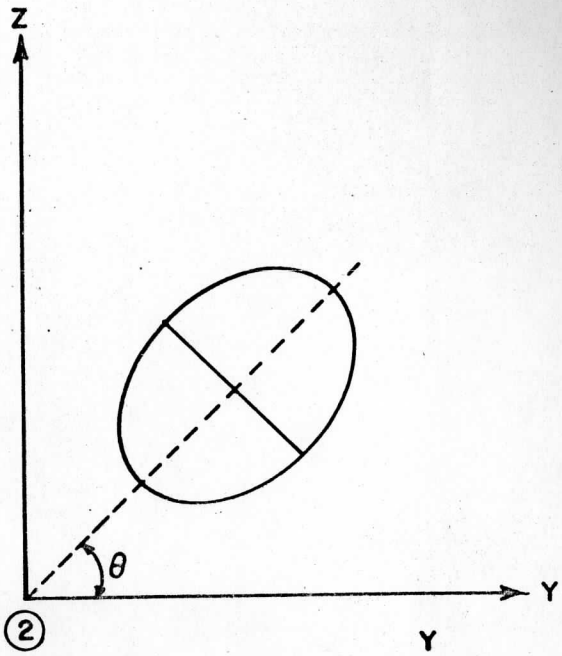
Z
Y
θ
2

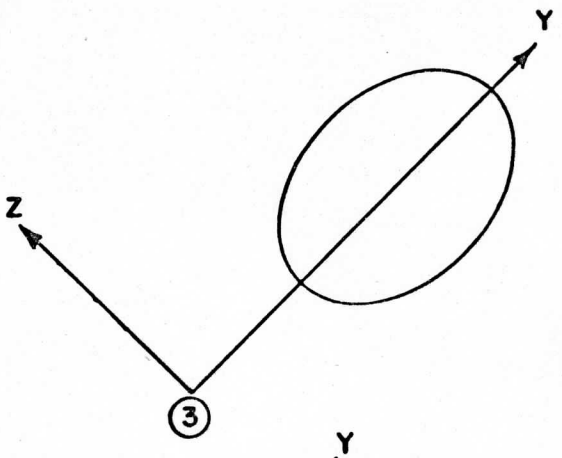
Y
Z
3

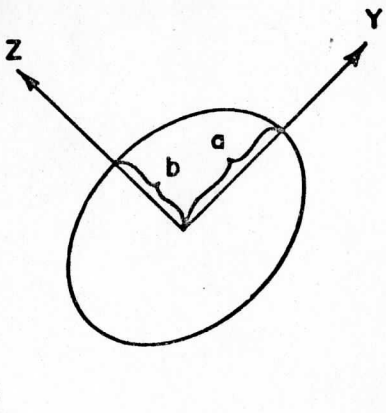
Z
Y
b
a
4

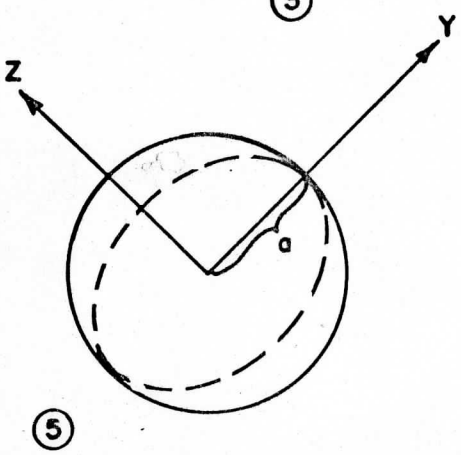
Z
Y
a
5

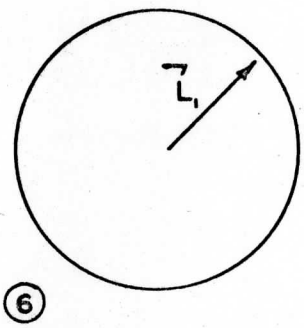
L1
6

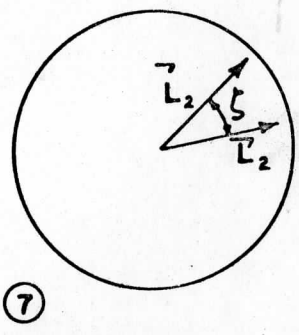
L2
ζ
L2
7

FIG A-2

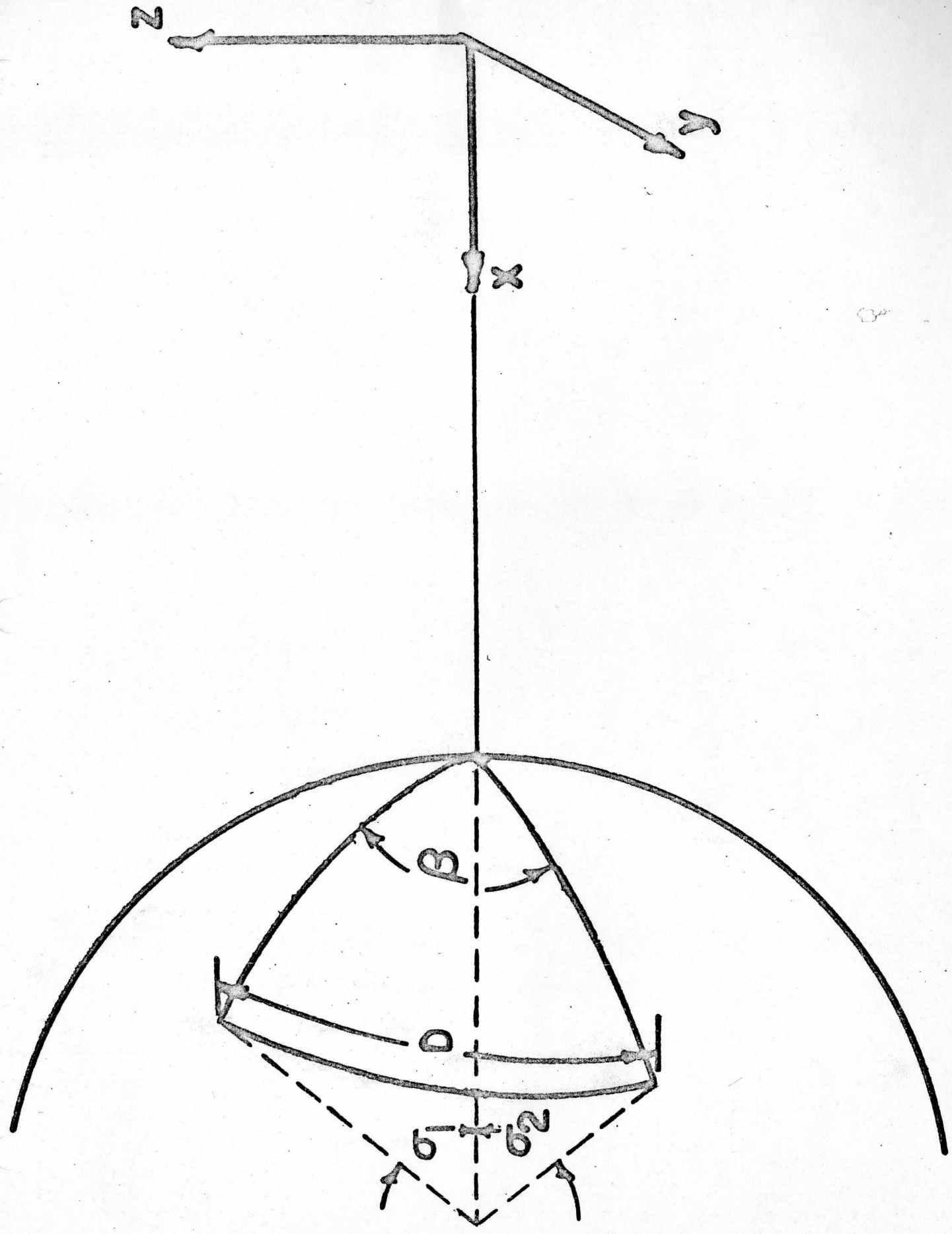

FIG A-3

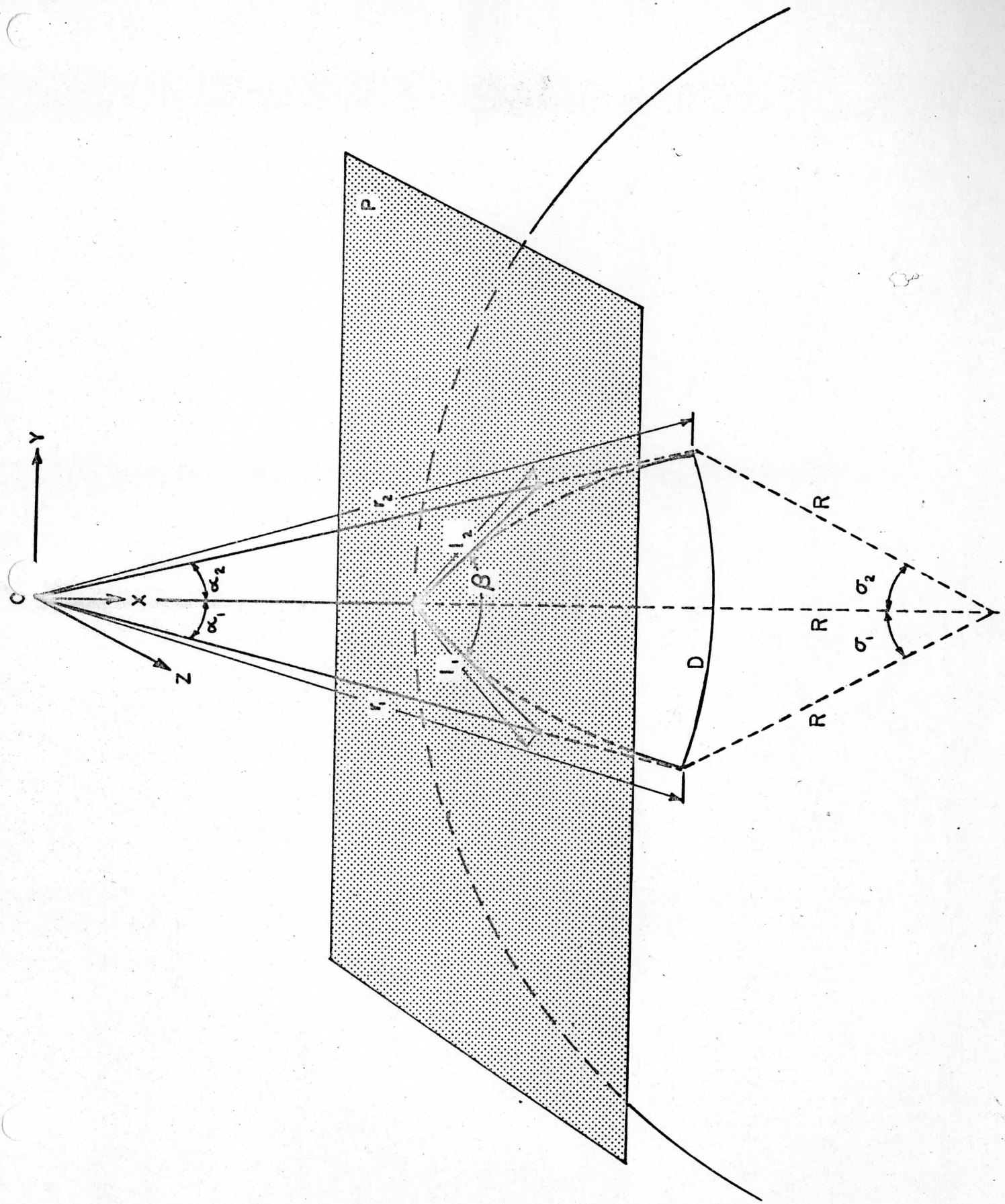

FIG A-4

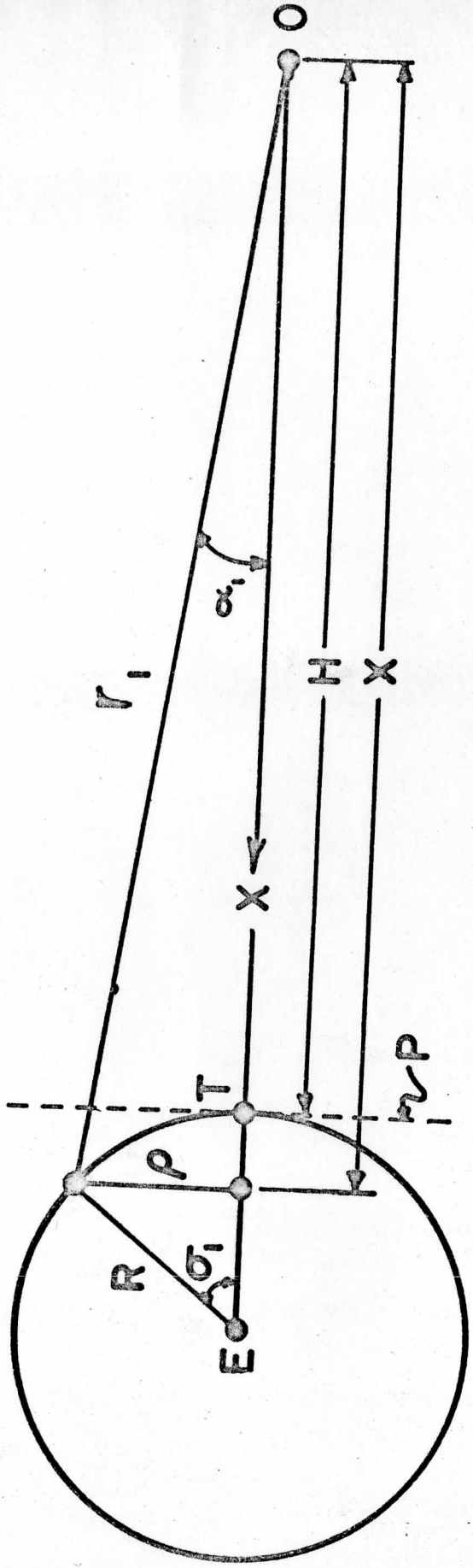

FIG A-5

#22 Second revision

DISPLAY AND ANALYSIS OF ATS-1 AND ATS-3 SPIN SCAN CLOUD CAMERA PICTURES THROUGH TIME-LAPSE MOVIE TECHNIQUES

A. F. Hasler
and
J. Kornfield

University of Wisconsin
Madison, Wisconsin

1. INTRODUCTION

The ATS-1 and ATS-3 Spin Scan Cloud Cameras (SSCC) offer the scientific community its first opportunity to view the time evolution of clouds and cloud systems from the vantage point of space. Time-lapse movies made from the SSCC pictures provide an effective way of displaying the change in the cloud field over a wide range of time and space scales. By varying the time intervals between pictures, the speed of projection, and the size of the area viewed, one may observe the atmosphere from perspectives never before available. The space scales available for study range from the smallest meso-scale (less than 10 n.mi.) to macro-scale (10^4 n.mi.). The time scales may be varied from periods of a few hours with pictures at the shortest 23 minute intervals[1] viewed up to 10,000 times faster than actual speed to periods of weeks or more at 24-hour or longer intervals which can be viewed advantageously at even faster rates. It is now possible using SSCC pictures to tailor-make a time-lapse movie which enables the study of an extremely wide range of atmospheric phenomena.

2. MOVIE PRODUCTION TECHNIQUES

A simple alignment and registration technique has been developed by which SSCC time-lapse movies may be produced with a minimum of time and expense.

When making a movie from a single day's set of ATS-1 SSCC data the following procedure is used: The duplicate negative of the picture taken at local noon is selected and aligned to the negative which follows it by 23

---

[1] Limited areas can be scanned at even shorter intervals by putting the camera in the "back to back" mode. The picture interval is then proportional to the vertical dimension of the area scanned.

minutes. Each adjacent negative is successively aligned until all afternoon pictures are aligned (the morning pictures are aligned in reverse order). Alignment is accomplished by using land marks when available. Baja California and orographic clouds over Hawaii are nearly always visible during a good part of the day. When no land marks are visible the earth's limb and clouds must be used. Care must be taken to minimize the effect of cloud motion. Registration is accomplished by punching holes in the negatives on a jig.

The advantage of this technique is that adjacent pictures have maximum similarity and therefore allow more accurate alignment than any technique using pictures taken at greater time intervals or using secondary alignment aids such as grids. However, the alignment error is cumulative and may build up over long series of pictures. This means that the movie will have very little bounce or jitter, but there may be a gradual shift or rotation over a long series of pictures. Most SSCC movies produced at the University of Wisconsin have a total shift or alignment error of less than 100 nautical miles (nm)[1]. The best alignment to date gives a total alignment error which is less than 35 nm. Alignment techniques are being investigated which would allow more accurate quantitative use of the movies for a longer series of pictures.

When a movie is made for long time periods using pictures at 24-hour intervals, all negatives are aligned using land marks to a master negative for that set. There is no advantage to using adjacent pictures in this case because of large changes in the cloud field over a 24-hour period.

Once a set of SSCC negatives or positive transparencies is aligned and registered, the negatives are mounted on the registration jig (which is transparent to allow back-lighting) and shot one at a time with a 16 mm movie camera in single frame mode. The number of movie frames used for each SSCC picture depends on the time scale of the movie. When pictures taken at the shortest time intervals (23 minutes) are used, it is

---

[1] at the subsatellite point

found that 3 movie frames per picture give an adequate time scale for viewing when projected at 24 frames per second. This allows one to view a twenty-hour satellite day in 8 seconds or a speed up in time by a factor of about 10,000.

Since a movie of the whole earth viewed at this rate displays a tremendous amount of information in a very short time, it is desirable to view it repeatedly (usually in loop form) concentrating one's attention on a limited portion of the picture over several cycles.

When the interval between pictures is longer (1 hour to 24 hours or longer) it is often desirable to view the movie very slowly or even view one picture for extended periods. Since it is also useful to view this type of movie at a rapid rate, it is best to retain the 3 movie frames per picture shooting rate and use a variable speed projector. This allows a maximum speed-up in time of 600,000 times for pictures taken at 24-hour intervals. If no variable speed projector is available then rates of 3 to 30 movie frames per picture are useful.

3. TYPES OF TIME LAPSE MOVIES

As was mentioned in the introduction, it is possible to vary both the time and space scale of movies made from ATS-1 pictures through a very large range. All film types which have been produced or are planned are listed in Table 1 according to their time and space scales.

a) Complete Day Movies

Movies using the maximum standard time resolution and the full picture area of the satellite are called Complete Day movies when an entire complement of pictures (twenty or more) is available. This type of movie is very well suited to obtaining an over-all view of the complete set of data.

Cloud motions and their growth and decay are clearly evident at this time scale. Trajectories of individual clouds may be seen as well as the motion and development of synoptic scale disturbances. The diurnal build-up of clouds over continents and islands and the occasional development of cirrus plumes[1] or streamers originating over islands may often be seen. Lines of cumulus cloud groups and rings imbedded in the easterlies are often observed in the trade wind areas of the Pacific (ATS-1-CU-3)[2].

b) Close-Up Movies

The 16 mm movie frame is incapable of preserving the maximum spatial resolution of the SSCC pictures. A resolution of 50 to 118 lines per millimeter depending on the contrast of the subject has been specified by Kodak for Plus-X Reversal Film. The vertical dimension of a standard 16 mm projector aperature is .284" or 7.22 mm so one could expect between 360 and 720 lines to be resolved. However, this would be somewhat reduced for duplicate films. Since the maximum resolution of the SSCC is 2400 discreet lines, it is evident that the full resolution can not be retained on the 16 mm format although some improvement can be achieved with higher resolution film. For this reason, it is desirable to limit the field of view by using Close-Up techniques. It can also be advantageous to limit one's attention to a particular meso-scale phenomenon. Some features which have been studied in this way are: a hurricane in the southwestern Pacific[3], traveling waves in clouds associated with a polar jet (ATS-1-CU-1), and the build-up of orographic clouds over Hawaii during the day.

---

[1]Cirrus plumes are particularly evident originating over small islands near Fiji in a movie filmed from ATS-1 pictures by T. Fujita at the University of Chicago.

[2](ATS-1-CU-3) is the classification of the film listed in Table 2 which best illustrates this example.

[3]Suomi, V. E., T. Fujita, The Life Cycle of a South Pacific Typhoon as Revealed by Time-Lapse ATS-1 Motion Pictures, (Paper presented at the Conference on Hurricanes and Tropical Meteorology, Caracas, Venezuela, November 20-28, 1967)

c) Daily Series Movies

Movies made from a series of SSCC local noon pictures, and covering the whole picture area are called Daily Series movies. These have been made in lengths varying from one month to one year and they are very useful for obtaining a synoptic view over long time periods. The daily series can be used as a convenient data retrieval system if the frames can be viewed individually. Depending on the speed of projection, Daily Series movies can be used to observe in detail the day-to-day motion of synoptic-scale disturbances (slow speeds) or to get an impression of the earth's general circulation (high speeds). In the high speed mode mid-latitude cyclones move rapidly toward the east, and cloud masses in the tropics apparently move toward the west. Another interesting feature of the Pacific which is seen are the undulations in equatorial cloud bands which appear to travel toward the west (ATS-1-DS-2 or OS-1).

d) Long Time Scale Movies

Longer time-scale films, that is weekly, monthly, quarterly, etc. movies, are being made now that the satellite has been in orbit long enough to make them possible. Another type of film which allows the observation of longer time scales is the "Average" movie. Fifteen-day and monthly photographic cloud cover "averages" described elsewhere in this volume by Kornfield and Hasler have been shot using the same time-lapse techniques to give a new vantage point for climatological studies (OS-A-1, 2, 3, 4). Two of the most dramatic features which can be observed in the "average" movies are the variations in cloud cover associated with the monsoon circulations of the earth and the variations in intensity and position of the cloud bands which are thought to mark the intertropical convergence zone.

e) Special Time Series Movies

Movies which are made from discontinuous data or which use pictures at special time intervals are called Special Time Series (STS) movies. One film was made using pictures at three-hour intervals over several days to give an accelerated view of a cyclone. The two hurricane movies (ATS-1, STS-CU-2, & STS-5-W/CU) which have been made to date use all data which is available for periods up to three weeks; but since there are some data gaps, they are classified as STS movies. A movie showing a close up of the United States during a "Tornado Watch" period (ATS-III, STS-CU-2) was made from ATS-III pictures taken at 14-minute intervals. The special 14-minute time interval (therefore the STS classification) is made possible by scanning only the Northern Hemisphere for each picture.

4. NEW FILMING TECHNIQUES

Many new filming techniques have been used or are planned which will aid in the analysis of the satellite pictures; three examples worth considering are a quasi-Lagrangian coordinate system, a "traveling mean" technique, and an "auto correlation" technique. To study the life of Typhoon Sarah (Pacific, September, 1967), a film (ATS-1-STS-5-W/CU) was made using a quasi-Lagrangian coordinate system centered on the storm[1], as well as using the conventional Eularian coordinate system. This allows one to concentrate on the storm's development rather than its motion. A technique which is planned for use in making the "average" movies is the "traveling mean." The present procedure is to take five movie frames of each 15-day or monthly "average." This gives a rather abrupt transition between each individual "average." The "traveling mean" technique will involve making "averages" which would be stepped forward one day at a

[1] The field of view is centered on the storm but does not rotate with it.

time instead of 15 or 30 days at a time as is presently done. These would be filmed at a rate of one movie frame per "average" and would give a more detailed view of the data as well as insuring perfectly smooth transitions. Finally, an "auto correlation" technique is being applied using different time lags which are selected to help analyze periodic time variations in cloud patterns.

5. FILMS AVAILABLE AT THE UNIVERSITY OF WISCONSIN

A list of films available for purchase is shown in Table 2. Requests for films and updated film lists should be directed to the authors' attention, Department of Meteorology, University of Wisconsin, Madison, Wisconsin.

6. ACKNOWLEDGMENTS

This project was supported by grants from the National Aeronautics and Space Administration and Environmental Science Services Administration. The authors would like to thank Professor V. E. Suomi, principal investigator on the ATS-I Spin Scan Camera project, for his support and NASA for providing us with the Spin Scan Camera negatives. The assistance of Dave Cadle and Jack Lund, University of Wisconsin, has also been indispensable in the production of these films.

LIST OF TABLES

TABLE 1: Types of Time Lapse Movies

TABLE 2: ATS-1, ATS-III, ESSA III and ESSA V experimental films presently available at the University of Wisconsin (June 1968).

.BLE I

	FILM TYPE	TIME SCALE	SPACE SCALE	MOVIE FRAMES PER PICTURE	USES
1)	Complete Day	23 minutes (ATS-I) 28 minutes (ATS-III)	Whole picture	3	Over-all view of complete data Cloud motions and other phenomena
2)	Close-UP	23 minutes (ATS-I) 28 minutes (ATS-III)	Depends on area covered by the phenomena to be viewed (10 to 10^4 nm)	3	Meso-scale phenomena
3)	Daily Series	24 hours	Whole picture	3 to 30 (Variable speed projector is very desirable)	Over-all view of long time periods Convenient data retrieval Synoptic scale disturbances over long time periods
4)	Weekly Monthly Quarterly Etc.	7 days 30 days 90 days Etc.	Whole picture	3 to 30	Climatology
5)	"Averages" See article in this volume by (Kornfield and Hasler)	15 days 30 days	Whole picture	3 to 30	Climatology
6)	Special Time Series	Any non-standard picture interval	Depends on area covered by the phenomena to be viewed (10 to 10^4 nm)	3 to 30	Observation of disturbances over non-standard time periods

TABLE 2

1. ATS-I Loops and Short Movies

A. Complete Days

1. Loops

CD-1	January	7-8, 1967 (U); 36 pictures, 23 minute intervals
CD-2	February	18-19, 1967 (U); 47 pictures, 23 minute intervals
CD-3	February	19-20, 1967 (U); 43 pictures, 23 minute intervals
CD-3.1	April	13-14, 1967 (U); 37 pictures, 23 minute intervals
CD-3.2	April	14-15, 1967 (U); 45 pictures, 23 minute intervals
CD-3.3	April	15-16, 1967 (U); 27 pictures, 23 minute intervals
CD-4	April	16-17, 1967 (U); 47 pictures, 23 minute intervals
CD-4.1	April	17-18, 1967 (U); 40 pictures, 23 minute intervals
CD-5	April	18-19, 1967 (U); 41 pictures, 23 minute intervals
CD-6	April	19-20, 1967 (U); 41 pictures, 23 minute intervals
CD-7	April	20-21, 1967 (U); 45 pictures, 23 minute intervals
CD-8	April	21-22, 1967 (U); 43 pictures, 23 minute intervals
CD-9	April	22-23, 1967 (U); 43 pictures, 23 minute intervals
CD-10	April	23-24, 1967 (U); 36 pictures, 23 minute intervals
CD-16	June	21-22, 1967 (U); 39 pictures, 23 minute intervals
CD-17	July	15-16, 1967 (U); 41 pictures, 23 minute intervals
2CD-1	February	18-20, 1967 Two Complete Days (U); 97 pictures; 23 minute intervals

2. Short Movies

12CD-1 April 13-24, 1967 (U); Twelve Complete Days; 425 pictures, 23 minute intervals, 50 ft.

12CD-1 W/CU April 13-24, 1967 (U); Twelve Complete Days; with close-up of cyclone April 13-20, 100 ft.

B. Close-Ups (Loops)

CU-1 February 19-20, 1967 (U); Cloud Waves in a Polar Jet
CU-3 June 21-22, 1967 (U); Easterly Waves South East Pacific

C. Daily Series

1. Loop

DS-2 January 21-February 28, 1967 (U); 35 pictures at approximately local noon (2200U)

2. Short Movie

DS-1967 Complete Year 1967; 300 pictures at approximately local noon (2200U) 5 frames per day repeated three times, 100 ft.

D. Special Time Series

1. Loop

STS-CU-2 April 6-15, 1967 (U); Birth and Death of a Hurricane

2. Short Movie

STS-5 W/CU August 31 - September 22, 1967 (U); Typhoon Sarah - Life History (with close up), 100 ft.

II. ATS I 400 ft. Movies

"Weather in Motion" - consists of the following films: CD-1, CD-3, CD-4, DS-2 STS-CU-2, CU-1; repeated up to 15 times each.

"Mesoscale Cloud Motions From ATS Synchronous Satellites" - consists of the following complete days and selected close-ups: CD-3, CU-1, CD-16, CU-3, 12CD-1 W/CU, STS-5 W/CU, STS-CU-2, parts of ATS-3 Color Movie (B & W Copy)

III. ATS-III Loops

A. Complete Day Color Loop
CD-C-1, November 18, 1967; 35 pictures, 30 minute intervals

B. Special Time Series Black and White loop
STS-CU-2, April 19, 1968 (U); "Tornado Watch" (Close-up of United States) 30 pictures, 14 minute intervals

IV. ATS-III 400 ft. Color Movie

"Weather in Motion and in Color" - consists of complete day (November 18, 1967) with selected close-ups.

V. Other Satellite Loops (Made from ESSA III and V Computer Composite Pictures)

A. Daioy Series

OS-1 - January 21 - February 25, 1967; Mercator Projection, Pacific Ocean (three frames per day)
OS-2 - January 26 - March 25, 1967; North Polar Projection (three frames per day)
OS-5 - January 10 - May 31, 1967; North Polar Projection (three frames per day)
OS-6 - January 10 - May 31, 1967; South Polar Projection (three frames per day)

B. Averages

OS-A-1 - Complete Year 1967; Monthly "Averages", Mercator projection, Pacific Ocean (five frames per month)
OS-A-2 - Complete Year 1967; Monthly "Averages", Mercator projection, Atlantic and Indian Oceans (five frames per month)
OS-A-3 - Complete Year 1967; 15-Day "Averages", Mercator projection, Pacific Ocean (five frames per "Average")
OS-A-4 - Complete Year 1967; 15-Day "Averages", Mercator projection, Atlantic and Indian Oceans (five frames per "Average")

This list is subject to change without notice.

Original

CLOUD MOTION AND GROWTH

FROM DIGITIZED ATS1 PICTURE PAIRS

C. L. Bristor, M. Frankel and E. Kendall

National Environmental Satellite Center, ESSA

October, 1967

ABSTRACT

Early computer experiments are discussed whereby digitized ATSI picture pairs are utilized to deduce the motion and growth of cloud fields. Variable grey shade cloud brightness topographies are reduced to single binary "event" and "void" arrays by simple thresholding logic after which certain pattern recognition techniques are employed. An "erosion" procedure is applied in order to reduce "event" clusters to singular "fingerprint" patterns. Cloud displacements are deduced through successive trial juxtapositions which yield an optimum match between features of the picture pair. Comparisons of the "erosion" required in the mated regions of the two pictures provides cloud growth information. Programs are presently diagnostic in nature in order to provide insight concerning convergence to realistic solutions, and to indicate computer practicalities in terms of memory requirements and running speeds. The possibilities for operational programs are encouraging.

1. Introduction

The National Environmental Satellite Center, ESSA, has cooperated with NASA's ATS project and with Professor V. E. Suomi since late 1966 as a co-experimentor in the utilization of digitized ATSI Spin Scan camera image information. Experiments in automatic processing of the digitized imagery at NESC have emphasized the development of capabilities for generating real time products and operational procedures. Whitney and others, 1967, have described most of these efforts elsewhere in this volume.

The present paper deals with the unique attribute of a geostationary satellite -- its ability to provide continuous surveillance of selected regions. Despite problems of deducing the three dimensional wind field from cloud motions, the challenge presented by the ATSI images has prompted a variety of approaches for the extraction of cloud motion information from picture sequences.

The "loop" movies produced by Fujita, 1967, have provided strong impetus and represent one approach. Apart from this and other efforts (e.g. Hubert, 1967) which utilize analog images and optical hardware techniques, there would appear to be advantages in using digital automation techniques. Objectivity is perhaps the key advantage in the digital pattern recognition approach. Hopefully, an algorithm can be developed with sufficient sophistication and speed so as to compete with methods which require interpretor/operator skills.

Without digressing into a discussion of pattern recognition, mention should perhaps be made of the progress of such techniques in several application areas. For example, in the analysis of biomedical subject imagery (e.g. Ruddle et al, 1967) and in the analysis of bubble chamber patterns of nuclear particles (White, 1967), computerized techniques are reaching an operational testing status. Also, in the area of analysis of metallurgical microstructures, some results of computerized techniques are more precise than hand interpreted information. Moore, 1966, has developed a hierarchy of programs for metallurgical applications and some of these ideas are applied in the present study. The following listed items provide a brief description of the operational method from the conceptual standpoint. The items are then amplified in corresponding separate sections of the paper, explaining actions taken in the present diagnostic effort:

(a). The raw digitized video raster data is first calibrated and earth located so that a pair of image brightness topographies, separated by a short time interval, are available as coincident views ready to serve as a source of information concerning cloud changes that have occurred during the specified interval.

(b). "Event" arrays are next extracted as compressed source information for the remaining pattern treatment. Ideally, the resulting binary arrays are obtained as a result of brightness slicing coupled with "neighbor" tests in order to retain only those features which represent the class of cloud features being treated.

(c). An "erosion" process is next employed in order to reduce pattern clusters to single event "fingerprint" form. A record of the eroded samples is retained in sub-sector table form for each picture.

(d). Sub-sectors of the first picture eroded array are then displaced in the "near realm" of the second picture array until successive tests yield the best match. The resulting pattern displacement is regarded as the mean motion of the cloud pattern in the sector.

(e). Once the equivalent sector boundaries are defined on the second picture, an interpolation of the (saved) eroded elements can be made. An individual difference can then be obtained using the saved eroded population for each pre-selected sub-sector of the first picture, and using the interpolated eroded population for the mated equivalent sector of the second picture. These differences represent cloud growth information.

2. Input data

The automated approach, as conceived, deals with a pair of image sectors which have been mapped onto a standard (Mercator) projection in order to simplify the program logic which otherwise would be required to deal with distortions arising from variations in perspective and with relative coordinate systems. Ideally, the image brightness topographies also require calibration to remove camera system response anomalies and to provide normalization for variations in illumination.

The location precision attainable in the input data relates directly to the minimum permissible time span between picture pairs. If one must minimize the time between pictures in consideration of the life cycle of tracer cloud features, then there is need for compromise on a practical time difference. Considerable compromise has been made with these conceptual ideals in the present diagnostic programming effort. Some requirements have been sidestepped and others ignored and therefore accepted as secondary contaminants.

In the case of mapped arrays, the problems described in the companion paper (by Whitney et al, 1967) have been set aside since, clearly, the success of an automated operational program depends upon being able to map the imagery with practical precision. Brightness sample arrays have simply been taken directly from the unrectified image rasters with minor orthogonal shifts in the coordinate reference system in order to approximate a one-to-one correspondence in array earth location. Displacement results will therefore represent only relative motions. The basic data input array, indicated in Fig. 1, consists of 1.8 million 8-bit brightness samples comprised of 1200 scan lines, each containing 1500 samples with sample-to-sample spacing along each line approximating the line-to-line spacing. The number of samples per degree of geocentric arc varies from about 30 near the center to perhaps 15 at the corners, but, for the present purpose, local resolution variations are a secondary consideration.

Similarly, brightness corrections have been set aside as of secondary importance. Array test sub-regions are selected away from areas of sun glint and the remaining frame-to-frame illumination change ranks in the same secondary category with the omitted response calibration.

Beyond the questions of brightness corrections and earth positioning, the volume of data requires further compromise in terms of computer resources. Even with a large scale CDC 6600 computer, the manipulation of two large arrays totalling nearly 29 million bits presents problems of segmenting and efficient data flow. Although practical data volumes could be obtained if basic arrays are broken into "local" sectors of the first image and a larger corresponding realm in the second image, a great complexity remains in the logical treatment of brightness topographies having such a large count range.

The initial investigation has therefore followed common pattern study practice wherein a "slice" of the picture patterns becomes the means of comparison. The following section describes the pattern techniques which deal with the resulting single bit arrays. From the viewpoint of the input data problem, the advantage is clear, since two input array patterns may now be stored in input data storage buffers representing a total of 60,000 (60-bit) words. With more than 131,000 words of high speed memory available, ample space remains for program logic and auxiliary work space.

3. Event arrays

There are, no doubt, many possible techniques for the reduction of full range brightness topographies to a desired class of black/white patterns. In the case of clouds, the techniques employed -- whether utilizing tests for brightness gradients, pattern amplitude variability, absolute brightness, or whatever -- should depend upon the attributes which best define the class of cloud patterns which are to be isolated for comparison.

In the present study, regions with stratoform high cloud clusters were selected beforehand in order to delimit the scope of this first effort. The area selected is shown in Fig. 2. The test subregion is displayed for both the first and second pictures using a modified full range table (see Whitney et al, 1967). And the simplest thresholding logic is used to compress the data stream as it enters the computer memory. After examining line brightness profiles graphically, the discriminant brightness parameter was set to define an "event" as any brightness value of 100 or greater (where zero is darkest and 255 is brightest). The resultant equivalent binary arrays are shown in Fig. 3.

The arbitrary image class selection is recognized as a restriction. The generalizing of this logic sector would, ideally, permit the program to decide which attributes to employ in the subsequent binary event definition. Since the data stream enters serially, large 8-bit sample arrays would be needed for such generalized logic. At present there is also question of

the precise description of the separate cloud classes.

Some flexibility has been built into the present program in an effort to produce meaningful inputs to the following portions of the study. The brightness discriminant is a program card parameter and the logic portion is easily alterable to provide a brightness slice or other attribute of each sample as the criterion of an "event". The (FORTRAN) program is otherwise flexible, for example, in terms of row and sample indexing. A semi - hand option is available for the elimination of unwanted "events" in the binary array. In this way, clutter can be removed, and the absence of more sophisticated event classification logic does not compromise the testing of the following program logic segments. An inverse of this logic is also available for the arbitrary "plating in" of unwanted pattern voids.

4. Erosion

Since simple Boolean match tests are to be employed in the subsequent displacement logic, it is important that the event arrays be reduced to the most elementary and singular features. In that the approach involves arbitrary bounded image sectors which are matched in the displacement logic, there is need to establish a standard sector size. An arbitrary 60x60 element choice has been made -- partly because this sector is comparable to an NWP (Numerical Weather Prediction) grid square and because of manipulating convenience in the 60-bit word length computer.

The erosion process consists of repeated scans of the matrix to remove the first only of each set of consecutive bits in horizontal or vertical alignment. One pass is made successively along each row in a forward direction (ascending locations), then along each row in a backward direction, then down each column in a forward direction and finally, up each column in a backward direction. The whole cycle is repeated until no bits are removed during a sequence of passes. The reverse direction passes are performed logically only; the actual erosion of bits is performed during the forward pass, since the combined effects are to remove the first and last bits of a string of bits, and both these results can be performed during the forward sweep. The bits (brightness events) which remain from this erosion process have no adjacent neighbors laterally or vertically, and may be considered the "cores" of a mass of brightness.

For each pass, a count is accumulated of the number of bits removed from each column or row during the pass; when the count becomes zero that column or row is omitted on subsequent passes. Two counts are also accumulated of the number of non-zero columns and rows, and when one of these is zero that portion of the cycle is omitted. The process ends when both counts are zero. Total counts are also accumulated by 60x60 sample squares.

Provision has been made in the program for optional visual inspection of sections of the original events matrix and of the final eroded matrix. An event is represented on the printed output by an asterisk. The initial and final lines and the initial and

final spots of the picture that are desired to be printed are read from a card. More than one area may be printed; the program reads cards and performs the indicated printout until a blank card in encountered. The size of the printed rectangles are limited only by the dimensions of the original matrix. But if the width is greater than 130 spots the printout will consist of several sections of a maximum of 130 spots each.

A computer printout of an event array -- both before and after the erosion process -- is shown in Fig. 4. An alternate version used the "plating" option to fill certain voids before the erosion process. This is indicated in Fig. 5.

5. Displacement

In displacement matching, a 60x60 array sector is selected from the first image. This table of sixty (60-bit) words is set aside for comparison with a similar set from the second image. Once the displacement guess has been decided upon, a similar sixty word table can be made of standard second picture sets. The first picture table and the derived second picture table are next multiplied logically with a Boolean AND operation. The match is then expressed as the percent of "hits" -- the number of mated "events" divided by the total population of "events" in the first image sector.

Operationally, the displacement guess should be automatic and several approaches may be considered. For the beginning sector, one might use some "climatological" guess or derive the answer through a spiral search starting with a zero displacement

guess. Once an answer has been obtained for the beginning sector, it might then serve as a first guess for adjacent neighbor sectors. An approach of this type could doubtless be devised to minimize the number of match-and-test operations.

The present interest is directed more at the question of the validity of the preceding manipulative steps and their adequacy in providing inputs suitable for the matching operation. For that reason the diagnostic matching program has been constructed to scan through a specified realm of the second image and evaluate the matching percentage for all possible row and column displacements of the first picture image sector. The resulting match topographies provide interesting diagnostic information. Two localized areas illustrate this approach. Fig. 6 indicates the eroded fields for the first and second pictures. Two selected 60x60 test sectors are marked on the eroded patterns -- their starting locations on the first picture and their equivalent deduced locations on the second picture. A larger realm is also indicated on the second picture within which the search was made for the displaced upper 60x60 sector. Fig. 7 is a closeup view of the mated fields for this upper 60x60 sector. The indicated sector boundary on the second picture is one which would likely be made after subjective inspection. However the selection is made automatically on the basis of the match percentage field shown in Fig. 8. The match topography has been smoothed by grouping the percentages; blank is 0 - 5%, dot 5 - 10%,

asterisk 10 - 20%, and W is 20 - 100%. There appears to be some tendency toward secondary match peaks, perhaps resulting from an alias effect as cyclic features become partially aligned. However, the optimum match position appears to have been selected properly by computer logic. (Perhaps some added spatial smoothing of the match field would be needed to minimize the chance of wrong selection.) A close view of the mated regions for the lower 60x60 array is shown in Fig. 9. Again, this selection was based on the match percentage field shown in Fig. 10. For this sector the clustering is not as well marked as that shown in Fig. 8 for the upper 60x60 sector. This appears to result from the somewhat oversimplified erode logic which does not recognize diagonal neighbors as "contiguous". Since the eroded fields thereby contain diagonal strings of events, partially overlapped arrays thus aligned will tend to yield higher match percentages. With all of the simplifications and crudities of the present diagnostic effort, these tentative indications are very encouraging. Nine sector displacements were tried in the initial test. Automatically selected displacements were judged correct in five cases. Three sectors were displaced beyond the match boundary (by almost two thirds of their area) and are thereby disqualified. One sector case was in error where the larger maximum in a double node match profile was the incorrect choice. A guess from a known neighbor sector displacement would have corrected this case. Ideas

at hand for the improvement and embellishment of the program logic segments described in the preceding sections would seem to offer good prospects for the programming of a procedure which could automatically and reliably select the optimum displacement.

6. Growth

Fig. 11 presents the count of eroded elements as described in section 4 above for a six by five group of (60x60) sectors from both the first and second pictures. If one now delineates the mated 60x60 arrays from Figs. 7 and 9 above on these two fields, the individual growth factor for the two clusters might be obtained by subtraction. A topographic hand analysis was tried for the two erosion fields in order to attempt such substraction graphically. Since the gradients were effectively discontinuous in some sectors, this attempt seemed futile. However insight is gained toward the remaining programming step required to automatically obtain such growth information. The extreme nonliniarity in the eroded count fields suggests that there will be difficulty in interpolating a representative count for the deduced terminal position of the 60x60 array on the second picture even using automated higher order interpolation techniques. The eroded counts, at least for the second image, will likely be required in finer subsectors. And, of course, the growth information will only have meaning in terms of the relative success of the displacement logic.

7. Discussion

The sample indications presented above can in no way be regarded as meaningful results. They serve only as indications, and, within the freedoms permitted in this first diagnostic effort, these indications are encouraging. Ample experimentation with added case samples using this program (with variations) are expected to produce substantial additional insight toward the development of an operational version. Meanwhile some added discussion is in order as a means of highlighting problems alluded to earlier. Added discussion may also provide a better assessment of the capabilities of the eventual operational system.

First the need for calibration of the raw response and the companion need to correct for illumination variations cannot be overemphasized. The difficulty in making the latter correction in strong sunblint regions will likely restrict application. Certainly the "growth" information will depend strongly on such calibration. Also the earlier mentioned need for accurate mapping should be stressed. In trying to determine the optimum time space between frames, these items interact. If, for example, a twenty minute time difference was required in order to utilize some short lived cloud pattern feature as a tracer, then a net 5 nautical mile mapping error would, of course, be reflected as a 15 knot speed error. It is expected that features resolvable with presently used sample (spacial) resolutions would be longer

lived so that an hour or larger time span would be desirable. This would improve the skill in speed evaluations and would likely render "growth" information more meaningful. Even so, there may well be some 5 or 10 knot uncertainty in derived speeds. More tests with the present diagnostic program can help in determining the best time span by noting differences in the match topographies, even though the displacements are only relative.

In the "event" classification portion there is much to be done. An ultimate system would read in and hold in memory a sufficiently large array of full (8-bit) range imagery so that its general cloud category could be established. The suitable software algorithm would then be brought to bear using all pertinent attributes of the scene - brightness, element size, brightness gradients, variability of cloud brightness (disjunction), organization of elements (streakiness) etc. - and thereby determine the binary "event" field. Some work of this type is planned since there is an ample supply of ideas in the pattern recognition literature which might apply. A minimum sized working buffer of over 10,000 60-bit words would be required for this input test cycle along with efficient routines which would yield test results with reasonable running speeds.

Efforts of this sort appear worthwhile even if the most general solution is not attained. So long as "indeterminant" regions are rejected without confusion, any substantial remainder of categories yielding meaningful outputs would seem well worthwhile.

And if certain required program array operators proved too impractical with the available computer facility, some different hardware (perhaps a hybrid) arrangement may be suggested.

As mentioned, the erosion logic could be improved. Plans call for the insertion of diagonal scans. This should not greatly increase the computation time since elements should be eroded at about the same rate whether there are two or four scan directions. Machine language bit manipulating routines are expected to reduce the erosion time for the two 1200 x 1500 element arrays to a total of about 15 minutes from the present 35-40 minute span.

In the displacement logic the match criterion is more meaningful if the sectors to be tested are approximately balanced in terms of total event populations. Using the number of eroded events as an indicator, sectors with counts below 50 are not tested. Present tests also exclude matching attempts where one population of eroded samples differs from the other by a factor of 1.5 or more. Displacements over differing backgrounds could greatly complicate such logic. There is also the dilemma of compound motions. Where event classification cannot separate the cloud classes - and this may be very difficult in cases where a lower cloud regime moving in one direction is partially visible through the upper regime which has a different motion - the fields may have to be omitted from further treatment. In instances where the two fields do not yield some interacting "group velocity" vector, a bimodal match pattern may be produced

yielding solutions for both vectors. Experiments with arrays of this type will be attempted.

As mentioned, the present growth treatment does not appear adequate. For satisfactory interpolation of erosion count for the mated sector area of the second picture, there will likely be need for saved erosion data on a fine mesh - perhaps 10 x 10 or 6 x 6 subsectors. Ideally each event might be represented by a 2-bit byte. History of the uneroded field could thereby be carred along and the erosion count re-evaluated as the new sector boundaries became known. This, unfortunately, doubles memory requirements. Practical solutions appear likely.

A final comment should be made concerning defects in the approach, generally. The selection of arbitrary 60 x 60 element arrays implies that the imagery for all classes of cloud regimes will always be adequately represented by boxes of such scale. And the assumption is made that boundaries that cut sizable cloud clusters will not overly compromise the system. Also there is an assumption that the sectors move without rotation, shear or deformation. Such crudities seem justified in a first attempt - particularly if a goal is the simulation of wind measurements which are to apply as inputs for a macro-mesh NWP analysis. There are, of course, more complex approaches wherein the sector boundary is established by the scale of the cloud feature to be tracked. And the match logic could be extended to permit deformation, shear and rotation. Once the present programs have been exercised to gain all possible insight, various generalizations will be considered.

8. Conclusion

A seemingly tractable beginning has been made toward an operational system whereby digitized image pairs can be used to automatically generate cloud displacement information. At this stage, however, the evidence is only in the form of encouraging indications. Additional tests using other input patterns should provide more substantial evidence. Various secondary alterations to the existing program system can further enhance the indications. Other amendments can likely improve its running efficiency for such tests without mounting a major effort toward a streamlined operational version.

This programming needs guidance and support from other efforts directed at the relationship between cloud motion and wind. Ideally, inputs to this program would define clouds in terms of computerizable descriptors which would categorize them in terms of the relationship of their motion to winds and not necessarily in terms of the classic categories.

Finally, this effort should help define future hardware needs. Greatly enlarged and faster computers with bit/byte addresability and Boolean neighbor communication characteristics appear to be required. With more sophisticated "event" definition, a large scratchpad buffer or hybrid (analog) array filter may be indicated.

Acknowledgment: Advice and counsel provided by L. F. Hubert involving the use of stereo viewing equipment is appreciated. Encouraging support for some of the speculations expressed above has been provided through discussions with Dr. John Leese, IBM, concerning a somewhat parallel company - sponsored preliminary

(but more formal) investigation.

REFERENCES

1. Whitney, M. B. Jr., R. C. Doolittle and B. G. Goddard, 1967, Processing and Display Experiments Using Digitized ATS1 Spin Scan Camera Data, ATS1 Volume, University of Wisconsin.
2. Fujita, T., 1967, ATS1 Volume, University of Wisconsin.
3. Hubert, L. F. and E. Ramey, 1967, Analysis of ATS1 Pictures by Photogrammetric Techniques, ATS1 Volume, University of Wisconsin.
4. Ruddle, F., M. Legator, and R. S. Ledley, 1967, Computer Analysis of Overlapping Chromosomes and Automatic Determination of Mitotic Index, Proceedings - Symposium on Photointerpretation, Thompson Book Co., Washington, D. C.
5. White, H., 1967, Digital Automatic Pattern Recognition in Bubble Chamber Pictures, Proceedings - Symposium on Photointerpretation, Thompson Book Co., Washington, D. C.
6. Moore, G. A., 1966, Application of Computers to Quantitative Analysis of Microstructures, National Bureau of Standards Report No. 9428.

LEGENDS

Figure 1. Cathode ray film display of digitized ATS1 picture recorded on June 26, 1967, starting at 2152Z. This is the first image involved in the picture pair tests. The corresponding second picture recording began at 2240Z.

Figure 2. Features in this test area have been sharpened in terms of spacial resolution by using overlapping samples and extra (interpolated) scan lines. The same raw count-to-display grey shade table as Fig. 1 was used.

Figure 3. The augmented array of Fig. 2 is employed in these equivalent threshold sliced patterns. The computer program employs a non-overlapping subset for pattern manipulation.

Figure 4. Computer printout of portion of the array from the first picture shown in Fig. 3; after the event logic has been applied (left) and after the erosion process (right).

Figure 5. The same patterns shown in Fig. 4 but with certain void regions filled before the erosion process.

Figure 6. The eroded field of Fig. 5 is repeated (left) along with the equivalent eroded pattern from the second picture. Two selected 60x60 sectors selected on the first picture are outlined (left) together with their computer deduced new positions on the second picture (right). The dashed corner indicates area searched in displacing the upper sector (I).

Figure 7. This is a closeup repeat of the upper (I) array sectors marked on Fig. 6.

Figure 8. Percentage of 60x60 sector I points which were "hits" for all test displacements. The percentage key is provided in the text.

Figure 9. A closeup repeat of the matched sectors for the lower sectors (II).

Figure 10. Match topography (as in Fig. 8) for sector II.

Figure 11. The number of eroded elements are indicated for each of 30 picture sectors in the case of the first (upper) and second pictures. The discussed sectors I and II are indicated on both arrays.

Fig. 1

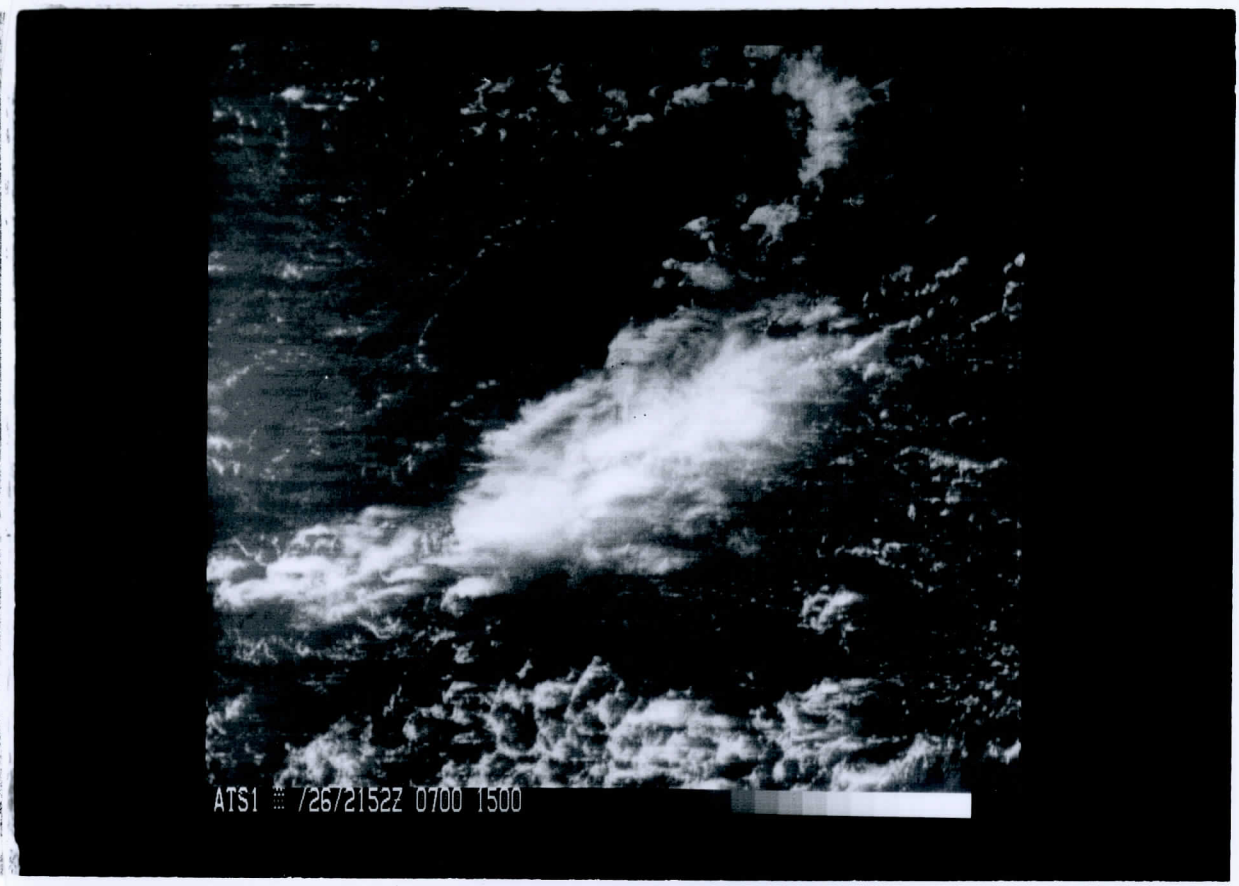

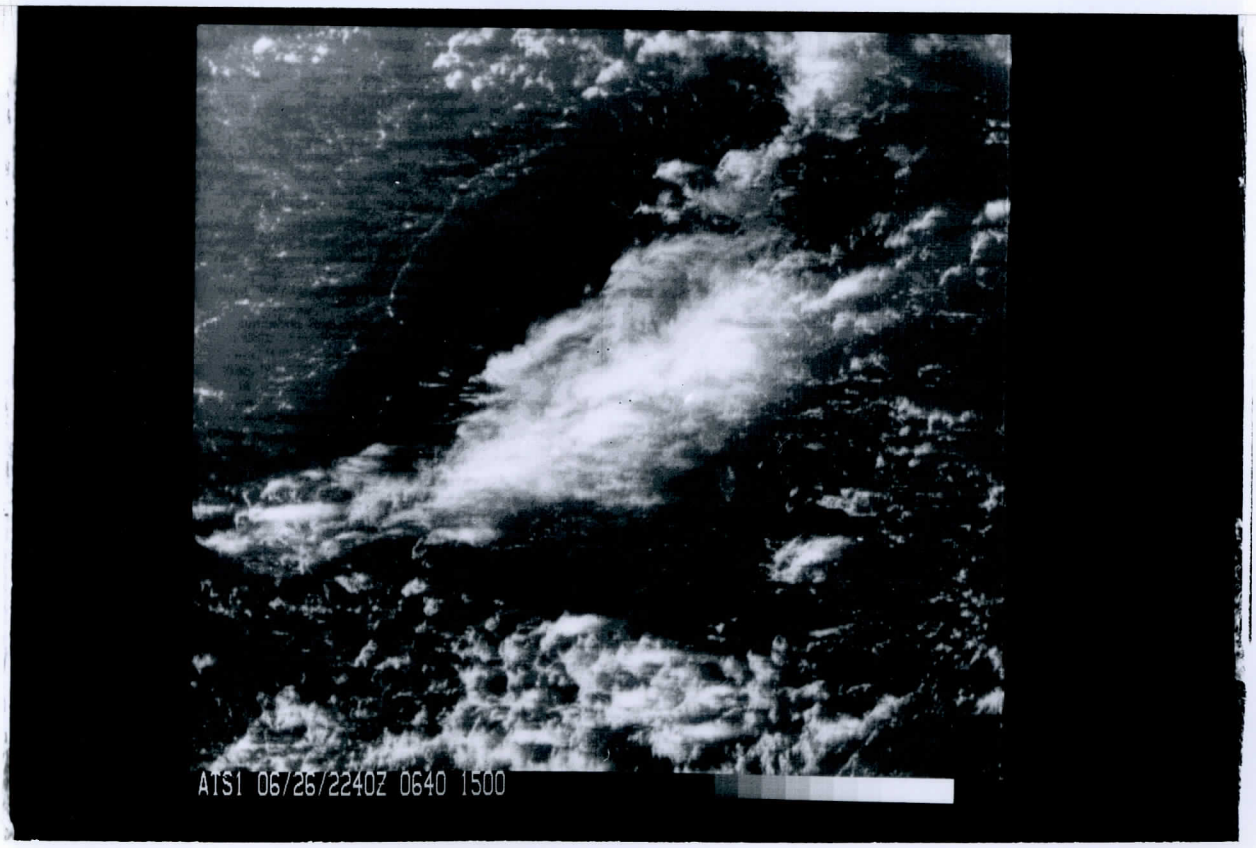

FIG. 2

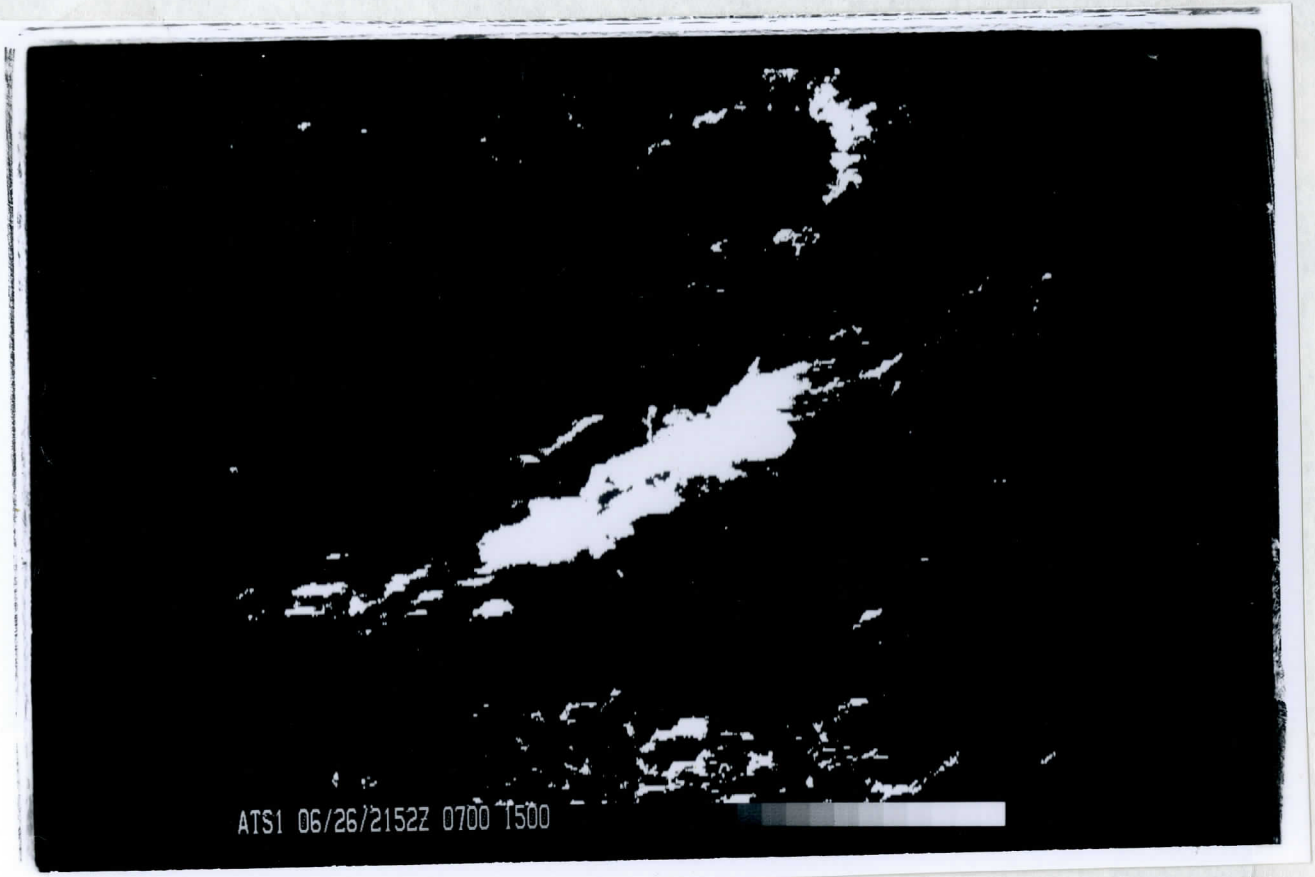

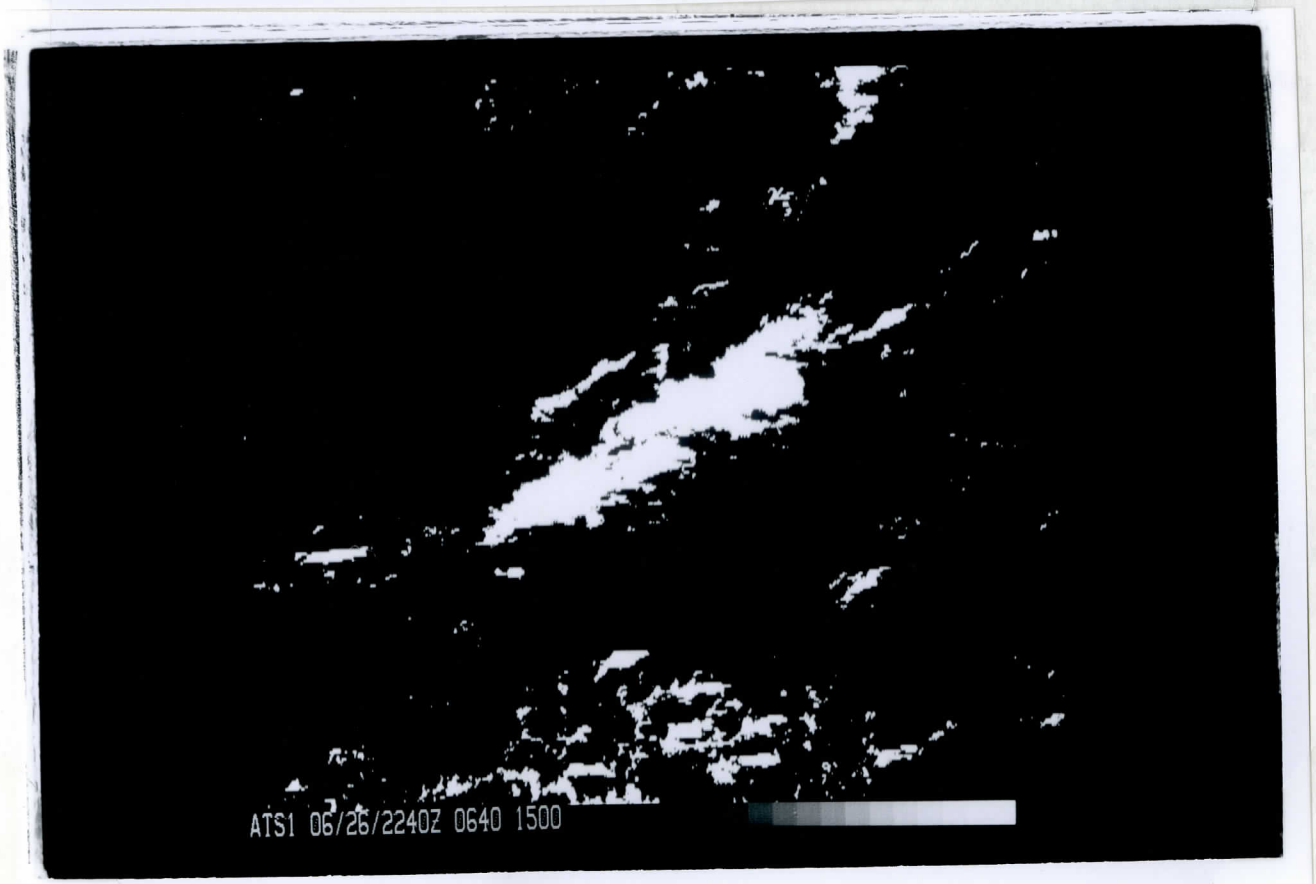

FIG. 3

FIG. 4

FIG. 5

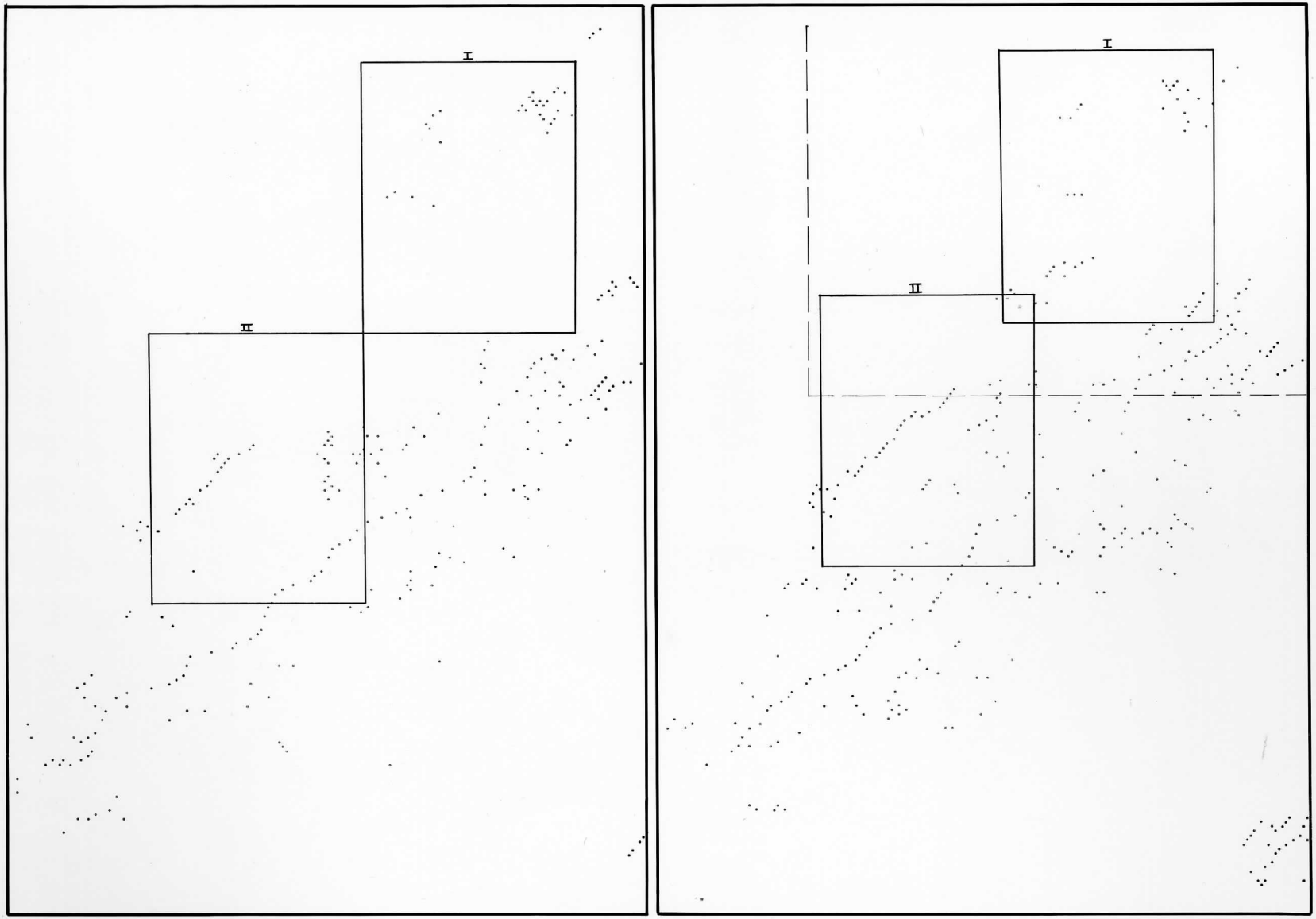

FIG. 6

FIG. 7

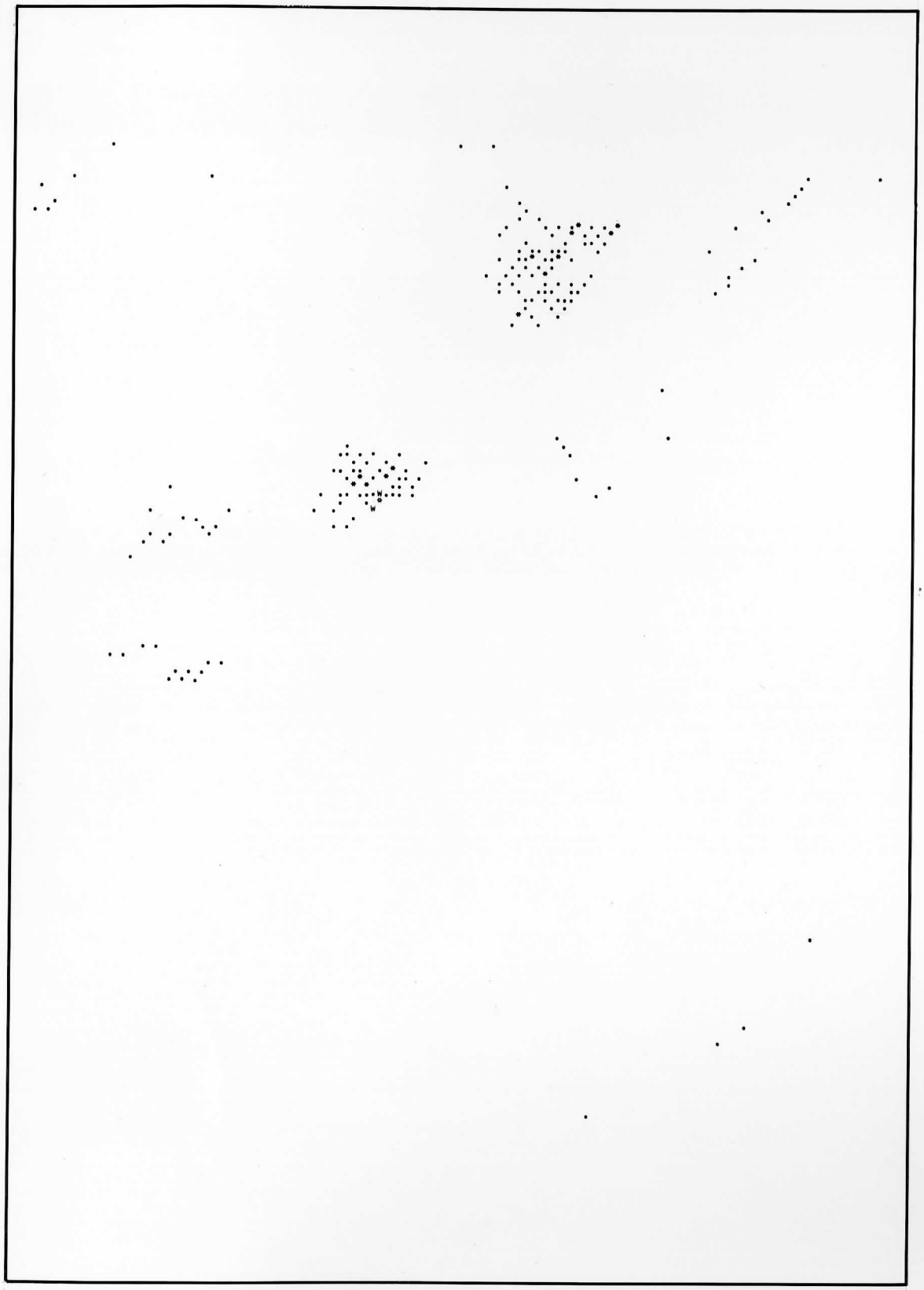

FIG. 8

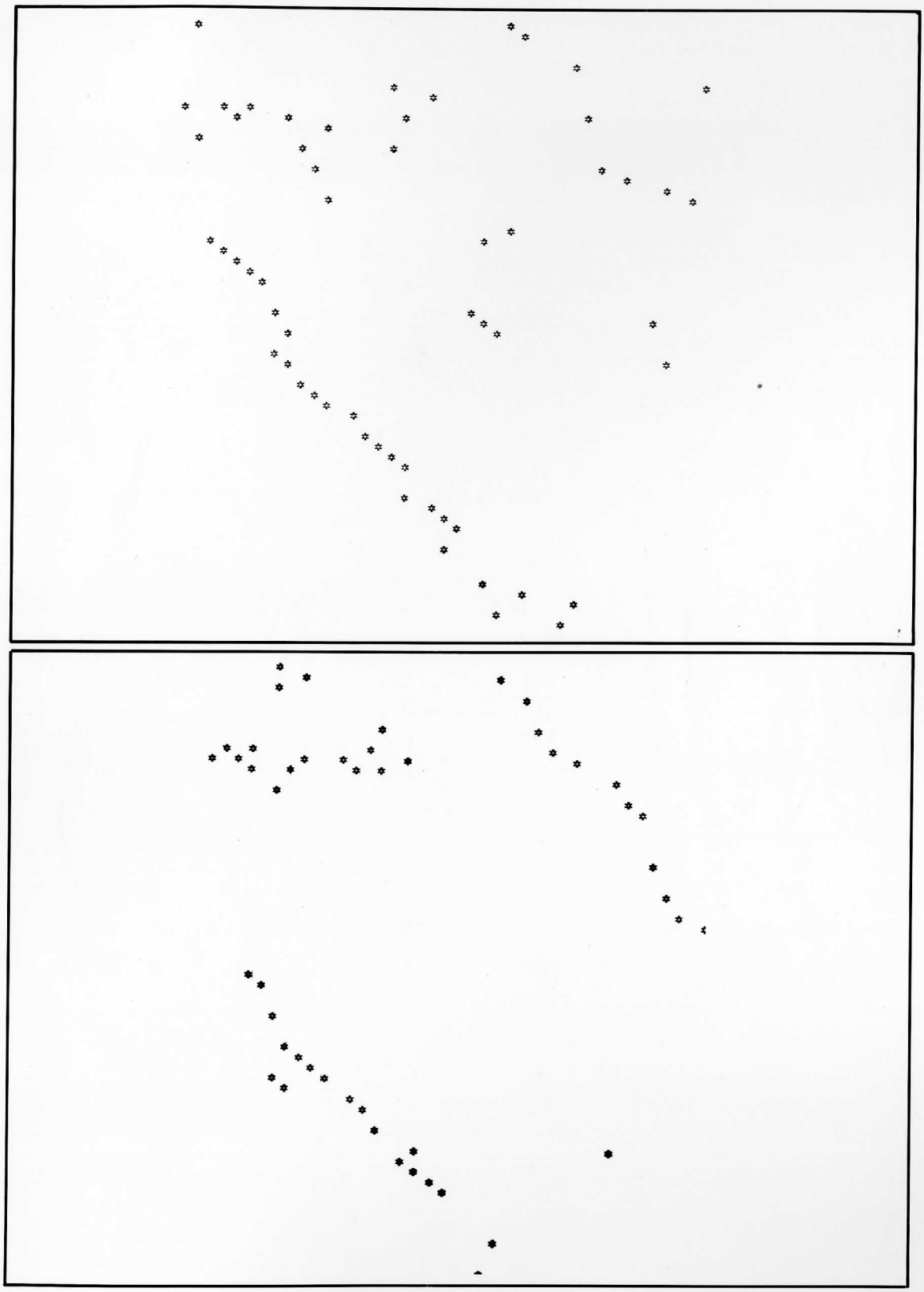

FIG. 9

FIG. 10

5	2	9	77	424	0
0	0	0	(I) 50	12	33
0	7	(II) 785	1667	72	0
167	545	1156	11	24	0
5	4	133	223	66 FIRST	121 PICTURE

5	8	7	71 (I)	303	0
0	0	27 (II)	424	154	49
0	65	1657	1353	11	2
120	302	296	0	87	5
27	88	458	489	94 SECOND	357 PICTURE

FIG. 11

ANALYSIS OF ATS-1 PICTURES BY PHOTOGRAMMETRIC TECHNIQUES

by

Lester F. Hubert
National Environmental Satellite Center

and

Everett Ramey
Coast and Geodetic Survey

Washington, D. C.

~~September 1967~~

FINAL Version:
Revised per Reviewers
suggestions:
5/16/68 L.H.

Copy #1

CONTENTS

1. Introduction

2. ATS-1 Data

3. The Registration Problem

4. Stereographic Analysis on the B-8 Aviograph
   a. Results of B-8 Analysis

5. Stereographic Analysis on the STK-1 Comparator
   a. Mathematical Stereo Model for the STK-1
   b. Results of STK-1 Measurements

6. Potential of Photogrammetric Techniques for ATS-1 Data

7. Sources of Error

8. Variable Dimension Changes of Film in the Photographic Generations Subsequent to Production of the Original Negatives

9. Summary

10. Acknowledgements

APPENDIX

ANALYSIS OF ATS-1 PICTURES BY PHOTOGRAMMETRIC TECHNIQUES

1. Introduction

When ATS-1 pictures taken at intervals of 23-minutes or more are viewed with an ordinary desk stereo viewer, a three-dimensional effect is produced; the various cloud layers appear to lie at different heights above the earth's surface. This is not caused by a real height variation of the cloud layers, rather it is a false stereo effect caused by the motion of a layer of clouds relative to the earth or relative to another cloud layer.

The satellite is fixed relative to the earth, there is but a single camera position so no stereo base and no true stereo exists. No information concerning cloud heights can be derived directly from the geometry of the picture.

The fact that large stereo effects do appear in the pair, such as those shown on Fig. 1, is evidence of two important characteristics of these pictures. Of greatest significance is the fact that the overall cloud patterns change so little in 46-minutes (the time interval between the "stereo" pair of Fig. 1) that each eye viewing separate pictures sees the same scene. If this were not so, the viewer would experience discomfort because he could not fuse the two images into a single view. The second characteristic is that the geometric shapes of various parts of a given cloud layer maintain nearly the same relationship on each picture. If this were not true, extensive layers of clouds would not appear at a uniform "height." In some regions the zonal cloud speed has a large meridional variation and this is clearly seen in Fig. 1 where stereographic viewing reveals a strong north-south slope of the "highest" clouds, mainly of those bands near the jet stream in the northwest and southwest quadrants of the photographs.

These characteristics suggest that transforming the apparent parallax (that which produces the three-dimensional effect) to lateral cloud displacement could produce accurate measurements of cloud motion ~~during the period involved~~ between pictures.

The human eye (coupled to the high capacity analogue computer to which it supplies data) is a marvelously flexible integrator and adjustor of patterns. Thus, minor distortions of scale and shape that produce discrepancies between stereo pairs such as Fig. 1, are suppressed for the "eye" interpretation. This is the opposite of the situation in the preceding article. This is not the case, however, when a multitude of points in the pattern are reduced to digital location coordinates; discrepancies in quantitative data are not easily neglected. For that reason the stereo effect so clearly visible in Fig. 1 becomes an intricate quantitative problem.

This paper describes the photogrammetric analyses applied to these data, the equipment used, and the mathematical stereo models employed.

2. ATS-1 Data

The geometric character of the photographic images depends critically upon the orientation of the satellite and upon an intricate ground system for generating synchronization pulses that are reference points for the television line-scan pictures. Each scan line on the receiving T.V. tube must begin along a line that remains precisely fixed relative to the earth's image. If each scan were not laid down in the correct relationship to the preceding line, the image of the earth would be distorted. The synchronization pulse to accomplish this is computed on basis of the sun's position sensed at each rotation of the satellite. Since the angular relationship between the satellite, the earth, and the sun changes during each picture-taking interval, this synchronization pulse must be

computed for each scan line. Any error introduced in this computation appears as the distortion of the image which, as will be shown later, affects the photogrammetric evaluation. For example, if each successive scan line (scanning from west to east across the earth) were laid down with a few microseconds lag relative to the preceding line, the earth's image would be sheared toward the southeast as illustrated in Fig. 2a.

The system is designed to operate with the spin axis of the satellite parallel to the earth's axis. In general these axes are out of parallel by about one degree and this also affects the photogrammetric analysis. Figure 2b illustrates schematically the motion of the picture format relative to the earth which is produced by non-parallel axes. While this does not seriously distort the picture it must be taken into account for the following reasons.

The basic requirement in deriving parallax is that the two images be precisely in register throughout the whole field of view. That is, they must exactly match in scale, aspect ratio (ratio of length to width) and orientation. If the pictures were not exactly at the same scale or if the north-south line of one picture were rotated slightly relative to the north-south line of its neighbor, erroneous parallax (displacement) would be introduced. This is critical here because the diameter of the earth's disc is about 12,000 km while the cloud displacements in an hour are generally less than 100 km and cloud motions as small as 10 km should be detectable. Registration or scale errors as small as 1/1000 therefore introduce noticeable errors.

3. The Registration Problem

Most of the ATS-1 pictures are sheared to some degree (Fig. 2a) and distorted by other minor aberrations. These various non-linear distortions change from picture to picture. For that reason the registration (matching) of a picture pair preliminary to making parallax (displacement) measurements is the crux of this photogrammetric approach. The work reported here is directed toward developing a technique for the accurate registration of ATS picture pairs. Once this has been accomplished and a large number of cloud features identified at two different times, their positions relative to the earth can be determined.

The ATS satellite, being located at approximately 150°W, has few landmarks in its field of view. Figure 3 shows that the area encompassed by the image is mostly ocean. Australia is so near the edge of the field that no specific landmarks are adequately resolved in the picture. New Zealand and the smaller islands do not contrast sufficiently with the ocean backgrounds to be visible and even the Hawaiian Islands, not too distant from the picture center, are not always visible. Only the west coast of North America is regularly seen so only lower California and parts of the Mexican coast, contrasting highly with the ocean background, are dependable landmarks.

Visible ground control points are therefore too few to permit picture resection by standard photogrammetric methods. For that reason scale distortion, picture shear, and other non-linear distortions must be determined from the position and shape of the horizon, and the top and bottom borders of the picture.

4. Stereographic Analysis on the B-8 Aviograph

Quantitative parallax (motion) measurements can be made by use of a large variety of equipment, ranging from the simple parallax bar to the sophisticated equipment that utilizes electronic computers for the analysis. Due to the fact that the ATS-1 photos as received from the ground equipment are distorted, application of the simple parallax bar is not adequate. For that reason the first pair of ATS pictures were analyzed by use of a stereo device known as the Wild Aviograph B-8.

The picture pair were printed on glass plates. These diapositives when mounted on the B-8, could be adjusted in scale, aspect ratio, etc. by changing the projection focal length, by tilting, by translation, and by rotation of the image planes.

Optical corrections through this projection system were applied until the horizons as well as cloud features near the limbs of the earth of both pictures were closely matched. East-west displacement of cloud masses at the extreme eastern and western horizons along the equator produce negligible displacement on the image plane because of foreshortening due to the earth's curvature. An attempt was made to use clouds at the northern and southern borders of the image for the north-south control, but they were less satisfactory because the picture format cuts off the polar cap so cloud features at the horizon are not photographed. In addition to the horizon and cloud control points, the Mexican coast, and the center of the cloud ring surrounding the large island of Hawaii, were also used as ground control points.

Once the best register between pictures was accomplished by making a subjective best fit of horizons and control points, the operator identified a series of individual cloud features on the picture pair on which to set the "floating index point." When this dot lay at the apparent elevation of

the cloud feature, a parallax figure was read and written at the corresponding point on an enlarged duplicate of the photograph. By use of the projection geometry of the B-8 equipment and the projection geometry from earth to image plane, this parallax figure in the image plane could be related to the displacement distance of the cloud feature relative to the earth.

In this equipment as in the ordinary stereo viewing equipment, the only visible parallax is parallel to the line between the eyes of the viewer. That is, if the images are viewed such that the line between the viewers eyes were east-west on the image pair then only east-west parallax will be visible. In order to measure north-south parallax the image pair must each be rotated 90°. After measuring a number of east-west cloud displacements on the B-8 equipment each of the diapositive plates was rotated 90° and the various trial and error optical corrections were repeated to attain register for measuring the north-south displacements. The output from this procedure was a graphic display from which "height" measurements were converted to cloud movements.

a. Results of B-8 Analysis. The analysis of the displacements obtained by use of this stereo equipment showed that the register was inadequate to permit satisfactory measurements of cloud motions. This was revealed by apparent displacement of the geographical features that could be identified as well as unreasonable unrealistic values of cloud displacements.

Apparently the north-south scale adjustment and control points were inadequate. For example, some clouds that appeared to have a southward displacement were proved, by independent data, actually to have a northward motion, indicating that the photographs were not properly registered relative to the y-axis.

Further analysis revealed that this north-south error was not constant over the whole field and therefore was not amenable to a simple constant correction.

~~The conclusion suggested by~~ The above, as well as other details of the analysis, suggested that adjustment of scale and the tilting of the image plane in the projection were inadequate to achieve proper registration. The use of the B-8 equipment was therefore abandoned in favor of the Wild STK-1 Stereo-comparator wherein photographic coordinates are digitized and manipulated mathematically.

5. Stereographic Analysis on the STK-1 Comparator

The STK-1 is mechanically much simpler than the B-8 because it provides for no adjustment of the image planes. The basic operating principle involves viewing a diapositive pair and placing the floating index dot on the point of photograph number 1, translating photograph number 2 until the index lies on that same image point, then pushing a button to record on punch card the x-y coordinates of photograph 1 and the parallax of photograph 2. These measurements are made at many points around the horizon as well as at all control and cloud points. All of the coordinates thus determined are then fit to the appropriate mathematical model.

The flexibility of analytic manipulation permits linear or non-linear scale changes, allows for picture axes to be rotated independently and enables the horizon curve to be fit to a theoretical curve, for there are no optical projection restraints. A further advantage is that the parallaxes in both the x and y axes are measured without changing position of the diapositives. This eliminates the 90° rotation

and re-register problems and the need to make a second identification of the cloud element measured earlier.

a. Mathematical Stereo Model for the STK-1. The data of the measurement program with the STK-1 Stereo-comparator are x and y coordinates for points of photograph 1 and x and y parallaxes for the corresponding points of photograph 2, measured in the plane of the photographs. These raw data (for both control points and cloud element points) are measured relative to coordinate axes that are arbitrary and different for each photograph. The mathematical model applied by a digital computer performs the following:

1. Makes a first gross adjustment of parallaxes of photo 2 into coordinates of photo 1 in the following steps:
   a. Translates the origin of photo 2 coordinate system to coincide with the origin of photo 1 coordinates.
   b. Determines a mean linear equation for the scan line direction ($y = ax + b$) for each photograph relative to its coordinate system, (using several data points read along the bottom, truncated part, of each picture) and rotates the coordinate system of photo 2 so that the scan lines of the picture pair are parallel.
2. Initializes the error equation program by establishing "first guess" values for five parameters as follows:
   α, the x-coordinate of picture center, computed by bisecting the east-west dimension of the earth's image.
   β, the y-coordinate of picture center, was loaded in the program from a previous analysis of these photographs. A simple change to the program can provide an equation to compute β from the length of the bottom (or top) truncated picture border.

R, the radius, is taken as half the east-west dimension of the earth's image, approximately through the image center.

D, the shear coefficient, is set equal to zero.

S, the coefficient to correct y-axis compression, is set equal to 1.02.

3. Solves by iteration for each photograph a differential error equation (see Appendix) that achieves a least square fit of 20 to 70 horizon points to a circle*. The iteration minimizes residual erros by:

   a. Translation of "first guess" picture center to the center of the best-fit circle.

   b. Scale adjustment which is different along the x and y axes and different for each photograph.

   c. Derivation of an east-west, linear shear (the distortion illustrated in Fig. 2a).

4. Performs the final transformation of the scale of photo 2 to the scale of photo 1 by use of the ratio R_1/R_2 (radii of the best fit circles of photo 1 and photo 2, respectively).

5. Determines the angle through which photo 2 must be rotated (about the best fit circle center) to coincide with the rotation position of photo 1 by fitting the visible geographical features.

At this fifth step all of the final parameters have been derived that are used in transforming cloud element data of the photographs to a common coordinate system.

---

* Projection of the earth's image on the undistorted image plane is not precisely a circle but the deviation is less than 0.2% of the radius and was neglected at this stage.

6. Transform all cloud and control data to the common coordinate system, by translation, rotation, differential x-y scale adjustments and linear shear, using the final values of the 5 parameters.

7. Compute Δx and Δy (parallaxes) for all control points and cloud element points, relative to the common coordinate system.

When the residuals are sufficiently reduced, the program prints out: (a) point identification, (b) Δx and Δy parallaxes, (c) distortion and translation coefficients, (d) radii of the best fit circles and their mean, (e) residual errors in fit of the horizon points to the best fit circles, (f) miscellaneous analysis data such as number of iterations, sum of error residuals, etc.

b. Results of STK-1 Measurements. The three pictures analyzed were, No. 22 - (Start time) 2124 GMT 18 Feb. 1967, No. 24 - (Start time) 2219 GMT 18 Feb. 1967, and No. 26 - (Start time) 2306 GMT 18 Feb. 1967. The first two are the stereo pair of Fig. 1. The analysis that follows involves only the control points and their manipulation. Many cloud points were also measured in this program and their displacements computed but because cloud displacements include errors as large as the registration errors, there is little point at this stage of the work, in analyzing the cloud motions in relation to the known wind field. Preliminary indications are that the mathematical model has not yet obtained adequate registration of the pictures, so the immediate task is to improve the mathematical treatment of the data.

Non-linear distortions that vary over a single photograph as well as between pictures are also sources of error but it appears that such aberrations can be partly corrected by this technique so that any residual error may be neglected. This is suggested by analysis of the circle fitting.

Figure 4a presents results of the circle fitting and scale adjustment of picture 22; Fig. 4b shows the same data for picture 26. Two mathematical models were applied to the horizon (control) points of both pictures; first the best fit circle was determined without allowing for shear, and second the best fit circle was computed including a shear correction. Plotted near the horizon curves of Figs. 4a and b are points representing the deviation of the horizon point coordinates from the best fit circle. The radial distance of each point from the horizon curve is proportional to the deviation. Thus in Fig. 4a the first point on the northeast horizon lay 20 microns* outside the circle fitted without shear and lay 12 microns inside the circle fitted with shear. The maximum deviation was 80 microns and the RMS of all horizon point residuals, with shear for both pictures, ranged from 25 to 40 microns.

The STK operator made repeatability tests to estimate the accuracy to which he could read the horizon points and he estimated that some 99% of the measurements were repeatable to $\pm$ 20 microns. Since the measurement uncertainty is essentially equal to the RMS of the residual errors, it appears that the mathematical model achieved a satisfactory circle fit. Moreover, comparison of the residual errors with and without shear shows that the circle is better fitted by including the shear

---

* These distances were measured at the scale of the diapositives on which the earth images were about 44,000 microns in radius. At the subpoint, 100 microns at model scale is equivalent to 14 km on the earth.

correction. This correction would produce relatively greater improvement on other photographs that are more severely sheared.

The entire problem of registering stereo pairs is not solved by successful horizon fitting, however. This is illustrated by displacement of the circle centers. The center of the best-fit circle for picture 22 (Fig. 4a) was displaced 15 microns along both the x and y axes when the shear correction was included, and for picture 26 (Fig. 4b) the center was shifted 160 microns (Δ x) and 115 microns (Δ y). The sensitivity of center location to the number and distribution of horizon data was confirmed by computing other best fit circles after withholding selected data points.

The picture center location directly influences cloud motion because all displacements are computed relative to the common coordinate system origin which is the center of the best-fit circle. It is not evident at this stage whether this large shift of the center (produced by inclusion of shear) achieved the best registration of the entire image interior, indeed there are indications that it increased the errors.

A measure of the parallax errors is revealed by the apparent motion of geographical features. Picture-pair 22 and 24 yielded parallaxes shown in Fig. 5a, while Fig. 5b shows parallaxes derived from picture-pair 24 and 26. Points a to d are, respectively, Hawaii, two landmarks on Baja California, and one on New Zealand. In addition to landmarks, two horizon points designated e and f at the extremities of the equator were also used as x-axis check.

The random parallax errors for geographical check points were expected to be larger than they were for horizon points because the STK operator estimated that the repeatability of measurement was much poorer for landmarks. Nevertheless the errors for geographical features comprise a coherent pattern, suggesting that it is not random error due to the data measurement, rather is a systematic error due to lack of proper registration. For example on the pair 22-24, all four geographical points showed an (erroneous) parallax toward the east and toward the south. On pair 24-26 the northern hemisphere points were in error toward the east and north.

Discrepancies in x-parallax at points e and f, Fig. 5, suggest some error also may have been introduced in adjusting the scale of the pairs. For example, the pair 22-24 (Fig. 5a) shows a Δx error radially inward, while in the pair 24-26 (Fig. 5b), the Δx error is radially outward. Neither shear (D) nor scale (S) corrections directly affects the x-parallax on the x-axis, but these errors could have been produced by scale adjustments between the photographs (by application of the factor R_1/R_2). If, for example, the radius of the best fit circle for picture 24 were too large while the radii determined for pictures 22 and 26 were correct, scale adjustment would produce erroneous parallaxes similar to that shown for points e and f on Figs. 5a and b. Further analysis will localize this error source, but it has not been completed at this writing.

In addition to registration error sources already mentioned, the effects of rotation (of photo 1 relative to photo 2) must also be carefully evaluated.

Rotation of the pictures to match the visible geographical features may be a serious flaw because Hawaii and Baja California for the features are located in portions of the image that are

known, from independent data, frequently to have serious non-linear distortions. It is possible, by use of independent data, to compute the rotation necessary to match the north-south meridians of the picture pair, without recourse to landmarks. If this were incorporated into the mathematical model the landmarks could then be used as redundant check points and a possible source of secondary correction data.

6. Potential of Photogrammetric Techniques for ATS-1 Data

This approach appears to be promising despite the difficulties reported here. The analytic treatment of digital data provides many degrees of freedom not easily achieved by other methods. The present advantage of graphical methods, such as time lapse movie analysis reported elsewhere in this volume, is that a skilled movie producer can subjectively weight data during his grid-fitting on the basis of the type of distortion he encounters. In principle there is no reason the same decisions cannot be incorporated into the analytic method. Refinement of the mathematical model must proceed along those lines.

With further development there is hope that the accuracy will be limited mostly by the reliability to which points can be measured. The repeatability test already made indicates this limit may be approximately 5 km. Thus, cloud displacement measurements may include errors of up to 10 km due to this factor (5 km on each photograph of the pair), implying an average vector error of about 7 km.

Is this a tolerable degree of accuracy? The answer is "Yes" if the proper time interval between pictures is used. Experience with ATS-1 photographs indicates that many cloud features remain identifiable for more than one hour, and some can be followed much longer.

For the purpose of illustration, assume that the average vector error (due to all sources) is 10 km and that the time interval between pictures is 69 minutes (three picture intervals on ATS-1). Under those conditions an actual cloud speed of 10 kts would be computed with an uncertainty of $\pm$ 25° in direction and $\pm$ 4.7 kts in speed. A 20 kt wind would be uncertain to $\pm$ 13° and $\pm$ 4.7 kts. These uncertainties would be reduced somewhat when many independent cloud displacements were computed for a given region because the random part of the error could be removed by areal averaging.

Clearly cloud motion information of this accuracy would be highly useful in the vast areas not observed by other means.

7. Sources of Error

The laborious analysis reported here suggest the question, "Is this trip necessary?" That is, cannot the images be delivered to the user without troublesome distortions? It is clear that if no distortions existed, simply fitting the horizons and rotating to match a single landmark would attain the required registration. Such images are attainable because the source of distortions and thereby the source of parallax errors, appears to be chiefly in the ground-based equipment, not in the satellite.

The analog video signal transmitted by the satellite is generated by a mechanical line-by-line stepping of the telescope in the north-south direction between each rotation of the satellite; the satellite rotation generates the scan line in the east-west direction. Satellite-generated sources of geometric distortion therefore can be caused only by irregular stepping, irregular rotation rates or instability of the satellite itself.

Pre-flight tests showed that the stepping was repeatable to within ± 1 step in a total of 2,017 steps (lines). Whether this irregularity produces a random double-line step or a random line-repetition step it would cause a displacement of the image equivalent to 4.8 km at the sub-point, an error no larger than that due to reading point locations on the stereo equipment, and is therefore an insignificant source of error.

The rotation rate of the ATS-1 satellite changes slightly during the 20-minute picture taking cycle in response to changes in the moment of mass. While this can and has produced non-linear distortions, it need not be an error source because concurrent sun pulses are transmitted so that the rotation rate is always known. To the authors' knowledge, analysis of various telemetry has yielded no evidence of a short period nutation or disturbance to the spin axis of the satellite. Transmission from the spin-scan camera system, therefore, contains accurate data together with all of the information required to produce virtually distortion-free images.

Some sources of error introduced by the ground-based equipment are:

1. The circuit logic that computes the timing of the synchronization pulse of the cathode ray tube (the television monitor) from the raw sun data.
2. Computation parameters (input by the operator) relative to longitude of the sub-point, time of day, etc.
3. Deviation of the cathode ray tube beam sweep rate from the camera sweep rate.
4. Non-linear north-south deflection of the beam in the cathode ray tube.
5. Lens distortion in the copy camera optics.
6. Dimensional instability of the copy camera film.

8.7. Variable Dimension Changes of Film in the Photographic Generations Subsequent to Production of the Original Negatives.

Photogrammetric analysis has not provided data to assess the errors of each of these sources but the largest error sources can be identified. Non-linear distortions within the field of view, especially at high and middle northern latitudes, and the shear distortion (figure 2a) are caused by the first two sources listed above.

Although not evaluated, it is suspected that the dimensional instability of the standard polaroid film used in the copy camera introduced some error. Photogrammetric measurements of a rectangular grid reproduced on the cathode ray tube would determine the errors produced by items 3, 4 and 5. However, the analyses are not deemed worth the effort in view of the large errors caused by the first two listed items.

After this work had been completed, improved experimental equipment was developed, reducing the error sources 1 and 2. Development work at Hughes Aircraft Co., Space System Division under N.E.S.C. support, produced equipment used for experimental readout of ATS I. The images produced revealed very good geometric fidelity and great resolution and dynamic range. The analog signal was digitized in that experiment, and reproduced on a mechanical scanner. While no photogrammetric analysis has been performed on these images at this writing, many movie sequences have been made. The high quality of the resulting movies proves that some of the distortions discussed in this paper can be eliminated by improving the ground equipment.

9.8. Summary

Development of this photogrammetric approach is planned but the analysis of three photographs has already provided guidelines for further investigation. Analysis of this small sample of three pictures shows that the present mathe-

matical model must be refined in order to derive useable cloud displacements. The results discussed here suggest the following features may be responsible for the unsatisfactory behavior of the model at this stage:

1. Great sensitivity (of picture center location) to the pattern of distortion in the image horizons. Photographs that show only a portion of the horizon appear to be unduly sensitive to the distortion pattern (e.g., Fig. 4b).
2. The scale of each image, based on the radius of the best fit circle may not be the most representative scale for the entire field of view. For example, due to non-linear distortions, the image distance between two geographical features may reveal a scale different from the image distance from picture center to the horizon.
3. Non-linear distortions within the field of view may be undetected by the measurement program and uncorrected by the mathematical model.

It appears that the first-listed item is the primary error source. If this is corroborated by further analysis, various refinements can be made. For example, the circle fitting may be more stable if less weights are given to the horizon points that contribute the largest residual errors.

Significant registration errors may be due to the present method of scale normalization (use of the ratio R_1/R_2) and due to picture orientation (rotation to match the visible landmarks). The analysis already completed provides guidelines for refinement along these lines.

Highly useful meteorological data can be obtained if the mathematical model can derive cloud displacements with about 10 km average vector error.

New ground equipment which produces much greater geometric fidelity of the images promises to yield more accurate results than were obtained with the material used here.

10. Acknowledgements. The authors acknowledge the unstinting cooperation of Mr. Charles Theurer of the Photogrammetric Division of the Coast and Geodetic Survey who made available the technical assistance and facilities for this work, and the helpful discussions with him and Mr. William D. Harris, Office of Geodesy and Photogrammetry.

Special thanks are extended to Mr. Edward Rolle for his painstaking labor in setting up the stereo models and his hours of careful data collection.

APPENDIX

The program which operates on the horizon point data makes a least square fit to a circle by permitting simultaneous adjustments in (a) x and y scale, (b) radius of the circle, (c) location of circle center, and (d) linear shear parallel to the x-axis.

Following the first "gross adjustment" of photo 2 coordinates (see text: Step 1 in "Mathematical stereo model"), the computer iterates the adjustments until the residuals have been reduced to a specified magnitude and then exits with the following derived parameters for each picture:

$R \equiv$ radius of the best fit circle.

$\alpha, \beta \equiv$ x and y coordinates, respectively, of the circle center.

$S \equiv$ Coefficient to correct y-axis compression.

$D \equiv$ Coefficient to correct linear shear.

These coefficients are used to transform the "gross adjusted" (x_g, y_g) coordinates to the final coordinates as follows:

In order to achieve a best fit circle the y-coordinates of each horizon point (y_g) must be adjusted to a corrected (y_c) value by,

$$y_c = S\, y_g$$

The best fit requires the x-coordinates (x_g) be adjusted to a corrected value (x_c) by,

$$x_c = x_g + Dy_c$$

The basic error equation for computing the circle of best fit is:

$$[(X_i + Y_i \cdot D - \alpha)^2 + (Y \cdot S - \beta)^2]^{1/2} - R = V_i$$

By Taylor's Theorem applied to standard least square procedures, the differential error equation becomes:

$$a_{i,1} \cdot \delta R + a_{i,2} \cdot \delta D + a_{i,3} \cdot \delta\alpha + a_{i,4} \cdot \delta S + a_{i,5} \cdot \delta\beta - L_i = V_i.$$

The coefficients of the observation equation to be used in the least squares matrix are:

$$a_{i,1} = \frac{\partial F}{\partial R} = -1.0$$

$$a_{i,2} = \frac{\partial F}{\partial D} = \frac{X_i + Y_i \cdot D_o - \alpha_o}{R_o} \cdot Y_i$$

$$a_{i,3} = \frac{\partial F}{\partial \alpha} = -\frac{(X_i + Y_i \cdot D_o - \alpha_o)}{R_o}$$

$$a_{i,4} = \frac{\partial F}{\partial S} = (Y_i \cdot S_o - \beta_o) \cdot Y_i/R_o$$

$$a_{i,5} = \frac{\partial F}{\partial \beta} = (Y_i \cdot S_o - \beta_o)/R_o$$

$$L_i = R_i - R_o = [(X_i + Y_i \cdot D_o - \alpha_o)^2 + (Y_i \cdot S_o - \beta_o)^2]^{1/2} - R_o$$

Definition of Symbols

X_i, Y_i ≡ Data points coordinates.

R ≡ Radius of best fit circle.

V_i ≡ Residual which is reduced to a specified value before iteration is stopped.

The subscript "i" indicates value of the variable as its latest, updated value.

The numerical subscript (1 to 5) refers to the column of the observation equation matrix in which the variable is placed.

The subscript "o" denotes the approximate value in each case.

LEGENDS

Figure 1. One of the "stereo" pairs analyzed by the photogrammetric technique, from ATS-1 satellite 18 February 1967. Left photograph started at 2219 GMT; the right photograph started at 2124 GMT. The clouds moving from left to right (eastward) appear to be at a greater elevation than the westward moving clouds. North-south motions produce no stereo effect in this view.

Figure 2a. Schematic of earth's limb as seen on ATS-1 pictures with no distortion (solid line) and with east-west shear (broken line). Shear distortion of this type is produced when each T.V. scan line on the receiving display equipment is started with a small lag relative to its predecessor.

Figure 2b. Motion of the picture format relative to the earth's disc caused by satellite axis being non-parallel to earth's axis. (Motion is schematic and exaggerated for easy illustration).

Figure 3. Total field of view from ATS-1 satellite above 151°W longitude when the spin axis is parallel to the earth's axis.

Figure 4a. Plot of deviation of horizon points (photograph 22) from the best fit circle. Solid line connects deviations of points where circle was fit with no shear correction. Broken line connects points fit with shear correction. Radii through each point intersects the horizon circle where the horizon point was measured. All distances in microns.

Figure 4b. Same as 4a, for photograph 26.

Figure 5a. Parallax (erroneous motion) of geographical features derived from photo-pair 22 and 24. All parallax in microns (component vectors not to scale).

Figure 5b. Same as 5a, for photo-pair 24 and 26.

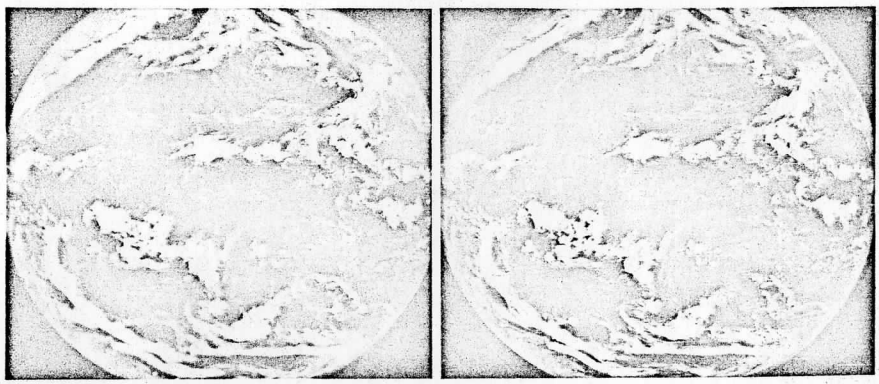

Fig 1
Hubert & Ramey

Fig 2a

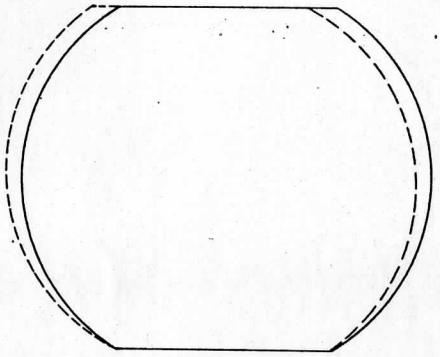

Fig 2a

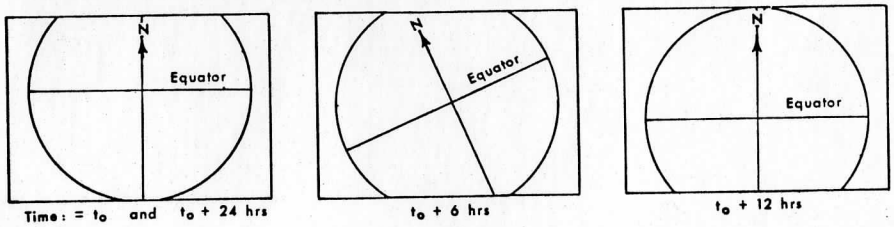

Fig 2b

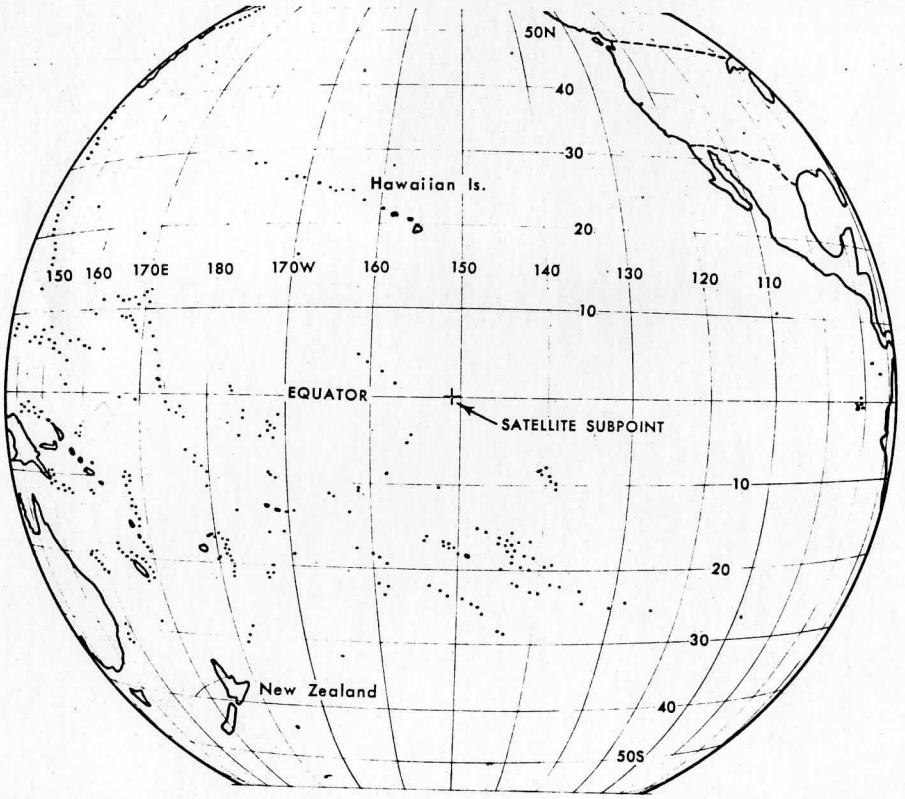
50N
40
30
Hawaiian Is.
20
150 160 170E 180 170W 160 150 140 130 120 110
10
EQUATOR
SATELLITE SUBPOINT
10
20
30
New Zealand
40
50S

Fig 3

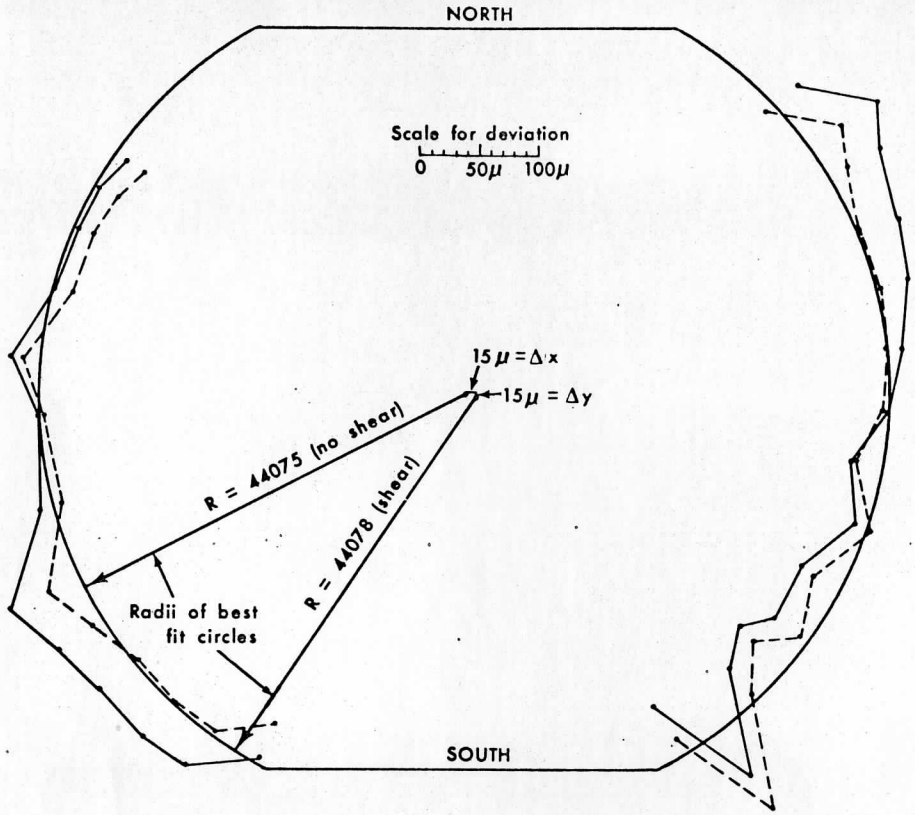
NORTH
Scale for deviation
0 50μ 100μ
15μ = Δx
15μ = Δy
R = 44075 (no shear)
R = 44078 (shear)
Radii of best fit circles
SOUTH

a

Fig 4

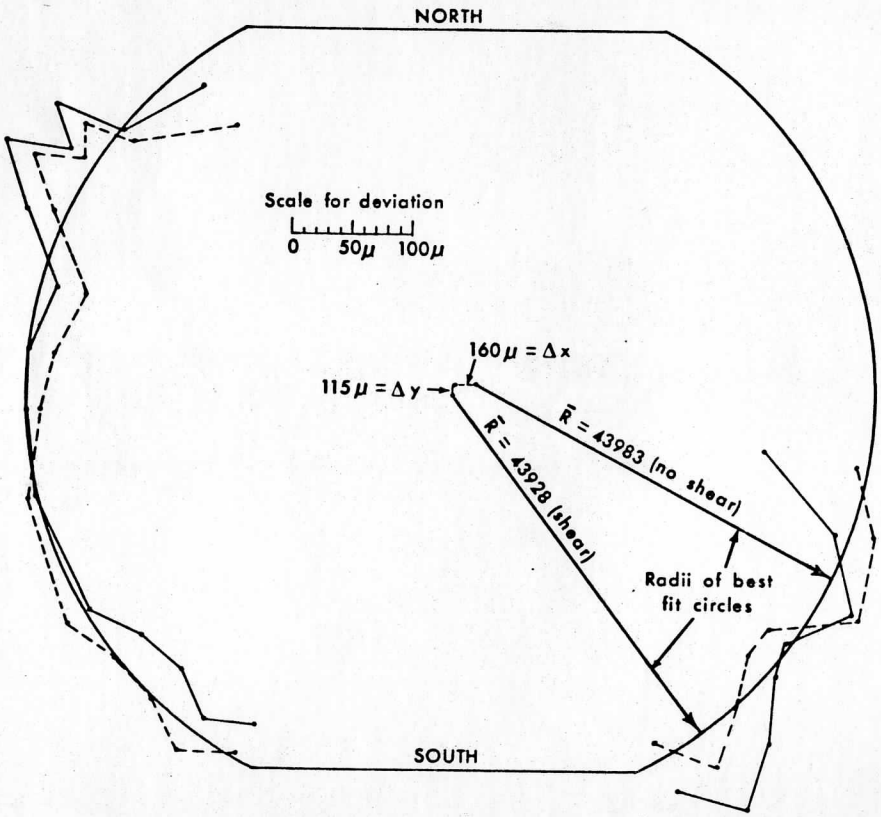
NORTH
Scale for deviation
0 50μ 100μ
160μ = Δx
115μ = Δy
R̄ = 43983 (no shear)
R̄' = 43928 (shear)
Radii of best fit circles
SOUTH

b

NORTH
SOUTH
a.
62
66
b.
124
95
70
c.
39
e.
41
25
f.
d.
26
66

SOUTH
d.
261
187
179
e.
168
f.
NORTH.
385
a.
199
250
b.
485
229
c.
507

Fig 5a

The use of ATS satellites for ionospheric studies.

T. Norman and S. V. Venkateswaran
University of California, Los Angeles

I. Introduction

In addition to monitoring tropospheric weather phenomena, as discussed by the majority of papers in this volume, the ATS satellites have proven to be invaluable in conducting ionospheric studies. A convenient method for this purpose is to measure the amount of ionospheric Faraday rotation impressed on the satellite VHF telemetry signals. The Faraday rotation is related in a fairly simple manner to the total electron content along the propagation path between the satellite and the observer. Since the ATS satellites are geostationary, the propagation paths remain fixed. Time continuous records of total electron content obtained in this manner provide useful material for the pursuit of investigations like the following: 1) the response of the ionosphere to changing solar radiation conditions during sunrise and sunset and solar eclipses; 2) ionospheric effects of solar flares and geomagnetic storms; 3) structure and movement of ionospheric perturbations, including naturally occurring traveling ionospheric disturbances and scintillations, and man-made disturbances and 4) maintenance of the night-time ionosphere.

In the present paper, which constitutes a preliminary report of our investigations along these lines, the basic theory of ionospheric Faraday rotation is briefly reviewed in Section II. This is followed in Section III with a description of a radio polarimeter suitable for Faraday rotation measurements with high time resolution. Section IV gives some details of the signal analysis procedure. The concluding

Section V contains a selection of illustrative experimental results.

II. Basic Theory of Satellite Signal Polarimetry

The ionosphere which is permeated by the earth's magnetic field acts as a birefrigent medium for the propagation of electromagnetic waves. In this medium, an elliptically polarized beam of radiation like the VHF transmission of the ATS travels in two distinct modes. Each of these modes is circularly polarized; but they have opposite senses of rotation as viewed along the direction of propagation. The phase velocities of these two modes are different so that when they are recombined at the end of their propagation paths, there results an elliptically polarized beam which has its major axis rotated with respect to its initial orientation at the satellite. To an observer in the Northern Hemisphere, the rotation is in the anti-clockwise sense (Figure I). The amount of rotation can be calculated knowing the refractive indices of the medium for the two propagating modes. These are given by the well-known Appleton-Hartree formula which can be simplified due to the fact that the propagating frequency is much higher than the characteristic frequencies of the ionospheric plasma. As a result,

$$\Omega_i = \frac{K}{f^2} \int N H \cos\gamma \, ds \qquad (1)$$

where Ω_i = amount of Faraday rotation,

N = electron density,

H = magnetic field strength,

f = propagating frequency,

γ = angle between the earth's magnetic field and the direction of propagation

and K = constant, depending on units used; integration is along the ray path. The formula assumes that the differential refraction effects on the exact phase paths of the two modes are negligible. Because of the typical distribution of electrons in the ionosphere and of the nature of variation of the earth's magnetic field, the predominant part of the Faraday rotation is introduced in a relatively narrow altitude range. A suitable average value of $H \cos \gamma$ is generally chosen to be that which exists at about 400 km altitude.

Writing

$$ds = dh \sec \chi \tag{2}$$

where h = altitude

and χ = zenith angle of the ray path at 400 km;

the rotation formula becomes

$$\Omega_i = \frac{K}{f^2} \overline{H \cos\gamma \sec\chi} \int N dh \tag{3}$$

This is the form in which the formula is often used in ionospheric studies by satellite radio polarimetry.

For a geostationary satellite, the quantity in front of the integration sign in the above formula is a constant for any given observing station. For example, for our observing station at China Lake, California (Lat. 35.7°N, Long. 117.6°W), the values of this constant evaluated at 400 km altitude are:

$$69.7 \times 10^{-18} \quad \frac{\text{rad-meter}^2}{\text{electron}} \quad \text{for ATS-I at 151° W Longitude,}$$

and

$$61.4 \times 10^{-18} \quad \frac{\text{rad-meter}^2}{\text{electron}} \quad \text{for ATS-III at 90°W Longitude.}$$

Hence, for a reasonable mid-day maximum columnar electron content of 6×10^{17} electrons/meter^2, the major axis of the polarization ellipse will undergo approximately 6.5 complete rotations during its ionospheric traversal, while for a typical night-time minimum value of 0.5×10^{17} electrons/meter^2, the rotation will on the order of 0.5.

The amount of rotation is most conveniently measured in terms of a ground based coordinate system. In this system we have

$$\Omega_g + n\pi = \Omega_i + \Omega_s = \Omega \qquad (4)$$

where Ω_g = rotation angle measured at the ground, this angle being always less than 360°,

Ω_s = initial orientation angle of the signal polarization at the instant of satellite emission,

Ω_i = ionospheric Faraday rotation given by formula (1) or (3)

and n = 0, 1, 2....., an integer.

It is clear from the above relation that in order to obtain absolute values of Ω_i and hence of the electron content it is necessary to specify Ω_s, and to resolve the ambiguity of $n\pi$ in the rotation angle, Ω_g.

There are several ways of resolving this ambiguity. The most satisfactory method is to record the rotation angle at two closely spaced frequencies which are selected such that the difference in Faraday rotation between them is less than π radians. The simultaneous transmissions at 136.470 MHz and at 137.350 MHz that are occasionally available from ATS satellites are ideally suited for this purpose.

The initial orientation angle Ω_s is inferred from the orientation and radiation pattern of the satellite antenna structure. This structure consists of a turnstile array mounted on the Northern end of the satellite. The array consists of 8 quarter-wave whips at 45° intervals around the spacecraft circumference with each whip inclined at 20° to the satellite spin axis. The spin axis is accurately maintained parallel to the earth's spinaxis. An observer on the ground essentially obtains an edge-on view of the equatorial plane of the satellite. The geometry and phasing of the antenna elements described above are such that to this observer the satellite signal appears elliptically polarized, the major axis of polarization being along the projection of the satellite spin axis on to the observation plane

(that is, a plane perpendicular to the line of sight). This geometry of satellite signal emanation is illustrated in Figure 2. From this geometry it is found that the values of Ω_s from China Lake for the satellites ATS-I and ATS-III are 52° and 122°, respectively (Figure 3). The orientation angles for these satellites for any other ground station can be calculated in a similar manner.

As shown already, most of the Faraday rotation of the satellite signal takes place in the ionosphere in a relatively narrow range of altitudes. This is illustrated in Figure 4 showing the rotation as a function of altitude for two electron density profiles, typical for day and night-time conditions at sunspot maximum. It is readily seen from this diagram that the polarimetric method is most sensitive for detecting electron density changes in the topside ionosphere in the vicinity of the F-maximum. The method is relatively insensitive to changes in the electron density in the D and E regions below and in the magnetosphere above. This feature of the technique is advantageous for isolating F-region effects from simultaneous effects at other altitudes.

III. Signal Detection

A block diagram of the radio polarimeter used in our investigations is shown in Figure 5. A high-gain (12 db) 8 element Yagi array is the receiving antenna with element lengths and spacings adjusted for 137 MHz. The antenna is mounted on four pillow-block bearings, and the antenna shaft is coupled to a gear

motor so that the entire assembly can be continuously rotated about the antenna axis pointed towards the satellite. An inductive coupling is used to transfer the VHF signal off the rotating shaft. The output of the coupler is introduced into an Ameco CN-144 frequency converter tuned for 137 MHz. The converter reduces the received frequency to approximately 20 MHz which is then fed into a Collins R-390 military receiver used without AGC. The diode load of the receiver is band pass filtered and digitized at 50 samples/second. An oscilloscope monitor of the sampled signal is also provided. Two modes of data sampling are employed: three consecutive rotations of the antenna are recorded every minute on the minute (Mode 1); for the first two minutes of every hour the antenna rotations are recorded continuously (Mode 2). Data sampled in the first mode are used for rotation angle measurements. The second mode provides data for analysis of the scintillation spectrum (Section V). In addition to the signal, digital time codes and a phase reference signal are also recorded. The latter is generated by a magnet which is mounted on the end of the reflector element. This magnet produces a momentary reed switch closure once every rotation when the antenna elements swing through the vertical position. The phase reference signal is used in signal analysis.

IV. Signal Analysis

With an antenna rotation rate of 1 cycle/second, the receiver output consists of a basic 2 cycles/second component (Figure 6). The amplitude maxima

of this component are obtained when the antenna axis coincides, twice every rotation, with the major axis of the signal polarization. The amplitude minima occur when the antenna axis coincides with the minor axis of the polarization curve. It can be seen, moreover, from Figure 6 that the signal is modulated by the spins of the satellite and the polarimeter antenna systems. The lack of synchronization of the spin rates of these systems produces varying signal forms, as illustrated in the three sequential frames of Figure 6.

The signal analysis procedure consists essentially of performing a harmonic analysis of the digitized data and deducing the phase angle (time of maximum amplitude) of the 2 cycles/second component with reference to the phase reference signal provided by the magnetic switch (Section III). This phase angle is in turn converted to the rotation angle Ω_g from the known spin rate of the polarimeter antenna. The rotation angles determined in this manner will, however, be in error because of the spin modulation effects on the signals discussed above. This error can be calculated in terms of the satellite radiation pattern (Section II) and the spin ratio of the satellite and the polarimeter antennas. Calculations made for two different values of the spin ratio are shown in Figure 7. It can be seen that the spin effect can produce an error of as much as $\pm 4^{\circ}$ in individual rotation angle measurements. However, the error is reduced to $\pm 0.5^{\circ}$ by averaging results for three or more consecutive rotations of the polarimeter antenna. The resulting loss of time resolution in measurements is not serious for most ionospheric studies.

V. Illustrative Results

In this section are presented some initial results obtained with the radio polarimeter described above. Figure 8 shows the diurnal variation of electron content for two consecutive days selected at random during the months of August and December, 1967. The location of observation may be taken to be Lat. 32.8°N, Long. 120.8°W. This location corresponds to the sub-ionospheric point above which the propagation path of the ATS-I signal as observed at China Lake intersects the height of 400 km.

The most striking feature of the diurnal curves is the fact that the day-time electron content is greater during December than during August. This feature is the well known seasonal anomaly of the F-region (Ratcliffe and Weekes, 1960) and is probably produced by seasonal changes in atmospheric composition. In spite of the large variation in the day-time electron content observed between summer and winter, the night-time values remain approximately the same.

A consistent feature of the diurnal curves is the rapid increase of electron content at sunrise. The sunrise effect is delineated in detail in Figure 9 from observations made at China Lake of ATS-I and III on 23 January 1968. These satellites were stationed longitudes 151° and 89°, respectively, on that date. The sunrise times at ground level and at a height of 100 km along the propagation path are marked in the figure.

The rate of increase of electron content during sunrise is directly related to the production rate of electrons if it is assumed that loss rates and vertical motion

effects are negligible. The production rate is in turn related to the intensity of the ionizing flux of solar radiation in the extreme ultra violet and to the ionospheric scale height. The production rates calculated in this manner from previous satellite observations (Garriott and Smith, 1965; Titheridge, 1966), however, show seasonal variations which are unrelated to variations in the ionizing flux. These variations have been surmised to be due to variations of the densities of N_2 and O_2 which are minor constituents in the F-region but have a complete control on the loss rates of electrons. A careful study of the seasonal variation of the production rate might therefore establish the variations of these minor constituents relative to atomic oxygen. Used in conjunction with satellite drag measurements at lower ionospheric heights, this information might lead to useful inferences of the seasonal variation of the turbopause height above which all the constituents are in diffusive equilibrium.

Inspection of Figure 8 further shows interesting seasonal differences in the temporal behavior of the night-time ionosphere. For example, there is a marked decrease of electron content during the particular night in August, but no similar decrease is observed in December. The problem of maintenance of the night-time ionosphere has been discussed most recently by Titheridge(1968). He has argued that the night-time total electron content measurements are most readily explained if it is postulated that there is a nocturnal supply of ionization from the magnetosphere

to the ionospheric F-region, the amount of supply being greater during the winter than during the summer season. Observations of electron content from different geographic locations are needed before details of this magnetospheric contribution to the night-time ionosphere are firmly established.

In addition to day-to-night changes, records of total electron content quite often show fluctuations ranging in periods from hours to minutes. An example of such fluctuations is shown in Figure 10. These fluctuations are known to be produced by traveling ionospheric disturbances (TID's). These disturbances, most probably, are manifestations of vertically propagating gravity waves which are generated in the troposphere (Hines, 1960) and have leaked into the ionosphere. If this, in fact, is the most common mode of origin of these distrubances, their frequency content must depend upon the transmission properties (wind and temperature structure) of the intervening atmosphere. Faraday rotation measurements of electron content like those shown in Figure 10 provide an extremely sensitive method of studying the diurnal and seasonal variation of the frequency content of TID's.

Besides studying the periods of the disturbances, their apparent velocity of movement can also be studied if measurements of Faraday rotation are carried out from a suitably spaced triangle of stations. If more than one ATS satellite is available for observation the number of ground based stations required for this purpose can be still further reduced. Moreover, by having an additional mobile station whose position is varied such that the propagation path of the satellite signal

to it intersects the fixed propagation from the permanent stations at various desired heights in the ionosphere, it might be possible to determine the height of the perturbations as well. Obviously, the observational study of ionospheric perturbations is greatly facilitated with the launching of ATS satellites.

Extremely small sized irregularities of electron content in the ionosphere are believed to be responsible for "scintillations". Figure II gives an example of the scintillation spectrum of the ATS-I signal. This spectrum has been derived by the Fast Fourier Transform method from data sampled continuously for a period of two minutes (Section III). The scintillation spectrum is obviously contaminated by strong lines appearing at the spin frequencies (and their harmonics) of the satellite and polarimeter antenna systems and at their various combination frequencies. In addition, small-sized ionospheric irregularities give rise to transient fluctuations of power at other frequencies in the spectrum. It should be possible to abstract this latter information from spectra like those shown in Figure II. Details are not given in this paper.

The high time resolution attainable with the Faraday measurement makes it ideally suited for studying impulsive ionospheric effects such as are produced by solar flares. The method is all the more attractive because F-region effects can be studied directly in this manner. As is well known, the sudden enhancement of D-region ionization by flare produced X-rays prevents the probing of the higher F-region by conventional ionosonde methods during flare periods. As a result, the

F-region effects of solar flares are poorly understood (Knecht, 1962). However, the Faraday rotation method, because of its lower sensitivity to D-region ionization, can record F-region effects without serious interruption even during the most intense phase of a flare. This has been already demonstrated by Garriott, et al (1967). The results of these investigators for the flare of May 1967 seem to indicate that F-region effects of solar flares are highly variable both geographically and from one individual flare to another. The current phase of high solar activity is likely to yield further opportunities for observing flare produced effects in the ionospheric F-region.

Studies based on ionosonde records (Matsushita, 1959; Somayajulu, 1963; Kotadia, 1965) have led to inconclusive results regarding ionospheric effects of geomagnetic storms. A recent study by Titheridge and Andrews(1967)of an isolated storm during a low period of solar activity seems to indicate that the world-wide morphology of ionospheric storms may be more clearly revealed in total electron content measurements than from parameters readily scaled from ionograms. It is evident from their results that pronounced changes occur in the height distribution of electrons as a result of changes in the composition and thermal structure of the neutral atmosphere at ionospheric heights during the storm period.

Figures 12 and 13 are intended to show that changes in the vertical destribution of electron density produced by storm effects can be studied by a combination of results from Faraday rotation measurements and conventional

ionograms. In these figures are plotted $(f_o F_2)^2$ (the square of the critical frequency of the F_2 - layer) as abcissa versus Faraday rotation angle as ordinate for different times of the day for two consecutive days which were magnetically disturbed. The critical frequency data have been obtained from Pt. Arguello (Lat. 34.6°N, Long. 120.7°W) which is not far removed from the sub-ionospheric point referring to the Faraday rotation measurements. Since $(f_o F_2)^2$ is proportional to the peak electron density of F_2-layer, these plots reveal how the total electron content is related to the peak content.

If ionospheric layer variations are strictly shape preserving, it can be shown that the Faraday rotation angle would be related linearly to the peak content. In this case, the plotted points in Figures 12 or 13 would fall on a straight line, and this line would intersect the ordinate axis at a value of the rotation angle which equals the initial orientation angle, Ω_s, of the satellite signal polarization. This was first pointed out by Nakata (1966) who proposed this method for determining Ω_s. However, distortions of ionospheric layers bring about departures from the straight line relationships. Day-to-day changes in these departures appear to be most pronounced during the period of geomagnetic storms.

VI. Conclusion

It has been shown in the previous paragraphs that Faraday rotation measurements on the VHF telemetry of ATS satellites can give valuable information

on the detailed structure and behavior of the ionospheric region near the F_2 maximum. Among the topics that can be studied in this manner are sunrise and sunset effects, effects of solar flares and geomagnetic storms and the apparent velocity of movement of ionospheric disturbances. These topics of study form an integral part of a more ambitious investigation designed to study coupling effects between the troposphere and the ionosphere, and the ionosphere and the magnetosphere.

Acknowledgment

Financial assistance for this investigation has come partly from the Naval Weapons Center, China Lake, California. Encouragement and assistance from Mr. James G. Moore, Mr. Gary Babcock and Mr. Glen Bray of the Naval Weapons Center are gratefully acknowledged.

References

GARRIOTT O. K., SMITH F. L. and YUEN P. C.	1965	Planet. Space Sci. 13, 829
GARRIOTT O.K., et al	1967	J. Geophys. Res. 72, 6099
HINES C. O.	1960	Can. J. Phys. 38, 1441
JOHNSON F. S.	1965	Satellite Environment Handbook, Stanford University Press, Stanford, California
KNECHT R. W. and McDUFFIE R. E.	1962	J. Phys. Soc. Japan (A-1) 17, 280
KOTADIA K. M.	1965	J. Atmos. Terr. Phys. 27, 723
MATSUSHITA S.	1959	J. Geophys. Res. 64, 305
RATCLIFFE J.A. and WEEKES K.	1960	Physics of the Upper Atmosphere, Academic Press, New York and London, 429
SOMAYAJULU Y. V.	1963	J. Geophys. Res. 68, 1899
TITHERIDGE J. E.	1966	J. Atmos. Terr. Phys. 28, 1135
TITHERIDGE J. E. and ANDREWS M. K.	1967	Planet. Space Sci. 15, 1157
TITHERIDGE J. E.	1968	J. Geophys. Res. 73, 2985

Figure Captions

1. Illustration of Faraday rotation.

2. The geometry of signal reception.

3. Orientation angle, Ω_s, as a function of longitudinal separation between a geostationary satellite and a ground station at 35.7°N. The azimuth and elevation angles from such a station are also shown.

4. Faraday rotation angle, Ω_i, per km as a function of height for typical sunspot maximum electron density profiles taken from Johnson (1965).

5. Radio Polarimeter Block Diagram

6. Band pass filtered output of receiver.

7. Analysis of error due to spin effects. The error analysis have been performed for the cases where the spin rates of satellite and the polarimeter antenna systems are in the ratio 40/50 and 31/50, respectively. The top curves show the error in rotation angle as a function of consecutive rotations. The bottom curves show the error averaged over different numbers of consecutive rotations.

8. Diurnal variation of total electron content for a sub-ionospheric point at Lat. 32.8°N, Long. 120.8°W at which location local time is UT minus 8 hrs. Although the ambiguity of $n\pi$ is left unresolved in the ordinate of this figure, it is known that n = 0 from an independent calibration.

9. The Sunrise behavior of the total electron content. The angle ψ is linearly related to the Faraday rotation angle, Ω_g, mentioned in the text.

10. Fluctuations in total electron content for a sub-ionospheric point where local time is UT minus 8 hrs.

11. Spectral analysis of the satellite signal: the ordinate is the variance of power associated with the signal at a particular frequency on a (relative) logarithmic scale; the abcissa is the frequency parameter, k, related to frequency by $f(c/s) = 0.008\ k$. f_a denotes the frequency of the ground antenna rotation and f_s the frequency of satellite spin.

12. and 13. Plot of $(f_o F_2)^2$ vs. Ω_i (see text). The times shown on the plots are local times.

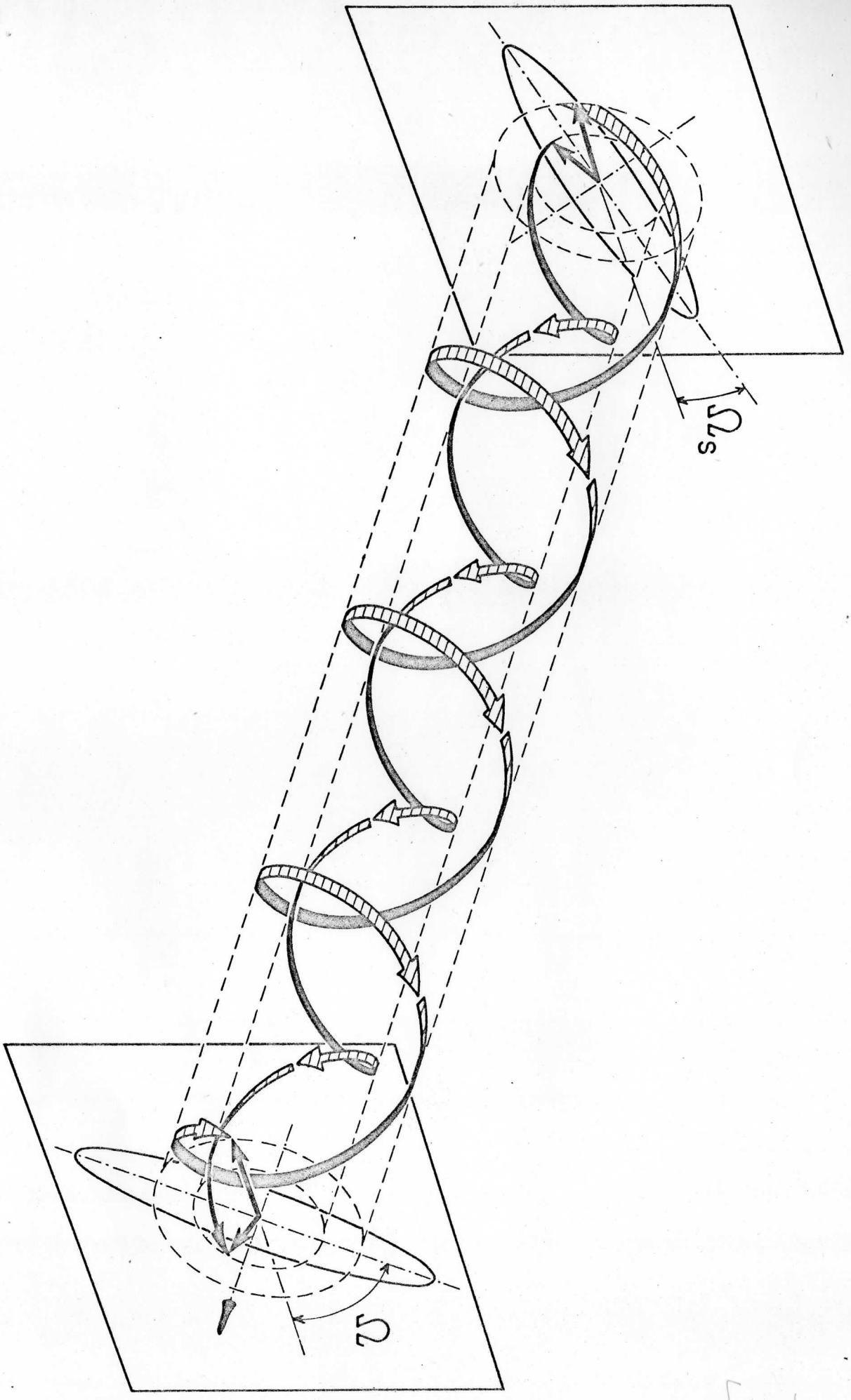

Fig 1

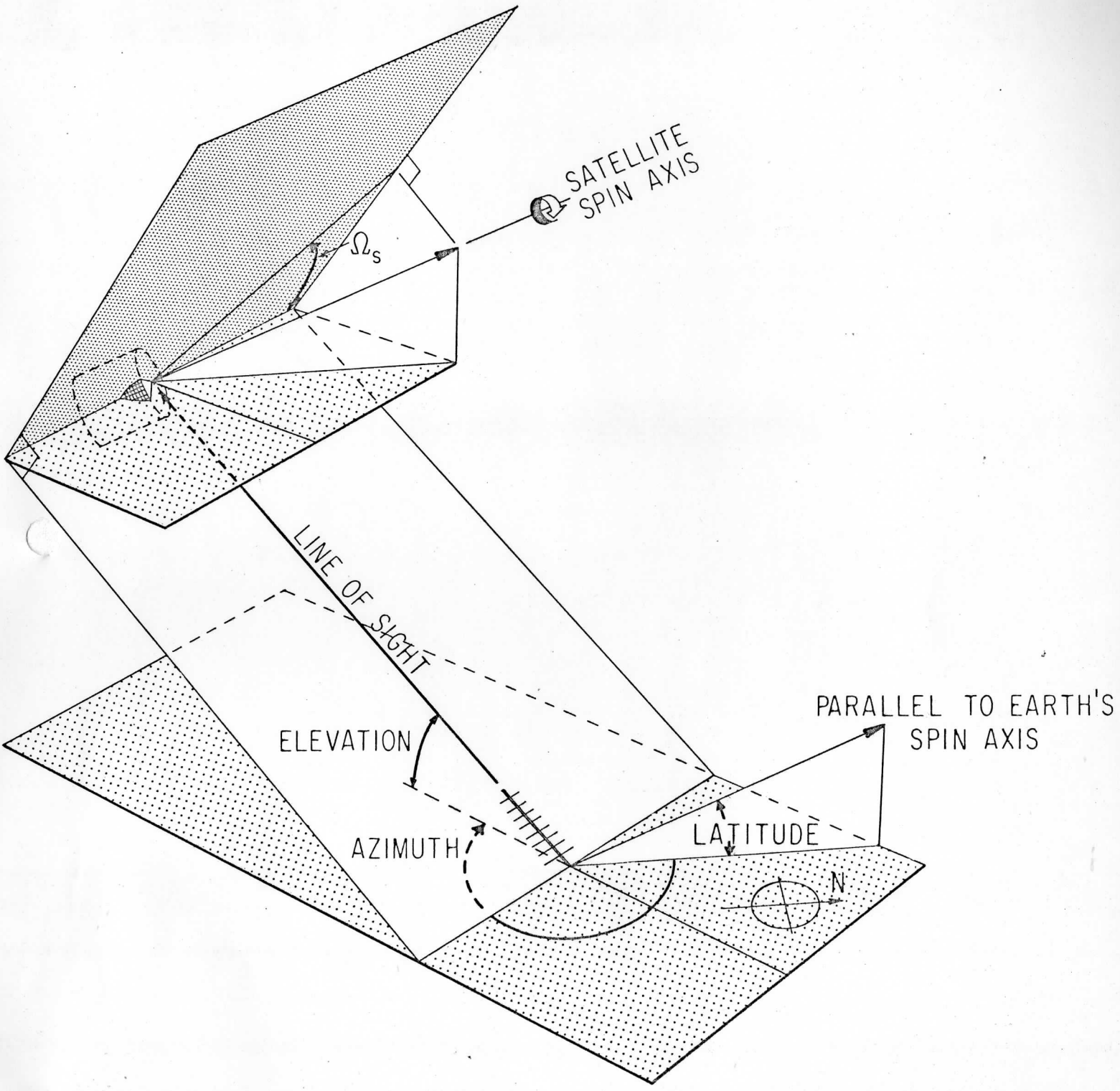
SATELLITE
SPIN AXIS
Ω_s
LINE OF SIGHT
ELEVATION
AZIMUTH
PARALLEL TO EARTH'S
SPIN AXIS
LATITUDE
N

Fig 2

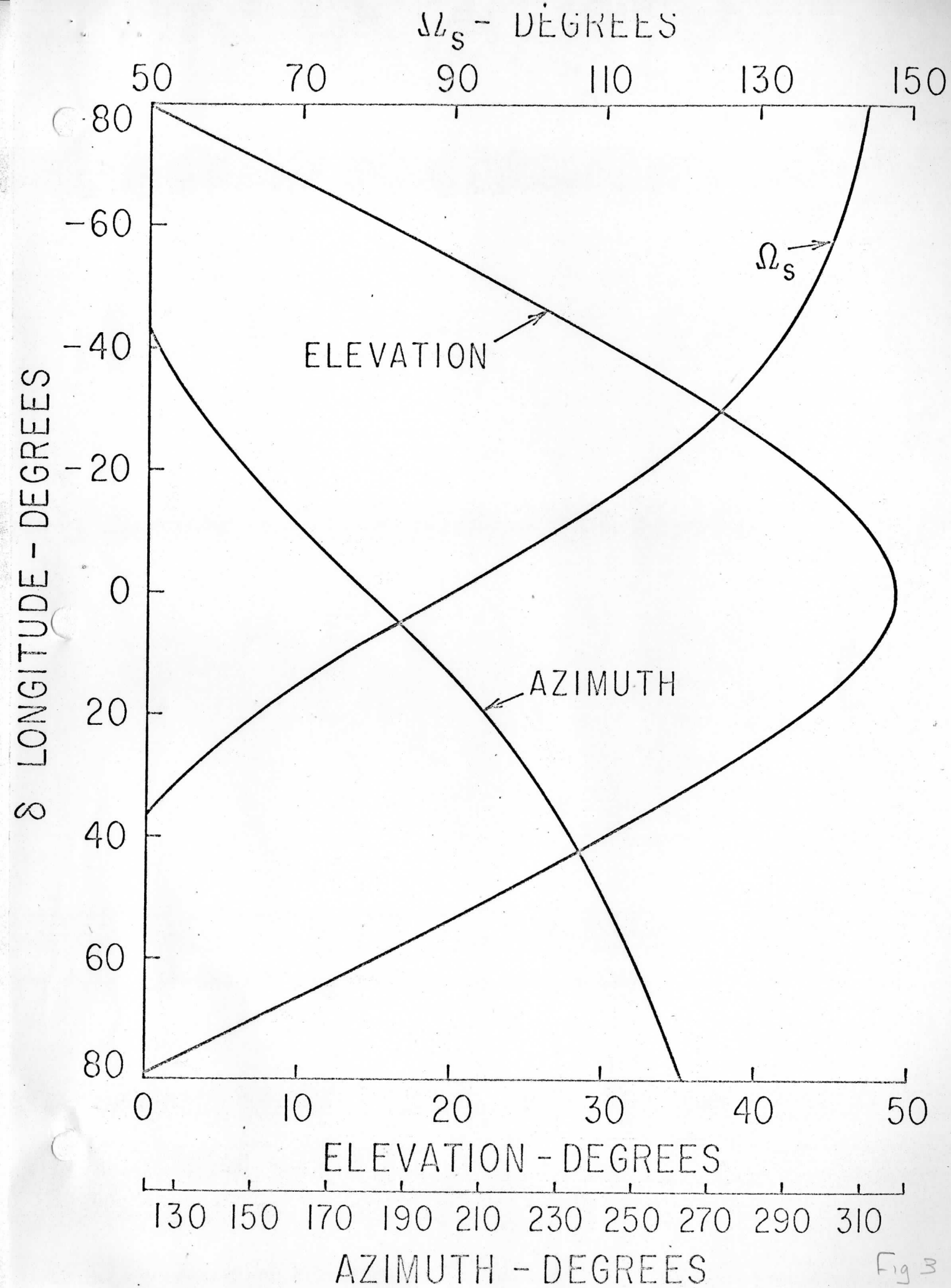
Ω_s - DEGREES
50
70
90
110
130
150
-80
-60
-40
-20
0
20
40
60
80
Ω_s
ELEVATION
AZIMUTH
δ LONGITUDE - DEGREES
0
10
20
30
40
50
ELEVATION - DEGREES
130
150
170
190
210
230
250
270
290
310
AZIMUTH - DEGREES

Fig 3

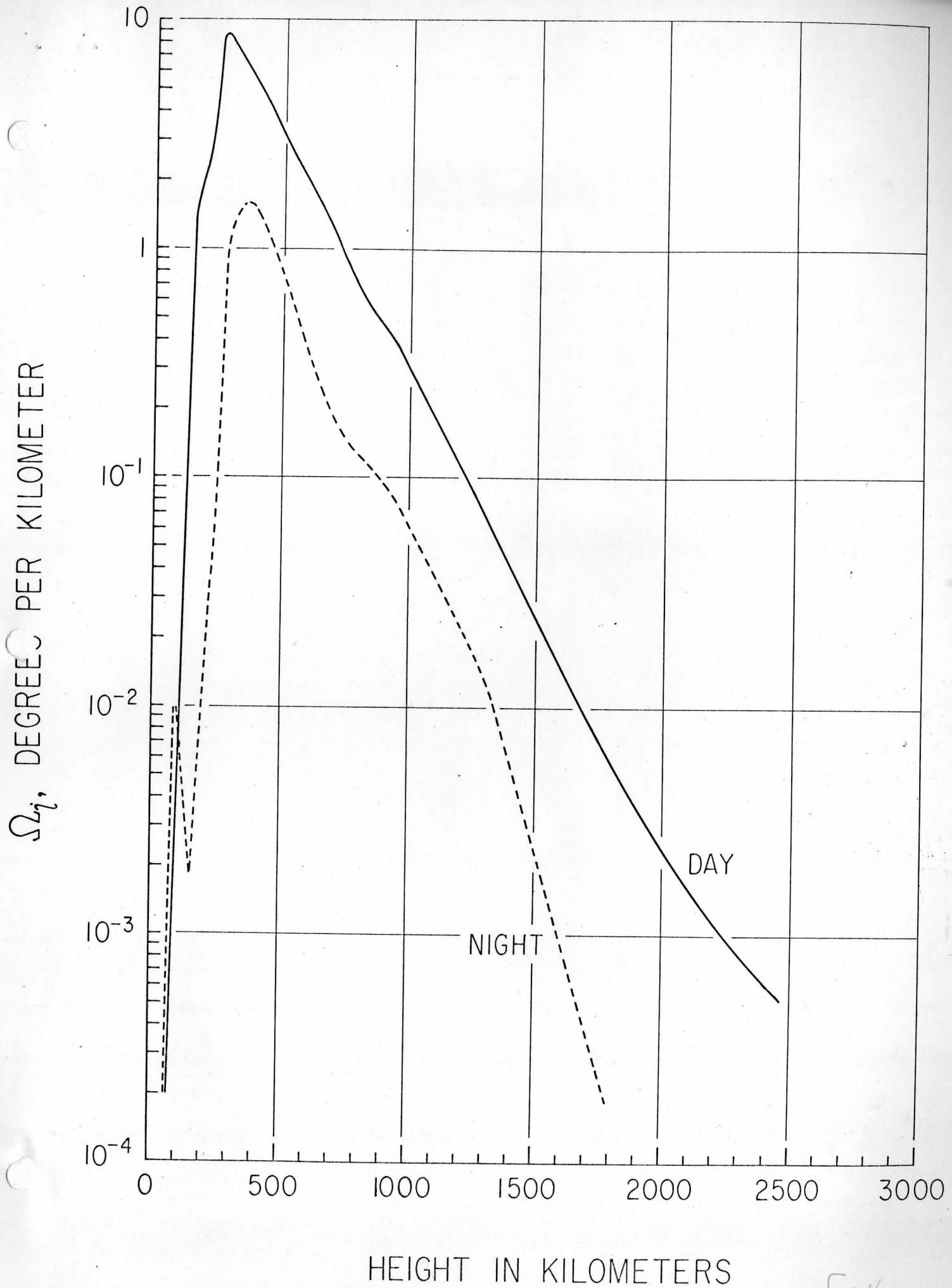
10
1
10^{-1}
10^{-2}
10^{-3}
10^{-4}
Ω_i, DEGREES PER KILOMETER
DAY
NIGHT
0
500
1000
1500
2000
2500
3000
HEIGHT IN KILOMETERS

Fig 4

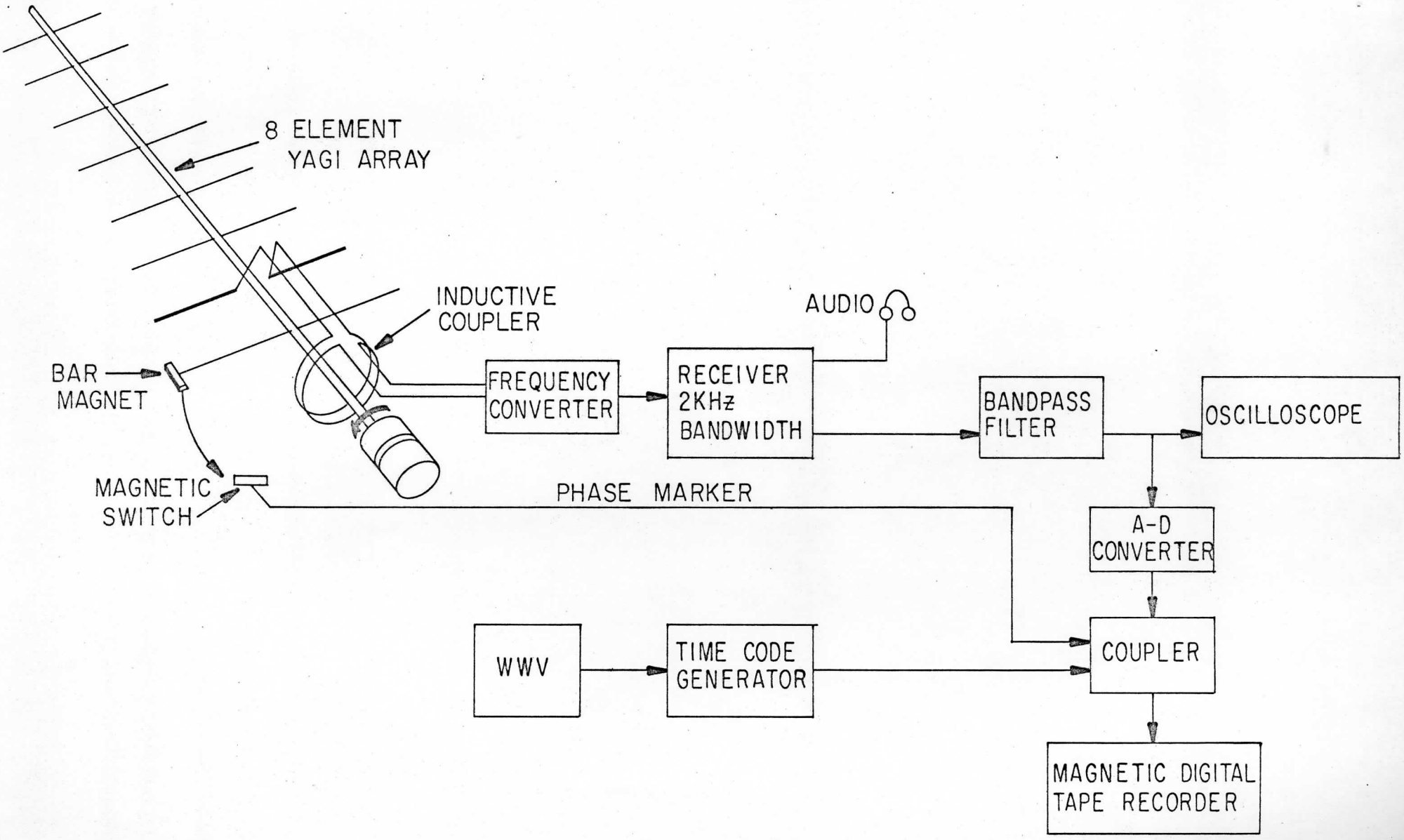

RADIO POLARIMETER BLOCK DIAGRAM

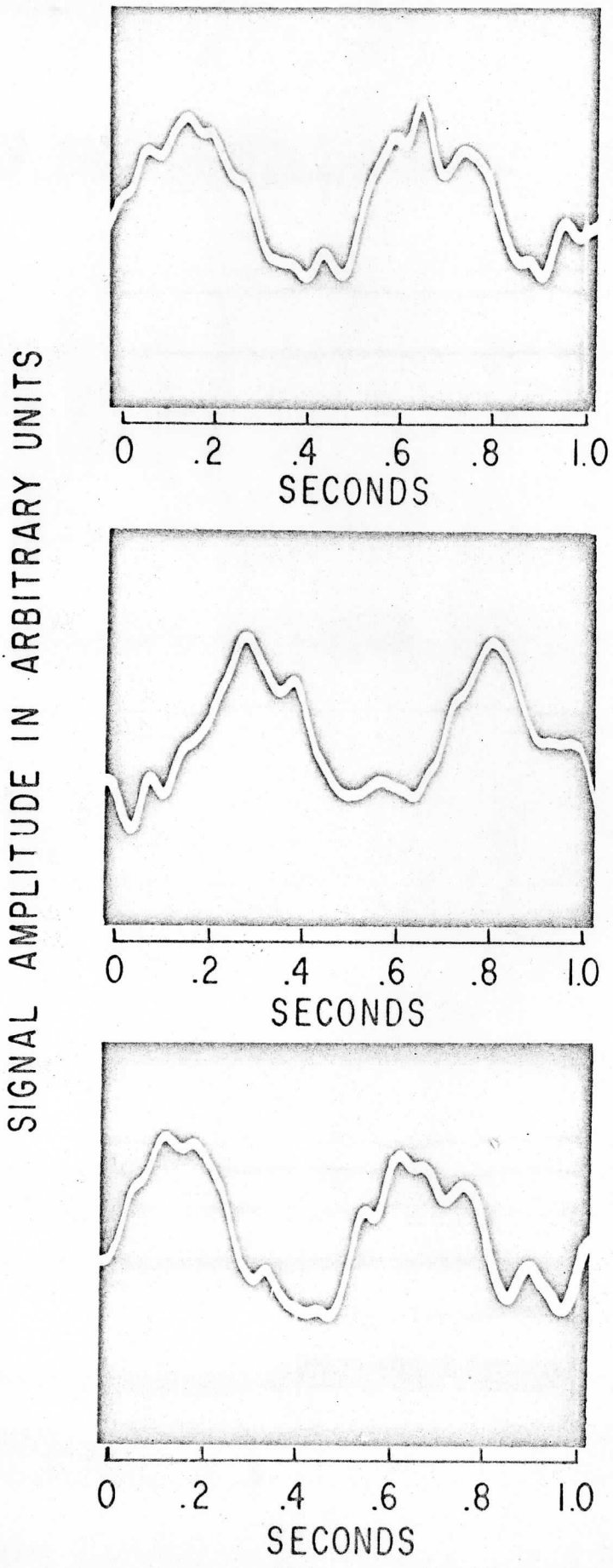
SIGNAL AMPLITUDE IN ARBITRARY UNITS
0
.2
.4
.6
.8
1.0
SECONDS
0
.2
.4
.6
.8
1.0
SECONDS
0
.2
.4
.6
.8
1.0
SECONDS

Fig 6

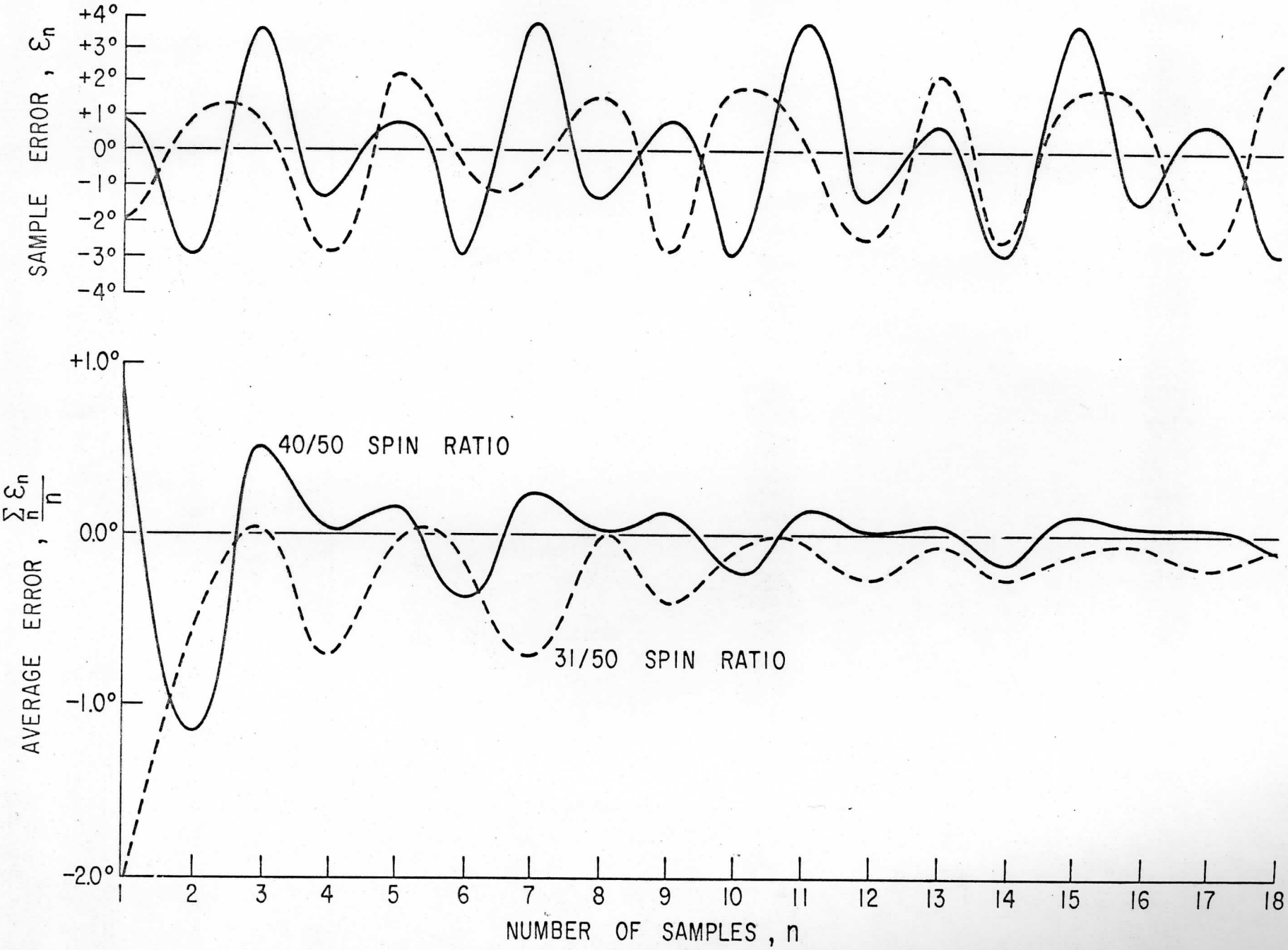
SAMPLE ERROR , ε_n
+4°
+3°
+2°
+1°
0°
-1°
-2°
-3°
-4°
AVERAGE ERROR , $\frac{\sum_n \varepsilon_n}{n}$
+1.0°
0.0°
-1.0°
-2.0°
40/50 SPIN RATIO
31/50 SPIN RATIO
1
2
3
4
5
6
7
8
9
10
11
12
13
14
15
16
17
18
NUMBER OF SAMPLES , n

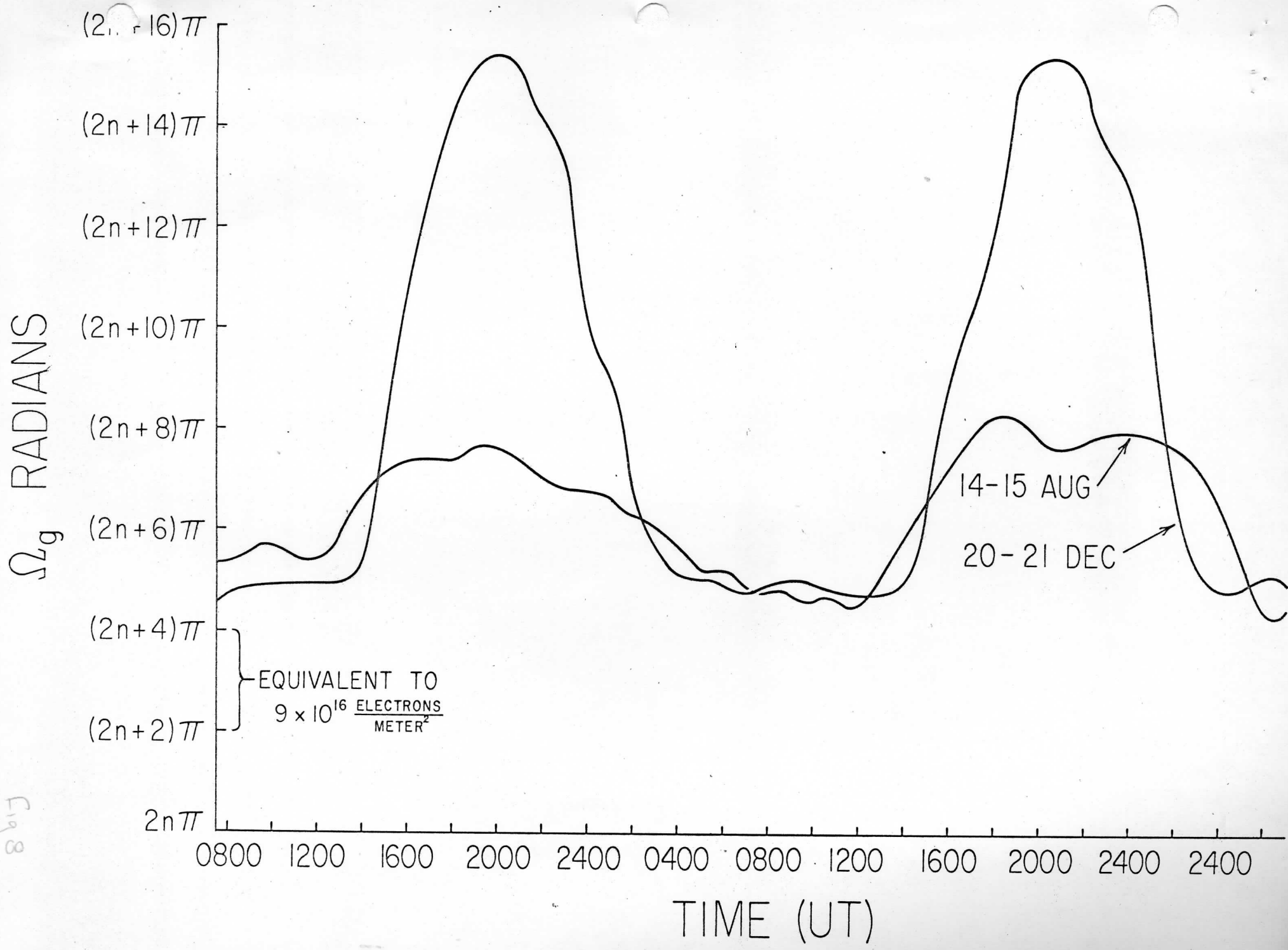
(2n+16)π
(2n+14)π
(2n+12)π
(2n+10)π
(2n+8)π
(2n+6)π
(2n+4)π
(2n+2)π
2nπ
Ωg RADIANS
EQUIVALENT TO
9 × 10^16 ELECTRONS / METER^2
14-15 AUG
20-21 DEC
0800
1200
1600
2000
2400
0400
0800
1200
1600
2000
2400
2400
TIME (UT)

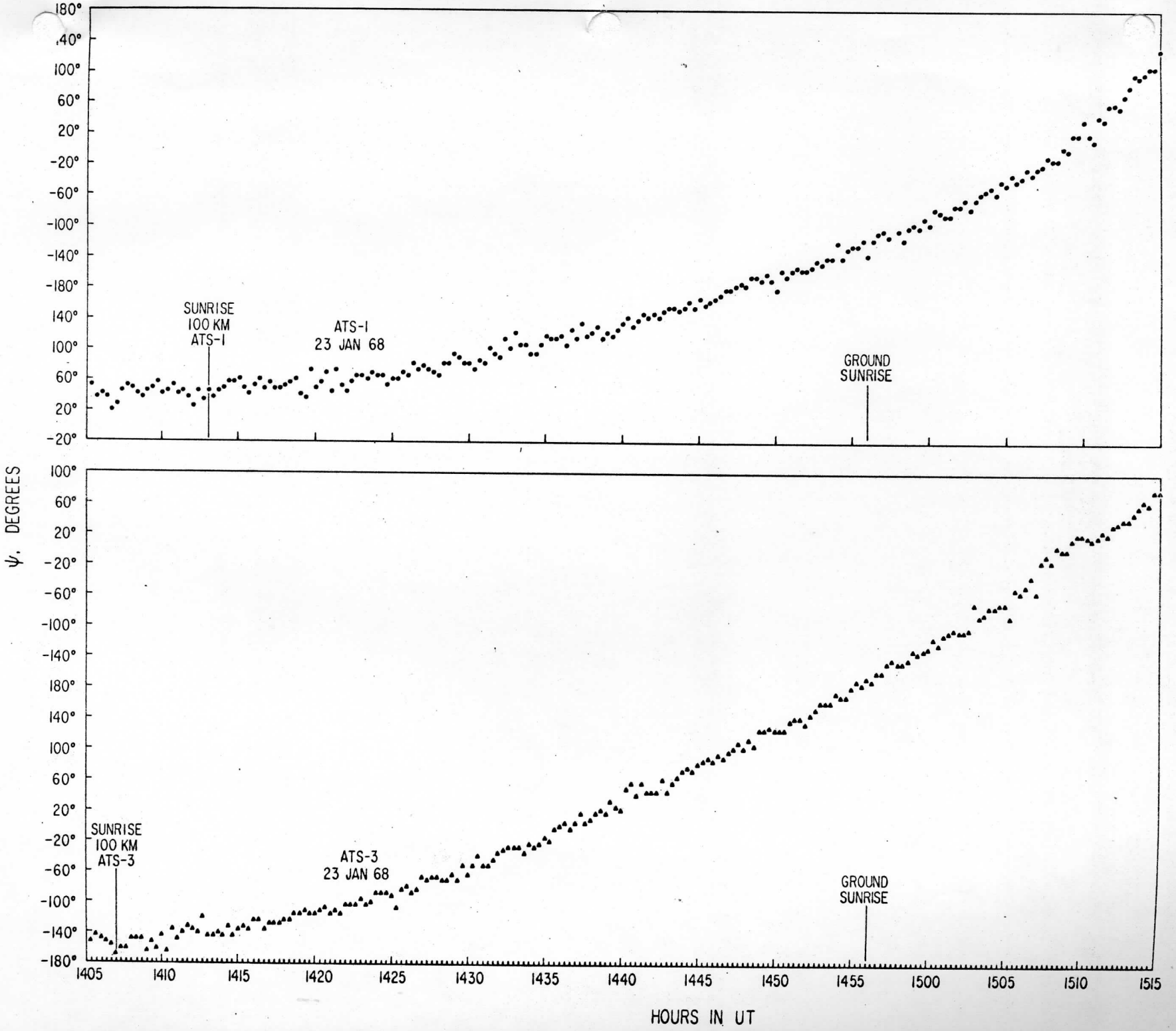
180°
140°
100°
60°
20°
-20°
-60°
-100°
-140°
-180°
140°
100°
60°
20°
-20°
SUNRISE
100 KM
ATS-1
ATS-1
23 JAN 68
GROUND
SUNRISE
100°
60°
20°
-20°
-60°
-100°
-140°
180°
140°
100°
60°
20°
-20°
-60°
-100°
-140°
-180°
SUNRISE
100 KM
ATS-3
ATS-3
23 JAN 68
GROUND
SUNRISE
ψ, DEGREES
1405
1410
1415
1420
1425
1430
1435
1440
1445
1450
1455
1500
1505
1510
1515
HOURS IN UT

F 59

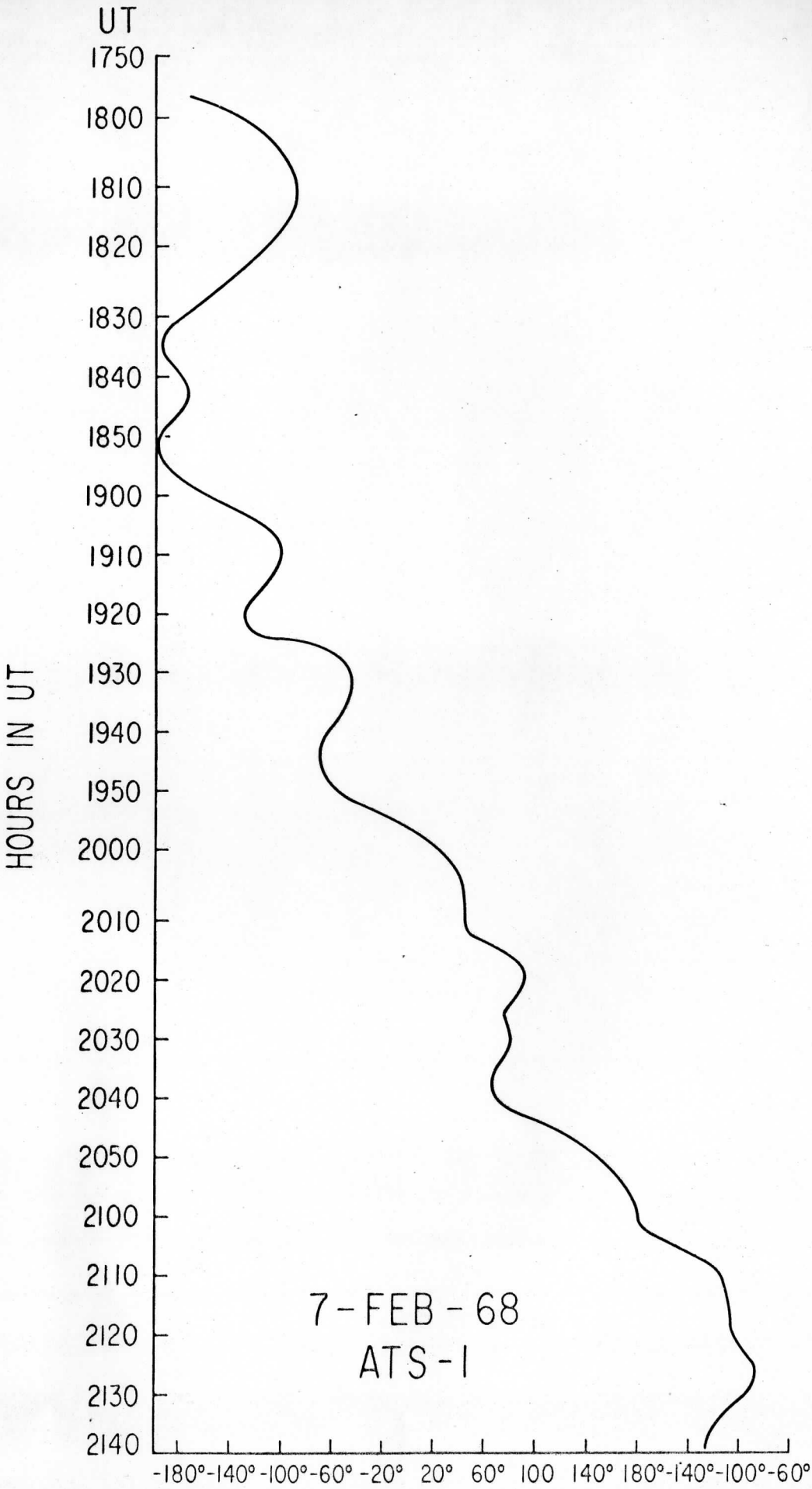
UT
1750
1800
1810
1820
1830
1840
1850
1900
1910
1920
1930
1940
1950
2000
2010
2020
2030
2040
2050
2100
2110
2120
2130
2140
HOURS IN UT
7-FEB-68
ATS-I
-180° -140° -100° -60° -20° 20° 60° 100 140° 180° -140° -100° -60°
ψ, DEGREES

Fig 10

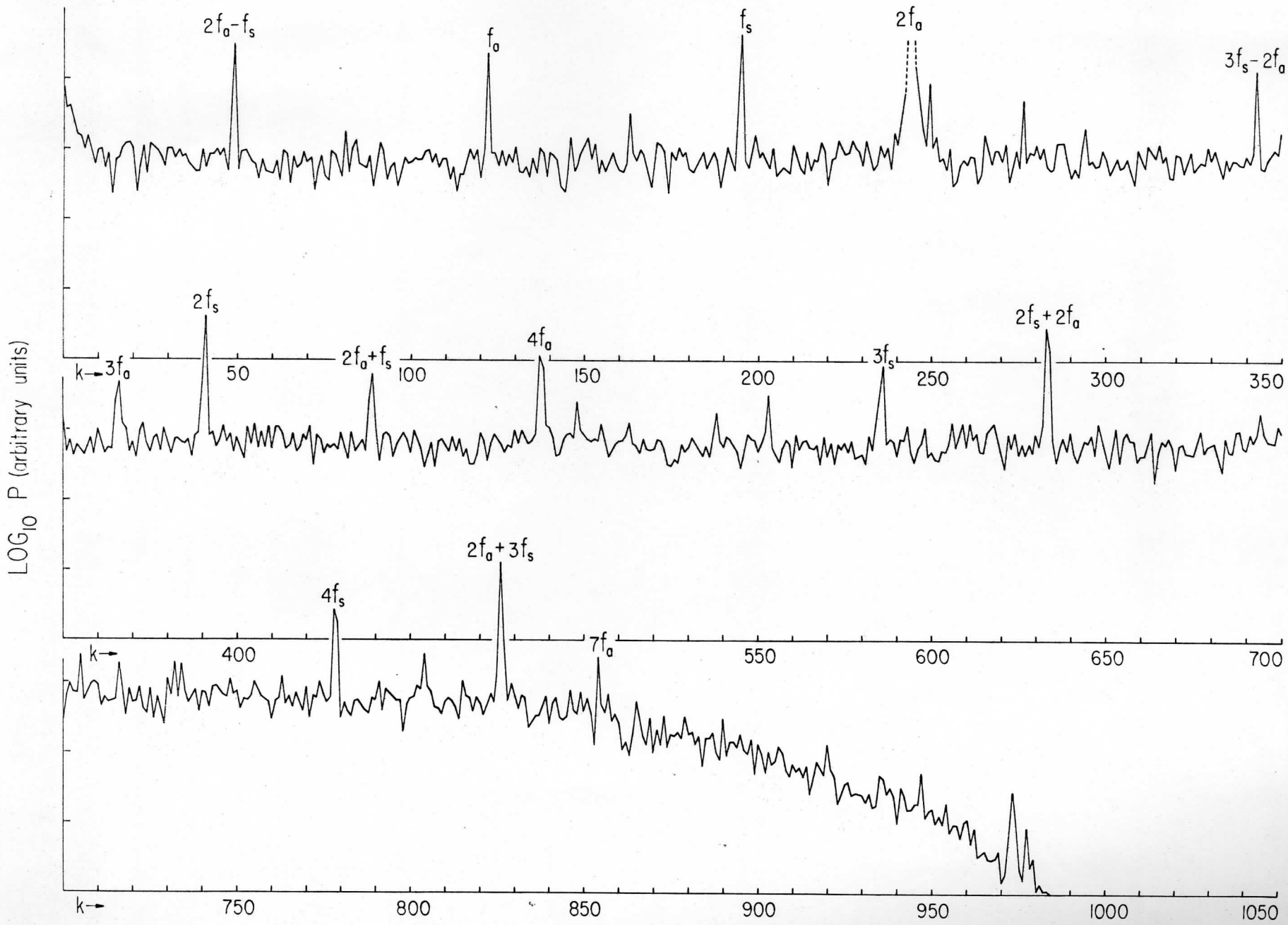
$2f_a - f_s$
f_a
f_s
$2f_a$
$3f_s - 2f_a$
$2f_s$
$4f_a$
$2f_s + 2f_a$
$2f_a + f_s$
$3f_a$
$3f_s$
$2f_a + 3f_s$
$4f_s$
$7f_a$
k→
50
100
150
200
250
300
350
400
550
600
650
700
750
800
850
900
950
1000
1050
LOG_{10} P (arbitrary units)

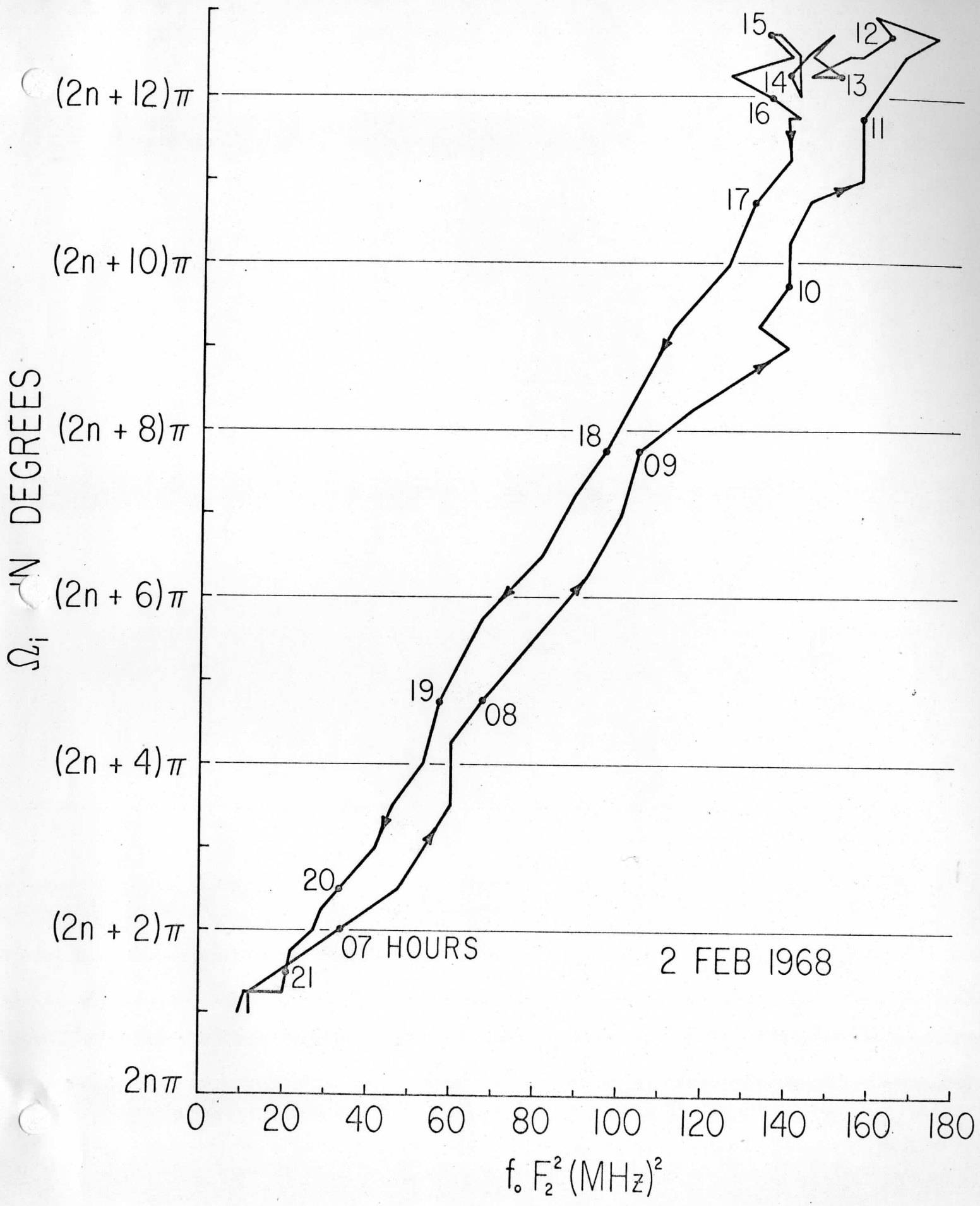
(2n + 12)π
(2n + 10)π
(2n + 8)π
(2n + 6)π
(2n + 4)π
(2n + 2)π
2nπ
Ω_i 'N DEGREES
0
20
40
60
80
100
120
140
160
180
f_o F_2^2 (MHz)^2
15
12
14
13
16
11
17
10
18
09
19
08
20
21
07 HOURS
2 FEB 1968

Fig 12

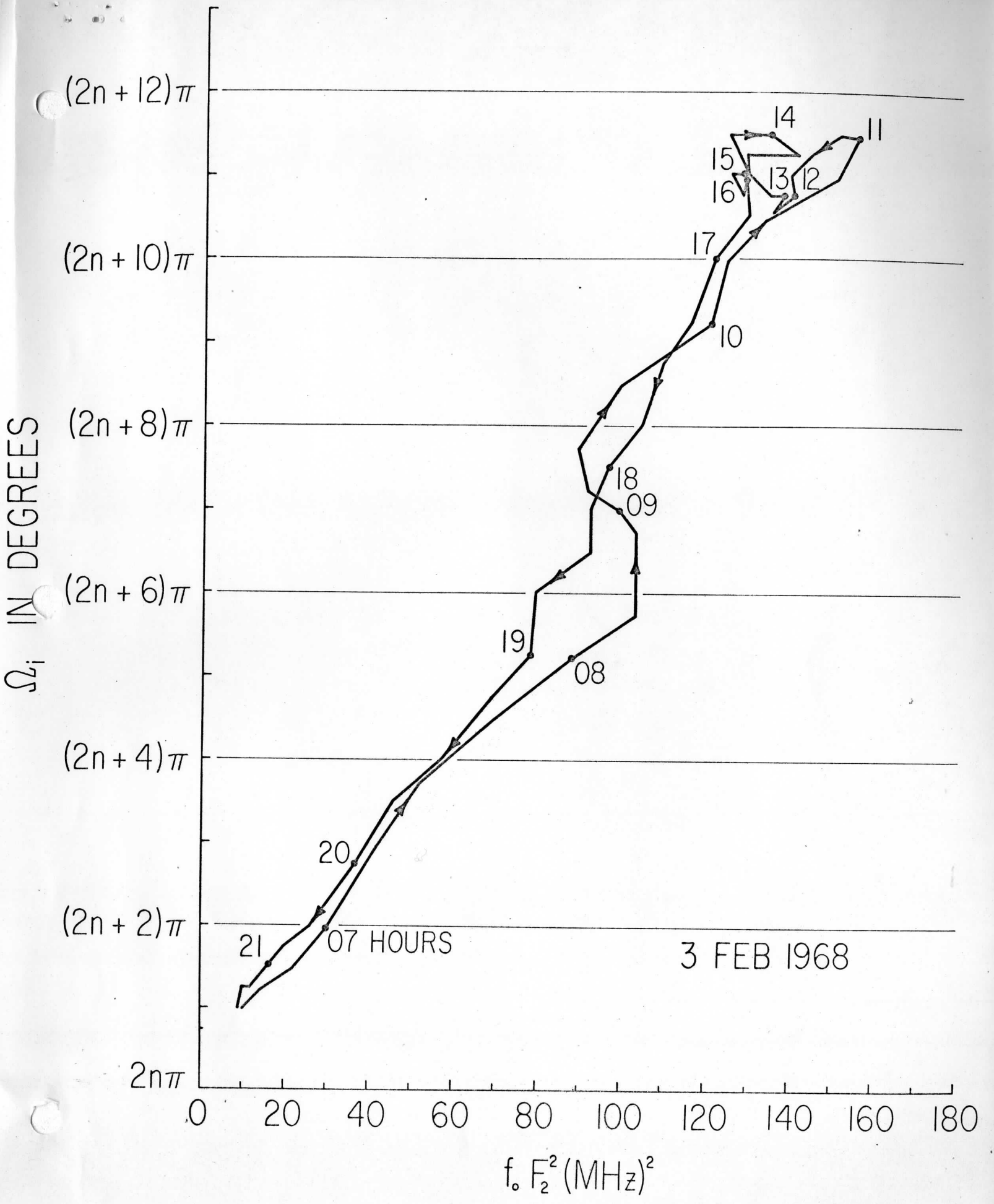
(2n + 12)π
(2n + 10)π
(2n + 8)π
(2n + 6)π
(2n + 4)π
(2n + 2)π
2nπ
Ω_i IN DEGREES
0
20
40
60
80
100
120
140
160
180
f_o F_2^2 (MHz)^2
14
11
15
13
12
16
17
10
18
09
19
08
20
21
07 HOURS
3 FEB 1968

Fig 13

Suomi

ATS-I SPIN-SCAN CLOUD CAMERA

by

R. Thomsen[1]
R. Parent and
V. Suomi

The University of Wisconsin

[1]Santa Barbara Research Center, Santa Barbara, California.

CONTENTS

	Page
GENERAL DESCRIPTION	1
OPTICAL DESIGN	3
MECHANICAL DESIGN	5
1. Housing	5
2. Telescope	5
3. Step Mechanism	6
ELECTRONIC DESIGN	7
COMMAND AND TELEMETRY DATA	10
1. Camera Commands	10
a. Normal Scan Command	10
b. Back-to-Back Scan Command	10
c. South Override Limit Command	11
d. North Override Limit Command	12
2. Telemetry Data	12
a. Scan Mode Indicate	12
b. Scan Direction Indicate	12
c. Telescope Temperature	12
d. Camera Input Voltage	13
e. Pressure Switch Monitor	13
TEST RESULTS	14

GENERAL DESCRIPTION

The Spin-Scan Cloud Camera, shown in Figure 1, is unique in that the spinning motion of the spin stabilized synchronous spacecraft is used to provide part of the required spatial scan. The camera contains a high resolution telescope with a photomultiplier light detector coupled to a precision latitude step mechanism. The latitude step motion combined with the spinning motion of the ATS synchronous vehicle provides complete scan coverage of the earth from 52.5° north latitude to 52.5° south latitude and from the west limb to the east limb. This area is scanned west to east in 2,000 lines. The optical resolution is 2.0 nautical miles when the telescope is pointed at nadir from a synchronous equatorial orbit, 22,752 nautical miles from the earth center. An artist's concept of the Spin-Scan principle is shown in Figure 2.

The telescope is stepped once in each spacecraft revolution by a command from the spacecraft PACE* system. The step occurs approximately 158° after the camera has scanned past the north-south earth centerline. After 2,000 steps, requiring approximately 20 minutes, the telescope reaches a south latitude limit position and a limit switch is actuated to initiate retrace. In retrace, the output of a self-contained 17-Hz oscillator is substituted for the PACE command and the step motor phase

*PACE—An on-board command system providing outputs with direct reference to the earth's position at any time.

sequencing is reversed. This causes the telescope to return to the north latitude limit position in approximately 2 minutes. At this point, actuation of another limit switch initiates normal north-south stepping in synchronism with spacecraft rotation.

Four ground commands are available for remote control of the step motion sequence. The first two provide for early termination of the latitude stepping and retrace allowing for more frequent scanning of limited earth areas. These commands are called south limit override and north limit override. The other two ground commands are called normal scan command and back-to-back scan command. The normal scan mode command causes the camera step mechanism to follow the sequence previously described: 20-minute normal down scan and 2-minute retrace. The back-to-back scan command causes the camera step mechanism to step the telescope both down (north to south) and back up (south to north) at the same slow step rate. In this alternate mode, the 17-Hz retrace oscillator output is not substituted for the PACE step command.

The camera video amplifiers used to drive the spacecraft video ground link VCO's have provision for addition of a sun sensor output pulse. This pulse is positive going and the camera video negative going. The video output appears at two coaxial connectors on the camera housing at a 75 ohm impedance level. The two outputs are identical except that one has a 10-db higher output level than the other. The video bandwidth

at these outputs is 0.1 Hz (-3db) to 100 kHz (-1 db).

Camera power input voltage, two telescope temperatures, scan mode, scan direction, and drive mechanism pressure state are telemetered to earth.

Detailed specifications for the spin-scan camera are listed in Table 1. A cut-away drawing of the spin-scan camera is shown in Figure 3. The telescope is shown in the center frame or neutral position.

OPTICAL DESIGN

The camera optical telescope is a two-element reflective system composed of a 5-inch diameter fused quartz parabolic primary and a flat 1.8-inch diameter secondary. The equivalent focal length is 10 inches. The optical surfaces are evaporated aluminum overcoated with magnesium fluoride. The effective area of the entrance aperture is 104 cm^2. A field defining aperture is located at the focal plane and provides a circular instantaneous field of view of 0.1-mrad. This field aperture consists of a 0.001-inch diameter hole in a titanium-gold evaporated film on a quartz substrate. Quartz was chosen for its excellent resistance to damaging radiation (UV, IR, etc.), titanium for adherence properties, and gold for high reflectivity. Intermittent exposure to focused solar radiation requires such properties.

Radiation collected by the optical system and focused at the field aperture plane passes through this aperture and is spread over the 1-inch diameter photocathode of the photomultiplier tube by a diverging lens. The lens also provides the required blue cutoff filtering because it is made from Corning-type 3-71 filter glass.

The f/2 optical system required the use of an invar structure and fused quartz optical mirror substrates to provide the necessary dimensional stability with temperature. A compensating type of structure could have been used with an associated reduction in weight; however, expected nonuniform thermal gradients and a tight program schedule ruled out this approach.

In operation, the entire camera is constantly exposed to a force of approximately 6 times gravity due to spacecraft rotation. This constant load required that the optics be hard mounted if defocus was to be avoided. Mounting surfaces were carefully lapped to prevent optical surface distortion by the retaining forces.

Tests on the completed telescope to simulate the centrifugal force loading were performed. Loads of several times those predicted produced no detectable change in optical performance.

A diagram of the optical configuration employed is shown in Figure 4. The completed telescope assembly is shown in Figure 5.

MECHANICAL DESIGN

The major mechanical components of the Spin-Scan Cloud Camera are the main housing, the telescope and the precision step mechanism (see Figure 3).

Housing

The housing is a lightweight dip-brazed aluminum structure. It is composed of two halves to provide ease of assembly. Final machining was done with the halves bolted together for accurate location of the mounting surfaces. The two electronics areas are completely accessible from the outside by removal of lightweight protective covers.

Telescope

The telescope consists of a tubular structure made from rolled sheet stock, a spider assembly with secondary mirror holder and a photomultiplier tube housing. All parts are made from Invar with the exception of the aluminum light baffled aperture housing. The telescope housing parts are dip brazed prior to final machining of the mirror mounting surfaces.

Two Bendix flexural pivots support the telescope in the main housing and allow the limited $\pm$ 7.5° telescope motion. The flexural pivots have the advantage that they are bearings with no radial play and do not require lubrication. Any radial play in the telescope bearings would introduce

error in the step scan linearity and step position repeatability. Step position tests on both the prototype and flight model cameras affirm the choice of the flexural pivots.

Step Mechanism

The camera telescope is rotated through 27 seconds of arc about its pivot axis each step. The precision angular step is accomplished in approximately 10 msec (6° of spacecraft rotation). A schematic of the step drive mechanism which is coupled to the telescope to provide the angular motion is shown in Figure 6.

The step drive sequence starts with rotary motion from a 90° stepper motor. The motor has four windings which are energized sequentially by the camera electronics. A 90° rotation of the stepper motor shaft through a 10.4:1 gear reduction to a drive nut produces a 0.0006 inch linear motion along the axis of the 40 thread per inch lead screw. The linear motion of the lead screw is converted to an angular motion of the telescope through a rectangular box structure, drive bands and drive sector arms (see Figure 3).

Several advantages are apparent in the drive concept: 1) the stepper motor provides a high starting torque without additional gear reduction, 2) any step position is repeatable since the motor is always stopped in one of four positions, 3) average power consumption is low because

the motor is electrically off between steps, 4) all bearings are run at very low speed, and 5) the system has very little backlash without the use of antibacklash devices.

The drive mechanism has two electrical limit switches to signal the ends of mechanism travel. Two positive mechanical stops are also provided which act as a backup should the switches fail. If these mechanical stops are encountered, they provide for a nonbinding mechanism stall, and a manual command can be used to perform the limit switch function.

The camera step mechanism is sealed and pressurized to maintain lubrication of all moving parts.

ELECTRONIC DESIGN

The electronic block diagram (Figure 7) illustrates the simplicity of the camera electronics. Four major electronic items shown are: 1) video amplifier, 2) photomultiplier tube, 3) photomultiplier high-voltage power supply, and 4) logic.

The video amplifier has an input for the photomultiplier tube video and one for a sun pulse obtained from a sun sensor on the spacecraft. The amplifier input stage contains a gain adjustment of from 1 to 10 which is set to a specific value at the time of calibration. There are two video output channels with one having a camera signal amplitude

3.16 times (10 db) greater than the other. The sun pulse applied to the camera video appears in both outputs at the same amplitude and opposite in polarity to the video information (video negative going—sun pulse positive going). The camera sun pulse processing circuitry clips approximately 10% of the sun pulse skirt to eliminate camera video distortion due to the sun sensor seeing the earth. This is necessary since the camera and sun sensor are aligned to within a few degrees of each other in azimuth.

The photomultiplier tube is an EMR type 541A-01-14-05600-M-49. This is an end looking, ruggedized, 14-stage type with an S-11 equivalent photocathode. The manufacturer performed a 100-hour burn-in at 5 microamps anode current on each tube prior to delivery. A review of the burn-in data indicated a need for further burn-in. An additional 150 hours showed good tube stabilization. The only change in tube response since burn-in was observed when the flight model was in the dark in the thermal vacuum chamber for about 4 days. The response increased by approximately 10%. Response reduction for the final 150 hours of burn-in was 25% to 40%. Therefore, some recovery (tube gain) was experienced as predicted by the manufacturer. Since average anode current while scanning in space will be well below 1 microamp, excellent tube stability is expected during the life of the camera.

The average photomultiplier tube load on the high voltage supply is determined by the dynode bleeder string resistance. This is approximately 25 microamps and depends on the value of high voltage selected. Momentary direct looks at the sun by the camera will nearly double this value. The tubes have 90 megohms of bleeder string resistance and the high voltage supply is fixed resistor adjustable from 1935 to 2500 volts. A specific high-voltage value was selected for each camera prior to acceptance testing.

The camera logic performs the control functions associated with latitude scanning. These circuits receive camera, spacecraft and ground commands, relay these commands at the proper time and provide telemetry indications of camera command responses. Due to the simplicity of the logic and drive circuits, a detailed description is not included. The electronic design in general is based on simplicity and generous safety margins in component ratings. Also, a careful analysis was made of the logic to ensure that no combination of commands or transient situations could cause logic circuit hang-up.

The simplicity of the over-all design approach is illustrated in Figure 8 which shows the electronics installed in the camera frame. The photomultiplier tube power supply can be seen at the lower left in this photo.

COMMAND AND TELEMETRY DETAILS

The following is a description of ground commands and telemetry outputs which are available.

Camera Commands

1. Normal Scan Command—This command can be initiated at any time but is ideally performed during telescope north-to-south stepping (20 minute period). If this command is given while the camera logic circuits are already in this mode no change of scan mode will occur. When the camera logic is in the Back-to-Back Scan Mode, initiation of the Normal Scan Command will cause a change of scan mode which will be detectable immediately at the telemetry output labeled Scan Mode Indicate as a "0" state. The camera stepping rate will not be altered until the scan direction has been reversed and retrace begins. Retrace will then take place at a 17 Hz stepping rate and will not be synchronized with spacecraft rotation as the down scan was, so no useful video information will be produced.

2. Back-to-Back Scan Command—This command can also be initiated at any time but again is ideally performed during the telescope north-to-south stepping. Again, if this command is given while the camera logic is in this mode, no change of stepping rate will occur. When the camera logic is in the Normal Scan Mode (telemetry indicates a "0" state)

initiation of the Back-to-Back Scan Command will cause a change of scan mode which will be immediately detectable by a change in telemetry scan mode indicate to a "1" state. When the telescope reaches the south end of the frame, retrace will begin at the down scan rate and will remain in synchronism with spacecraft rotation. The video information during retrace, while in the Back-to-Back Scan mode, will be identical to the down scan frame information but will be reversed in time (the south latitude information preceding the north latitude information).

It should be noted that either of the above commands causes the camera logic to lock in and remain indefinitely in that mode until commanded to change or until the camera is turned off.

3. South Override Limit Command—This command is designed to end the north-to-south stepping at any time prior to the telescope reaching the south latitude limit position. If this command is initiated during retrace (south-to-north stepping), the camera logic will not respond. If more than one frame is to be shortened, this command must be sent for each frame. Therefore, some ground timing consisting of step counting is required to make the best use of this command. The telemetry output called "Scan Direction Indicate" will signal a "zero state" during north-to-south scan stepping and a "one state" during south-to-north retrace stepping. The sampling rate of this telemetry channel is such

that a maximum error of five lines is possible and this therefore must be considered in the ground timing.

4. North Override Limit Command—This override command is identical with the south override limit command except that it is intended to end retrace stepping at some time prior to the telescope reaching the north latitude limit position. The combination of the two override commands allows for more rapid frames of shorter latitude dimension to study specific earth areas.

Telemetry Data

1. Scan Mode Indicate—As mentioned above, this telemetry channel will have the following output indications:

   a. "0" state for the Normal Scan Mode

   b. "1" state for the Back-to-Back Scan Mode

2. Scan Direction Indicate—The following outputs will occur:

   a. "0" state for north-to-south scan stepping

   b. "1" state for south-to-north scan stepping or retrace

   Maximum indication error from the 3-second access encoder will be five scan lines for each change of state when the camera is in the Back-to-Back Mode.

3. Telescope Temperature—The temperature of the forward and aft end of the optical telescope is available on two telemetry channels. These two locations were chosen to monitor the differential temperature expected

due to the telescope interior exposure to cold space. The telescope is designed to operate with a relatively large thermal gradient between optical elements but actual thermal data could be very useful for future lightweight designs. Temperature Monitor No. 1 is located on the telescope near the primary mirror and Monitor No. 2 is located at the forward end of the telescope housing near the secondary mirror.

4. Camera Input Voltage—The camera input voltage from the experiment supply voltage regulator is available in one analog channel of the telemetry. A voltage of -3.41 volts at this output represents -24.0 volts at the spacecraft regulator input to the camera. Any change in this output therefore represents a change in the regulator output by this ratio.

5. Pressure Switch Monitor—A pressure switch is used to monitor the internal nitrogen pressure of the camera step mechanism housing. The housing is sealed to prevent failure due to loss of lubrication. Initial pressurization is 2 atmospheres absolute. A drop of approximately 10 psi will cause the switch to open. An analog telemetry channel indicates normal pressure when the output is 0 volts and -4.2 volts is an indication of pressure loss. This information is useful for verifying mechanism life expectancy. A step mechanism life expectancy prediction based on the initial pressure and the elapsed time to the switch opening was made. The minimum operating life in orbit is expected to be 2.5 years.

TEST RESULTS

Four important performance parameters, latitude step scan linearity, optical resolution, input-output linearity and dynamic range emphasize the major advantage of the spin-scan camera concept to other comparable electronic camera systems. The last two performance parameters are covered in detail in Chapter VI-21 (Calibration).

The latitude or step scan linearity measurements were made by viewing the pin-hole aperture with a theodolite at various step positions throughout the frame. Results show the step scan linearity to be within $\pm$ one step of a true linear step scan at any point within the 2017 step frame. Additionally the results of many measurements indicated the step position repeatability to be better than one-quarter of a step at any position in the frame. Since a latitude step is 2.7 nautical miles at the nadir, step scan position repeatability can be stated as approximately 0.7 nautical mile.

The optical resolution of the SSCC was measured by Modulation Transfer Function (MTF) techniques. A test calibrator which projected moving, closely spaced light and dark bars on the aperture plate of the camera verified the optical resolution. The bar pattern was such that the bar widths varied from many times wider to many times narrower than the pin-hole aperture. Acceptance criteria was that the SSCC output modulation amplitude for a bar width equal to the aperture size

be 50% or more of the amplitude from the very wide bar. Optical resolution is thus conservatively stated and could be referred to as "low contrast optical resolution."

Figure 9 is an attempt to use the MTF test data to construct the shape of the SSCC instantaneous field-of-view (IFOV). Results of the ATS-1 flight have shown the optical resolution test that was used to be accurate and sufficient.

Figure 10 is a plot of the SSCC relative spectral response. Table II is the tabulated data of Figure 10. Camera output response to a composite source which is defined by the camera field of view and which produces a known spectral irradiance $H(\lambda)$ at the camera entrance aperture can be predicted as follows:

Given: $H(\lambda)$ = spectral irradiance in watts cm^{-2} nm^{-1} at camera entrance aperture.

$$P_{eff} = A \int_0^{\infty} H(\lambda)R(\lambda)d\lambda$$

Where: P_{eff} = effective input power in watts at camera entrance aperture

A = area of entrance aperture = 104 cm^2

$R(\lambda)$ = relative spectral response of camera (Figure 10)

Then: Locate the output (millivolts) for corresponding P_{eff} on Figure 11. This provides the photomultiplier tube output

and must be multiplied by 2.62 or 8.25 to give the camera electronic output for Channel 1 and 2 respectively.

For more detailed information regarding calculation of camera output refer to other chapters of this volume.

ILLUSTRATIONS

LIST OF FIGURES

Figure 1. ATS-I Spin Scan Cloud Camera, Flight Model F-1.

Figure 2. An artist's concept of the Spin-Scan principle.

Figure 3. Cut-away drawing of the ATS-I Spin-Scan Cloud Camera.

Figure 4. ATS-I Spin-Scan Cloud Camera optical configuration.

Figure 5. ATS-I Spin-Scan Cloud Camera optical telescope assembly.

Figure 6. Schematic of ATS-I Spin-Scan Cloud Camera precision step drive mechanism.

Figure 7. Block diagram of the ATS-I Spin-Scan Cloud Camera electronics.

Figure 8. View of electronics installed in the Spin-Scan Cloud Camera

Figure 9. Probable shape of the field of view of the Spin-Scan Cloud Camera derived from test data.

Figure 10. Overall Relative Spectral Response of the ATS-I Spin-Scan Cloud Camera.

Figure 11. ATS-I Spin-Scan Cloud Camera Photomultiplier System Signal and Noise Output Voltage as a Function of Effective Radiant Input Power, P_{eff}.

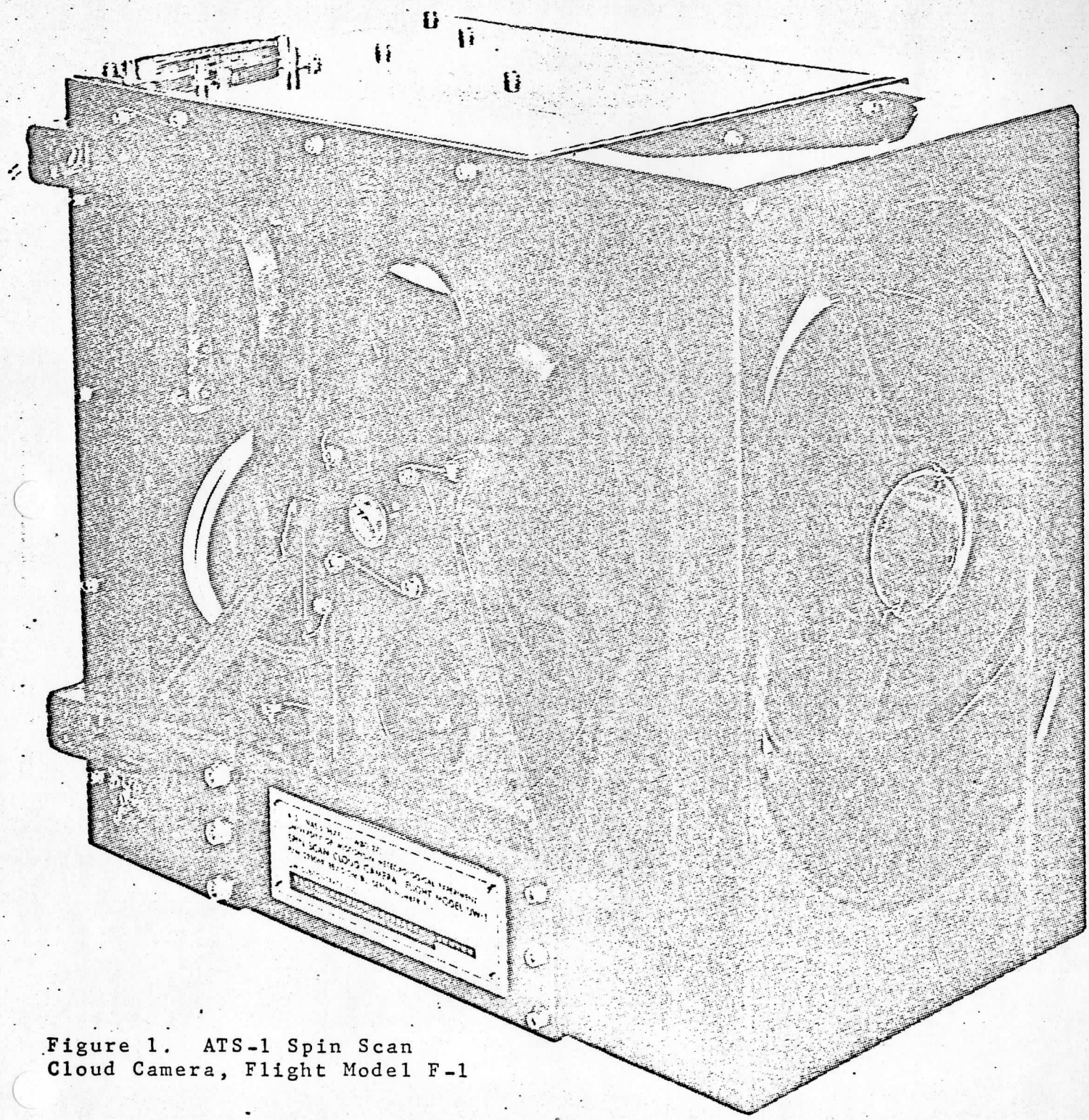

Figure 1. ATS-1 Spin Scan Cloud Camera, Flight Model F-1

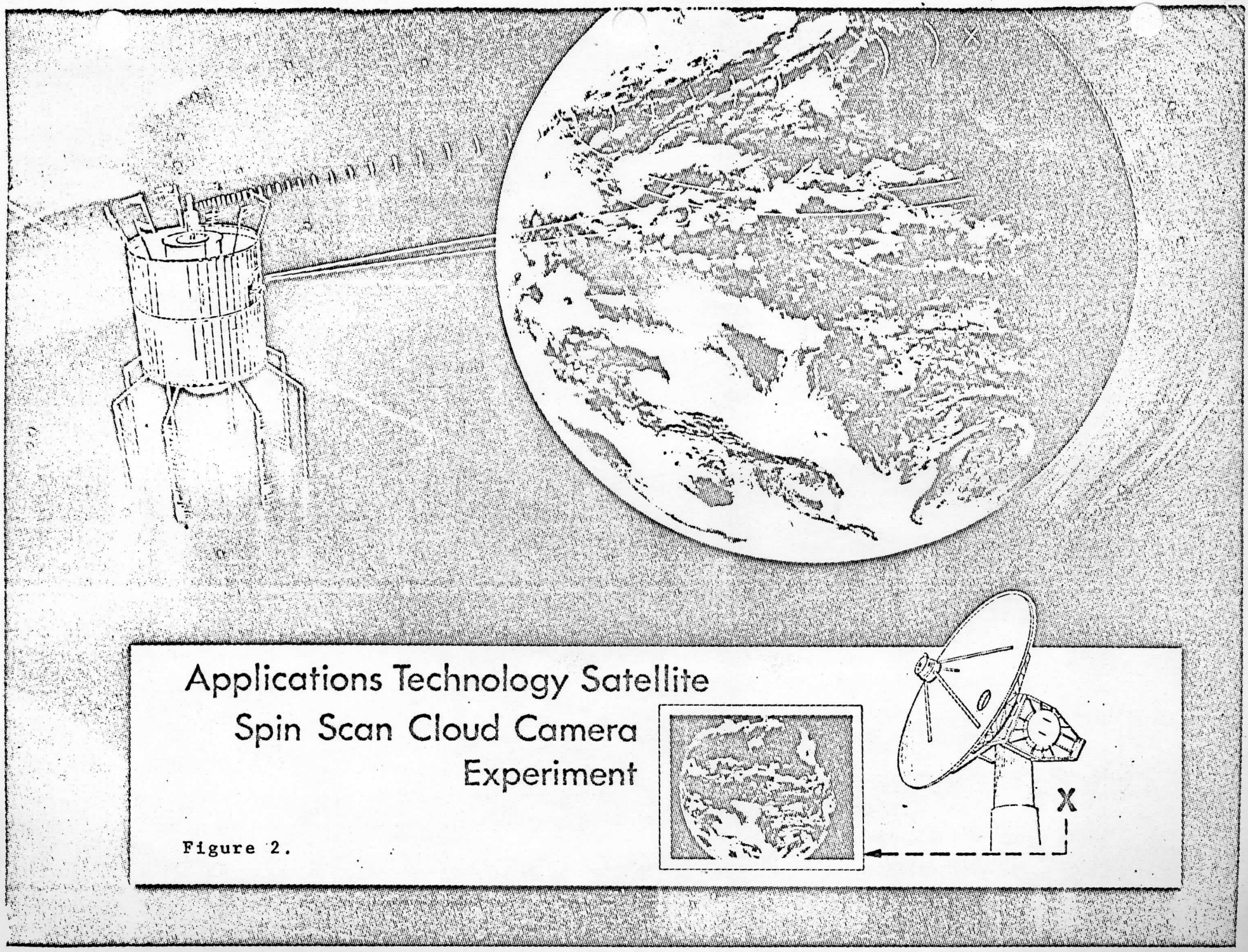
Applications Technology Satellite
Spin Scan Cloud Camera
Experiment
X

Figure 2.

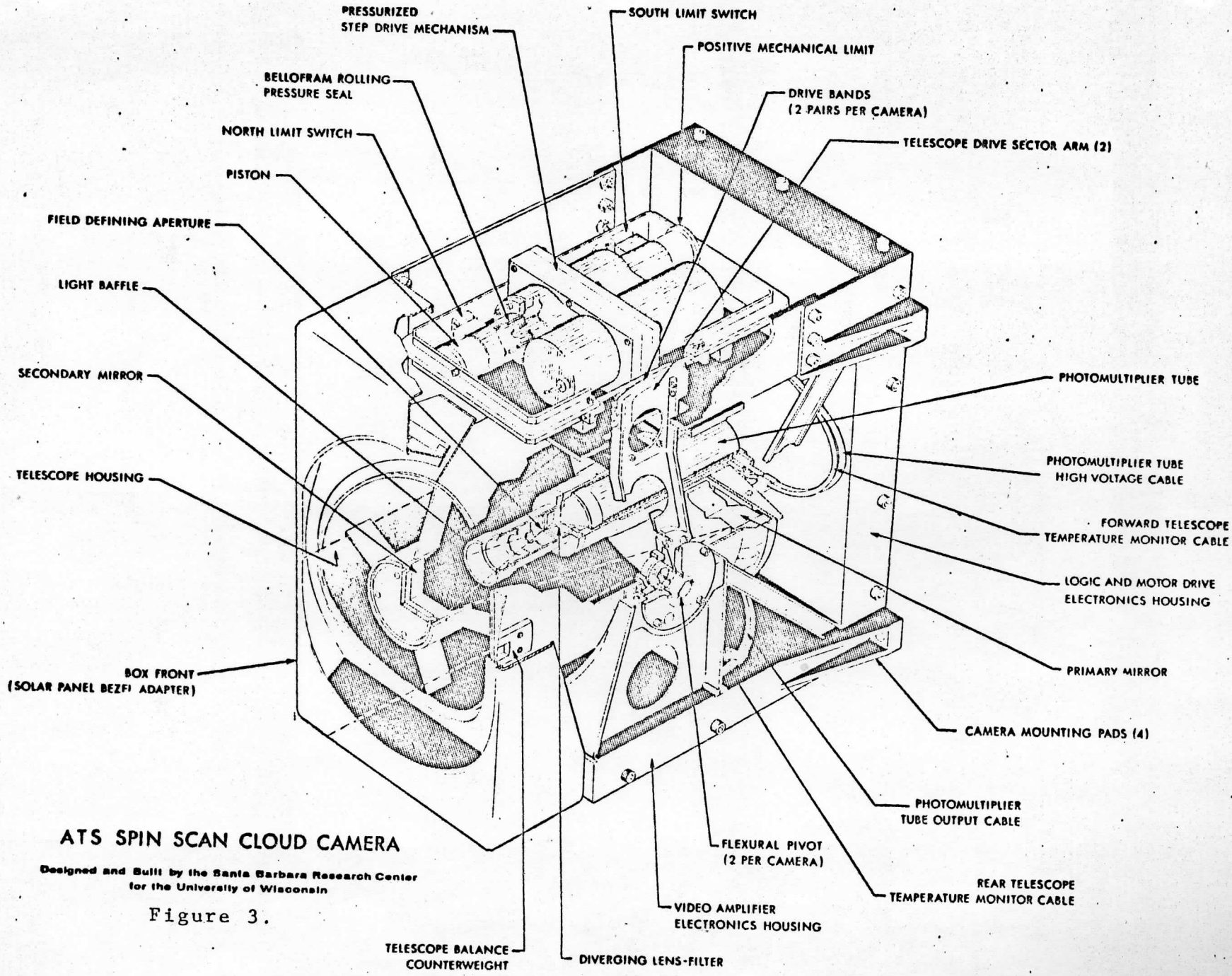

ATS SPIN SCAN CLOUD CAMERA

Designed and Built by the Santa Barbara Research Center for the University of Wisconsin

Figure 3.

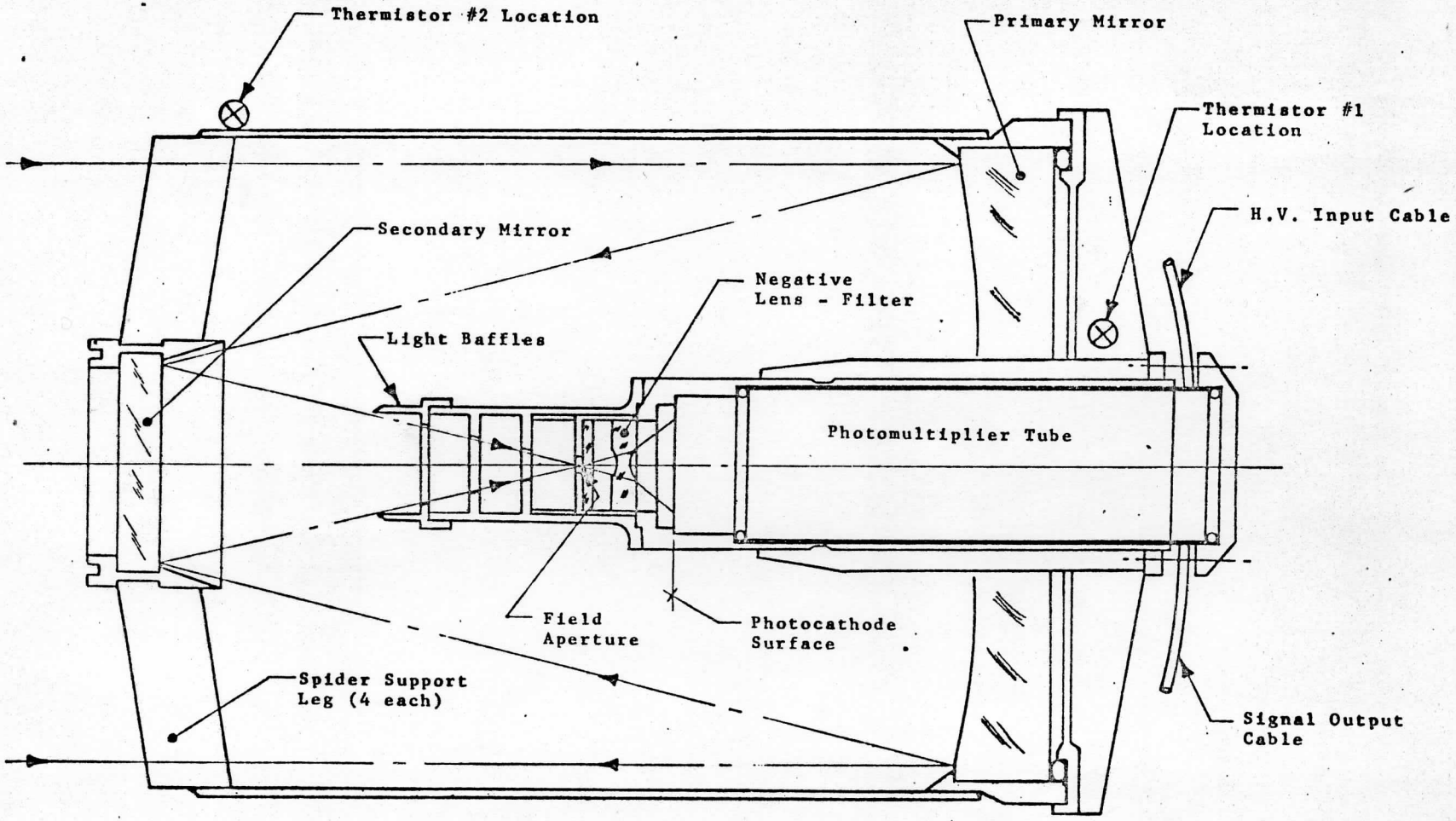

Figure 4. ATS Spin-Scan Cloud Camera Optical Configuration

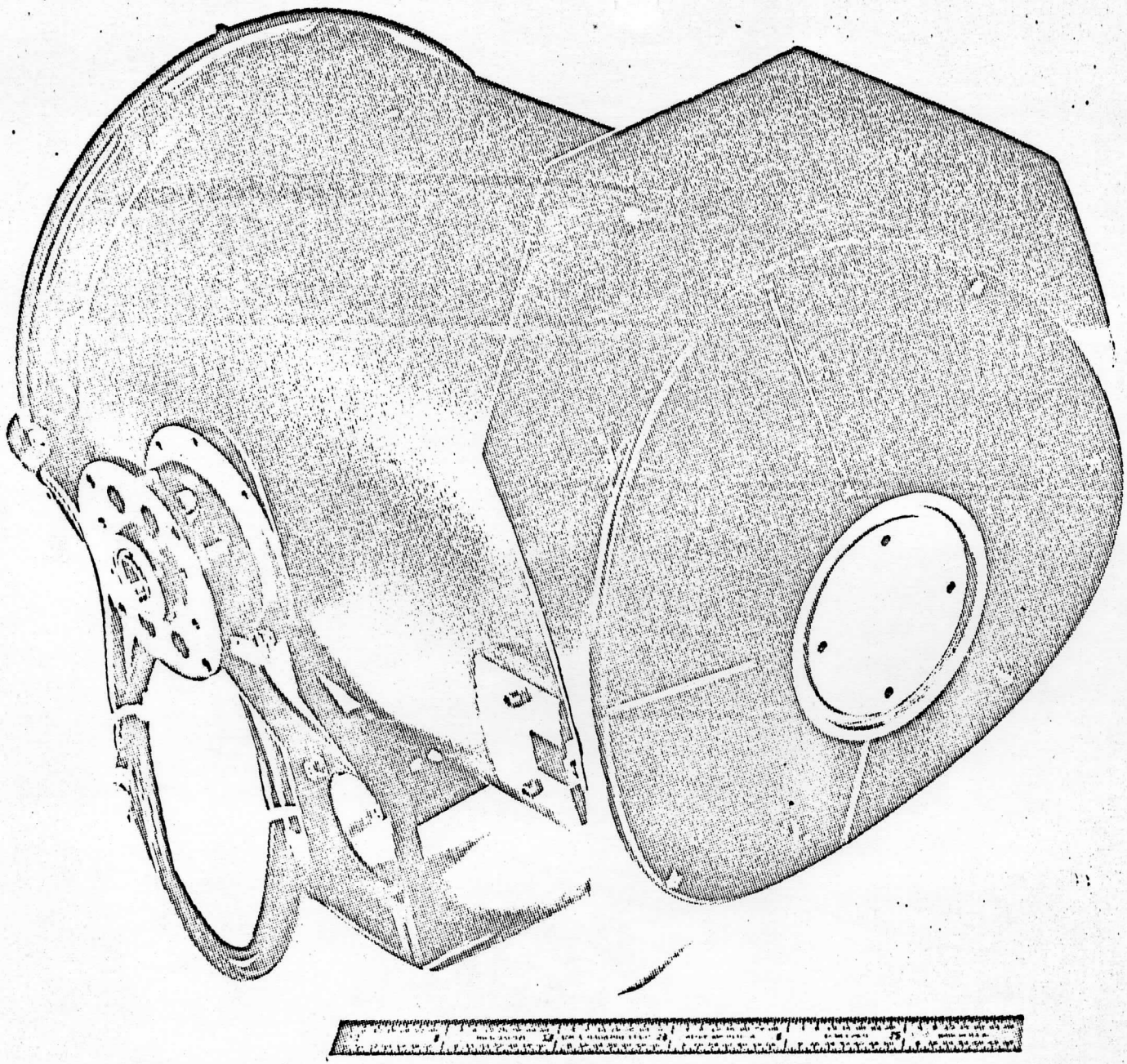

Figure 5. ATS-1 Spin Scan Cloud Camera Optical Telescope Assembly

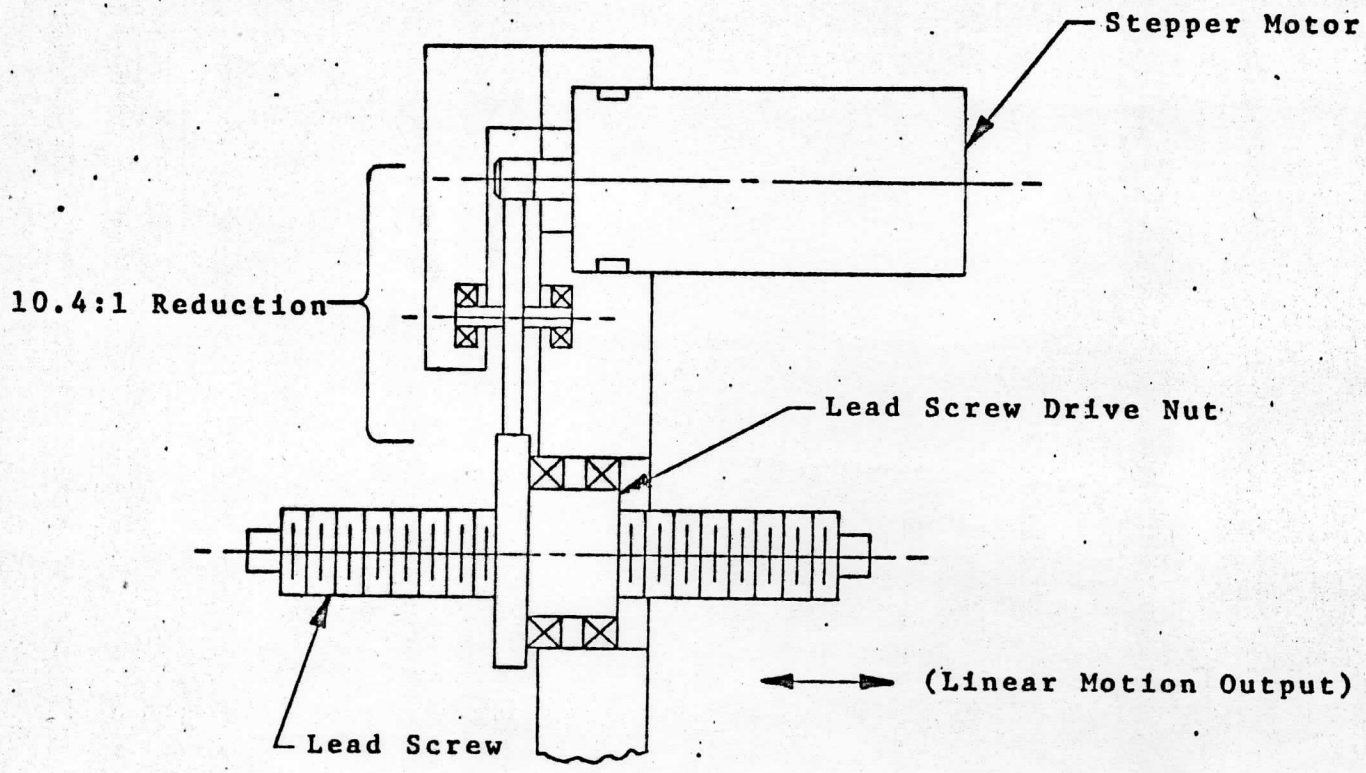

1. 90° Step Motor rotation per step pulse
2. 10.4:1 reduction to lead screw nut
3. 0.025 inch linear travel per revolution of lead screw nut

$$90°/\text{pulse} \times \frac{1}{10.4} \times 0.025 \text{ inch}/360° \text{ rotation}$$

$$= \frac{0.025}{41.6} - 0.0006 \text{ inch/pulse linear travel}$$

Figure 6. Schematic of ATS-I Spin-Scan Cloud Camera precision step drive mechanism

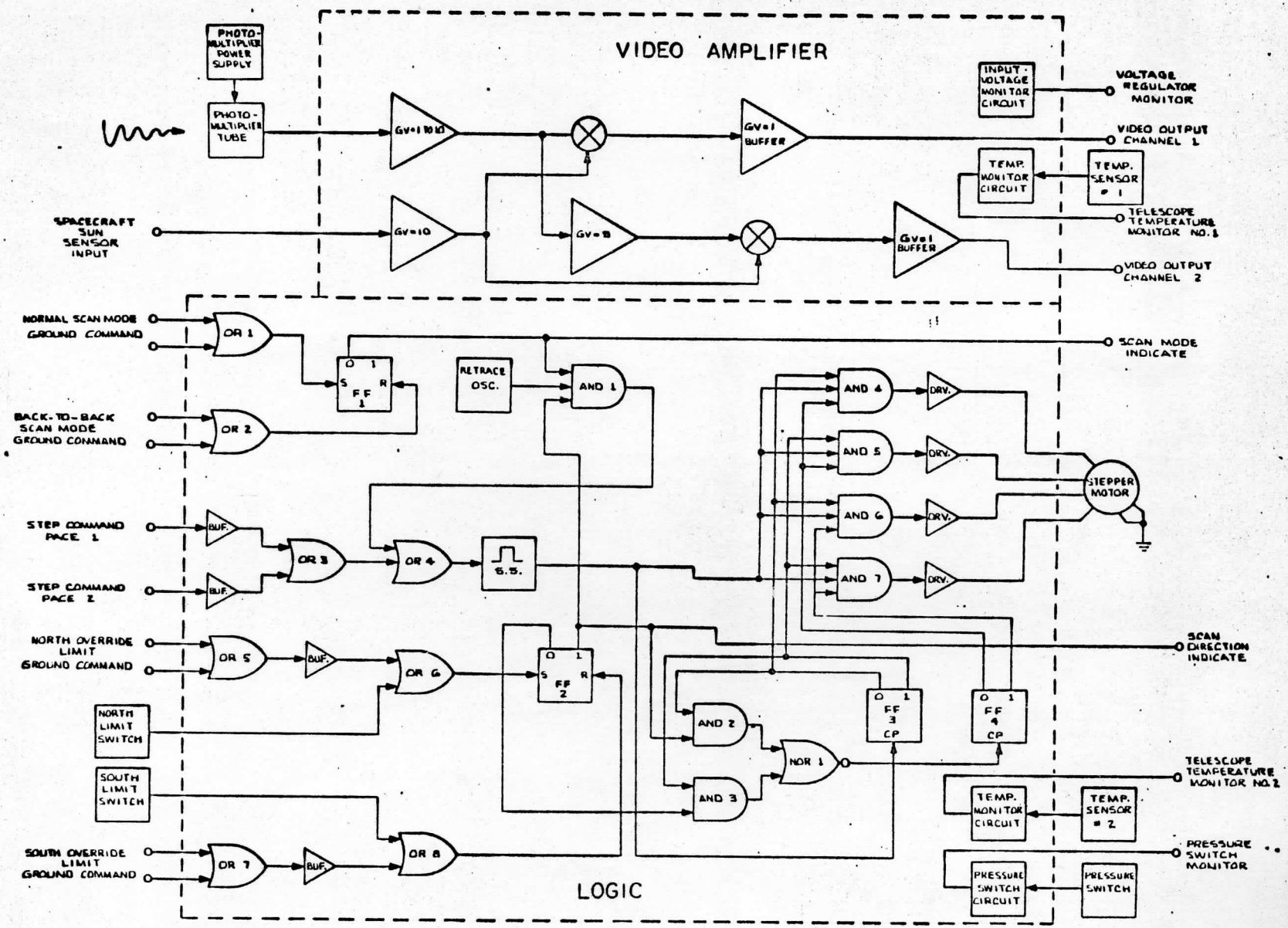

Figure 7. Block diagram of the ATS-I Spin-Scan Cloud Camera electronics

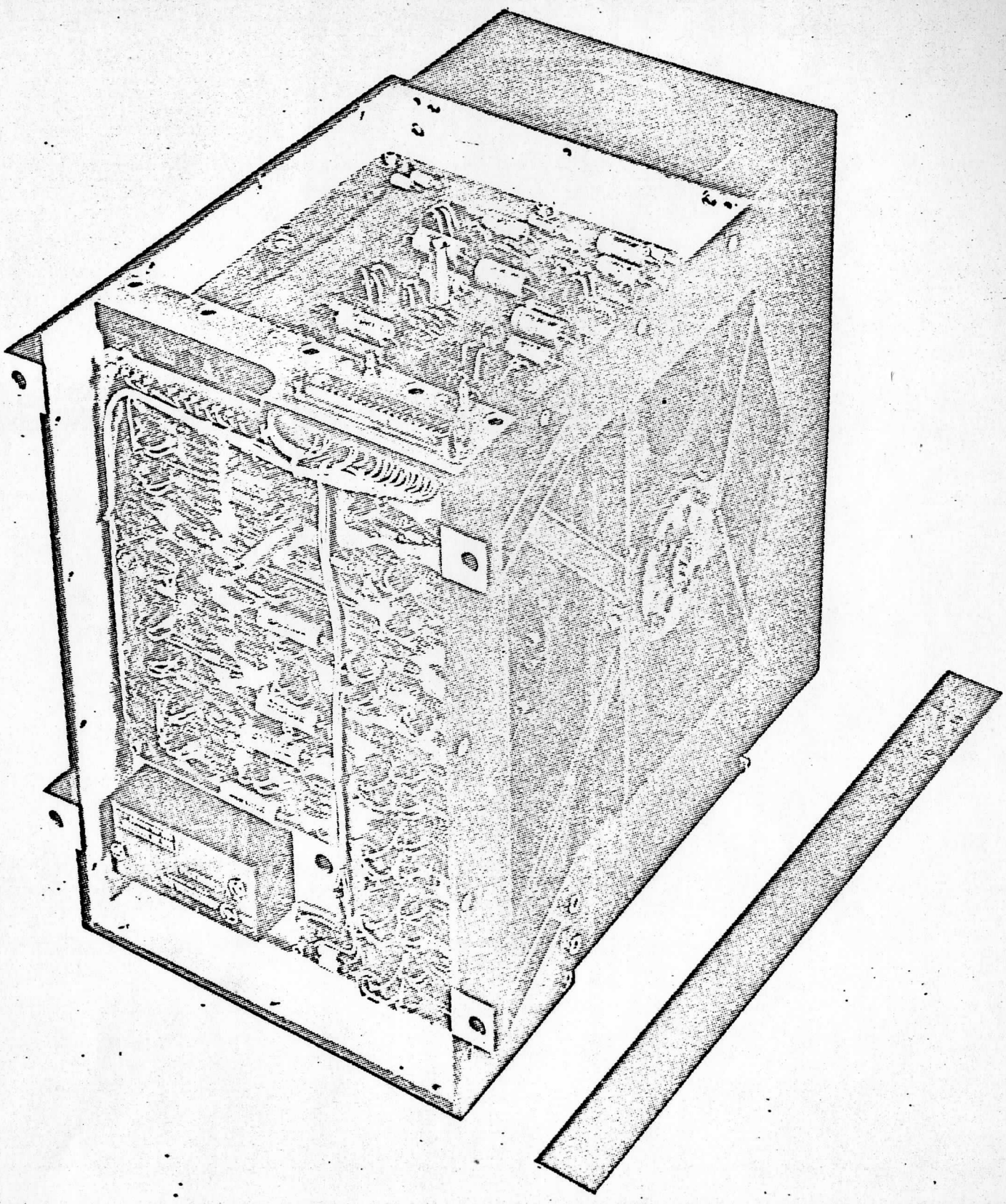

Figure 8. View of electronics installed in the Spin-Scan Cloud Camera

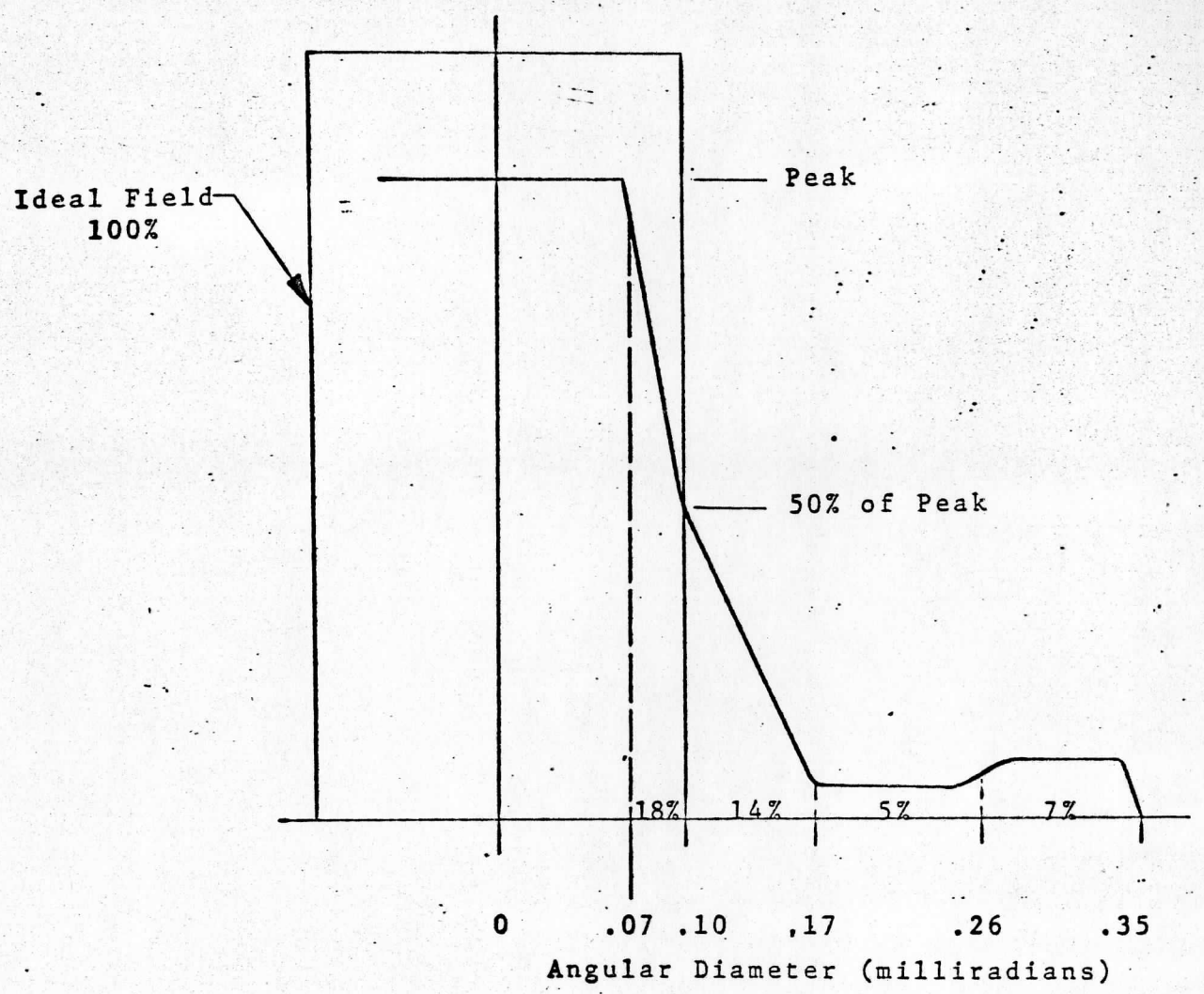

Figure 9. Probable shape of the field of view of the Spin-Scan Cloud Camera

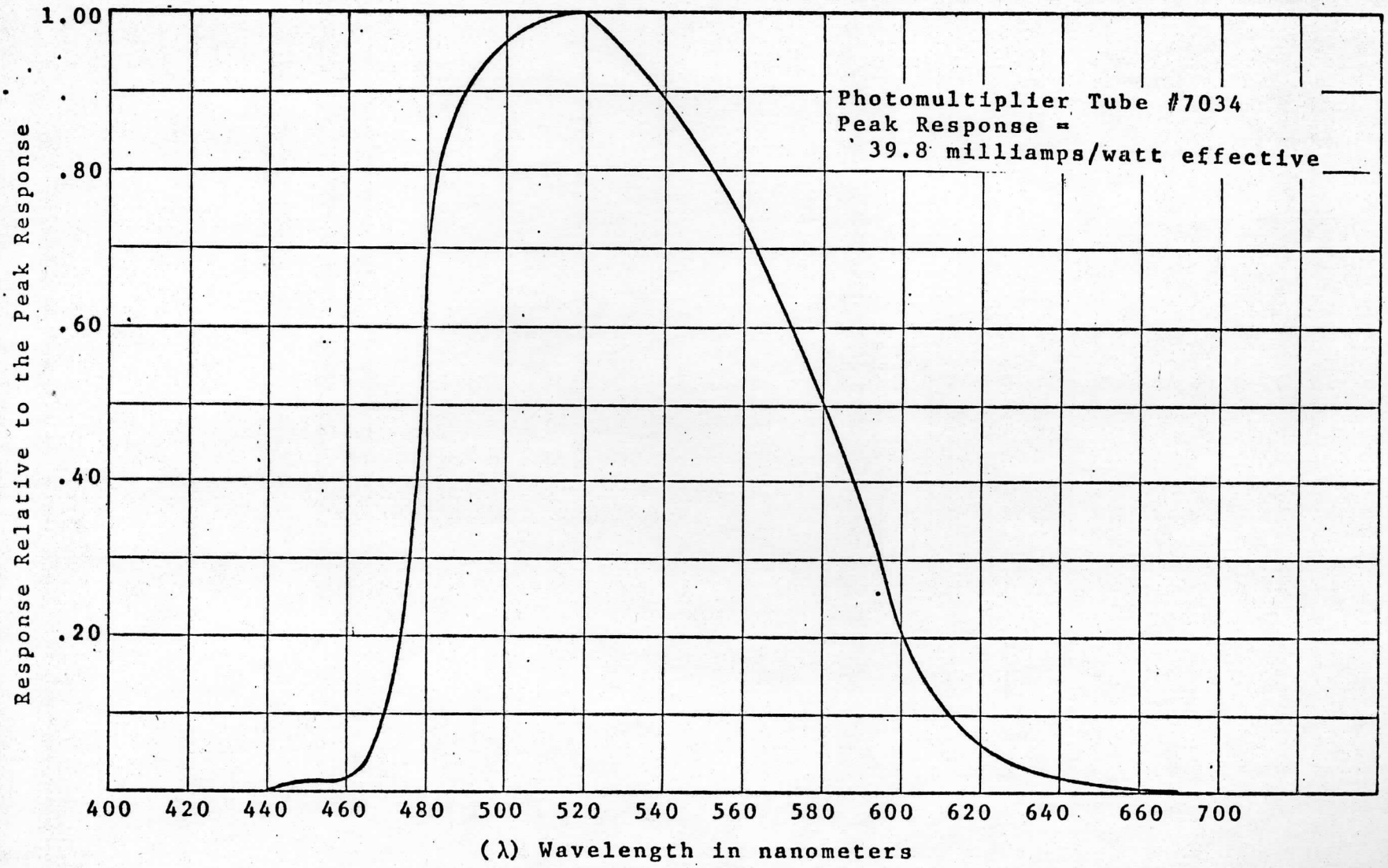

Figure 10. Overall Relative Spectral Response of the ATS-I Spin-Scan Cloud Camera

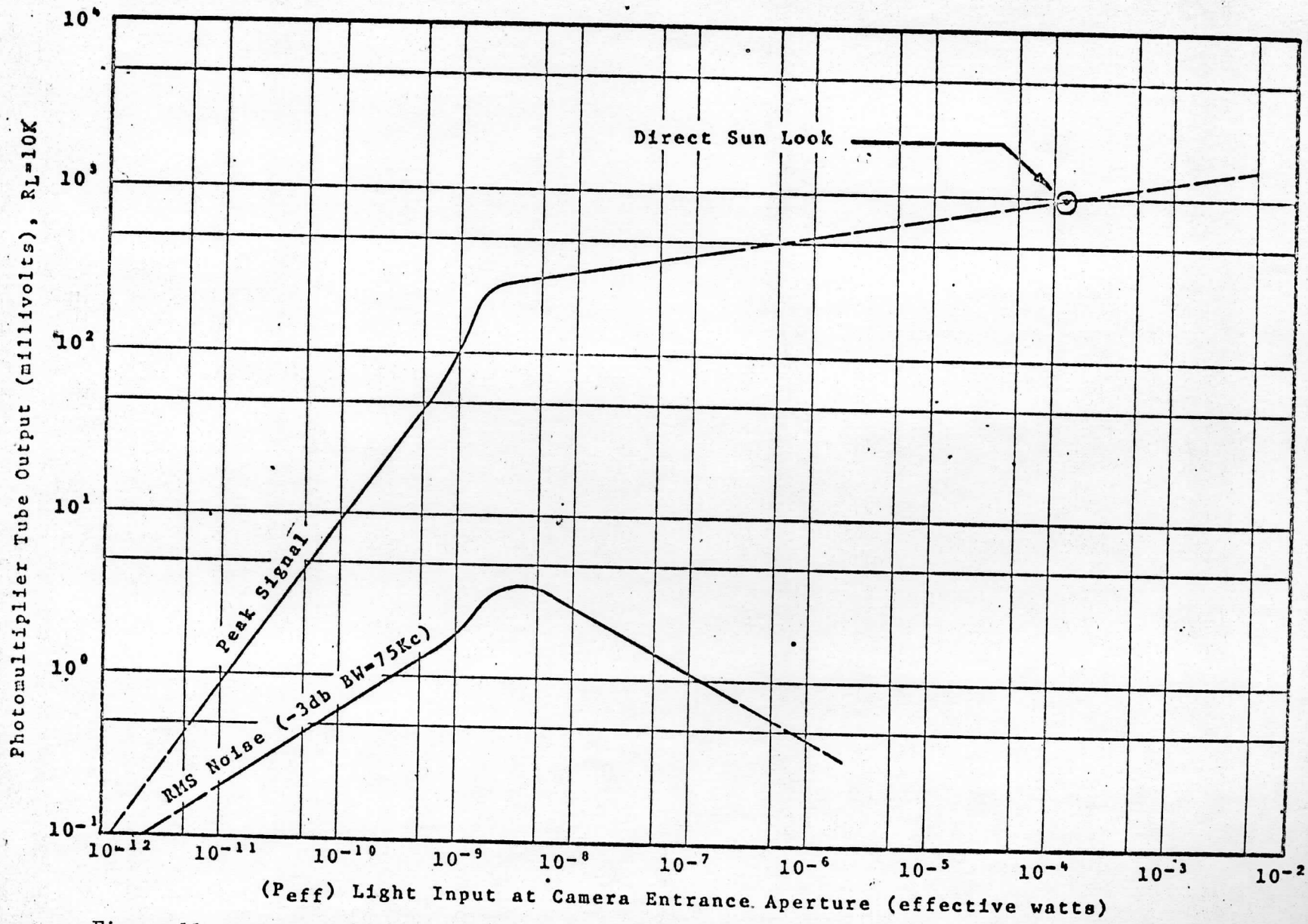

Figure 11. ATS-I Spin-Scan Cloud Camera Photomultiplier System Signal and Noise Output Voltage as a Function of Effective Radiant Input Power, P_{eff}.

LIST OF TABLES

Table 1. ATS Spin-Scan Cloud Camera Specifications.

Table 2. Relative Response as a Function of Wavelength SSCC F-1 (Tube 7034).

TABLE 1

Optical System	
Type	Two-element reflective
Primary mirror	5-inch diameter paraboloid, 10-inch focal length
Secondary mirror	2-inch diameter, flat
Instantaneous field of view	0.1 ± 0.02 mrad diameter (1/2 power points)
Field stop diameter	0.001 ± 0.0001 inch
Mirror substrate material	Fused quartz
Spectral bandpass	4750Å to 5800Å (defined by optical filter and photocathode) (see Fig. 10)
Photomultiplier	
Type	EMR Model 541A-01-14
Photocathode	S-11 type surface, 1-inch diameter
Scan System	
Line scan	Spacecraft rotation, 100 rpm nominal
Latitude or step scan (15° total)	Camera step provided by sealed mechanical drive (one step per line)
Lines per frame	2000 ± 50 lines
Frame time	20 minutes (100 rpm SC spin rate)
Vertical retrace time	Approximately 2 minutes
Dwell period (time for instantaneous field to scan a point source)	9.6 μsec (100 rpm SC spin rate)

Table 1 continued

Electronics	
Voltage gain (video amplifier)	1-10 (fixed resistor adjustable) (set at 2.62)
Gain stability 0° C to 50° C	± 5%
Dynamic range	≥ 1000/1 (video amplifier)
Linearity	± 2% over dynamic range specified
Electronic upper frequency cutoff	100 kHz (-1 db)
Electronic lower frequency cutoff	0.1 Hz (-3 db)
Signal output	1 volt p-p (nominal), 75 ohms. Two outputs provided. Channel No. 2 provides a camera signal 10 db higher voltage swing than Channel No. 1.
Sun pulse input	An input is provided for connection to a spacecraft sun sensor. A 200-400 mv positive sun pulse at this input is added to the camera video and appears in both camera outputs in the opposite polarity as the video.
Size	10 × 11 × 7 inches
Weight	15.5 lb.
Power (maximum)	-24 vdc, < 1 amp

TABLE 2

Wavelength λ (nm)	Relative Response
440	0.000
450	0.013
460	0.128
470	0.116
480	0.644
490	0.898
500	0.961
510	0.992
520	1.000
530	0.938
540	0.888
550	0.813
560	0.719
570	0.624
580	0.505
590	0.365
600	0.212
610	0.124
620	0.063
630	0.030
640	0.022
650	0.015
660	0.007
670	0.003
680	0.000

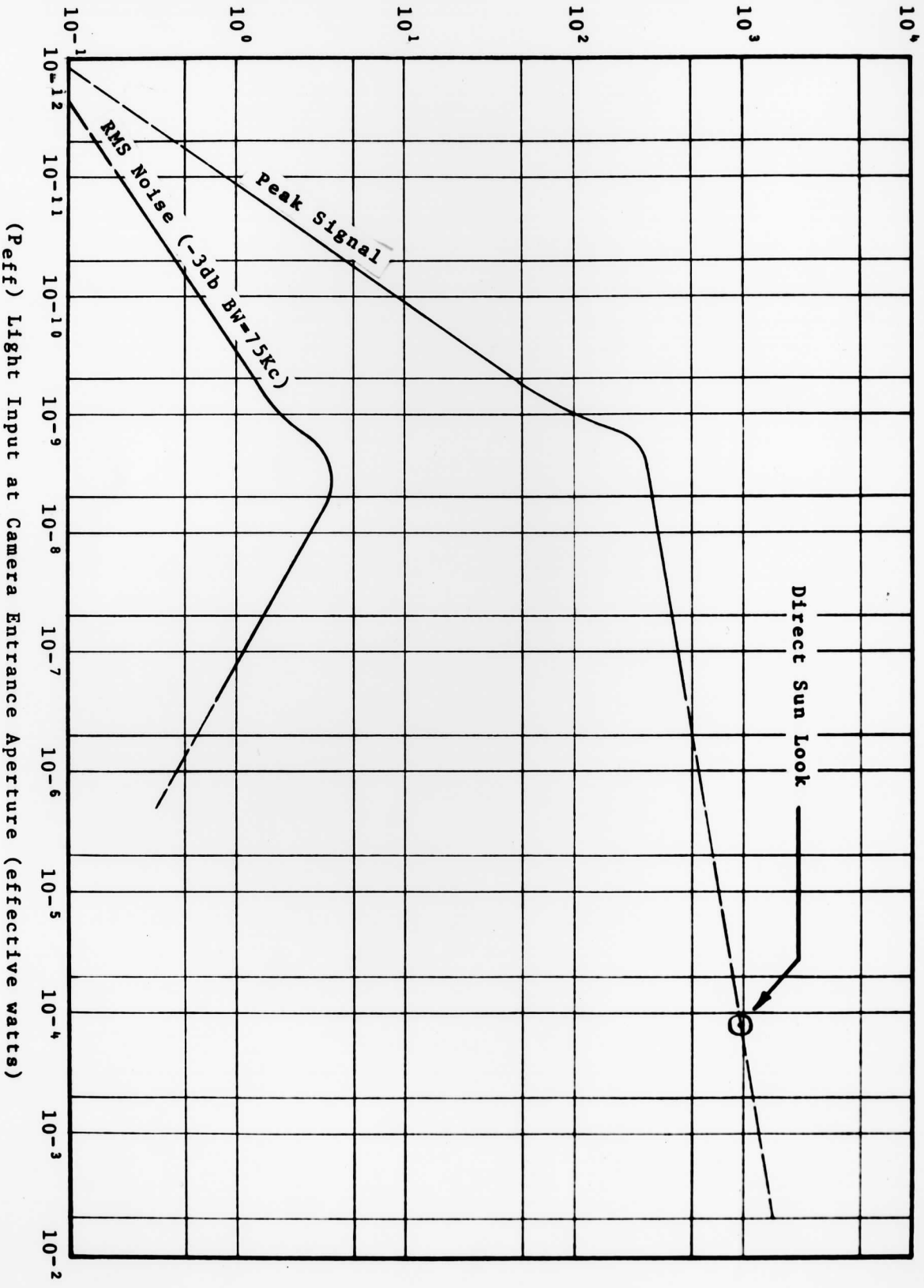
Photomultiplier Tube Output (millivolts), R_L=10K
10^{-1}
10^{0}
10^{1}
10^{2}
10^{3}
10^{4}
10^{-12}
10^{-11}
10^{-10}
10^{-9}
10^{-8}
10^{-7}
10^{-6}
10^{-5}
10^{-4}
10^{-3}
10^{-2}
Peak Signal
RMS Noise (-3db BW=75Kc)
Direct Sun Look
(Peff) Light Input at Camera Entrance Aperture (effective watts)

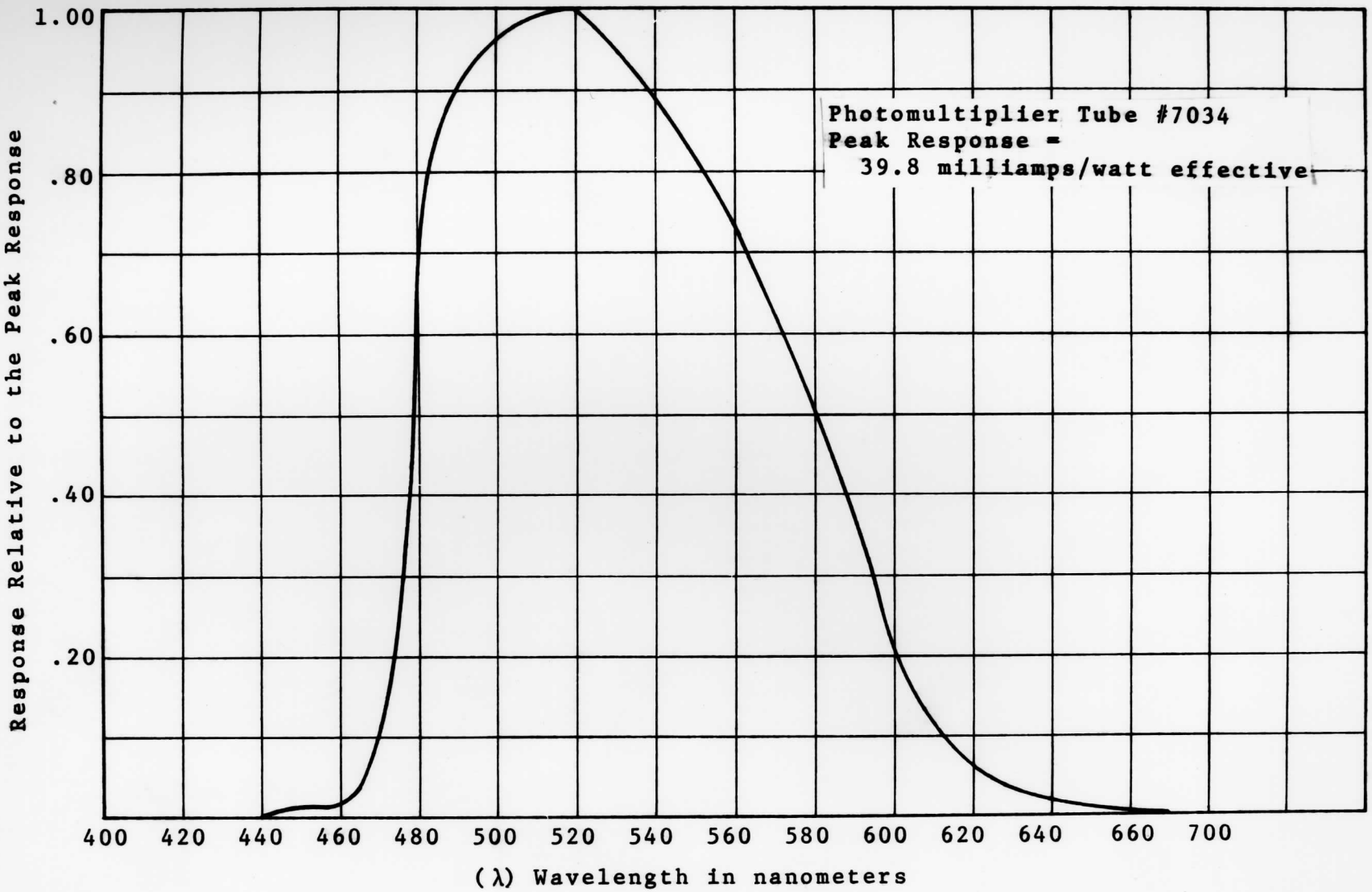
Photomultiplier Tube #7034
Peak Response =
39.8 milliamps/watt effective
Response Relative to the Peak Response
1.00
.80
.60
.40
.20
400
420
440
460
480
500
520
540
560
580
600
620
640
660
700
(λ) Wavelength in nanometers

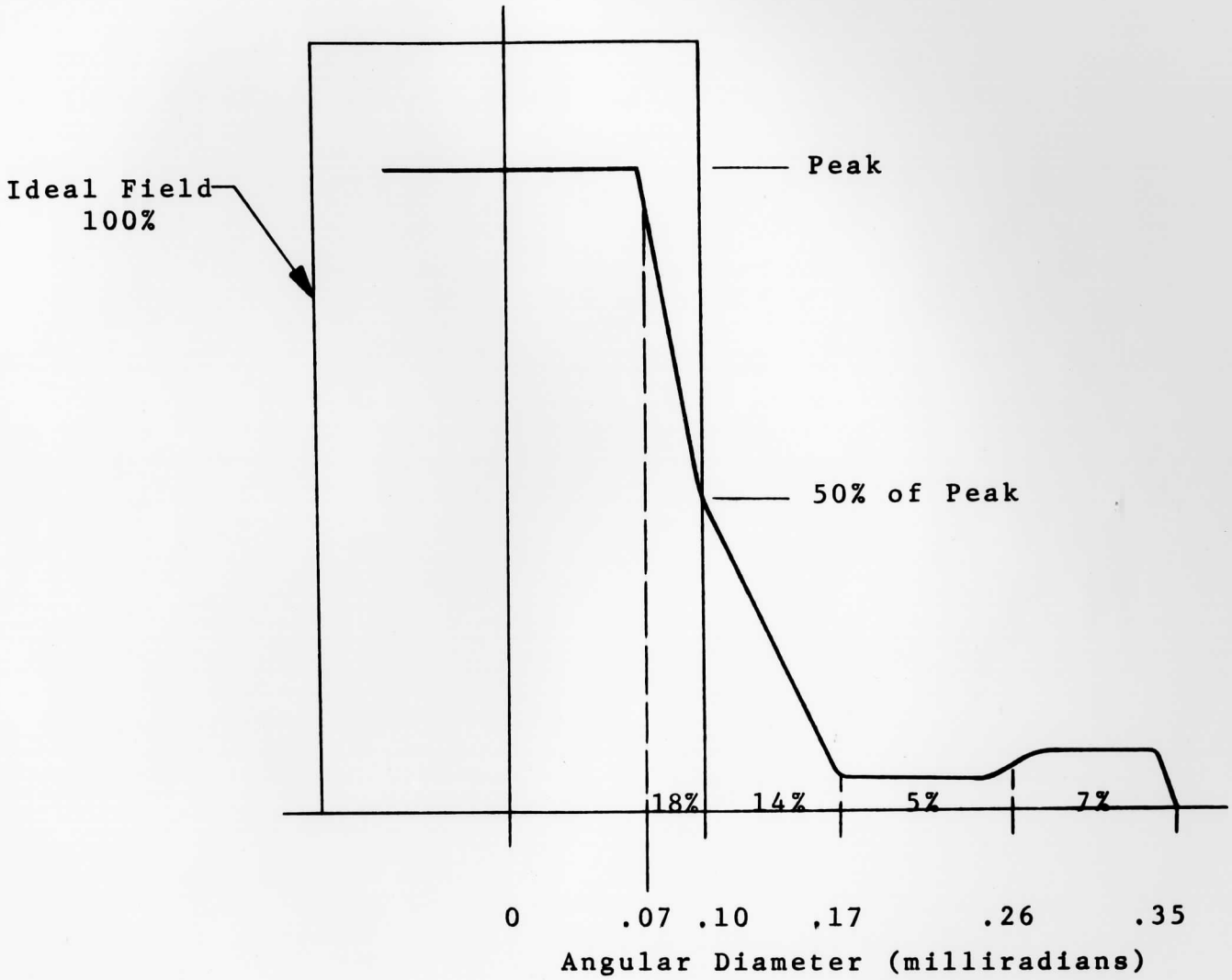
Ideal Field
100%
Peak
50% of Peak
18%
14%
5%
7%
0
.07
.10
.17
.26
.35
Angular Diameter (milliradians)

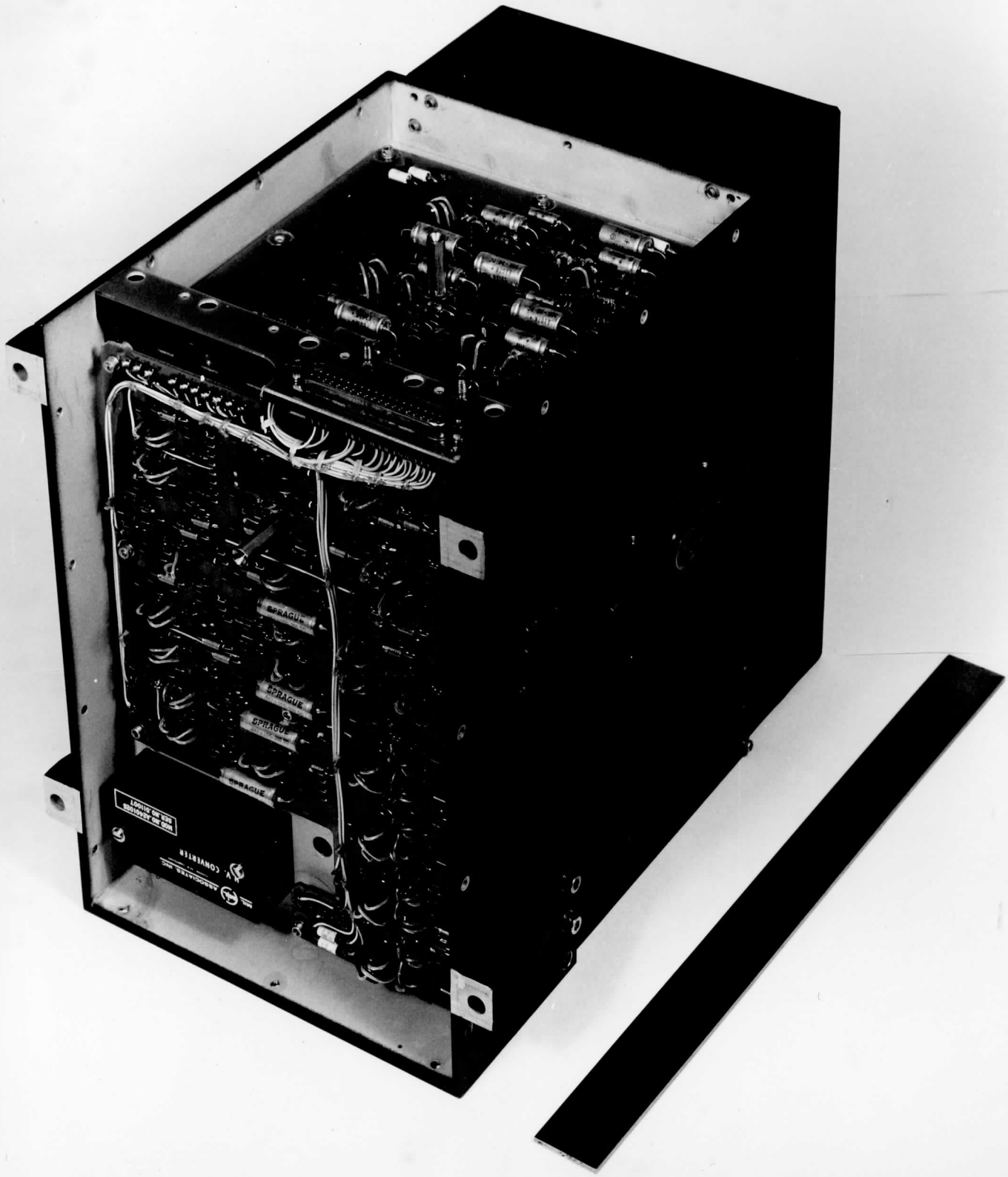
SPRAGUE
SPRAGUE
SPRAGUE
SPRAGUE

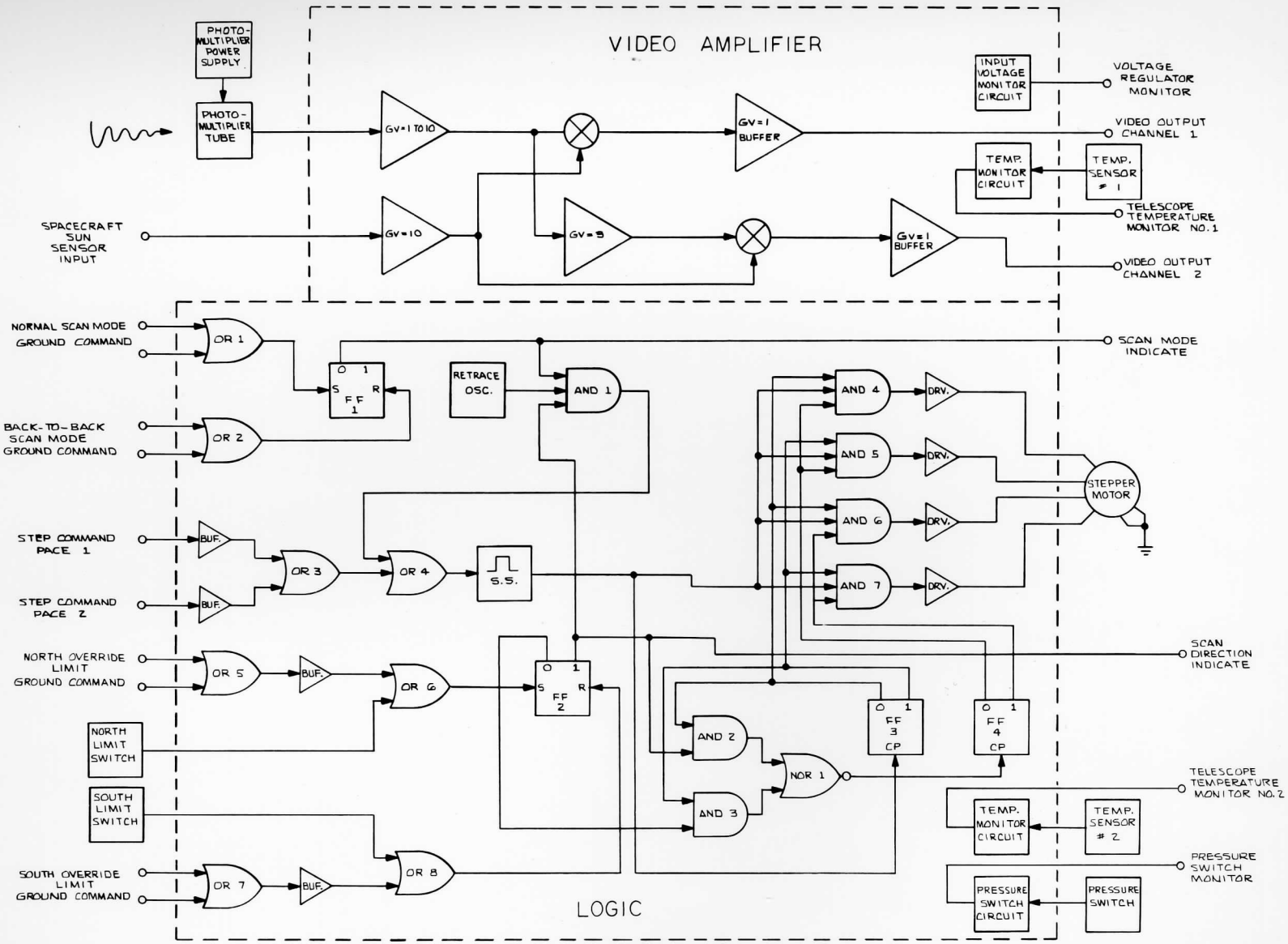

ELECTRONIC BLOCK DIAGRAM

SPIN-SCAN CLOUD CAMERA

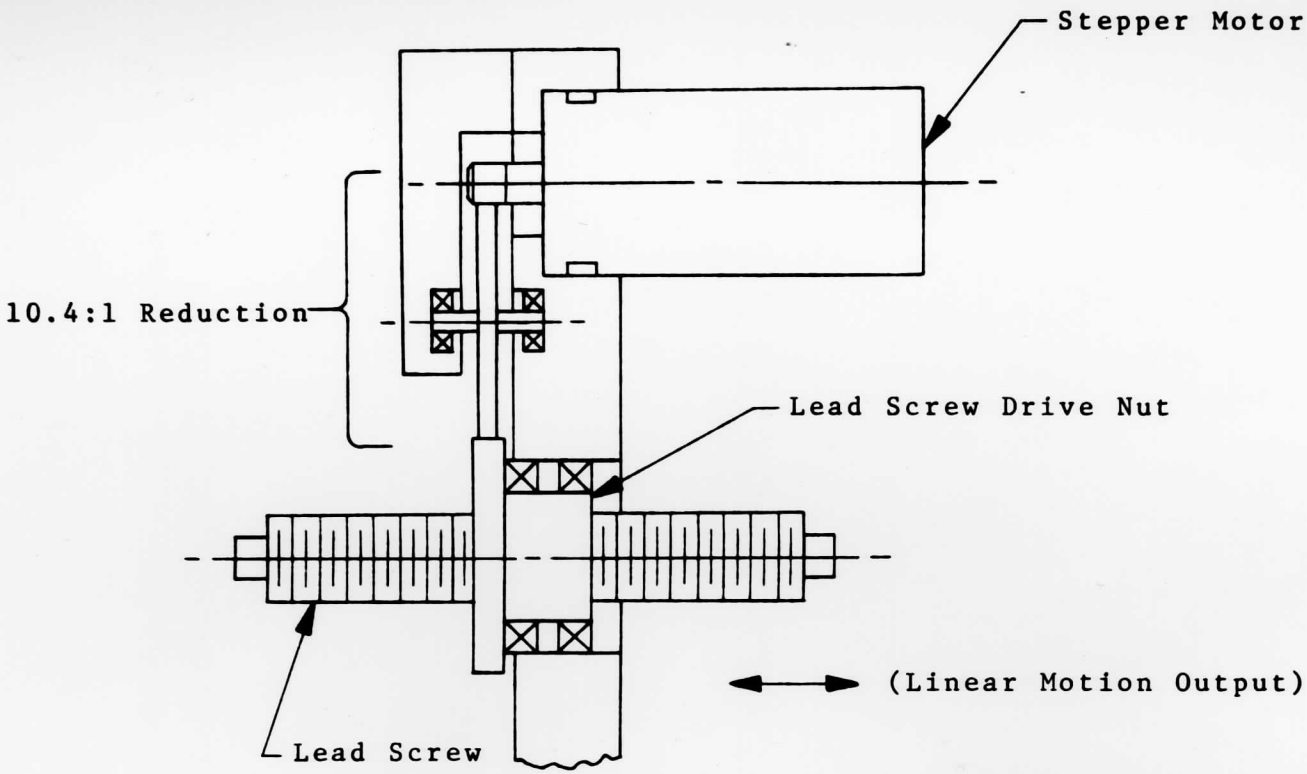

1. 90° Step Motor rotation per step pulse
2. 10.4:1 reduction to lead screw nut
3. 0.025 inch linear travel per revolution of lead screw nut

$$90°/\text{pulse} \times \frac{1}{10.4} \times 0.025 \text{ inch}/360° \text{ rotation}$$

$$= \frac{0.025}{41.6} - 0.0006 \text{ inch/pulse linear travel}$$

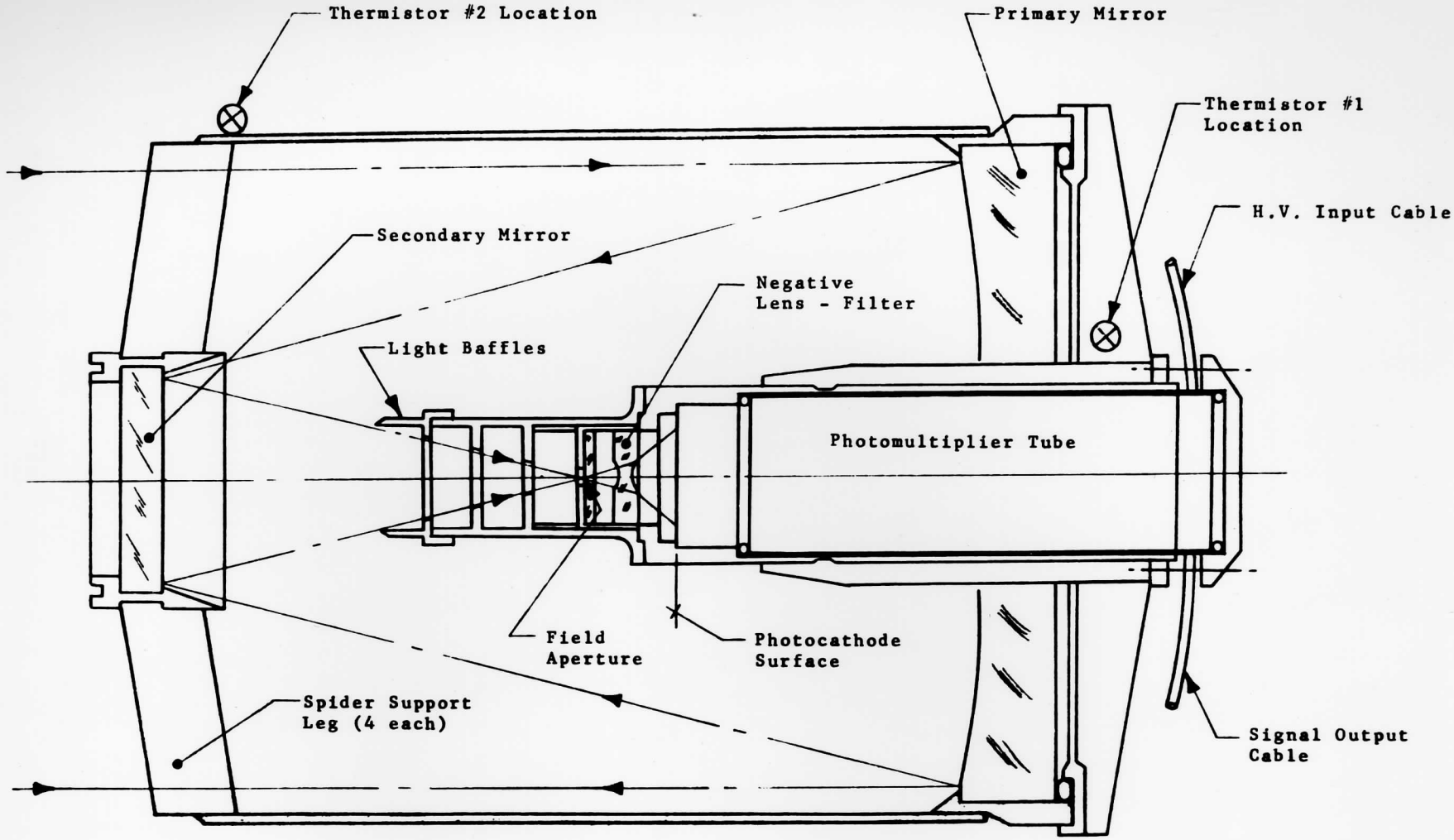
Thermistor #2 Location
Primary Mirror
Thermistor #1 Location
H.V. Input Cable
Secondary Mirror
Negative Lens - Filter
Light Baffles
Photomultiplier Tube
Field Aperture
Photocathode Surface
Spider Support Leg (4 each)
Signal Output Cable

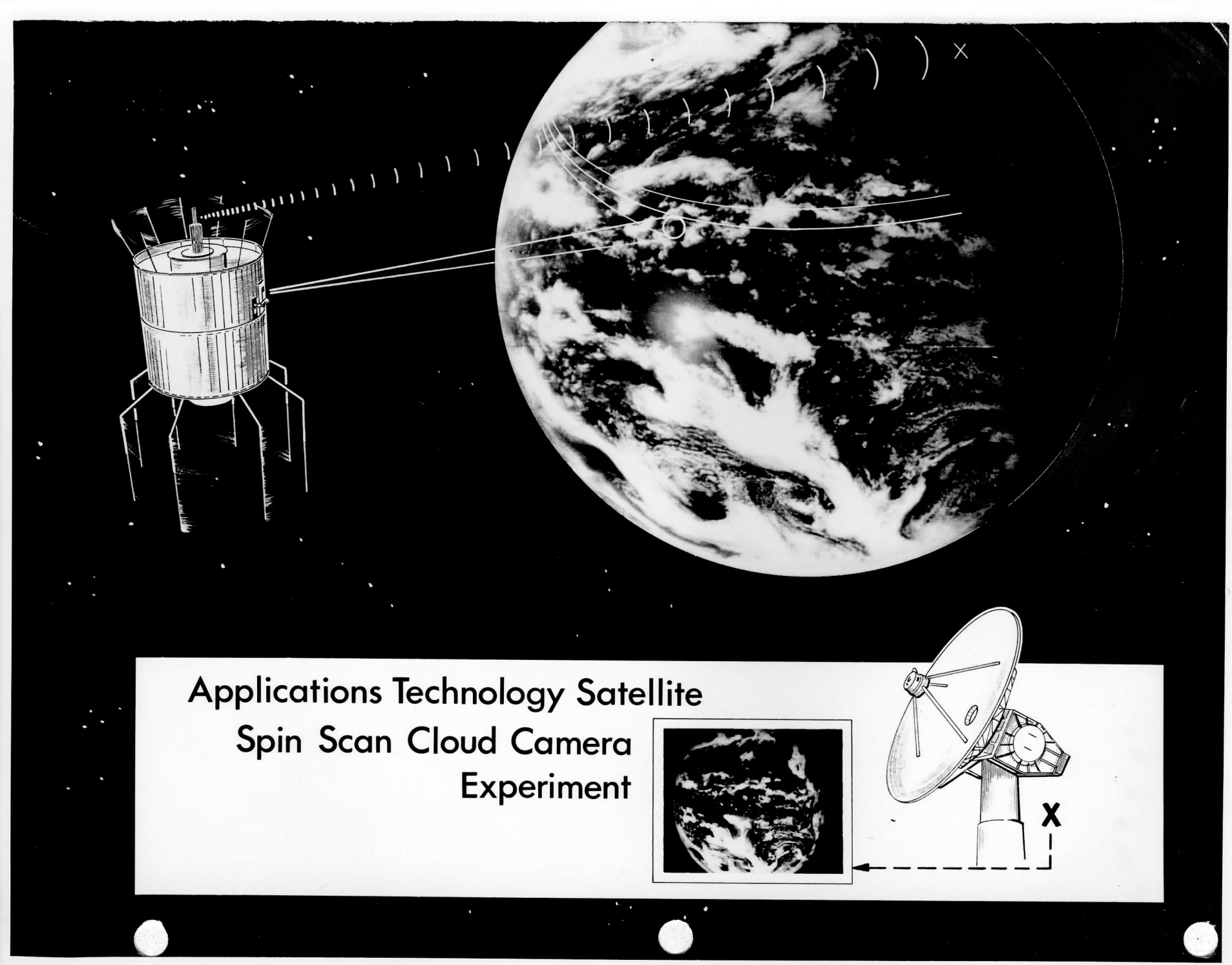

Applications Technology Satellite Spin Scan Cloud Camera Experiment

ATS-I (NAS 5-9677) - (WBG-27)
UNIVERSITY OF WISCONSIN METEOROLOGICAL EXPERIMENT
SPIN SCAN CLOUD CAMERA - FLIGHT MODEL UW-1
P/N 298069 REVISION B, SERIAL NUMBER F-1
UW SUBCONTRACT NO. 1
SANTA BARBARA RESEARCH CENTER
GOLETA, CALIFORNIA

III
A. 25

(25)
revised
3/3/70

Ground Display and Recording Equipment for the Spin Scan Camera System

Wendell S. Sunderlin

John P. Lahzun

National Aeronautics and Space Administration

Goddard Space Flight Center

Greenbelt, Maryland

CONTENTS

	Page
Introduction	1
System Description	3
SHF Receiver	6
Video Processor	6
Phase Lock Loop	9
Timing Subsystem	12
Fudicial Marks	15
Gray Scale	15
Limited Scan Controller	16
Digital Tape Recording System	17
Recording Mode (core unloading)	19
System Status	20
Photofacsimile Recorder	22
Acknowledgements	26

INTRODUCTION

The SSCC camera scans the earth by rotating the camera sightline across the earth on successive spins of the satellite. The elevation angle of the camera sightline is advanced on each revolution, in order to trace over a slightly different latitude on each sweep, thus forming a complete picture.

In order to form a clear picture with the received data, each received line of data is displayed such that the longitude of each picture element is essentially identical to the longitude of the picture element directly below or above it. Thus, a synchronizing signal must be provided to start each line in order to achieve the above criterion as closely as possible.

The resolution of the earth's edge is not sufficient to determine the synchronizing, so the time at which the sun-sensor sweeps past the center of the sun has been used instead. The satellite rotation rate is determined by using the sun-sensor pulses together with orbital information about the satellite and the sun. This rotation rate, together with knowledge of the satellite's motion with respect to a geographic reference, is then used to provide the synchronizing signal to start each new line of data on the photofax display.

The angle β, which must be determined, is the angle through which the satellite rotates between the sun-sensor's passage over the sun, and the camera sweep over a given earth reference line. It is seen in Figure 1, that this angle β, is the angle between the projections of the satellite-sun line and satellite-earth line into the satellite spin plane. Since the angle varies with time, means of providing an initial β and $\dot{\beta}$ is provided. The angle β depends on sun and satellite position, satellite attitude, time of year, and satellite motion with respect to its nominal subpoint.

Measured at the spacecraft, the earth subtends an angle of 17.3°, but the camera video data is presented and stored for a 20° azimuth band as shown in Figure 2. As the camera scans the earth, in a west-east direction, a video signal is produced by the photomultiplier tube. The requirement of the ground equipment is then to display and record this video data as a function of camera azimuth and elevation. The camera is at zero azimuth when it is in the plane defined by the satellite spin axis and the earth center. The camera elevation is defined as the mechanical tilting of the camera in a fixed increment during each revolution of the satellite. The camera elevation limits are $\pm 7.5°$, corresponding to about $\pm 50°$ of latitude on the earth. In the normal mode of operation, the camera steps from north to south at one step per revolution. In this manner the camera travels from the north limit to the south limit in approximately 20 minutes. Once the camera has reached the south frame limit, it retraces at a rate of 17 steps per second, taking approximately two minutes to retrace to the north frame limit. At that point, the camera begins to scan south again at one step per revolution.

The composite video from the spacecraft is separated in the ground equipment, resulting in the earth video burst and the sun pulse. The sun pulse serves as the input to the phase locked loop, which generates a smoothed sun pulse, the trailing edge of which occurs at the center of the real sun pulse. The synchronizer also receives two manual inputs, β and $\dot{\beta}$. β is the angle indicated in Figure 1 and $\dot{\beta}$ is the time rate of change of this angle. The limited scan controller receives the scan mode and scan direction signals from the pulse code modulation data handling equipment (PCM/DHE). With these inputs, the ground equipment will automatically send the video, along with the required timing signals, to the photo-recorder, the analog tape

recorder, and the digital tape recorder.

In the back-to-back mode of operation, the camera steps north to south at a rate of one step per revolution. Once the camera has reached the south frame limit, the camera reverses direction and scans towards the north frame limit at the same rate of one step per revolution. It will continue to do this until the camera is either put in the normal mode or turned off.

SYSTEM DESCRIPTION

The ground station signal processing equipment for the spin scan cloud camera (SSCC) experiment is used to record video data received from the Applications Technology Satellite-I (ATS-1) camera via the SHF communications link.

Figure 3 is a block diagram of the ground equipment that is used to process and record the camera video data. The ATS-1 spacecraft transmits the main data stream to the SHF receiver. This data consists of a carrier which is frequency modulated by the spin scan camera and the output from the sun sensor. The receiver provides the detected video and sun pulse signals to the video processor, which separates and amplifies the two signals. The video processor has four output channels, each having a separate internal gain control which are connected to the phase locked loop, and the output recorders.

The sun pulse signal is applied to the phase locked loop where it is utilized as the basic timing signal and the video signals are sent to the analog and digital tape recorders and the photofax recorder. Signals from the timing subsystem are applied to the video processor to provide dc restoration, and also to modify the amplitude of the video so that fiducial marks and phase lock loop error indications are placed on the photographic copy. The phase locked loop error signal is displayed by producing a series of short white lines to the left of

the earth cloud cover picture obtained on the photofax recorder.

The PCM data handling equipment supplies the scan direction and scan mode information to the system through the limited scan controller. In the normal mode, a frame start occurs whenever the scan direction changes from north to south; in the back-to-back mode, each scan direction change will start a new picture frame. During limited scan operation, the ground system commands the scan direction of the camera.

The timing subsystem accepts the smoothed sun pulse and VCO pulses from the phase locked loop and in turn generates the timing signals which are applied to the three recorder units. The start of the first picture line occurs after the first smoothed sun pulse following a frame start. The delay between the sun pulse and the line start pulse is equal to the handset line delay. The second and successive line start pulses are delayed by the handset line delay plus a delay proportional to the line delay rate. These handset qualities are set only once a day; however, they may be adjusted as often as once per frame. A computer generated chart is provided to indicate the correct settings of these parameters as a function of time of day and year.

The timing subsystem sends frame and line start pulses to the photofax and tape recorders. The photofax unit also receives picture element pulses (PEP) to step the X deflection of the photofax recorder, and a reset signal at the end of each picture frame.

The digital tape recorder receives essentially the same video signals as the photofax recorder except that sampling occurs twice as often and the video is digitized. The digitized video is stored one line at a time in a high-speed core memory unit, and during the time when the camera is not facing the earth, this data is read from the core memory onto magnetic tape. Identification data such as time of

recording and phase lock loop error is placed on digital tape at the beginning of each line of video data.

The digital tape recorder system operates in two modes--record and playback. Due to the received data rate, the record mode consists of two sequential modes of operation for each line of data. The first operation (phase 1) consists of converting the analog video input to 8192 digital words consisting of 8 bits per word, and storing this data in a core memory. Phase 2 consists of unloading the core memory and writing the digital video on magnetic tape.

In the playback mode, the digitized data is recovered from the tape, processed, and sent to the photo-recorder unit to produce a playback picture.

The station oscillator provides a stable 1 MHz signal to a divider in the $\dot{\beta}$ generator. The resulting 500 pps signal combined with the output of the $\dot{\beta}$ storage register produces an output correction signal to the sun-earth angle counter. The correction signal thus generated serves to compensate for changes in the earth-sun angle.

A simulated video signal, consisting of 32 black and white bars followed by an equal period of black, is generated by the synchronizer logic. Associated with this periodic bar pattern is a simulated sun pulse occurring at the end of every other black and white bar pattern, with a 512 msec period. These two logic signals are combined in the video processor to form a composite video signal which is inserted into the system in place of the normal camera video. It is possible to lock-up the synchronizer on the simulated sun pulse and record the bar pattern on the photo-recorder, analog tape recorder, or the digital tape system. Thus, it is possible to check all recording and playback systems with the simulator mode.

SHF RECEIVER

The SHF receiver receives the composite camera video signal from the ATS satellite in the form of a frequency modulated carrier at 4119.599 or 4178.591 mHz. This signal is demodulated by a conventional discriminator which has a linear response of ±1% for frequency deviations up to 20 mHz P-P.

The discriminator output is then applied to a video amplifier which has a ±0.4 db amplitude response from 0.1 Hz to 10 mHz, and a 3 db bandwidth from about 0.035 Hz to about 14 mHz. The amplifier has an adjustable gain of 40 db with a nominal output of 2 volts P-P. A typical response curve for the amplifier is indicated in Figures 4 and 5. The response from 100 Hz to 1 mHz is essentially flat.

The video amplifier output is then coupled to the pre-emphasis amplifier in the video processor.

VIDEO PROCESSOR

The functional purpose of the video processor is to control the video amplitude and waveform of the signal that is received from the video amplifier output. A simplified block diagram of the video processor is indicated in Figure 6.

The pre-emphasis amplifier in the video processor is provided to modify the frequency response of the camera video signal as compensation for the low frequency characteristics of the spacecraft voltage controlled oscillator. A typical response characteristic for the pre-emphasis amplifier output indicated in Figure 7 is then applied to a 200 kHz filter which has a response as indicated in Figure 8.

The signal inputs to the video separator circuit that is contained in the video processor are either the composite video signal from the spacecraft, or a simulated video and sun pulse waveform. The composite video signal is separated into two parts, permitting the sun pulse to

be used by the phase lock loop, and the video to be amplified and sent to the analog, digital and photofax recorders. The video signals are optionally dc restored by clamping the video signal to ground for a period controlled by a dc restore signal from the timing subsystem. The dc restore pulse occurs immediately before or after the video signal to restore the baseline of the video signal to a near ground potential.

Also contained in the video processor is a 12 db video amplifier consisting of a variable attenuator followed by a 12 db non-inverting amplifier. This amplifier is used to vary the gain of the input video from 0 to 12 db in 2 db steps.

The output buffer amplifiers of the video processor are used to provide low impedance video outputs to drive the recording equipment. The outputs to the analog recorder and the digital recorder are normally adjusted for a maximum video signal of 1.5 volts peak, and the output of the photofax recorder is adjusted to 1.0 volt peak.

Tests of the video processing system have provided a means of measuring performance of the system at specific points. The test results are as follows:

1) With a shorted input to the SHF receiver video amplifier, approximately 20 MV of predominently 60 Hz noise, out of a signal scale of 1 volt peak, exists at the unit output. Measurements of this condition in the laboratory indicated an output noise level considerably less in value (5 MV), indicating a source of noise external to the unit. A test of the video processor unit with a shorted input on a functional block basis indicated little additional noise. Most of the noise appeared near the front end at the output of the pre-emphasis network (1.5 MV), with no discernable increase in noise level in the stages following that point.

The important observation is that the video processor chain is not introducing sufficient noise to cause video degradation. On the other hand, noise is getting into the receiver video amplifier unit which causes slight video distortion (approx. 2%). This may be attributable to ground loops.

2) The system was checked for drift (with a 150 uf coupling capacitor at the input to the receiver video amplifier). The overall drift was less than 20 MV., well below the threshold for video degradation. The pre-emphasis network is the major source of drift value since it magnifies low frequency fluctuations in the input signal. Following that point, the video processor produces no discernable drift.

3) A square wave response test was used to check the transient response of the system. A signal input was applied to the receiver IF amplifier and the resulting square wave output from the discriminator was used as a test signal for the video processing system. The signal approximates the actual video in terms of its pulse characteristics and repetition rate. Results indicate that there is some overshoot and ringing at the output of the video processor input filter which will cause some distortion of the actual video. Since the actual video does not have the short rise and fall times of the test signal (the test signal rise and fall times were 3 microseconds versus 20 microseconds for the actual video), the video distortion will be less. Calculations indicate a video distortion of 3 to 5%. Generally the distortion would be 3% except for points in the picture with a white-black edge. No additional distortion appears following the input filter.

The test effort was primarily focused on investigating the amount of video distortion occurring in the video processing system. Results

of waveform evaluation relative to noise, drift and square wave response indicate an overall video distortion of approximately 5%.

PHASE LOCK LOOP

The basic function of the phase lock loop indicated in Figure 9 is to reduce the jitter of the received sun pulse by forming a smoothed sun pulse, and to divide the spin period into a large number of equal intervals, each representing about .02 milliradians. Given the composite video from the spacecraft, the key synchronization requirement is then to provide a line start pulse when the spacecraft camera is at -10°azimuth. Secondly, the video data which is present from -10° azimuth to +10° azimuth must be divisable into equal intervals for control of the sampling processes associated with the photofax and tape recorders. The numbers of equal intervals selected was 16,384 for the following reasons:

1) It is 4 times the 4096 parts required for the photofax sampling process.

2) At spin rates of 50 to 150 rpm, it corresponds to a frequency of approximately 250 kc to 750 kc--a range readily achieved on available frequency synthesizers with good stability.

3) It is 2 times the 8192 parts required for the digital sampling and recording process.

4) The azimuth spacing between these basic pulses is only about 0.2 milliradians, or about one-fifth the camera resolution.

The sun pulse input from the video processor is initially passed through a filter and threshold detector to reduce the high frequency noise and to form a rectangular pulse suitable for subsequent digital handling. The low pass filter has a 3 db cut-off frequency of 1 kHz and a 12 db per octave roll-off above 1 kHz. The threshold level of the sun pulse is adjustable between +1 and +5 volts. Whenever the

input is above the set threshold, the nominal output is +6 volts, and whenever the input is below the threshold, the nominal output is 0 volts. The rise time of the output pulse is about 0.1 microsecond.

Basically, the phase locked loop operates in two modes; acquisition and tracking. During the acquisition mode, the leading edge of the sun pulse is used to transfer selected bits of the sun angle counter into the correction counter, and then to reset the sun angle counter to zero. The correction count is then added to the digital integrator with the proper multiplying factor. This closed loop operation continues until the VCO frequency has been adjusted to the point where the difference between the sun pulse and the smoothed sun pulse is small enough so that the correction counter will be operating in the linear region during the tracking mode. The system then switches to the tracking mode, and for the next sun pulse, a full correction from the counter is fed back into the sun angle counter to align it with the center of the sun pulse. Thereafter the operation is identical to the tracking mode.

During the tracking mode, the phase locked loop supplies a smoothed sun pulse to the timing subsystem. The generation of the smoothed sun pulse then occurs in the following manner. The sun angle counter generates an early gate and a late gate. During the early gate and when the sun pulse exceeds a threshold, the correction counter is fed with VCO clock pulses and thereby accumulates a number proportional to the portion of the sun pulse which occurs during the early gate. Likewise, during the late gate, the number in the correction counter is decreased by a number proportional to the part of the sun pulse which occurs during the late gate. Therefore, the resultant number in the correction counter is proportional to how far the center of the sun pulse is from the smoothed sun pulse. The smoothed sun pulse occurs at

the transition between the early and late gates.

Some time after the smoothed sun pulse occurs (dependent on the un-earth angle), the number in the correction counter is added to a digital integrator (digital accumulator). The resultant number in the digital integrator then controls the frequency of the frequency synthesizer (VCO). At the same time that the number in the correction counter is being added to the digital integrator a fraction of it is added to the sun angle counter via the phase correction circuit. The VCO clock pulses are then counted by the sun angle counter which automatically cycles at a pre-set count corresponding to the number of counts (294912) in one revolution of the satellite. The sun angle counter then generates the early and late gates for the next sun pulse, thereby closing the loop.

Operation of the phase locked loop is completely automatic once it has been initiated. The operator need only push a "start" button to acquire and lock-on the sun pulse. Prior to pushing this "start" button, the operator must however set the preset frequency dial, on the control panel, to the approximate frequency. This setting may be in error by 20% without introducing any problem. It is employed by the phase locked loop as an initial VCO setting to avoid possible ambiguities in tracking. The digital frequency input to the VCO is then displayed in a six decimal digit readout.

The frequency synthesizer (VCO) is a major part of the phase lock loop. The sine wave output from the VCO is applied to a pulse circuit to generate a 1 microsecond pulse train, at the VCO frequency. The VCO output is the basic clock frequency that is proportional to the satellite spin rate.

Whenever the phase lock loop is locked up on a camera sun pulse, a TSI counter can be configured to give spin period measurements.

There are two basic methods for obtaining spin period measurements from the TSI counter: direct manual readings by the SSCC operator, and utomated recording of spin period measurements using the Spin Period Acquisition Program, SPAP, in conjunction with the SDS-910 computer. Under most circumstances, a 10-period average is sufficient. If other spin rate averaging periods are desired, they can be obtained by setting the multiplier switch on the counter to the desired number of periods to be averaged.

TIMING SUBSYSTEM

The timing subsystem, indicated in Figure 10, accepts the smoothed sun pulse, and VCO pulses from the phase locked loop and generates most of the timing signals employed by the recording units. All of the timing pulses occur coincidently with a VCO pulse, and the time between leading edges of adjacent VCO pulses varies from approximately 1.36 microseconds to approximately 4.07 microseconds, depending on the satellite spin rate. Because of this variation, times are designated in terms of VCO pulses and Picture Element Pulses (PEP).

The earth angle counter is similar to the sun angle counter of the phase locked loop. The initial information for the sun-earth angle is set up on dials on the control panel. The earth angle counter then cycles through zero at a fixed angle with respect to the earth. The contents of the sun-earth angle counter is incremented at a rate controlled by the handset sun-earth angle rate $\dot{\beta}$.

The smoothed sun pulse generated in the phase locked loop is then used to transfer the contents of the sun-earth angle counter into the earth angle counter. The number in the sun-earth angle counter is directly proportional to the current azimuth angle between the sun and the earth (offset by a fixed angle).

Timing control signals are generated by decoding selected counts

of the earth angle counter. These include line start, line end, picture element pulses, A/D sample pulses, and the DC restore pulse. The DC restore signal causes DC restoration of the video for a satellite angular change of 10° either immediately preceding or following the earth scan; a switch on the control panel selects the desired case. In addition, the timing subsystem generates the mark signals used by the video processor to produce the fiducial marks and sync (PLL) error. The fiducial mark section of the timing subsystem consists of the necessary gating to decode the 19-bit earth angle counter in the timing subsystem, and the 11-bit vertical line counter in the limited-scan controller to produce a white mark signal to the video processor when the counters reach the appropriate states. A switch on the control panel controls the use of this option. This option may be employed in normal or limited scan modes.

Another section of the timing subsystem generates the simulated video and sun pulse signals. This simulated signal consists essentially of a 250-bit/sec pulse train with a pulse width of 2 msec each. Every 128th pulse simulates the sun pulse; the remaining pulses simulate the video signal. The time between simulated sun pulses is 0.152 seconds, and corresponds to a satellite spin rate of 117 rpm. With the synchronizer sun-earth angle counter rate set to zero, this simulated signal produces a series of 32 black and white vertical bars followed by an equal period of black. Approximately 7.1 black and white cycles are displayed on the photofax recorder. With the sun-earth angle rate not set to zero, these bars assume an oblique angle instead of the previously vertical ones. Variation of the sun-earth angle setting causes a horizontal shift of these bars. This same signal can be simultaneously employed for testing the analog and digital recorders. The timing control signals that are generated by decoding selected counts of the

earth angle counter are as follows:

1) Picture Element Pulse - This signal provides 4096 equally spaced pulses during the time that the camera azimuth angle lies within a 20 degree sector. This sector is normally adjusted to be centered on a line joining the satellite and the earth's axis. The picture element pulse occurs simultaneously with every other A/D sampling pulse.

2) Line Start - The line start pulse will occur 75 VCO pulses prior to the first picture element pulse of each line.

3) Frame Start - In the normal mode of operation, a frame start pulse occurs coincident with the first line start pulse following a change of scan from the north to south direction. In the back-to-back limited scan mode, a frame start pulse occurs coincident with the first line start pulse following the first change in scan direction after generation of a frame end pulse.

4) Frame End - In the normal mode of operation, a frame end pulse occurs coincident with the last picture element pulse of the last line. The last line is either the 2048th line of a frame, or the first line to be completed after a south-north scan direction change, whichever occurs first. In the back-to-back limited scan mode, a frame end pulse occurs coincident with the last picture element pulse of the 2048th line after frame start.

5) DC Restore - This signal caused DC restoration of the video for a satellite angular change of 10 degrees immediately preceding or following the earth scan. A switch on the control panel selects the desired case.

6) Scan Direction - This is the direction of stepping of the ATS-1 camera. Logical zero indicates south-north stepping. In the back-to-back limited scan mode, the scan direction changes when a command

is sent to the satellite. Otherwise, the scan direction level changes when the telemetry indicates a scan change.

7) Mode - This signal identifies the normal or back-to-back camera mode. A logical zero indicates the normal mode. This level is changed when the telemetry channel indicates a change in mode.

8) A/D Sampling Pulse - These 8192 sequential pulses are provided to the analog to digital converter and they occur simultaneously with every other VCO pulse. The first sampling pulse occurs on the first VCO pulse after the zero count of the earth angle counter.

9) Line End - The line end pulse which is used by the digital recorder occurs simultaneously with the 8192nd A/D sampling pulse.

FIDUCIAL MARKS

The fiducial mark generator contains gating circuits to decode the earth angle counter and the vertical line counter to produce a fiducial mark signal to the video processor. These fiducial marks are of fixed size and fixed position with respect to each other and the edges of the picture. The fiducial marks occur in the corners of the picture which will not overlap the earth. The marks are 64 lines high and 128 picture element pulses (PEP) wide. The vertical bar is 4 PEP's wide and the horizontal bar is 2 lines high.

GRAY SCALE

A gray scale signal is added to all photofax, analog, and digital recorder video signals. The scale appears as a 1/8 inch vertical bar at the right edge of the picture frame. The scale consists of 10 levels of gray from black at the top segment to peak white at the tenth segment and is controlled by a shift register and a D/A converter. The video levels referenced to the photofax recorder input are as follows:

Step	Shade	Photofax recorder input voltage
1	Black	.000
2		.004
3		.008
4		.016
5		.031
6		.063
7		.125
8		.250
9		.500
10	White	.996

LIMITED SCAN CONTROLLER

By sending signals to the command console and master control console (MCC) at the proper times, the limited scan controller causes the spacecraft camera to traverse a fraction of the normal scan limits (see Figure 11). While the system is in this mode, the satellite camera scans over a smaller angle, between preset north and south limits. These non-normal limits are preset by means of rotary switches on the control panel. While in the limiting scan mode, the contents of a line counter are compared with the contents of the north and south limit registers, and when a match is found, the vertical line counter is stopped and its direction reversed. When a match occurs, an execute pulse is then sent to the MCC for transmission to the spacecraft. Prior to each execute pulse, a command must be loaded into the command console to indicate the direction of the change. This is accomplished by using the scan direction signal from the PCM/DHE. Therefore, if the camera is scanning north it will be told to expect a south scan command next, and vice versa.

The line counter displays a four-digit decimal readout and provides the operator with an indication of the present camera elevation in the normal and limited scan modes.

Since there are two site locations either of which can provide commands to the satellite, a local/remote switch on the control panel

is set to indicate whether commands are generated at the local or remote station. Another switch places the system in an automatic or manual operation. In manual operation, frame start pulses are inhibited after a frame end occurs, and a warning light on the control panel is lit. As soon as this light comes on, the operator may change the photofax recorder film and the digital recorder tape. He then depresses the restart button, which transmits the next frame start pulse to the recorders.

DIGITAL TAPE RECORDING SYSTEM

The digital recording system has the primary role of converting the processed video data into digital form, and the subsequent storage of the data on a digital magnetic tape transport.. The recording system also contains the circuitry to play back the recorded data, and to make the data available for off-line local transmission to the photofax equipment for post-time reproduction of a picture frame.

The principal parts of the digital recording system includes the analog to digital converter, core memory, and a magnetic tape recorder.

The analog-to-digital converter is capable of 5,000,000 analog samples per second with 8-bit parallel word readout. In this application, the unit is operated synchronously by being interrogated for readout by the A/D picture element pulses.

The core memory stack size is 4096 words of 16 bits each, and is rated at 1 microsecond full cycle. The core memory system contains the complete read/write electronics, as well as manual self-test provisions, and displays the primary registers and status signals.

The magnetic tape transport has a tape speed of 45 ips, a packing density of 800 bpi, and 7 tracks (6 data and 1 parity). The transport contains the read/write circuits, parity generate/read circuits, transport DC power, and a local control panel. This transport is completely transistorized.

So that special (signature) data may also be writtin on tape, the system also multiplexes, by sample pulses derived from the first eight pictue element pulses, the following data:

1) Frame Identifier: Two thumbwheel switches, with a range of 00 to 99, provide two sets of BCD lines for a total of 8 bits. The switches are located on the recorder control panel and their use is at the operator's discretion, e.g., year 68 or tape number.

2) Phase-Locked Loop Error: These are 11 lines (straight binary) derived from the synchronizer prior to the first picture element pulse and represent the correction count within the phase-locked loop.

3) Scan Direction: One binary bit is obtained to indicate scan direction. The south-to-north scan is indicated with a binary "one", and the north-to-south scan is a binary "zero".

4) Ground Video Gain: Three bits of BCD data, ranging from 0 to 6, are obtained from one deck of a synchronizer cabinet panel switch to indicate ground video gain setting.

5) Satellite Video Gain: One binary bit is obtained from a switch on the synchronizer cabinet panel wherein binary "one" is equal to high gain and binary "zero" is equal to normal gain.

6) Day-of-Year: Three BCD thumbwheel switches, located on the synchronizer cabinet panel, with a range of 000 to 399, provide 10 lines of parallel data.

7) Time-of-Day: GMT time is derived from the computer system via the synchronizer as 20 lines of BCD data with a range of 00:00:00 to 29:59:59, expressed as the maximum value possible for each column or digit over a 24-hour period, e.g., 19:58:39.

8) Scan Mode: One binary bit for the normal mode is indicated with a binary "one", and the back-to-back mode is indicated by a "zero".

9) Vertical Line Count: Obtained from the synchronizer are 14 lines of BCD which are used to indicate the camera (elevation) vertical line count, (range 0000 to 2048).

(10) Digitized Video: Processed video signals are interrogated and digitized by the A/D converter in the recorder assembly. Each A/D conversion yields an 8-bit straight binary count.

Items (1) to (9) form the signature data which is placed at the beginning of every line of each frame. The first 18 A/D sample pulses are used to load the signature data. Thereafter, the remaining A/D sample pulses are used to acquire the digitized video from the analog to digital converter.

The word format of the data as it enters the core memory is shown in Figure 12. As shown, bits occur only where there are letters in the illustrated bit configuration.

Successive locations of core are loaded on every even A/D interrogator pulse, although the converter itself is not interrogated until the 19th A/D interrogator pulse, and thereon through the 8192'nd pulse. Loading of the core is therefore synchronized to the rate of the A/D interrogator pulses from the synchronizer. During core loading no other recorder functions will occur.

RECORDING MODE (CORE UNLOADING)

After the core is loaded with a line of data, phase two, or core unloading, shall occur. Precision clocks are enabled to synchronously strobe out each successive core address starting at location 0000.

Each core word, of 16 bits, is "stretched" to 18 bits by the pseudo-addition of two zeros at the most significant bits such that

three 6-bit bytes can be derived from each word for placement on tape. The most significant 6-bit byte is placed on tape first, followed by the middle 6-bits, and ended by the least significant 6 bits. Figure 13 illustrates the foregoing statements on word dissassembly.

All data is placed on tape at a rate of 36 kHz, that is 80 BPI at 45 IPS. Thirty-six hundred foot reels of 1 MIL tape, 7-track certified for 800 BPI, is required to record one frame of 2048 lines of data. The exact length required for 2048 lines frame is:

$$\left[\begin{array}{l}4097 \text{ wds} \\ (\text{incl.} \\ \text{LRCC})\end{array} \times \frac{3 \text{ chars}}{\text{word}} \times \frac{1 \text{ inch}}{800 \text{ chars}} + 0.75 \text{ inch (gap)}\right] \cdot \left[\frac{1 \text{ ft.}}{12 \text{ in.}}\right] \cdot \left[2048\right]$$

= 2750 feet + 25 feet (leader)

= 2775 feet (thereby exceeding the standard 2400' reels by 375 feet)

Beyond the load-point gap, each line of data (plus longitudinal check character) shall equal one record and each line (or record) is separated only by 0.75 inch blank record gap until the end of the frame (anywhere from 1950 to 2048) records dependent on scan mode). After the last record of a frame, there is a 3.5 inch blank gap followed by the end-of-file characters (double even-parity octal 17's). All picture frame tapes are written in the binary mode, thus requiring odd parity on record data. After the EOF mark is written, the transport is commanded to Rewind/Unload.

SYSTEM STATUS

Experimental test results indicate that encoded data is being correctly time buffered via core storage, and properly formatted and read-out to the photofax recorder and digital tape unit. Signature data is being correctly loaded and attached to the front end of each data line. Analysis of results indicates suitable encoding of analog data, and except for possible smaller effects discussed in the next

paragraphs, A/D calibration appears adequate, and the distribution of digital data values is in line with what is expected of the input data.

Diagnostic analyses of some difficulties in digitizing the video data are presented by Hanson (paper No. 27) and by Whitney, et. al (paper No. 21).

The performance of the digital tape unit appears satisfactory from the point of view of tape transport operation as well as quality of tape data. Transport operation is sensitive to the mechanical and pneumatic condition of the unit and will apparently be satisfactory so long as proper preventive maintenance is applied. Preventive maintenance also aids in reducing tape data errors, since the collection of tape particles is not allowed to build up to the point of distorting or obstructing proper tape motion.

Tape error indications encountered in the playback of tapes have been small in number; normally no more than a few records per reel contain errors. Errors have been predominantly parity errors.

In order to evaluate the digital recording system, a single frame was acquired on June 15, 1967 (Day 166 at 2142 GMT). This particular tape was generated after all significant system problems were corrected at the Rosman ATS ground station.

The tape had 1990 records; the first was at line count 32 and the last at line count 2021. The first line count was 32 as a result of a late start by the operator. Scan mode and direction were both zero, indicating normal mode and N-S scan. The frame identifier had been arbitrarily set to one and the day was set to 166.

The phase lock error was initially negative, reaching a maximum negative value of -15 at line count 50. This number is twice the number of VCO pulses between the smoothed (predicted) sun pulse and the center of the actual sun pulse. Each unit error is very nearly 0.01 milliradians. The maximum positive value reached was +7. The

computed average sync error was +2.8 and the computed rms sync error was 3.2.

The video data content is apparently satisfactory. Of the approximately 16 X 10^6 video samples only 66 (about 0.0004%) were at or above the maximum encoding level of 255.

An analysis of the camera response to a black/white edge indicated that at most the sample-to-sample change would not exceed about 0.18 of full scale, or 0.18 X 255 = 46. Data on this tape did however exceed this difference in 0.0062 percent of the cases. Possible reasons for this include:

1) Camera resolution was ten percent better than the nominal value--this would reduce the excess to 0.0024 percent.

2) Noise produced in the video and/or A/D converter.

PHOTOFACSIMILE RECORDER

The photofax recorder operates from real time or tape playback data, and produces on Polaroid 55 PN film, a positive print and a negative. The print is basically for monitoring purposes and the negative is of high resolution and quality for subsequent enlargements.

The photofax recorder receives the analog video from the video processor and timing signals from the synchronizer. The video information is then displayed on a high resolution five inch cathode ray tube and projected on the film. The mechanism for the tube deflection is basically a digital one. The recorder has both X and Y deflection. The X deflection corresponds to the azimuth sweep and the vertical deflection corresponding to some particular elevation of the camera. The deflection wave form is generated by two digital counters - one for horizontal and another for vertical, whose numerical output, after digital-to-analog conversion, drive the deflection amplifiers. The net effect is like that of locating a given cell on cartesian coordinate

graph paper by giving its numerical coordinates. Once a cell has been located, a gate turns on the cathode ray tube (CRT) electron beam. The light that is given off when the electrons hit the CRT phospher is divided by a half-silvered mirror into two components, one of which is directed to the film and the other to a photomultiplier tube. The photomultiplier integrates the light output and continuously compares its reading with the brightness dictated by the incoming video signal for that cell. When the two values coincide, a gate turns off the electronic beam and the system is ready to move on to a new cell. This process is continued until the complete picture is generated. When such a picture is built element by element, a certain sequence of events must occur for each element. The required sequence of events, with some overlap, goes as follows:

1) Generate the digital deflection coordinate
2) Convert the digital deflection to an analog deflection voltage
3) Deflect the beam
4) Turn the beam on
5) Make the exposure
6) Turn the beam off

The horizontal deflection register has 12 bits or 4,096 states, while the vertical deflection register has 11 bits with 2,048 states. Thus, 4,096 uniformly spaced spots can be placed in a horizontal line, and in the vertical direction a total fo 2,048 lines. Intensity information can be presented from analog video or 8-bit digital data for each spot. The exposure capabilities of the recorder is accurate to approximately two percent of the video level, and sixteen shades of gray may easily be displayed. The gray scale and fiducial mark locations are indicated in Figure 14.

After the photofax recorder was installed, it was checked for

focus, aspect ratio, and exposure. In addition, a digital tape generated with a computer was run to check the square wave modulation response of the recorder. The resulting negatives were then checked using a microdensitometer.

The test data was obtained by taking the average transmission of a test bar pattern for each video level. The slope of the straight portion of the density-exposure curve when plotted on semi-log paper is the film gamma, which was 1.1 and 0.97 respectively for test film A and test film B. This test indicates that, although there is a non-linear section near fog level, the D log E curve closely approximates a standard film gamma curve. This non-linearity near fog is typical of film and no technique is incorporated in the recorder to correct this.

The film gamma characteristic shows little curvature at the maximum density recorded, which indicates that no saturation occurred for the negatives tested. The maximum density measured on the negatives was 1.74, where density = log 1/T. The density of fog level obtained was 0.252 for film A and 0.224 for film B. Therefore, the usable dynamic range of the film is a maximum minus the minimum density and is approximately 1.5.

Film grain noise was maximum near fog and decreased as the film reached saturation. This noise was sufficient to render parts of the trace for the video run on film A indiscernable in the fifth set of bars. In the sixth and seventh set of bars, the noise level was greater than the video. (The peak-to-peak noise as recorded on the densitometer was greater than the density change from step 5 to step 6. After step 5 only noise was present to the densitometer.)

The densitometer plot of the various test bar patterns must first be converted to spatial frequency numbers before usable data can be

obtained. Note that the length of a scan line is 100 mm while the vertical frame height is 75 mm for 2018 scan lines. The maximum spatial frequency for film A is then 13.5 cycles/mm and film B is 10.1 cycles/mm.

Since the linear output function results from plotting 1/T versus input, the transfer function was calculated by the following formula:

$$MTF = \frac{\frac{1}{T_{max}} - \frac{1}{T_{min}}}{\frac{1}{T_{max}} + \frac{1}{T_{min}}}$$

The MTF was plotted for the video levels of 256, 64 and 16 for film A and B. These curves were then extrapolated to give limiting resolution at 5% response. Resolution in TV lines may be obtained by multiplying the spatial frequency in cycles/mm by [2 TV lines/cycle] [75 mm] = 150 TVL mm/cycle for film A and 200 TVL mm/cycle for film B.

A summary of the resolution is listed in the following Table for various video levels. These values are for square wave responses.

Input	MTF(%)	Film A(TVL)	Film B(TVL)	Film A(cy/mm)	Film B(cy/mm)
256	5%	2175	3360	14.5	16.8
256	50%	450	560	3	2.8
256	90%	158	208	1.05	1.04
64	5%	2175	3920	14.5	19.6
64	50%	450	580	3	2.9
64	90%	158	208	1	1.04
16	5%	2450	5240	16.3	26.2
16	50%	645	880	4.5	4.4
16	90%	316	300	2.12	1.5

The difference in TVL resolution between data for film A and B is due mostly to the longer dimension for film B.

Assuming that the film has no effect on the 50% MTF point, a sample calculation of effective spot size gives an idea of the distortion of spot size present. The resolution at 50% response obtained on the film was 3 cycles/mm for film A. For a square wave response it has been

established that the beam diameter is very nearly one-half cycle at the 50% response point of the MTF. Thus 3 cycles/mm yields a beam diameter of 0.167 mm or 6.6 mils. Resolution increases somewhat with decreased video drive indicating spot growth occurs with increased video drive. However, no significant improvement occurs between video level 256 and 64. This can partially be explained in the following manner. If the best focus is set at maximum video drive, the tube will defocus with decreased current. The spot does not decrease in size as much as expected because of the decreased beam current. However, at much decreased beam current the spot size would decrease at a faster rate than defocussing occurs.

Figures 16 through 20 show typical pictures taken with the spin scan camera system and reproduced on the photofax recorder.

ACKNOWLEDGEMENTS

The Santa Barbara Research Center, A Subsidiary of Hughes Aircraft Company under contract to the University of Wisconsin designed and built the Spin Scan Cloud Camera for use aboard the NASA Applications Technology Satellite (ATS-1).

The Westinghouse Defense and Space Center under contract to NASA Goddard Space Flight Center developed the ground equipment for synchronization and processing of the received camera data.

The Electronic Photofax Recorder was developed by Electronic Image System Corporation, Boston, Massachusetts under a NASA Goddard Space Flight Center contract.

ILLUSTRATIONS

Figure 1	Satellite Rotation Earth-Sun Reference Angle β
Figure 2	Camera Angle α
Figure 3	Spin Scan Cloud Cover Experiment Ground Equipment Block Diagram
Figure 4	Frequency (Hz)
Figure 5	Frequency (MHz)
Figure 6	Receiver Video Amplifier and Video Processor Block Diagram
Figure 7	Frequency (HZ)
Figure 8	Frequency (KHz)
Figure 9	Phase Locked Loop Block Diagram
Figure 10	Basic Parts of Control Panel and Timing Subsystem
Figure 11	Limited Scan Controller Interface Diagram
Figure 12	Word Format for Core Memory Stored Line Data
Figure 13	Phase Two Core Unload -- Record Pattern
Figure 14	Gray Scale and Fiducial Mark Locations
Figure 15	Pictures taken with the Spin Scan Camera System
Figure 16	Spin Scan Camera Photograph taken on September 17, 1967
Figure 17	Spin Scan Camera Photograph taken on September 19, 1967
Figure 18	Pictures originally taken with the Spin Scan Camera System
Figure 19	Picture taken with the Spin Scan Camera System

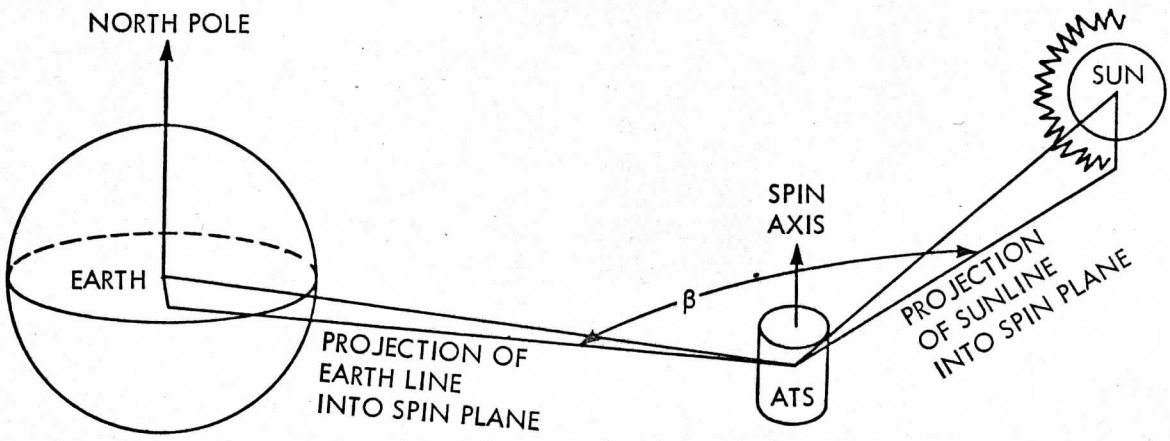

Figure 1 - Satellite Rotation Earth-Sun Reference Angle β

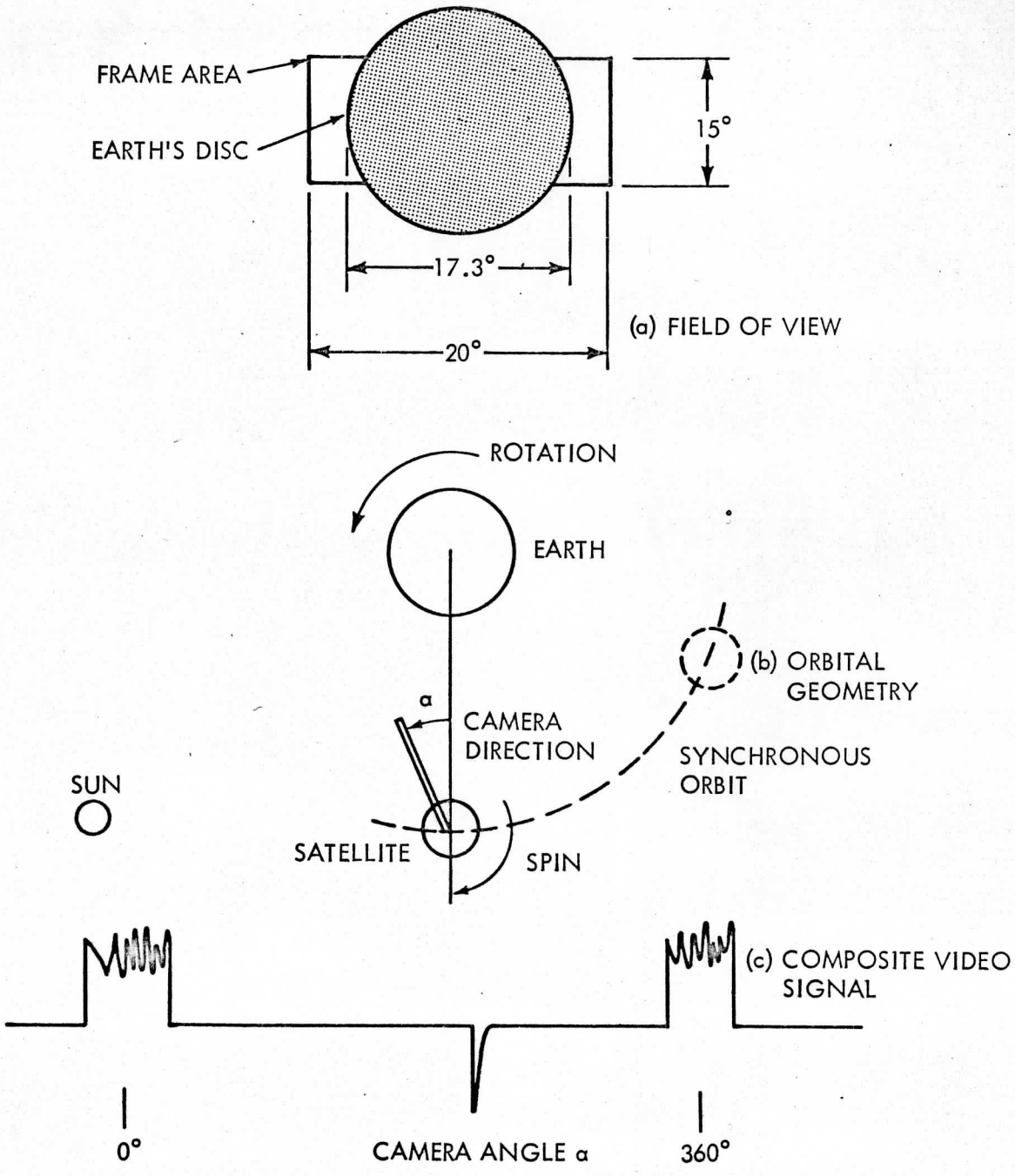
FRAME AREA
EARTH'S DISC
15°
17.3°
20°
(a) FIELD OF VIEW
ROTATION
EARTH
(b) ORBITAL GEOMETRY
α
CAMERA DIRECTION
SYNCHRONOUS ORBIT
SUN
SATELLITE
SPIN
(c) COMPOSITE VIDEO SIGNAL
0°
CAMERA ANGLE α
360°

Figure 2

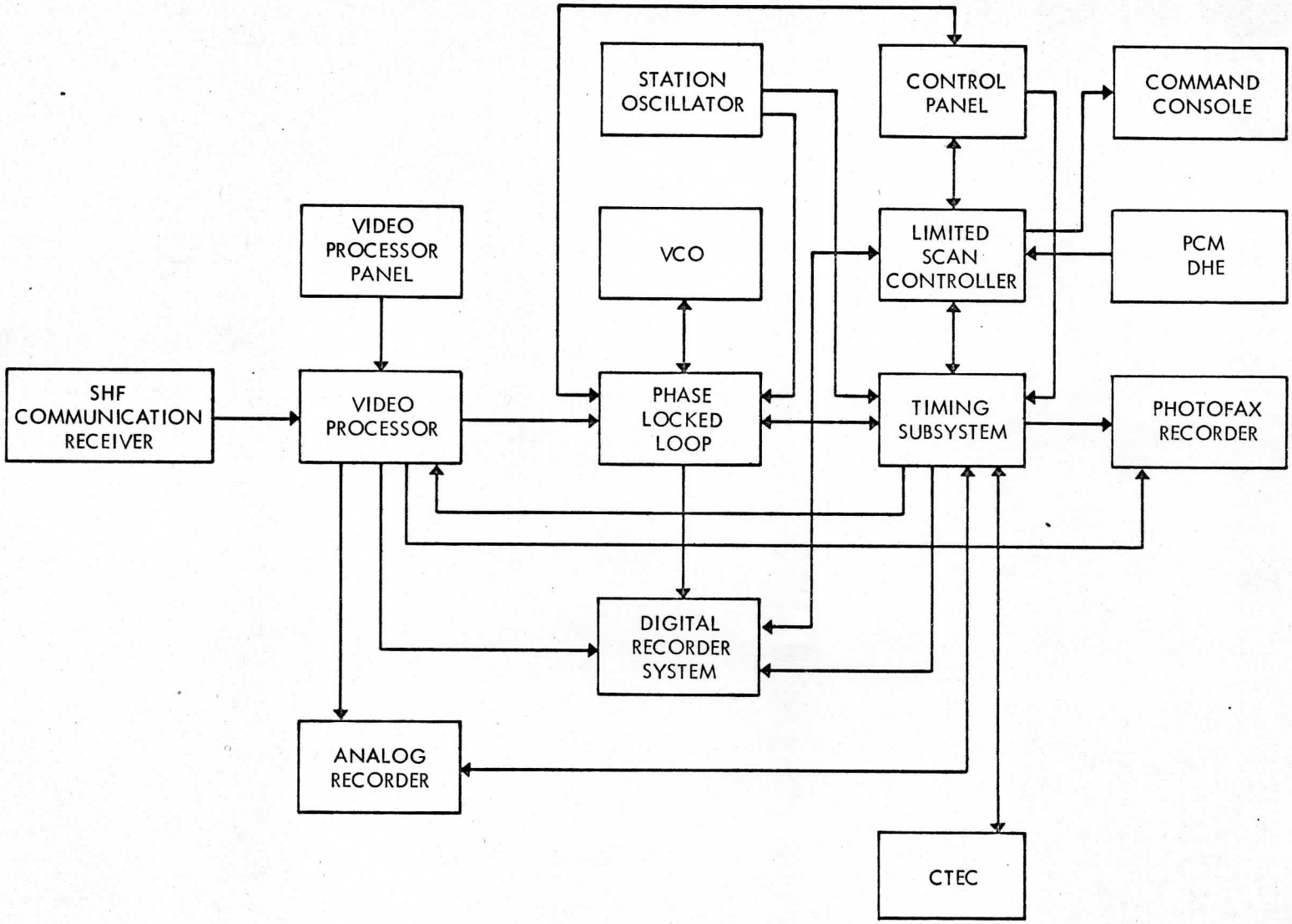

Figure 3 – Spin Scan Cloud Cover Experiment Ground Equipment Block Diagram

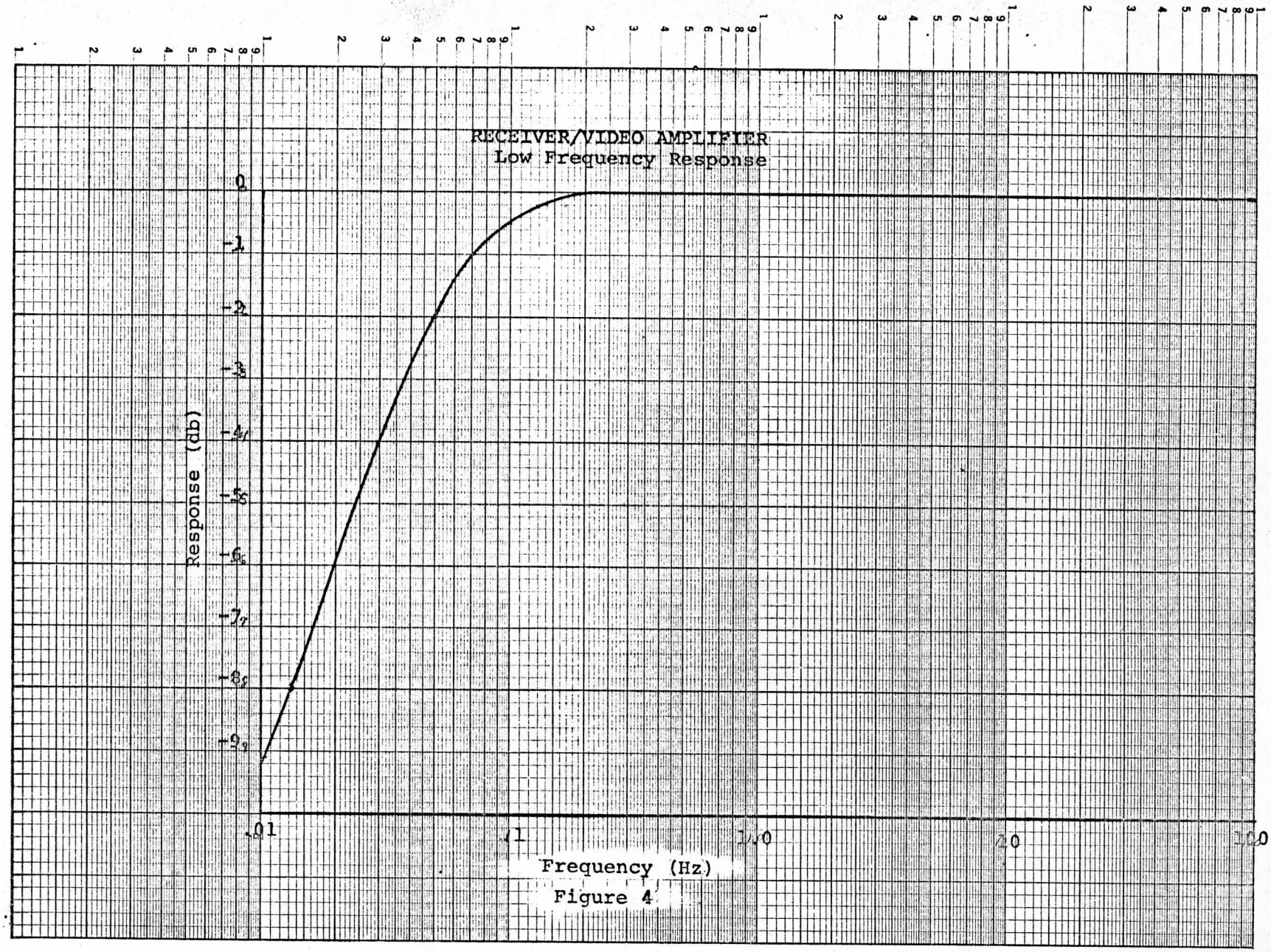
RECEIVER/VIDEO AMPLIFIER
Low Frequency Response
Response (db)
0
-1
-2
-3
-4
-5
-6
-7
-8
-9
.01
.1
1.0
10
100
Frequency (Hz)

Figure 4

RECEIVER/VIDEO AMPLIFIER
High Frequency Response
+0.5
0
-0.5
-1
-2
-3
-4
Response (db)
1.0
10
30
Frequency (MHz)

Figure 5

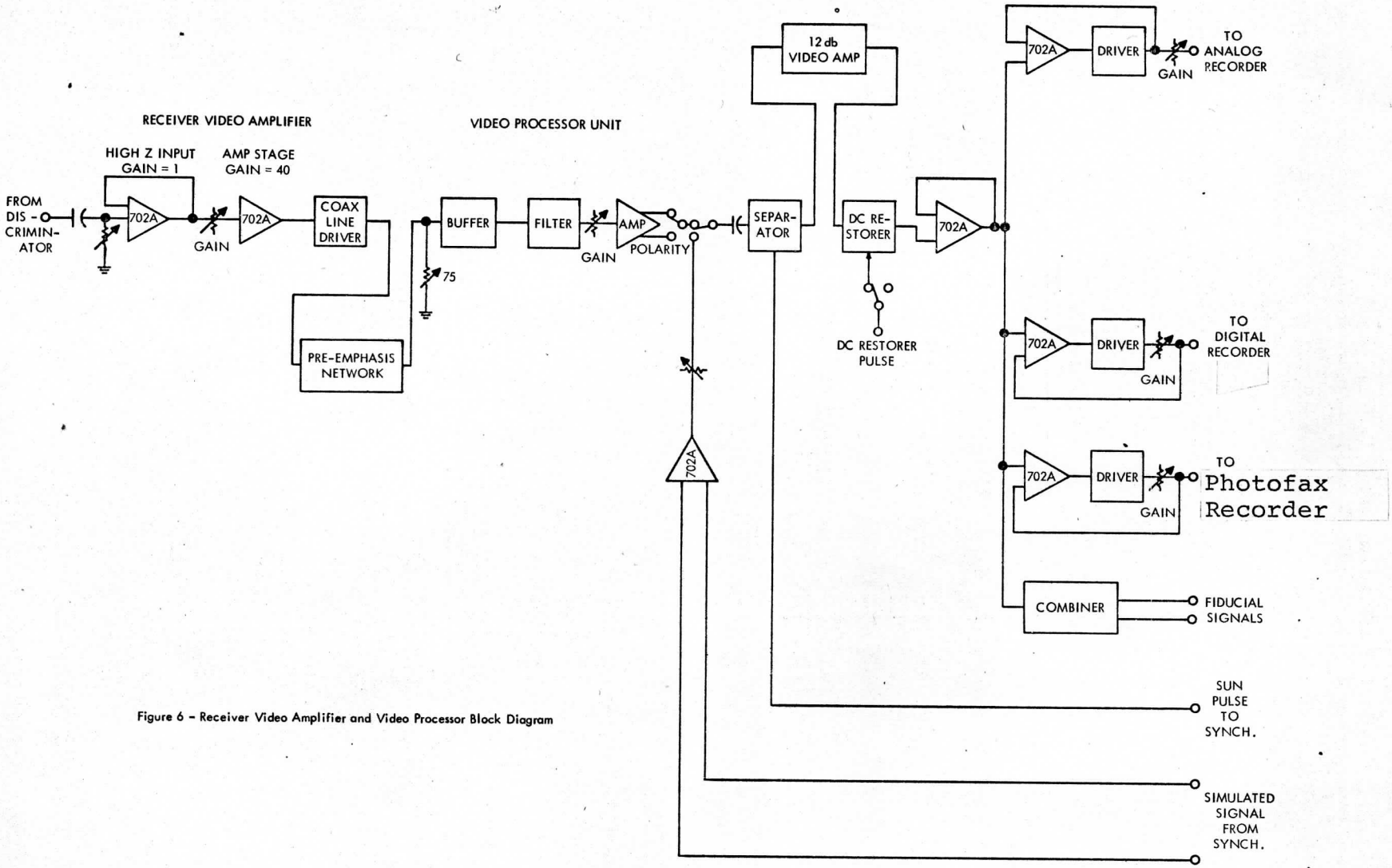

Figure 6 – Receiver Video Amplifier and Video Processor Block Diagram

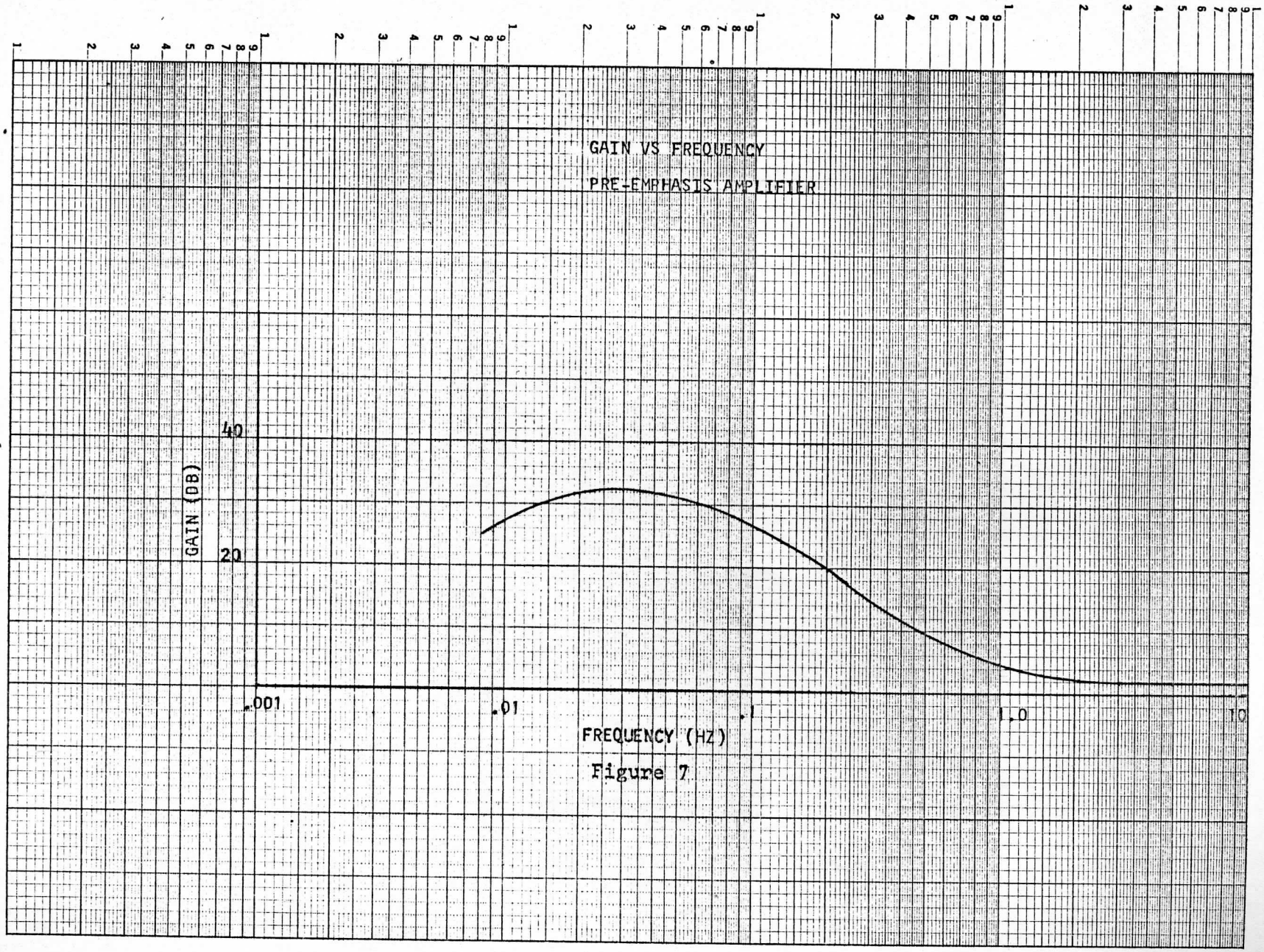
GAIN VS FREQUENCY
PRE-EMPHASIS AMPLIFIER
GAIN (DB)
40
20
.001
.01
.1
1.0
10
FREQUENCY (HZ)

Figure 7

VIDEO PROCESSOR
200 KHz Filter Response
Response (db)
0
-10
-20
-30
.1
1.0
10
100
500
Frequency (KHz)

Figure 8

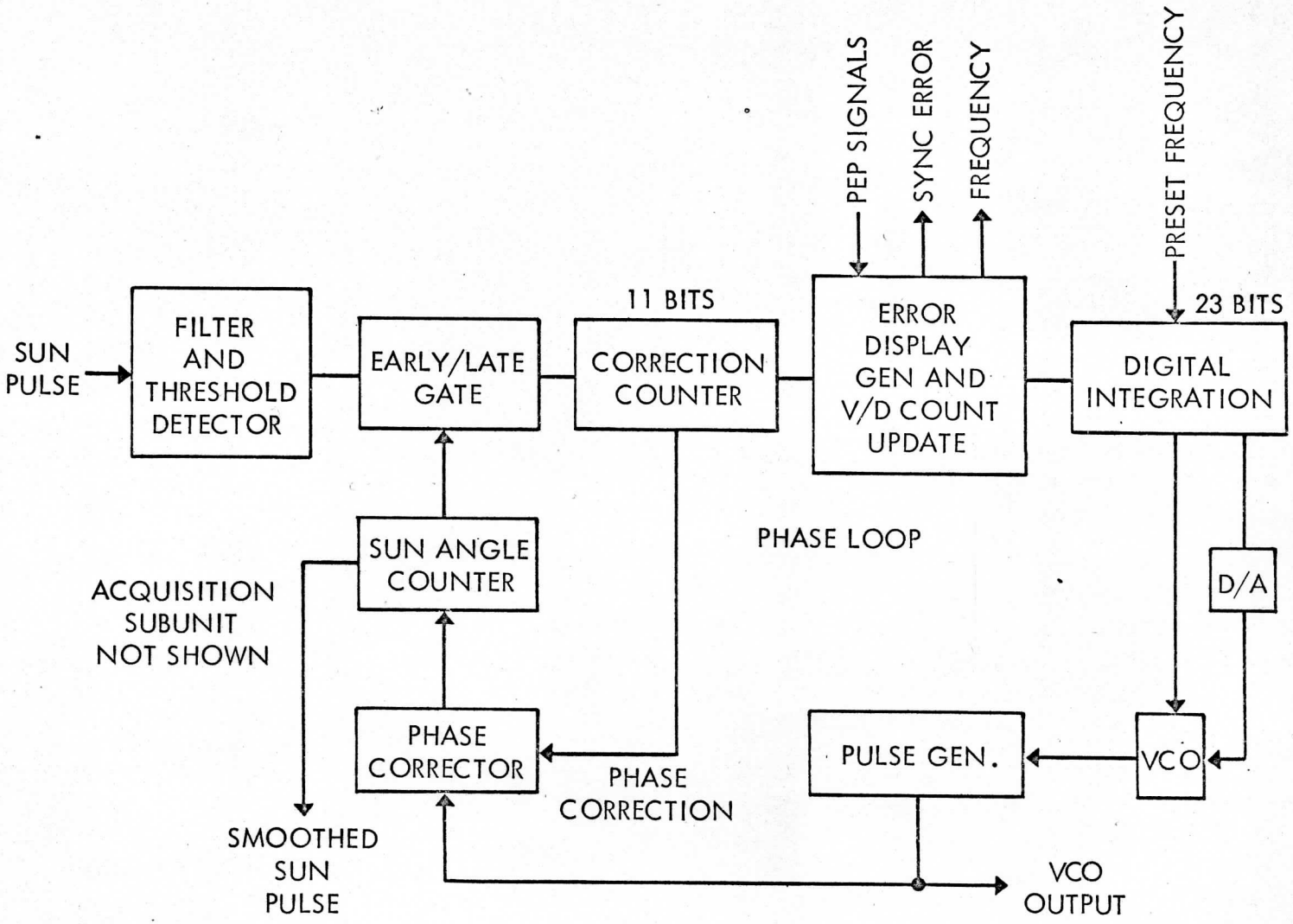

Figure 9 - Phase Locked Loop Block Diagram

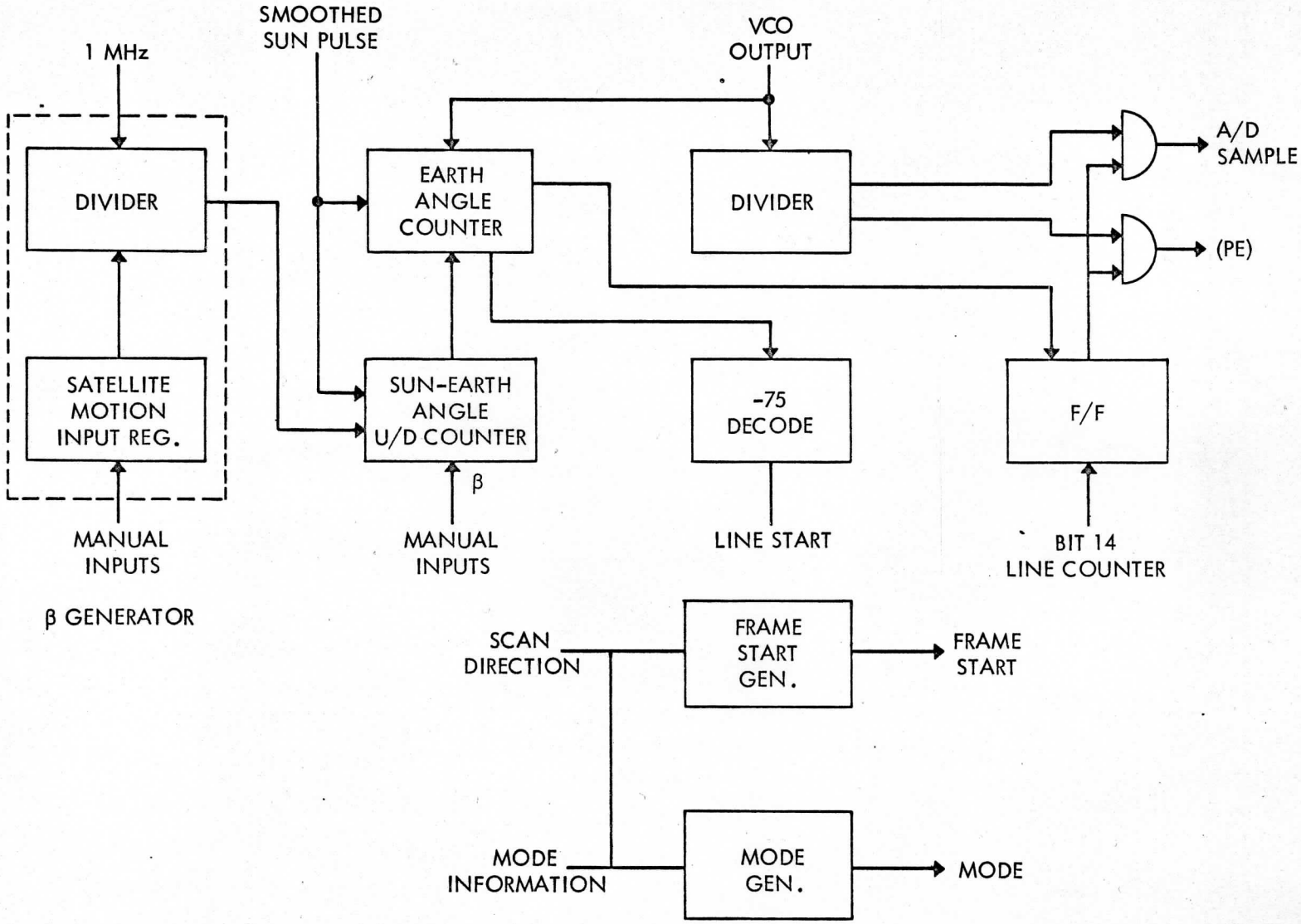

Figure 10 – Basic Parts of Control Panel and Timing Subsystem

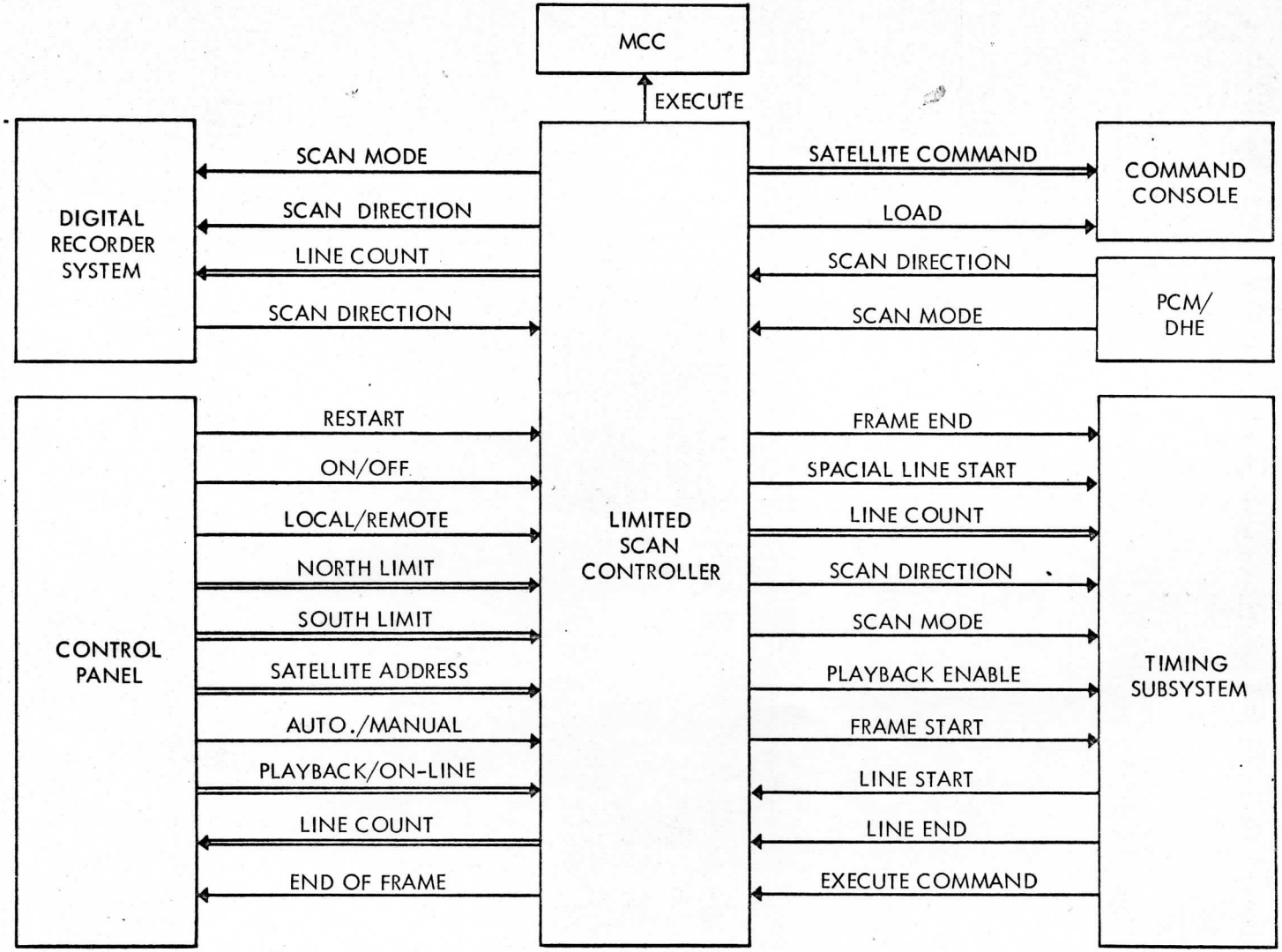

Figure 11 - Limited Scan Controller Interface Diagram

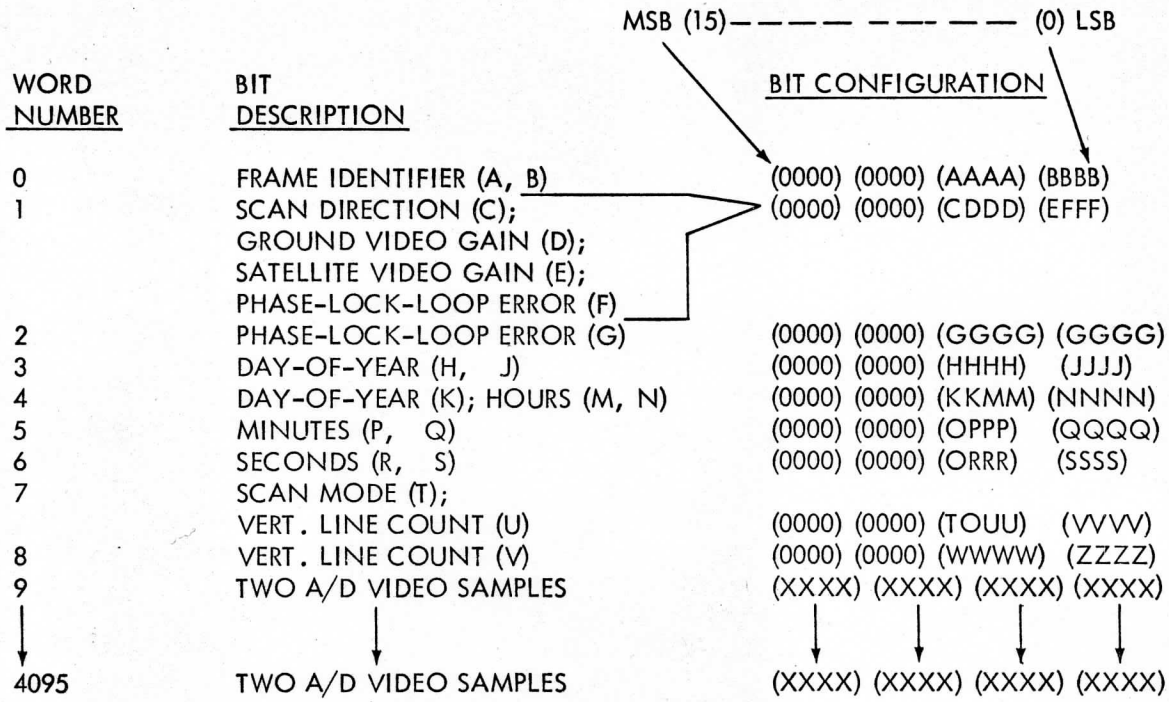

SYMBOLS:

A = TENS FRAME IDENT. BCD
B = UNITS FRAME IDENT. BCD
F = PHASE LOCK LOOP ERROR
2 HIGH-ORDER BITS (Binary)
H = TENS DAYS BCD
J = UNITS DAYS BCD
K = HUNDREDS DAYS BCD
M = TENS HOURS BCD
N = UNITS HOURS BCD

O = INTENTIONAL BLANKS ADDED IN FIRST NINE CORE WORDS

P = TENS MINUTES BCD
Q = UNITS MINUTES BCD
R = TENS SECONDS BCD
S = UNITS SECONDS BCD
U = THOUSANDS LINES BCD
V = HUNDREDS LINES BCD
W = TENS LINES BCD
Z = UNITS LINES BCD

Figure 12 - Word Format for Core Memory Stored Line Data

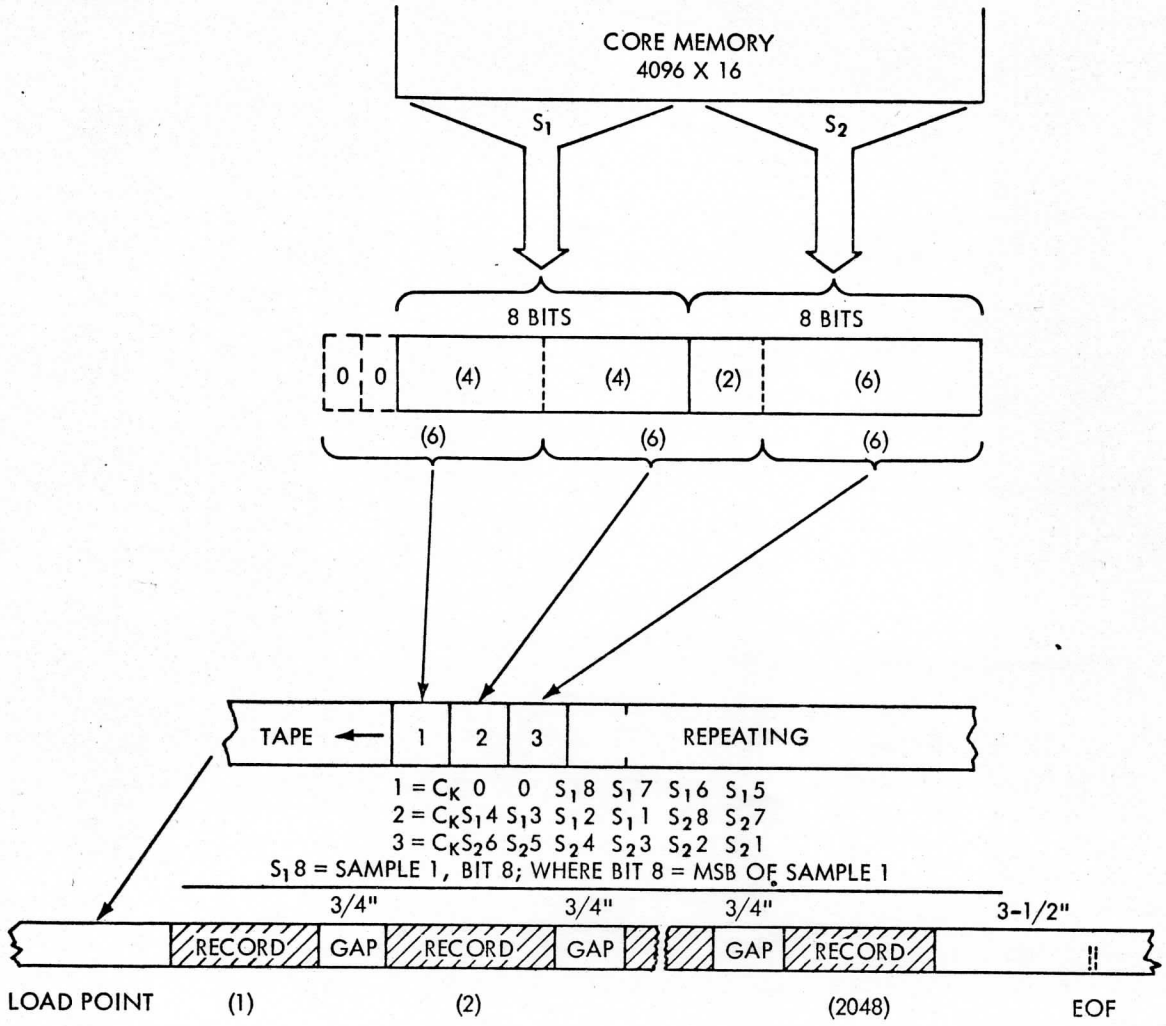

Figure 13 – Phase Two Core Unload – Record Pattern

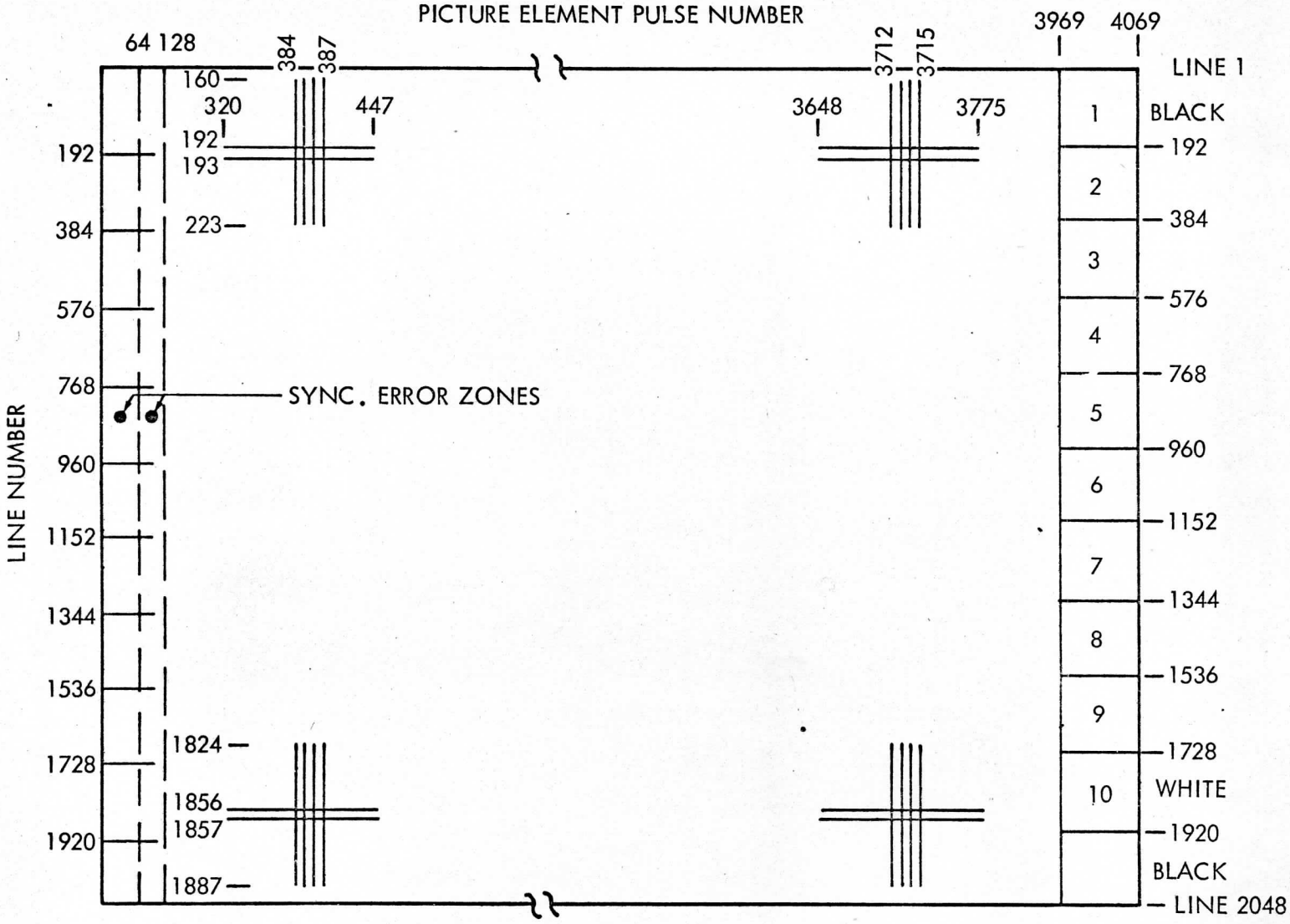

Figure 14. - Gray Scale and Fiducial Mark Locations

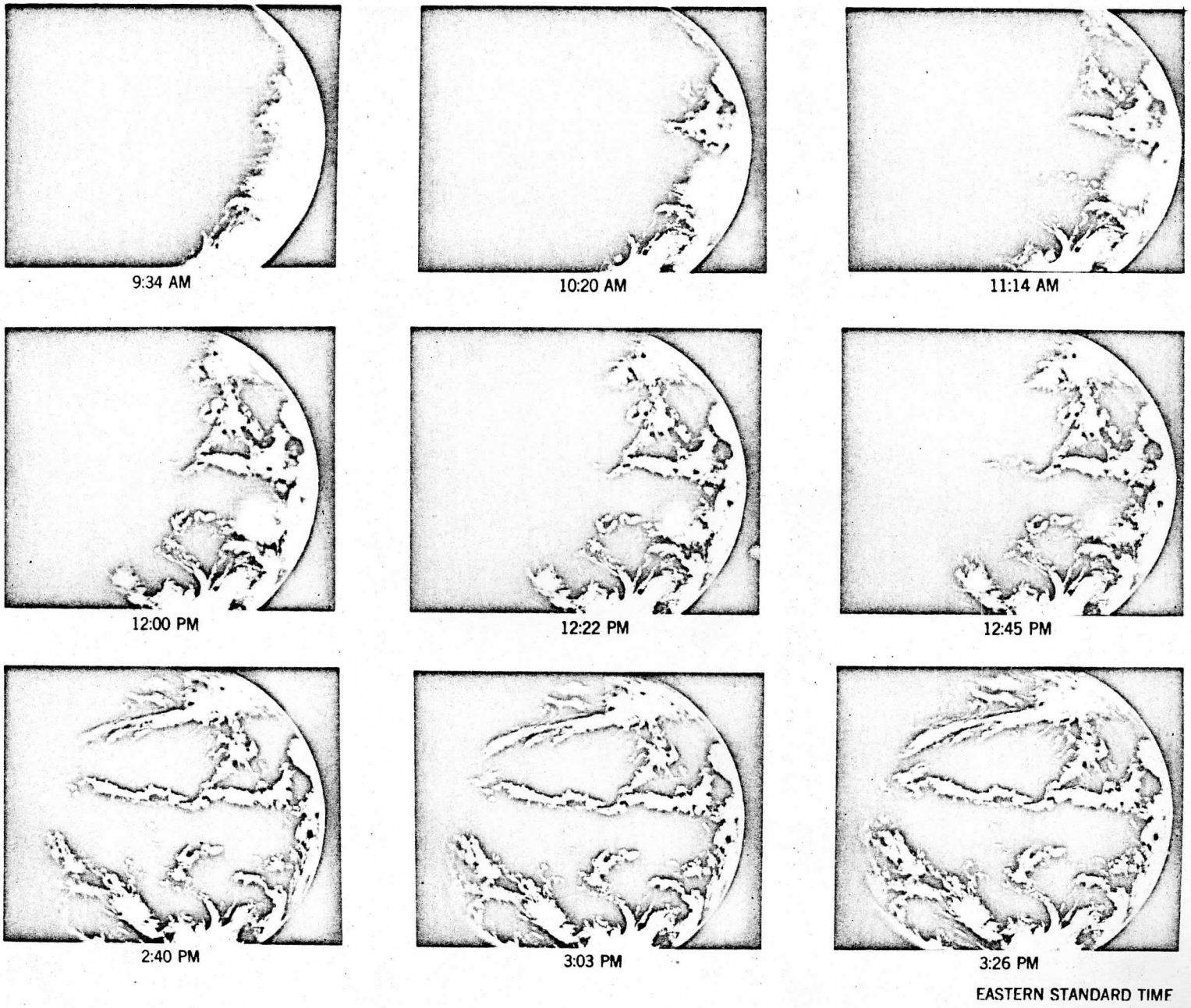

Figure 15. Pictures taken with the Spin Scan Camera System.

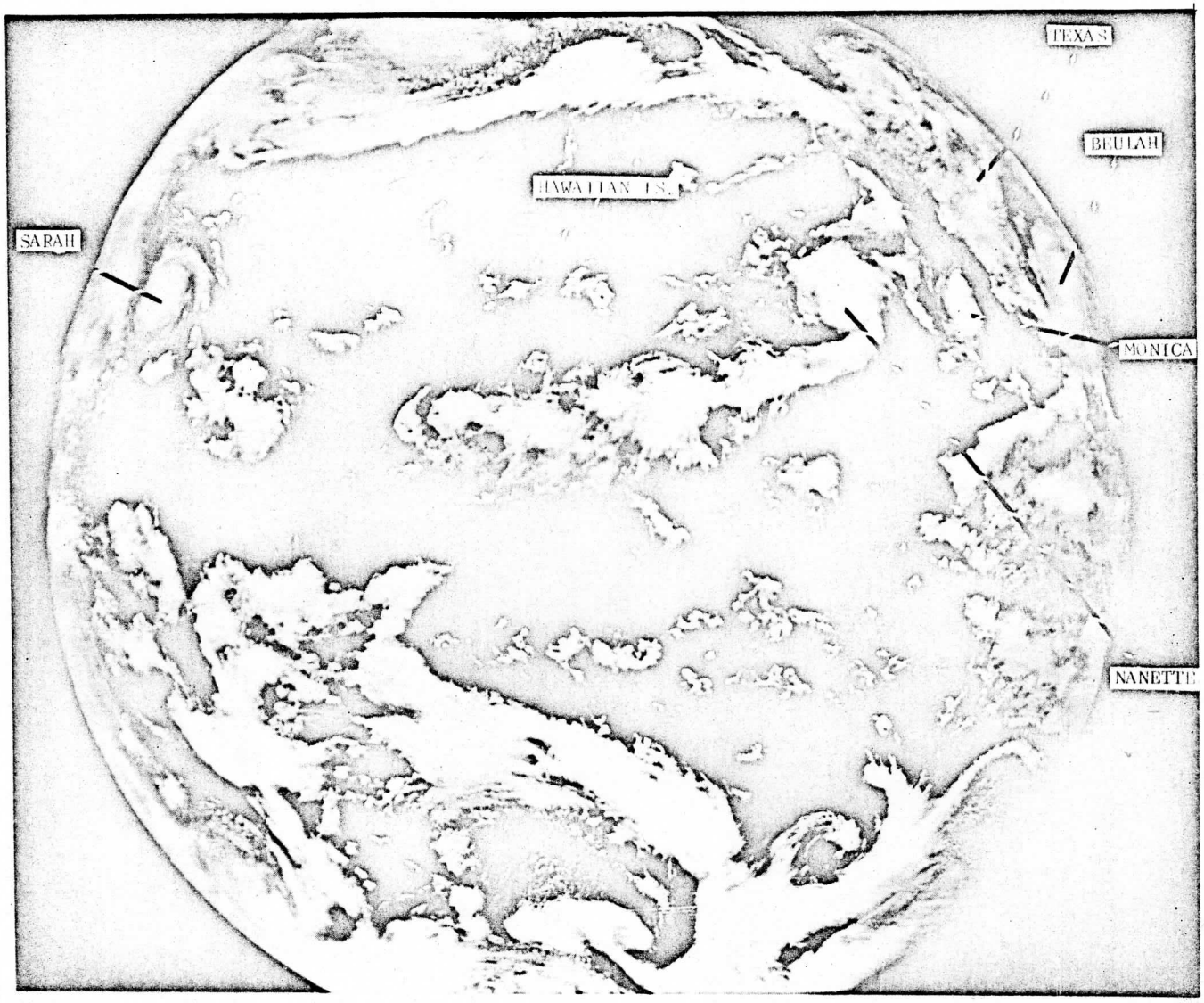

Figure 16. Spin Scan Camera Photograph taken on September 17, 1967.

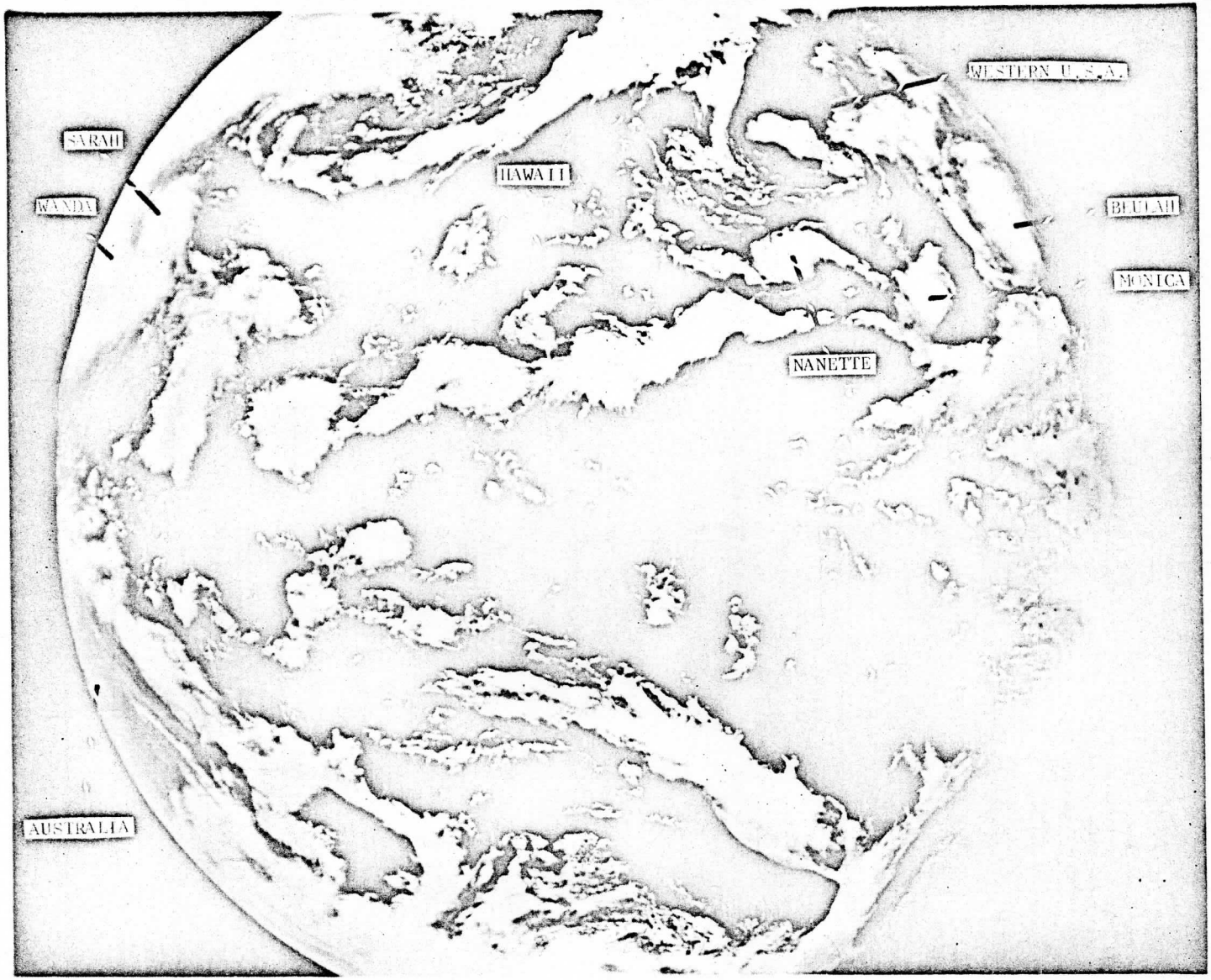

Figure 17. Spin Scan Camera Photograph taken on September 19, 1967.

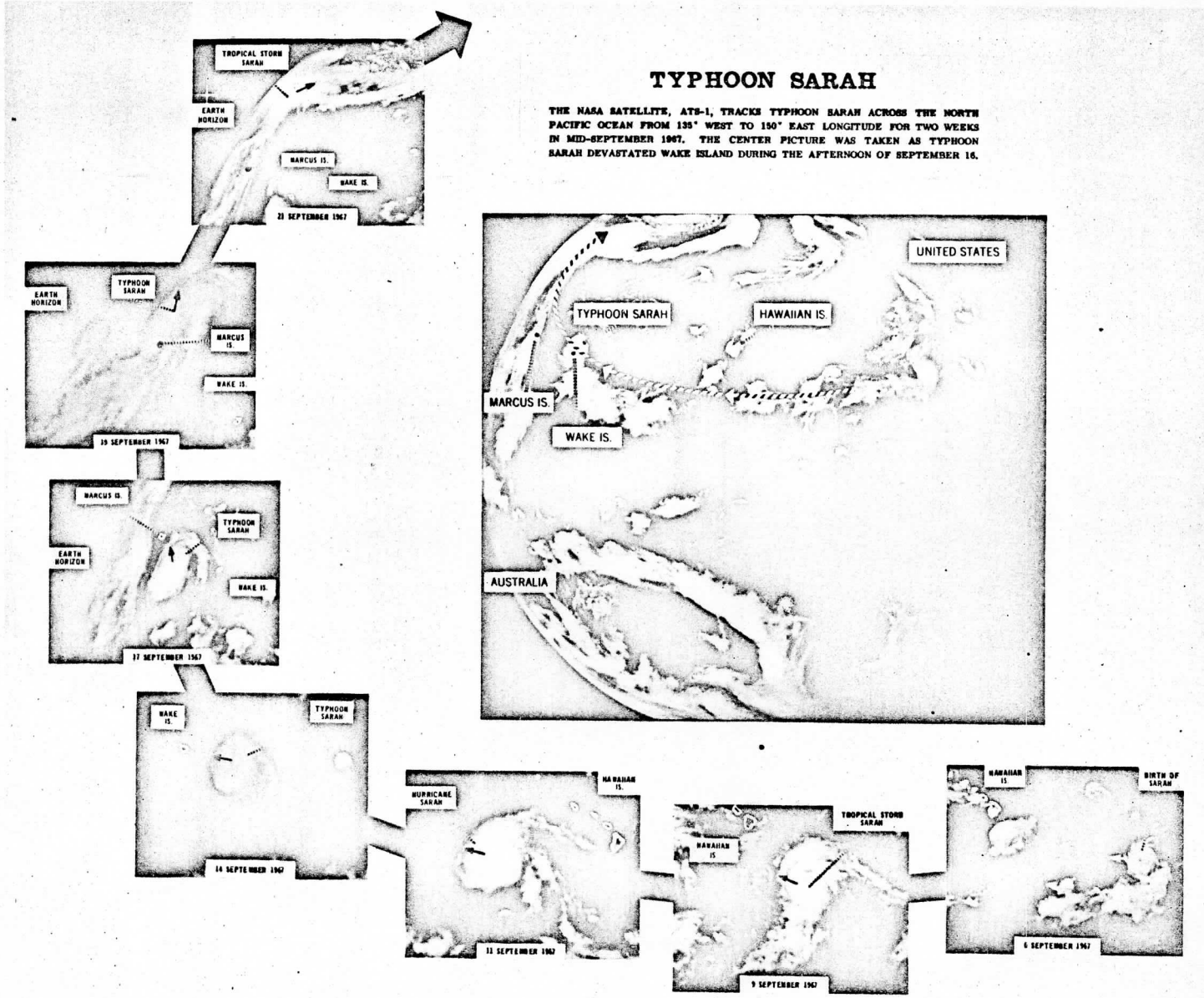

Figure 18. Pictures Originally taken with the Spin Scan Camera System.

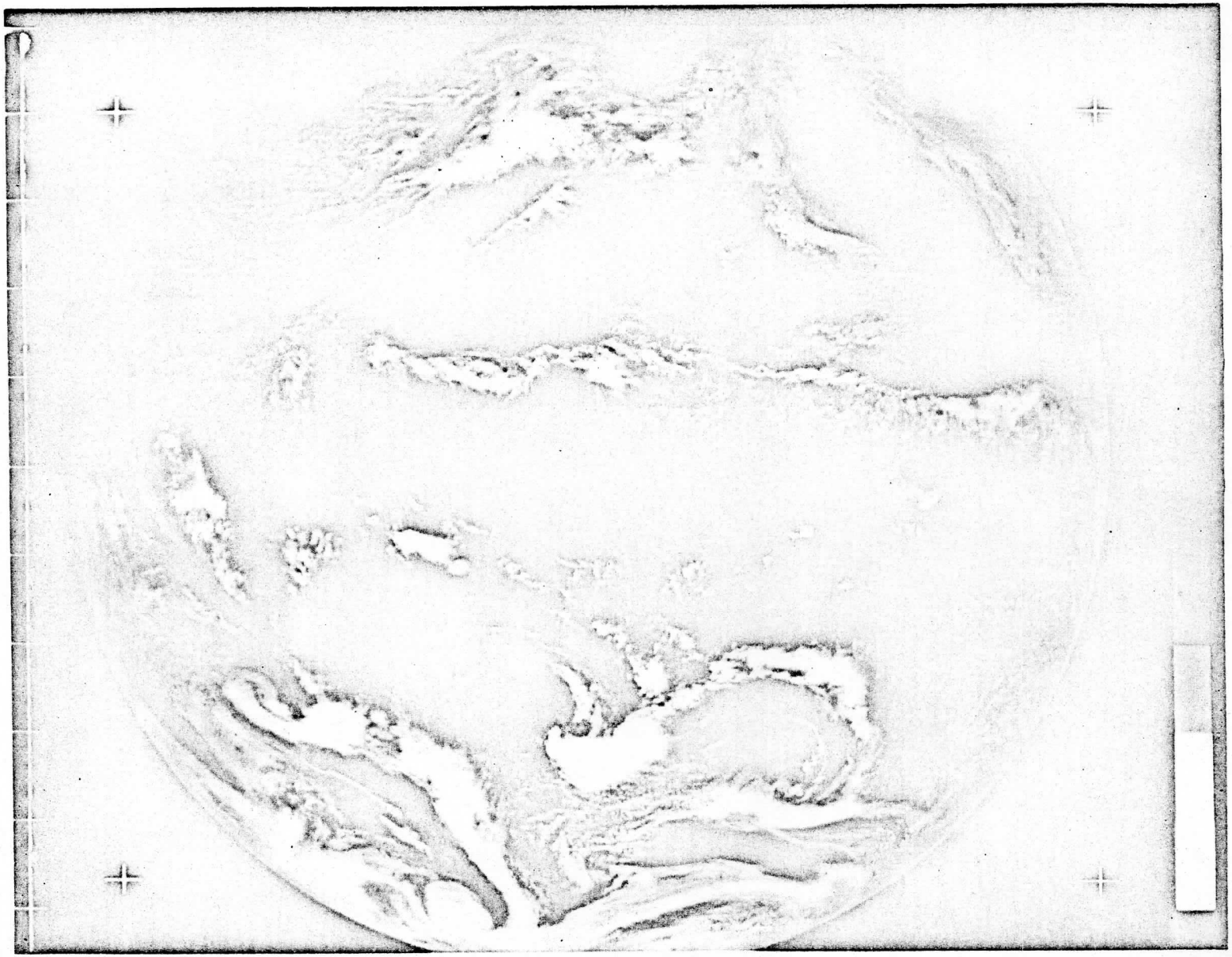

Figure 19. Picture taken with the Spin Scan Camera System.

Revised #23

WEFAX - A WEATHER DATA COMMUNICATIONS EXPERIMENT

by

David W. Holmes
ESSA

S-68

CONTENTS

1. Introduction

2. WEFAX System Description

3. ATS-1 Satellite
   a. Microwave Communication System
   b. VHF Communication System
   c. Spin Scan Cloud Camera System

4. WEFAX Receiving Stations

5. WEFAX Data

6. Evaluation of the Experiment

7. Conclusions

8. Future Plans

9. Hydrologic Data Experiment

10. Acknowledgement

1. INTRODUCTION

The Weather Facsimile Experiment (WEFAX) was begun December 14, 1966, to explore the operational feasibility of transmitting meteorological data directly from a central source to widely scattered remote weather stations via a communications satellite. The experiment is under the joint supervision of the National Aeronautics and Space Administration (NASA), Goddard Space Flight Center, and the Environmental Science Services Administration (ESSA), National Environmental Satellite Center. The Applications Technology Satellite (ATS-1) is being used to relay meteorological data to ground stations equipped to receive Automatic Picture Transmission (APT) signals from ESSA and Nimbus satellites. The receiving stations cooperating in the experiment are located over an area extending from the east coast of the United States to Australia and Japan. This experiment is providing experience to be used in developing a system that could be a part of the World Weather Watch Global Telecommunications System to furnish the various types of meteorological data required at meteorological facilities with a minimun time delay.

The objectives of the WEFAX experiment include the determination of the feasibility of providing additional processed weather data transmissions in facsimile format that can be recorded in existing APT ground stations. The intent of this new service is to provide the local user with weather information to supplement other meteorological data available at the station. An integral part of the WEFAX experiment consists of transmitting, for reception by APT ground stations,

selected cloud cover photographs taken by an experimental spin scan camera located on the ATS-1 Satellite, and selected ESSA satellite pictures and picture composites processed by computer at the National Environmental Satellite Center. This experiment provides supplemental weather data in a timely fashion to the local user and makes possible greater utilization of APT ground station facilities.

The APT stations participating in the experiment prepare daily and monthly evaluation forms which are forwarded, together with the samples of WEFAX transmissions received, to the WEFAX Project Office for evaluation. Analysis indicates that weather charts can be transmitted successfully from a central source through an earth synchronous satellite to widely scattered receiving stations. Stations at the periphery of the radio contact area of the satellite can operate with antenna acquisition angles as low as 3^{o} elevation with assurance of usable reception more than 90 percent of the time.

Use of the communications facilities of the ATS-1 spacecraft permits the transmission of data from one central location to all APT stations within radio reception range of the satellite (figure 1). Data originating at the National Environmental Satellite Center and the World Meteorological Center, Washington, D. C., are transmitted in facsimile format to the ATS ground station at Mojave, California, where they are sent to the spacecraft by the up-link transmitter. The VHF transponder aboard the spacecraft retransmits the data in a format patterned after that of the automatic picture transmission system. The WEFAX field center, a transportable ground station at Mojave, contains equipment for transmission of data and has the capability for providing a closed loop evaluation of the WEFAX transmissions to and from the satellite.

The contents of the WEFAX transmissions are experimental in nature and have been varied throughout the experiment. Some of the variations are in the types, scales, and projections of the weather charts and in the inclusion of supplemental information during special synoptic situations such as tropical storms. The WEFAX transmission periods vary since transmission times are shared with other experimental programs using the satellite. However, suffecient operations can be conducted to evaluate in depth all variables of the feasibility study and at the same time provide APT stations with useful information.

2. WEFAX SYSTEM DESCRIPTION

Figure 2 illustrates the ATS-1 WEFAX system. Weather maps, cloud cover pictures, and other meteorological data processed at the World Meteorological Center or at the National Environmental Satellite Center are transmitted via facsimile line to the Mojave ATS WEFAX field center.

Computer processed products transmitted from the National Environmental Satellite Center are gridded single frame ESSA 3 and 5 pictures and picture mosaics processed to an APT format. The computer process involves: (1) putting the raw digital image into a suitable format to facilitate digital processing; (2) normalizing the brightness of each AVCS frame to compensate for brightness inconsistencies; and (3) using the earth locator information computed for each raster point position to provide latitude-longitude grid lines and major coast line overprints for each image frame.

The computer derived digital information (frame or mosaic) is converted to analog form for transmission or recording purposes. The resulting product is an 800 x 800 point raster image in APT format with superimposed latitude-longitude grids and coast lines. The grid and

character imagery is added so that the brightness signal polarity is the reverse of that of the scene to permit this information to be easily distinguishable. The data from the facsimile encoder are then transmitted in APT form over the specially conditioned (equalized) 3 kHz land line to the WEFAX field center at Mojave for transmission to the ATS satellite.

Figure 3 is a block diagram of WEFAX functions at the ATS ground station, Mojave, California. The spin scan cloud camera picture data are received at the station from the satellite and digitized and recorded as analog signals. The digitized spin scan camera data, recorded on magnetic tape, are mailed to the National Environmental Satellite Center for processing in a manner similar to that for the ESSA 3 and 5 data described above. The analog spin scan camera data are converted into a photographic negative by a special camera processor. The negative is manually inserted together with an overlay grid in the flying spot scanner section of the photo recorder. The flying spot scanner has an electronic zooming capability so that specific sections of the positive can be selected and expanded for transmission. The output signal of the flying spot scanner is in a format compatible with APT ground station recorders.

The WEFAX field center also contains a facsimile scanner which can be used to transmit notices or an emergency weather data package if a disruption occurs in the land line from Suitland. The transmissions to and from the satellite (at 149.22 MHz and 136.60 MHz, respectively) are monitored on separate receivers. The output of each receiver is recorded on a tape recorder and displayed on a facsimile recorder.

3. ATS-1 SATELLITE

The ATS-1 spacecraft carries the following systems which are used in

the WEFAX experiment:

a. Microwave communication system.

The microwave communication system is designed to receive (earth to spacecraft) at frequencies of 6301 to 6312 MHz and to transmit (spacecraft to earth) at frequencies of 4195 and 4120 MHz. Receiving and transmitting antennas and traveling wave tube power amplifiers are used in conjunction with a dual mode communications transponder to provide a system element capable of accepting and handling any type of communications traffic or wide band communications. The spin scan camera data is transmitted from the satellite to the Mojave field station via the microwave communications link.

b. VHF communications system.

The very high frequency communication system is an active frequency translator. The receive frequency (earth to spacecraft) is 149.22 MHz. The transmit (satellite to earth) frequency is 135.60 MHz. this system is used to demonstrate the feasibility of various applications for which operation in the very high frequency bands is either desirable or necessary. The phased array antenna system is electrically despun to produce a beam pointed constantly toward the earth.

c. Spin scan cloud camera system.

The camera is described in detail elsewhere in this volume.

4. WEFAX RECEIVING STATIONS

The APT ground station equipment used to receive pictures transmitted directly from Nimbus and ESSA spacecraft can receive the WEFAX transmissions provided the ground stations have been modified to receive

the ATS-1 frequency of 135.6 MHz. In most cases the modification required is only the addition of a suitable crystal for the ATS frequency. At some locations where a radio frequency band pass filter is used, it may be necessary to change or modify the filter system. Many stations are using a frequency tunable band pass cavity type of filter capable of being tuned over the range of 135 to 138 MHz.

A WEFAX experiment participant's guide has been forwarded to all APT ground stations participating in the experiment. The participant's guide is an operating reference for use with the ATS-1 weather facsimile experiment and describes in detail the experiment, the aims of the project, and the methods of operation. The guide includes an azimuth-elevation overlay diagram which permits each station to determine its antenna look angles to receive the signals from the satellite. The ATS-1 WEFAX schedules are transmitted in a daily message (TBUS-3) over teletypewriter circuits covering the area of interest of the WEFAX experiment.

5. WEFAX DATA

Test charts, weather maps and cloud pictures have been transmitted. Typical examples are shown in Figures 4 - 7. Effects of satellite nutation, environmental conditions, and radio frequency interference are evaluated. The weather charts sent from ESSA's National Meteorological Center vary in content, format, and scale. Several types of pictures are used. Nimbus and ESSA pictures scanned by facsimile equipment, ESSA 3 and ESSA 5 AVCS picture data prepared in digital APT format with grids, and mosaicked ESSA 3 and 5 pictures for various areas of the Pacific are transmitted via WEFAX. In addition, the spin scan cloud

camera pictures are retransmitted by facsimile equipment from Mojave and experimental transmissions of computer processed spin scan pictures are transmitted from Goddard Space Flight Center and from the National Environmental Satellite Center.

6. EVALUATION OF THE EXPERIMENT

The APT stations cooperating in the experiment on a voluntary basis evaluate the effectiveness of the WEFAX experiment. The stations collect samples of charts and pictures to complete the WEFAX Daily Evaluation Reports (Figure 8) for specified periods and the WEFAX Monthly Evaluation Reports (Figure 9) and mail them to the experimenter.

Reports from the participating APT receiving stations are the primary source of data for evaluating the WEFAX experiment. Therefore, the important role of each of these stations cannot be over-emphasized. The cooperating stations have been requested to give high priority to the daily test charts since they will indicate communications link performance and will alert station personnel to equipment degradation. It is recommended that facsimile recorder copies be immediately protectively coated (for example, a clear lacquer spray) to avoid deterioration from exposure to light and temperature.

The lack of uniformity of receiving equipment, antenna angles, types of supplies available, etc., does not permit a single reception standard of evaluation to be used objectively for all receiving ground stations. However, in an attempt to maintain as much similarity as possible in individual subjective evaluations of legibility and quality, the following guidelines have been provided to the cooperating stations:

	Legible Information Available	Quality
Excellent	100% of data	Less than 10% imperfections
Good	At least 90% of data	Less than 30% imperfections
Fair	At least 70% of data	Less than 40% imperfections
Poor	At least 50% of data	Less than 50% imperfections
Unacceptable	Less than 40% of data	More than 75% imperfections

(The classification assigned should be the highest one satisfied by both characteristics; for example, if 80% of data legible and less than 30% imperfections, the chart should be classified "Fair.")

Since WEFAX transmissions are limited to about an hour each day, the experiment will be continued over a period of several months to permit collection of sufficient data for evaluation. All stations are encouraged to receive and evaluate as many of the test charts, cloud pictures and weather charts as possible to permit a more meaningful evaluation.

During December 1966, engineering checks were made of equipment, communication lines were placed in working order, and all operating procedures were activated and tested in both normal and emergency mode. Test transmissions of weather charts and spin scan camera pictures were made using the receiving stations at Mojave and GSFC to obtain the preliminary data required prior to the start of the overall experiment. A test WEFAX transmission of weather charts was started on December 14, 1966. Reception of WEFAX transmissions has been reported from APT stations in Australia, Canada, Canal Zone, Guam, Japan, New Zealand, Tahiti, and Wake Island, and also at stations in Alaska, California, Colorado, Florida, Hawaii, Louisiana, Maryland, Montana, South Dakota, Tennessee, Texas and Washington.

During 1967, nearly 50,000 WEFAX charts and pictures were evaluated by the participating stations and the WEFAX evaluators. Figure 10 shows the classification of weather charts and satellite pictures for January through December 1967. Satellite picture receptions were rated slightly higher than the weather chart receptions. Eighty-six percent of the charts were classified as "excellent" to "fair" and 14% as "poor" to "unusable." Ninety percent of the satellite pictures were classified as "excellent" to "fair" and only 10% as "poor" to "unusable." Figure 11 shows the monthly trend of charts and pictures classified as "excellent" or "good." The drop in the number of charts classified in the "good" or "excellent" caregory during July through September can be attributed to the reduced size of the charts transmitted. Seventy-five percent or more of the satellite pictures were classified as "good" or "excellent" beginning in July when the ESSA 3 and ESSA 5 mosaics were added to the WEFAX program.

The average number of grey scale steps discernible on the WEFAX test charts are depicted in Figure 12. Although the number of grey scale steps which are discernible is dependent upon the type of receiving equipment and the recording paper used, it is still a measurement of the capability of the WEFAX system. The average for all stations was 5.8 grey steps; however, two stations, Lake Jackson, Texas and Papeete, Tahiti, averaged 7.2 grey steps.

The major difficulties noted in WEFAX receptions are presented in Figure 13 as percentages of occurrence. Interference, which was the major reception difficulty, occurred 34% of the time. Noise was next at 30%, followed by jitter at 26%. The relatively high occurrence of jitter can be attributed to the use of tape recorders in recording the transmissions. The other reception difficulties were rather minor and

did not materially affect the WEFAX receptions.

Further discussions of monthly data evaluation are available in the ATS-Project Technical Data Report, or from the author.

7. CONCLUSIONS

Weather chart reception is of excellent quality with all of the participating stations reporting nearly 70% as good or excellent. Less than 5% of the charts that have been transmitted and received at participating stations have been classified as unusable; much of this unusable reception can be attributed to local problems. We feel this proves the feasibility of transmitting weather charts from a weather center through an earth synchronous satellite to widely scattered receiving stations, even to those with antenna acquisition angles as low as 3^{o}, and that useful reception can be assured more than 90 percent of the time. Over 70 percent of the receptions will contain at least 90 percent of the original data, and less than 30 percent will be imperfect, using present APT ground station equipment. It is obvious, therefore, that such a system could be incorporated into the World Weather Watch Program of the future.

8. FUTURE PLANS

WEFAX has been included in the ATS-3 program and is continuing with ATS-1. At present over thirty stations located in the United States and in five other countries are actively participating in the program on ATS-1. The extension of WEFAX on the ATS-3 satellite provides the opportunity for stations from many more nations to participate

in the experiment, and provides data for a large section of the earth (the Atlantic Ocean community) which is presently not being covered. Figure 14 shows the area of WEFAX coverage for both the ATS-3 and the ATS-1 and the location of many known APT stations. With ATS-3 over the equator at 47° West longitude the area of coverage for WEFAX extends to all of South America and most of Europe, Africa and North America. Approximately 30 nations and more than 150 APT ground stations are able to participate in the WEFAX experiment. This provides those nations with the opportunity of participating and contributing to the research required to develop specifications for a world-wide meteorological data link using synchronous satellites.

9. HYDROLOGIC DATA EXPERIMENT

There are currently several thousand sites in the United States, many remotely located, that form the basis of the reporting network in the river and flood forecast and warning service of the ESSA Weather Bureau Office of Hydrology. These reports are collected through all available communications media. However, data collection has not kept pace with the advances made in forecast preparation and dissemination. Increasing numbers of hydrologic sensors now have telemetering capability and the potential of the satellite for relaying hydrologic data is most promising.

A new system, under joint ESSA/NASA sponsorship, is being used experimentally to collect river and rainfall readings from hydrologic gauging stations by VHF relay through the ATS-1 satellite. Stations report when interrogated by a command sent from NASA's Mojave command

station through the satellite. The responses from the stations are received at Washington and recorded on a teleprinter.

Polling of the stations by Mojave is by magnetic tape loop having the pertinent address codes and sequences of stations recorded on it. A digital address scheme is used. Replies from the remote stations are in the form of audio signals forwarded to Washington via the WEFAX facsimile line on a real time basis. These data are recorded on a printer in the Hydrologic Services Office and on magnetic tape at Mojave.

At the remote stations the interrogation signal received from the satellite is fed to an address decoder. When the correct sequence of pulses for the particular station is received, the transmitter is turned on automatically and the data register is scanned at a teleprinter data rate. These data modulate the transmitter and the data message is transmitted to the satellite. The data register is updated at 15-minute intervals by the binary coded decimal output of the river stage and precipitation gauges. At the Washington end of the facsimile line the audio signals are demodulated and converted to print out the message on the teletypewriter.

The objectives of the hydrologic communications experiment include the determination of (1) the economic and technical feasibility of using satellites to relay hydrologic data from relatively unattended remote sites; (2) the utility of existing APT equipment as a medium for reception of data from these platforms; (3) the average transmitting power and receiver sensitivity required; and (4) an alternative system design including the central readout or several readouts.

In the initial test four platforms have been established; one near

Little Rock, Arkansas; the second near Sacramento, California; the third near Portland, Oregon; and the fourth in the Washington, D. C. vicinity.

The experiment was put into operation the first of August 1967. Results to date indicate that satellites can be used successfully to collect hydrological data from relatively unattended sites to existing APT stations or to a central facility. Experiments are continuing to determine the minimum transmitter power requirements and antenna configurations for the remote stations. These will provide essestial data for the design of a low cost operational system.

10. ACKNOWLEDGEMENT

The author wishes to express his appreciation to Mr. Paul Lehr for his editorial assistance, to Mr. Arthur Hall who aided in the data evaluation, Mr. Sheldon Wishna the WEFAX Technical Officer, and the many others within ESSA's National Environmental Satellite Center and National Meteorological Center and the NASA Goddard Space Flight Center's ATS Project who have aided in making the WEFAX experiment a success.

LEGENDS

Figure 1. ATS-1 WEFAX Reception Area

2. WEFAX Experiment Flow Diagram

3. WEFAX Field Center ATS Ground Station, Mojave, California

4. WEFAX Test Chart

5. Northern Hemisphere 300 MB Analysis Chart as received at Melbourne, Australia, and Papeete, Tahiti

6. ESSA 3 Pacific Mosaic received at Toronto on photofacsimile and paper facsimile

7. ATS-1 Spin Scan Cloud Camera Picture (full disc and section) received at Mojave, California

8. WEFAX Daily Evaluation Report

9. WEFAX Monthly Evaluation Report

10. Classification of WEFAX Reception, Jan. - Dec., 1967

11. Percentage of Excellent or Good Receptions by Months

12. Average Grey Scale Steps Received, Jan. - Dec., 1967

13. Percentage of Occurrence of Reception Difficulties During WEFAX Receptions, Jan. - Dec., 1967

14. Area of WEFAX Coverage for ATS-1 and ATS-3

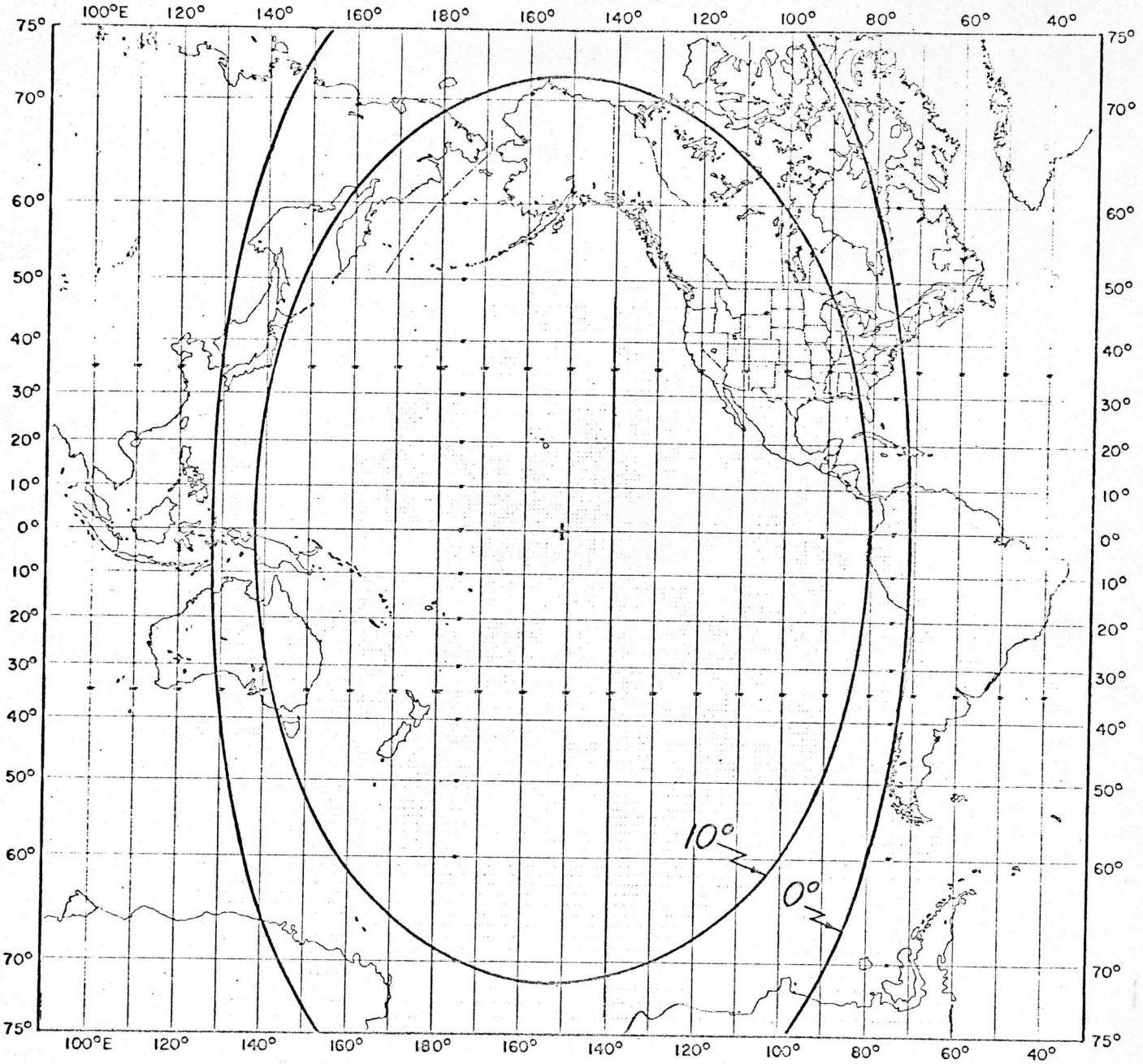
100°E
120°
140°
160°
180°
160°
140°
120°
100°
80°
60°
40°
75°
70°
60°
50°
40°
30°
20°
10°
0°
10°
20°
30°
40°
50°
60°
70°
75°
10°
0°

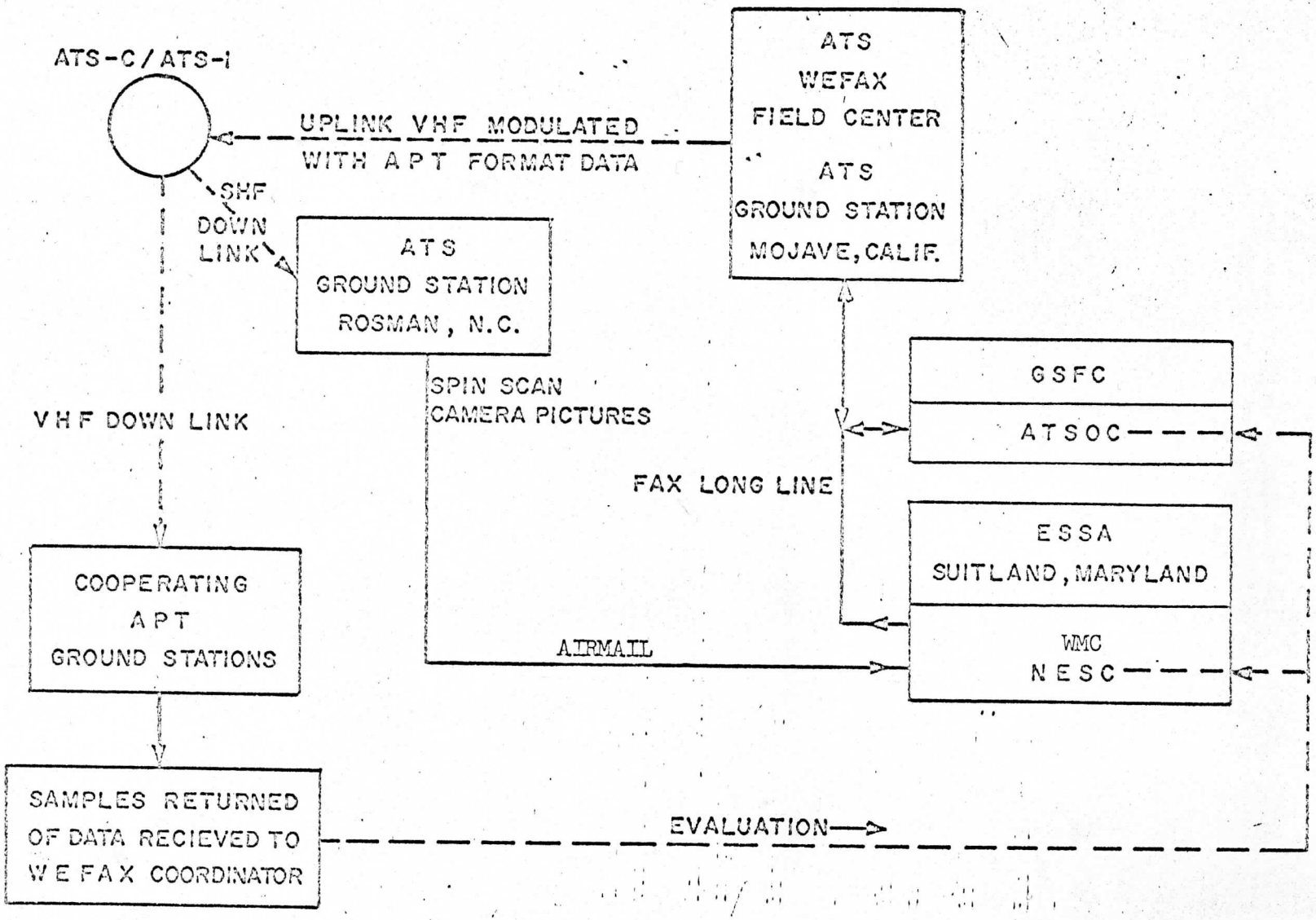
ATS-C/ATS-I
UPLINK VHF MODULATED
WITH APT FORMAT DATA
ATS
WEFAX
FIELD CENTER
ATS
GROUND STATION
MOJAVE, CALIF.
SHF
DOWN
LINK
ATS
GROUND STATION
ROSMAN, N.C.
SPIN SCAN
CAMERA PICTURES
GSFC
ATSOC
VHF DOWN LINK
FAX LONG LINE
ESSA
SUITLAND, MARYLAND
WMC
NESC
AIRMAIL
COOPERATING
APT
GROUND STATIONS
SAMPLES RETURNED
OF DATA RECIEVED TO
W E FAX COORDINATOR
EVALUATION

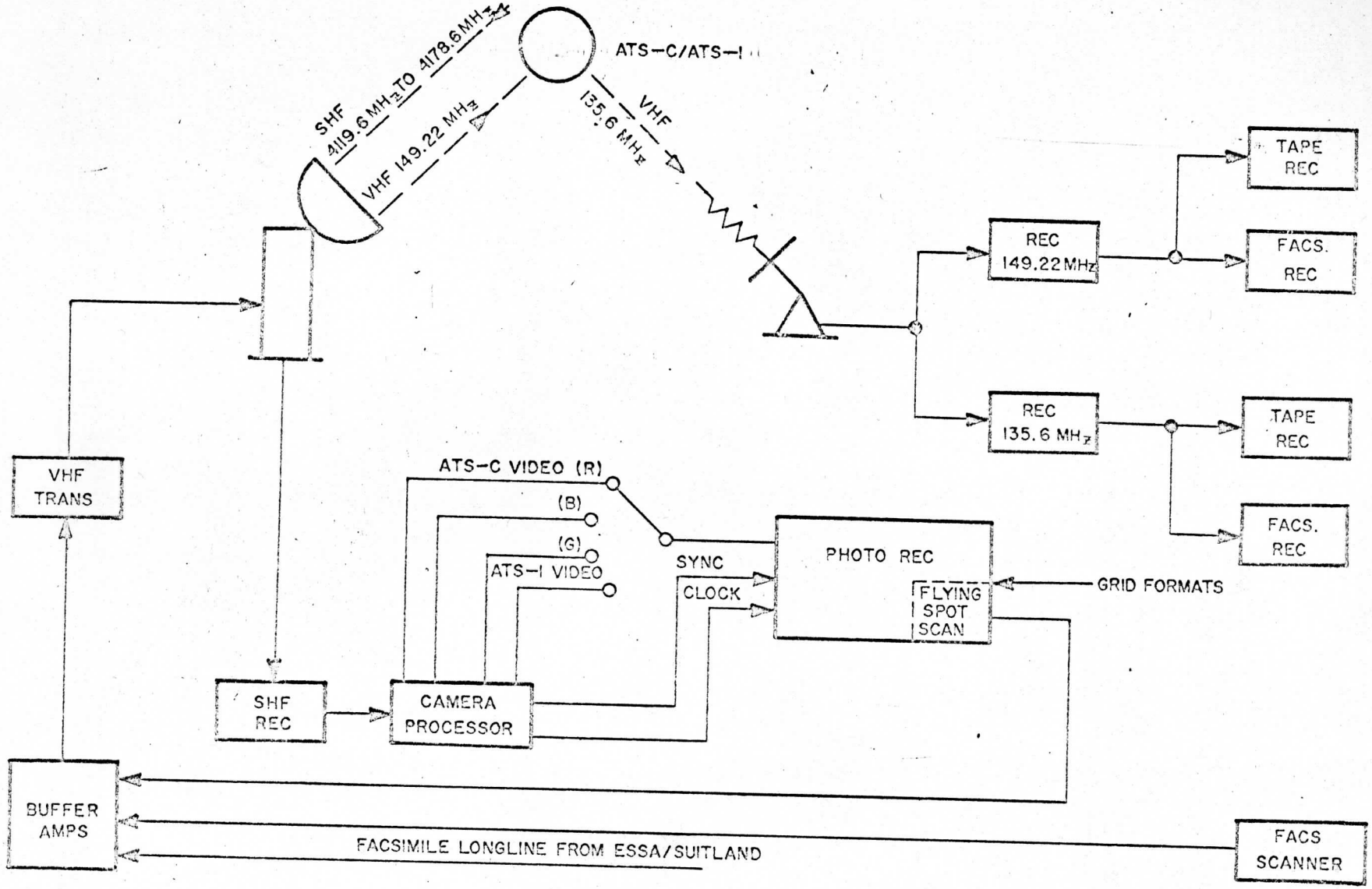
ATS-C/ATS-I
SHF
4119.6 MHz TO 4178.6 MHz
VHF 149.22 MHz
VHF
135.6 MHz
TAPE REC
FACS. REC
REC 149.22 MHz
REC 135.6 MHz
TAPE REC
FACS. REC
VHF TRANS
ATS-C VIDEO (R)
(B)
(G)
ATS-I VIDEO
SYNC
CLOCK
PHOTO REC
FLYING SPOT SCAN
GRID FORMATS
SHF REC
CAMERA PROCESSOR
BUFFER AMPS
FACSIMILE LONGLINE FROM ESSA/SUITLAND
FACS SCANNER

WEFAX DAILY EVALUATION REPORT

STATION (Location) _____ DATE(Z) _____

1. Receiver Signal Strength (Test Chart) _____ μv.
2. Antenna pointing angles: _____ ° azimuth; _____ ° elevation.
3. Interference _____ (yes/no); time _____ Z.

   Identification (characteristics) _____

   Brief description of interference _____

   _____

4. Number of steps of grey scale discernible on test chart _____.
5. Were recordings skewed more than 1/4 inch in 8 inches? _____ (yes/no)
6. Chart legibility and picture quality:

	Number of Charts	Number of Pictures
Excellent	_____	_____
Good	_____	_____
Fair	_____	_____
Poor	_____	_____
Unacceptable	_____	_____

7. Utility of charts and pictures: _____

   _____

   _____

   _____

8. Comments:

Signed _____

WEFAX Form No. 1

WEFAX MONTHLY EVALUATION REPORT

STATION (Location)_____ MONTH _____

1. Total number of charts received during month _____.

2. Total number of pictures received during month _____.

3. Chart legibility and picture quality:

	Number of Charts	Number of Pictures
Excellent	_____	_____
Good	_____	_____
Fair	_____	_____
Poor	_____	_____
Unacceptable	_____	_____

4. Comments (difficulties in data acquisition, reception, interference, chart legibility, chart formats, picture quality, usefulness, timeliness, etc.):

WEFAX Form No. 2

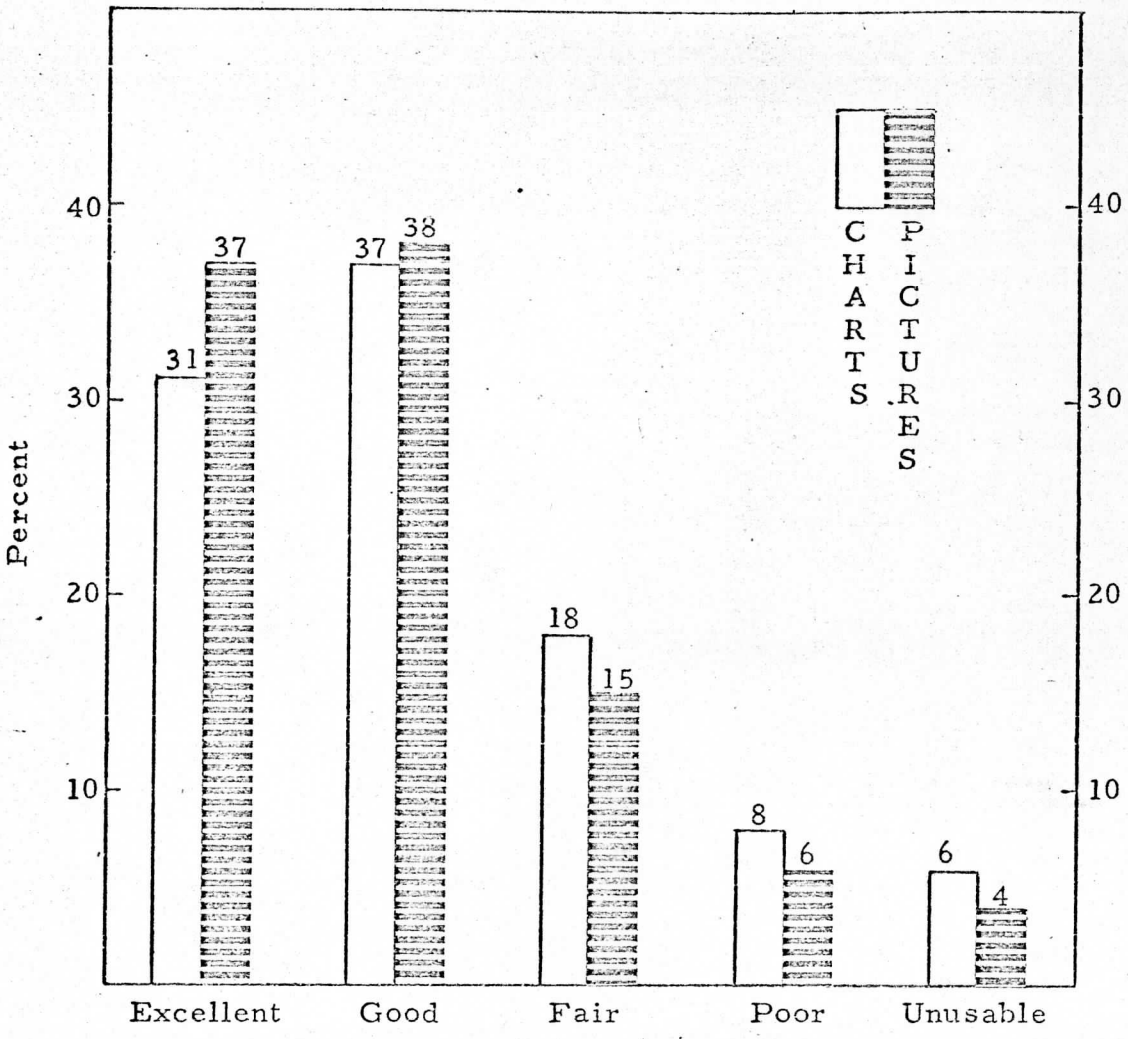

Classification Guidelines

	Legible Information Available	Quality
Excellent	100% of data	Less than 10% imperfections
Good	At least 90% of data	Less than 30% imperfections
Fair	At least 70% of data	Less than 40% imperfections
Poor	At least 50% of data	Less than 50% imperfections.
Unusable	Less than 40% of data	More than 75% imperfections

100
90
80
70
60
50
40
Percent
Charts
Pictures
J
F
M
A
M
J
J
A
S
O
N
D
Months During 1967

Station	Elev. angle	Grey Scale Steps
GSFC, Maryland	4°	
Aichi, Japan	5°	
Toronto, Canada	5°	
Fuchu, Japan	7°	
Tokyo, Japan	8°	
Howard AFB, C. Z.	10°	
MacDill AFB, Florida	11°	
Melbourne, Australia	11°	
Tampa, Florida	11°	
Nashville, Tennessee	13°	
Guam, Marianas	16°	
Aberdeen, South Dakota	18°	
New Orleans, Louisiana	18°	
Anchorage, Alaska	21°	
Lake Jackson, Texas	22°	
Christchurch, N. Z.	27°	
Seattle, Washington	29°	
Mojave, California	36°	
San Francisco, California	37°	
Pt. Mugu, California	38°	
Wake Island, Pacific	38°	
Kunia, Hawaii	65°	
Papeete, Tahiti	68°	
USS Oriskany, Pacific		

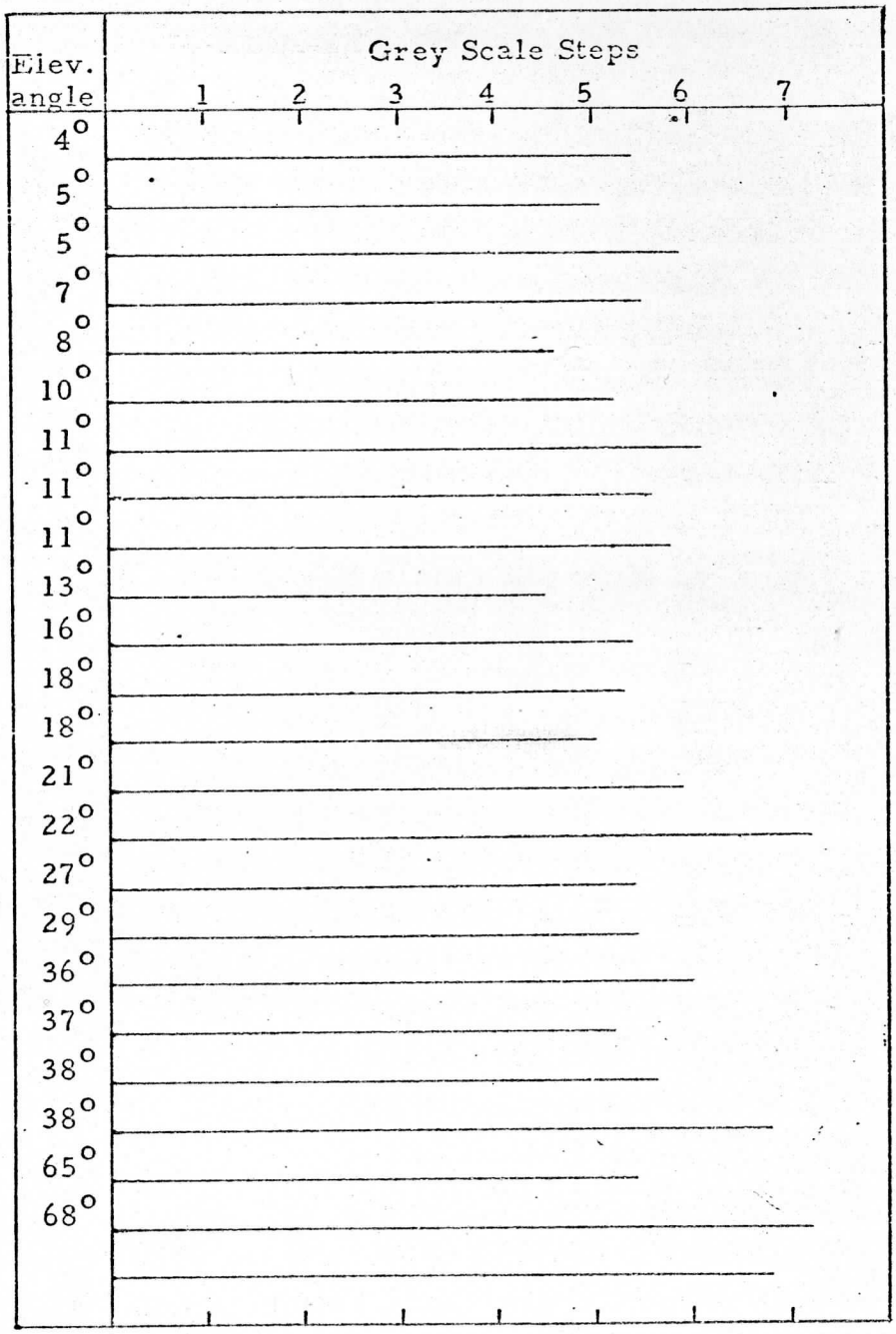

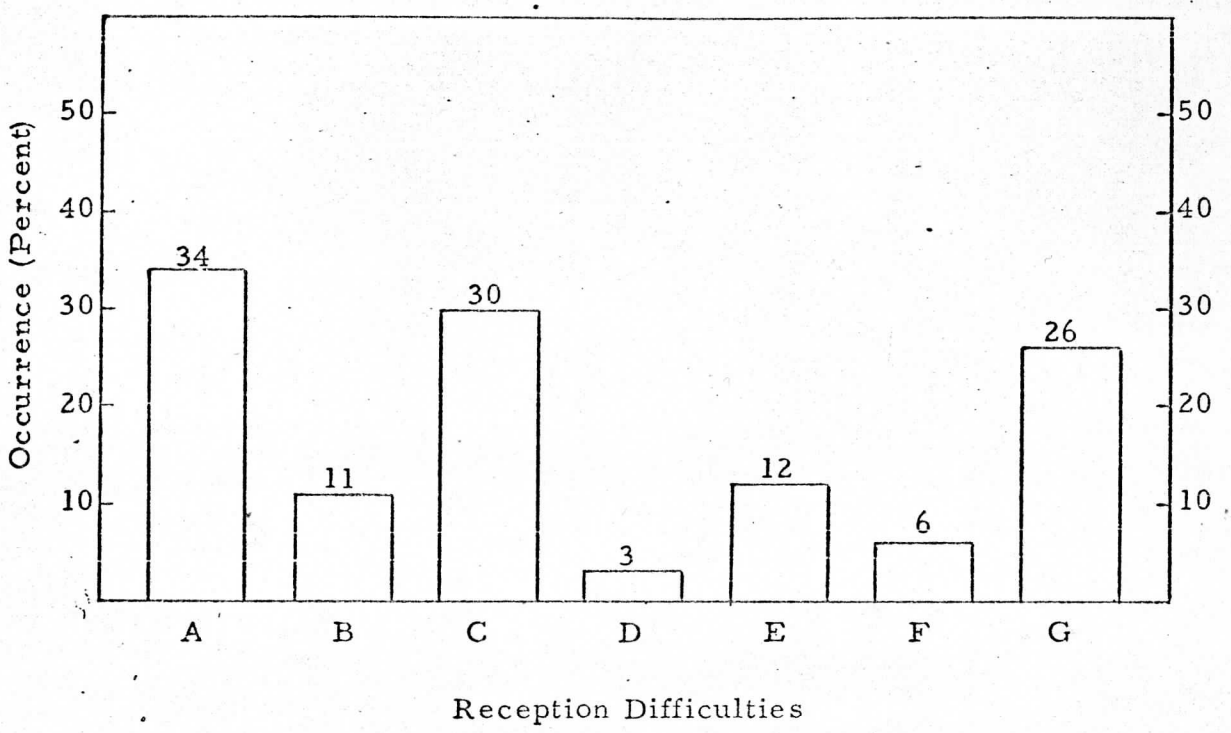

A - Interference - Visible patterns appearing on chart format as a result of external signal sources or internally generated beat frequencies.
B - Bleeding - Smearing and presentation on white areas by black.
C - Signal plus noise-to-noise - White or black streaks on chart, uniformity of tonal shades, snow effect.
D - Distortion - Large scale geometric deviation from time pattern.
E - Skew - Deviation of a vertical line from a vertical normal. Test limit - 1/4" in 8".
F - Multi-Image - The multiple chart reproduction (ghosts) caused by multiple path transmission or reflection.
G - Jitter - Periodic irregularities on lines and patterns.

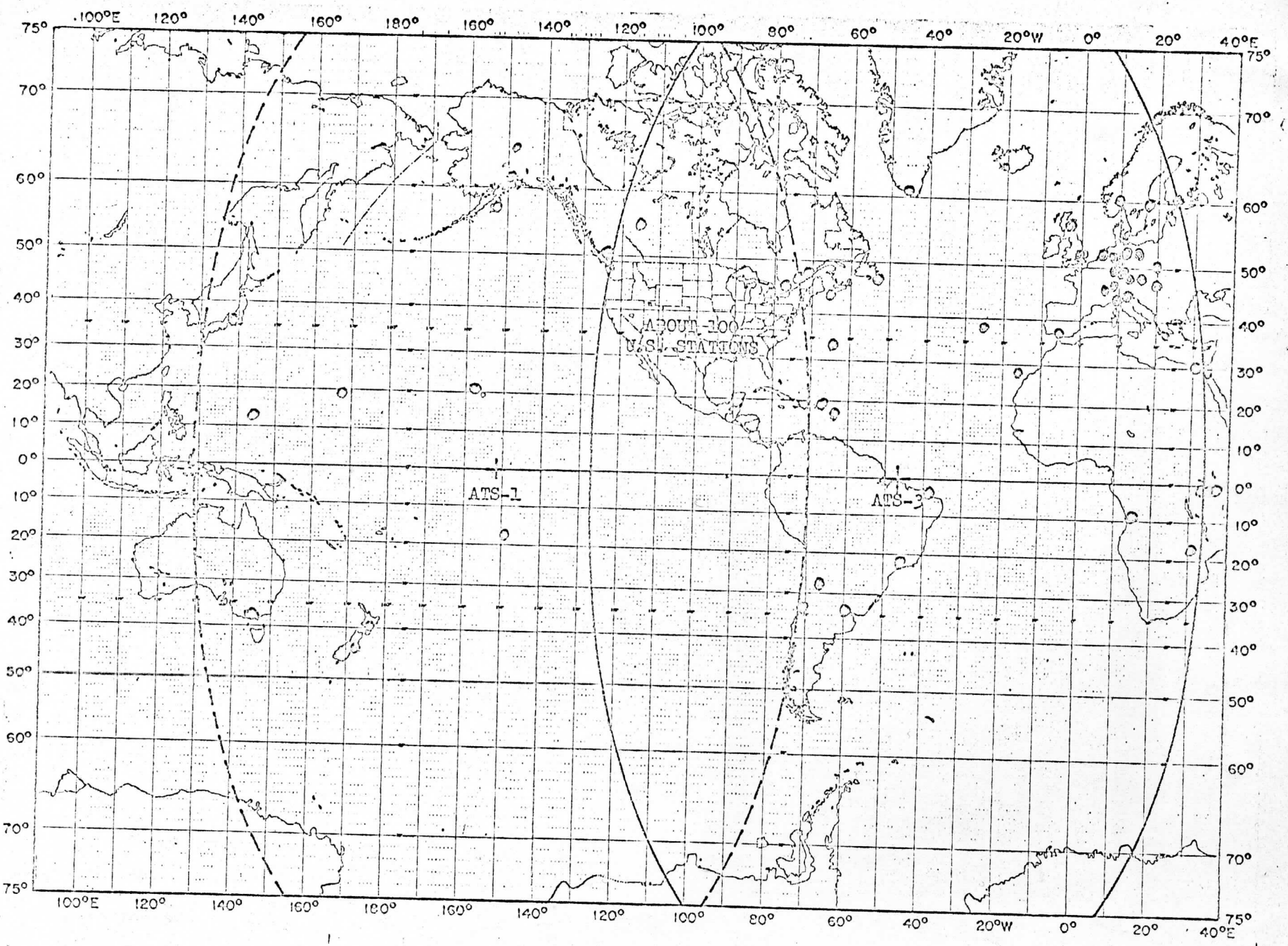
ABOUT 100
U.S. STATIONS
ATS-1
ATS-3
100°E
120°
140°
160°
180°
160°
140°
120°
100°
80°
60°
40°
20°W
0°
20°
40°E
75°
70°
60°
50°
40°
30°
20°
10°
0°
10°
20°
30°
40°
50°
60°
70°
75°

PRELAUNCH CAMERA CALIBRATION

by

Robert J. Parent
and
Verner E. Suomi

Space Science & Engineering Center
University of Wisconsin
Madison, Wisconsin

Prelaunch camera calibration, that is, camera response to a known light input, has been accomplished in two ways. The first method is to image a small area of a strip filament lamp on the camera field aperture. The lamp spectral characteristics and absolute output power are known (Bureau of Standards calibration) and the camera response is measured. If the input light level is within the linear range of the photomultiplier tube, a calibration point on the linear characteristic tube curve is established. The high light level or nonlinear region is known from both manufacturer's data and measurements made during extended tube burn-in.

The second method is to cause light to enter the camera entrance aperture from a known reflective surface exposed to direct sunlight. If the sun and camera are nearly normal to the reflective surface, and measurements are taken for various sun zenith angles, camera performance for bright clouds as viewed from space can be accurately predicted.

PROTOTYPE SPIN-SCAN CAMERA CALIBRATION

All photomultiplier tubes were operated at various multiplier gains and output voltages were recorded as a function of multiples of light input prior to and after SBRC burn-in. This data established tube output voltage as a function of relative light input. Because the lamp temperature was constant and the light was merely attenuated and no attempt was made to define the light input, the spectral characteristics of both lamp and photocathode need not be known. The idea was to define the shape of the tube response curve (linear region, saturation knee, etc.)

Using the photomultiplier tube data supplied by the manufacturer (assuming additional burn-in only reduces the tube gain) and the camera optical parameters, the relative light values can be converted to effective watts. These effective watts are simply watts of light entering the camera aperture from the scene within the field of view in the wavelength region of camera sensitivity. (For more details see papers by Peekna, Parent and VonderHaar and by Thomson, Parent, and Suomi elsewhere in this volume). Performance of the camera to any known light

input can be predicted from this plot and performance of the actual camera compared with this prediction.

Figure 1 shows such a plot for the prototype with the measured point shown in close agreement with the curve. (Similar curves for the flight camera may be found in the paper by Thomson, Parent, and Suomi elsewhere in this volume).

Because of the delivery schedule, no time was available for outside sun reflection measurements.

FLIGHT-MODEL SPIN-SCAN CAMERA CALIBRATION

The primary purpose of the calibration is to establish the relationship between the energy intercepted by the camera as it views a suitable target illuminated by sunlight and the camera output signal. A second purpose of the experiment is to set the level of the camera signal so typical targets on the earth (clouds, etc.) will generate voltages which fall within the design range of the satellite telemetry system.

There are a number of difficulties which make the calibration procedure awkward.

1. Non-availability of a calibrated radiation source whose spectral composition is similar to that of sunlight.
2. The exact spectral distribution of the specific quartz-iodine lamps which were used as a variable source was not available.
3. The spectral response of the spot photometer, which was used for relative calibration, did not match the spectral response of the camera.
4. The California sunshine is not as pure as the typical Californian would have us believe!

In principle it should be possible to determine the camera's performance in sunlight from first principles alone without the need for an artificial radiation source or without the need for an instrument such as the spot photometer. The light box source and spot photometer were used only as relative measures to aid in setting the sensitivity of the system. The absolute calibration of these devices was not employed. It is awkward to use the sun as a variable source, so the light box was used for this purpose. This box, on loan from the National Environmental Satellite Center, contains 5 quartz iodine lamps whose distance to the diffusing screen can be varied. Thus, the light intensity can be varied

over wide limits without changing its spectral content. The limits can be varied by turning off some of the lamps, as well.

Because the spectral energy distribution of the light from the quartz-iodine lamps is less intense in the blue portion of the spectrum compared to sunlight, and because the pass band of the camera and spot photometer are not matched, it is necessary to use about 20 percent higher readings on the spot photometer to get the equivalent sunlight performance in the camera.

The camera has a filter which allows light in the band from about 4500 to 6500 Å to be measured. As can be seen in Figure 2, the solar spectrum is fairly flat in this portion of the spectrum, whereas the energy of the quartz-iodine lamp changes rapidly with wavelength. Thus, even though the spot photometer and camera have slightly different pass bands, their sensitivities will be quite similar in sunlight. On the other hand, the camera will tend to read lower using the radiation from the quartz-iodine lamps.

Photomultiplier Sensitivity Tests

The light box was used in laboratory tests to determine the "knee" of the photomultiplier response curve; the test setup is illustrated in Figure 3. In these tests the voltage on the photomultiplier tube was varied as well as the illumination. The resulting performance of the photomultiplier tube is shown in Figure 4. One obtains a better signal to noise ratio with higher photomultiplier supply voltage; however, the light level at which the photomultiplier saturates decreases with higher photomultiplier voltage. Thus for operational use, one would like to set the photomultiplier supply voltage as high as possible and yet not have it saturate when viewing the brightest clouds. A close approximation to what this brightness level is for the flight-model camera has been obtained from outdoor tests using the sun as a light source.

Photomultiplier Response in Sunlight

The flight model camera was tested outdoors at Santa Barbara, California on April 27, 1966. The test setup is shown in Figures 5 and 6. The chopper in front of the camera aperture produced an AC signal of almost perfect sinusoidal wave shape so measurement was simplified to reading a

true rms AC voltmeter and realigning the platform for changing sun zenith angle. The scattered light level was also measured by obscuring the direct sun and recording the camera output. Measurement of the direct sunlight was obtained as the difference between the total and scattered light. Data from this test is shown in Table 1. Peak-to-peak video signal levels were obtained by multiplying the rms by $2\sqrt{2} = 2.828$.

From a series of measurements using a spot photometer and the spin-scan camera, one may determine the illuminance of Kodak white paper as it would appear at the top of the atmosphere (m=0) normal to the sun's rays. After smoothing a time vs. illuminance plot to the brightest (cleanest) values, Figure 7 shows that one can indeed extrapolate to zero air mass with some confidence.

In order for the camera to view a bright target in the atmosphere having high luminance values similar to those obtained for the Kodak white paper extrapolated to the outside of the atmosphere, it would be necessary to:

1. Have a cloud whose albedo is greater than 90 percent.
2. Have the cloud extend high into the atmosphere so a small amount of attenuating atmosphere lies above it.
3. Have the zenith angle of the sun near zero.
4. Have the nadir angle of the camera near zero also.

Only when local noon is at the subsatellite point will all these conditions prevail. There are other phenomena such as specular reflection which gives rise to sea glint and non-isotropic forward scatter when the sun is low on the horizon. These phenomena will yield abnormally high light values, but they are the exceptional cases.

If the video gain is set to include all these phenomena, most meteorological phenomena will have light values near the low end of the detectable video range. We chose, therefore, to set the gain so most cloud systems would give signals near mid-scale. A small percentage of the very brightest targets would therefore saturate the photomultiplier.

Camera Characteristics in Operational Use

For operational use, the upper limit of the linear range of the video has been kept above 10,000 foot lamberts by setting the photo-

multiplier supply voltage to 2100 v. Figure 4 shows that this supply voltage keeps the "knee" of the response curve sufficiently high.

The other required prelaunch adjustment of the video level is to set the video amplifier gain A. The adjustable range is between 1 and 10. From the laboratory and outdoor tests, the desired A-value was found to be 2.72.

Figure 8 shows the camera video response with (1) the quartz-iodine light source, (2) a photomultiplier supply voltage of 2100 v., and (3) A-values of 1.0 and 2.72. The data are also give in Table 2.

From these measurements and from a knowledge of the spectral distribution of light from the lamps and sun and the spectral response of the camera and photometer, it is possible to estimate the camera video response to sunlight at the top of the atmosphere. Doing the necessary integration, we find that the camera response to sunlight (at m=0) is greater than to quartz-iodine light by a factor of 1.21. Thus, we may compute the camera response to sunlight at m=0 using this factor. The results are shown in Figure 8 as well as in Table 2.

The outdoor measurements serve as an excellent, independent check on the camera response curve in Figure 8, which was obtained with artificial light and was extended to sunlight by calculation. The advantage of using the outdoor measurements for a check on the artificial-light method is that there is less difference between the spectral distribution of sunlight at the top and bottom of the atmosphere than there is between quartz-iodine light and sunlight at the top of the atmosphere.

Using the camera and photometer response to sunlight on Kodak white paper at the top of the atmosphere, as shown in Figure 7, and applying an A-value of 2.72, we see the camera output would be 680 mv. for a target of 15,500 ft. L. This single value is plotted as a point in Figure 8 and falls on the response curve for an A-value of 2.72. This verifies results with the artificial-light method.

Using the procedure described above, we have established the magnitude of the camera signal that will be generated by a surface having the same spectral reflectivity characteristics as Kodak white paper near normal to the solar beam above the atmosphere. (The spectral reflectivity

characteristics of Kodak white paper are shown in Figure 9). If the sensitivity of the photomultiplier tube were stable with time in a space environment, it should be possible to obtain the albedo of clouds for the camera spectral pass band. Unfortunately, despite a substantial effort to "burn-in" the photomultiplier photocathode to make it more stable, the photomultiplier becomes temporarily about 10-15 percent more sensitive when it has a short history in total darkness or low light levels. This increase in sensitivity is evident in the early readings of the calibration experiment. Thus, we cannot use this calibration as a precision calibration for the instrument sensitivity in space.

Use of the Moon as a Camera Stability Check

The camera scans about 70 lines across the face of the moon. Thus it is possible to use portions of the moon's surface or the mean value of the whole moon as a check of the camera sensitivity stability. Of course all the appropriate astronomical parameters will have to be taken into account.

It is possible to get a good estimate of the absolute value of camera sensitivity using the moon as a light source. This requires one to carry out a series of moon brightness measurements from a high mountain top using a carefully calibrated spot photometer having a spectral pass band identical to that of the camera. Since the pass band of the camera does not include any significant absorption bands in the CO_2 or H_2O spectrum and Mie scattering is small, an extrapolation of photometer measurements made on earth to the top of the atmosphere making use of Beers law attenuation should allow calibration of the spin-scan camera when viewing the moon without an intervening atmosphere.

A calibration of this type was carried out from White Mountain, California in September, 1967 and is presented in another paper in this volume by Hanson and Suomi.

Table 1. Spin-Scan Cloud Camera F-1 Calibration Test Data--Camera and Photometer Output as a Function of Reflected Sunlight from Kodak White Paper at Various Times of Day

Time (Pacific Daylight)	Camera Output (mv)		Photometer Output (ft. lamberts)	
27 April 1966	Direct and Scattered	Scattered	Direct and Scattered	Scattered
11:52	514.7	92.76	9800	2050
12:03	503.4	96.15	9490	2090
12:05	503.4	91.91	9330	2000
12:15	494.9	94.74	9580	2100
12:20	494.9	91.91	9820	2060
12:33	486.4	90.50	9660	2140
12:45	480.8	87.67	9700	2100
13:00	472.3	90.50	9580	2230
13:15	469.4	80.60	9700	1990
13:30	466.6	79.18	9850	2080
13:43	466.6	75.51	9980	2080
13:55	458.1		9899	
14:03	458.1	77.77	9900	2120
14:15	446.8	78.34	9650	2250
14:39	431.3	83.43	9550	2360
14:52	429.9	79.75	9500	2230
15:00	424.2	80.32	9460	2220
15:15	412.9	79.18	9330	2210
15:35	401.6	78.62	8890	2300
15:45	303.1	80.32	8890	2280
16:00	384.6	82.01	8750	2320
16:15	364.8	80.32	8400	2390
16:27	345.0	83.14	7900	2350
16:45	322.4	83.99	7410	2310
17:00	302.6	80.60	6930	2210

Table 2. Spin-Scan Cloud Camera F-1. Measured Camera (Channel 1) and Photometer Output with Quartz-Iodine Light and Photomultiplier Supply Voltage of 2100 V. Computed Camera Output (Channel 1) for Sunlight at the Top of the Atmosphere.

Photometer	Quartz-Iodine Light			Sunlight
	Measured		Computed (from A=2.5)	Computed (from A=2.72)
(ft. L.)	A = 1.0 (mv)	A = 2.5 (mv)	A = 2.72 (mv)	A = 2.72 (mv)
1000	12.8	31	32.7	39.5
1520	19.8	48	52.2	63.0
2000	27.5	63	68.7	83
3000	42.0	100	109	132
4500	68.0	154	168	203
6000	96.0	215	235	284
8000	132	300	326	395
10000	165	390	425	515
12000	188	450	490	592
15000	210	500	545	660
17500	218	530	578	698
20000	225	540	588	710
25000	228	550	599	723

FIGURE

1. Prototype (P-1) Spin-Scan Cloud Camera Photomultiplier Tube Output as a Function of Effective Radiant Input Power at the Entrance Aperture (HV = 2500 volts)

2. Relative Intensity of Sunlight (at m = 0) and Quartz-Iodine Lamp, and Relative Sensitivity of ATS Spin-Scan Cloud Camera and Spot Photometer.

3. Test Setup for Photomultiplier Response Using the Quartz-Iodine Light Box

4. Photomultiplier Response with Quartz-Iodine Light Box

5. Flight Model Camera Calibration Using Reflected Solar Radiation Source

6. Schematic of Test Setup for Calibration of F-1 Using Reflected Solar Energy

7. Camera Video Response Using Reflected Solar Radiation Source

8. Camera Video Response

9. Spectral Reflectivity Characteristics of Kodak White Paper

TABLES

1. Spin-Scan Cloud Camera F-1 Calibration Test Data-Camera and Photometer Output as a Function of Reflected Sunlight from Kodak White Paper at Various Times of Day

2. Spin-Scan Cloud Camera F-1. Measured Camera (Channel 1) and Photometer Output with Quartz-Iodine Light and Photomultiplier Supply Voltage of 2100 V. Computed Camera Output (Channel 1) for Sunlight at the Top of the Atmosphere.

Fig for #28
Prelaunch Camera Calibration

FIGURE

1. Prototype (P-1) Spin-Scan Cloud Camera Photomultiplier Tube Output as a Function of Effective Radiant Input Power at the Entrance Aperture (HV = 2500 volts)

2. Relative Intensity of Sunlight (at m = 0) and Quartz-Iodine Lamp, and Relative Sensitivity of ATS Spin-Scan Cloud Camera and Spot Photometer.

3. Test Setup for Photomultiplier Response Using the Quartz-Iodine Light Box

4. Photomultiplier Response with Quartz-Iodine Light Box

5. Flight Model Camera Calibration Using Reflected Solar Radiation Source

6. Schematic of Test Setup for Calibration of F-1 Using Reflected Solar Energy

7. Camera Video Response Using Reflected Solar Radiation Source

8. Camera Video Response

9. Spectral Reflectivity Characteristics of Kodak White Paper

TABLES

1. Spin-Scan Cloud Camera F-1 Calibration Test Data-Camera and Photometer Output as a Function of Reflected Sunlight from Kodak White Paper at Various Times of Day

2. Spin-Scan Cloud Camera F-1. Measured Camera (Channel 1) and Photometer Output with Quartz-Iodine Light and Photomultiplier Supply Voltage of 2100 V. Computed Camera Output (Channel 1) for Sunlight at the Top of the Atmosphere.

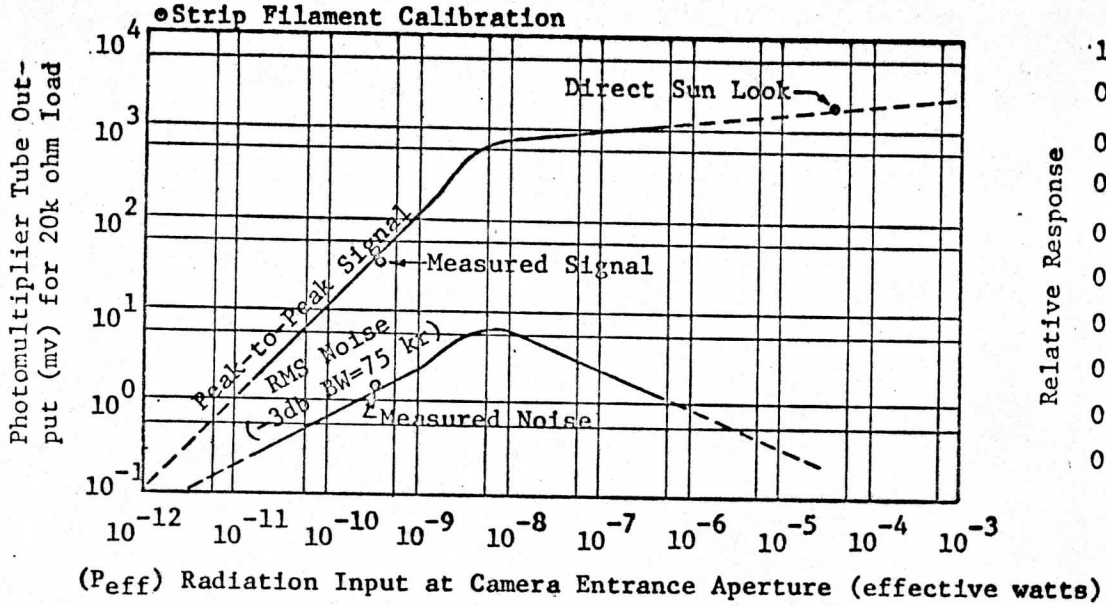

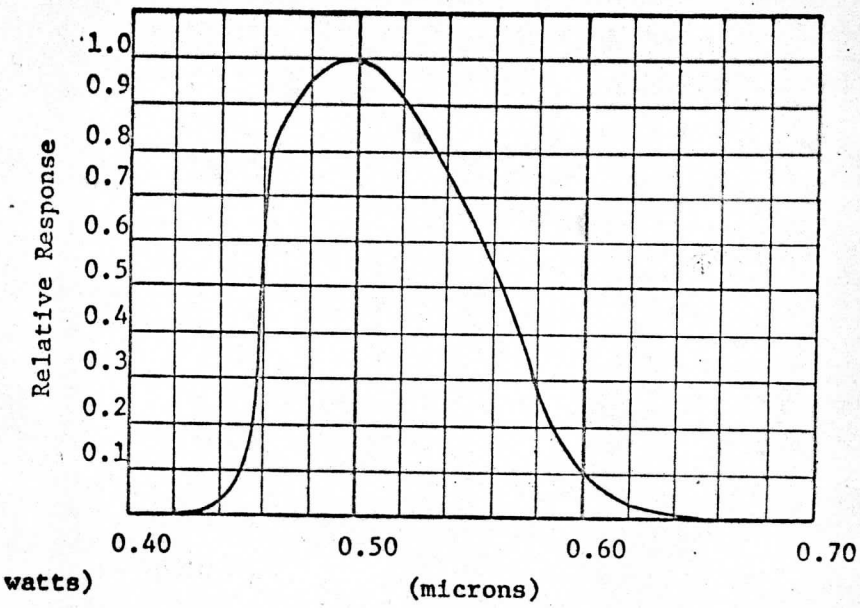

Combined Response of Camera Optical System and EMR Photomultiplier Tube #5489. Peak Response $R(\lambda) = 33.7 \times 10^{-3}$ amps/watt effective.

The photomultiplier response in millivolts (for a 10k ohm load) for any light input can be found as follows:

Given $H(\lambda)$ in watts $cm^{-2}\ \mu^{-1}$ at camera entrance aperture from scene within field of view.

$$P_{eff} = \int_0^\infty H(\lambda)\, S(\lambda)\, d\lambda$$

Where: $S(\lambda) = AR(\lambda)$

A = area of camera entrance aperture

= 104 cm^2

$R(\lambda)$ = camera spectral response shown above.

Then: Locate output (mv) for corresponding P_{eff} on curve for both signal and noise.

Fig. 1 Prototype (P-1) Spin-Scan Cloud Camera Photomultiplier Tube Output as a Function of Effective Radiant Input Power at the Entrance Aperture (HV - 2500 volts)

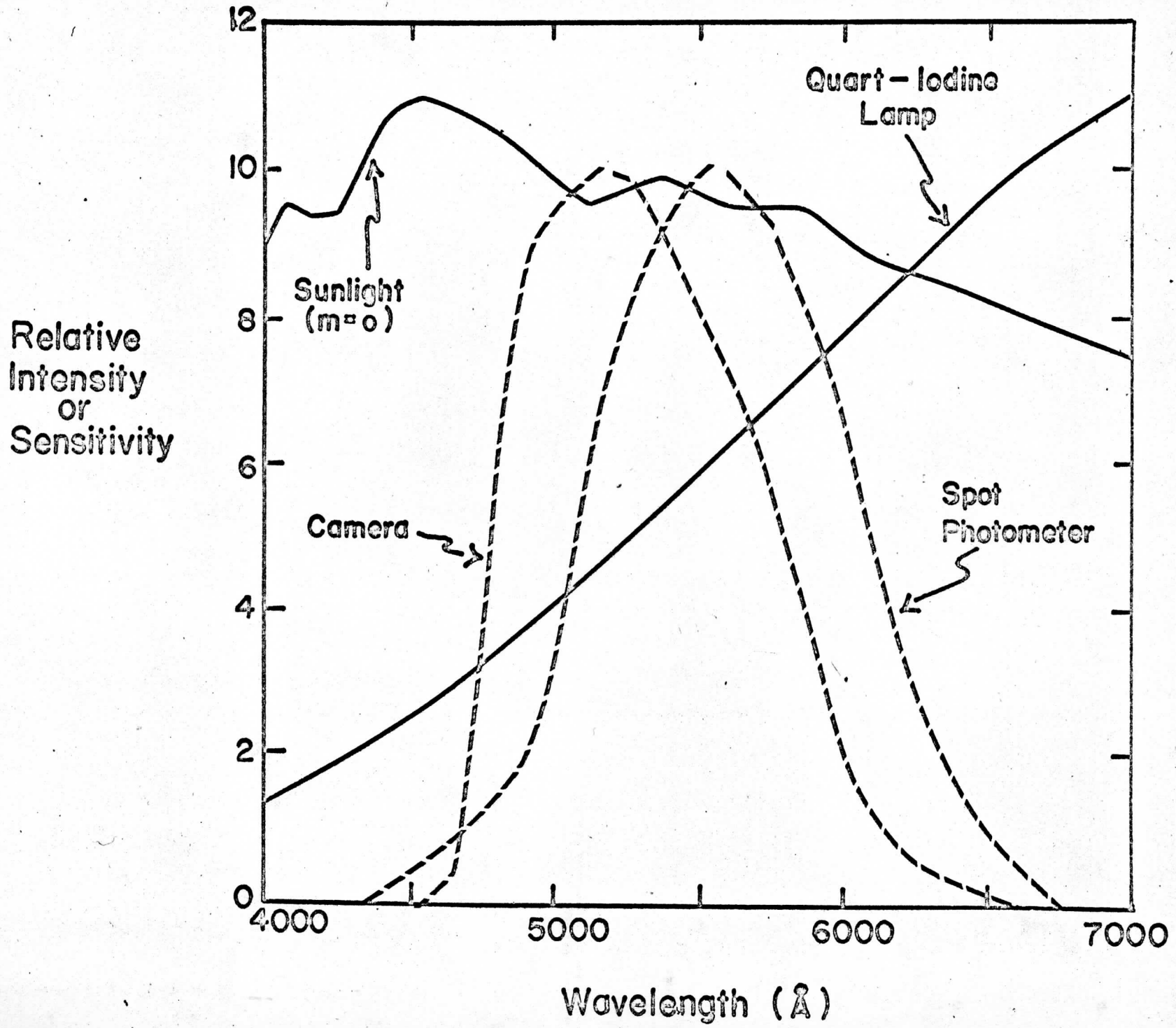
12
10
8
6
4
2
0
4000
5000
6000
7000
Quart – Iodine Lamp
Sunlight (m=0)
Camera
Spot Photometer
Relative Intensity or Sensitivity
Wavelength (Å)

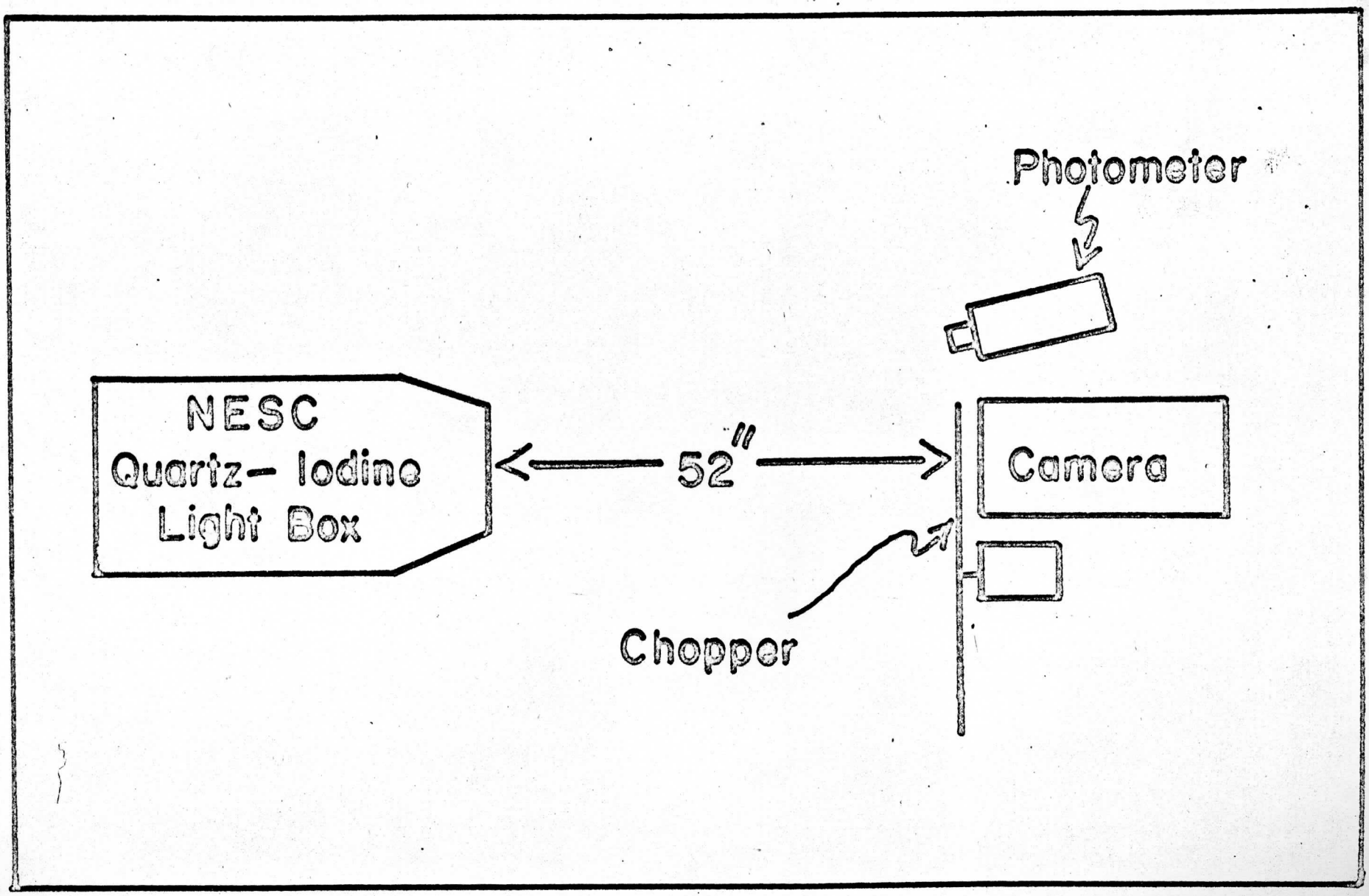
Photometer
NESC
Quartz- Iodine
Light Box
52"
Camera
Chopper

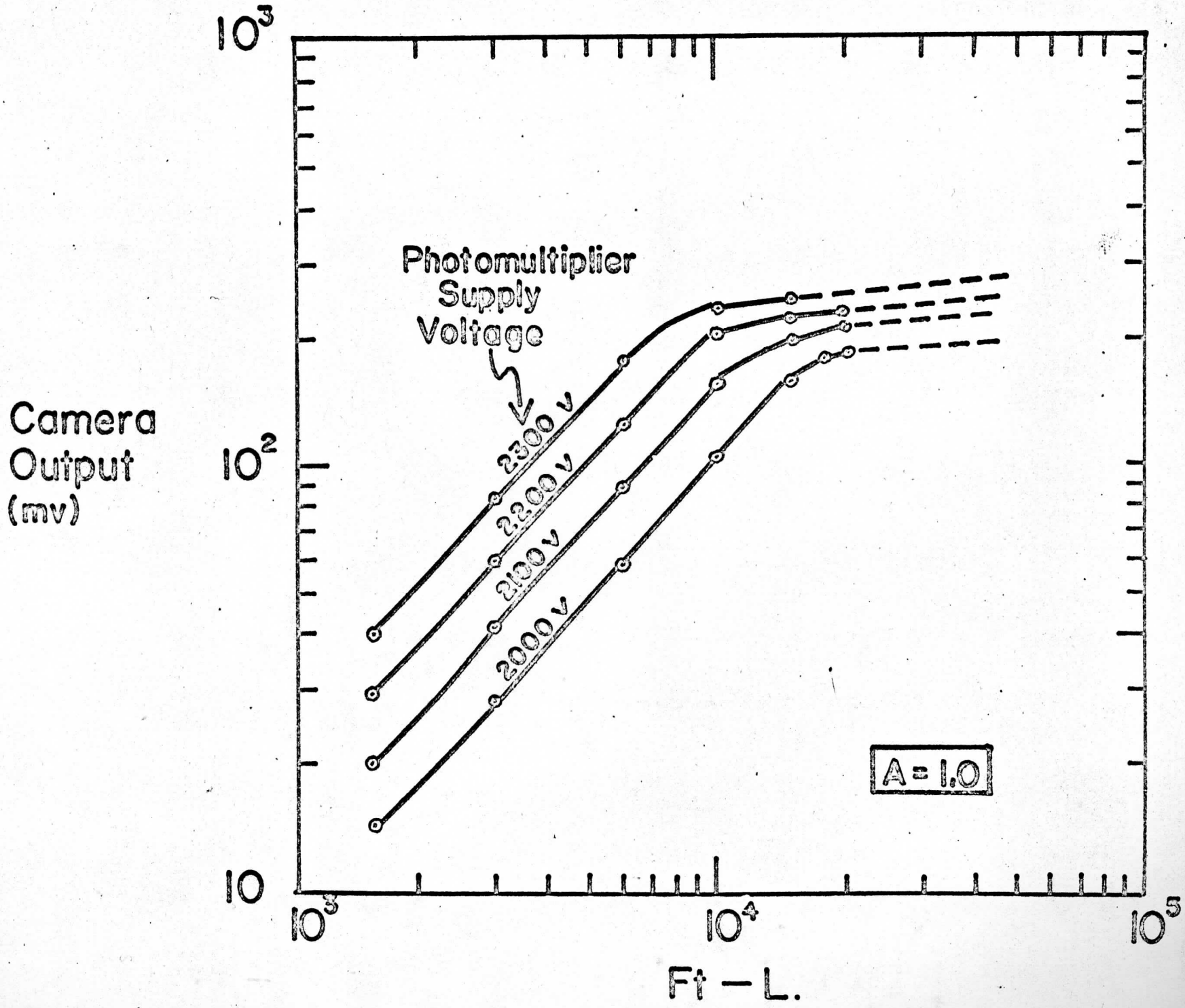
Camera Output (mv)
10^3
10^2
10
10^3
10^4
10^5
Ft — L.
Photomultiplier Supply Voltage
2300 v
2200 v
2100 v
2000 v
A = 1.0

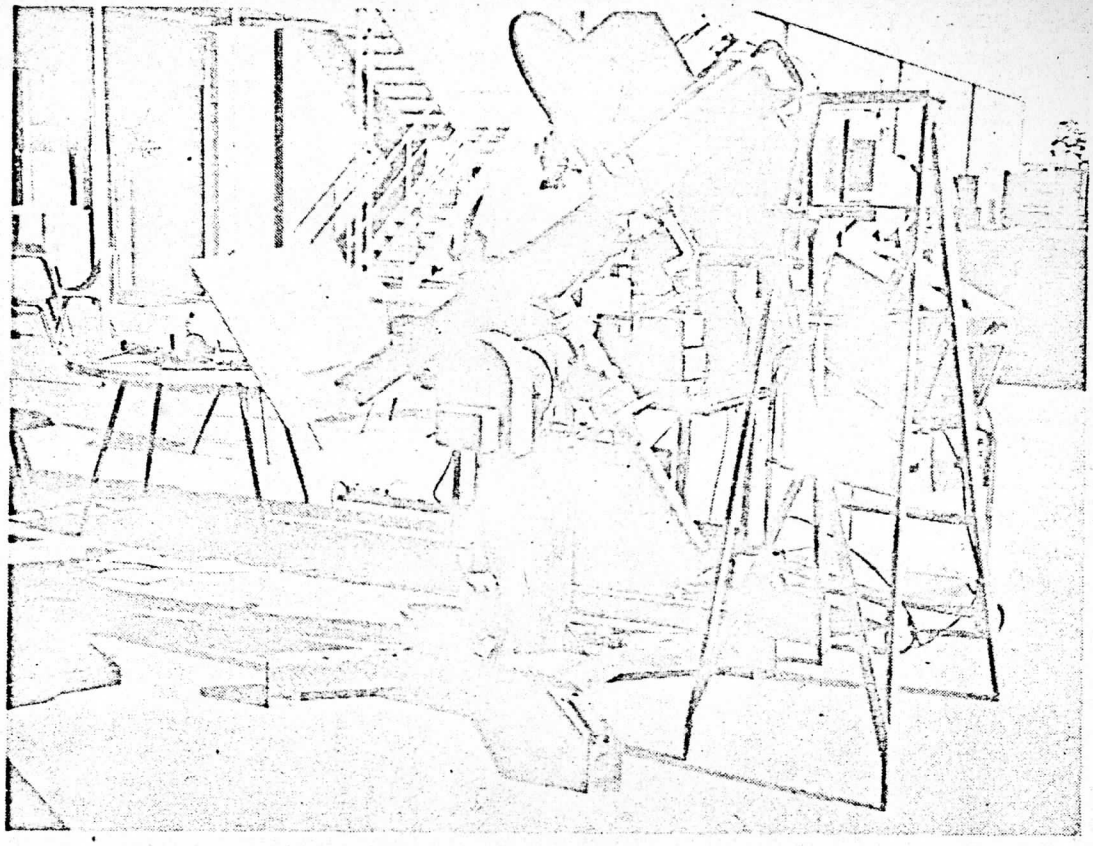

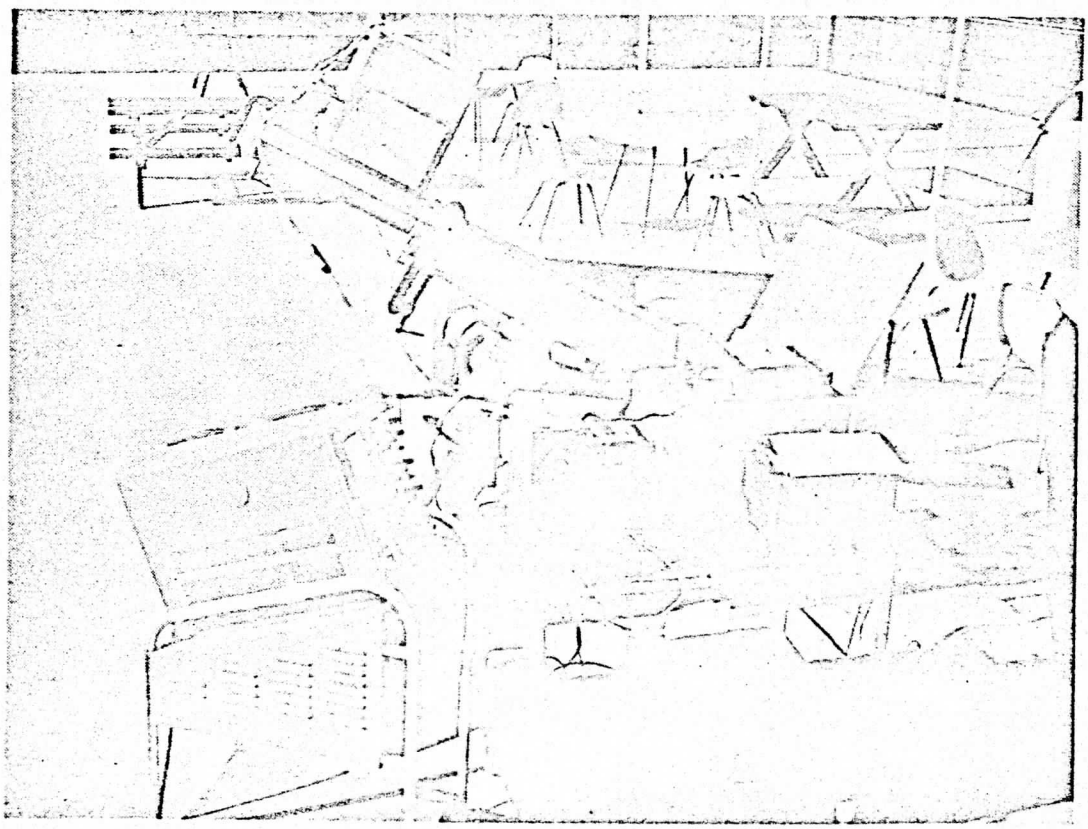

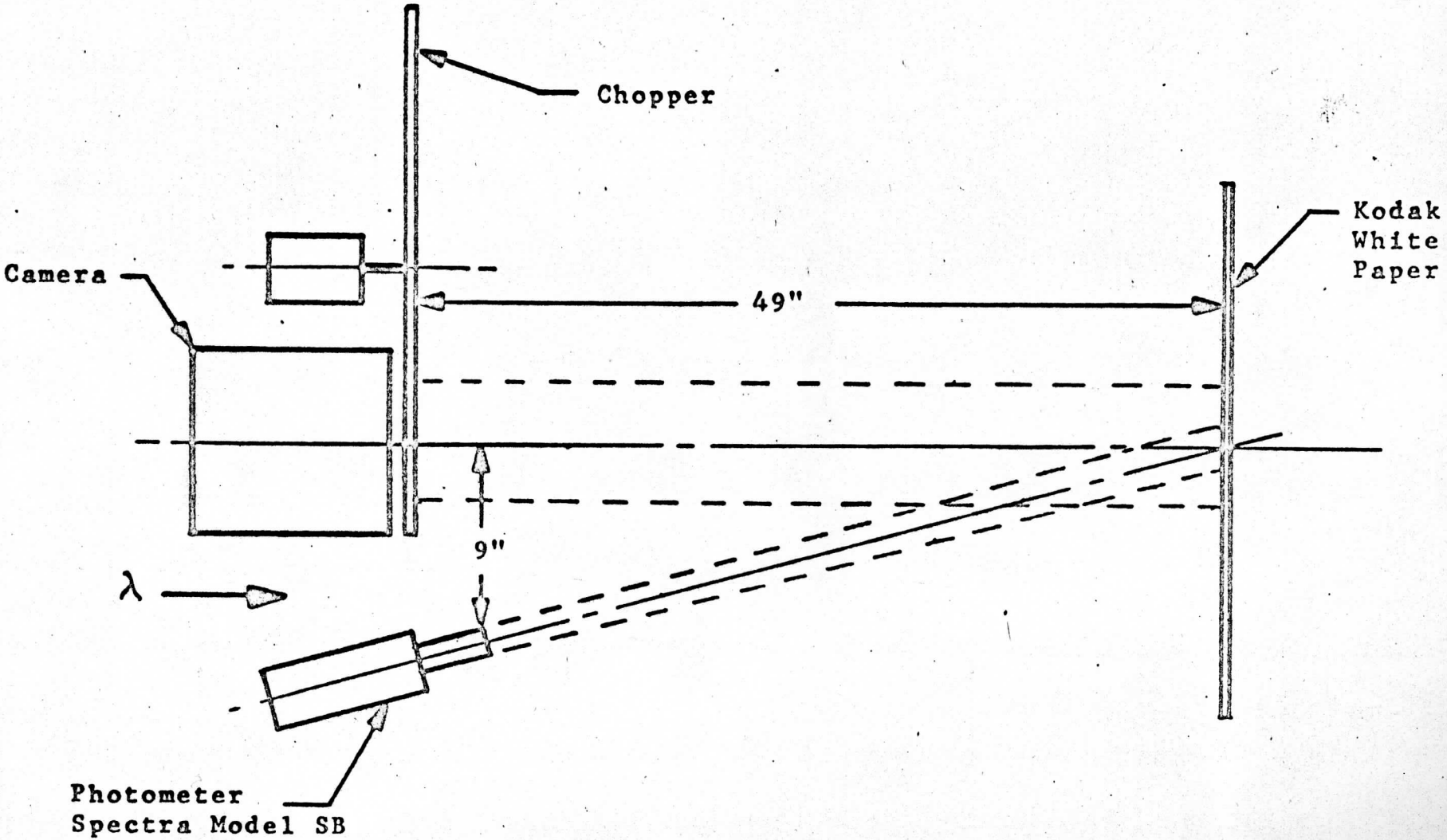
Chopper
Kodak
White
Paper
Camera
49"
9"
λ
Photometer
Spectra Model SB

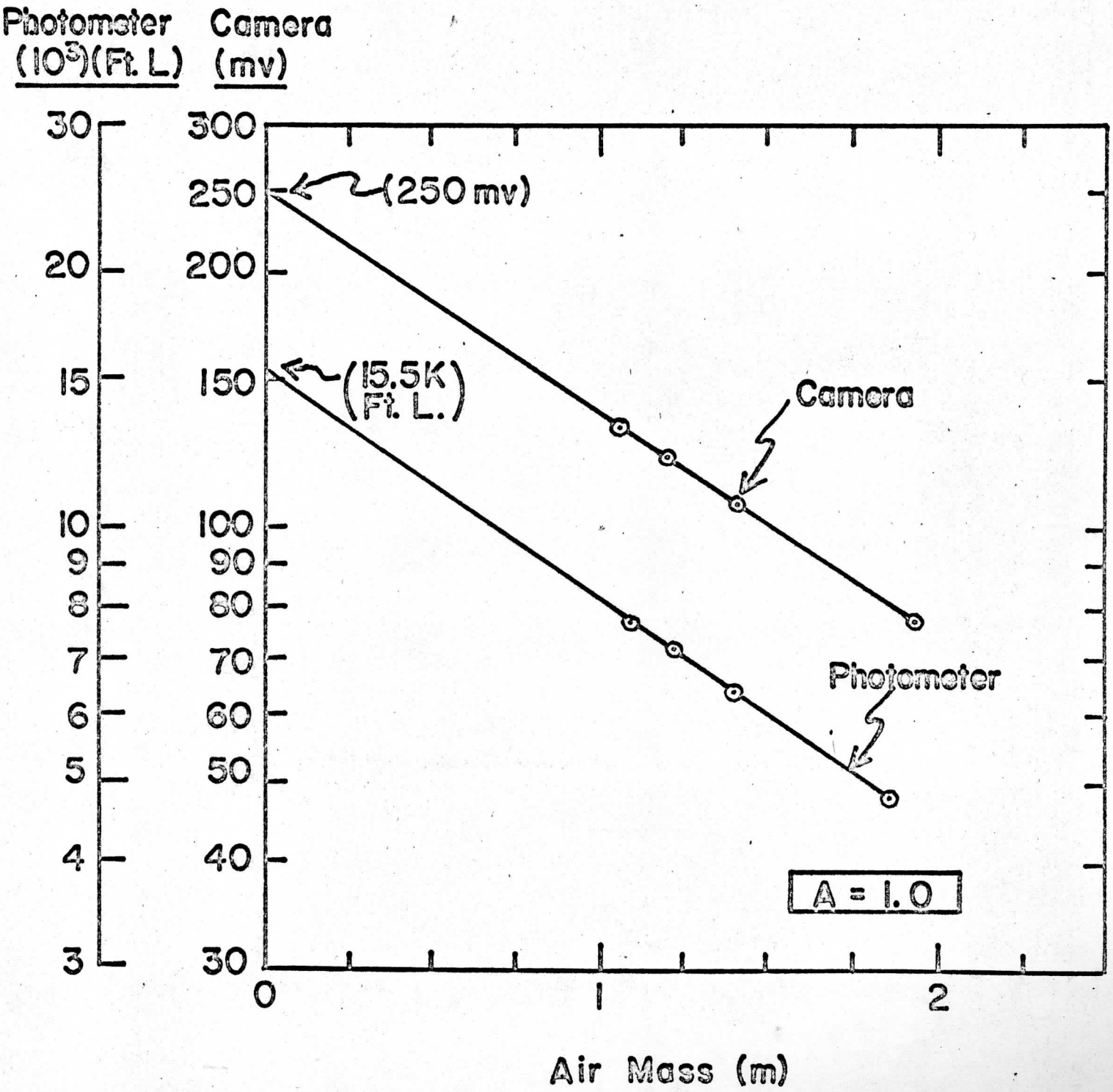
Photometer (10³)(Ft. L)
Camera (mv)
30
20
15
10
9
8
7
6
5
4
3
300
250
200
150
100
90
80
70
60
50
40
30
(250 mv)
(15.5K Ft. L.)
Camera
Photometer
A = 1.0
0
1
2
Air Mass (m)

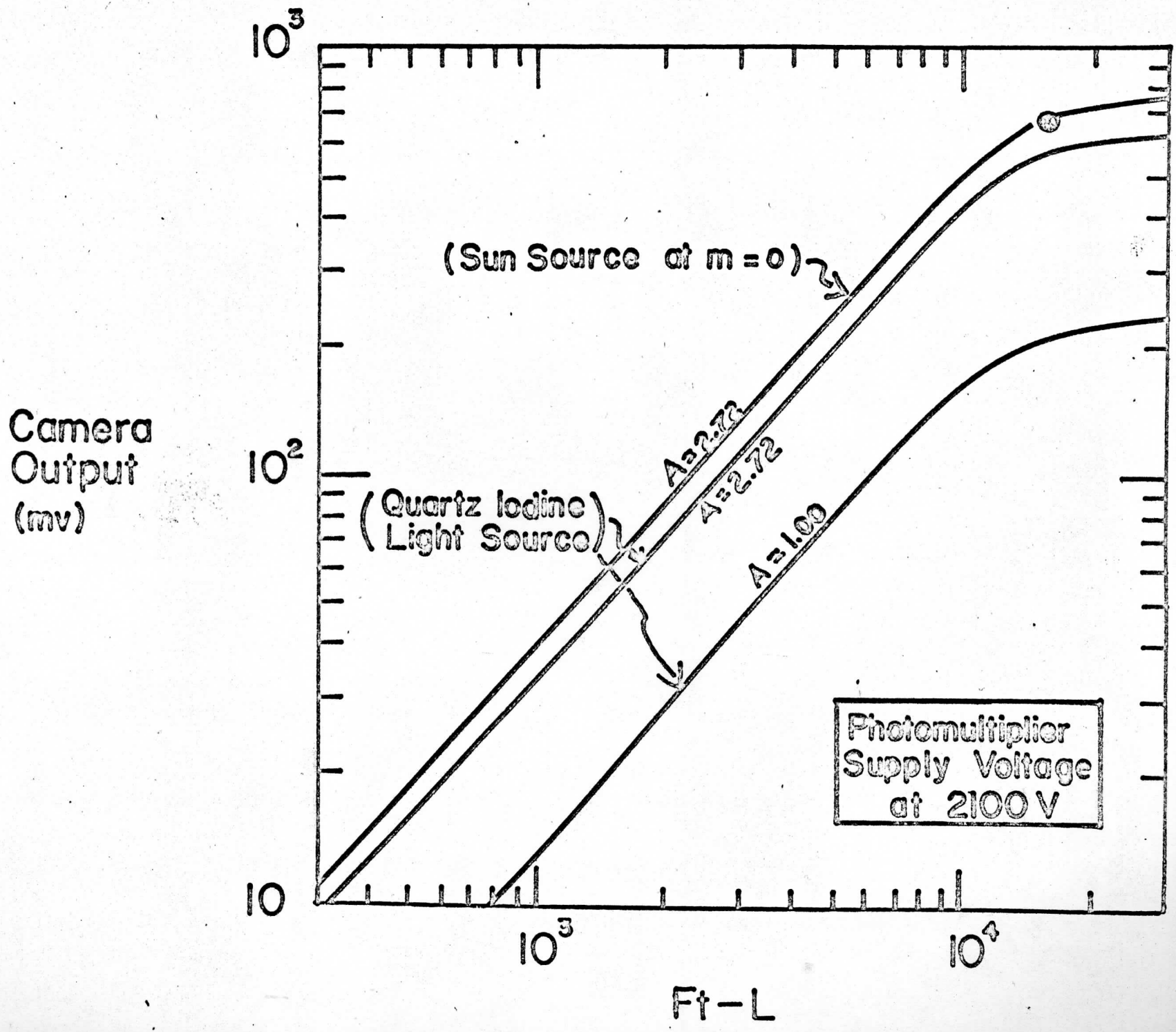
Camera Output (mv)
10^3
10^2
10
(Sun Source at m = o)
A=2.73
A=2.72
A=1.00
(Quartz Iodine Light Source)
Photomultiplier Supply Voltage at 2100 V
10^3
10^4
Ft-L

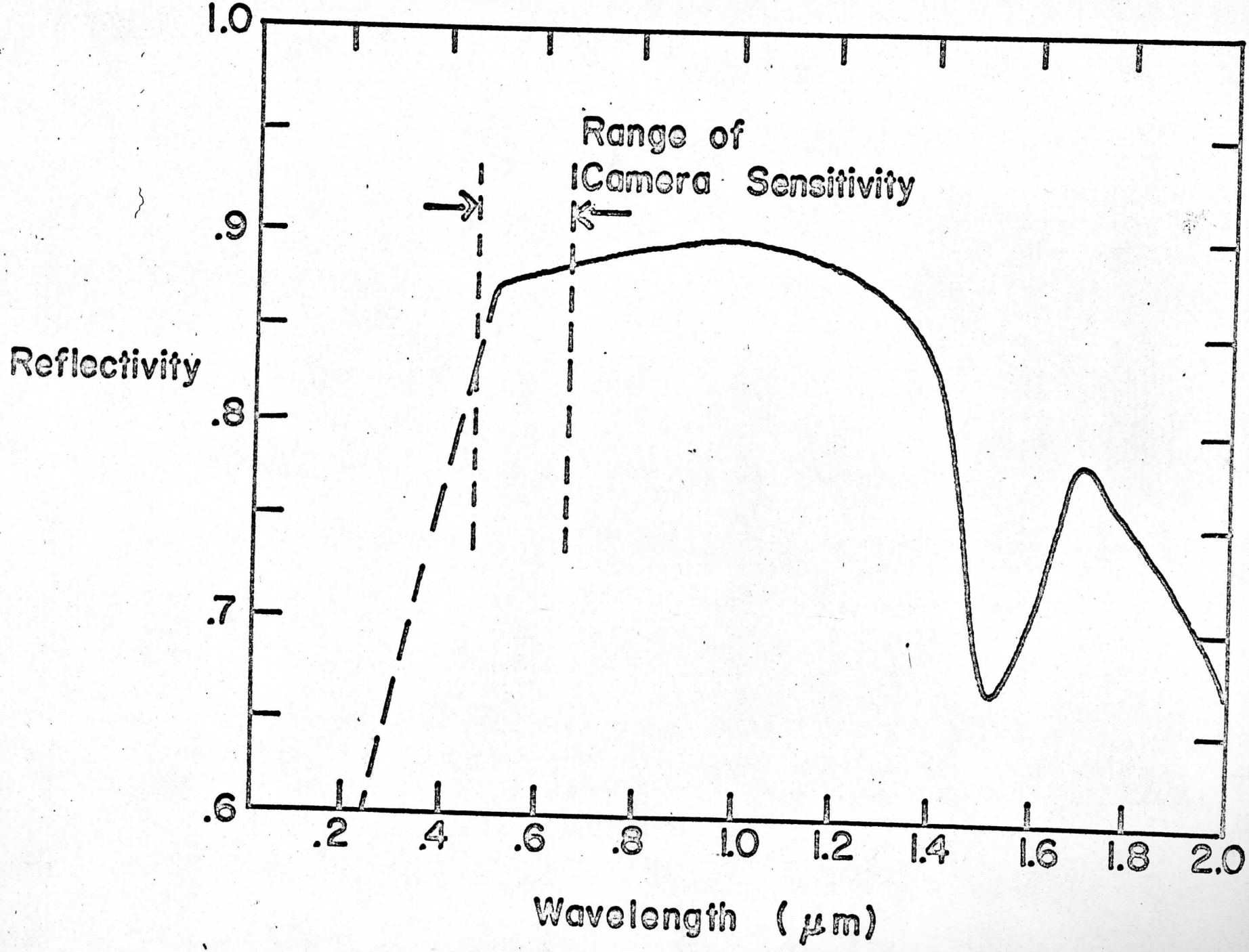
Range of
Camera Sensitivity
Reflectivity
1.0
.9
.8
.7
.6
.2
.4
.6
.8
1.0
1.2
1.4
1.6
1.8
2.0
Wavelength (μm)

aug 26

ANALOG RECORDING SYSTEM

by

R. Parent and
J. Sitzman

The University of Wisconsin

CONTENTS

	Page
Introduction	1
System Description	2
SK-1600A Functional Description	3
Data Processor Functional Description	5
Acknowledgements	7

ANALOG RECORDING SYSTEM

R. Parent and J. Sitzman

INTRODUCTION

The video information from the ATS-1 Spin Scan Cloud Camera (SSCC), along with associated timing and experiment status data, has been recorded on a real time basis at the Rosman, North Carolina, and Mojave, California, STADAN Stations. Three basic methods of video data recording have been employed.

1. Photographic - film negative plus positive print
2. Magnetic tape - digital
3. Magnetic tape - analog, duty cycle improved

The first two methods are described by W. Sunderlin and J. Lahzun in this Volume and so will not be discussed here. The third method, analog recording of video data, is the subject of this paper.

A unique method of recording the video data makes it possible to effect a 16:1 saving in magnetic tape over conventional methods.

SYSTEM DESCRIPTION

The Analog Recording System provides the capability of economically storing all of the spin-scan camera video data, along with the timing and logging information required for subsequent retrieval. The system described here was developed for analog recording of ATS-1 spin-scan data and operated at the Mojave STADAN station*.

The heart of the system is the SK-1600A Video Weather Data Accumulator (Fig. 1) specially developed by Ampex Corporation for application in the SSCC experiment. The unique design of this recorder permits recording of successive lines of video data, each line corresponding to the 20° of spacecraft rotation which includes the earth scan, with only a relatively small gap between records. Tape utilization is improved by a factor of 16 over that of conventional recorders in this application. While recording, the speed of the transport is accurately slaved to the spin rate of the spacecraft to produce data records which are uniform in length and spacing in tape. This uniform data format reduces design requirements for systems to process or display data reproduced at fixed tape speeds from conventional transports.

A Data Processor unit, developed at the University of Wisconsin Space Science and Engineering Center, interfaces the SK-1600A with the ground equipment. It combines timing signals, data logging information and camera video for recording on a single analog channel and supplies the external control signals to the recorder transport servos.

*A similar system, capable of recording either ATS-3 or ATS-1 data, has since been built and forms part of the Rosman Station spin-scan ground equipment.

SK-1600A FUNCTIONAL DESCRIPTION

The SK-1600A consists of a high performance precision tape transport and associated high quality recording and control systems.

A wide-band FM, with bias, record electronics system is used to preserve the DC to 150 kHz video data bandwidth. This method of recording, combined with the low flutter and mechanical noise characteristics of the transport, yields a peak signal-to-RMS ratio in excess of 40 db for the record/reproduce system.

The SK-1600A is capable of recording and reproducing one track at a time up to a maximum of 4 tracks on, or from, 1/2 inch magnetic tape. The track spacing conforms with IRIG standards for 1/2 inch tape, but only the odd-numbered tracks are used.

When recording, tape is transported longitudinally by both an upper record drive capstan and a lower reproduce drive capstan suitably tensioned by vacuum chamber control. The tape is guided around a rotating record head drum and reproduce head, as illustrated in Fig. 2. The rotating drum contains the 4 track record head and rotates at four times the spacecraft spin rate. Every fourth revolution, the record driver electronics are gated on to record a line of data. A control system maintains phasing of the drum so that the head is in the proper position for recording at the start of each video scan line. The phasing reference signal is a Pre-line Start pulse, generated by the Synchronizer unit of the ground equipment (see Sunderlin and Lahzun), which occurs 64 Picture Element pulses before the normal Line Start pulse. The Pre-line Start pulse also triggers a monostable multivibrator which turns on the record electronics for the duration of a scan line. The speeds of the drum and capstans are always precisely controlled by an externally supplied Recorder Reference Frequency. During the record process,

this frequency is derived from the voltage controlled oscillator (VCO) of the Synchronizer, so tape and drum speeds are proportional to the spacecraft spin rate.

At the nominal spin rate of 100 rpm, the longitudinal tape speed is 7.5 inches per second (ips) and the interval between video scan lines is 0.6 sec., so the distance on tape between the starts of two successive records is 4.5 in. The 400 rpm rotation of the drum, approximately 5.4 in. in diameter, moves the record head past the tape at 112.5 ips to give a relative head-to-tape speed of 120 ips. The duration of each scan line, generated over 20° of spacecraft rotation, is 33.3 ms., so each scan line record occupies 4 in. of tape. Since tape and record head motions are both slaved to the spacecraft rotation, the length and spacing of the scan line records on tape remain constant, independent of the actual spin rate.

The four-track head stack for the single reproduce channel is located near the reproduce drive capstan. Data may be reproduced for monitoring purposes only seconds after being recorded. The transport may also be operated in a Reproduce Only mode, in which the record drive capstan is disengaged, the scanning drum is stationary, and the Recorder Reference Frequency is derived from a crystal oscillator source. Tape is then transported only by the reproduce drive capstan at precise speeds of either 7.5 or 3.75 ips, as selected.

The precise speed control and low time base error mentioned result from the use of position-sensitive servos to control the rotation of the scanning drum and both capstans. An optical encoder disc, with 4096 radial grid lines photo-engraved about its circumference, form part of the drum and capstan assemblies. The output of each encoder disc is compared with the Recorder Reference Frequency signal so as to resolve the position of every grid line. The use of high-torque, low-inertia printed circuit motors holds position errors to a minimum. The reeling system is

isolated from the capstans by buffer vacuum chambers, further improving overall time base stability.

The scanning drum optical encoder also provides a separate "once-around" pulse output, which is compared with the Pre-line Start signal by the control system which adjusts drum phasing. This phasing servo is non-linear, and corrects drum phasing only if the error exceeds a fixed threshold value. A Pre-line Start pulse occurs with every 16,384th cycle of the Recorder Reference Frequency. This number of cycles (4 times 4096), applied to the drum servo input, advances the position of the scanning drum through exactly four revolutions. As a result, once the transport has been started and proper phasing established, further phase adjustments, which momentarily change drum speed, are not normally required.

Specifications of the SK-1600A recorder are summarized in Table 1.

DATA PROCESSOR FUNCTIONAL DESCRIPTION

The Data Processor formats the camera video, digital data logging information and timing signals so that all may be recorded upon a single data track of the SK-1600A. In addition, it supplies the Pre-line Start signal and Recorder Reference Frequency to the recorder drum and capstan servos. A block diagram of the Data Processor is shown in Fig. 3.

The NRZ Encoder is a digital subsystem which generates a serial 64-bit binary code Data Identification Word (DIW) at the start of each video scan line,as shown in Fig. 4. The contents of the DIW, listed in Table 2, are encoded at a bit rate determined by the Picture Element frequency (one-fourth the VCO frequency) and occupies the first 0.3° of the 20° video scan line. The coding used indicates a data binary "one" by a transition between the two output levels and a "zero" by no transition. This is analogous to the NRZ(M) method of digital tape recording

in which the direction of magnetization is changed each time a data "one" occurs. The Line Start pulse input initiates the encoding operation, as well as an Extended Line Start encoder output pulse. The encoder output appears as 0 or +1 volt levels applied to the recorder input.

The video input from the Video Processor is clamped to ground while the DIW is generated, but is otherwise supplied to the record input as a +1.5 volt peak signal from a 0 volt baseline.

Two reference frequencies, a 200 kHz tape speed reference and the A/D Sampling Pulse frequency (nominally 245.76 kHz) are summed with the video and Encoder output as 100 mv. peak-to-peak sinusoids. These superimposed frequencies can be separated from the video and Encoder data by filtering and used in off-line processing of the data.

On playback, the A/D frequency information is used for the same purposes as the real time A/D (or PE) Sampling Pulses, i.e., as a sample command in transcribing the data to digital tape or as a horizontal position reference in generating photographic displays.

The center frequency of the FM modulator in the record electronics is fixed, although the record head-to-tape speed is proportional to spin rate. When reproduced at a fixed tape speed, the FM center frequency and, hence, the DC level and gain of the demodulator output depend upon spin rate. The 200 kHz reference frequency provides recording speed information which may be used to correct the demodulated output.

The output of a divide-by-18 counter supplies the Recorder Reference Frequency to the SK-1600A. Either the Analog Recorder Sync. Signal (ARSS) input from the Synchronizer, or a 245.76 kHz crystal oscillator source is selected by the Reproduce Only command as the counter input. The crystal oscillator source is used when the recorder is operated in the Reproduce Only mode.

ACKNOWLEDGEMENTS

NASA Goddard Space Flight Center provided the support to the University of Wisconsin under Contract NAS 5-9677.

The Ampex Corporation developed and built the SK-1600A Video Weather Data Accumulator for the University of Wisconsin.

The Westinghouse Defense and Space Center, under contract to NASA Goddard Space Flight Center, provided the necessary interfacing between their ground equipment and the University of Wisconsin Data Processor.

The University of Wisconsin Space Science and Engineering Center provided technical management and designed and built the Data Processor to provide the interface between the ground equipment and the SK-1600A.

LIST OF FIGURES

Figure 1. SK-1600A Recorder/Reproducer

Figure 2. SK-1600A Tape Transport Diagram

Figure 3. Analog Recording System Interface and Data Processor Block Diagram

Figure 4. Data Timing and Record Input Levels

LIST OF TABLES

Table 1. SK-1600A Weather Data Accumulator Specifications.

Table 2. Data Identification Word Format.

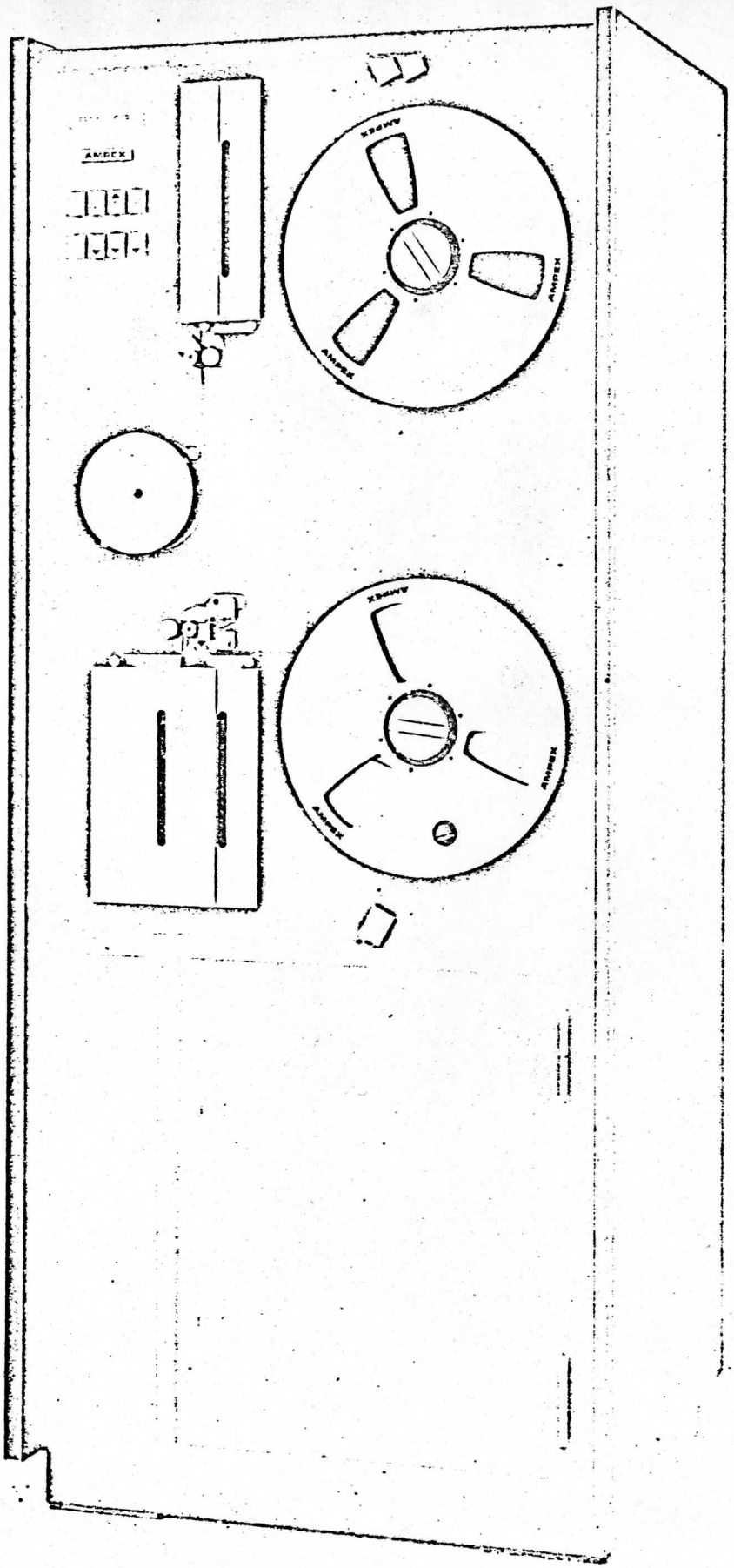

Figure 1. SK-1600A Recorder/Reproducer

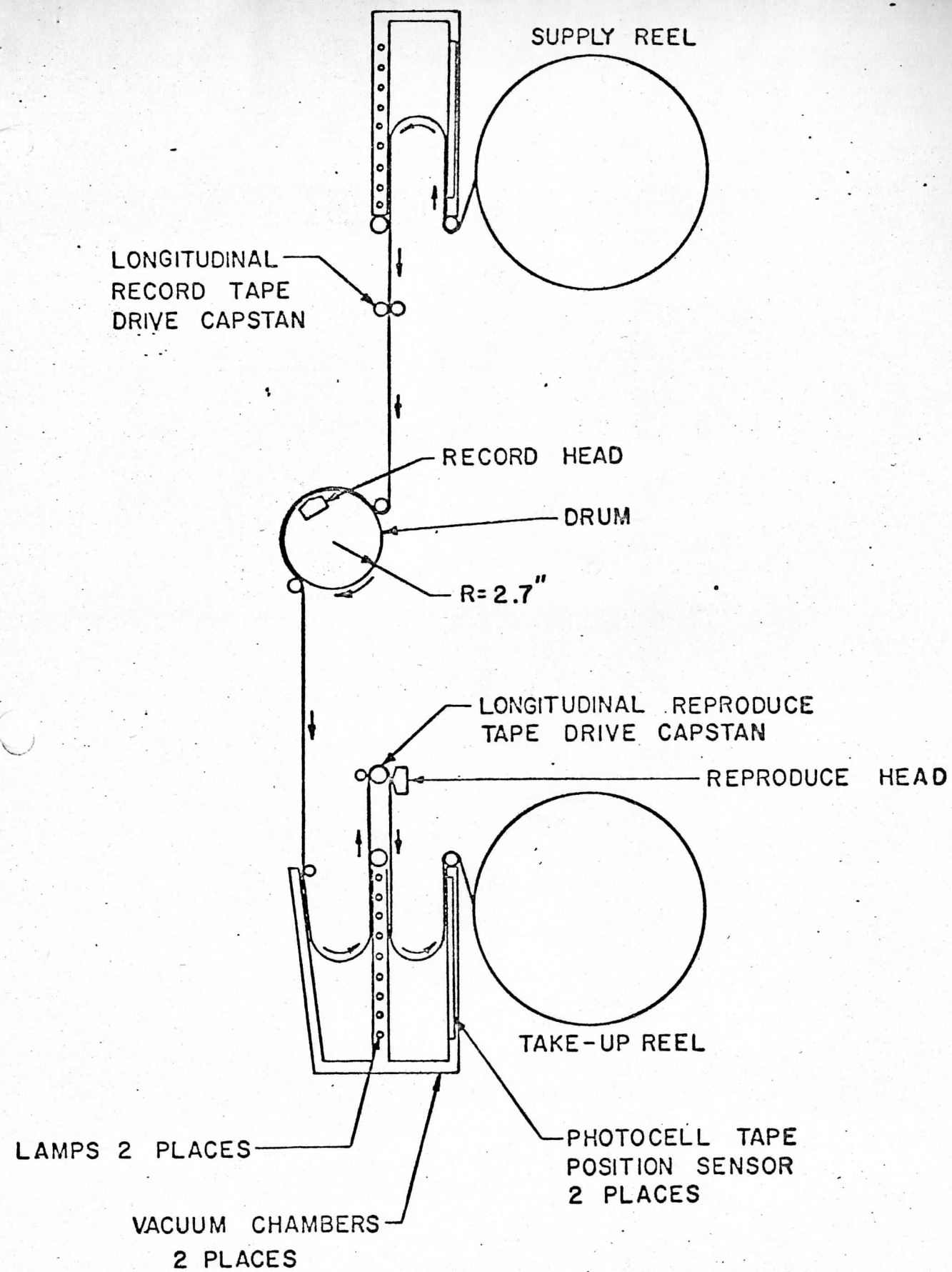

Figure 2. SK-1600A Tape Transport Diagram

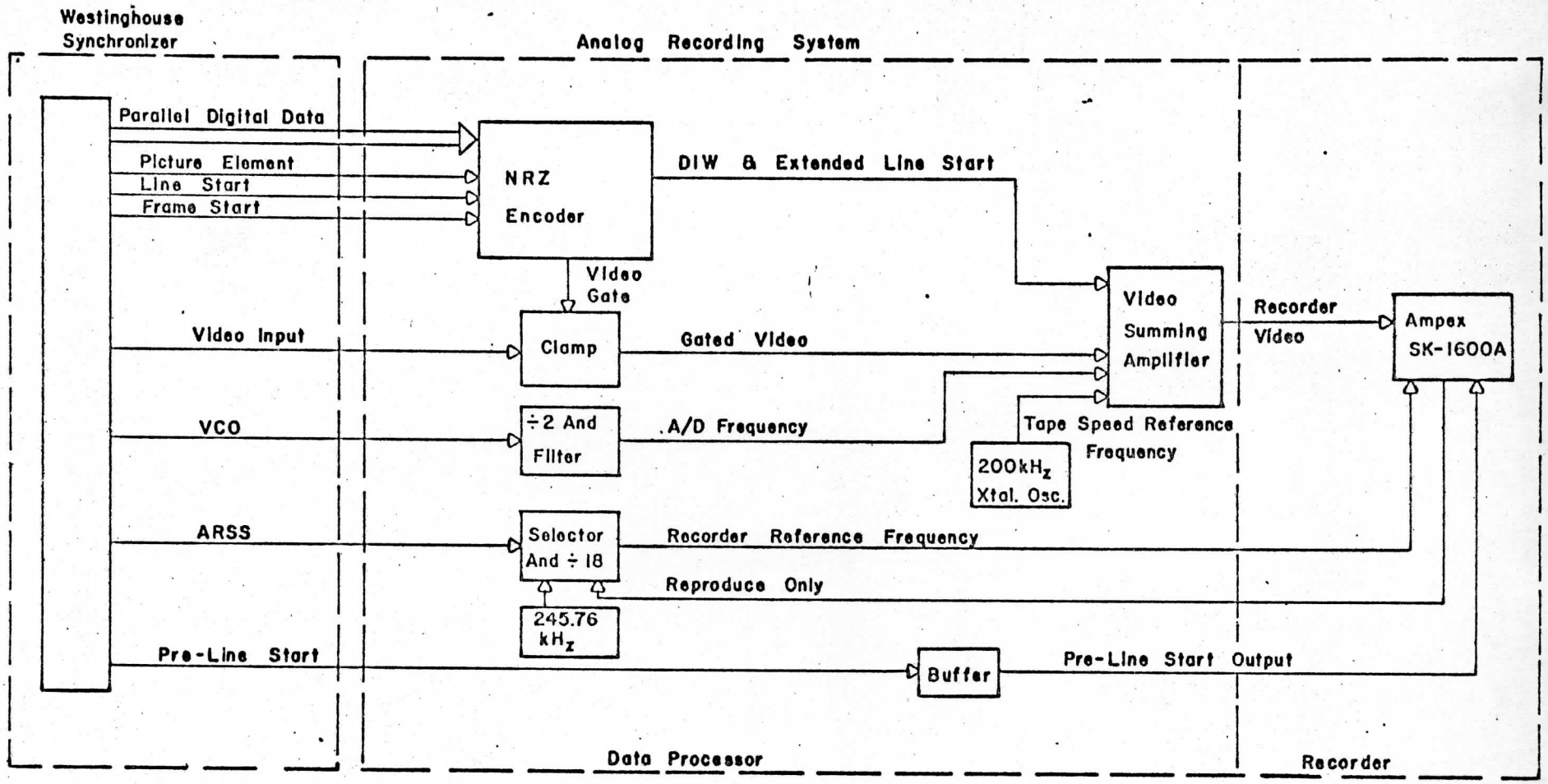

Figure 3. Analog Recording System Interface and Data Processor Block Diagram

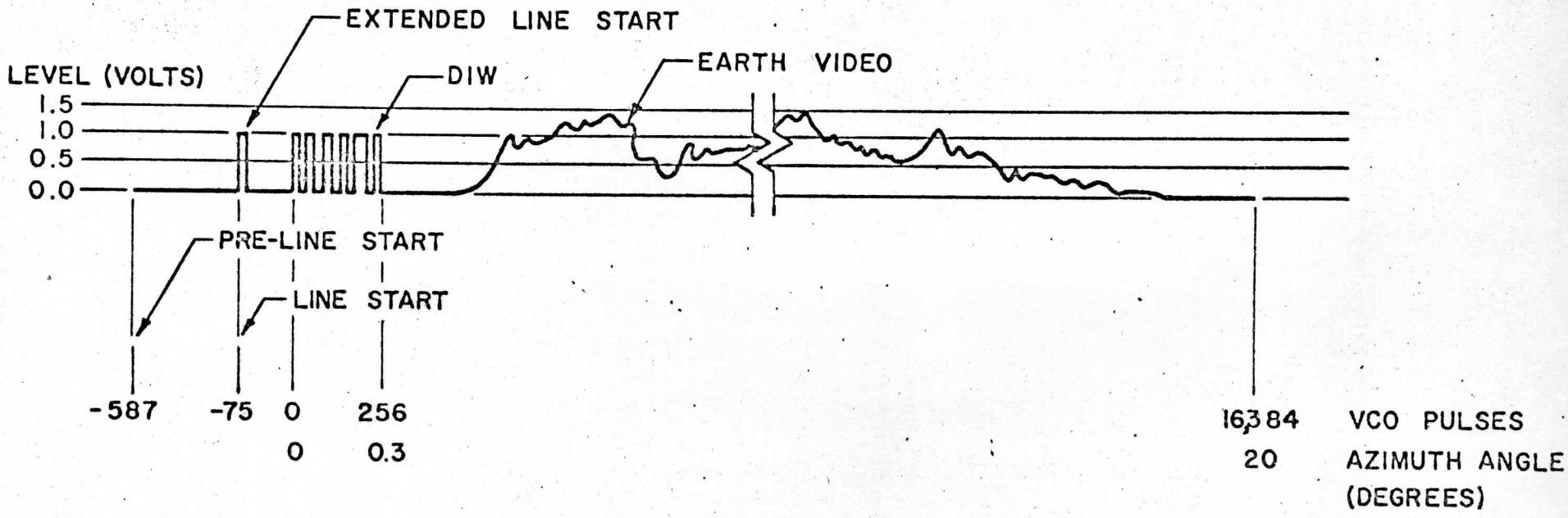

Figure 4. Data Timing and Record Input Levels

Table 1. SK-1600A Weather Data Accumulator Specifications

Storage Capacity	
Tape size	1/2 inch wide
Reel size	14" diameter
Number of Tracks	4
Track Format	IRIG spacing
Reel capacity	
1.5 mil tape	7200 ft.
1.0 mil tape	9600 ft.
Picture capacity per track	
7200 ft. reel	9
9600 ft. reel	12
Record/Reproduce Electronics	
Type	Wideband FM with bias
Record modulator center frequency	900 kHz.
Deviation	± 40%
Bias frequency	7.7 MHz.
Record/reproduce frequency response for DC to 100 KHz record bandwidth	± 0.5 db
Data input sensitivity	0 to +1.5 v. peak signal produces full modulation
Output level	2.6 v. p-p into 75Ω with fully modulated signal
Transport	
[1]Recording longitudinal tape speed	7.5 ips
[1]Record head-to-tape speed	120 ips
Reproduce Only tape speeds	3.75 or 7.5 ips
Scan line record length	4.0 inches, approximatel
Time base expansion	16:1
[2]Line jitter (variation in signal timing at line end relative to line start) at 7.5 ips reproduce (while recording)	60 microseconds

Noise and Distortion

Record/reproduce system peak signal to RMS noise ratio	≥ 40 db
Harmonic Distortion @ 1 kHz. record frequency $(2d^2 + 3d^2)^{1/2}$	1%

Miscellaneous

Power	115v., 60Hz., 1 phase
Size	30"w. x 28"d. x 72" h.
Environment	Normal laboratory type

[1]Values are proportional to spin rate. Those given apply to a spin rate of 100 rpm.

[2]Jitter error distribution is assumed to be gaussian, the specification values given are the 2σ (twice the standard deviation) values.

Table 2. Data Identification Word Format

BIT POSITIONS	DATA DESCRIPTION
1 - 9	Fixed Marker, 111110110
10	Frame Start, F.S. = 1, No. F.S. = 0
11	Fixed Marker, 0
12	Scan Direction, South-to-North = 1, North-to-South = 0
13 - 15	Ground Video Gain, 0 to 6, BCD
16	Satellite Video Gain, High = 1, Normal = 0
17 - 18	Day-of-Year, Hundreds, BCD
19 - 22	Day-of-Year, Tens, BCD
23 - 26	Day-of-Year, Units, BCD
27 - 28	Time-of-Day, Hours, Tens, BCD
29 - 32	Time-of-Day, Hours, Units, BCD
33 - 35	Time-of-Day, Minutes, Tens, BCD
36 - 39	Time-of-Day, Minutes, Units, BCD
40 - 42	Time-of-Day, Seconds, Tens, BCD
43 - 46	Time-of-Day, Seconds, Units, BCD
47	Scan Mode, Normal = 1, Back-to-Back = 0
48 - 49	Vertical Line Count, Thousands, BCD
50 - 53	Vertical Line Count, Hundreds, BCD
54 - 57	Vertical Line Count, Tens, BCD
58 - 61	Vertical Line Count, Units, BCD
62 - 63	Fixed Marker, 0 0
64	Parity

Note: BCD digits begin with MSB.

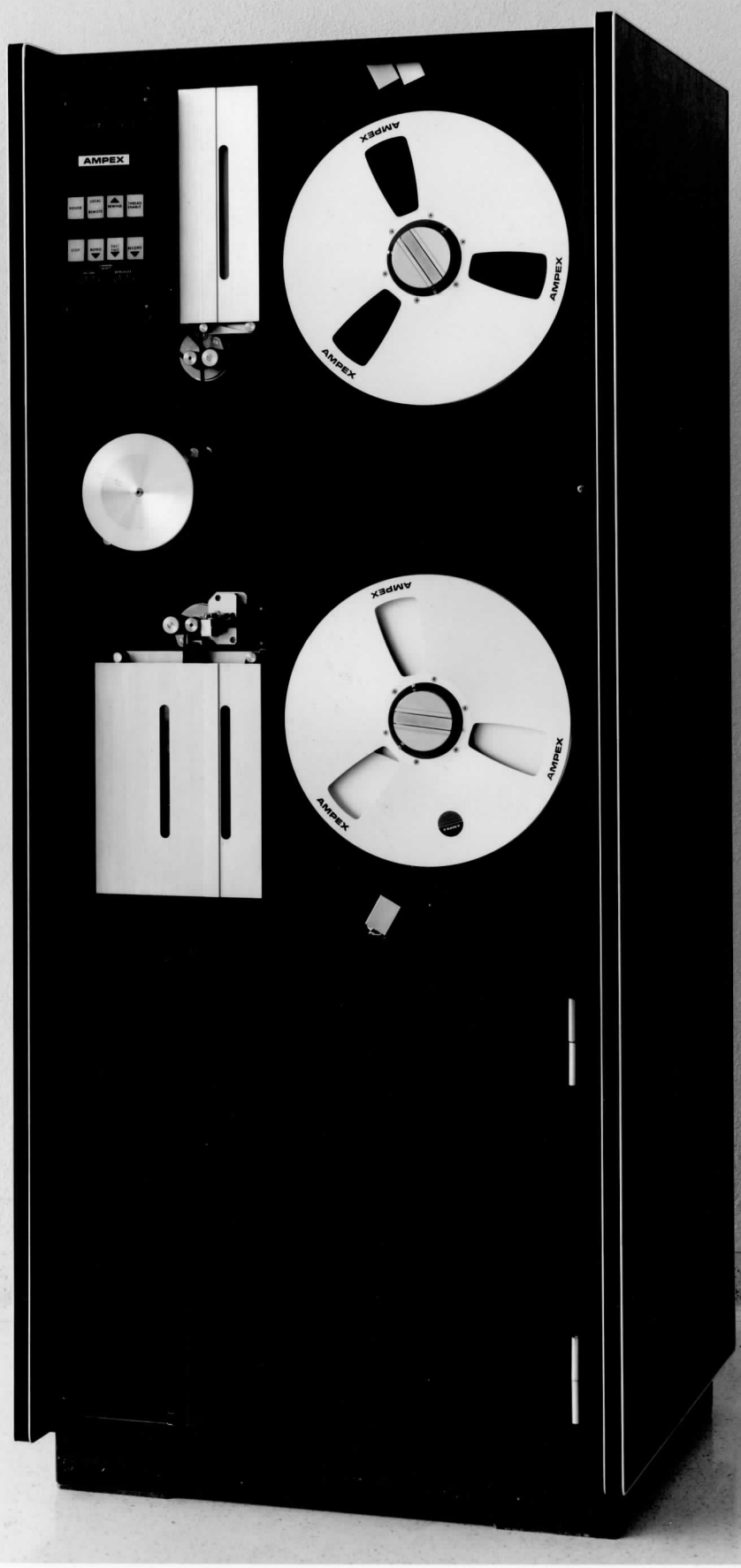
AMPEX
AMPEX
AMPEX
AMPEX
AMPEX
AMPEX

Figure 1. SK-1600A Recorder/Reproducer

PHOTOGRAPHIC DEPT.
9896-1
AMPEX CORPORATION

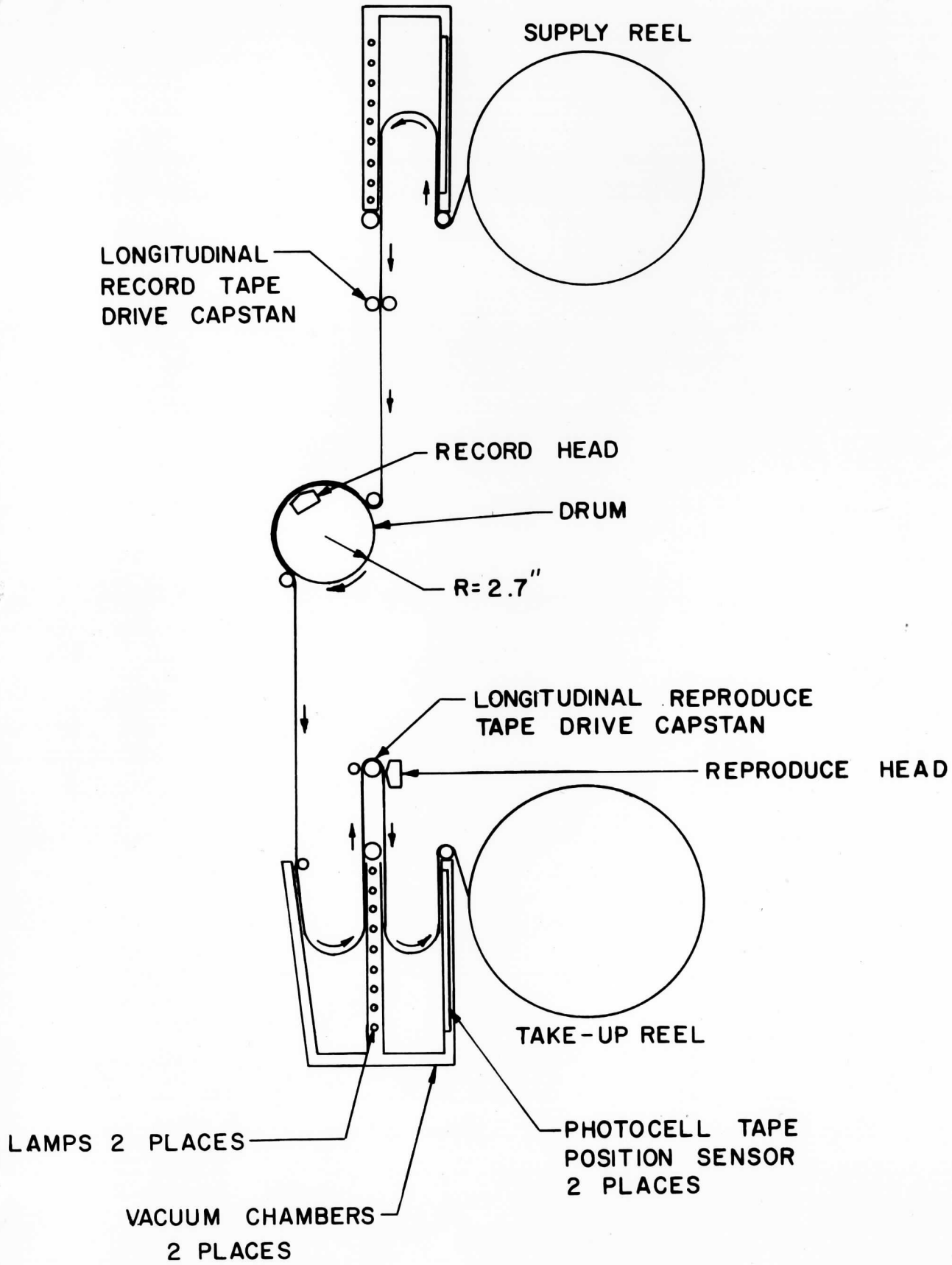
SUPPLY REEL
LONGITUDINAL
RECORD TAPE
DRIVE CAPSTAN
RECORD HEAD
DRUM
R=2.7"
LONGITUDINAL REPRODUCE
TAPE DRIVE CAPSTAN
REPRODUCE HEAD
TAKE-UP REEL
LAMPS 2 PLACES
PHOTOCELL TAPE
POSITION SENSOR
2 PLACES
VACUUM CHAMBERS
2 PLACES

Figure 2. SK-1600A Tape Transport Diagram

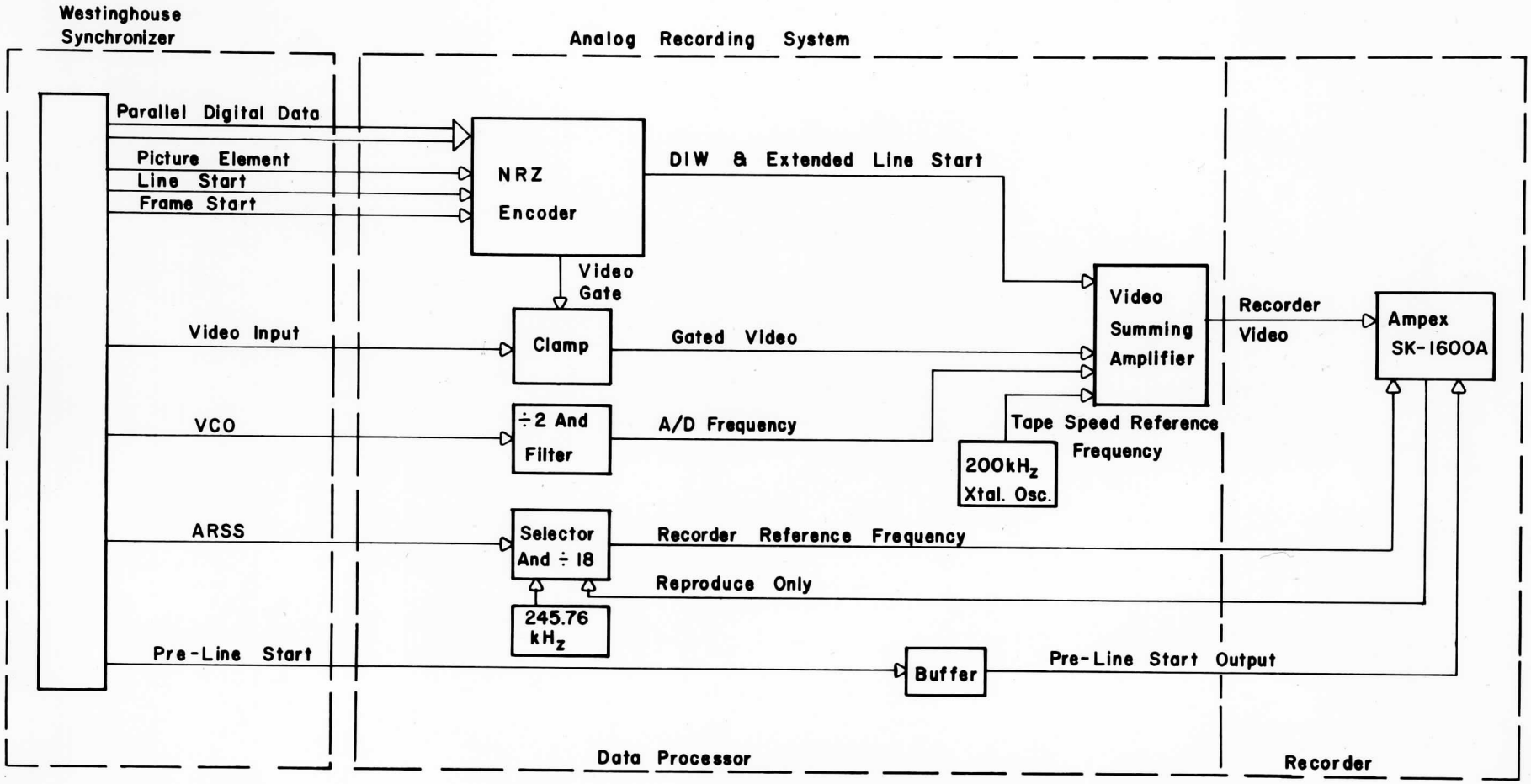
Westinghouse
Synchronizer
Analog Recording System
Parallel Digital Data
Picture Element
Line Start
Frame Start
NRZ
Encoder
DIW & Extended Line Start
Video
Gate
Video Input
Clamp
Gated Video
Video
Summing
Amplifier
Recorder
Video
Ampex
SK-1600A
VCO
÷2 And
Filter
A/D Frequency
Tape Speed Reference
Frequency
200kHz
Xtal. Osc.
ARSS
Selector
And ÷ 18
Recorder Reference Frequency
Reproduce Only
245.76
kHz
Pre-Line Start
Buffer
Pre-Line Start Output
Data Processor
Recorder

Figure 3. Analog Recording System Interface and Data Processor Block Diagram

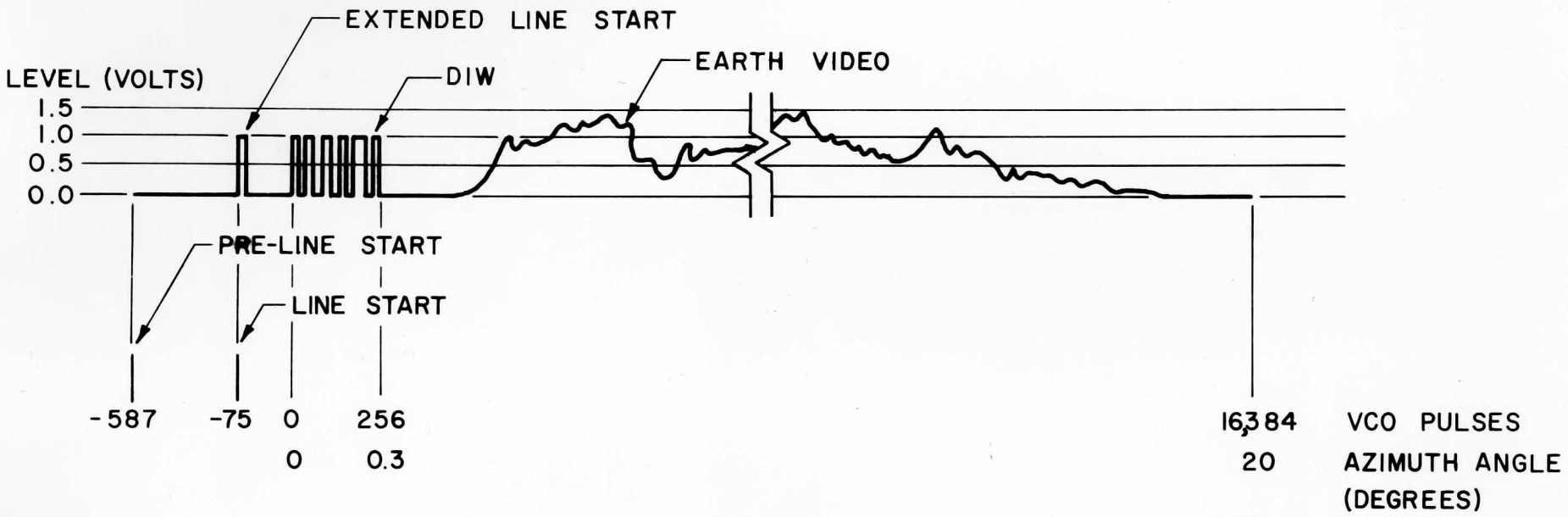
EXTENDED LINE START
DIW
EARTH VIDEO
LEVEL (VOLTS)
1.5
1.0
0.5
0.0
PRE-LINE START
LINE START
-587
-75
0
256
0
0.3
16,384
20
VCO PULSES
AZIMUTH ANGLE
(DEGREES)

Figure 4. Data Timing and Record Input Levels

SOME DISPLAY AND ANALYSIS TECHNIQUES FOR ATS DIGITAL DATA USERS

by

Eric A. Smith and Thomas H. Vonder Haar

1. INTRODUCTION

This paper describes simple, yet flexible, display and analysis techniques that have been developed for use with the ATS digital data. All of the techniques were designed for scientific applications, although some byproducts are useful for engineering and quality assessment purposes. Standardized programs that can be adapted to any large-core computer allow the scientific user to work directly with the recorded satellite data. Standard data input is from a magnetic tape and the display techniques use an on-line highspeed printer and an off-line X-Y plotter. Five types of display and analysis techniques discussed in this paper are shown in the data flow sequence illustrated in Figure 1.

ATS measurements are stored in digital form as "brightness" values ranging from 0-255 digital counts. These values are directly related to the output voltage of the camera and, in turn, to the effective radiance reflected from the region in view (see Peekna et. al. (1968)). This same reference and others in this volume discuss the digitizing procedure and other important facts concerning the digital data. The reference frame used in this paper is the scan line number (increasing from north to south) and the digital element or sample (increasing from west to east).

2. PRELIMINARY DATA TRANSFORMATION

Transformation of the data (digital counts) is often desired before it is input to the display programs. Methods that are most often required have been integrated in a standardized input package utilized by all the display programs. The features of this "front-end" routine include options to sample or average the data over both elements and scan lines of a pictures block. An enhancement

routine is available so that brightness values may be replaced by an enhanced value on a one-to-one basis. This is used not only to improve contrast where needed, but is a method for improving poor quality data if the characteristics are known. Also available is an option to convert brightness value to their natural logarithm value, which serves to improve separation at the lower end of the brightness scale. Finally, before transferring a prepared data block to a display program, an option is available to output a brightness frequency distribution of the block.

3. NUMERIC AND CHARACTER GRID DISPLAYS

Numeric grid display or numeric posting is a representation of the actual brightness values in a gridded format. The scale size of the output displays is variable, enabling latitude and longitude to be preserved, if required. Although the raw product would not generally be used pictorially, detailed hand analysis can be carried out very effectively because one works with the exact brightness values at camera resolution. Furthermore, if the display is shaded or colored at brightness intervals; or manually contoured at brightness levels, a detailed visual product can be produced.

Character display gridding is another method of displaying the data. In this case printer characters are selected to represent specific brightness intervals so that each data element is displayed by a single character. If the characters are chosen on the basis of size, a very smooth gray scale can be established. In Figure 2 we have displayed a large storm to the north-west of the Hawaiian Islands. We chose four brightness levels, represented by an asterisk, a slash, a period and a blank. For better contrast, the cloud areas

(blanks) have been outlined in black. The cloud covered Islands can be seen in the lower right of the picture and circulation features of the storm are easily spotted. A more carefully analyzed display, for the Baja California region, is seen in figure 3. Five brightness intervals have been used, and approximate latitude-longitude lines have been drawn (by hand). A problem with this type of display results from the paper size factor of the computer product. Figure 2 represents 22 sheets of computer paper taped together. The original dimensions of this may were approximately six feet by six feet which is, quite obviously, a bulky size to work with. If necessary, we resolve this problem by the use of an off-line X-Y plotting device.

4. PLOTTING TECHNIQUES

In Figure 4, an individual scan line (near 60°N) has been displayed by plotting the brightness values of the individual elements. Each sample of the scan line is included in the upper plot, while in the lower plot every four elements were sequentially averaged for smoothing purposes. As is readily seen, the numbered features on the plots correspond to distinctive cloud features on the accompanying blow-up of an ATS photograph. The edge of a cold front moving towards the north-west coast of the U. S. (feature 5) appears as a sudden rise in brightness, whereas the convective clouds following the front (feature 4) appear as a series of sharp spikes. When used in conjunction with the photographic originals, scan line plots have successfully been used to determine such things as data quality, brightness of characteristic features, and cloud patterns and types. Levanon (1968) is presently able to determine ocean surface characteristics (ultimately winds) from analyzed scan line plots

over sun glint areas of clear or partly cloudy ocean. An option to this program allows for plotting north-south scans. This is helpful, for example, in studying brightness variations and cloudiness across latitude zones such as the intertropical convergence regions. Hanson and Vonder Haar (1968) have used line plots combined with character displays to study several meteorological phenomena.

Two dimensional plotting of brightness values is accomplished by the use of objective contouring techniques. With these programs, display size, scaling and the contour levels are all variable, thus allowing for flexible usage. We have shown at the bottom of Figure 5 a contour plot of the island of Hawaii, at brightness level 35. As can be seen, the resolution is far better than that of a standard ATS picture. Directly above the picture we have included a contoured region of the storm already seen in Figure 2. In this case the individual contours have been labeled according to their brightness level. A scan line plot through this region (heavy black line with lettering), seen at the top of the figure, has been included to demonstrate the visual and informational properties of both systems when used together in conjunction with a photograph. Vonder Haar et. al. (1968) have used the contour displays to study the time variation of ring-like cloud patterns in the tropics.

A three dimensional technique (in perspective) for plotting an ATS data grid is seen in Figure 6. The area represents a typical region of well-developed convection in the tropics. This type of isometric plotting, although qualitatively quite descriptive, is still being developed and has not yet been applied to ATS data in a quantitative fashion.

5. CLOUD POPULATION ANALYSIS

The most versatile program that has been used for quantitative analysis of

the digital data utilizes a technique which determines and plots individual cloud boundaries while simultaneously measuring area, mean brightness, and position of these clouds. After upper and lower brightness thresholds have been established (distinguishing cloud elements from non-cloud elements), the program scans through a data grid, plotting the cloud boundaries and keeping an "information census" on each cloud. Upon completion of the scanning process, individual clouds on the display have been given an index number which is referenced in a cloud information program. From this information, a cloud size frequency plot and a cloud mean brightness frequency plot are generated. The percentage of total cloud cover, the mean picture brightness and an element brightness frequency distribution are also computed.

The left of Figure 7 shows an area analyzed in this way at three different thresholds. The top display considers as clouds all elements ranging from brightness 35 to 255, the middle display from 50 to 255, the bottom display from 75 to 255. Various cloud masses have been indicated by the letters A-E. In Table 1, we have prepared from the three cloud information tables generated by the program, a specialized information table associated with all three cloud depiction displays. The column headed ID indicates the individual clouds, as they are found at the three thresholds, for each cloud mass. The mean brightness and area is given for each of these clouds. For example, at BT=35 cloud mass A is identified by ID-11* and has a mean brightness of 59 digital counts and an area of 56 square nautical miles. The two brightest portions of this mass are shown at the BT=75 level to have areas of 2 and 4 sq. n.mi. These small bright areas may identify the thick convective towers from the high and low level clouds associated with them. The letter C marks two small clouds at BT=35, but at the next level (BT=50) only one remains and neither of the clouds are brighter than the equivalent

of 75 digital counts. Points D and E are related to a large cloud-covered region about 900 sq. n.mi. at the lower brightness threshold. Display at a higher level (BT=75) yields a 75% reduction in area together with a 25% increase in mean brightness. This indicates that the cloud mass is rather uniform with a slightly brighter center portion and thinning toward the edges. At the right of the figure, a contour analysis at BT=50 is seen. Although this product is visually more pleasing, it does not provide the wealth of quantitative information that is available with our cloud population process. The region we have displayed is seen in the upper right hand corner of the figure (outlined in white). The advantage of the display techniques over the standard ATS picture is quite obvious.

By using this technique over time sequenced pictures, change in cloud positions can be measured very accurately. This offers another possibility of inferring the wind field from cloud motion. The advantage of this method over that of a correlative displacement method for measuring cloud motion, is that the meteorologist can apply human decision to the process rather than leave all the decisions up to the computer. This advantage becomes apparent when studying meso-scale activity, such as individual cloud growth and decay or wave patterns in convergence or divergence regions, when meteorological decision-making is not easily programmable.

6. SUMMARY

The display and analysis techniques discussed in this paper have been developed to aid the scientific utilization of quantitative ATS satellite observations. They have already saved thousands of man-hours of data plotting and analysis. At the same time their flexibility allows and requires frequent input

judgement from the scientific users.

Detailed information regarding these techniques and the programs is available from the authors. A program time-cost summary is shown in Table 2.

ACKNOWLEDGEMENTS

Programmers in the Space Science and Engineering Center of the University of Wisconsin have contributed to the display routines and to the associated data reduction techniques.

REFERENCES

1. Hanson, K. and T. Vonder Haar, 1968: Cloud motion and modeling information in ATS-I digital data, The ATS-I Volume, University of Wisconsin Press.

2. Levanon, N., 1968: Studying the statistical geometry of the sea surface from a synchronous satellite utilizing the sun glitter, The ATS-I Volume, University of Wisconsin Press.

3. Peekna, S., R. Parent and T. Vonder Haar, 1968: Possibilities for quantitative radiance measurements in the 450 - 650 nm region from the ATS-I satellite, The ATS-I Volume, University of Wisconsin Press.

4. Vonder Haar, T., K. Hanson, V. Suomi and U. Shafrir, 1968: Phenomenology of convective ring clouds in the tropics as derived from geosynchronous satellite observations. Proceedings of the International Conference on Cloud Physics, Toronto.

TABLE 1: Cloud statistics table associated with figure 7

(BT=brightness threshold, ID=cloud identification number,
$\overline{B}$=cloud mean brightness, A=cloud area)

REGION	BT	ID	$\overline{B}$	A(Sq n.mi.)
A	35	11*	59	56
	50	6*	61	32
		143	79	8
		146	56	2
	75	13	79	2
		14	101	4
B	35	13*	64	210
	50	8*	87	78
		9*	73	18
		Others		
	75	17	95	12
		20	89	4
		21	125	2
		5*	112	34
C	35	129	59	2
		130	50	2
	50	144	54	2

TABLE 1 CONTINUED

Region	BT	ID	$\bar{B}$	A(Sq n.mi.)
	75			
	35	12*	79	898
D	50	10*	74	60
		165	55	2
		166	62	2
	75	4*	93	16
		19	119	2
	35	12*	79	898
E	50	7*	101	504
	75	3*	119	184

TABLE 2

PROGRAM TIME-COST SUMMARY

(Valid for a 100 Scan Line X 300 Element Grid of ATS Data Input to The CDC 3600 Computer)

TECHNIQUE	PROGRAM NAME	INPUT/OUTPUT TIME(SEC)	PROCESSING TIME(SEC)	COST* ($)
Numeric or Character Display	ATSDSPLY	10#	10	$5°
Scan-line Plot +	ATSPLOT	2#	20	$5°
2-Dimensional Objective Contour Analysis	ATSCNTUR	10#	20	$6°
Isometric Plot	ATSMPLT	10#	25	$6.50°
Cloud Population Depiction and Statistics	CLOUDPOP	10#	25	$6.50°

* total time rate of $400 per hour
\+ refers to a 7000 element scan, not a grid
\# assumes data block is at beginning of tape
o this is an average cost representing, handling charges, program load time, and tape skip time not included in above table.

FIGURES

Figure 1: Data flow sequence for ATS digital data display and analysis programs.

Figure 2: Character display of a storm to the north-west of the Hawaiian Islands. (1967 ATS Picture from Day 109, Time 2425 Z).

Figure 3: Character display of the Baja California region. (1967 ATS Picture from Day 81, Time 2058 Z).

Figure 4: Scan line plots and photograph of the northern Pacific region. (1967 ATS Picture from Day 81, Time 2339 Z).

Figure 5: Contour maps and scan line plot of Hawaiian Island region. (1967 ATS Picture from Day 109, Time 2425 Z).

Figure 6: Isometric plot of the brightness field over tropical convection.

Figure 7: Cloud population maps of a small region in the Line Islands area.

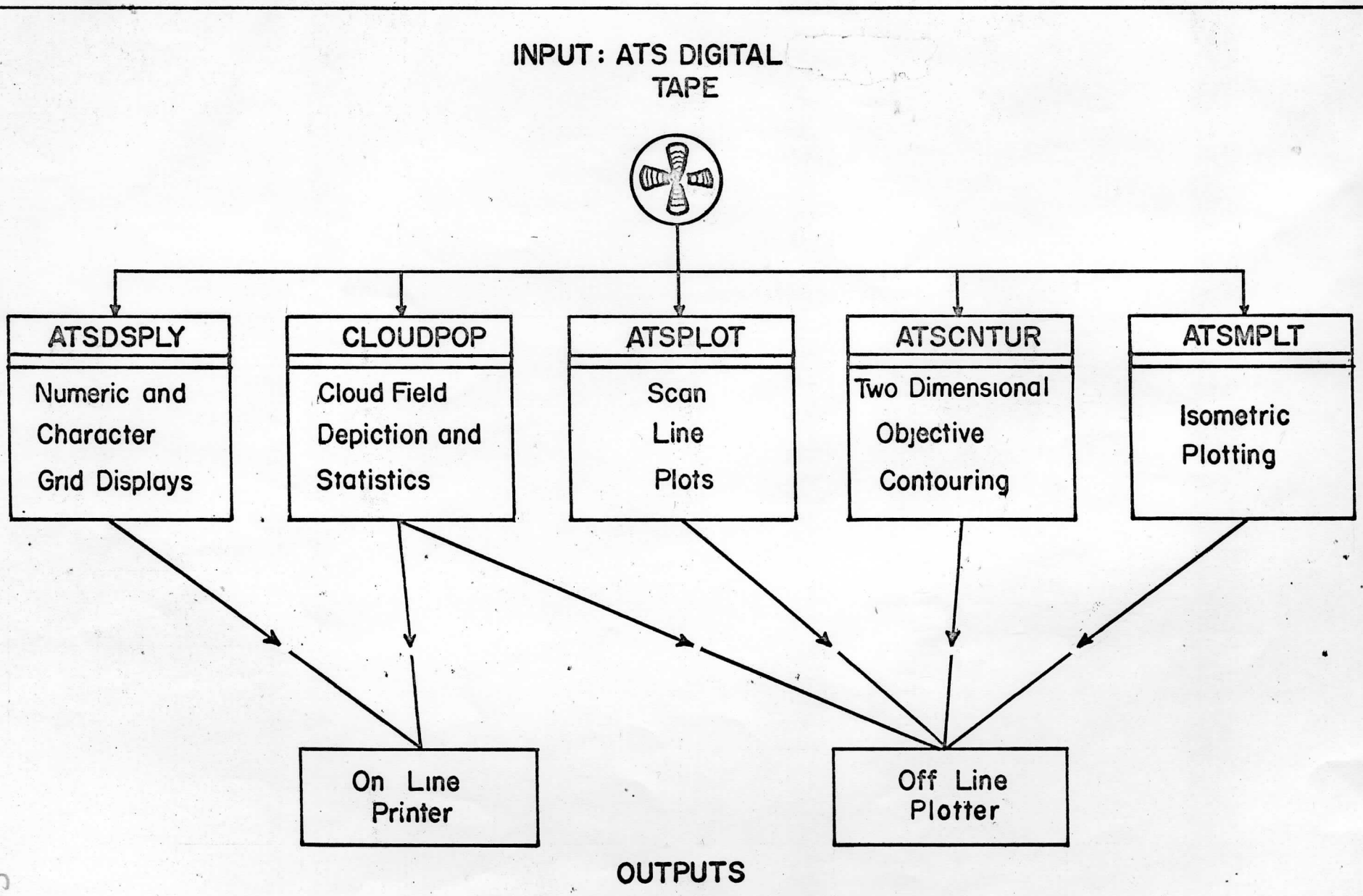
INPUT: ATS DIGITAL TAPE
ATSDSPLY
Numeric and Character Grid Displays
CLOUDPOP
Cloud Field Depiction and Statistics
ATSPLOT
Scan Line Plots
ATSCNTUR
Two Dimensional Objective Contouring
ATSMPLT
Isometric Plotting
On Line Printer
Off Line Plotter
OUTPUTS

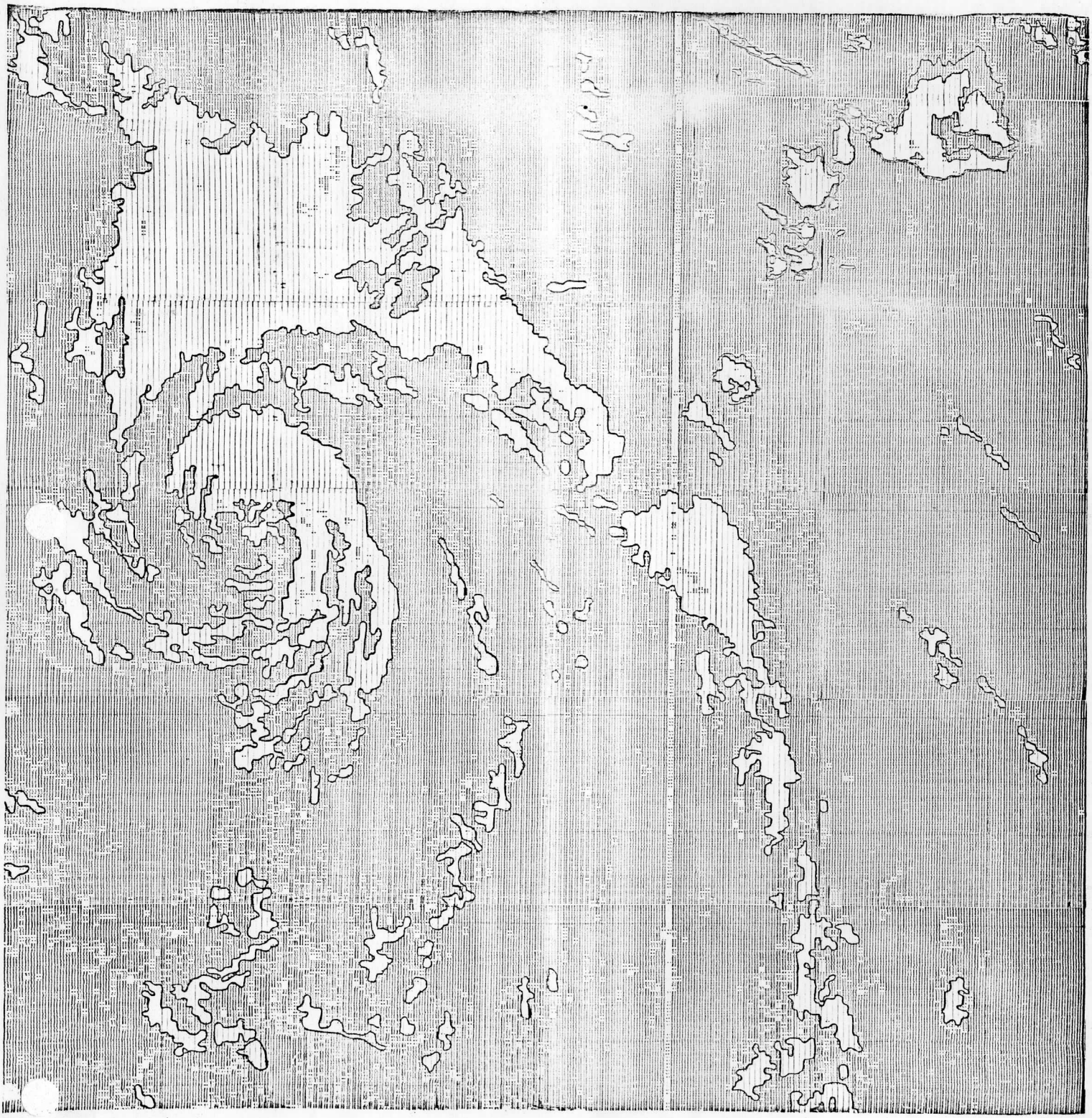

Fig 2

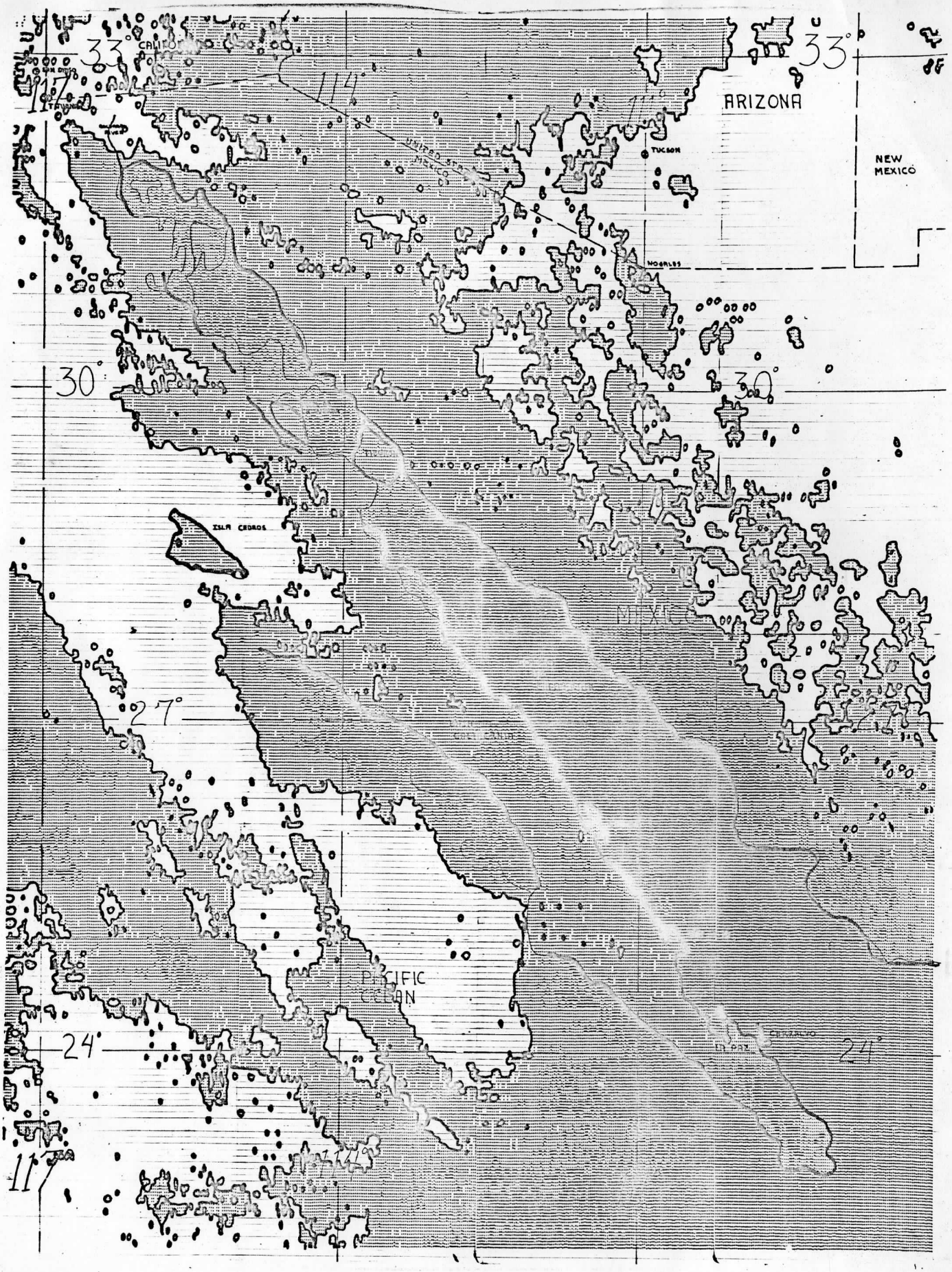
33°
117°
114°
ARIZONA
NEW MEXICO
TUCSON
NOGALES
30°
ISLA CEDROS
MEXICO
27°
PACIFIC OCEAN
LA PAZ
24°

fig 3

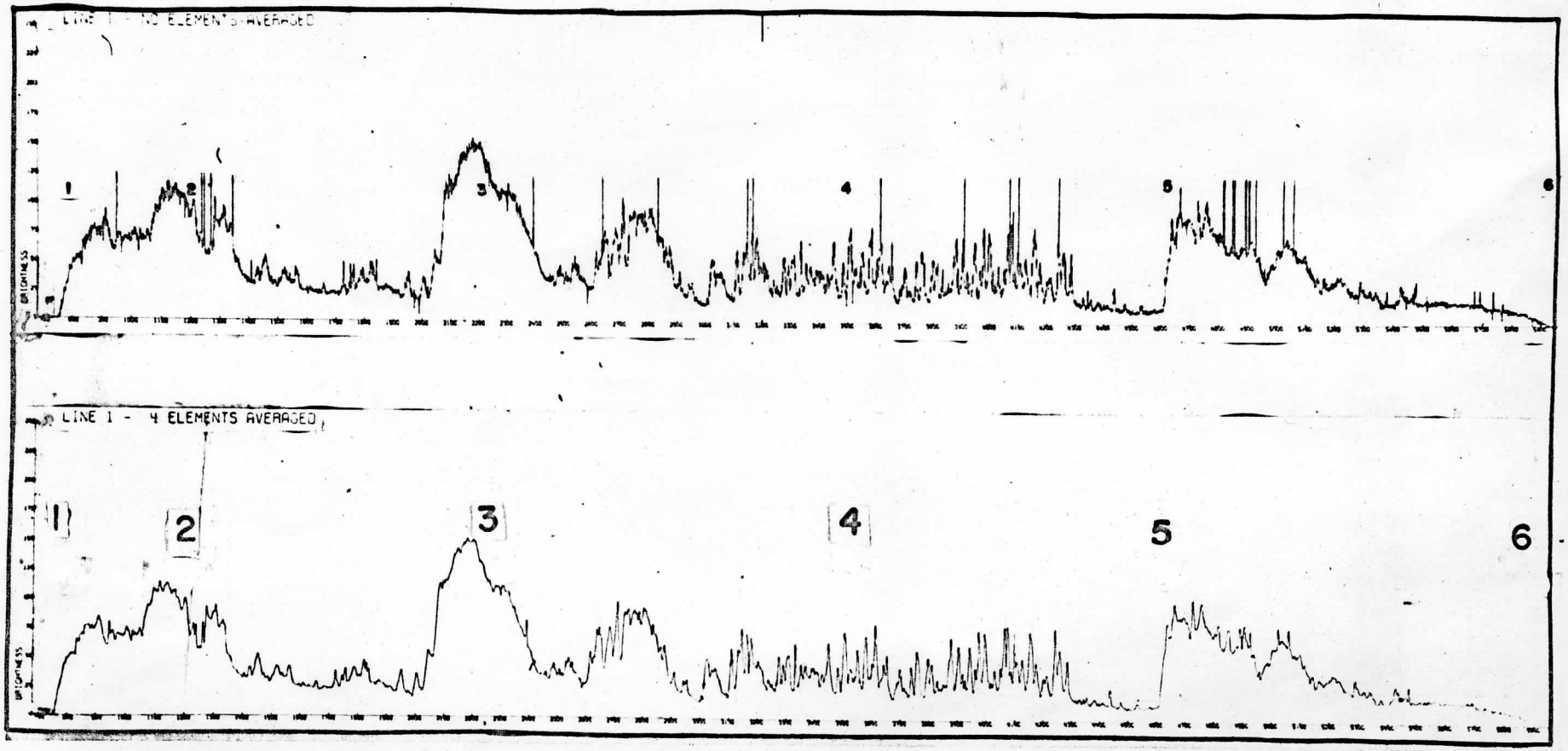
LINE 1 - NO ELEMENTS AVERAGED
BRIGHTNESS
1
2
3
4
5
6
LINE 1 - 4 ELEMENTS AVERAGED
BRIGHTNESS
1
2
3
4
5
6

Fig 4

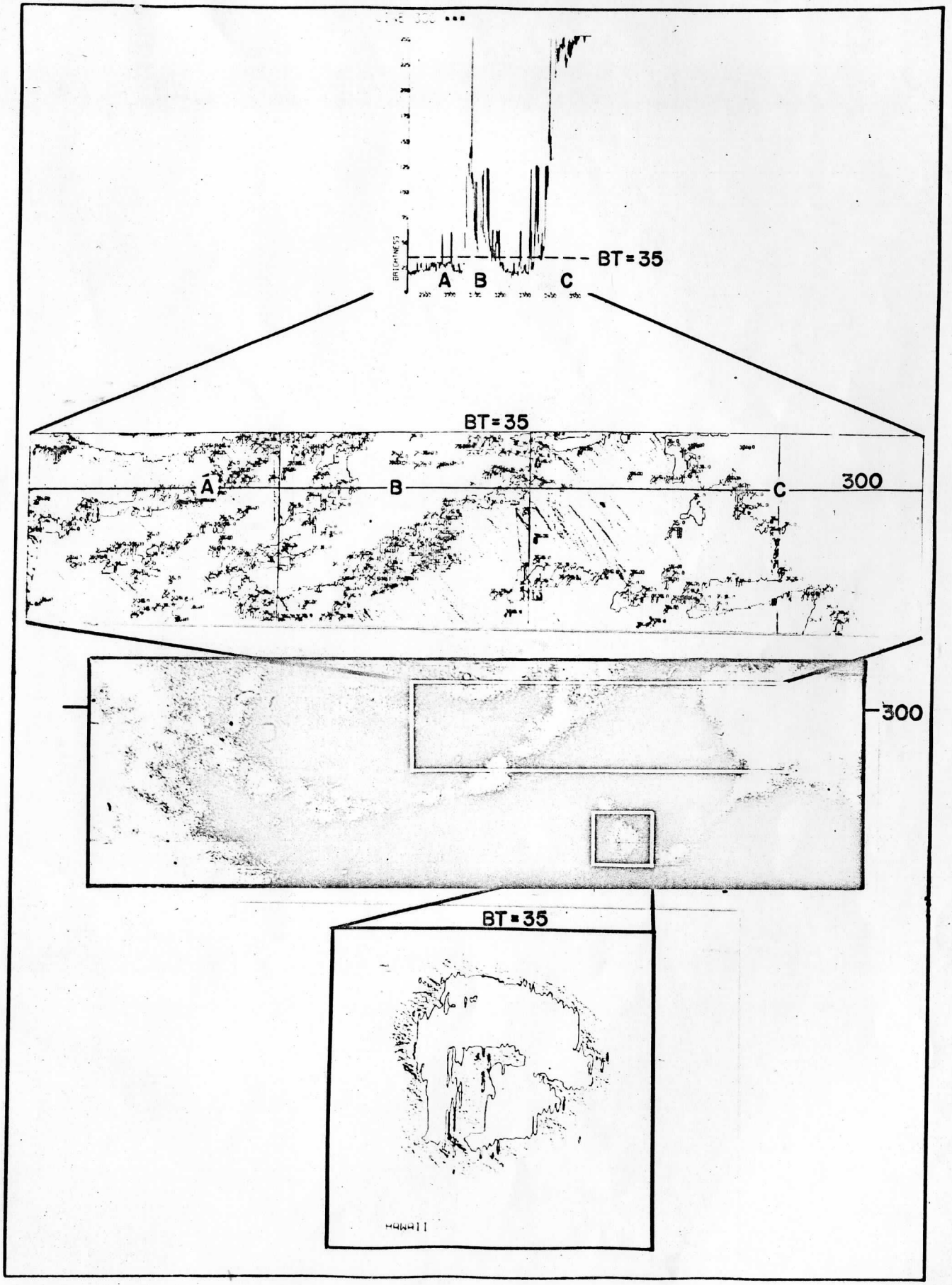

Fig 5

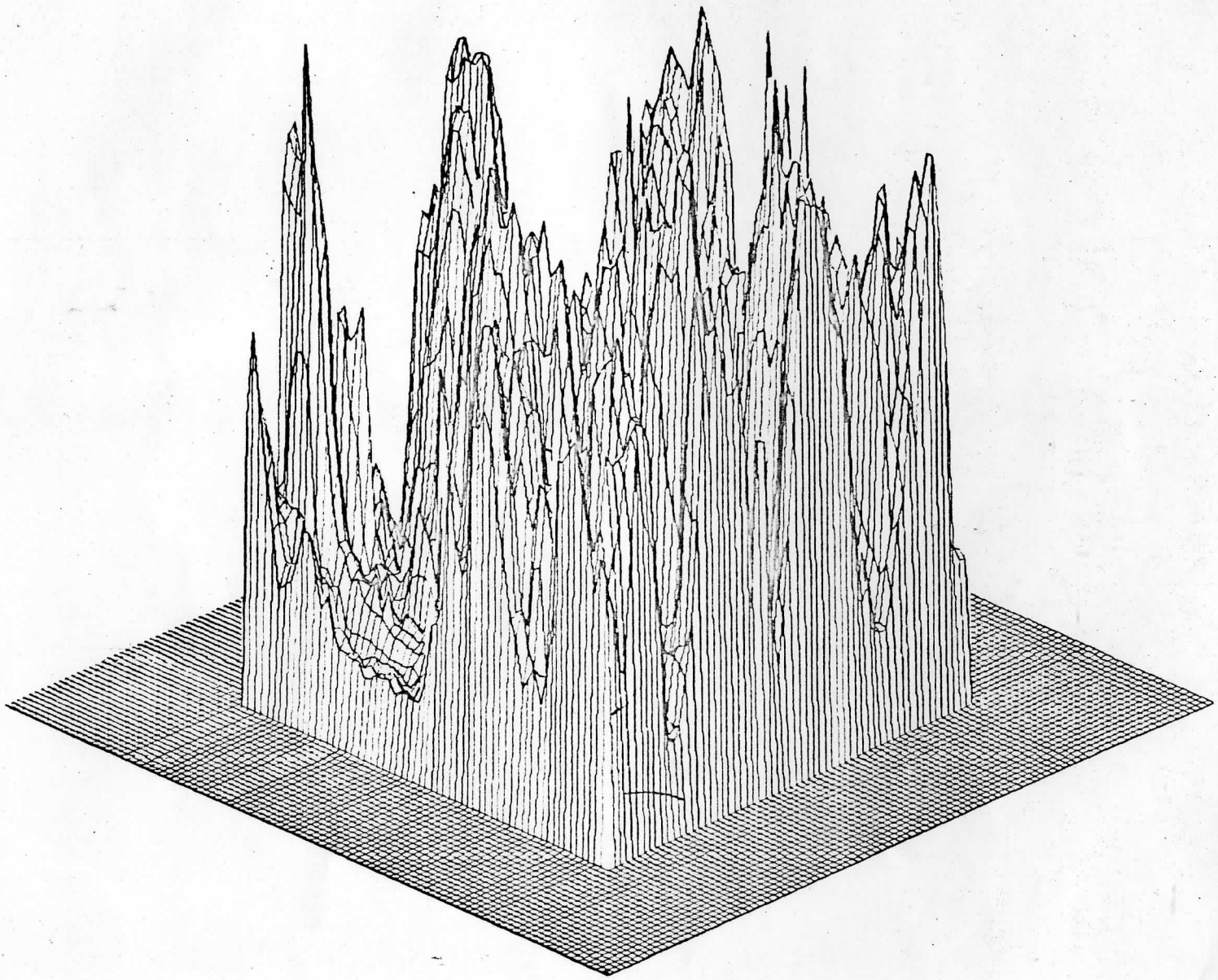

HEIGHT PROJECTION TEST

Fig c

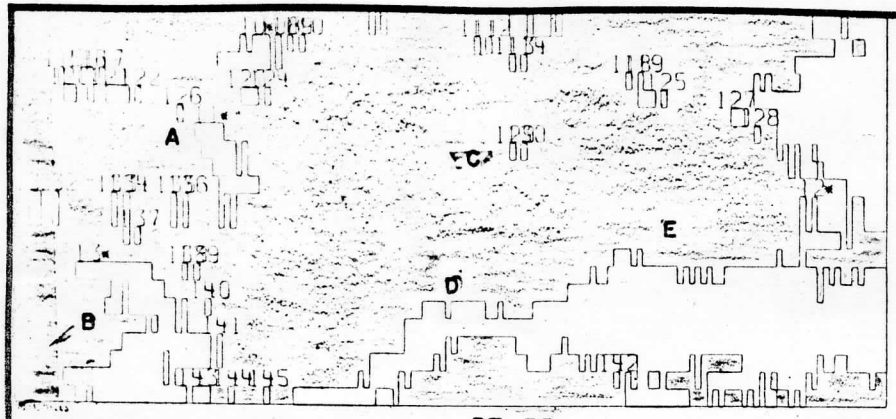

BT-35

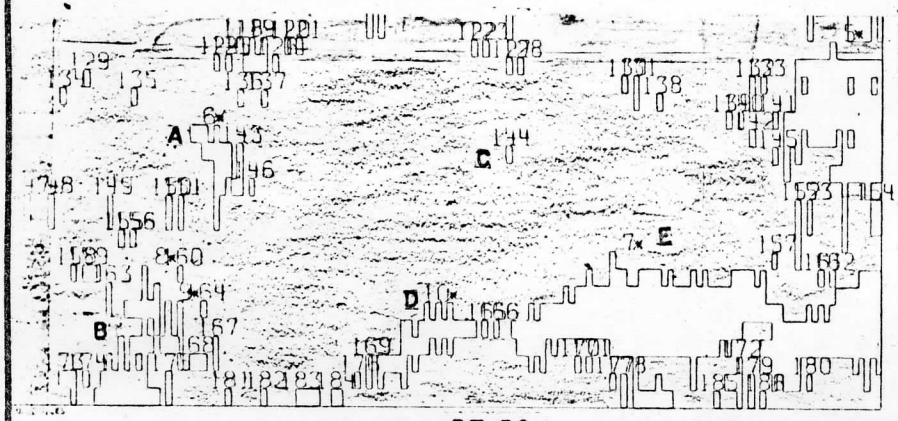

BT-50

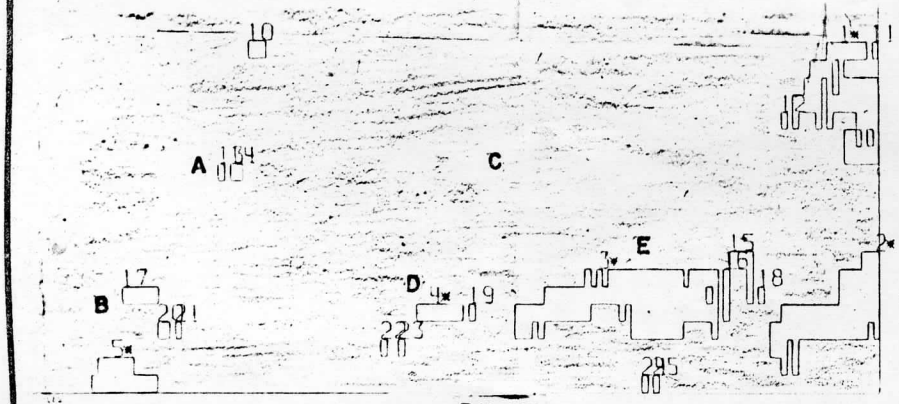

BT-75

LINE ISLANDS AREA

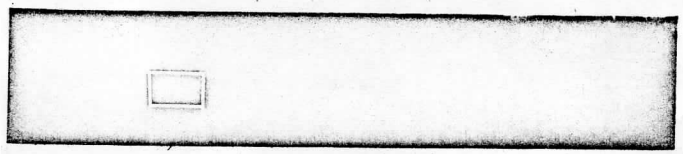

19 APR 67 2148Z.

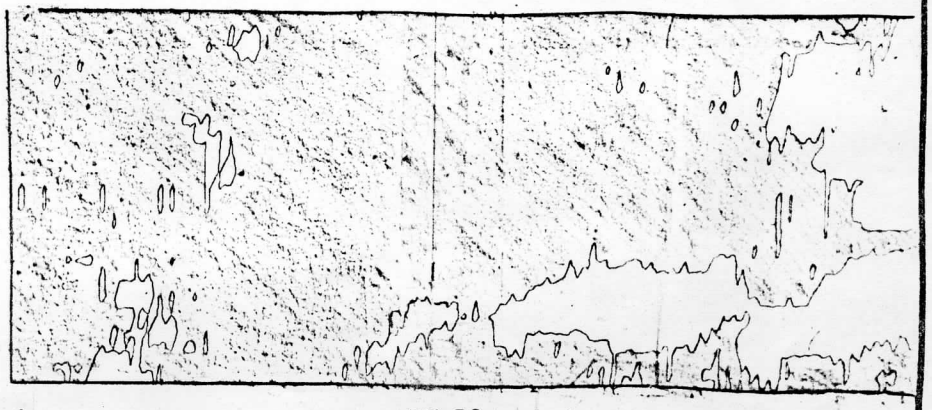

BT-50

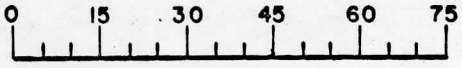

N. MI.

$$[\rho']_{t_0} = 0.03265 \quad [sr^{-1}]$$

In addition, by Eqs. (12) and (18), the numerical value for the constant b is,

$$b = 0.03265 \ [sr^{-1}] \tag{31}$$

The only remaining constant to be determined is c. The constant c is defined in Eq. (12) as $\omega_\odot \int_0^\infty N_{\odot\lambda} R_\lambda \, d\lambda$. If we assume the solar spectral radiance $N_{\odot\lambda}$ and spectral sensitivity of the ATS-1 camera are both constant with time - which is a good assumption - then c is truly a constant at t_0. A numerical integration of this term gives,

$$c = 191.45 \quad [WM^{-2} \, sr^{-1}] \tag{32}$$

based on solar spectral irradiance data of by Valley (1956), (1956) and the spectral sensitivity of ATS given in table 1. The latter is also illustrated in Peekna's Figure 1 (this volume).

Thus, numerical values have been determined for the constants a, b, and c.

4. CALIBRATION EQUATIONS AND THEIR APPLICATION

In the second section of this paper it was shown that Eq. (11),

$$MV = \frac{a}{b \cdot c} N_r', \quad [\text{millivolts}]$$

or its equivalent, expressed camera output as a function of the effective input radiance N_r'. However, to make it useful, we had to determine

numerical values of the calibration constants a, b and c. The latter were evaluated in the previous section and are given in equations (23), (31) and (32). With these known values, equation (11) can now be written as,

$$(MV)_{1,0} = 6.482 \times N_r' \quad \text{[millivolts]} \tag{33a}$$

Here the constant has units of $[mv/Wm^{-2} sr^{-1}]$; thus, the effective radiance has units of $[WM^{-2} sr^{-1}]$.

This form is both simple and useful because it answers the question, "What is the effective radiance from the earth and atmosphere within the field of view, given the camera output with nominal gain settings ?" There are also other useful forms, of course, and these should be given for continuity. They are,

$$(MV)_{1,0} = 6.482 \int_0^\infty N_r R_\lambda \, d\lambda \tag{33b}$$

$$= 6.482 \rho' \cos\delta \, \omega_\odot \int_0^\infty N_{\odot\lambda} R_\lambda \, d\lambda \tag{33c}$$

$$= 6.482 \cos\delta \, \omega_\odot \int_0^\infty \rho'_\lambda N_{\odot\lambda} R_\lambda \, d\lambda \tag{33d}$$

a. Estimating Total Radiance from Effective Radiance

For many applications we wish to estimate the total radiance from our measurements which represent only a limited portion of the spectrum that is, from effective radiance. Our only basis for making such an estimate is that we know these two quantities for the solar spectral distribution.

We can proceed by defining a quantity, $N_{r\odot}$, which is identical to N_r but has the additional constrant that the distribution of energy is the same as for the radiance of the sum. That is, the relative distribution of $N_{r\odot\lambda}$ is that of $N_{\odot\lambda}$; although their absolute values need not agree. From solar radiance data know then that

$$\frac{N_{r\odot}}{\int N_{r\odot\lambda} R_\lambda \, d\lambda} = 7.257 \quad [-] \tag{34}$$

This simple says that if the energy is distributed spectrally as for the sun, then the ATS-1 camera would "see" or sense only (1.7.257)th of the total amount of energy. Now by combining (34) with (33b) and rewriting we have

$$N_{r\odot} \times \frac{\int N_{r\lambda} R_\lambda \, d\lambda}{\int N_{r\odot\lambda} R_\lambda \, d\lambda} = 1.120 \times (MV)_{1,0} \; [WM^{-2} \; sr^{-1}] \tag{35}$$

Equation (35) is useful for handling problems dealing with various spectral distributions of radiance from the atmosphere. These distributions are of two types for discussion purposes - solar distribution and nonsolar distribution, and they are discussed below.

1. Solar Spectral Distribution. This is a special case of (35) in which we require that the radiance from the earth and atmosphere is essential with the solar spectral distribution. The case might be expected to occur in nature when a bright, neutral reflectance surface is located high in the atmosphere - such as with deep convection. In this case, the numerator integral on the left hand side of (35) approaches

$\int N_{r\odot\lambda} R_\lambda \, d\lambda$ and equation (35) becomes simply,

$$N_{r\odot} = 1.120 \times (MV)_{1,0} \quad [WM^{-2} sr^{-1}] \tag{36}$$

Or to go in with DN instead of MV, by equations (20) and (36),

$$N_{r\odot} = 2.196 \times (DN)_{1,0} \quad [WM^{-2} sr^{-1}] \tag{37}$$

These are very helpful equations to use for estimation of radiance, under the conditions assumed. The reader might also find it helpful to recall that the radiance, $N_{r\odot}$, from a perfect, Lambert reflector at the top of the atmosphere is 442.2 $[WM^{-2} sr^{-1}]$. This means that for Lambertian reflectance surfaces, the maximum camera output will be about 394.8 [millivolts] or a digital number of 201, assuming nominal gain settings of (0, 1) are used.

2. Non-solar Spectral Distribution. If the distributive is something other than the solar distribution, then Eq. (35) is a very useful form. It is useful because the ratio of the integrals allows one to correct for the error in calculation of N_r, which results from $N_{r\lambda}$ having a non-solar distribution. The equation is

$$N_r \times \frac{\int N_{r\lambda} R_\lambda \, d\lambda}{\int N_{r\odot\lambda} R_\lambda \, d\lambda} = 1.120 \, (mv)_{1,0} \quad [WM^{-2} sr^{-1}] \tag{35}$$

This equation is particularly useful if one knows or can estimate the spectral distribution of N_r; and this is often available from aircraft or satellite measurement, or from radiation model estimates.

If, however, one knows or can estimate the spectral reflectance properties of the medium within the field of view, then it is desirable to write (35) in terms of the bidirectional spectral reflectance.

$$N_r \cdot \frac{\int N_{\odot\lambda}\, \rho'_\lambda\, R_\lambda\, d\lambda}{\bar{\rho}' \int N_{\odot\lambda} R_\lambda d\lambda} = 1.120 \times (MV)_{1,0} \quad [WM^{-2} sr^{-1}] \tag{38}$$

5. SUMMARY

The ATS-I cloud camera was calibrated by observing the moon on September 19, 1967. This paper presents both the theory and data for that calibration. In this calibration the moon served simply as a passive brightness source with which to relate the camera response to sunlight reflected from a known reflectance surface. The moon's bidirectional reflectance was determined by comparison with a secondary-standard reflectance surface (Kodak white paper), which had been calibrated by comparison with a Mg O_2 reflectance surface.

It has been shown that the camera input and output are related by,

$$(MV)_{1,0} = 6.482 \times N_r' \qquad [\text{millivolts}] \qquad (33)$$

where the input is N_r', the effective radiance within the camera field of view, and the output is $(MV)_{1,0}$ in millivolts when the camera gain and ground station gain are nominal. The nominal gain settings are 1 and 0, respectively.

It is also possible to estimate the (true) radiance (rather than effective) within the field of view if one has some idea of the distribution of the spectral radiance. This is determined from

$$N_r \times \frac{\int N_{r\lambda} R_\lambda \, d\lambda}{\int N_{r\odot\lambda} R_\lambda \, d\lambda} = 1.120 \times (MV)_{1,0} \qquad [W m^{-2} sr^{-1}] \qquad (34)$$

Here, $N_{r\lambda}$ is the normalized spectral radiance within the field of view, and $N_{r\odot\lambda}$ is the same normalized spectral radiance, but having a solar distribution. That is, we require that the integral values of $N_{r\lambda}$ and $N_{r\odot\lambda}$ be equal,

$$\int N_{r\lambda} \, d\lambda = \int N_{r\odot\lambda} \, d\lambda$$

although the distributions of $N_{r\lambda}$ and $N_{r\odot\lambda}$ may differ. In this way the integral

ratio in equation (34) serves as a correction for calculating the value of N_r.

Consider the special case in which the radiance in the field of view has a solar spectral distribution, e. g. with radiance from bright clouds high in the atmosphere. In this case the integral ratio in equation (34) approaches unity; thus,

$$N_r = 1.120 \times (MV)_{1,0} \qquad [wm^{-2}sr^{-1}] \tag{35}$$

For users, it is somewhat more handy to determine the radiance from digital numbers (DN) on the digital data tapes, rather than from camera MV values. Therefore, equation (35) will be written in its other form as,

$$N_r = 2.196 \times (DN)_{1,0} \qquad [wm^{-2}sr^{-1}] \tag{36}$$

Both (35) and (36) have the limitations of this special case.

ILLUSTRATIONS

FIGURE

1. Definition of notation, which is principally an adaptation of that of Nicodemus (1963 and 1965).
2. The phase function of the moon. Abscissas, the phase angle in degrees. Ordinates, magnitudes V on the U, B, V system, reduced to 1 AU distance from the sun and 384,400 km from the earth (after Gehrels, et al. (1964)). The dashed linear extrapolation to phase angle (α) = 0 has been added for the present study so that our value may be normalized to a "full moon" equivalent. A V_m value of -12.74 at α = 0 was adopted for this purpose.
3. Computer display of the ATS-1 picture of the moon, 261-7-162755. The lightest areas of the picture correspond to the brightest areas on the moon. The isolines correspond to digital numbers of 75, 50, and 35 - the latter value is approximately on the lunar limb.
4. Measurements at White Mountain on September 19, 1967. Abscissas, the optical air mass above the 12,470 ft. high station. Ordinates, measured brightness of Kodak white paper, 1001 to 1723 PDT (top illustration), of the moon, 1947 to 2400 PDT (bottom illustration). Brightness units are foot-Lamberts.

TABLE

1. Relative Spectral Response of ATS-1 camera.

APPENDIX

Significant Constants

1. Astronomical Constants

AU - Earth-sun mean distance - 1.496×10^{13} [cm]

- Radius of the sun - 6.975×10^{10} [cm]

- Earth-moon mean distance - 3.844×10^{10} [cm]

$\omega_{\odot}$ - Solid angle subtended by the sun at the earth's mean distance - 6.793×10^{-5} [sr]

$\omega_{\odot}/\omega_{\odot}^{*}$ - Solid angle of sun at earth and moon - 0.9948

2. ATS-1 and Related Constants

a	- Calibration constant	- $(40.55)_{1,0}$ [millivolts]
a*	- Angular field of view of ATS-1 camera	- 0.1 [m rad.]
A_c	- Aperature area of ATS-1 camera	- 104. [cm^2]
A_f	- Area ratio	- 1/8.263
b	- Calibration Constant	- 3.265×10^{-2} [sr^{-1}]
B_M/B_P	- Measurement ratio	- 0.9196×10^{-2}
c	- Calibration constant	- 191.45 [WM^{-2}]
F_{α}	- Phase function value at α = 19.87 deg.	- 0.6096
$\int N_{\odot\lambda} R_{\lambda} d\lambda$	- Effective solar radiance	- 2.818×10^{6} [$WM^{-2}sr^{-1}$]
$\int H_{\odot\lambda} R_{\lambda} d\lambda$	- Effective solar irradiance	- 191.45 [WM^{-2}]
$\int N_{r\lambda} R_{\lambda} d\lambda$	- Effective radiance	- 60.94 [$WM^{-2}\ sr^{-1}$]

$P_{r(max)}$	- Maximum power input to ATS-1 camera aperature	- 36.5×10^{-9} [W]
$P'_{r(max)}$	- Maximum effective power input to ATS-1 camera	- 4.98×10^{-9} [W]
ρ'_M	- Bidirectional reflectance of full moon	- 0.03265 [sr^{-1}]
ρ'_P	- Bidirectional reflectance of Kodak white paper at specified angles	- 0.2633 [sr^{-1}]
ρ_P	- Directional reflectance of Kodak white paper	- 0.90
ω_c	- Solid angle field of view of ATS-1 camera	- 0.786×10^{-8} [sr]

3. Radiation Constants

N_O	- Solar radiance	- 2.045×10^{7} [WM^{-2} sr^{-1}]
H_O	- Solar irradiance, at earth's mean distance	- 1389.1 [WM^{-2}]
$N_{r(max)}$	- Maximum earth radiance	- 442.2 [WM^{-2} sr^{-1}]
	- Brightness associated with $N_{r(max)}$	- 44109. [lumens $M^{-2}sr^{-1}$]
		- 12873 [ft. L.]

REFERENCES

Gehrels, T., T. Coffeen and D. Owings. 1964. Wavelength Dependence of Polarization. III. The Lunar Surface. Astrj.,69, 10, 826-852.

NASA, 1964. Tech-Center Division, Cook Electric Co., "Fundemental Description and General Reference Specifications for the Wisconsin Experiment Package, Orbitting Astronomical Observation A." NASA Contract 5-1348, sub 1. Section 2, Page 4.

NASA, 1966. Operational Procedure, Spin Scan Camera Experiment ATS-B. p. 3. (copies available from authors).

NBS, 1939. Preperation and Colorimetric Properties of a Magnesium-Oxide Reflectance Standard. Letter Circular, LC-547. March 17, 1939 National Bureau of Standard, Washington D. C.

Nicodemus, Fred E., 1963. Radiance. am. J. phy.,31, 5, 368-377.

Nicodemus, Fred E., 1965. Directional Reflectance and Emissivity of an Opaque Surface. Applied Optics, 4, 7, 767-773.

Parent, Robert, 1967. Private Communication on ATS-1 Digitizer Conversion. Based on information from J. Luhzun (GSFC/NASA) on 9/11/67.

Richmond, Joseph C., Physical Standards of Emittance and Reflectance. pp 142-153 in Radiative Transfer from Solids. MacMillan, New York. Edited by Henry Blau and Heinz Fisher.

Suomi, V. and R. Parent, 1967. ATS Spin-Scan Cloud Camera and Prelaunch Calibration Procedure, in Studies in Atmospheric Energetics based on Aerospace Probings. Annual Report on WBG-27, amendment no. 1, 1966, pp. 1-40. Department of Meteorology, University of Wisconsin, Madison.

Valley, Shea L., 1965. Handbook of Geophysics and Space Environments. Air Force Cambridge Research Laboratories, Office of Aerospace Research, USAF. (Chapter 16).

TABLE 1

Relative Spectral Responses ATS-1 Camera and Spot Photometer

Wavelength (μ)	Relative Response ATS-1 Camera
.400	.000
.405	.000
.410	.000
.415	.000
.420	.000
.425	.000
.430	.000
.435	.000
.440	.000
.445	.010
.450	.015
.455	.020
.460	.020
.465	.040
.470	.095
.475	.210
.480	.440
.485	.840
.490	.900
.495	.930
.500	.960
.505	.980
.510	.995
.515	1.000
.520	1.000
.525	.980
.530	.950
.535	.925
.540 .545	.900 .860
.550	.820
.555	.770
.560	.720
.565	.675
.570	.610
.575	.560
.580	.500
.585	.440
.590	.350
.595	.275
.600	.200

(continued next page)

Wavelength (μ)	Relative Response ATS-1 Camera
.605	.145
.610	.120
.615	.085
.620	.060
.625	.050
.630	.030
.635	.025
.640	.020
.645	.015
.650	.010
.655	.005
.660	.000
.665	.000
.670	.000
.675	.000
.680	.000
.685	.000
.690	.000
.695	.000
.700	.000

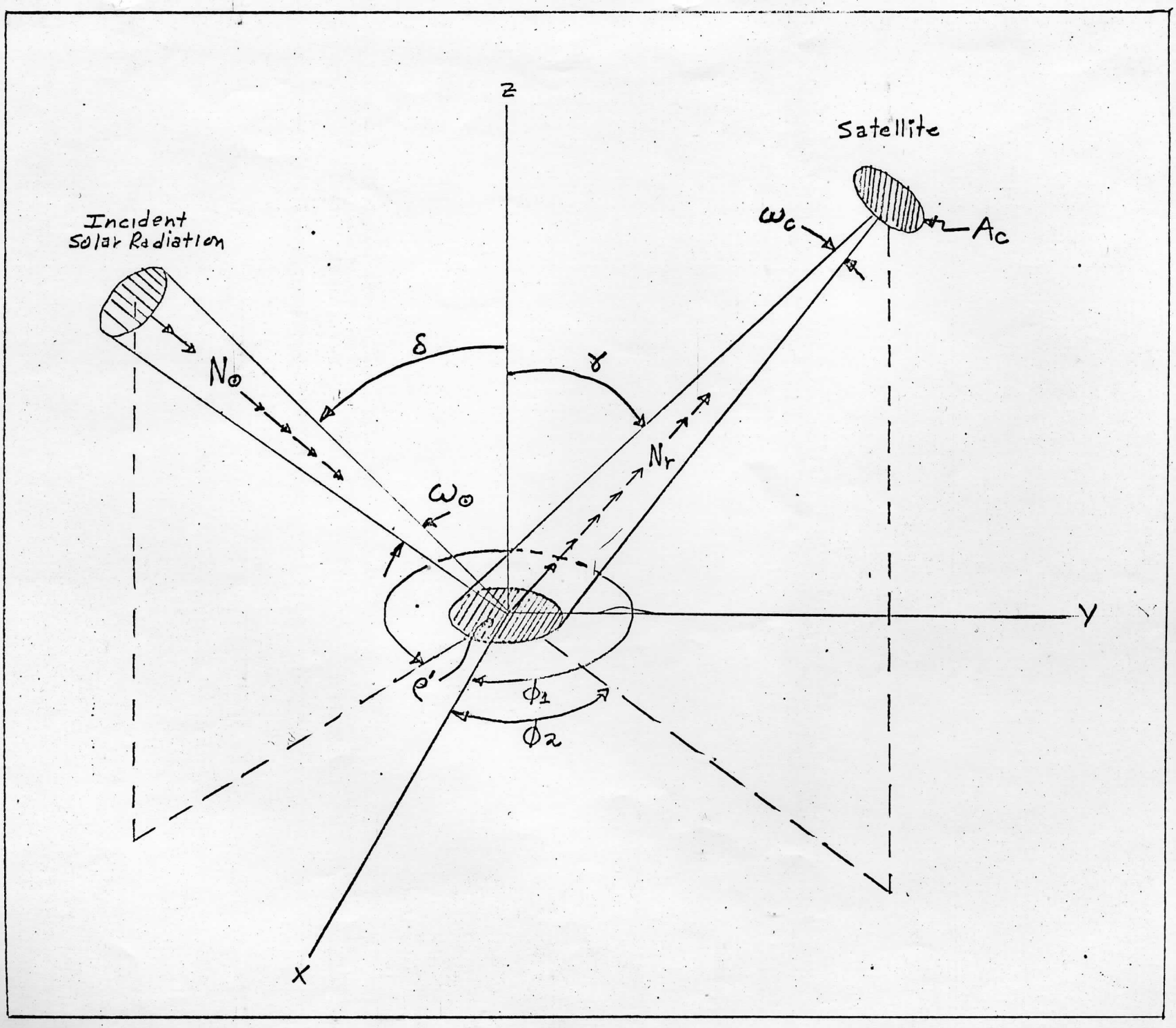
z
Satellite
Incident
Solar Radiation
ω_c
A_c
$N_\odot$
δ
γ
N_r
$\omega_\odot$
Y
ρ'
ϕ_1
ϕ_2
X

Fig. 1

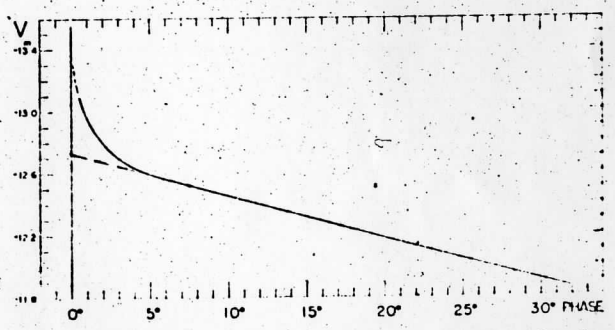

FIG. 5. The phase function of the moon. *Abscissas*, the phase angle in degrees. *Ordinates*, magnitudes V on the *U*, *B*, V system, reduced to 1 a.u. distance from the sun and 384 400 km distance from the earth.

Fig. 2

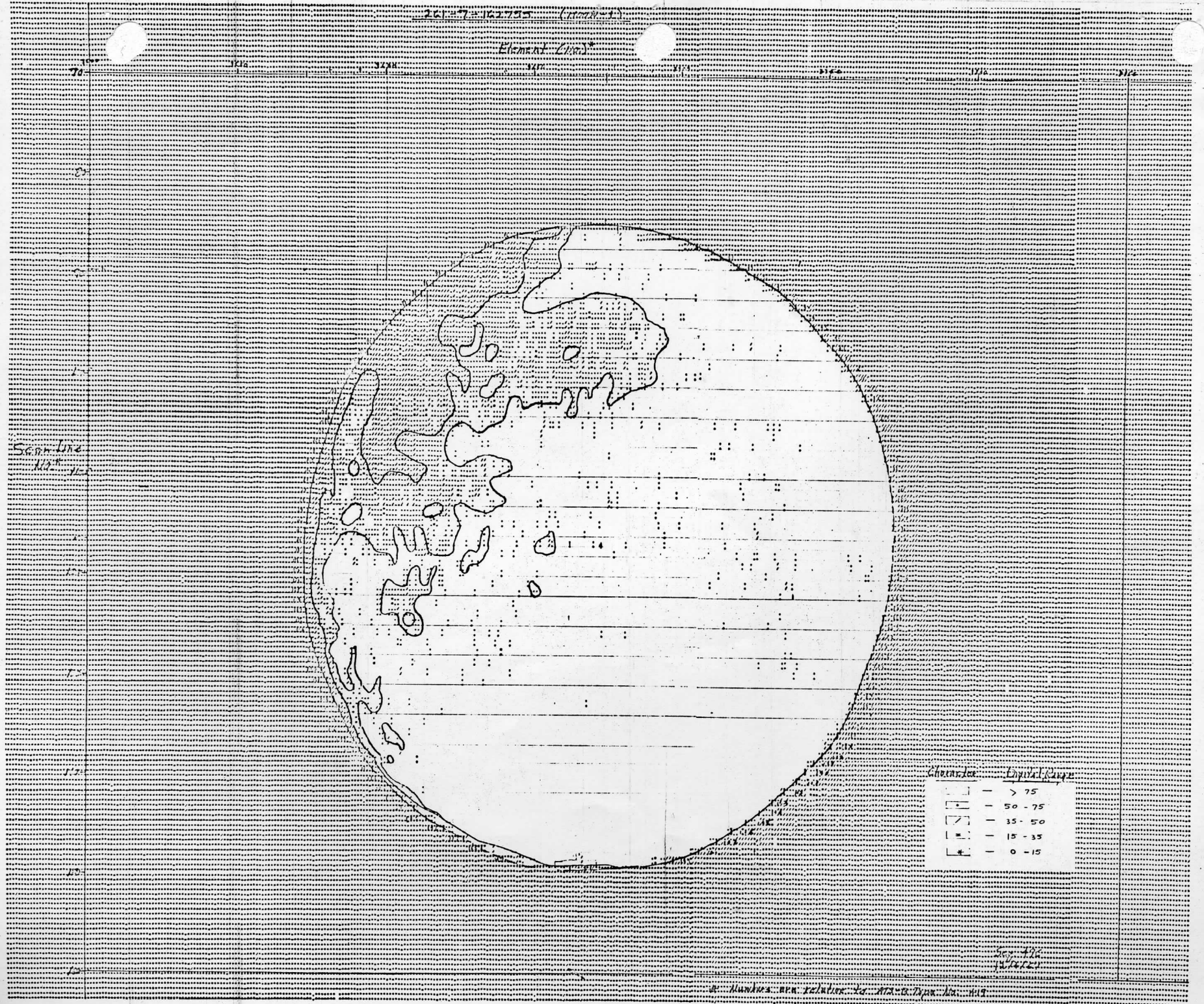
261-7-162795 (11-80-1)
Element Class*
Scan Line
Characteristic
Typical Range
> 75
50 - 75
35 - 50
15 - 35
0 - 15
Sept 1972
(Update)
* Number and relative % of 0 type in each

Fig 3

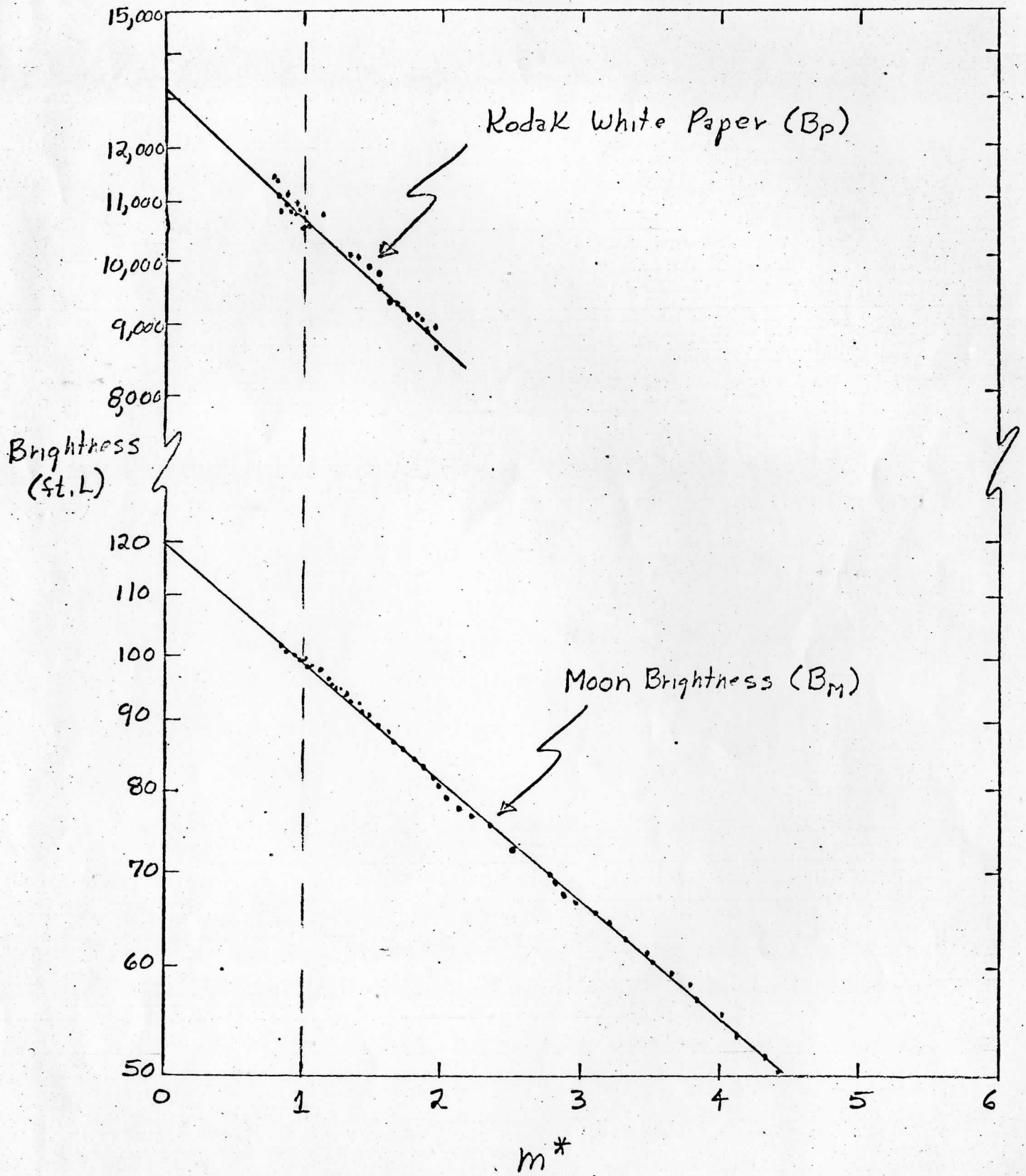
15,000
12,000
11,000
10,000
9,000
8,000
Brightness (ft.L)
120
110
100
90
80
70
60
50
Kodak White Paper (B_p)
Moon Brightness (B_M)
0
1
2
3
4
5
6
m*

Fig. 4

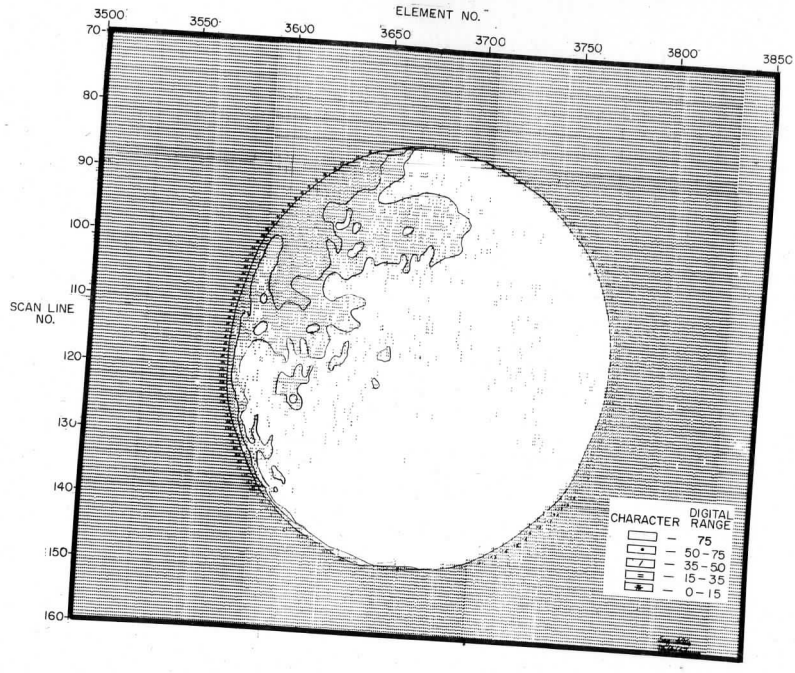
ELEMENT NO.
3500
3550
3600
3650
3700
3750
3800
3850
70
80
90
100
110
120
130
140
150
160
SCAN LINE NO.
CHARACTER
DIGITAL RANGE
– 75
– 50 – 75
– 35 – 50
– 15 – 35
– 0 – 15

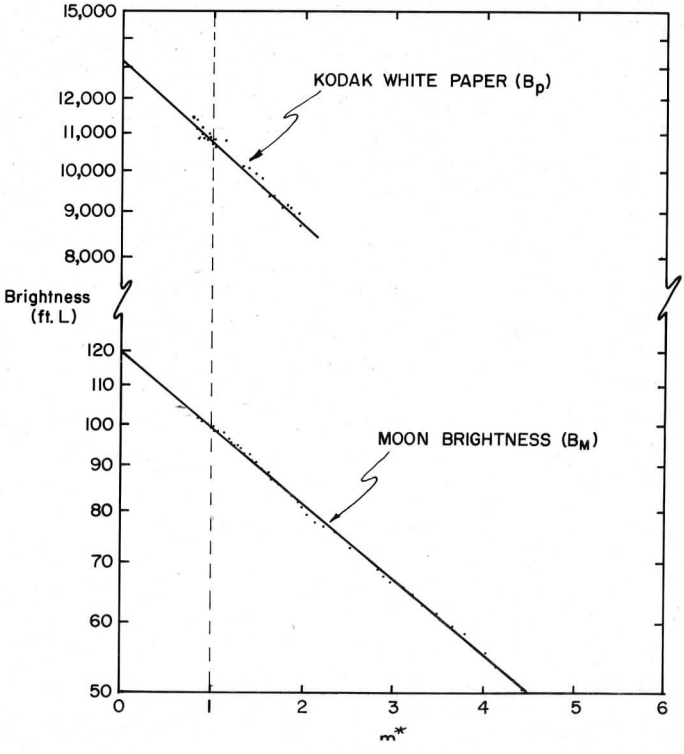
15,000
12,000
11,000
10,000
9,000
8,000
Brightness (ft. L)
120
110
100
90
80
70
60
50
KODAK WHITE PAPER (B_p)
MOON BRIGHTNESS (B_M)
0
1
2
3
4
5
6
m*

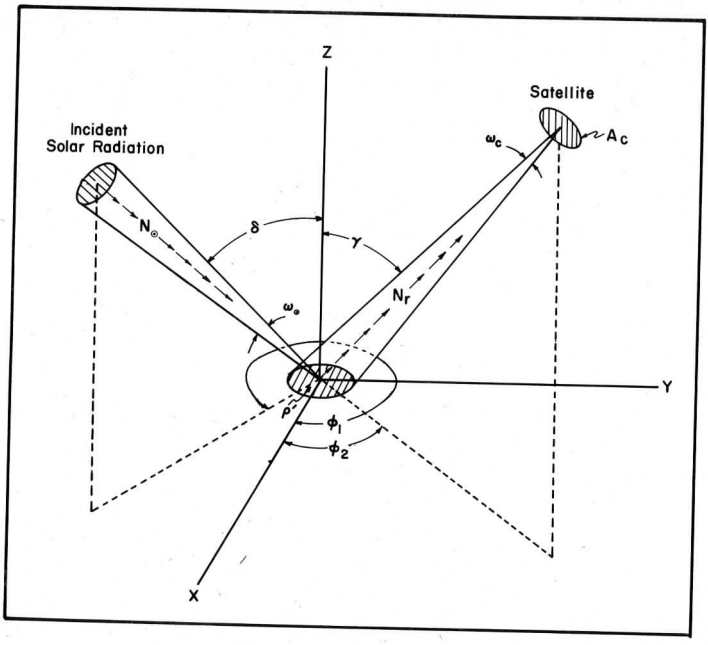
Z
Satellite
Incident
Solar Radiation
ω_c
A_c
$N_\odot$
δ
γ
N_r
$\omega_\odot$
Y
ρ
ϕ_1
ϕ_2
X

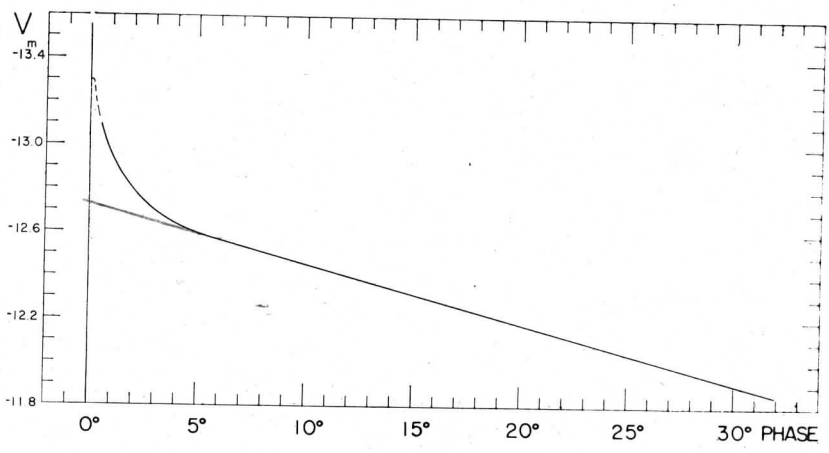
V_m
-13.4
-13.0
-12.6
-12.2
-11.8
0°
5°
10°
15°
20°
25°
30° PHASE

U.S. DEPARTMENT OF COMMERCE
ENVIRONMENTAL SCIENCE SERVICES ADMINISTRATION
NATIONAL ENVIRONMENTAL SATELLITE CENTER
WASHINGTON, D.C. 20233

January 16, 1969

IN REPLY REFER TO:

S112

Mr. Kirby J. Hanson
Executive Director
Space Science and Engineering Center
1225 West Dayton Street
Madison, Wisconsin 53706

Dear Mr. Hanson:

As I promised in our phone conversation this afternoon, I enclose an extra copy of our revised paper Processing and Display Experiments Using Digitized ATS1 Spin Scan Camera Data. We have made minor changes to delete from this revision the material not in paper No. 22. I enclose 2 prints of new figure 3a as per your suggestion of December 11, 1968. The figure legend and text have been modified to fit figure 3a and 3b.

In paper No. 11 there is a reference to NESC-44. The year of publication was 1968 and the reference is changed. An additional reference, Bristor (et al), 1966 has been added to the same paper. We also should change the figure legend references of figure 7 from figure 3.1 to figure 6 and on figure 8 from figures 3.1 and 3.2 to figures 6 and 7.

I hope this will help with the publication.

SSEC

JAN 20 1969

Very truly yours,

Merle B Whitney

Merle B. Whitney, Chief
Programming Branch
Data Processing and
Analysis Division

Attachments

Table of contents of Weather Motions from Space.
Papers 9, 10, 11 and 22
Suggestions in paper 22

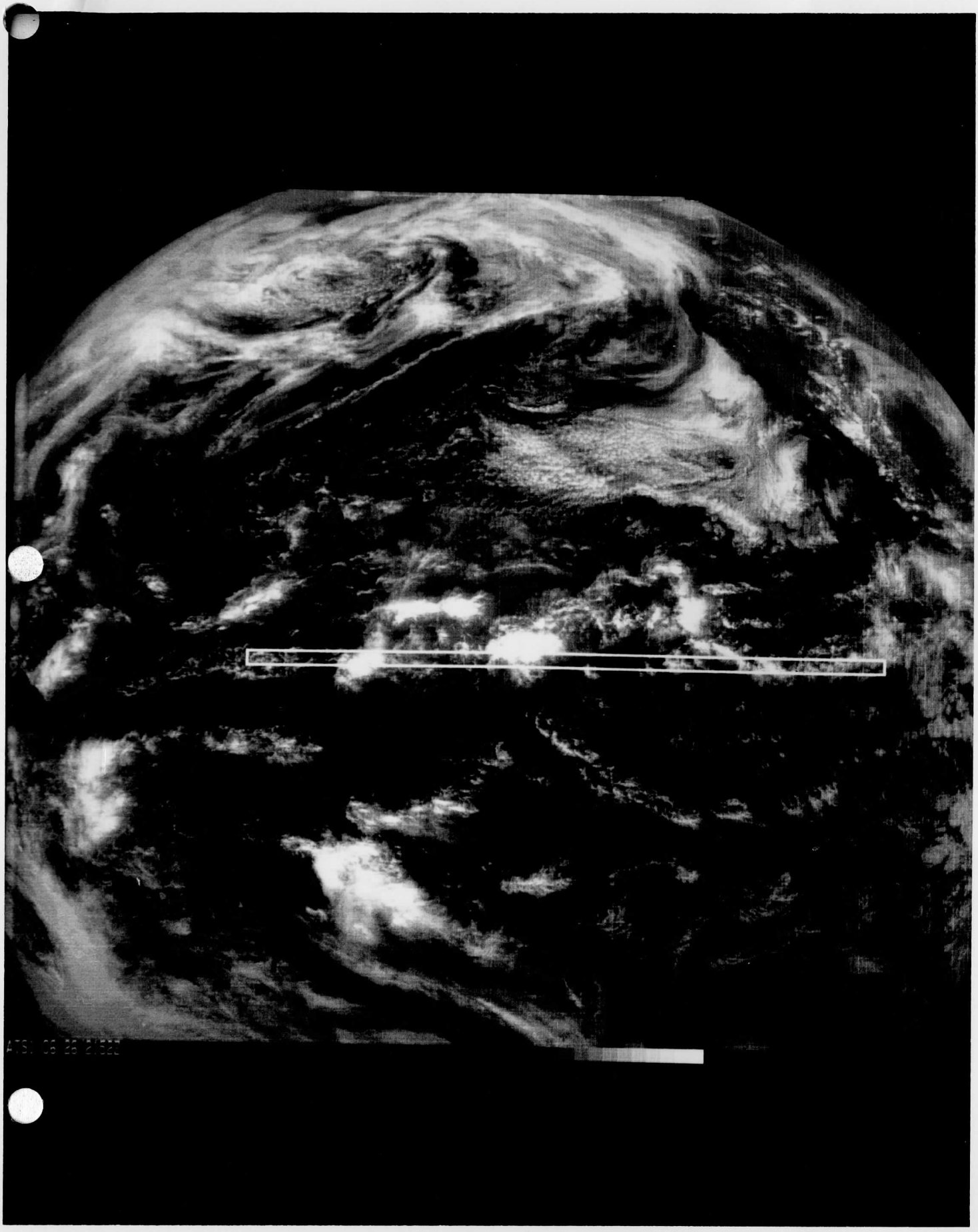

Figure 3 a (New)
3b is power spectrum

Processing and Display Experiments Using Digitized ATS1 Spin Scan Camera Data

Merle B. Whitney, Russell C. Doolittle, and Brent Goddard

National Environmental Satellite Center, ESSA

October 1967

Revision Oct 3 1968

edited for Paper #22

M B Whitney

15 Jan 69

FIGURE LEGENDS

Figure 1 Profiles of lines which pass through the ITC section depicted in Figures 7, 8, and 9. The upper two profiles (records 980 and 981) are adjacent lines through the lower middle of the section. The lower middle profile (record 890) passes through the middle bright mass, the bottom profile (record 790) through the bright mass at the top of the section.

Figure 2 Profiles of another portion from the same four records in Figure 1 which also pass through a very bright mass in the center of Figure 4.

Fig. 3. The data continued within the rectangle in 3a was used to obtain the power spectrum shown in 3b.

Figure 4 The full earth disk using every third data sample and every data line.

Figure 5 The EIS produced frame (From NASA).

Figure 6 A. Hawaiian Area with low enhance table. B. Photographically scaled map of Area.

Figure 7 ITC Area. A. Full range table. B. ESSA-5 Frame.

Figure 8 ITC Area. A. Low enhance table. B. Portion of EIS frame, for same area.

Figure 4.6 ITC Area. A. Mid enhance table. B. High enhance table.

Figure 4.7 Baja California Area. A. Low enhance table. B. Portion of EIS frame for same area.

Figure 4.8 Baja California Area. A. Horizon table. Insert Mid enhance table. B. ESSA-5 Frame.

1. Introduction

Inclusion of a digital recording system for the ATS1 Spin Scan Cloud Camera (SSCC), has provided source data for a variety of automatic data processing experiments. Of particular interest within the National Environmental Satellite Center (NESC) are those experiments which provide experience and insight toward an eventual operational geostationary environmental satellite. Specifically, there are questions concerning the quality and information content of the cloud picture data stream, and the problems involved in automatic earth location of the images. Practical problems also arise in displaying large raster, high dynamic range images.

In addressing these questions, a series of data handling and diagnostic programming activities are described in the first portion of this paper. Some indications and conclusions are given. Attitude and earth locator studies are next discussed, followed by a description of available display equipment with indications of future requirements.

Some additional technical detail related to tape formats, display devices, and computational procedures for attitude determination not included here are available as Appendices in ESSA Technical Report NESC-44.

2. Diagnostic Activities

Each SSCC digitized picture, with 8,192 8-bit data samples per line and over 2000 lines, is contained on an entire reel of magnetic computer tape. With the capability of producing almost three pictures per hour, the spin scan camera can provide an overwhelming volume of data. Since

the data volume is so large, a question could be raised as to the information content of the overlapped samples and the 0-255 (8-bits) brightness count range. A graphic display of the raw data values provides a qualitative answer to the question. Such profiles are shown in Figures ~~2.1~~ 1 and ~~2.2~~ 2. These were produced on the UAC Fax encoder. All the data samples are displayed in full dynamic range. Close inspection of portions of the profile reveal impressive sample to sample variability suggesting large contributions to the image information content from the non-redundant portions of the overlapped samples. Broad scale continuity ~~on~~ of the brightness masses is maintained from line to line. Large differences in the small scale features from contiguous lines indicate the absence of overlap between successive scan lines. The ability of the sensor to utilize the full 0 to 255 count range is also indicated by the profiles.

A data quality check was maintained with programs which extract line documentation content and raw data values for diagnosis. Other programs computed and displayed means, and frequency distributions of the data. Some of the problems uncovered were bad cable connection, analog-to-digital converter difficulties and noise.

The great variety of interesting brightness profiles displayed by the line graphics program invites study from a spectral standpoint using statistical tools. The data for a picture taken at 2152Z on June 26, 1967, ~~(Figure 4.1)~~ in lines 976 thru 1000 and points 1501 thru 5500, were subject to a spectral analysis to determine along-the-line signal characteristics. The spectrum peaks at a half wavelength of about 500 spots or about 350 miles and drops smoothly off to either side. This is some indication of the average breadth of cloud structures in the band measured but how well spectrum analysis can be used

to recognize cloud structures has not been investigated. Secondary peaks are frequent at lower wavelengths but are too small to interpret validly. That these occur, however, implies that there is at least enough information to warrant the present sampling rate and that there may be even more information. The absence of sharp peaks would indicate the absence of appreciable quantities of oscillatory degradation from the electronics. Figure 2.~~2~~ 36 shows the plot.

3. Earth Location of Picture Data

Geographic location of digitized image brightness from the spin scan cloud camera is required as an aid to the meteorological interpretation of the data.

Digital computer programs to produce latitude/longitude grids for satellite cloud pictures (Frankel and Bristor, 1962) and to rectify picture imagery to either Mercator or Polar Stereographic map projections (Bristor et al., 1966) are both in daily operational use at NESC. A major purpose of the present investigation was to ascertain the changes required to modify these programs, which were developed for conventional photographic perspective, for use with data from the spin scan camera.

Changes are required both in program logic and in input information. These are described fully in ESSA Technical Report NESC-44 and will be discussed only briefly below.

These changes were made in "off-line" versions of the operational programs and tested with spin scan camera data from the Applications Technology Satellites-ATS-1 and ATS-3. Figure 3.1 is a photographic copy of a facsimile display of a picture taken near local noon on January 18, 1968. (Horizontal lines in the implanted rectangular grid are spaced 100 scan lines apart. Vertical lines are spaced 100 samples apart in the reduced sample population used for the facsimile display or

TABLE 3.1

BASIC STEPS IN COMPUTATION OF COORDINATES FOR A POINT ON A GEOGRAPHIC (latitude-longitude) OVERLAY GRID

PROGRAM LOGIC	INPUT INFORMATION
1. Assign latitude and longitude of grid point.	
2. Compute orientation of perspective ray from earth to camera with respect to earth coordinate system.	Camera (satellite) location
3. Compute orientation of perspective ray with respect to camera coordinate system.	Camera attitude (orientation angles)
4. Compute position of grid point in an undistorted picture.	Camera constants
5. Compute position of grid point in picture to be gridded.	Image distortions.

TABLE 3.2

BASIC STEPS IN COMPUTATION OF MAP COORDINATES FOR AN IMAGE POINT (DATA SAMPLE)

PROGRAM LOGIC	INPUT INFORMATION
1. Assign image coordinates of point to be mapped.	
2. Compute distortion free image coordinates	Image distortions
3. Compute orientation of perspective ray with respect to camera coordinate system.	Camera constants
4. Compute orientation of perspective ray with respect to earth coordinate system.	Camera attitude (orientation angles)
5. Compute latitude and longitude of earth intersection of perspective ray from camera.	Camera (satellite) location
6. Compute map coordinates of point.	Map projection constants and scale.

every 300 samples in the full-resolution data.) Figure 3.2 shows the same picture with superimposed latitude and longitude lines, coast lines, and the horizon outlining the earth's disk. Figure 3.3 shows the Mercator mapped imagery for the portion of the picture between latitudes 50° north and 50° south and from longitudes 45° west to 145° west.

Basic steps in the computation of coordinates for a point on a geographic overlay grid are listed in Table 3.1, together with the necessary input information. Table 3.2 lists the basic steps in the computation of map coordinates for a data sample from its image coordinates (scan line number and sample number).

A comparison of Tables 3.1 and 3.2 shows that essentially the same items of input information are required for gridding and mapping. The map projection constants are independent of the data collection system and need not be considered further. In the operational system referred to above, camera location is computed by an "orbit generator" program obtained from the National Aeronautics and Space Administration. Inputs to this program are orbital elements for a given epoch (supplied by NASA) and the date/time of the data. No change is required here unless operational experience should show that an orbit generator designed for the large orbits of earth synchronous satellites is necessary for accuracy.

Because of the great height of the ATS satellite, accuracy in mapping spin scan camera data is critically dependent upon those items of input information used to compute, from scan and sample numbers, the corresponding pointing direction of the telescope with respect to a geocentric coordinate system fixed in the earth, (e.g., Z axis along north polar axis, X axis equatorial in Greenwich meridianal plane). The errors in computed latitude and longitude resulting from errors in pointing direction vary with the orientation of the ray and of the

pointing error. One example will illustrate order of magnitude: a tilting of the spin axis from horizontal by 0.01 degrees in the north-south plane through the satellite will cause displacements in earth position of about 3 nautical miles at the subsatellite point, and 12 nautical miles at the corners of a Mercator map area, covering 100 degrees of latitude and of longitude, centered at the subsatellite point. This order of accuracy is acceptable if it can be maintained operationally.

The relevant input items listed in Table 3.2 are:

a. "Camera constants" required to convert two-dimensional image position into coordinates in a three-dimensional camera coordinate system. For the spin scan camera these constants are the scan and sample numbers corresponding to the telescope position at the center of the picture, and the angular change in the orientation of the telescope between successive scans (0.0075 degrees), and between successive samples (0.00244 degrees). It may be noted that the change in pointing direction between successive scan lines or samples is less than 0.01 degrees.

b. "Camera attitude" angles which define the orientation of the camera coordinate system with respect to the geocentric system. These angles specify the rotations required for converting camera coordinates corresponding to the telescope pointing direction, into components parallel to the earth coordinate axes. The orientation of the satellite vehicle (and therefore also of the camera) is continually changing so that operational mapping of spin scan camera data is not possible without practical and accurate procedures for measuring attitude. Two methods which make use of the spin-scan picture data have been tested

experimentally. One method is described in ESSA Technical Report NESC-44 and is based on the amount of shift of the earth disk from top to bottom of the image field in pictures taken at different points in the orbit. This procedure requires the detection of image horizons in a sequence of pictures to obtain one determination of the spin axis orientation. Attitude was computed for two orbits with accuracy in one case approaching 0.01 degrees.

The other method uses standard photogrammetric techniques with landmarks as control points, and permits complete determination of camera orientation from a single picture. It's accuracy is dependent upon the number of recognizable coast line points in the picture, their distribution in the image field, and the precision with which their scan and sample numbers are determined. Experiments are now underway to see whether landmark coordinates can be found by computer search of the picture data. If suitable pattern recognition techniques can be developed for the identification of coastlines it will eliminate the time consuming process of landmark identification and manual coordinate reading from special picture displays containing coordinate scales.

As of this writing operational mapping of the spin scan data with either or both of these procedures would presuppose that changes in attitude are sufficiently regular over periods of several days to permit use of predicted values extrapolated from previous determinations. It may well be that the eventual practical solution for operational mapping will be found in celestial attitude determination using stars.

c. "Image distortion" tables to correct for observed error in camera coordinates computed from scan and sample numbers. These corrections are required in mapping vidicon camera data to remove optical and systematic electronic distortions present in the image field even when all equipment is operating perfectly. Other errors which may be present in some pictures due to equipment malfunction are not predictable and are ignored. For the spin scan camera systematic variations in the angular change from sample-to-sample or from scan-to-scan could be corrected if known. However, the sample-to-sample change, which is equal to the ratio of angular velocity about the spin axis to the digitizing sample rate, is closely controlled by the electronics and the scan-to-scan change is controlled by the precision of the stepping mechanism. Neither is believed to cause any significant distortion. Unpredictable larger errors which may occur due to doubled or omitted rachets in the spin scan stepping mechanism, or to incorrect synchronization of the data from line-to-line may be classed as camera malfunctions and would be ignored in operational mapping of the data.

4. Display

The large dynamic range of the sensor allowed ample opportunity to experiment with data-to-display conversion techniques. At NESC we have two display devices, which can use digital tapes as their input source.

The United aircraft Facsimile Encoder is an electronic converter which reads information from a digital magnetic tape and changes the information to electrical signals. These signals are fed to a standard

weather facsimile recorder which displays in sepia on a specially moistened paper roll. This machine may be operated to produce displays either in the black and white mode or with an eight shade gray scale.

The Link Division Weather Satellite Digital and Analogue Display (LINK) is a cathode ray tube device which produces 35 mm film and/or Polaroid prints. The input data may be either analogue or digital signals. Automatic switching between the two modes may be carried out under program control, to produce an analogue picture with a superimposed digital grid by double exposure. Another display option is available for drawing of solid or dashed lines or for outputting of typed characters.

~~These two devices are normally operated offline from the computer.~~

Details of the programs which control these devices are contained in ESSA Technical Report NESC-44. The conversion tables used by the programs to produce the images in the following section are given in Table 4.1. There was no attempt to calibrate, to apply solar illumination corrections, or account for the possible different gain settings on the satellite or ground station.

The samples of the digital data in the following set of figures are made from the picture taken on June 26 at 2152Z. All pictures were developed without the aid of a greyscale wedge on the film. The vertical dark lines are caused by display equipment problems and are not contained within the source data.

A display using the full range table is shown in Figure 4.1. The bright tropical clouds have been clipped at the high end at the ground station. A print made from the second generation negative of the

TABLE 4.1

ATS1/LINK BRIGHTNESS TABLES

LINK	FULL RANGE	a LOW-ENHANCE	c MID-ENHANCE	b HIGH-ENHANCE	c HORIZON
14	235 - 255	171 - 255	159 - 255	244 - 255	235 - 255 6 - 7
13	215 - 234	101 - 170	149 - 158	235 - 243	215 - 234
12	196 - 214	51 - 100	140 - 148	226 - 234	196 - 214
11	179 - 195	43 - 50	132 - 139	221 - 227	179 - 195
10	163 - 178	38 - 42	125 - 131	215 - 220	163 - 178
9	118 - 162	33 - 37	118 - 124	210 - 214	118 - 162
8	133 - 147	28 - 32	112 - 117	205 - 209	133 - 147
7	118 - 132	25 - 27	106 - 111	200 - 204	118 - 132
6	102 - 117	22 - 24	99 - 105	195 - 199	102 - 117
5	85 - 101	19 - 21	92 - 98	190 - 194	85 - 101
4	78 - 84	16 - 18	84 - 91	184 - 189	78 - 84
3	60 - 77	13 - 15	75 - 83	178 - 183	60 - 77
2	41 - 59	10 - 12	66 - 74	171 - 177	7 - 59
1	21 - 40	7 - 9	56 - 65	161 - 170	21 - 40
0	0 - 20	0 - 6	0 - 55	0 - 160	0 - 5

Electronic Image System (EIS) cathode ray tube display was enlarged photographically to the same size as Figure 4 and is shown in Figure 5.

The Hawaiian Islands area was chosen to test an enlarging program using a 2x2 sample matrix. This area is located just a little left of center in Figure 4. The very low range table was used in an attempt to enhance the geographical features. The results is shown in Figure 6, along with a Hawaiian map section enlarged to the same scale. The islands appear to be mostly cloud covered except for the peaks on the Island of Hawaii. Any attempt to increase the size of the sample matrix, i.e., 3x3, 4x4, would greatly increase the graininess and probably destroy eye appeal.

A cloud area on the Intertropical Convergence (ITC) just to the right of center in Figure 4 is depicted in Figures 7, 8, and 9. The full range table was used in Figure 7a. It demonstrates the difficulty in applying a linear table as the less bright clouds are either missing or barely discernible. This difficulty will be compounded when calibrations, different gain settings, and sun angles, are included in the computations. The ESSA-5 frame taken 1½ hour earlier is shown in Figure 7b. To try to bring out as much detail as possible and still retain some eye appeal, the low-enhance table was used to produce Figure 8a. The same section from the EIS photo, again increased to the same scale, is shown in Figure 8b. Of interest is the thin cloud line in the lower right center which can be faintly seen on the ESSA-5 frame. The mid-enhance table was used to produce Figure 9b. The protrusions of the central bright areas are more clearly defined. The three finger-like cloud structures are also clearly shown although the separation is better in the full range

depiction. In Figure 9a, the disappearance of the left-most finger and the distinct separate bright areas of the central cloud mass are features brought out when the high-enhance table is applied to the data.

Baja California, at approximately 6° azimuth, is a prominent landmark in the SSCC pictures. Views of it, the Gulf of Mexico, and the horizon are shown in Figures 10a and 10b. The low-enhance table was used in Figure 10a to bring out terrain features. The channel between Tiburon Island and the mainland is discernible. The EIS section, again to scale, is shown in Figure 10b. To help with attitude detection, the display of the horizon was thought to be useful. Figure 11a was produced using the horizon table. The view of the same area from ESSA-5, 27 minutes earlier, is shown in Figure 11b. The insert is the portion over the Gulf of Mexico which was digitally enhanced using the mid-enhance table and then further enhanced photographically.

4. Summary

The ATS1 spin scan cloud camera experiments provides a basis for eventual operational use with a group of geostationary satellites. New problems have been met in the areas of data quality, information content, earth location of data, and display.

High volume of data, new sensors, and new techniques have necessitated a variety of diagnostic programs. Tests to date show significant sample to sample and line to line variations. With the available data stream there is a wealth of non redundant data available.

Accuracy requirements for earth location of spin scan camera data require the spin axis orientation to be determined to within 0.01 degrees. This accuracy has been approached by two procedures, one using the

position of horizons, the other landmarks. Satisfactory mapping of the data on an operational basis is possible provided the attitude remains sufficiently stable to predict several days in advance. For a non-stable attitude, operational use of the data would require a fully automated detection of landmarks by computer search or application of a different attitude determination system, based on other data such as star observations.

Visual display of ATS1 data has been accomplished within the limits of available equipment. The data volumes and dynamic range point to the need for higher speed displays of about 8000 by 8000 elements which also should allow adequate use of high dynamic range available.

Acknowledgements

We wish to thank Mr. C. L. Bristor of the Data Processing & Analysis Division of NESC for helpful comments and suggestions. We wish also to thank Dr. S. Fritz of the Meteorological Satellite Laboratory (MSL) for important discussions in connection with scale of cloud systems, and Mr. L. F. Hubert, MSL, for discussions on the geometry of the spin scan cloud camera.

Our thanks also to Messrs. R. E. Bradford and A. Booth for work on spectral analysis, to Mr. Marcus Shellman for his programs which merge grid information with picture brightness for input to the digitally driven display devices, and to Mr. William Callicott who wrote the mapping routines.

References

Bristor, C. L., 1966, Satellite Data Collection, Proceedings of the IBM Scientific Computing Symposium on Environmental Sciences, Thomas J. Watson Research Center, Yorktown Heights, New York, pp 5-17.

Bristor, C. L. and W. M. Callicott and R. E. Bradford, 1966. Operational Processing of Satellite Cloud Pictures by Computer, Monthly Weather Review, Volume 94, Number 8, pp 515-527.

Doolittle, Russell C., 1963, Calibration of Image Distortion in TIROS Wide Angle Photography, U. S. Weather Bureau, Meteorological Satellite Laboratory, Report Number 15.

Frankel, M. H. and C. L. Bristor, 1962, Perspective Locator Grids for TIROS Pictures, U. S. Weather Bureau, Meteorological Satellite Laboratory, Report Number 11.

Fig. 3. The data contained within the rectangle in 3a was used to obtain the power spectrum shown in 3b.

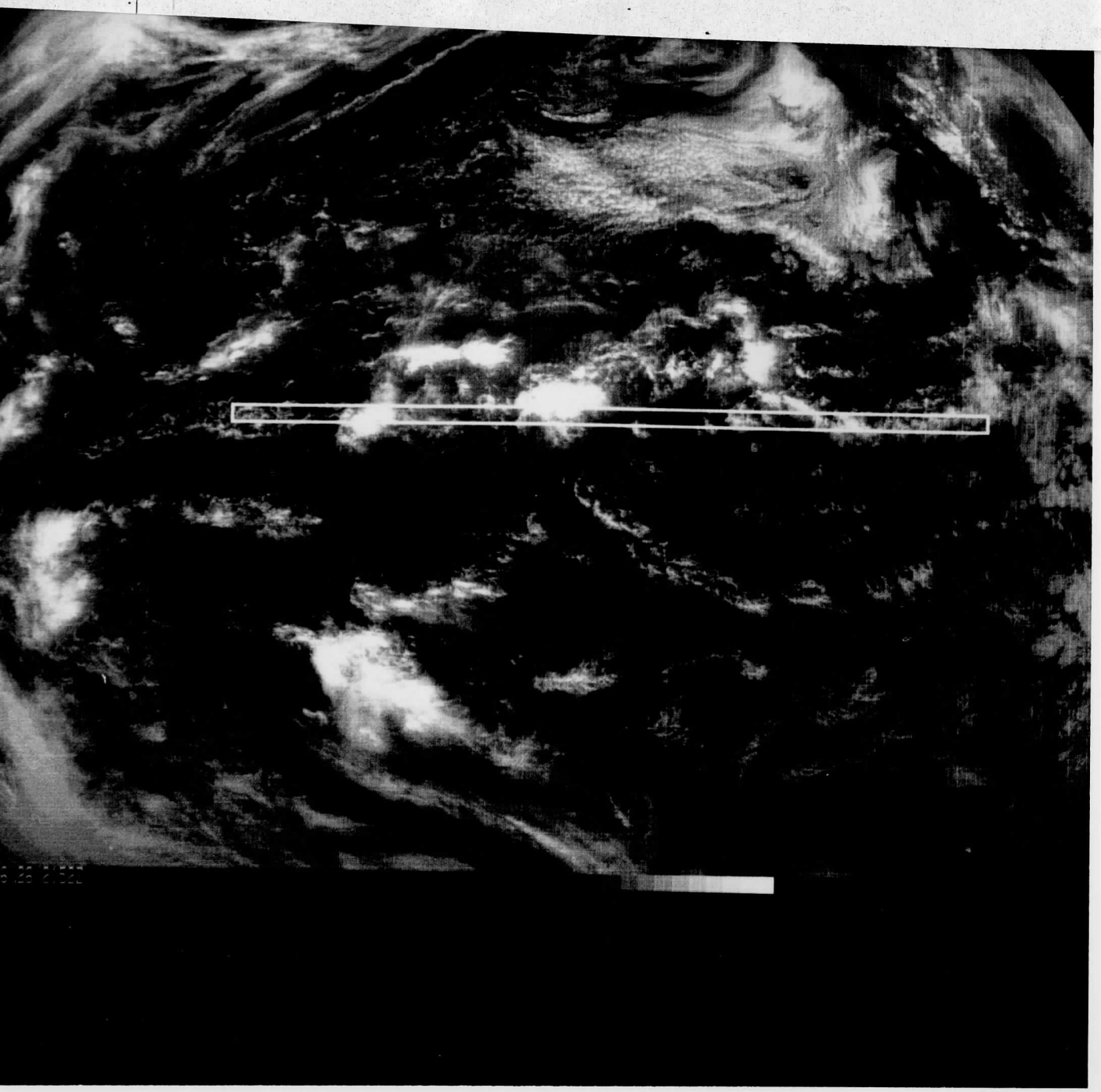

Figure 3a (new)
3b is power spectrum

Suggest to M. Whitney on Paper No. 22

(1) In Figure 3, it would be helpful to show in Figure 3a the ATS-I picture for June 26 (2152Z) with the area marked off for which the statistical analysis was done. Then put the line drawing in as Figure 3b.

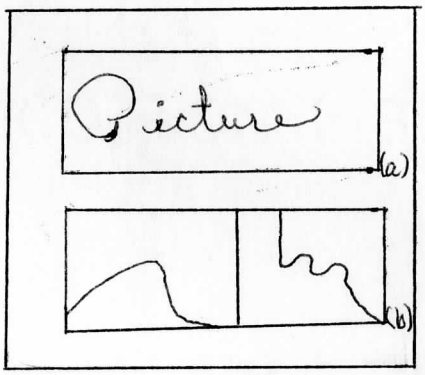

Figure 3

(2) Correct the references in text and Reference page.

complete set of
illustrations for:

Paper (22)

by Whitney
Doolittle
Goddard.

Nov. 27 '68

Fig 1

Fig. 2

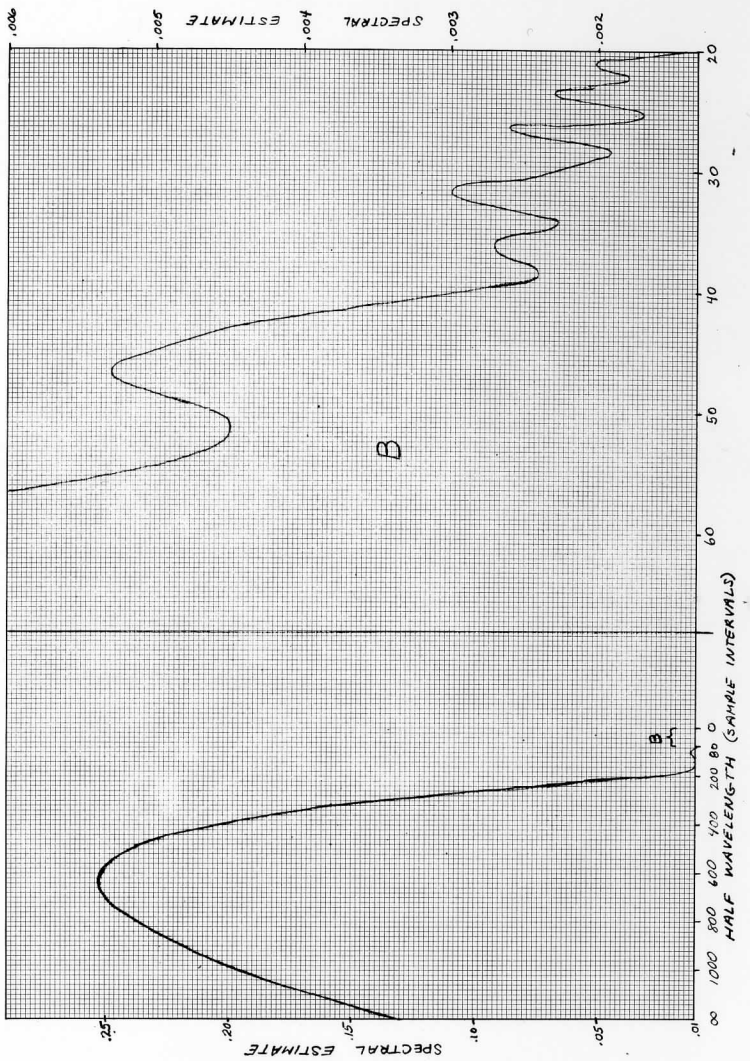
SPECTRAL ESTIMATE
.25
.20
.15
.10
.05
.01
.006
.005
.004
.003
.002
B
B-L
0
80
200
400
600
800
1000
20
30
40
50
60
HALF WAVELENGTH (SAMPLE INTERVALS)

Fig 3

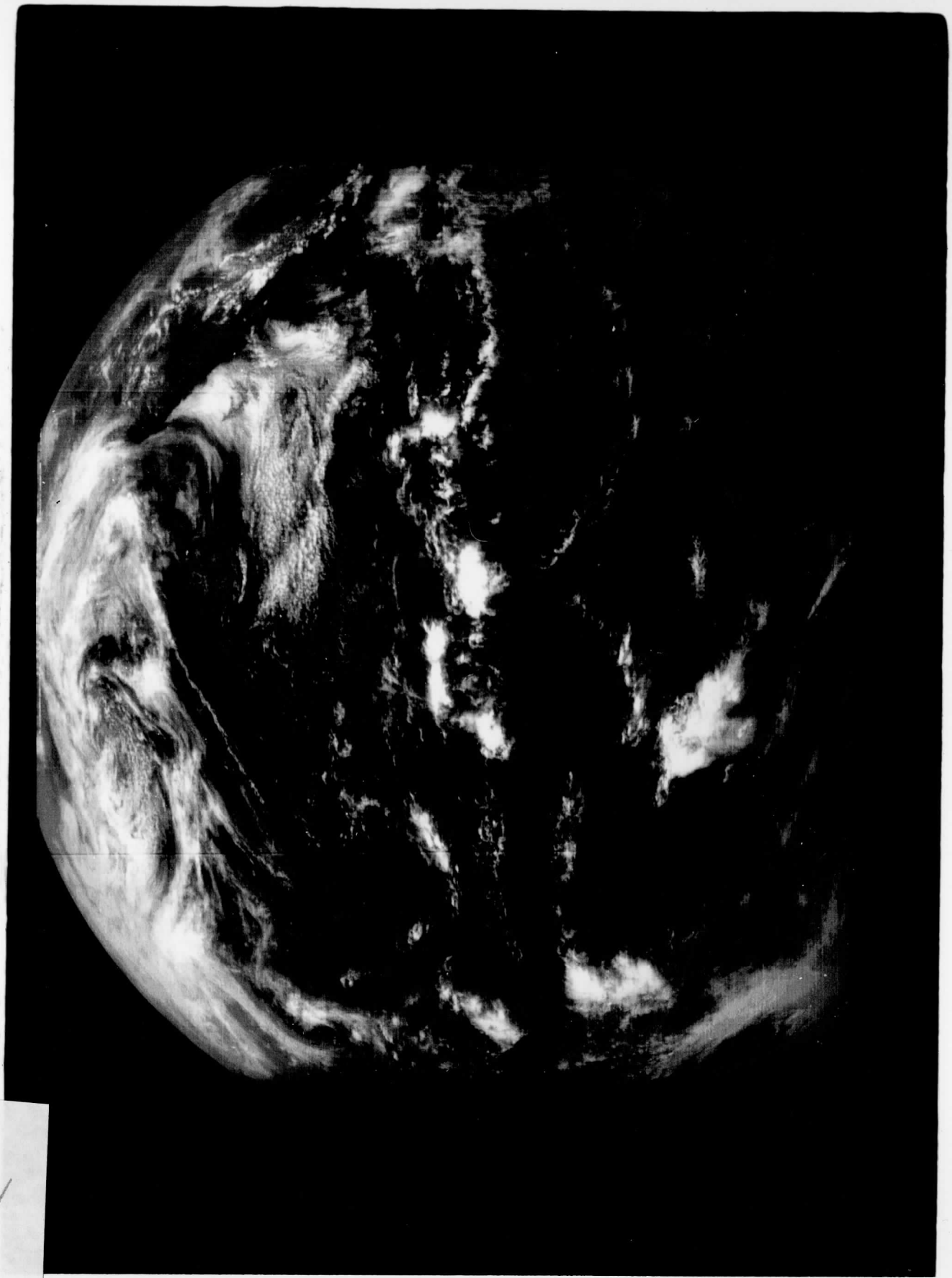

Fig 4

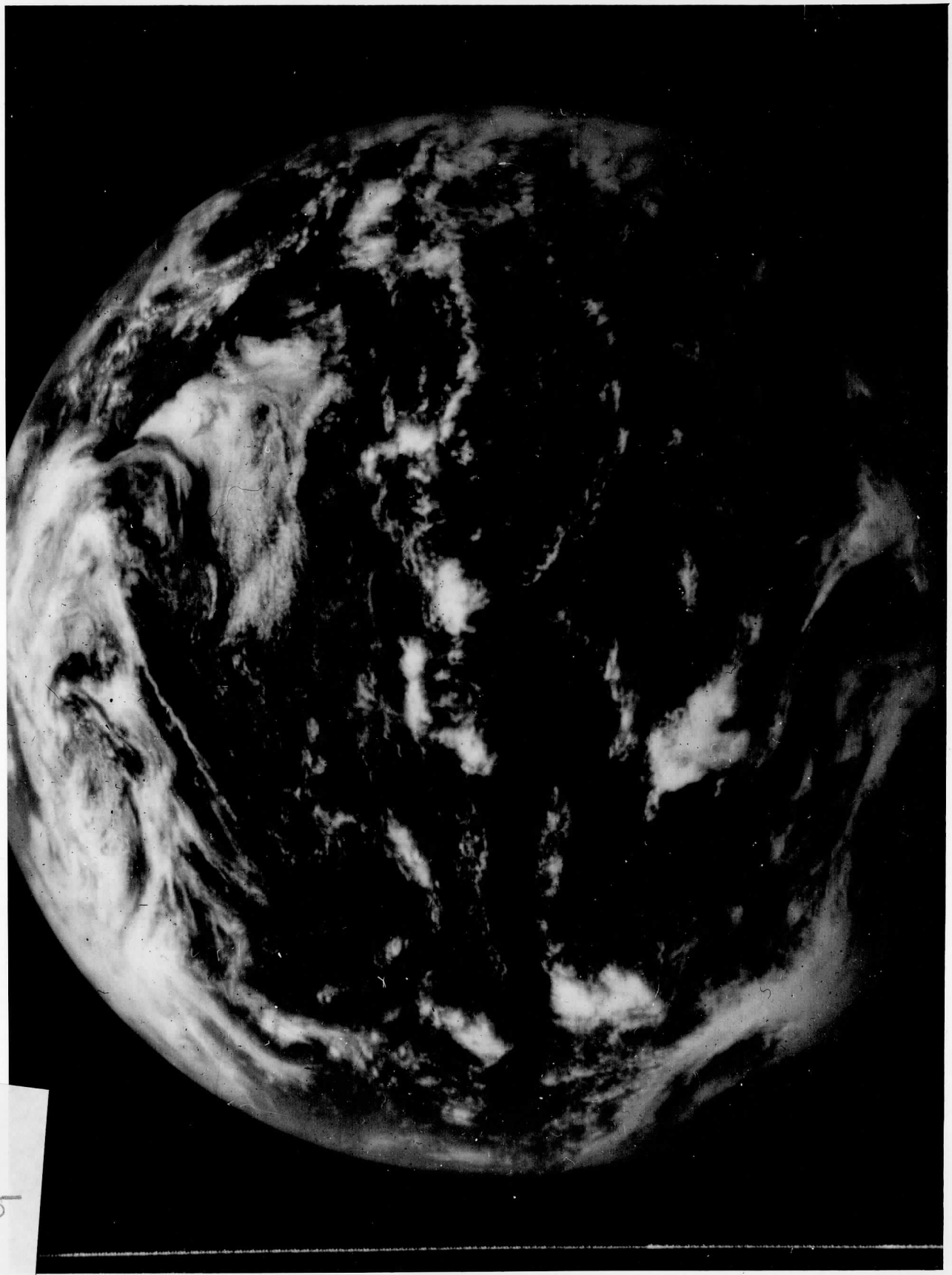

Fig 5

Fig 6a

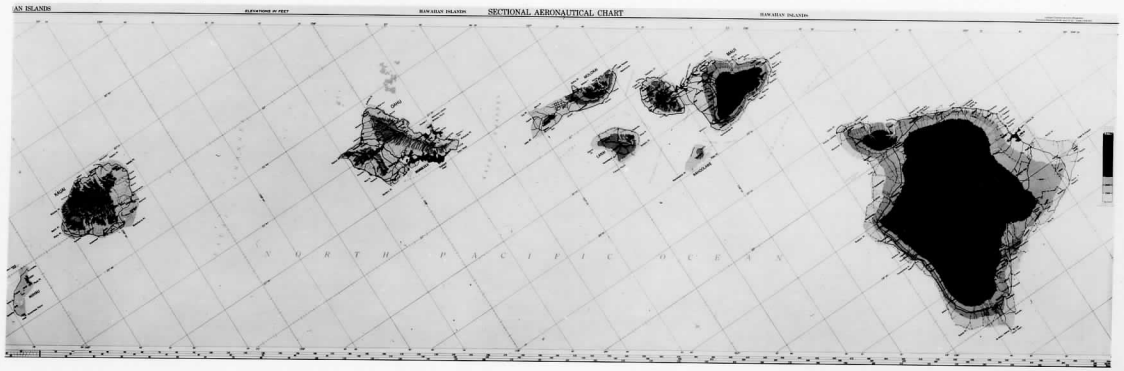
AN ISLANDS
ELEVATIONS IN FEET
HAWAIIAN ISLANDS
SECTIONAL AERONAUTICAL CHART
HAWAIIAN ISLANDS
NORTH PACIFIC OCEAN

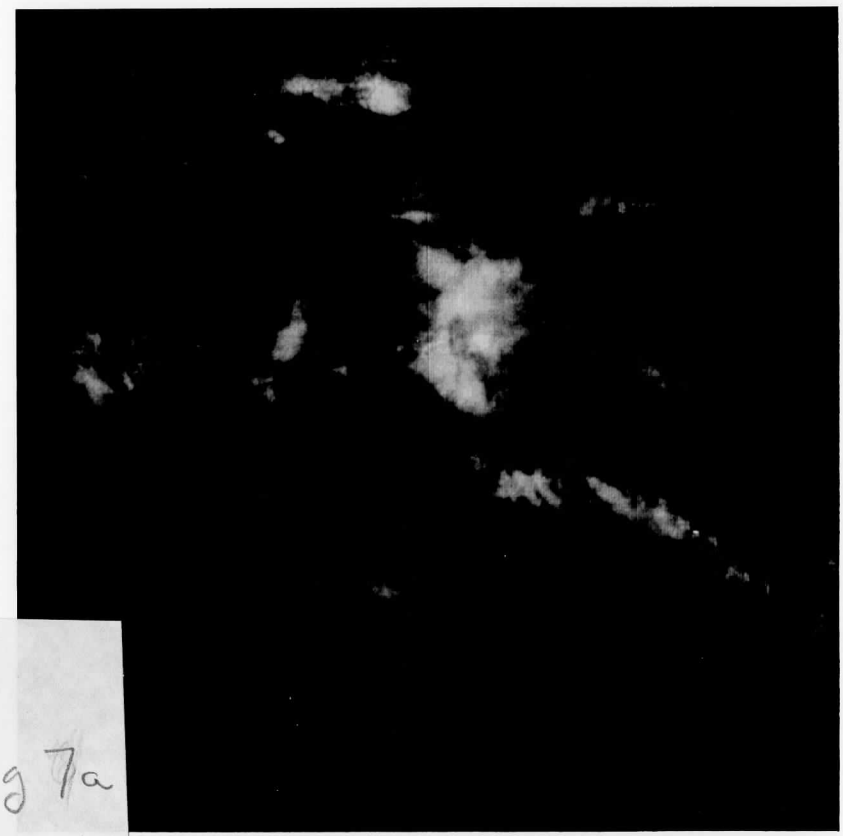

Fig 7a

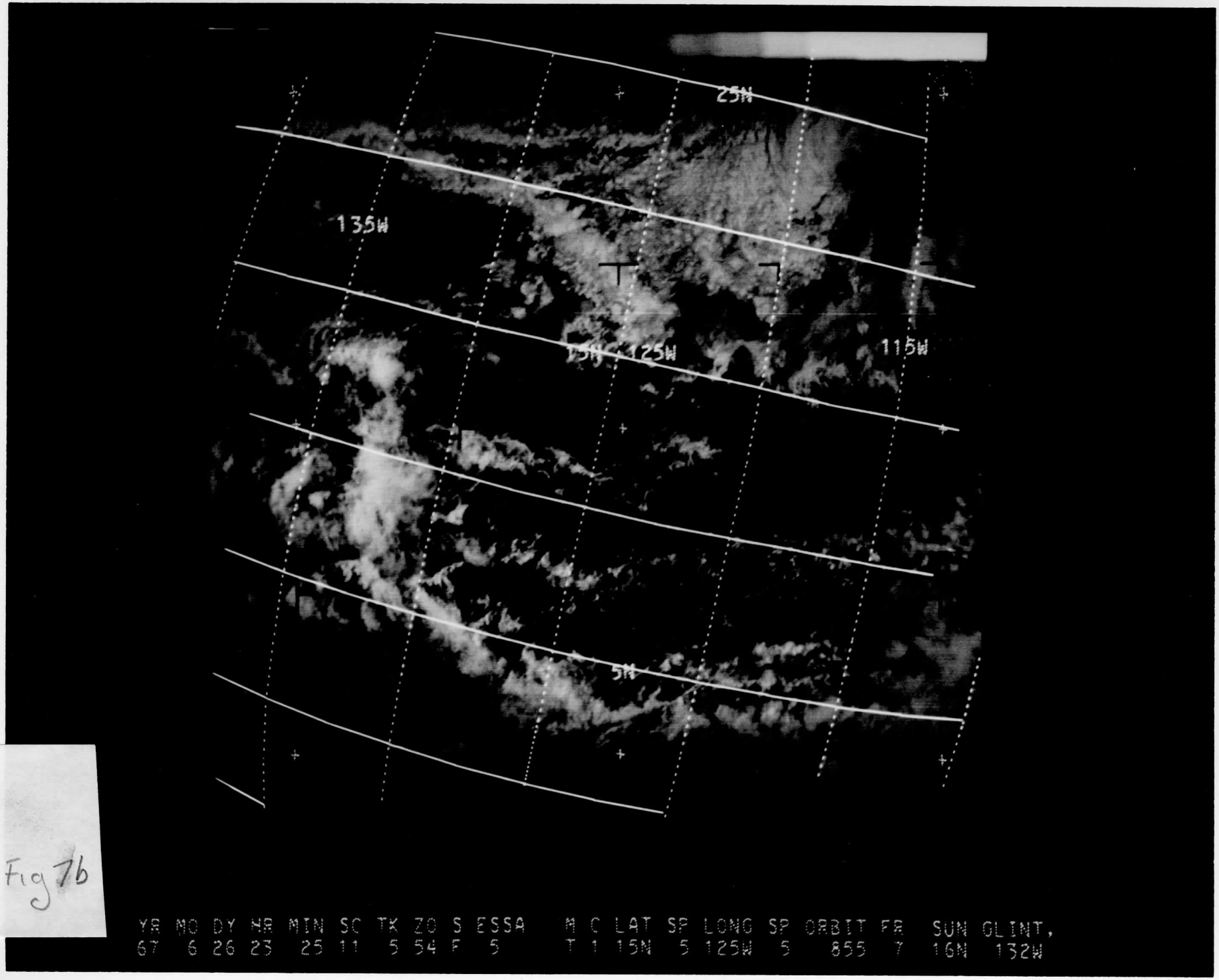
25N
135W
15N
125W
115W
5N
YR MO DY HR MIN SC TK ZO S ESSA M C LAT SP LONG SP ORBIT FR SUN GLINT,
67 6 26 23 25 11 5 54 F 5 T 1 15N 5 125W 5 855 7 16N 132W

Fig 7b

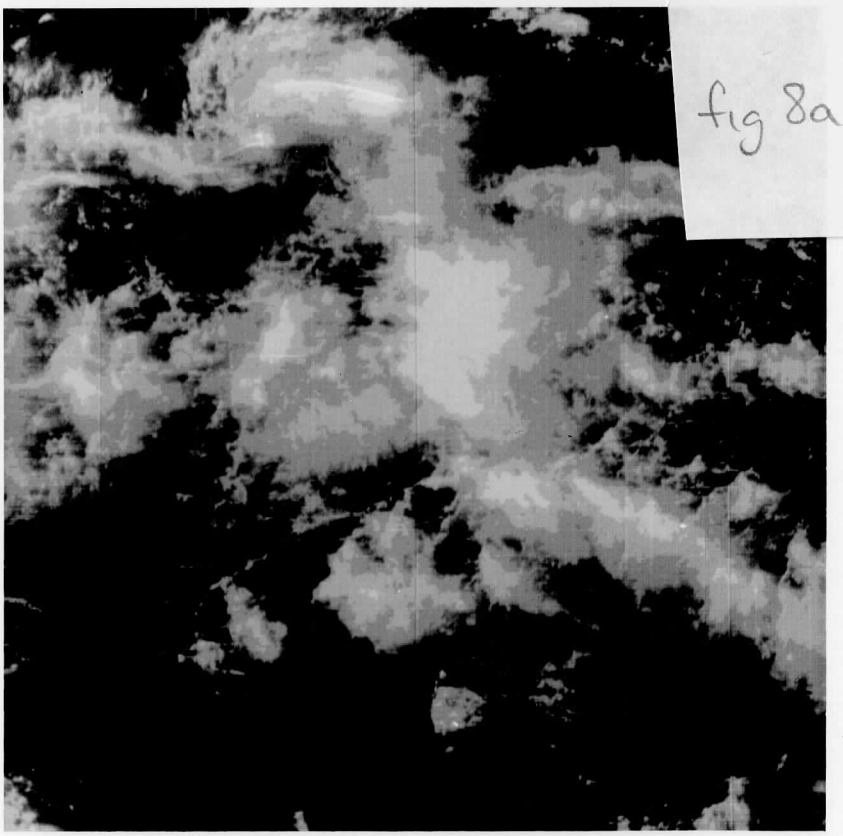

fig 8a

Fig 8b

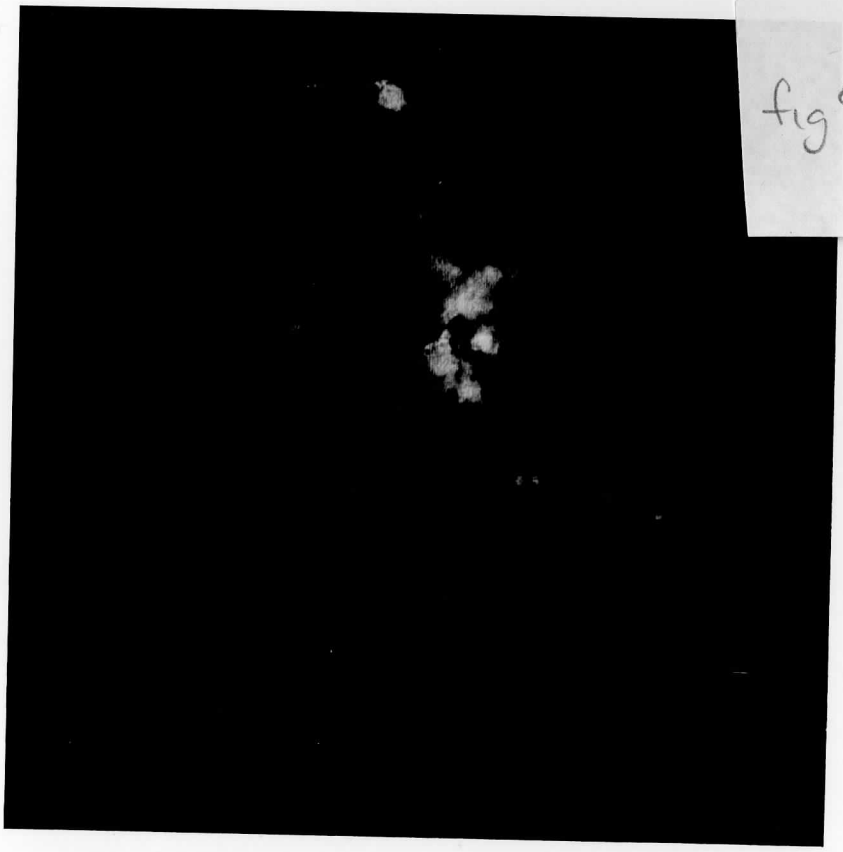

fig 9a

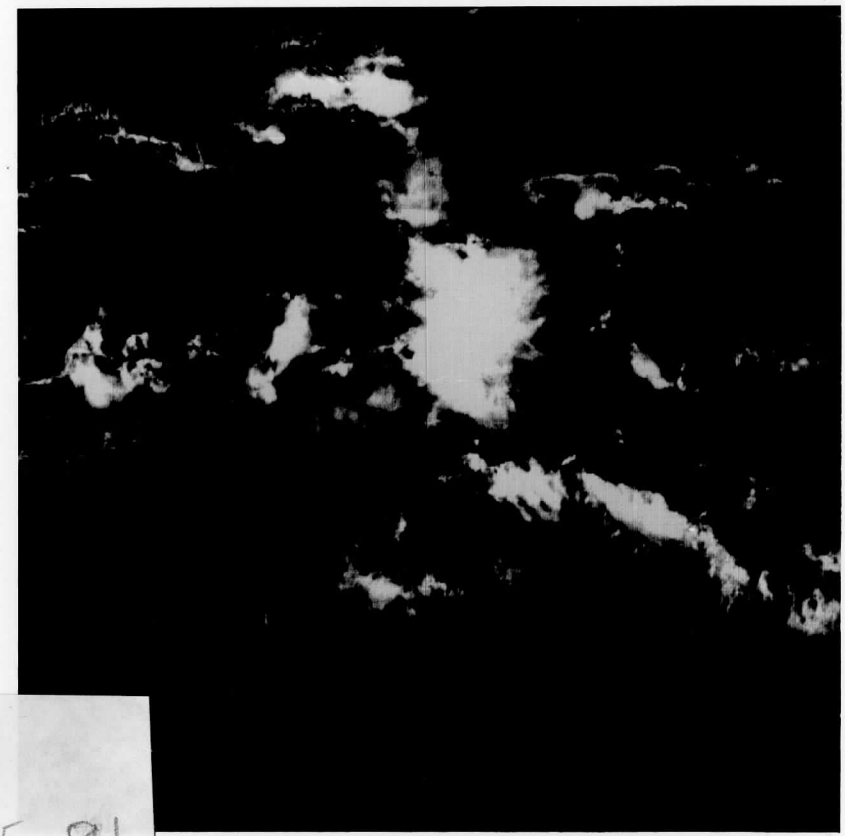

Fig 9b

Fig 10a

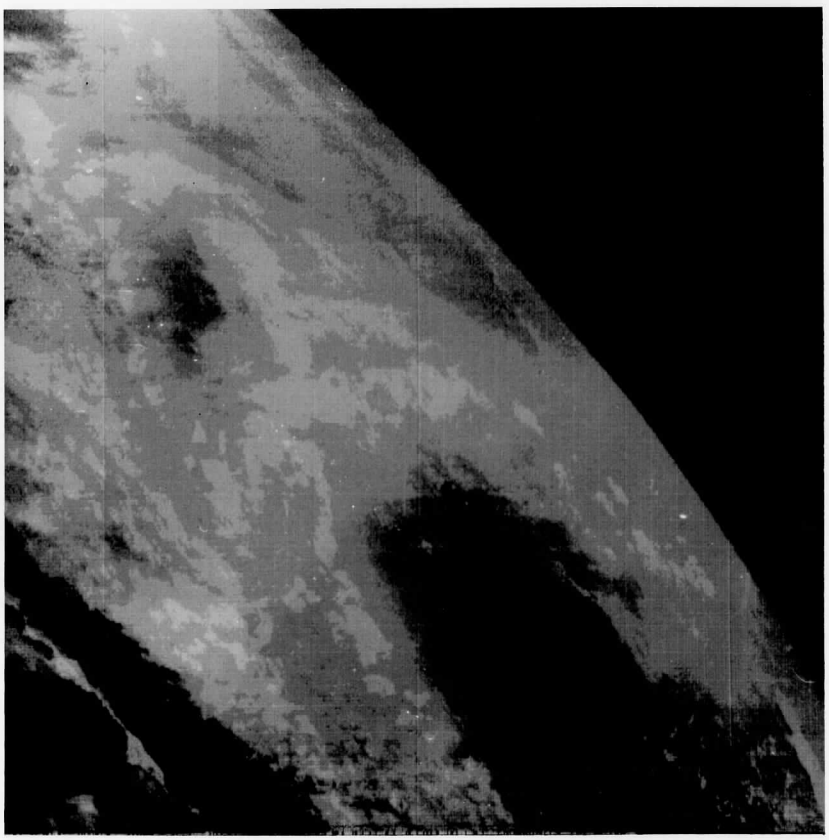

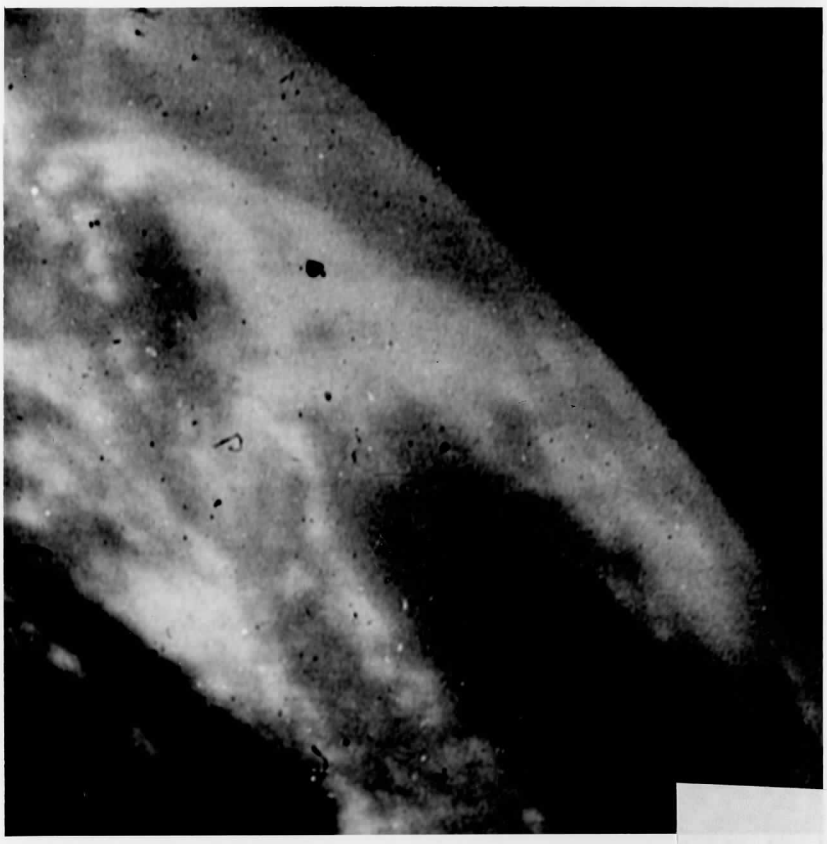

fig 10b

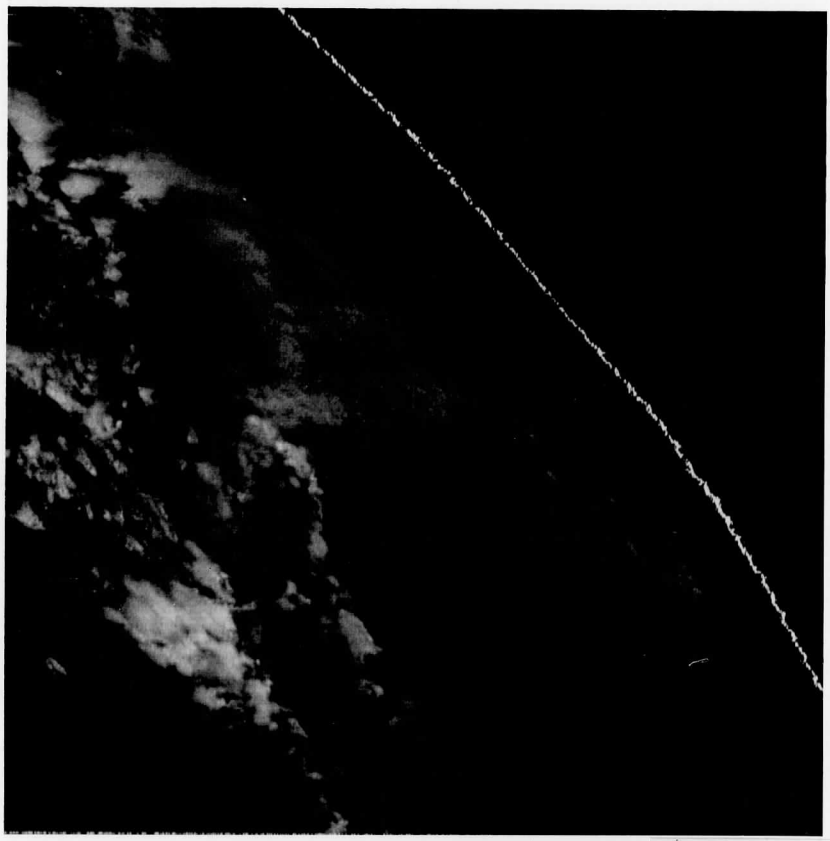

fig. 11

FORM CD-121 (9-22-59)
(PRES BY A.O. 206-10)

UNITED STATES GOVERNMENT

Memorandum

U.S. DEPARTMENT OF COMMERCE
WEATHER BUREAU

AUG 14 1967

TO : Professor Suomi

DATE: August 9, 1967

In reply refer to:

FROM : Kirby Hanson

SUBJECT: ATS-1 Book

Mr. Lee Ruiz of Allied Research called to say that NASA had made a decision that Mr. John Lindstrom would be author of the paper (No. 23) "Data Cataloging".

Kirby

MAR 29 1968

PROCESSING, ARCHIVAL AND DOCUMENTATION OF THE ATS-I SPIN SCAN CLOUD CAMERA PHOTOGRAPHIC DATA

By: John Lindstrom
NASA/Goddard Space
Flight Center

In October 1966, the then existing Nimbus Data Utilization Center was given the additional responsibility of processing, cataloging and archiving the photographic sensory data from the Applications Technology Satellite meteorological experiments. Thus, less than two months before the launch of a totally new sensory system, which would produce a unique class of meteorological data, development of a capability for handling the SSCC experiment data within the framework of a combined, integrated Nimbus/ATS Data Utilization Center was initiated. This effort was added to the contractual responsibility of the Goddard staff of the Geophysics Division, Allied Research Associates, Inc., which, under NASA management, plans for and carries out the operational functions of this combined data utilization effort.

Based on experience gained in the successful processing of Nimbus photographic meteorological data, an original ATS-I data utilization plan was devised which called for a final production, distribution and archival of gridded, individual 8x10 Spin Scan Cloud Camera pictures. User acquisition of desired data from the National Weather Records Center, Asheville, N. C., was to be based on catalog information incorporating a modified version of the Nimbus II Sensory Information Processing (SIP) program which provided for extraction, classification and coding of observed meteorological phenomena by geographical zones within the picture. With such information available, the user would have a basis for ordering specifically desired pictures.

After receipt of the first actual experiment data it was obvious that grid lines permanently induced on the pictures would obliterate much of the recorded messoscale phenomena. It was also determined that the cost of individual 8x10 transparencies to a potential researcher would be almost prohibitive when considering the volume of consecutive data the experiment was capable of producing. These factors required a post-launch change in the data handling system, the results of which will be described.

For ease of presentation the existing photographic data processing system, its problems and results will be described by functional sections.

Data Reception: The location of the experiment ground recording systems at both Rosman and Mojave sites presented problems in both duplication and delayed receipt of data. All processed negatives with an accompanying form containing the recording parameters are enveloped and mailed daily to the GSFC. In the beginning this created a five to seven day delay in any data processing since data from both sites had to be merged to assure full coverage and to avoid duplication. Now, with data being recorded at Mojave only, an average 4 day delay between recording and receipt of the original ATS-I negatives is being experienced. Negatives received in the initial phases were often scratched and dirty as a result of improper handling, and reflected a visible variation in both earth image size and film density from picture to picture and day-to-day. Ground station

recording and film handling techniques improved markedly with experience. The daily volume of recorded data has ranged from zero data to 49 pictures. Data volume has now stabilized at a normal 7-9 pictures per day with a minimum routine experimenter requirement of one at mid-morning, five centered about local noon and one at mid-afternoon. This can and does vary to meet specific experimenter requirements.

Initial Data Processing: On receipt of the original negatives the sequential order of the recorded data, and individual picture start times, are established and verified from the negative transmittal forms completed at the recording site. The annotated negatives are then evaluated to insure they contain usable data. Even though a usable picture was not created because of ground processing problems when the experiment was transmitting data, it is possible that a tape containing usable data is available for the missing picture. Thus, when pictures are annotated to indicate the universal date, start time and sequence number, missing sequence numbers in the archival files indicate a picture was scanned but usable photographic data were not processed. Initially, because of the lack of a tape playback capability, such a simple thing as a box of bad film at the recording site resulted in data loss. Also, during the period when sunlight was reflected into the telescope and over-riding the sun synch detector, there was data loss. However, even in cases where part of the earth image is totally misshapen because of recording problems the remaining portion

of the presentation can contain usable data and the picture is included in the archival files. During 1967, of 3690 possible pictures recorded, 3442 contained sufficiently usable data to be processed through to archival.

Photographic Processing: A data utilization center photographic facility has been established for ATS/Nimbus flight operations support. Here each annotated negative is subjected to demsitrometric measurement to insure that the ground photographic system is operating within established tolerance. Deviations from established limits are reported to the ground system engineers to guide necessary equipment adjustments.

An initial production of enlarged prints is made from the archival negative for distribution to the experimenter and to approved prime interest research groups. These are nominally 8x10 glossy prints on which every effort is made to hold the enlarged earth diameter on the image to a scale of 7.87 inches.

Duplicate film transparencies are also produced for distribution to the approved prime data users. Initially, these duplicates were created by contact printing four original 4"x5" negatives to a sheet of 8"x10" film. Since any deviation in the pressure plate on the printer could cause an occasional duplicate to be out of focus, this process was changed to a small vacuum frame utilizing a high intensity point light source. While this assured the highest possible resolution in transferring data to the duplicate film, it became obvious that an

essentially dust free environment is required for this system of film duplication. Even though high resolution transfer is maintained, the most minute pollutants in the air between the light source and the vacuum frame are induced on the film. With the installation of a new optical step and repeat printer and a strip-film print processor for formatting and production of archival film files, all initial duplicate film production is now being accomplished on five inch roll film stock. While a minimal loss of resolution may occur in this type of processing, a clean negative with an apparently expanded dynamic range is created.

During the period January 1 to December 31, 1967, the photographic facility produced the following volume of photographic film products from recorded ATS-I SSCC data in support of the experimenters, approved prime researchers, spacecraft and ground system engineers and the Public Information Office. Densitometric and sensitometric controls were maintained during all phases of this photographic processing.

4x5 film	22,385 sheets
8x10 film	386 sheets
4x5 prints	1,356 sheets
8x10 prints	53,773 sheets
5" roll film	10,615 feet

All film products created are returned to the GSFC data utilization area for further quality control checks and distribution.

Data Extraction, Gridding and Cataloging: From each universal day's set of 8x10 prints, a daily data listing is created. An experienced meteorologist, from an analysis of each picture, completes a computer input form which will, for each picture, list sequence number, start time, picture quality (the "no usable data" code here indicates a sequence number missing from the archival film file), and appropriate remarks. In addition, for one to three pictures a day, the data listing will contain, by defined geographical zones, coded descriptors indicating the visible geomorphological and meteorological phenomena as analyzed by the meteorologist. During this process, grids are matched to the pictures to insure that the grid appropriate to the day's satellite subpoint can be accurately fitted. Inability to fit an appropriate grid to a picture will be noted in the daily data listing.

When it was determined that the lines of a permanently induced grid would obliterate too much visible data, a system of overlay grids was devised. This resulted in a family of eleven grids centered on the equator at one degree longitude intervals between 146W and 156W. Grids have not been generated for a latitudinal drift component since the nominal drift is so small. Experience has shown that minor changes in attitude can be compensated by slipping or rotating the grid without increasing location errors. The routine grid fitting system practiced has given accuracies of better than one degree at the satellite subpoint and better than three degrees near the horizon. Greater accuracies can be attained with additional effort. The full

family of grids is routinely incorporated in the archival film file, the daily satellite subpoint is included in the catalog daily data listing. Scaling of the appropriate grid and picture to the specific size desired for grid melding is left to the discretion of the data user.

The best full disc picture from the daily sequence is selected for catalog publication. The periodic ATS Meteorological experiment data catalog to be published and distributed by the ATS Project, will include a brief summary of experiment operation, overall quality of data reception, and listings of spacecraft maneuvers affecting SSCC data presentation during the catalog period. Orbital elements will be presented along with the daily data listing and the "picture of the day". The initial catalog, covering the period January 1, 1966 to June 30, 1966, also included an ATS-I SSCC Data Users Guide, briefly describing the spacecraft, on-board and ground experiment systems, and describing in detail the data processing procedures and techniques. Distribution of the first ATS-I SSCC photographic data catalog was completed in January 1968.

It is anticipated that the second periodic catalog published will contain an ATS-III meteorological experiment User Guide, and include appropriate data listings and pictures for the ATS-I SSCC experiment, the ATS-III Multicolor SSCC experiment and the ATS-III Image Dissector Camera System Experiment. For future catalog documentation of synchronous orbit meteorological data a more dynamic presentation is being investigated.

Archival of SSCC Film Data: Since the ATS-I SSCC pictures constitute photographic meteorological data, these data will, by agreement with the Environmental Data Service, ESSA, be stored at the National Weather Records Center, (NWRC), Asheville, N. C., for fulfilling user requests. The original negatives produced at Rosman and Mojave will be retained in the Nimbus/ATS Data Utilization Center at GSFC.

Reproduced copies of the archival picture data are being furnished NWRC on five inch film stock in both positive and negative form, with an appropriate family of grids attached to each roll of film. Should the satellite subpoint change materially a new family of grids will be generated and provided with the appropriate reels of transparencies. Approximately 300 4x5 inch transparencies are provided on each 125 foot length of film. The total number of pictures per reel varies since only full days' coverage are included. The total archival data for the 1 January - 30 June 1966 period can be obtained on 9 reels of film.

ATS-I SSCC data may be ordered from NWRC by complete reels only. Individual pictures cannot be provided. Data will be furnished by NWRC as either positive or negative transparencies on 125 foot reels of 5 inch film. The data for 1967 has been archived as follows:

Reel 1	January 1 through 20, 1967
Reel 2	January 21 through February 17, 1967
Reel 3	February 18 through March 11, 1967
Reel 4	March 12 through April 4, 1967
Reel 5	April 5 through 17, 1967

Reel 6 April 18 through 22, 1967

Reel 7 April 23 through 30, 1967

Reel 8 May 1 through 31, 1967

Reel 9 June 2 through 30, 1967 (No data available on June 1, 1967)

Reel 10 July 1 through August 4, 1967

Reel 11 August 5 through September 10, 1967

Reel 12 September 11 through October 6, 1967

Reel 13 October 7 through November 18, 1967

Reel 14 November 19 through December 31, 1967

ATS - 1 NAVIGATION

by

Kirby Hanson
Tom Vonder Haar
Frank Nicholson

#26

CONTENTS

1. Introduction and Purpose

2. Perturbation Problems

   a. Perturbations due to the orbit

   b. Perturbations due to imperfect spin axis orientation

3. Navigation Parameters Defined

4. Significance of Apparent Pitch and Roll

5. Routine Determination of χ from Analog Picture Data

6. Transformation Between Perfect and Actual Picture Coordinates

7. Conclusion

8. References

Appendix 1: ATS - 1 Navigation Constants

1. Introduction and Purpose

Reflected shortwave radiation data observed by or measured from the ATS-1 cloud camera are not obtained relative to any common earth coordinate system. In their basic form, an array of these data comprise a scan line (L) and digital element (E) matrix, where the nominal east-west coordinate (E) is derived by sampling a continuous signal at a fixed rate. In order to fully utilize these data, it is necessary to facilitate easy transformation between the (L, E) system and one of latitude (ϕ) and longitude(λ).

The purpose of this study is to consider the problems inherent in such a transfer and also to consider some techniques to facilitate the transfer. These problems affect all ATS-1 data, regardless of the manner in which they are stored or displayed. However, because the original (L, E) system is preserved only when the data are stored in digital form on magnetic tapes the results of this study apply especially to the ATS "digital data."

The term "navigation" has been used in some previous discussion on this subject. For the present work, we will define navigation to indicate the technical ability to transfer between an actual ATS-1 picture matrix and the earth coordinate system, or vice versa. This two-way transformation is illustrated in Figure 1.

2. Perturbation Problems

If the ATS-1 orbit were perfect and if the satellite spin axis were parallel to that of the earth, it would be a straight forward geometrical problem to express the transformation between coordinate systems,

illustrated in Figure 1. We now know that the orbit is not perfect and the axes are not perfectly parallel. Thus, the transformation of coordinates is not simply the perfect orbit transformation, but requires consideration of the effect of these perturbations.

a. Orbital Perturbations - The orbital inclination (i) and position of the subsatellite point (SSP) have been determined as a function of time by NASA (1). This information is illustrated in Figure 2 and shows that the magnitude of $\dot{i}$ and SSP drift is small. Of additional importance is the fact that changes in these elements are of rather long - time period.

b. Spin - Axis Orientation - The perturbation resulting from the spin - axis being non - parallel to the earth's axis is a much more difficult problem. This is because the perturbation is both large and not known from ground measurements. Others (ATS Technical Data Report Vol. 5, (1967)) have found that the most precise method of determining the satellite spin axis orientation, relative to the earth's, is from the satellite pictures themselves. Therefore, our problem in navigation on the ATS - 1 picture is to determine from the data the numerical value of parameters with which to correct an actual picture coordinate matrix to the perfect picture coordinate matrix.

3. Navigation Parameters Defined

Before proceeding with methods of determining the numerical value these of parameters, it is necessary to first define the parameters.

Let us consider the case of a perfect orbit, i. e. $\underline{i} = 0$ and $\underline{h}$ = constant, and the axes not parallel. As shown in Figure 3, it is clear that the satellite undergoes an apparent pitch and roll relative to the earth. If we assume the satellite has no nutation, the spin axis orientation in space can be defined by two angles:

1. pitch (α) is the angular displacement of the spacecraft spin axis from a normal to the earth's equatorial plane, and
2. roll (β) is the angular displacement of the spacecraft spin axis from a plane through the earth's axis and center of the spacecraft.

If we suppose, as shown in Figure 3, that $\underline{\alpha}$ has some positive value $\underline{m}$ at time $\underline{t_1}$ and that $\underline{\beta}$ is zero, then at 6, 12 and 18 hours later, $\underline{\alpha}$ and $\underline{\beta}$ will have values as shown. Clearly $\underline{\alpha}$ and $\underline{\beta}$ are sinusoidal functions of time. In this example they are simply out of phase by 90 degrees. The apparent pitch (α) is also shown in the pictures at bottom of Figure 3. Pitch (α) appears in the picture as vertical displacement of the earth.

Apparent roll (β) is also discernable in the picture, providing there is a landmark which can be seen; this is illustrated in Figure 4. As shown in the top of the figure, the apparent pitch (α) shows up as vertical displacement, whereas, roll (β) causes an apparent rotation of the earth's disc in the picture. The example seen in the lower part of Figure 4 represents the orbital conditions specified in Figure 3. The circled dot on the earth's disc in the lower part of Figure 4 represents a landmark. The dashed line indicates the direction to the landmark when $\beta = 0$. The

apparent rotation of the landmark with time is clearly visible. Thus, it is possible to determine β as the angular displacement of a landmark relative to the SSP.

Since α and β are both sinusoidal functions having the same period (P), there is a relationship between them. If we let

$$a = \cos\alpha \tag{1}$$

$$b = \cos\beta \tag{2}$$

then, for the case given in Figure 3, we would expect a and b to vary with time as shown in Figure 5. Here $\Delta t = P/4$, which in this case is 6 hours between the functions. These functions are:

$$\alpha = 2\pi t/p \tag{3}$$

$$\beta = 2\pi (t + \Delta t)/P \tag{4}$$

Thus, for a specific time (t_1) it is possible to determine α from β, or vice versa, if Δt is known.

These relationships are simply,

$$\alpha_{(t_1)} = \beta_{(t_1)} - \left(\frac{2\pi}{P} \cdot \Delta t\right) \tag{5}$$

$$\beta_{(t_1)} = \alpha_{(t_1)} + \left(\frac{2\pi}{P} \cdot \Delta t\right) \tag{6}$$

The time variations of α and β are not measured by NASA tracking stations, nor have they been determined from the pictures. However, a cursory check of the EIS pictures indicate that α and β have daily maximum values of greater than 1.2 degrees for much of the period December, 1966 through May, 1967, but less than 1.2 degrees beginning in early June, 1967. Therefore, the example given in Figures 3, 4, and 5, in which pitch and roll were both taken as 2 degrees, is probably slightly larger than maximum

daily errors to be expected through much of the period for which data are available.

4. Significance of Apparent Pitch and Roll

To see how significant the errors associated with pitch and roll may be, consider the examples in Figure 6 in which both α and β individually have values of 2 degrees. The top illustration shows vertical displacement of the ATS - 1 picture due to a downward pitch ($-\alpha$) of 2 degrees. The resulting displacement is 266 scan lines from the corresponding scan lines of a perfect picture. If uncorrected, this is equivalent to a ν error in position on the earth's surface of 11.5 degrees of latitude in the tropics - or near 700 miles.

The bottom illustration in Figure 6 indicates how a roll (β) of 2 degrees would cause an apparent rotation of the earth on the ATS - 1 picture. At the intersection of the limb of the earth and equator, points are displaced vertically by 46 scan lines. This decreases to zero at SSP. At 40 degrees North latitude on the eastern limb, points are displaced northward by 32 scan lines and westward nearly an equivalent amount. If we wish to use the hook of Baja California as a landmark, we find that a 2 degree rotation gives an apparent displacement of Baja northward by only 31 scan lines and westward by 80 picture elements. This is also illustrated in Figure 7.

The important point to be learned from the examples in Fig. 6 is that with identical values of pitch and roll, we have considerably different displacements of earth features on the ATS - 1 pictures. In our example,

an α of 2° gives a displacement by 266 scan lines, whereas a β value of 2° gives a displacement of only 31 scan lines on the hook of Baja California.

Therefore, if one has the option of measuring either α or β, it is important to realize that a determination of α has at least 8 or 9 times the resolution of a determination of β.

In summarizing the navigation problem, we can say that the simple, one - step navigation procedure shown in Figure 1 is more realistically solved by a two - step procedure which is illustrated in Figure 8. The relationship between (a) and (b) is simply geometrical and can be determined precisely as shown by others. Second - order perturbations resulting from orbital variations as well as any yaw errors could be included in this step. The relationship between (b) and (c) can be determined from parameters α and β, which vary with time, of course. Only one parameter need be determined, because they are functions of each other. The resolution in determining α appears to be nearly an order of magnitude better than determining β.

5. Routine Determination of α from Analog Picture Data

A study was conducted to determine if the α values could be measured with sufficient accuracy for use in navigation in digital data tapes from measurements of earth displacement on the ERTS negatives. The results of this study showed that α can be determined to within 0.008 degrees, or within 1 scan line by this technique. This accuracy is sufficient for most

meteorological applications of the digital data and therefore is routinely useful.

a. Method - The vertical displacement of the earth on an individual picture was obtained by measurement on the EIS negative. The method simply was to determine the position of the earth center, relative to its vertical position in the picture. This is easily done, as shown in Figure 9, by:

1. Measuring from the left side of the negative (the start pulse), some arbitrary distance d to a point on the earth's upper limb. Then, measure the distance h_t from the top of the negative to this point.
2. The process is repeated for the point on the lower limb at which the distance from line start to limb is precisely d. As before, h_b is measured.
3. Finally the total picture height h is measured.

The earth center distance is simply the average of h_t and h_b, and therefore the scan line through the center of the earth SL_c can be calculated from,

$$SL_c = 2018 \left(\frac{h_t + h_b}{2h}\right) \quad (7)$$

This assumes the full picture is 2018 scan lines (Appendix 1).

The departure of SL_c from the "perfect SL_c" is given by

$$\Delta SL_c = SL_c - 1009 \quad (8)$$

and the α value in degrees for that particular picture is given by,

$$\alpha = .007512 \; (\Delta SL_c) \quad (9)$$

↑ should probably demonstrate how this number was obtained. It might not be clear to the reader.

b. Procedure - If one wishes to determine α from a single picture in order to determine the navigation parameters for that particular picture, it can be done as indicated above. However, we find that the error associated with single - picture determination of α is about 3 scan lines. Since α varies in a well defined (sinusoidal) manner with time, a more accurate determination of α can be made by making measurements of α on many pictures and fitting the data to the sine function by computor iteration in order to determine the associated constants. And then using the function and constants to derive dependent α values.

This procedure was used in the test case, mentioned above. A total of 69 individual picture measurements of ΔSL_c were used in the following equation to determine K_1 and K_2 by iteration.

$$\Delta SL_c = K_1 \left[\frac{\text{Cos } (2\pi (t - K_2))}{0.9973} \right] - 1009 \qquad (10)$$

These empirical constants were then used to derive dependent data. The standard deviation of the dependent data from the 69 initial measurements was 3.5 scan lines. We would, of course, expect the departure of a single dependent data point to be much less than 3.5 scan lines because of the large number of observations from which it was derived. In fact, since the error decreases by $1/\sqrt{n}$, where n=69 in our case, we would expect the error of a single dependent date point to be about 0.5 scan lines. This is equivalent to an error in α of about .004 degrees. Typical values of α are from 1 to 2 degrees.

6. Transformation Between Perfect and Actual Picture Coordinates

Correction for the pitch and roll problem is quite straightforward. In Fig. 10 is a pictorial representation of the problem where the origin 0, 0 is the center of the perfect picture, the angle β is the roll error, and $\geq, \alpha$ the pitching translation. Knowing that pitch and roll are a sine-cosine relationship and that yaw and heave are essentially zero, the elements (X_1) and lines (Y_1) which correspond to the actual picture coordinates can be rotated and translated according to the following transformations.

$$X = (X_1^2 + Y_1^2)^{\frac{1}{2}} \cos\left(\tan^{-1}\left(\frac{Y_1}{X_1}\right) + \beta\right) \qquad (11)$$

$$Y = (X_1^2 + Y_1^2)^{\frac{1}{2}} \sin\left(\tan^{-1}\left(\frac{Y_1}{X_1}\right) + \beta\right) + \geq \alpha . \qquad (12)$$

where, $\geq$ is the height of the satellite above the earth $\beta = \sin^{-1}(\sin\alpha + \pi/2)$, X and Y are the element (E) and line (L) values corresponding to the perfect orientation case.

This is a very close approximation, especially the translational part due to the fact that the arc of the pitch angle is assumed to be very nearly the same magnitude as the chord, and that the projections of the angle of translation introduce an insignificant error.

7. Conclusions

This paper has discussed the principal factors that effect "navigation" with the ATS - 1 data. Small ($\angle 2^\circ$) departures of the satellite's spin axis

from its nominal position parallel to the earth's axis cause the greatest problem. Apparent pitch and roll of the pictures, results from this effect and of the two, pitch variations are more evident in the data and cause greater navigation errors.

A technique for measuring pitch from standard photographic displays of the ATS - 1 data is discussed. These measurements together with a relation between pitch and roll provide the necessary data to convert actual line and element positions to values that correspond to the nominal attitude situation. For the resulting "perfect" case only a precise geometrical transformation is needed to assign the proper latitude and longitude to each ATS - 1 radiation measurement.

8. References

Technical Data Report for the Applications Technology Satellite ATS Program. Goddard Space Flight Center, Greenbelt, Maryland. 1967.

APPENDIX I

ATS - 1 NAVIGATION CONSTANTS

1.) Assumed Constant Values

Total No. Scan Lines = 2018

Vertical Sweep = 15.1594°

Total No. Picture Elem. = 8192

Horizontal Scan = $20.^{\circ}$

"Perfect" Picture Conditions

Earth Center Line = 1010.3

Christmas Island Line = 966.0

$\alpha = 0$

$\beta = 0$

Period = 0.9973 day

Altitude = 35,783 Km

Earth at Eq. = 17.4023 Deg

Eq. Radius = 6,378.15 Km

$0\text{-}5^{\circ}$ Lat, 23.68 Scan Lines = 1 Deg Lat

2.) Vertical Constants

1 Scan Line = .007512 Deg. at Satellite

1 Deg. at Satel. = 133.12 Scan Lines

Equator Line = 1010.3 Scan Line

1 Deg. of Lat. $(0\text{-}5^{\circ})$ = 23.68 Scan Lines

3.) Horizontal Constants

1 Picture Element = .002441 Deg. at Satellite

1 Deg. at Satel. = 409.6 Picture Elements

Earth Eq. Diam = 17.4023 Deg

Earth Eq. Diam = 7128. Picture Elements

ILLUSTRATIONS

1. ATS - 1 navigation problem, showing required two - way transformation.
2. ATS - 1 orbital elements from January - September, 1967. These are height (h), subpoint longitude (λ), and inclination (i).
3. ATS - 1 pitch (α) and roll (β) visualized in orbit, and apparent pitch in the ATS - 1 pictures.
4. Apparent pitch (α) and roll (β) in the ATS - 1 pictures. The circled dot on the earth represents a geographic feature. Note that when $\alpha = 0$ (at times $t_1 + 6$ and $t_1 + 18$) the location of the geographic feature is not unique.
5. Variation of a and b as a function of time.
6. Example of pitch error of 2 degrees (top), and roll error of 2 degrees (bottom).
7. Apparent displacement of the hook of Baja California due to a roll error of 2 degrees.
8. Block diagram of the logical step solutions to navigation on ATS - 1 data.
9. Measurements of ATS - 1 EIS negatives necessary to determine α value for that picture.
10. Translation and rotation due to pitch (α) and roll (β).

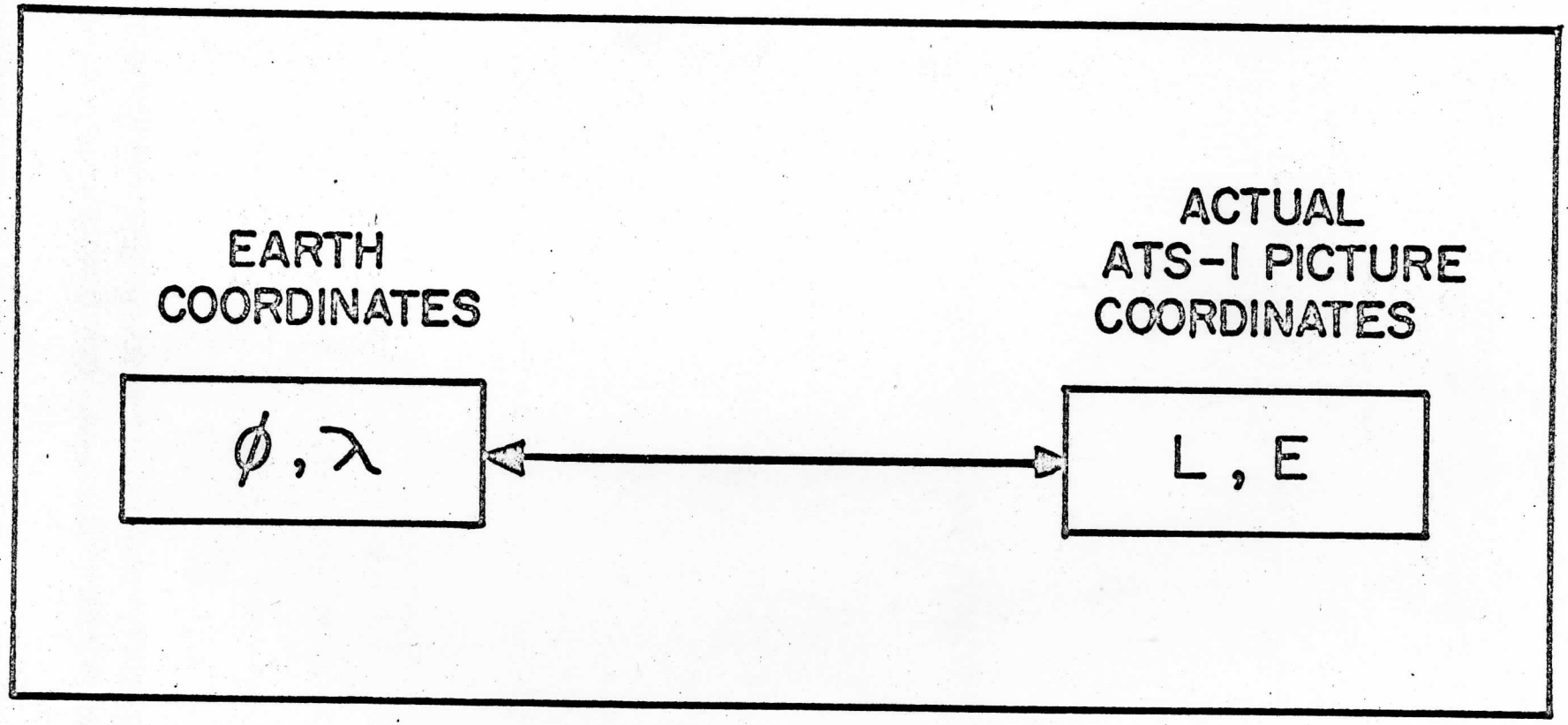

Fig. 1

ATS-I SELECTED ORBITAL ELEMENTS

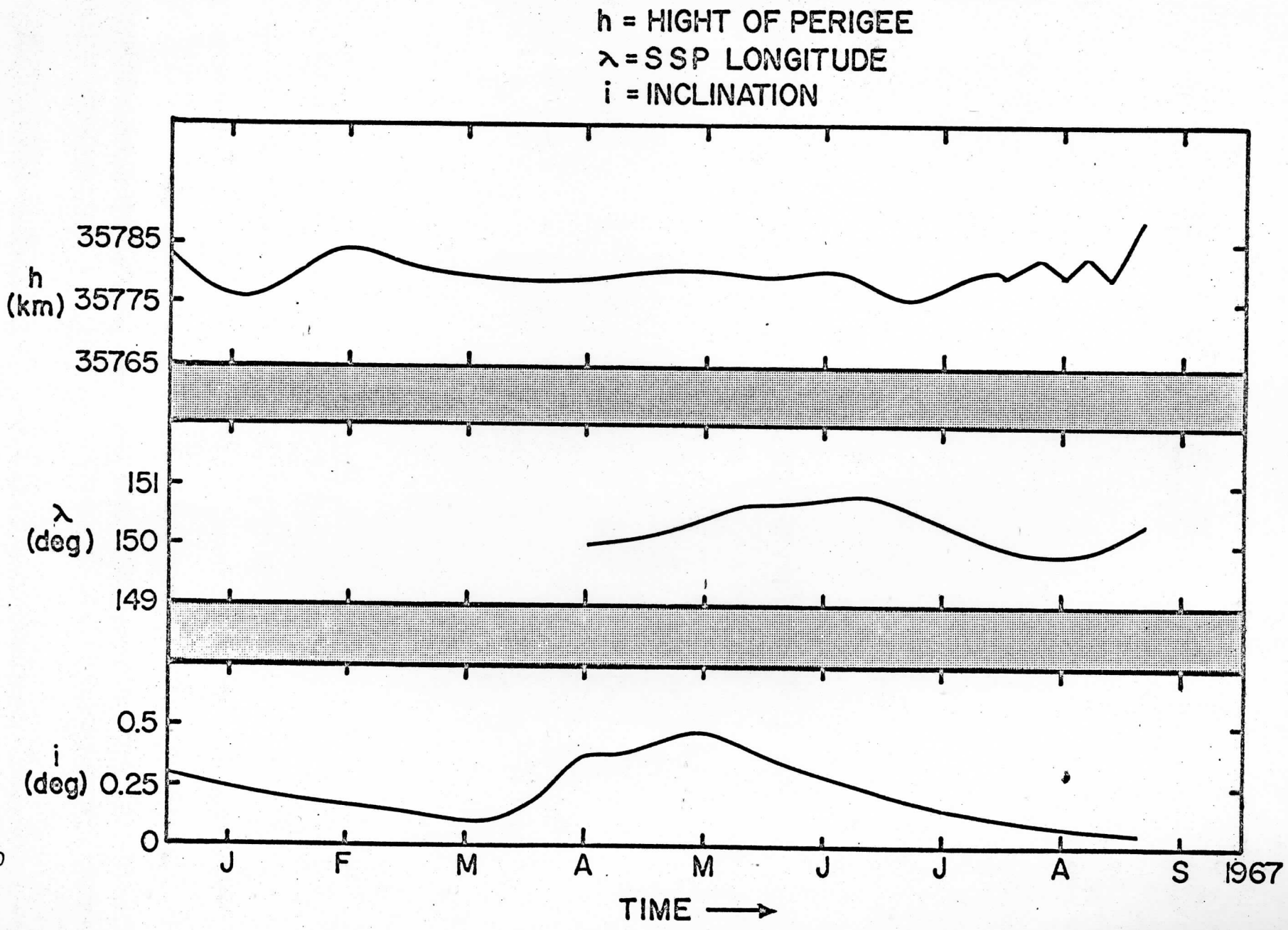

Fig. 2

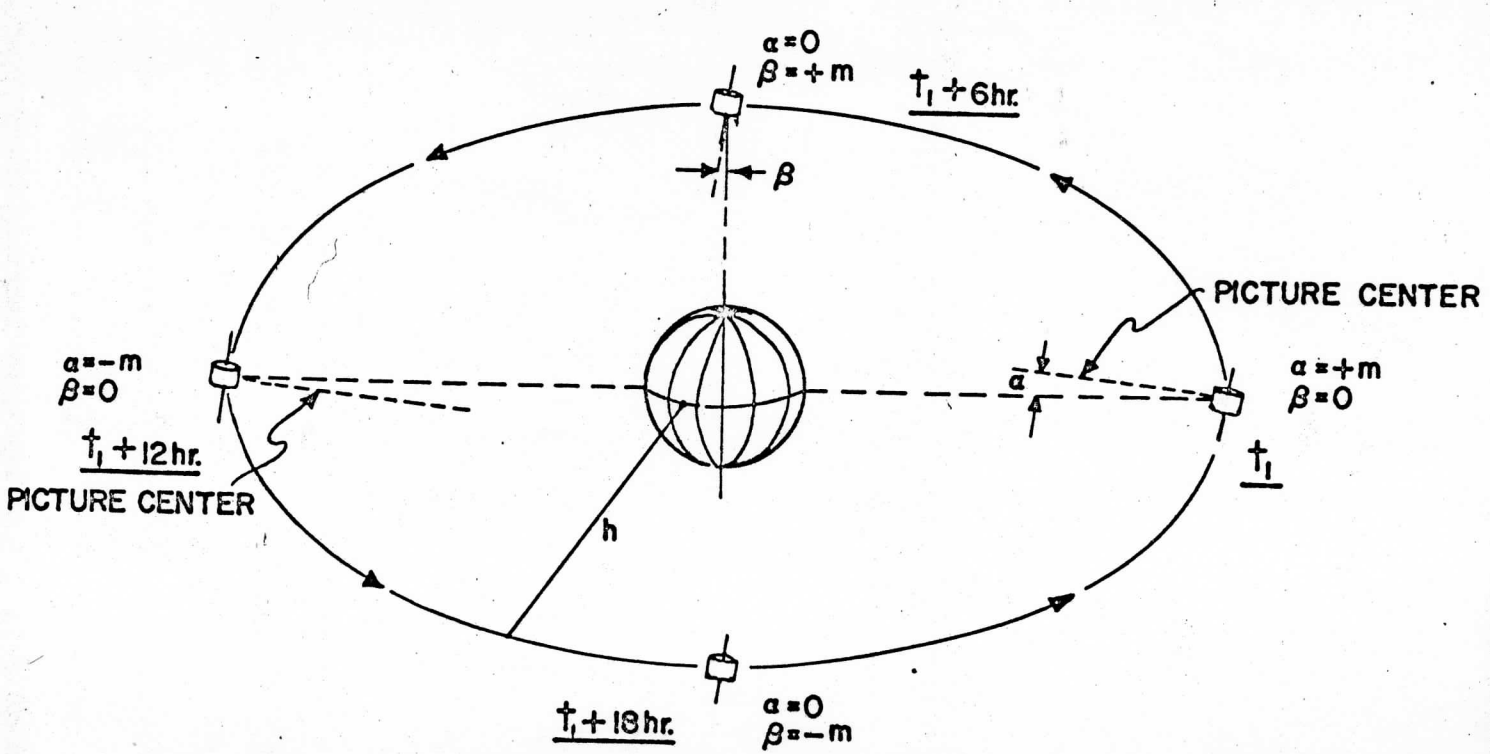

ATS – I PICTURES

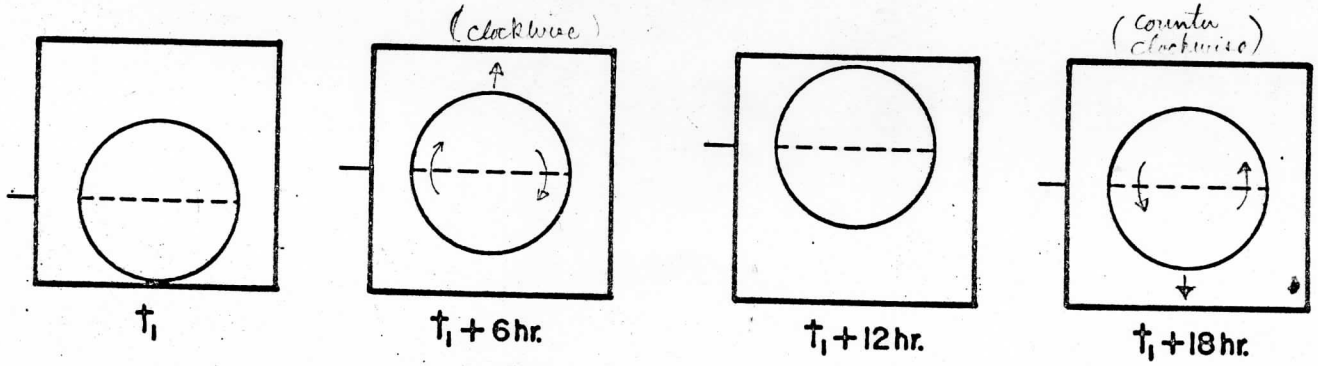

Fig. 3

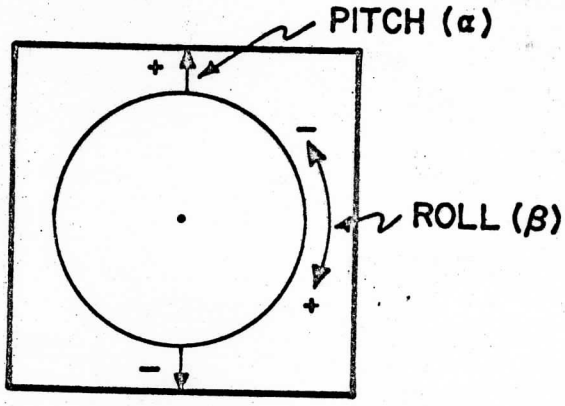

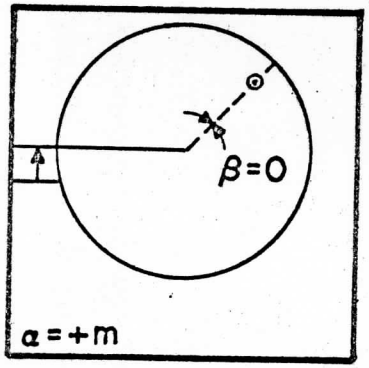

t_1

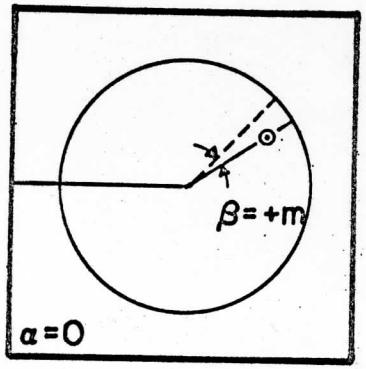

$t_1 + 6$ hr.

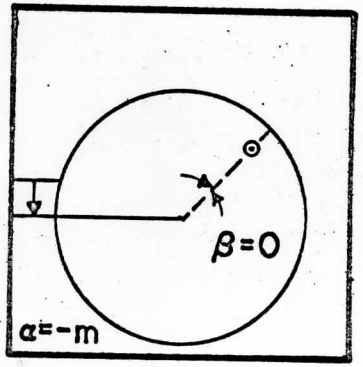

$t_1 + 12$ hr.

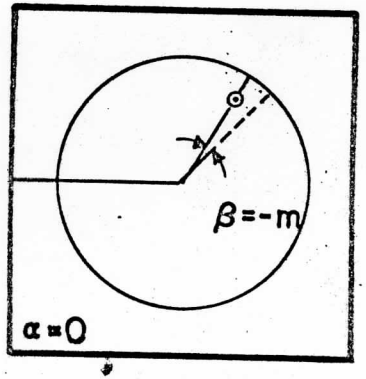

$t_1 + 18$ hr.

Fig. 4

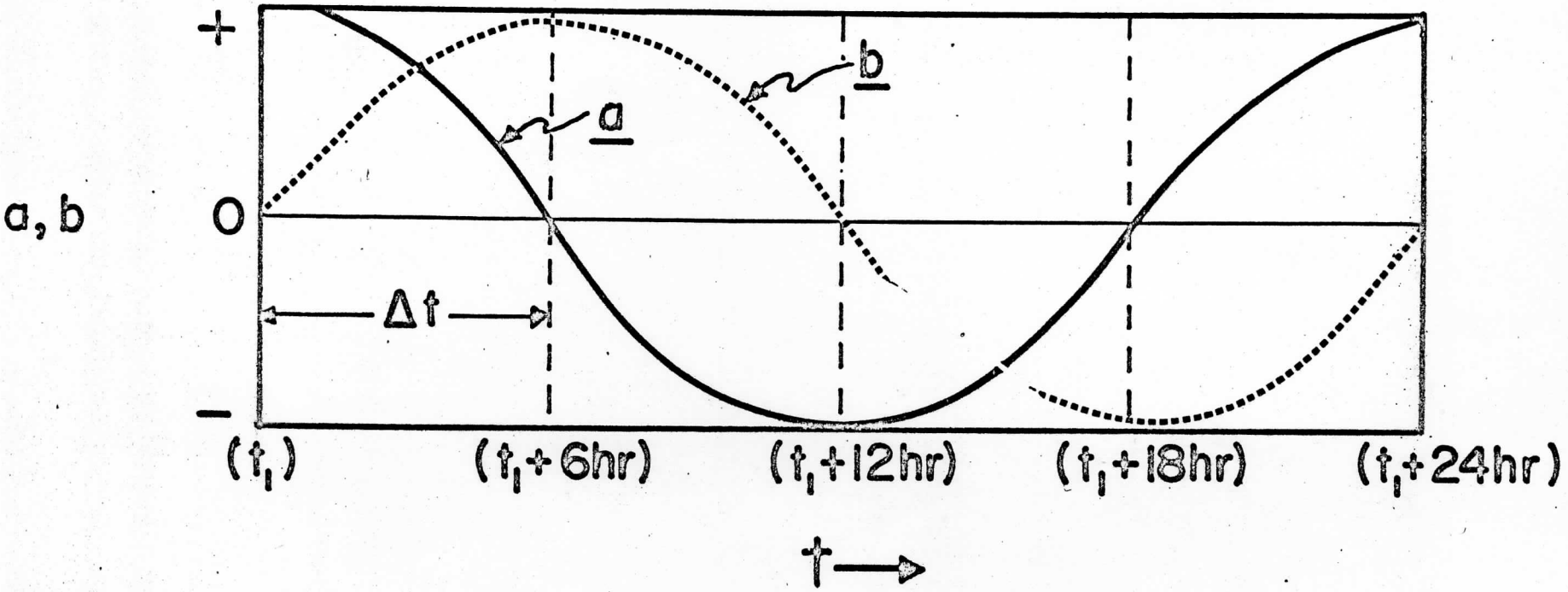

Fig. 5

VERTICAL DISPLACEMENT

DUE TO PITCH OF 2°

$\alpha = 2°$

$\beta = 0°$

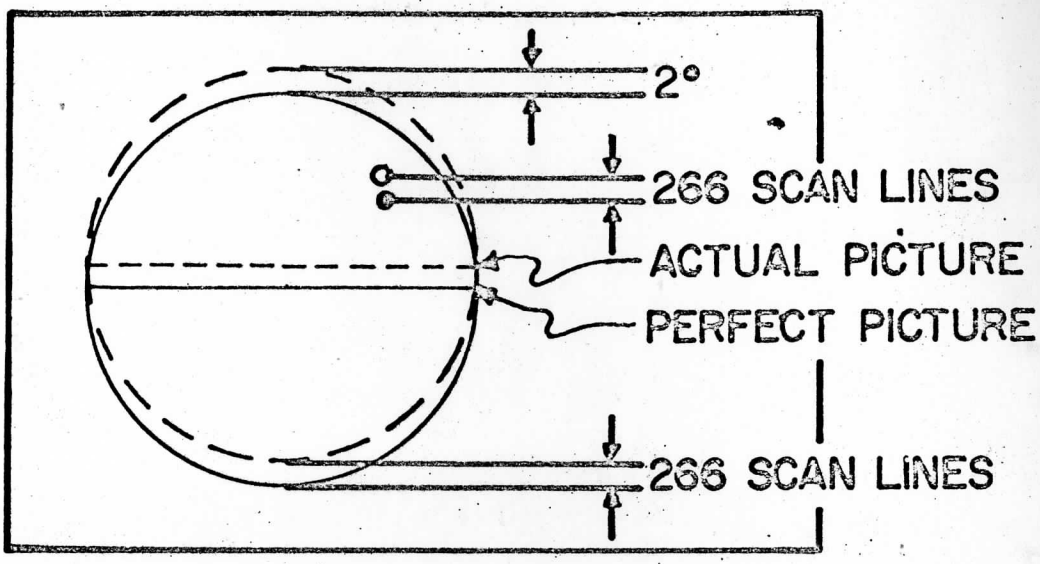

ROTATION OF EARTH

DUE TO ROLL OF 2°

$\alpha = 0°$

$\beta = -2°$

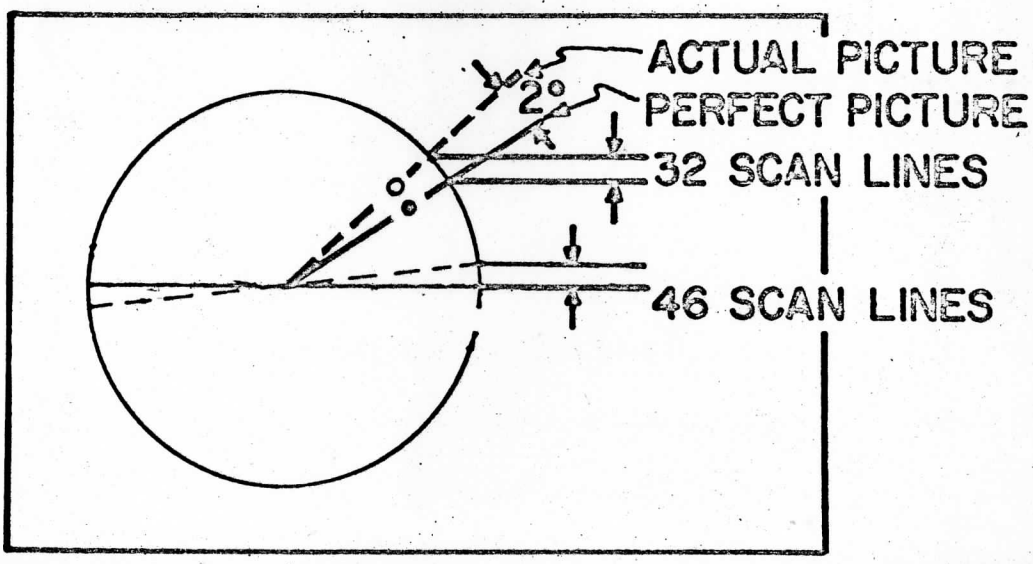

Fig. 6

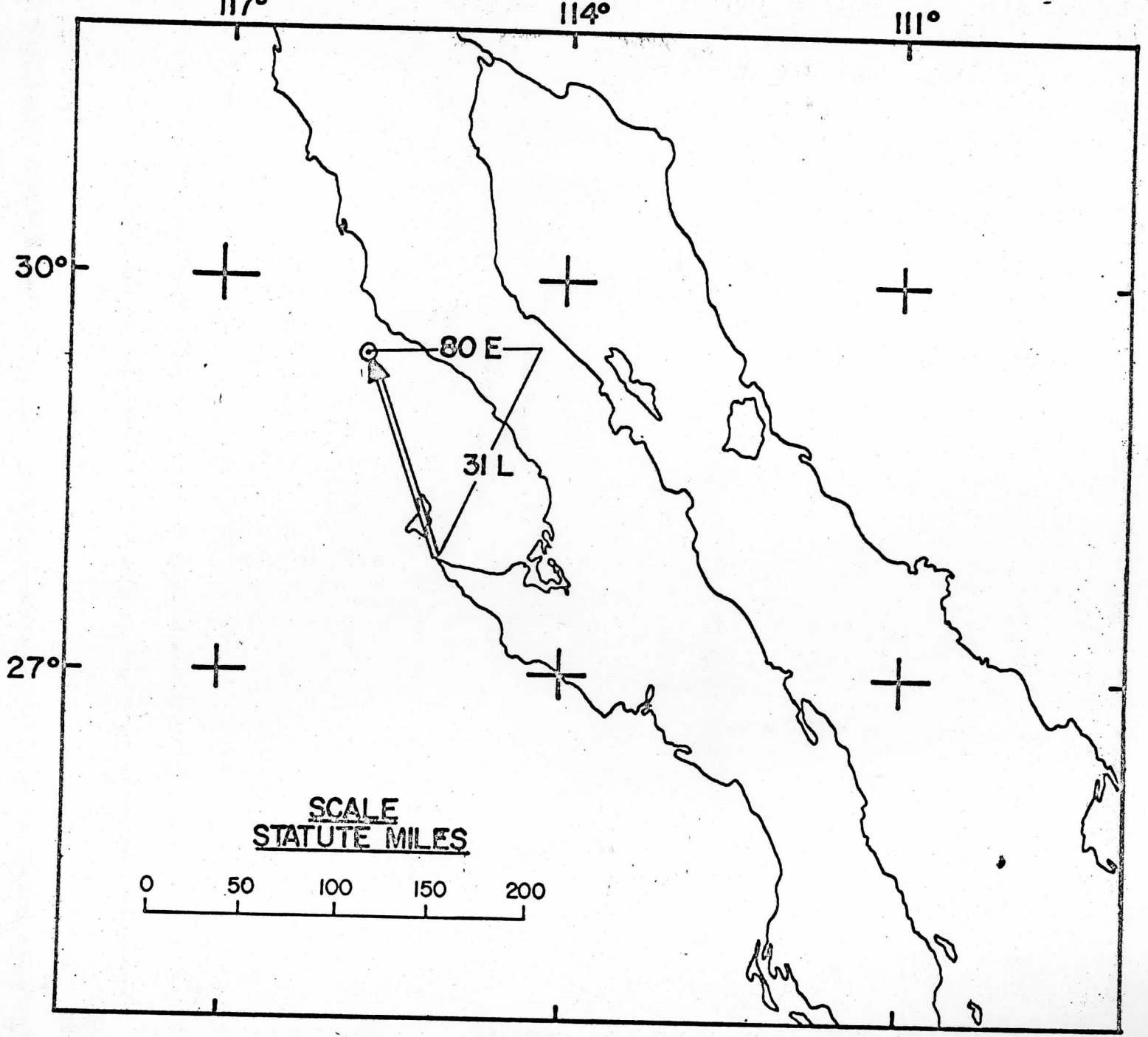

Fig. 1

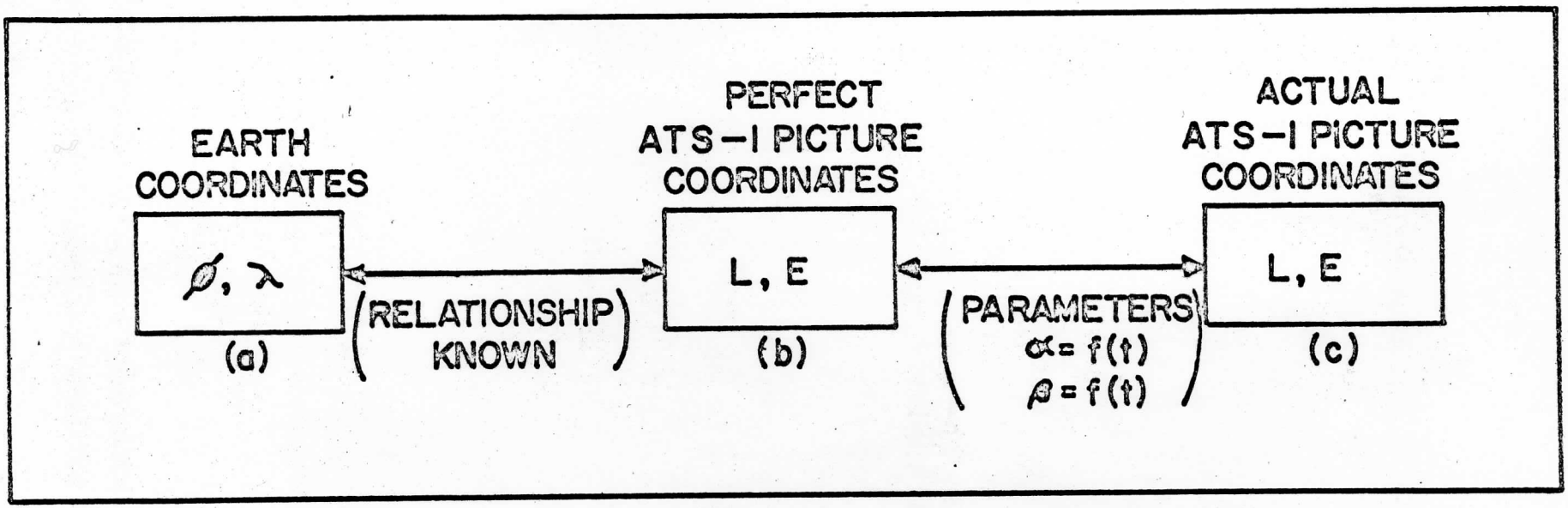
EARTH
COORDINATES
ϕ, λ
(a)
RELATIONSHIP
KNOWN
PERFECT
ATS-I PICTURE
COORDINATES
L, E
(b)
PARAMETERS
α = f(t)
β = f(t)
ACTUAL
ATS-I PICTURE
COORDINATES
L, E
(c)

Fig. 8

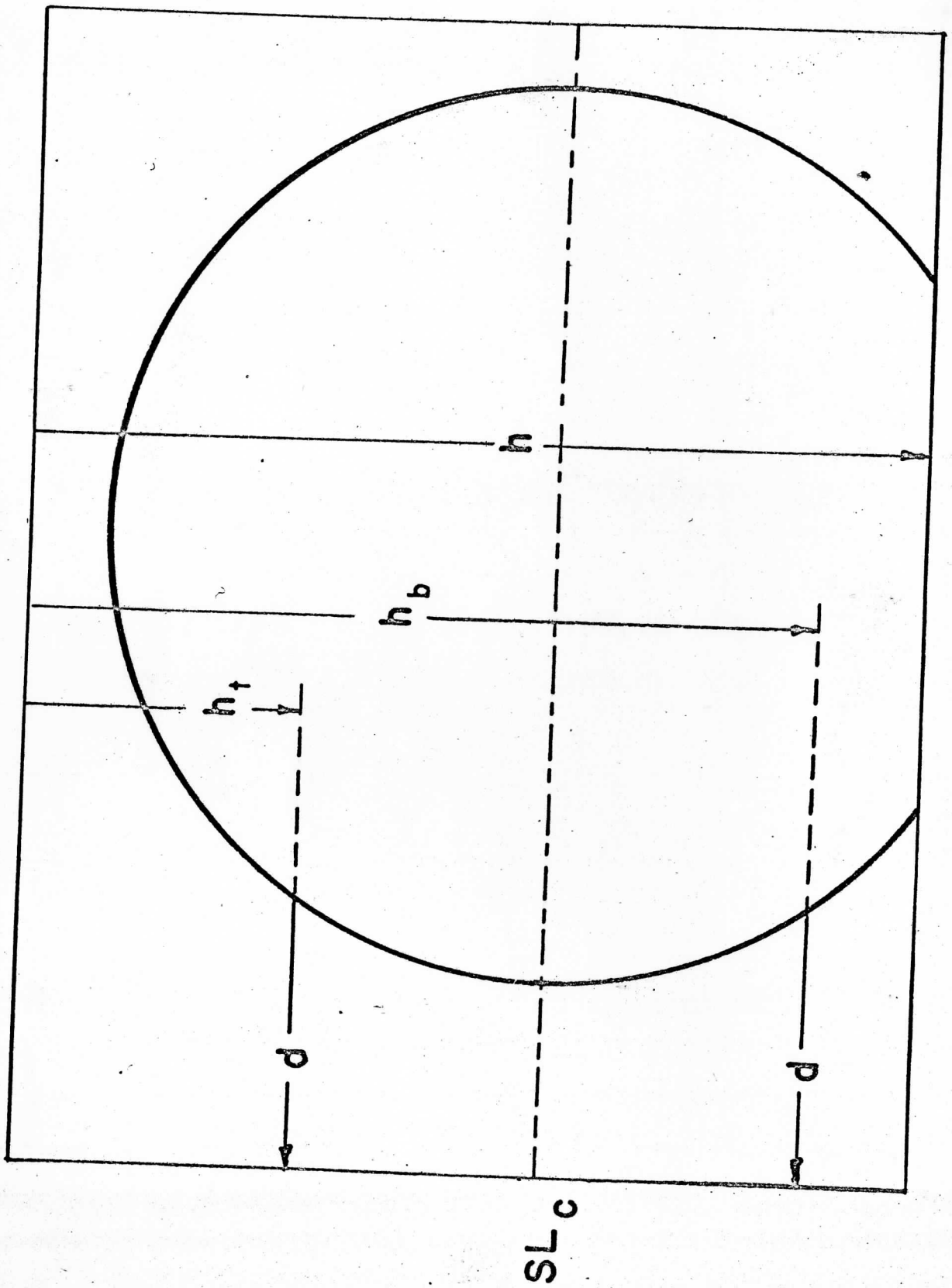

Fig. 9

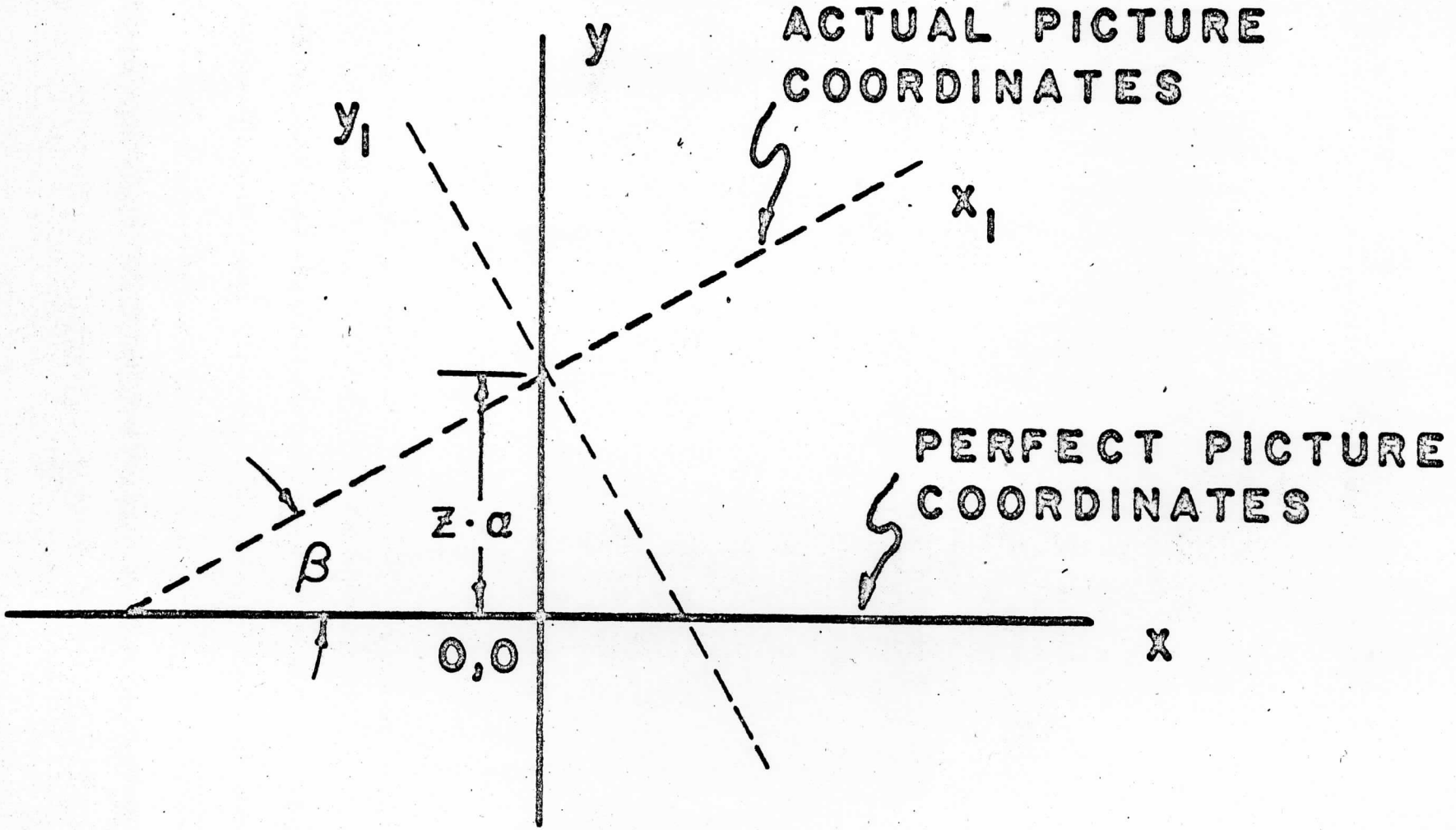
y
ACTUAL PICTURE
COORDINATES
y_1
x_1
PERFECT PICTURE
COORDINATES
$z \cdot \alpha$
β
0,0
x

Fig 10

#27

The Theoretical and Mathematical Justification for Navigation and Analysis from the ATS Satellites

by Francis H. Nicholson

1. Introduction

The successful launchings of ATS-1 and 3 have provided man with the opportunity of viewing the earth for the first time as though he were on a fixed platform in space. The phenomena which he can see in the visible spectrum allows him for the first time to have a truly uniform view of the weather from the scale of planetary waves to that of cumulus cell groups.

He can now observe the weather from a Lagrangian viewpoint as well as a time-integrated one. To get the most out of this vast new field of opportunity it is necessary that the observations by the scientist of the earth from these satellites be able to be used also as measurements, and that is the objective of this paper.

2. Geometry of the Satellite Orbit

The ATS satellite is inclined to the normal of the plane of its orbit about the earth by a small angle somewhat less than 5 degrees. The implications of this have been explored and explained by Mr. Kirby

Hanson, Mr. Tom Vonder Haar and myself in another paper in this volume and I suggest that the reader read this article first in order to get a more thorough understanding of the orbital peculiarities, especially the relation of pitch to roll.

This paper explains that the axes of the earth and the satellite are not parallel and hence the movement of the satellite in its orbit causes the angle of inclination of the satellite from the normal to its orbital plane to vary both its pitch and roll as a sine-cosine relationship.

3. Representation of Data by ATS

The spin-scan camera on the satellite works in such a way that what it sees is not exactly what it represents. Since the satellite is spinning on an axis nearly parallel to that of the earth and consequently does not increment pitch, the spin-scan camera within the satellite itself pitches to get a view of the whole earth, line by line (Fig. 1). This means that the vector defining the line of sight of the camera sweeps out a very flat cone. Where the camera sees the earth is in effect, then, the intersection of a series of cones and a sphere.

What the ground equipment display technique does, however, is to take these quasi-hyperbolas as seen by the camera and presents them as a series of straight lines as would occur if the satellite itself were pitching bit by bit so that the vector of the line of sight would sweep out a series of

planes hinged at the satellite and intersecting the earth (Figs. 2, 3). The hinge of this family of planes would be perpendicular to both the axis of rotation of the satellite and the vector describing a line drawn from the center of the satellite to the center of the earth, i.e., along $\underset{\sim}{y}$ in Fig. 4. The validity of measurements, then, on the data presented by the satellite depends, to a great extent on how realistic the view of the earth, as seen from ATS, really is.

Fortunately, the deviation is very small, as I shall demonstrate and does not significantly alter the true picture (Fig. 5, 5a)

where $R = Z$ (SATELLITE HEIGHT) + RAD$(1 - \cos\theta)$

$b = R \sec\alpha - y\cos\alpha$ $\qquad$ $H = R \sec\alpha \left(\frac{h}{b}\right)$

$h = y \sin\alpha$ $\qquad$ $x = R \sin\theta$

$H/R \sec\alpha = \tan\beta$ $\qquad$ $h/b = \tan\beta$ $\qquad$ $X = (H^2 + (R \sec\alpha)^2)^{\frac{1}{2}} * (x/(h^2 + b^2)^{\frac{1}{2}})$

and * is the mathematical symbol for multiplication

The maximum angle subtended by the earth is 17.4 degrees of celestial arc at the equator, given an equatorial radius of 6378 km. (Fig. 4)

For the ideal case in which the pitch is zero and the roll is zero, the greatest deviation is slightly greater than one part in a thousand at the limb of the earth, and this is at 16 degrees latitude, north and south. For the case of maximum pitch which is about 5 degrees at the very most, the deviation is 7.5 parts per thousand for 12 degrees of the latitude in the hemisphere in which the pitching error exists (Fig. 6).

4. Distortions Introduced by Photographic Representation Techniques and the Corrections for Them

Before the data is available for analysis, the EIS pictures of the earth from the ATS satellites undergo various deformations. Among these are the deformations that are introduced by the machinery in the formation of the EIS negatives and the stretching of the photographic paper in the drying process of both EIS and analogue precision display hard copy pictures.

Since multiple deformations are introduced it would be well to investigate the theory of strain relationships which are pertinent to the deformations.

The actual display system for the ATS negatives and corresponding positives and their enlargements introduce distortions or dilations which can be treated in terms of shear and plane strain. Their relationships can be treated by means of a Mohr strain diagram (Fig. 7). Plane strain can be defined as distortion per unit vector length (Eq. 1).

There are two principal dilations that are introduced. The first is due to shrinking (or stretching) of the vertical axis of the earth due to a lack of coordination in the mechanism by which the lines are incremented on the photograph. The lines are composed of elements and each line is separated from each other line by the equivalent space which is occupied by three elements. The incrementation of the lines on the

photograph is therefore by some other value than that which would result in a representation of the earth as a circular disk. This usually results in a flattening of the earth along the vertical axis. The secondary primary strain, and consequent dilatation is due to a rotation of the negative and stretching of the photographic paper in the drying process. In each case only plane strain is introduced, but the combination of two sets of plane strain results in a shear strain where the shear strain is the rotation of the major axes of the ellipse of deformation from the initial position. The strain in the j direction is constant and is independent of any parameter in the i direction.

The first deformation introduced, called the aspect ratio, flattens the earth so that a circle becomes an ellipse. If this ellipse is rotated and strained again not only will a new ellipse be formed, but the orientation of the original major axes will no longer be orthogonal, or shear strain is introduced.

This means that the new set of major axes of the secondary ellipse are not the same as those of the primary due to the introduction of additional plane strain (Fig. 8). So, in addition to a deformation of all the elements within the ellipse a correction of compound strain and conversion of its subsequent dilation to a simple magnification results in a rotational component, or shear strain, as well.

This may be more clearly seen in the mathematical explanation given below.

Looking at Fig. 7, and consulting the following equations which govern the interrelationships of shear and plane strain, it is evident that shear strain can be resolved into primary plane strains with a certain rotation. If u_i is the deformation in the x_i direction, then the dilation in a two dimensional strain diagram is

$$\phi = e_{ii} = \frac{\partial u_i}{\partial x_i} = e_{11} + e_{22} \qquad i = 1,2 \tag{1}$$

If the final picture is to be kinematically similar to the original, then the strains must be equal or $e_{11} = e_{22}$.

From equilibrium considerations the strains on the surfaces of the element rotated through an angle ϕ in a counterclockwise direction are (utilizing the Kronecker delta)

$$e'_{ii} = \frac{e_{ii} + e_{jj}}{2} + \frac{e_{ii} - e_{jj}}{2} \cos 2\phi + \delta_{ij}\, \gamma_{ij} \sin 2\phi \tag{2}$$

$$i \neq j \qquad i = 1,2; \quad j = 1,2$$

The shear strain, or rotation introduced upon the original circle by compound plane strains is given by the expression (Fig.8a)

$$\gamma'_{ij} = \gamma'_{ji} = \gamma_{ij} \cos 2\phi - \delta_{ij} \frac{e_{ii} - e_{jj}}{2} \sin 2\phi \tag{3}$$

$$i \neq j; \qquad i = 1,2; \qquad j = 1,2$$

The principal strains, which are the ones we will scale so that one equals the other for true magnification, i.e., $e_{11} = e_{22}$, are given by

$$e_i = \frac{e_{ii} + e_{jj}}{2} + \delta_{ij} \left(\left(\frac{e_{ii} - e_{jj}}{2} \right)^2 + \gamma_{ij}^2 \right)^{\frac{1}{2}} \tag{4}$$

and occur on the element rotated through an angle ϕ_n given by

$$\tan 2\phi_n = \delta_{ij} \frac{2\gamma_{ij}}{e_{ii} - e_{jj}} \tag{5}$$

The maximum shear strain is $(\gamma'_{ij})_{max} = \left(\left(\frac{e_{ii} - e_{jj}}{2} \right)^2 + \gamma_{ij}^2 \right)^{\frac{1}{2}}$ (6)

and occurs at an angle ϕ_s given by

$$\tan 2\phi_s = \delta_{ij} \left(\frac{e_{jj} - e_{ii}}{2\gamma_{ij}} \right) \tag{7}$$

Therefore we see that a circle subjected to multiple strains, and all the points within this circle, are relocated in a rotated ellipse. A further rotation and translation which occurs by taking data points off of either a hard copy print, analogue precision display print or digital tape contour dump gives us the original picture of the earth distorted, translated and rotated. Superimposed upon this is the fact that due to roll error the satellite looks at the earth only twice during its orbit such that the north pole of the satellite and of the earth are coincident. The obtaining of the original dimensions on the earth is made considerably simpler by solving for the center of the ellipse, its semimajor and semiminor axes and the angle of its rotation from the arbitrary coordinate system in reference to which data points have been extracted, about which we will treat later (Fig. 9).

Given four points on the limb of the earth, or several sets of four and solving each set, and taking the most probable of the solutions as a function of the distribution of their frequency of occurrence, we may, by solving simultaneously the following 5 equations, obtain the solutions yielding the quantities indicated above.

a. Elliptical Solution for Strains. The tensor equation for an ellipse is

$$\sum_{z=1}^{2} \frac{(\chi_{zh} - HK_z)^2}{AB_z^2} = 1 \tag{8}$$

where χ (chi) is a second order tensor and is the locus of points on the ellipse, HK the locus of the center of the ellipse, AB the semiaxes of the ellipse, and where $z = 1, 2$ or i, j and is summed within each equation using the summation convention, and $h = 1, 2, 3, 4$ or i, j, k, l and sums to four equations.

The transform-projection equation for an ellipse is

$$\frac{(x-h)^2}{a^2} + \frac{(y-k)^2}{b^2} = \cos^2\theta \tag{9}$$

where θ is the angle of rotation and $x' = x \sec\theta$; $y' = y \sec\theta$; $h' = h \sec\theta$; $k' = k \sec\theta$ where x' and y' are the axes of the rotated coordinate system.

Let

$$\begin{aligned} \chi_{ji} - \chi_{jj} &= \chi_{jm} \\ \chi_{ji}^2 - \chi_{jj}^2 &= \chi_{jm}^2 \end{aligned} \tag{10}$$

and so on for $j - k = n$; $k - l = 0$; $l - i = p$

$$\frac{(\chi_h - HK)^2}{AB^2} = \cos^2\theta \tag{11}$$

where $AB_1 = a$; $AB_2 = b$; $HK_1 = h$; $HK_2 = k$

iterating h so that

$$\frac{(x_{ii} - h)^2}{a^2} + \frac{(y_i - k)^2}{b^2} = \cos^2\theta \tag{12}$$

clearing the denominator for

$$b^2(x_i - h)^2 + a^2(y_i - k)^2 = a^2 b^2 \cos^2\theta$$

and expanding for

$$b^2(x_i^2 - 2hx_i + h^2) + a^2(y_i^2 - 2ky_i + k^2) = a^2 b^2 \cos^2\theta.$$

Expanding $(\chi_{jh} - HK_h)^2 / AB_h^2 = \cos^2\theta$, and subtracting from (12), we obtain

$$b^2(x_m^2 - 2hx_m) + a^2(y_m^2 - 2ky_m) = 0 \tag{13}$$

or by utilizing the Kronecker delta δ_{ij}

$$AB_j^2 \delta_{ij}(\chi_m^2 - 2HK_i\chi_{zm}) = 0 \tag{14}$$

Iterating the process to get the same tensor equation in χ_{zn}^2

$$AB_j^2 \delta_{ij}(\chi_{in}^2 - 2HK_i\chi_{in}) = 0 \tag{15}$$

Letting $A = y_m/y_n$ and multiplying (15) by A, we get

$$AB_j^2 \delta_{ij}(A\chi_{in} - 2HK_i\chi_{in}A) = 0 \tag{16}$$

but

$$A\chi_{jn} = \chi_{jm}$$

so by subtracting (16) from (14), we get

$$b^2(x_m^2 - Ax_n^2 - 2h(x_m - Ax_n)) + a^2(y_m^2 - Ay_n^2) = 0 \tag{17}$$

or by letting

$$\chi_{zm}^2 - A\chi_{zn}^2 = \chi_{zn}^2 \tag{18}$$

we get

$$AB_j^2 \delta_{ij}(\chi_{iu}^2) - AB_2 HK_1(\chi_{1r}) = 0 \tag{19}$$

By repeating the process letting $B = y_o/y_p$ and $\chi_{zh} = \chi_{zo} - B\chi_{zp}$ we get

$$AB_j^2 \delta_{ij}(\chi_{ir}^2) - AB_2 HK_1(\chi_{1r}) = 0$$

By adding Eqs. (20) and (19), grouping terms and factoring for HK_1, or h, we get

$$- AB_j^2 \delta_{ij} \frac{(\chi_{iu}^2 + \chi_{ir}^2)}{AB_2(\chi_{1u} + \chi_{1r})} = HK_1 = h \tag{21}$$

By a similar process we may solve for k letting $D = x_m/x_n$ and $E = x_o/x_p$

$$\chi_{zm} - D\chi_{zn} = \chi_{zs}; \quad \chi_{zo} - E\chi_{zp} = \chi_{zt} \tag{22}$$

$$k = HK_2 = - AB_2 j^2 \delta_{ij}(\chi_{is}^2 + \chi_{it})/AB_1(\chi_{2s} + \chi_{2t})$$

The original equation of course was

$$(\chi_{zh} - HK_z)^2 / AB_z^2 = \cos^2\theta$$

We now solve for R which is AB_2/AB_1 or b/a.

Multiplying both sides of the original equation by AB_2, we get

$$\frac{b^2}{a^2}(x_h - h)^2 + (y_h - k)^2 = b^2 \cos^2\theta \tag{23}$$

or $$\frac{b^2}{a^2}(x_m^2 - x_m h) + (y_m^2 - y_m k) = 0 \tag{24}$$

or if $R^2 = b^2/a^2$, then

$$R^2 = -\frac{(y_m^2 - y_m k)}{(x_m^2 - x_m h)} \tag{25}$$

Solving for AB_2 or b we have

$$\begin{aligned} R^2(x_k - h)^2 + (y_k - k)^2 &= b^2 \\ b &= (R^2(x \text{ etc.})^{1/2} \end{aligned} \tag{26}$$

Since in polar form, for an ellipse

$$r^2/\cos^2\theta = (x-h)^2 + (y-k)^2 = D \tag{27}$$

and

$$r^2 = a^2b^2/(a^2 \sin^2\theta + b^2 \cos^2\theta) \tag{28}$$

we may solve the polar equation for θ by substituting (27) in (28)

so that

$$(x-h)^2 + (y-k)^2 = a^2b^2 \cos^2\theta/(a^2 \sin^2\theta + b^2 \cos^2\theta) \tag{29}$$

but since

$$(b^2/a^2)(x-h)^2 + (y-k)^2 = b^2 \cos^2\theta, \tag{30}$$

$$(x-h)^2 + (y-k)^2 = \frac{a^2((b^2/a^2)(x-h)^2 + (y-k)^2)}{a^2(1-\cos^2\theta) + b^2 \cos^2\theta} \tag{31}$$

Since

$$b^2/a^2 = R^2 \tag{32}$$

then

$$D = (R^2(x-h)^2 + (y-k)^2)/((1 - \cos^2\theta) + R^2 \cos^2\theta) \tag{33}$$

Let

$$C = R^2(x-h)^2 + (y-k)^2 \tag{34}$$

so

$$D = C/(1 + \cos^2\theta(R-1) \tag{35}$$

or

$$\cos^2\theta = C/D(R-1) - 1$$

or

$$\theta = \cos^{-1}((C/D(R-1) - 1)^{1/2}) \tag{36}$$

b. Translation of Data. Therefore, knowing the angle of rotation of the ellipse, its translation and the ratio of its semiminor to its semimajor axes (as well as which is which), we may first translate the data points so that the origin of the coordinate system that we are measuring from becomes the center of the picture. Next, the data points are transformed into this coordinate system by multiplying them by the cosine of the angle by which the ellipse is rotated from the axes of our measuring coordinates.

The translation of the rotated ellipse was also accomplished by multiplying the amount of the translation by the same cosine as above, in accordance with the transformation equations (Fig. 10)

$$x = x' \cos\theta;\ y = y' \cos\theta$$
$$h = h' \cos\theta;\ k = k' \cos\theta \tag{37}$$

and subtracting h from each x, and k from each y.

To return the data points to a real model of what the "one-eyed" satellite sees, it is necessary to equate the strains so that $e_{xx} = e_{yy}$.

For the ellipse

$$a = r_{circ}\, e_{xx};\ b = r_{circ}\, e_{yy} \text{ so that } \frac{b}{a} = e_{yy}/e_{xx} \tag{38}$$

which multiplied by each x coordinate which is $x_{circ}\, e_{xx}$ will result in

$$x_{circ}\, e_{xx}\, \frac{b}{a} = x_{circ}\, e_{yy} \tag{39}$$

Hence, since the strains are equal, all the data points are now truly that of the model of the real earth, the dilatation now being simple magnification.

c. Model Ratio. The last step necessary to achieve real measurements of the earth from the satellite is the finding of the modeling ratio λ. If limb points were subjected to the preceding rectification process, it will be sufficient to know the equivalent radius of the earth seen from the satellite, and, by getting the distance from the model center to the model limb, the modeling ratio λ will be the real picture radius, r, divided by the pictorial radius, h. (Fig. 11)

The real "equivalent" radius can be obtained by considerations of the satellite-earth geometry (Fig. 3), where z is the altitude of the satellite and RAD is the radius of the earth,

$$\phi = \pi/2 - \sin^{-1}(RAD/(RAD + z)) \tag{40}$$

$$r/RAD = \sin\phi$$

therefore

$$r = RAD \sin \phi \tag{41}$$

or $$\lambda = r/h. \tag{42}$$

By multiplying all data points, both coordinates, by λ, we obtain the true "equivalent" distances rather than model distances. It is necessary to bear in mind that for each radial distance there is a specific defect of distance below the subsatellite point below which the "equivalent" radial distance meets the vector joining the satellite and the center of the earth so that due to the earth's geometry, each radial distance has an implied height from the center of the earth thereby granting the measurements in a cylindrical coordinate system. This height is defined by

$$z_0 = (RAD^2 - r^2)^{1/2} \tag{43}$$

(Figs. 3, 11).

d. Reorientation. Knowing this, there is one more thing we must do to get the true orientation of the earth, thereby correcting both for shear strain and for satellite roll. As part of the data set there should be a landmark such as a promentory on Baja California, or the northern tip of the island of Hawaii. Knowing the latitude and longitude of these landmarks and the subsatellite point, their real orientation can be compared to the orientation of the picture and suitable corrections made. The technique is as follows:

The angle $\Delta\theta$ between the longitude of the landmark and of the subsatellite point is computed (Fig. 11). The vertical distance y from the plane of the equator to the landmark is computed as $y = RAD \sin\phi$ where ϕ is the latitude. The distance from the center of the earth to this point of intersection, L, is also computed as

$$L = RAD \cos\phi \tag{44}$$

x is then the distance from the point of intersection to the subsatellite vector and is given by $L \sin\Delta\theta$ (Fig. 11, 14).

The arctangent of y/x, ψ, is the correct angle that the landmark in question should make in the cylindrical coordinate system from a perfectly oriented satellite. The same angle, ϕ, is recomputed from the rectified data points and the difference of the two, $\psi - \phi$, ρ, is added to the arctangent of every other set of data points (Fig. 13). Each x' coordinate becomes then x and y', y through the following transformation.

$$x' = (x^2 + y^2)^{1/2} \cos(\tan^{-1}(y/x) + \rho) \tag{45}$$

$$y' = (x^2 + y^2)^{1/2} \sin(\tan^{-1}(y/x) + \rho) \tag{46}$$

Finally we have a corrected earth. This leaves the problem of navigation, i.e., finding latitude and longitude. To solve for latitude and longitude of a point, it is first necessary to be able to find great circle distances.

e. Distance Measurements. Following is the solution for great circle distances between any two points found on the picture of the earth, once the previous rectifications have been made.

Let L_2/L_1 = RATIO2 = Rt2; RAD = R

Multiply h_1 to get two similar triangles (Fig. 13). Constructing a third triangle with sides $h_1 * RATIO2$, h_2 and angle α, we solve for d

$$a_1 = b \cos \gamma; \quad c = b \sin \gamma; \quad b_1 = a\left(\frac{L_2}{L_1}\right) - a_1; \quad d = (c^2 + b_1^2)^{1/2}$$

That leaves us with a fourth triangle of sides D, Rad & RAD * RATIO2 where the angle δ is opposite D (Fig. 14).

Solving for δ, (Fig. 15), we let

$a = RAD \cos \delta$

$b^2 = D^2 - C^2$

$b^2 = D^2 - R^2 \sin^2 \delta$

$b = RAD * Rt2 - RAD \cos \delta$

$b = RAD(Rt2 - \cos \delta)$

$ab = RAD^2 (Rt2 \cos \delta - \cos^2 \delta)$

$a + b = RAD * Rt2$

$a^2 + b^2 = (RAD * Rt2)^2 - 2ab$

$RAD^2 \cos^2 \delta + D^2 - R^2 \sin^2 \delta = R^2 Rt2^2 - 2ab$

$= R^2 Rt2^2 - 2R^2 (Rt2 \cos \delta)$

$+ 2 R^2 \cos^2 \delta$

Adding $\sin^2 + \cos^2$ to get 1 we get

$$D^2 - R^2 \sin^2\delta = R^2 Rt2^2 - 2R^2 Rt2 \cos\delta + R^2 \cos^2\delta + R^2$$

$$2R^2 Rt_2 \cos\delta = R^2 Rt2^2 + R^2 - D^2$$

$$\delta = \cos^{-1}((Rt2^2 + 1 - D^2/R^2)/2Rt2)$$

DISTANCE = $R * \delta$ (Fig. 14).

5. Navigation

D = 2 RAD sin(δ/2), Eq. (47), gives the chord of the angle subtended by the subsatellite point and the point in question by the method described above (Figs. 14, 16a).

$$d_3 = (D^2 - y^2)^{1/2}$$

$$d_4 = (d_3^2 - x^2)^{1/2}$$

$$d_5 = RAD - d_4$$

$$\theta = \tan^{-1}(x/d_5)$$

$$d_6 = d_5 \sec\theta$$

$$\phi = \tan^{-1}(y/d_6) \qquad (48)$$

Latitude = Lat of subsatellite point + θ

Depending on the sign of x and y, the longitude is east or west of the subsatellite point, and the latitude is north or south of it.

6. Analysis Techniques

It does little good to be able to find where we are on the satellite picture if we are unable to use what we see. So that the photographing of the earth from the satellite will result in more than an exercise in

aesthetics, it is necessary that we quantify what we see. The analyses of spirals and finding of irregular areas, especially, depend upon the ability to find spherical angles on the earth, as well as distances along the great circle from one point to another.

a. Irregular Areas. An irregular area either of a cloud or of a space demarked by a series of clouds can be found by finding the area of one or more inscribed polygons. The area of a polygon on a sphere is given by the following formula:

$$\text{Area} = \left(\sum_{i=1}^{n} \theta_i - (n-2)\pi\right)\text{RAD}^2 \tag{49}$$

where $\sum_{i=1}^{n} \theta_i$ is the sum of the angles within the polygon, and n is the number of sides. If the area in question can be considered circular, or if the area of a spiral band is of interest, then another technique can be applied which will be explained later.

Since the irregular area is based upon the ability of finding angles on a sphere within the polygon inscribed upon this sphere, we shall now explore the method of finding these angles.

First the angle in question, in this case $\angle abc$ is considered to be at the apex of a spherical triangle defined by points a, b, c, and in a plane normal to the vector, $\underset{\sim}{X}$, in an arbitrary Cartesian framework (Figs. 17, 17a).

These points are connected by the great circle segments labeled 1, 2 and 3. From the method of finding distances described above, we are able to find the angles subtending these distances from the center of the earth, 1, by δ_1, 2 by δ_2, 3 by δ_3 (Fig.18)

$$d_1 = RAD * \sec \delta_1$$

$$a = d_1 * \cos \delta_3$$

$$d_2 = RAD * \sec \delta_2$$

$$b = d_2 - a$$

$$c = d_1 \sin \delta_3$$

$$d = (c^2 + b^2)^{1/2}$$

$$A = RAD \tan \delta_1$$

$$B = RAD \tan \delta_2$$

We are now in possession of the dimensions of the sides of the three great circle distances projected onto a plane tangent to the sphere at point b. Therefore, in solving for the angle on the plane at we also get the angle on the earth. The angle is given by a modification of the Pythagorean theorem by which the angle in question

$$\beta = \cos^{-1}((A^2 + B^2 - d^2)/(2A * B)) \qquad (50)$$

Thus we can, by knowing the points, sum the angles, count the sides and find the area of the inscribed polygon.

From this knowledge of areas we can readily find a measure of divergence by marking the apices of the polygon with points at small

cloud elements moving with the wind field, and comparing one area with another at some later time.

b. Circular and Spiral Areas. Given three points on the picture of the earth it is possible to find the area enclosed by those three points on the surface of the terrestrial sphere. This area is a function of the solid angle subtended by this area and is given by the expression

$$A = 2\pi R^2 (1 - \cos(\frac{\gamma}{2})) \tag{51}$$

where γ is the solid angle subtending this area and R is the radius of the earth. Since the derivation of this expression is rather trivial and undoubtedly extant, I will not bore the reader with the details of the solution but rather I will give him an idea of how it was done.

A slice of the spherical cone into four equal parts along its axis of symmetry will enable us to visualize the process by which the area can be found (Fig. 18). First we must find the volume which is described by rotating Fig. 18 through 2Pi radians around the x axis. For the triangular portion the volume is $\int_0^{R\cos(\gamma/2)} \pi y^2 dx$ and for the rest $\int_{R\cos(\gamma/2)}^{R} \pi y^2 dx$ In the first case $y^2 = x^2 \tan^2\theta$ and in the second $y^2 = (R^2 - x^2)$ so that the above integrations are added with the above substitutions to get

$$R^2\pi \left\{ \int_0^{R\cos(\gamma/2)} \cos^2\frac{\gamma}{2} \tan^2\frac{\gamma}{2} dx + \int_{R\cos\gamma/2}^{R} (1 - \cos^2\frac{\gamma}{2}) dx \right\}$$

which when integrated and multiplied by the ratio of area of a sphere to

volume $4\pi R^2 / \frac{4}{3}\pi R^3 = 3/R$ gives us, after grouping terms, the formula

$$A = 2\pi R^2 (1 - \cos (\frac{\gamma}{2})) \tag{52}$$

The technique for finding $\gamma/2$ has as its data prerequisites three points on the picture, which are on the perimeter of the area in question. Using the technique for finding great circle distances between two points and the angles subtended by them we find the chord triangle dimensions, which is the planar projection of the spherical triangle, on a plane intersecting the sphere at the apeces of the spherical triangle. The angle subtended by side 1, α, is computed and the chord of the angle $S_1 = 2$ RAD sin $(\frac{\alpha}{2})$ is taken. For side 2, the angle β, $S_2 = 2$ RAD sin $(\frac{\beta}{2})$ δ, $S_3 = 2$ RAD sin $(\frac{\delta}{2})$, and for side 3, so that we have a chord triangle inscribed within the cone (Fig. 18a).

where α is given by $\alpha = \cos^{-1} (\frac{(S_1^2 + S_2^2 - S_3^2)}{2S_1S_2})$

The center is that point equidistant from the apices, and is also the center of an inscribed circle

$$(x-h)^2 + (y-k)^2 = r^2 \tag{53}$$

where $\sin (\frac{\gamma}{2}) = r/RAD$ or

$$\frac{\gamma}{2} = \sin^{-1}(\frac{r}{RAD}), \quad x_a = 0; \quad y = 0 \tag{54}$$

$$x_b = S_2 \cos \alpha, \qquad y_b = S_2 \sin \alpha$$

Expanding 1 we get $x^2 - 2xh + h^2 + y^2 - 2ky + k^2 = r^2$.

Substituting points a and b and c and subtracting, we get

$$h^2 + k^2 = r^2$$

$$h^2 + y_c^2 - 2ky_c + k^2 = r^2$$

$$x_b^2 - 2x_b h + y_b^2 - 2y_b k = 0$$

and

$$y_c - 2k = 0$$

$$k = y_c/2 \tag{55}$$

$$-2x_b h = -x_b^2 - y_b^2 - 2y_b y_c$$

$$h = (x_b^2 + y_b^2 + y_b y_c)/2x_b^2 \tag{56}$$

$$r = (h^2 + k^2)^{1/2} \tag{57}$$

$$\gamma/2 = \sin^{-1}(r/RAD) \tag{58}$$

c. Spirals and their Areas. To analyze for a spiral as in a cyclone, on the earth, it is perhaps best to calculate the constant of their axes. If it is indeed a constant, it should not vary more than an acceptable ϵ for all angles and radial arms. A spiral is best measured in polar coordinates, so that the great circle radial arm, ρ, is some simple function of θ. The simplest spirals are given below. (Fig. 19)

The curvilinear distance ρ and the angle θ can be found using the above techniques in sections 4e and 6a.

A section of area, knowing the ρ as a function of the angle θ can be found by subtracting $\langle \rho_1 \rangle$ from $\langle \rho_2 \rangle$ and multiplying by $\Delta\theta$ (Fig.20) incrementing θ from $\theta = 0$ to the final θ. By using the formula for circular areas on a sphere, and letting γ be the angle that subtends ρ

so that the area increment would be

$$\Delta\theta\ 2\pi\ RAD^2\ ((1 - \cos\ (\frac{\langle\gamma_1\rangle}{2}) - (1 - \cos\ (\frac{\langle\gamma_2\rangle}{2})) \tag{59}$$

or for an infinitesimal element the whole area is

$$A_{spiral} = 2\pi\ RAD^2 \int_0^{\theta_{final}} (\cos\ (\Phi_1\ (\frac{\theta}{RAD})) - \cos\ (\Phi_2\ (\frac{\theta}{RAD})))d\theta \tag{60}$$

where Φ is ρ as a function of θ, or by incrementing

$$A_{spiral} \simeq \sum_{i=1}^{n} \Delta\theta_i\ 2\pi\ RAD^2\ (\cos\ (\frac{\langle\gamma_1\rangle}{2}) - \cos\ (\frac{\langle\gamma_2\rangle}{2})). \tag{61}$$

7. Summary

Obviously, the only feasible way of handling all of this multitude of calculations is by computer. The above paper is the basis for a Fortran 63 Program which took nearly four months to write, including the derivations included in this paper. The program is very long, extremely complicated, and is in double precision to insure against significant round-off errors. It has 31 subprograms, 15 of which are functions and the remaining 16 subroutines. It takes 5 minutes just to compile and initiate execution on the CDC 1604. Obviously, if it were not for the advent of the computer as well as the satellite, the value of the data achieved from the satellite could never fully be appreciated.

Acknowledgments

The author takes pleasure in thanking the Environmental Science Services Administration and the National Aeronautics and Space Administration for the support for this research from their grants.

He also wishes to thank the editors, Prof. Verner E. Suomi and Mr. Kirby J. Hanson for their encouragement and support in the preparation of this paper. He also wishes to thank his colleagues, Mr. Jack I. Kornfield and Dr. Stephen K. Cox, for the stimulating discussions that they participated in with the author, and from which many of the ideas in this paper came. My special thanks to Mr. Peter Guetter for his great help in writing the computer programs based on these calculations, and to Mr. John W. Turner for his excellent drafting of the illustrations. Also I wish to thank Prof. E. G. Bombolakis of Boston College for the understanding of the concepts of the Mohr strain diagram and for the strain and tensor theory which he imparted to me, and which form a good part of the basis of this paper.

List of Illustrations

F. Nicholson

1. Scan Cones of Satellite's line of sight.

2. Scan Planes

3. Intersection of scanplanes and earth.

4. Earth-Satellite Geometry

5. Intersection of scan cones and earth and its projections.

6. Deviations of quasi-hyperbola from equivalent radial plane.

7. Mohr Strain Diagram

8. Multiply strained and rotated circular image.

8a. Shear vs. Plane strain.

9. Elliptical image of earth.

10. Rotated and translated axes.

11. Real "equivalent" radius vs. pictorial.

12. Rotation of points from landmark.

13. Similar triangles separated by $\angle$ delta subtending great circle distance between two points.

14. Great circle distance subtending $\angle$ delta.

15. Triangle displaying 3rd side in relation to two sides and intervening angle.

16. Navigation transformation from Pictorial Cartesian to real earth spherical coordinates.

16a. A different view of (16).

17. Spherical angle on earth, α.

17a. Side of tetrahedron with apex at point of interest.

18. Conal cross section with inscribed spherical and plane triangles.

18a. Conal cross section.

19 a) Spiral of Archimedes b) Logarithmic or Equiangular Spiral
c) Hyperbolic Spiral d) Parabolic Spiral

20. Cyclonic spiral in quasi polar coordinates.

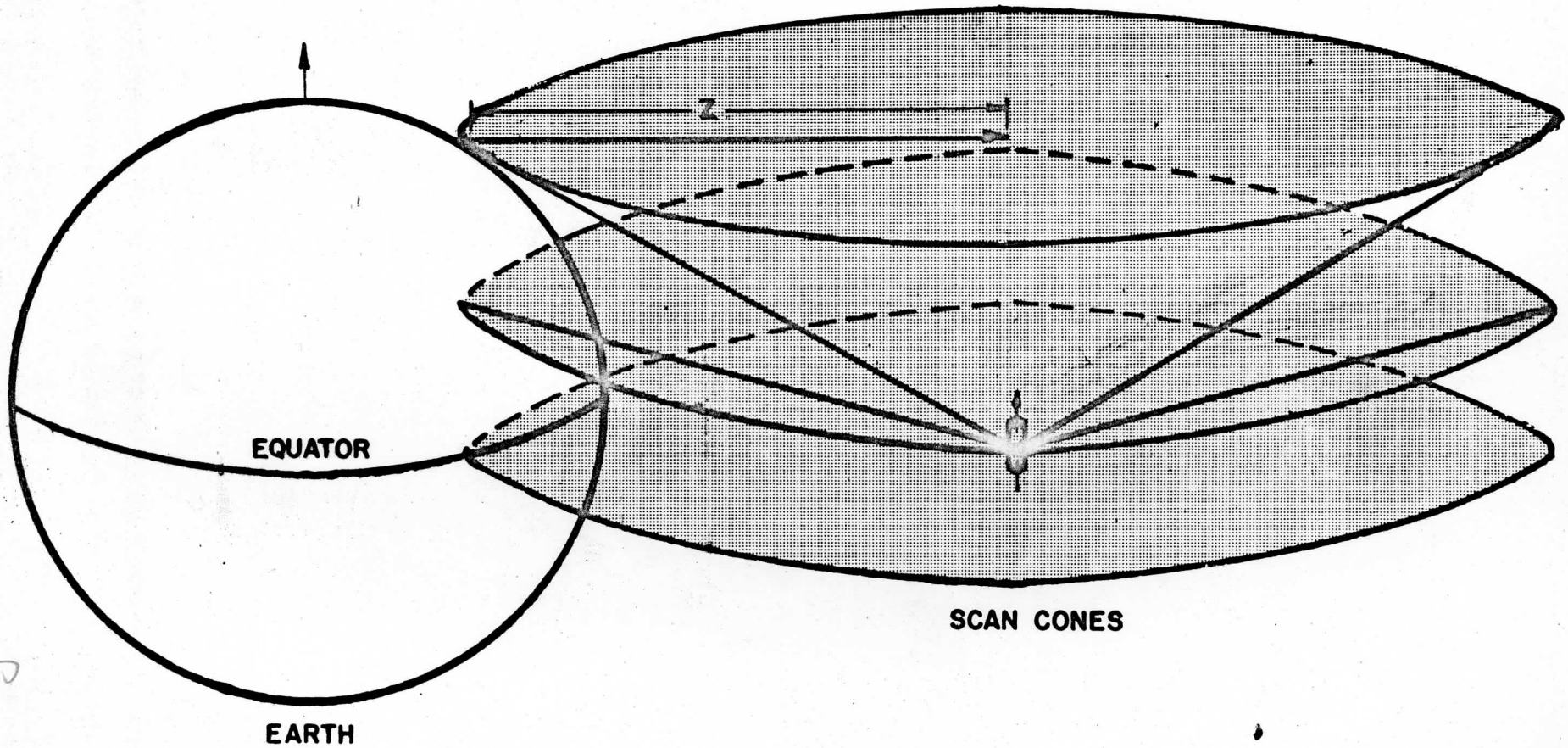
Z
EQUATOR
SCAN CONES
EARTH

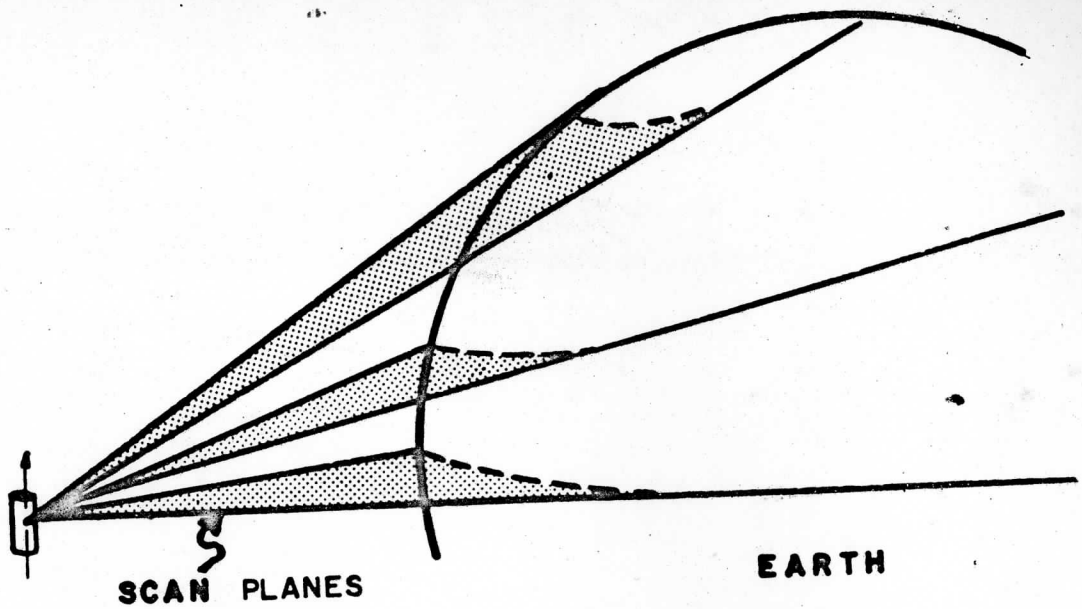

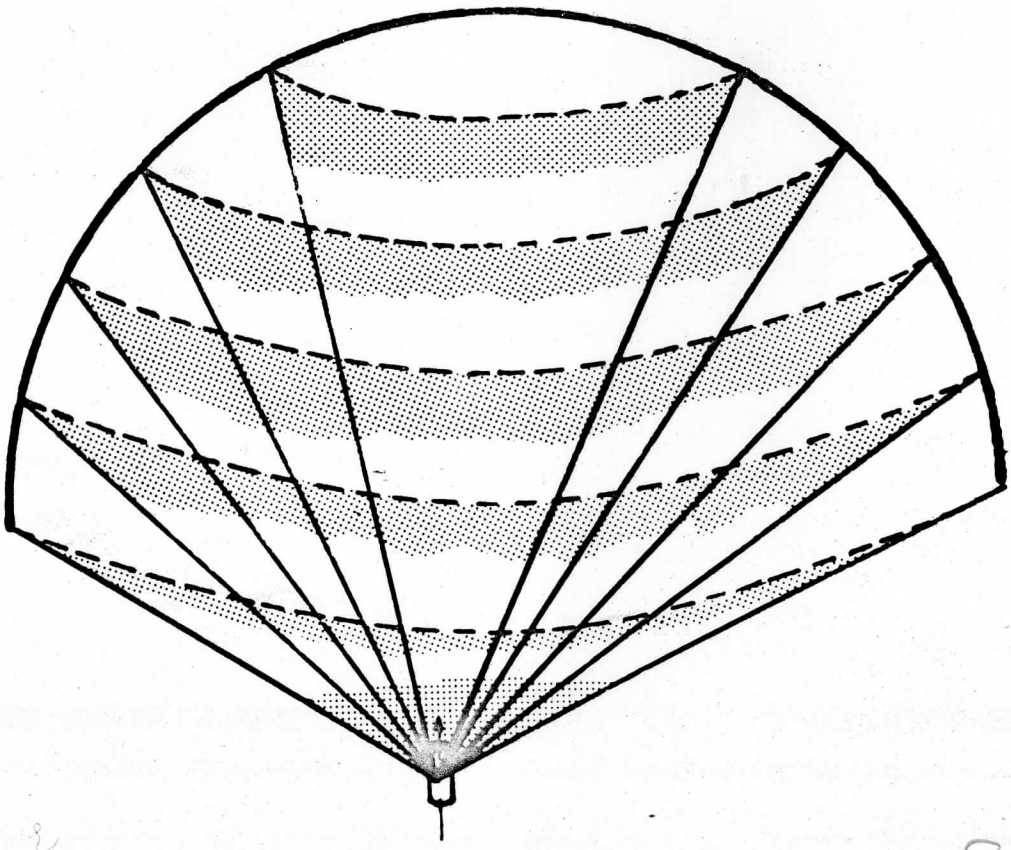

fig 2

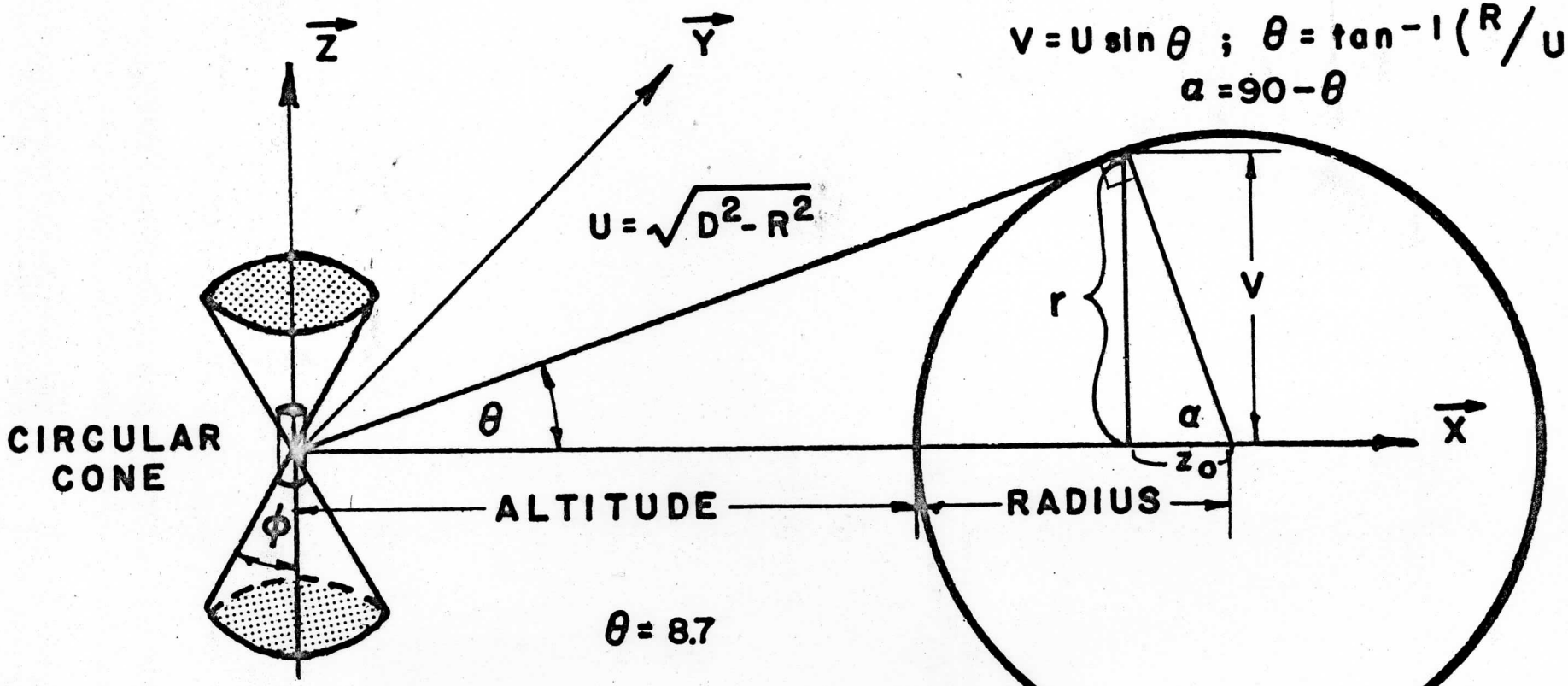

$\tan\phi = \text{DIST}/C$ DIST = ALTITUDE + RADIUS

$X^2 + Y^2 - \frac{\text{DIST}^2 Z^2}{C^2} = 0$ $(X - \text{DIST})^2 + Y^2 + Z^2 = \text{RAD}^2$

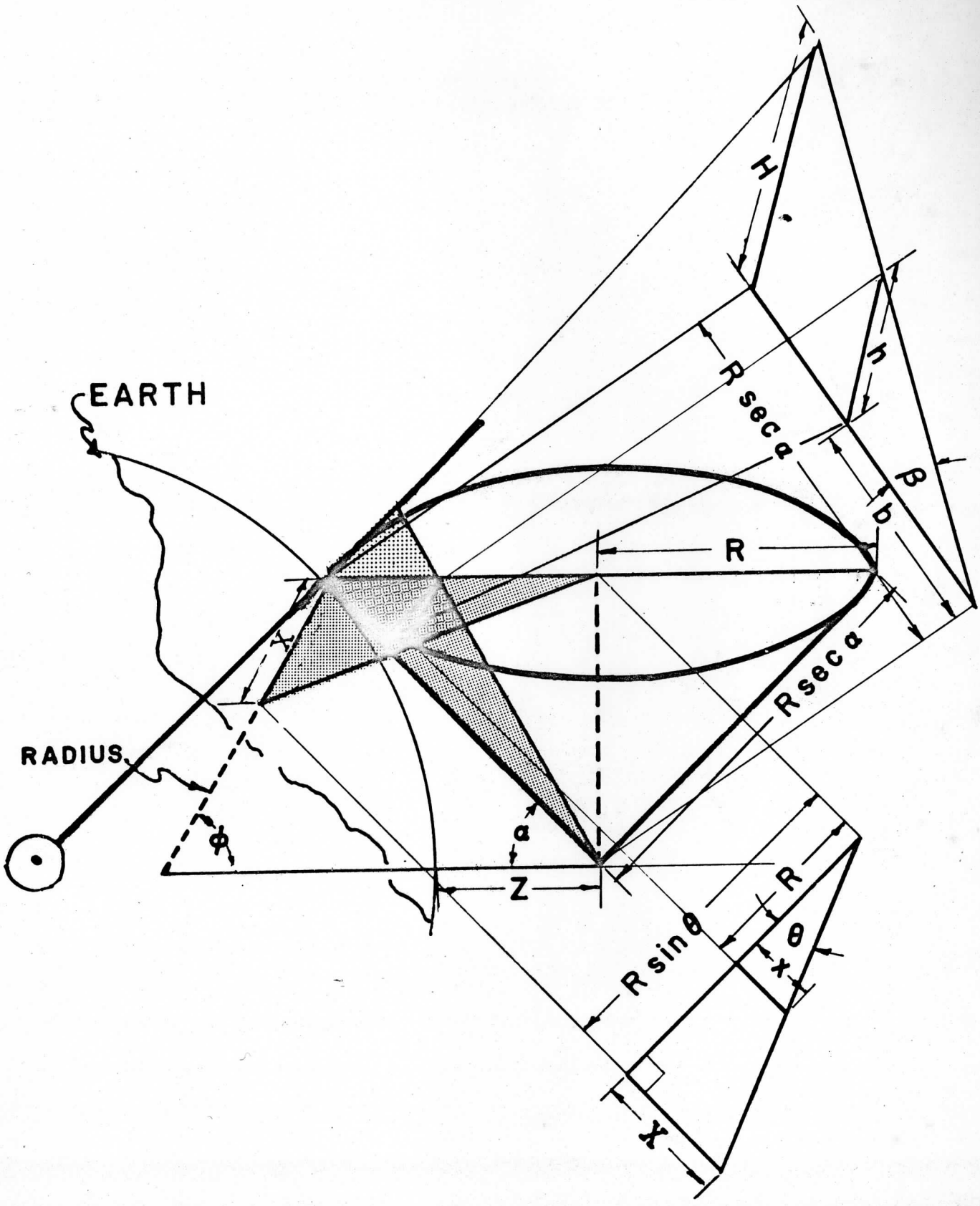

Fig 4

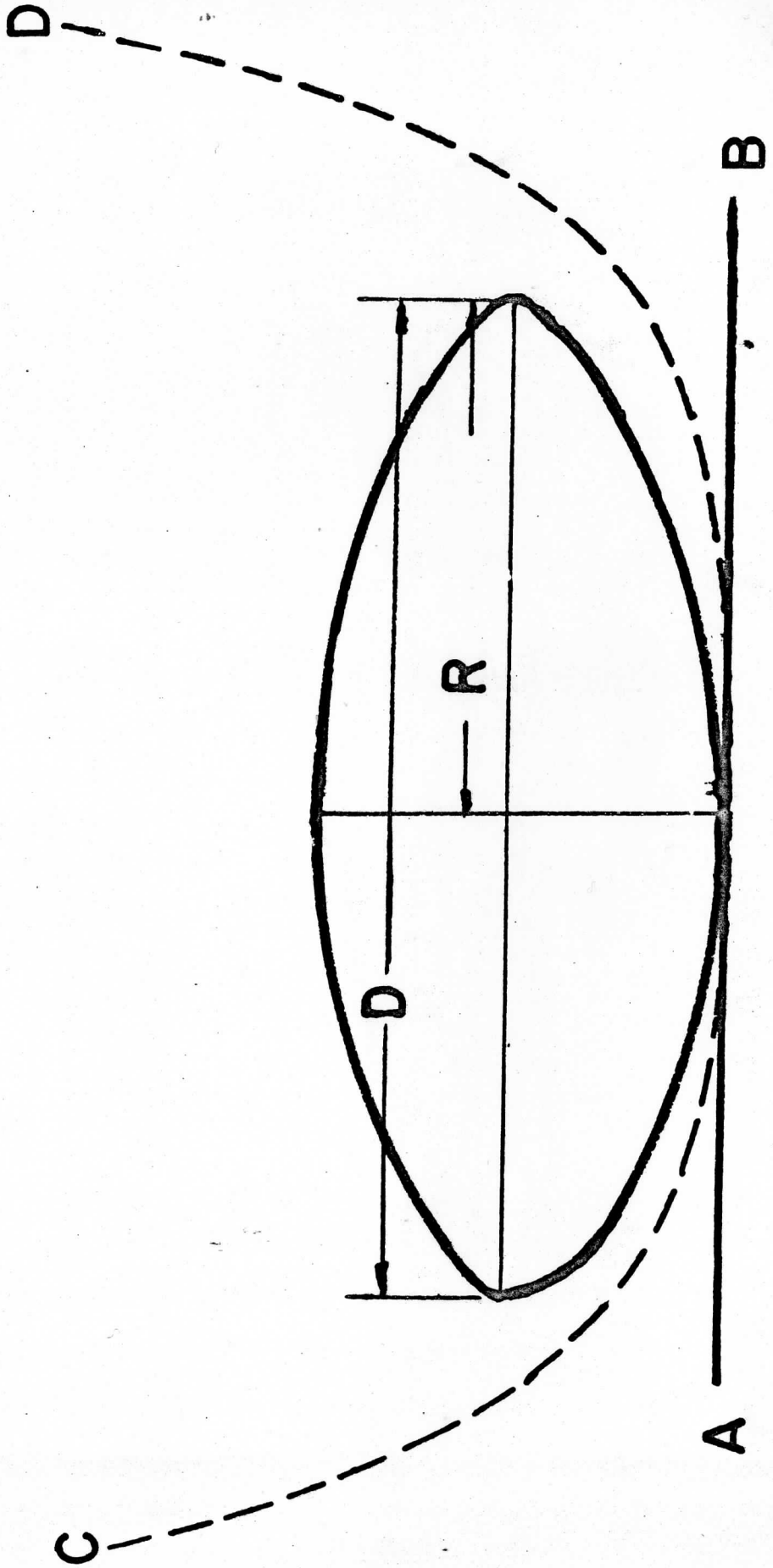

Fig 5

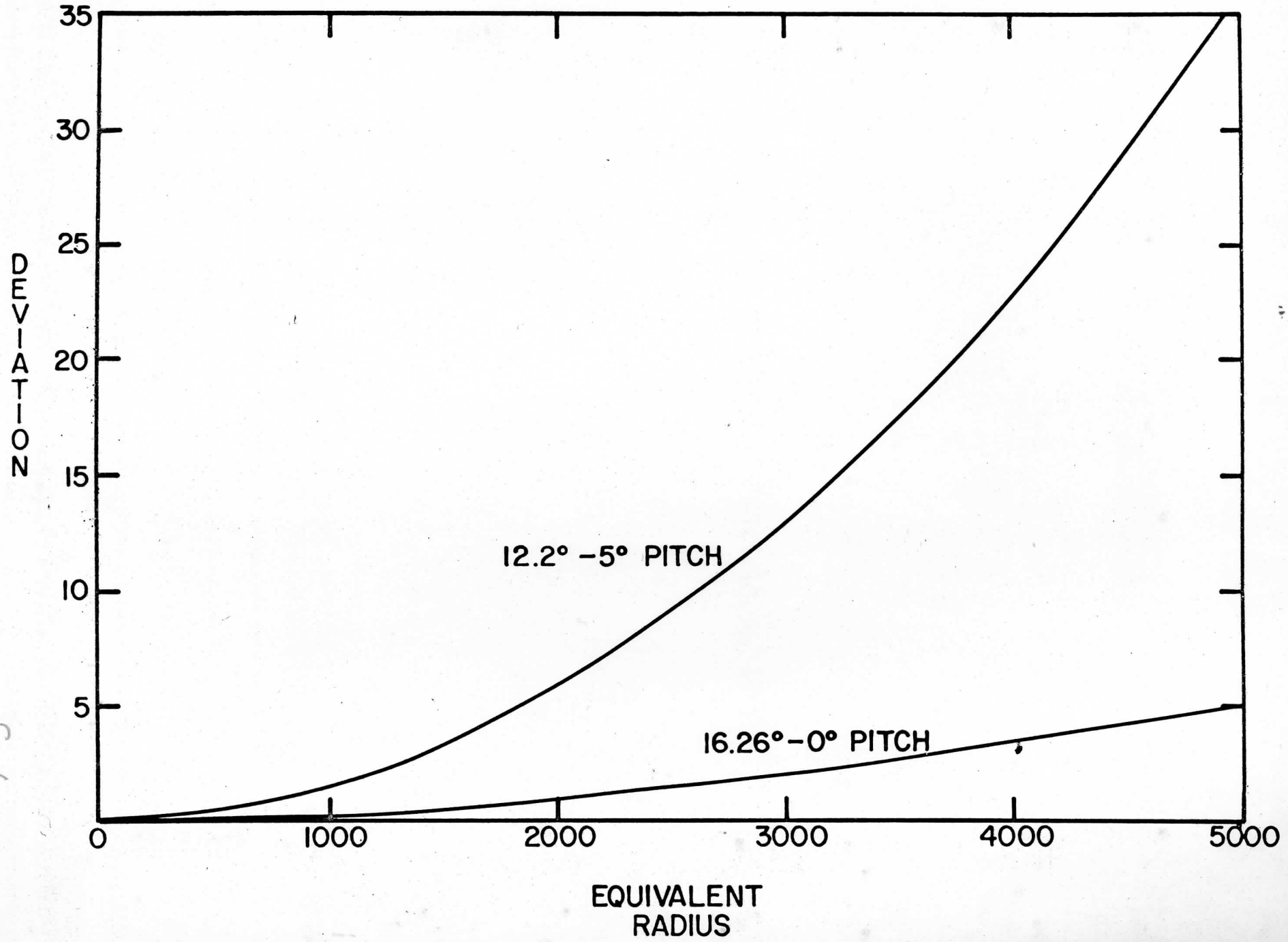
35
30
25
20
15
10
5
DEVIATION
12.2° -5° PITCH
16.26°-0° PITCH
0
1000
2000
3000
4000
5000
EQUIVALENT
RADIUS

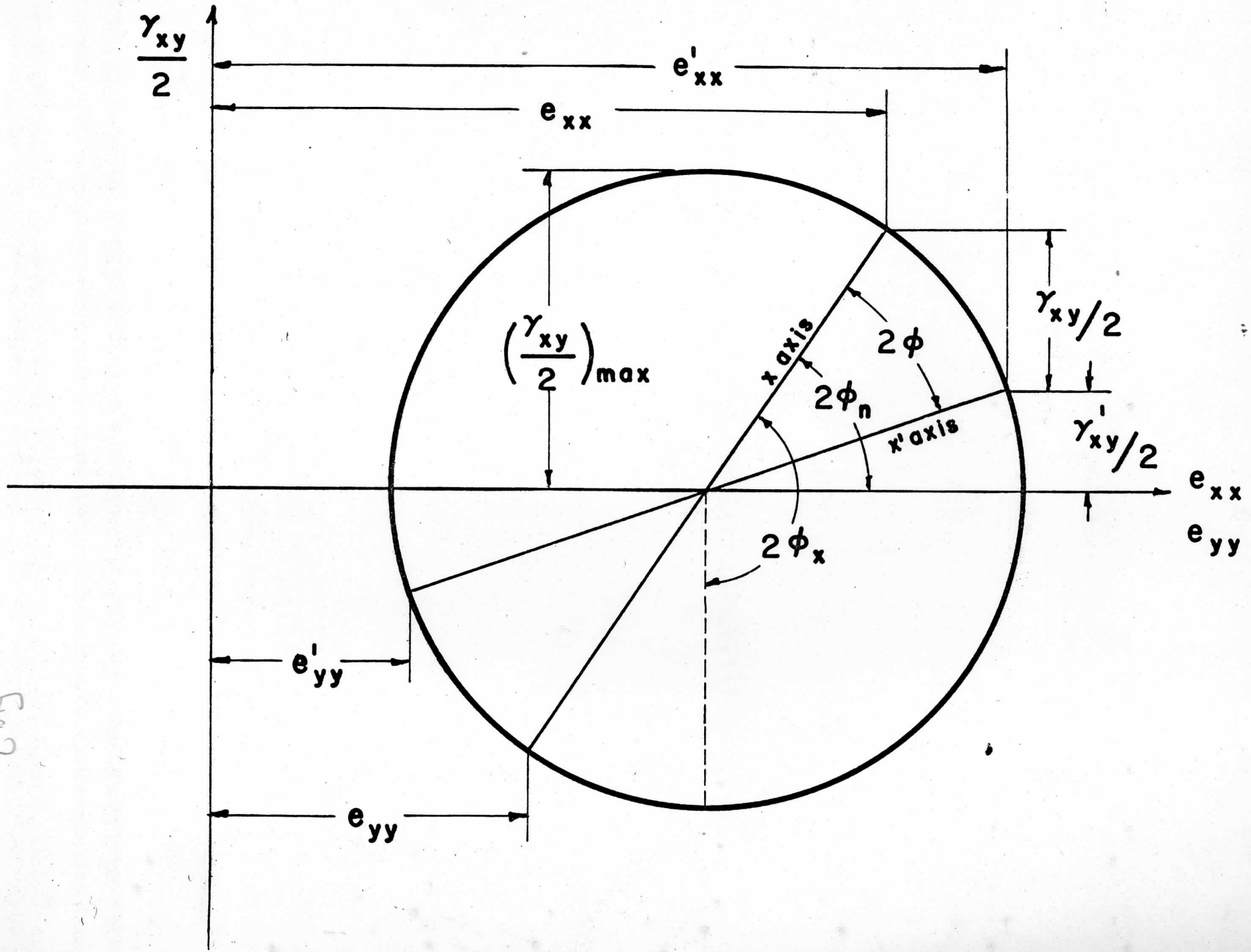
$\frac{\gamma_{xy}}{2}$
e'_{xx}
e_{xx}
$\left(\frac{\gamma_{xy}}{2}\right)_{max}$
x axis
2ϕ
$2\phi_n$
x' axis
$\gamma_{xy}/2$
$\gamma'_{xy}/2$
e_{xx}
e_{yy}
$2\phi_x$
e'_{yy}
e_{yy}

Fig 2

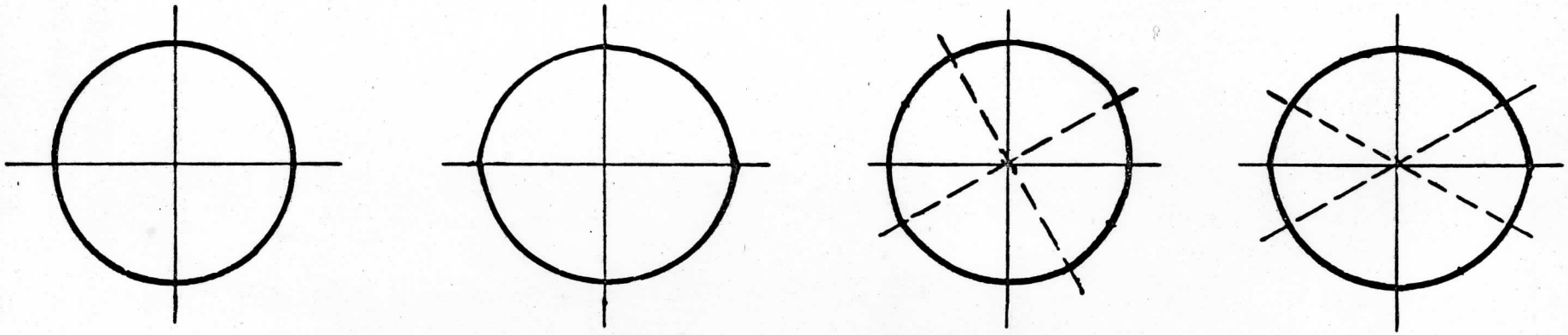

Fig 8

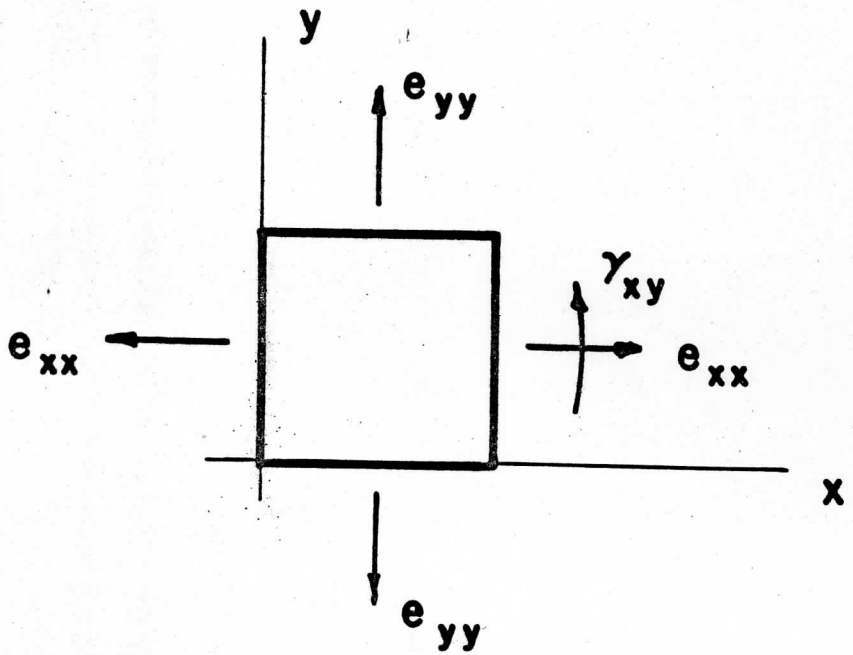
y
e_{yy}
γ_{xy}
e_{xx}
e_{xx}
x
e_{yy}

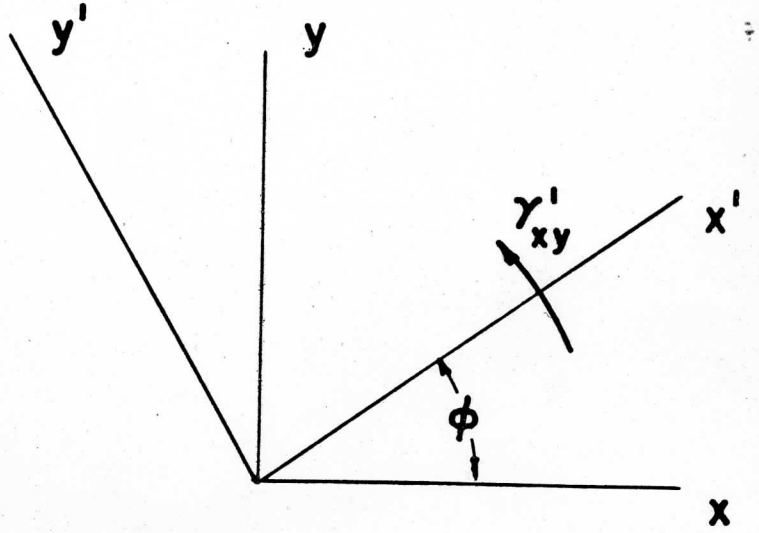
y'
y
γ'_{xy}
x'
ϕ
x

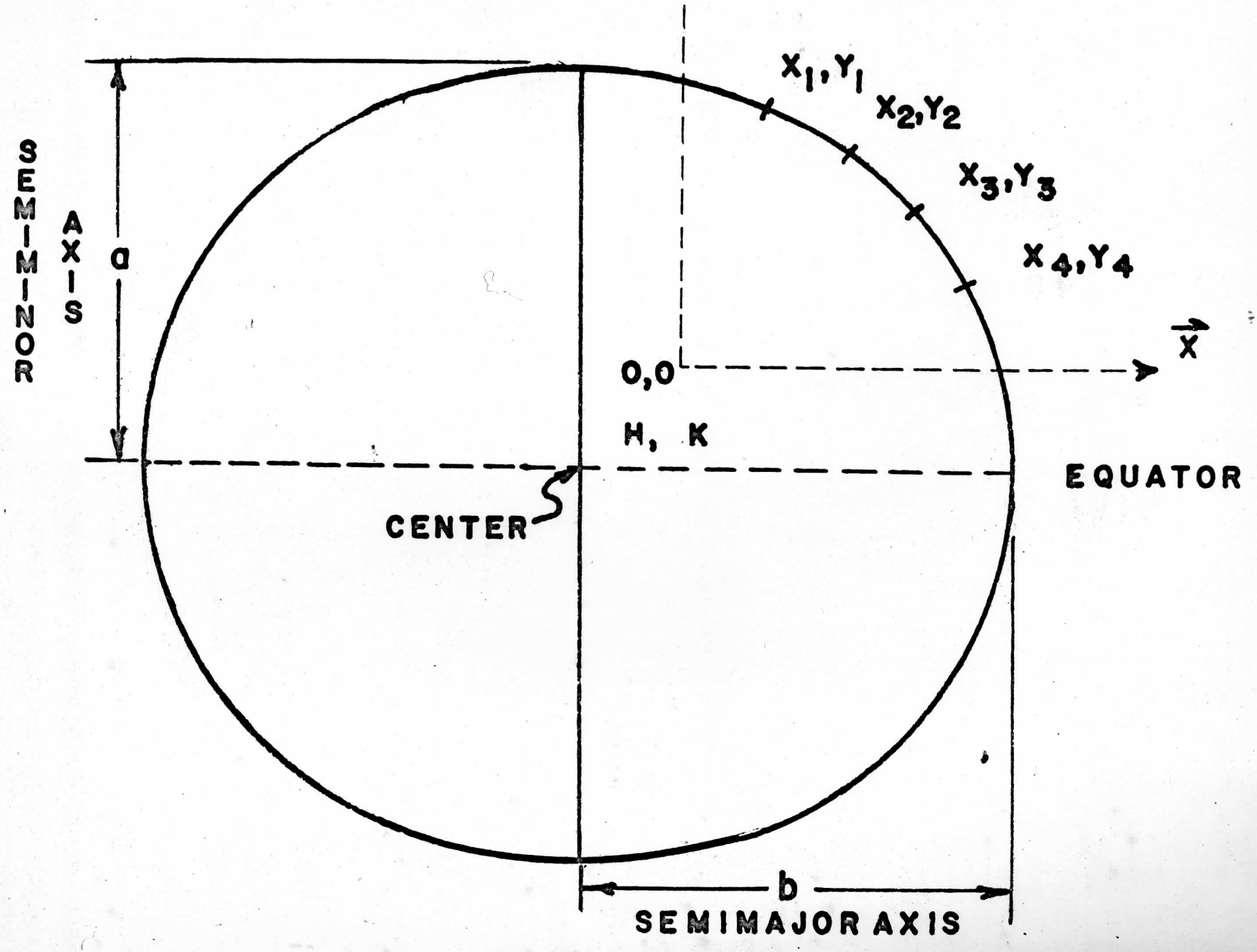
SEMIMINOR AXIS
a
X_1, Y_1
X_2, Y_2
X_3, Y_3
X_4, Y_4
$\vec{X}$
0,0
H, K
EQUATOR
CENTER
b
SEMIMAJOR AXIS

Fig 9

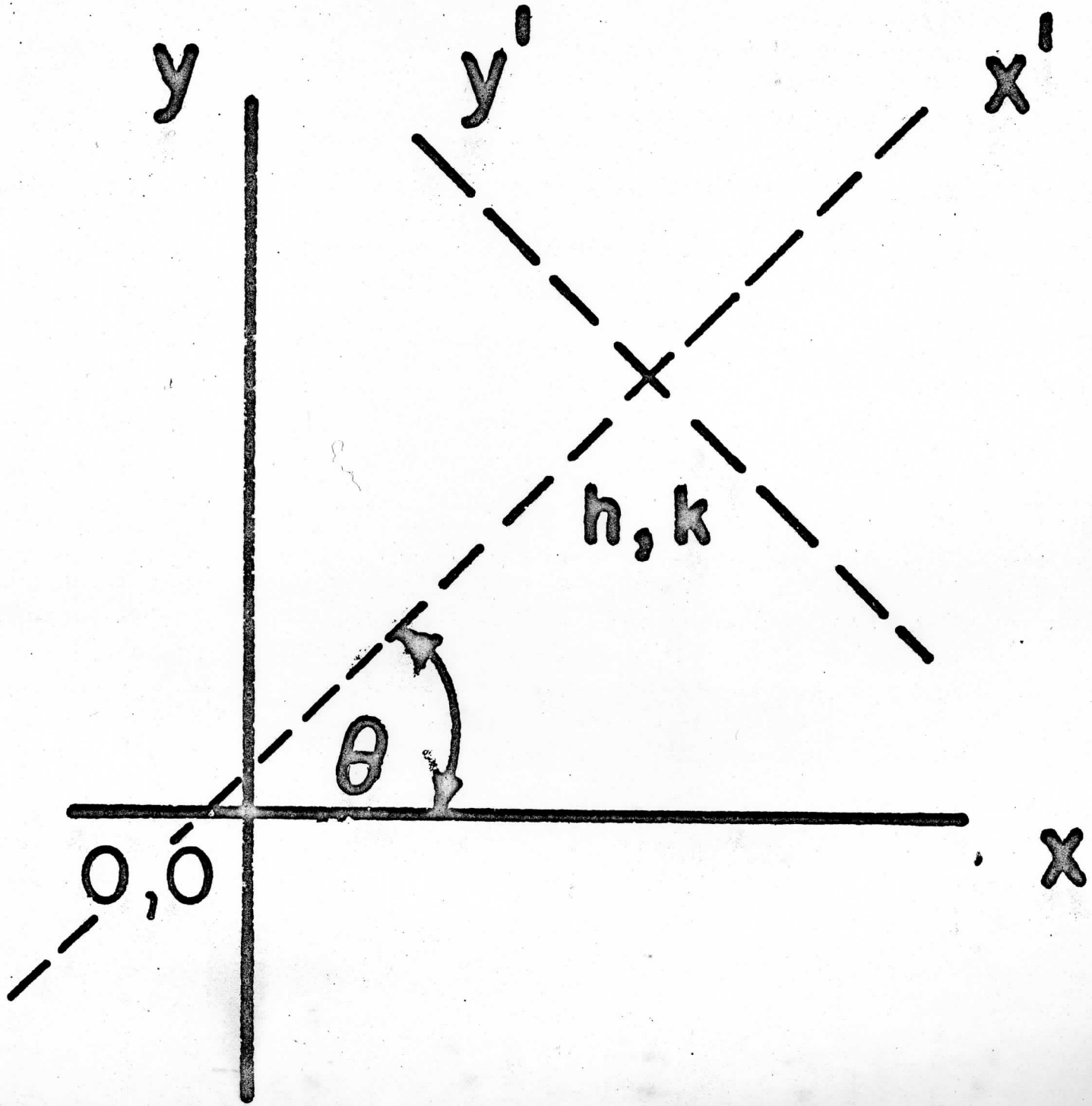

Fig 10

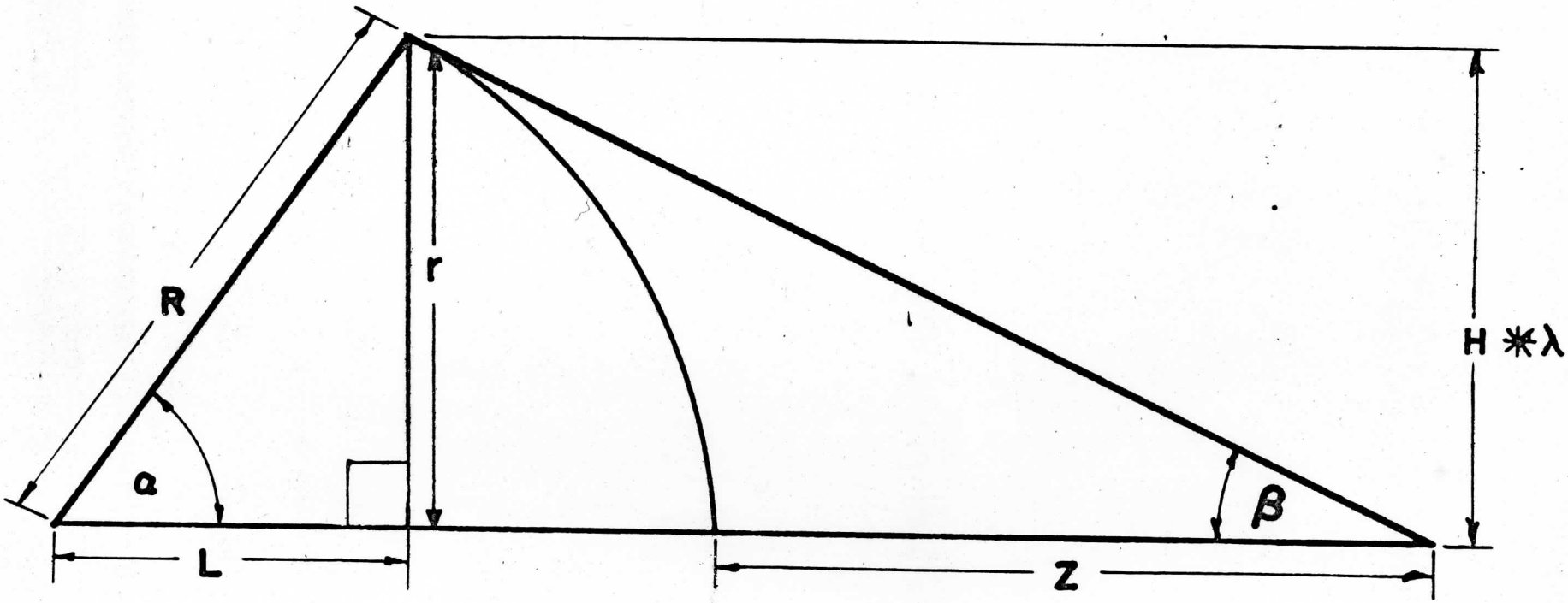

Fig 1

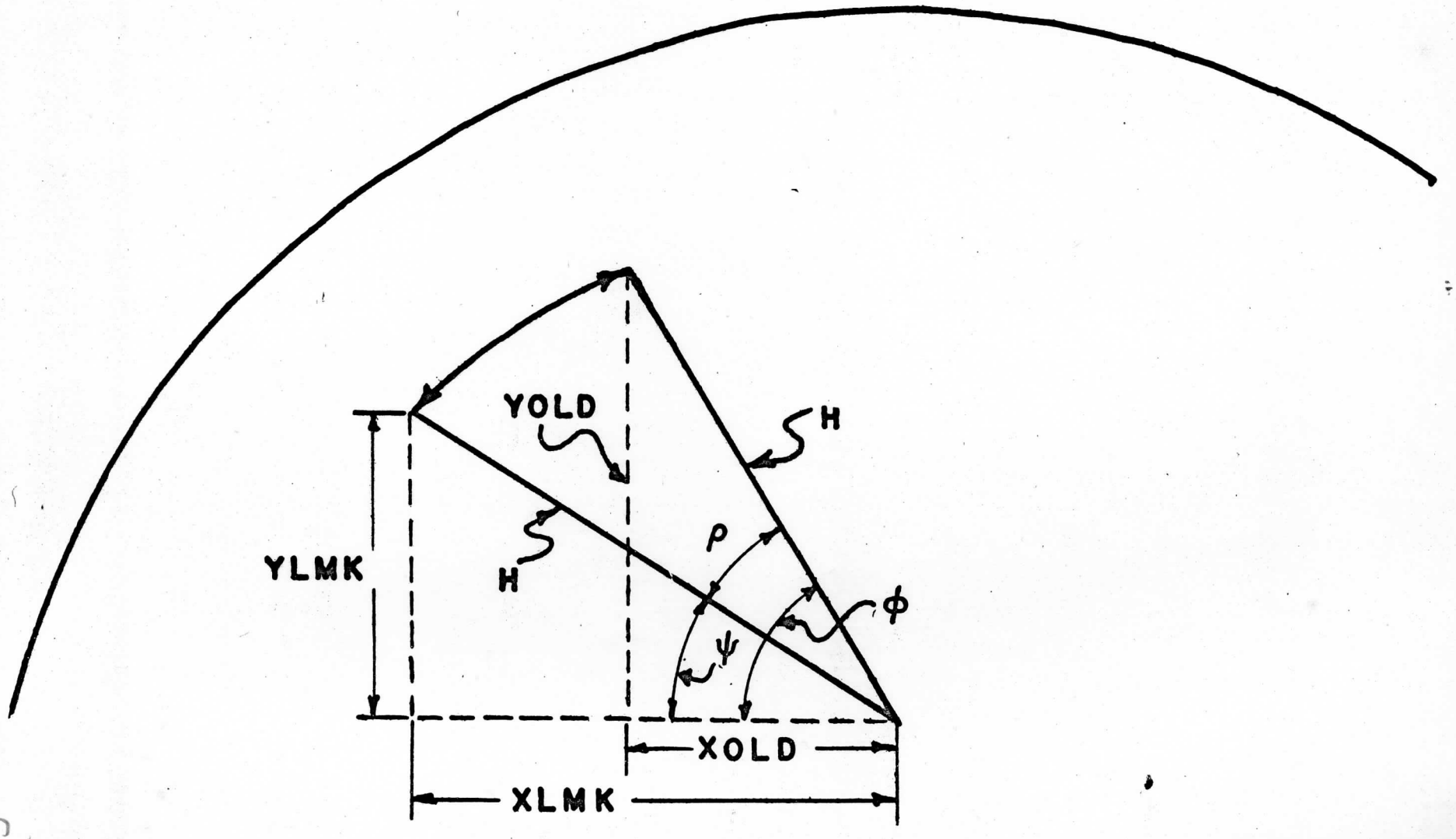

Fig 12

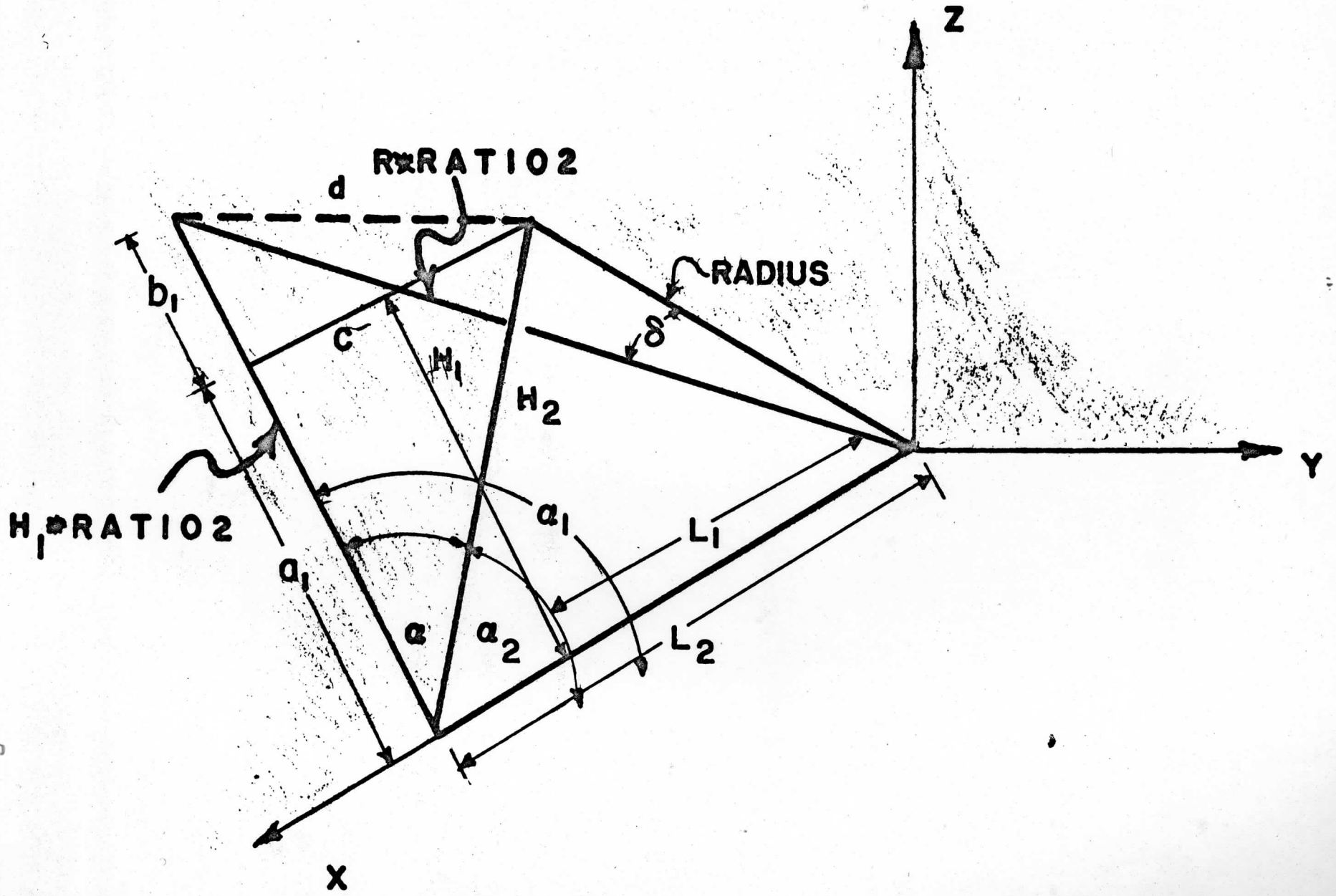

Fig 13

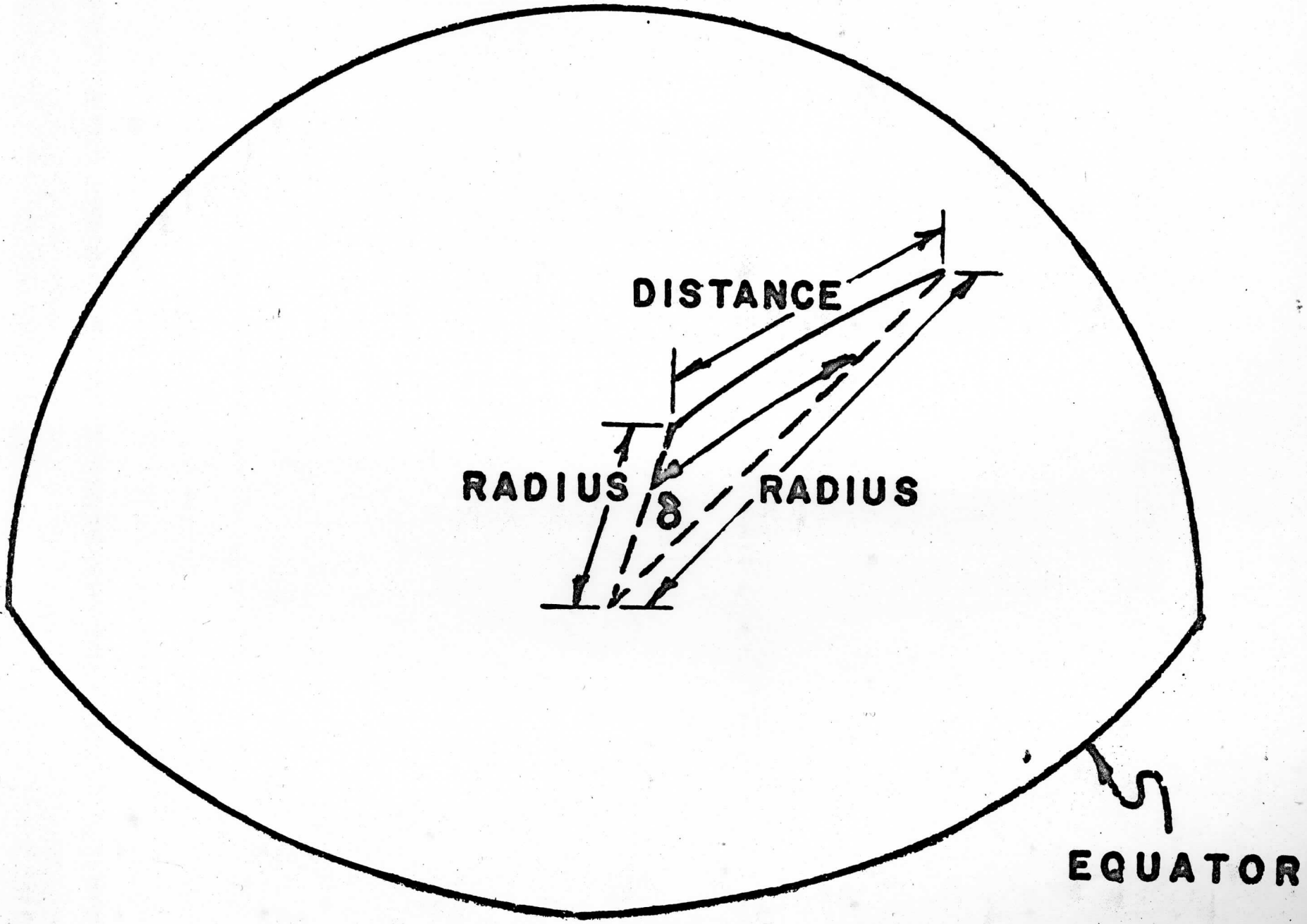

Fig 14

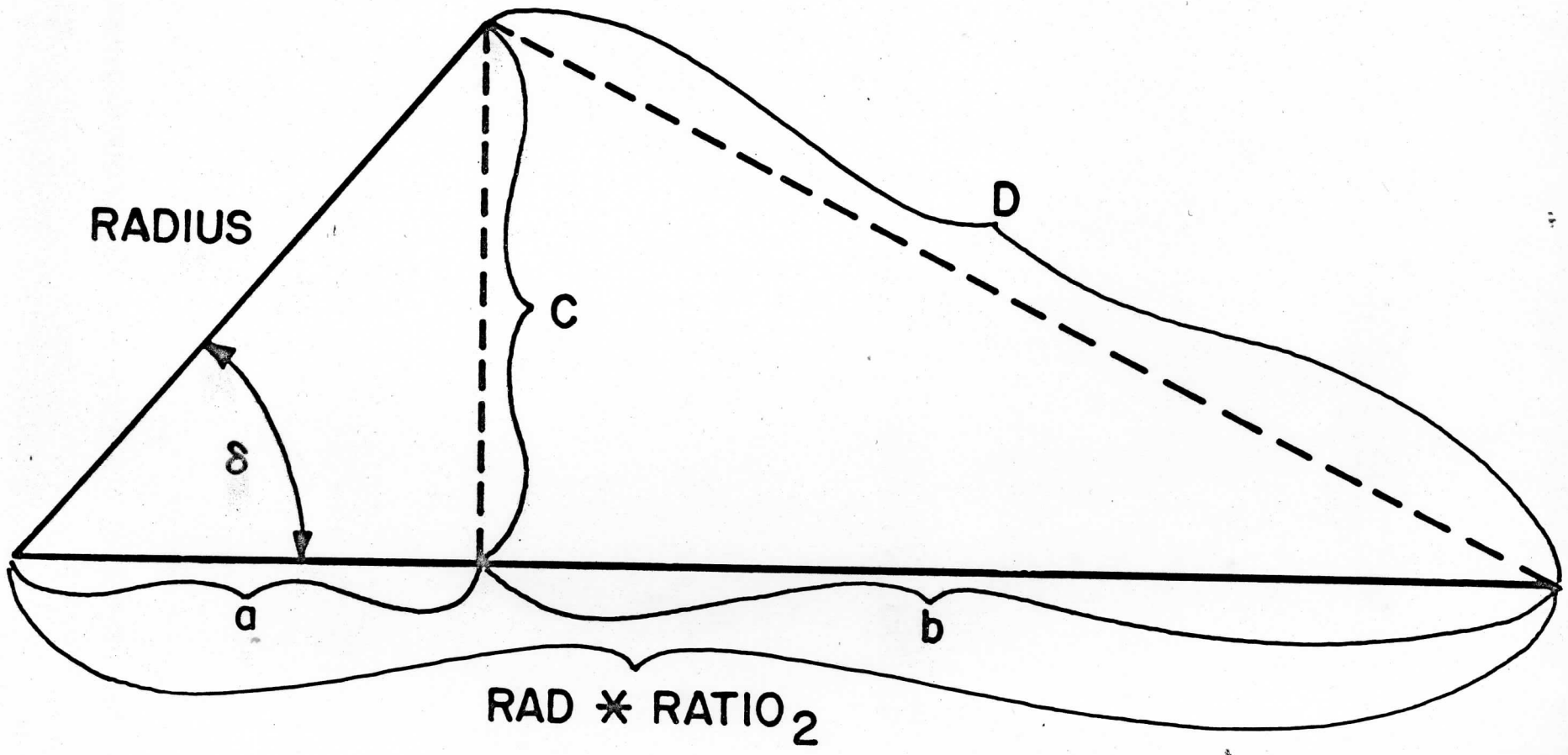

Fig 15

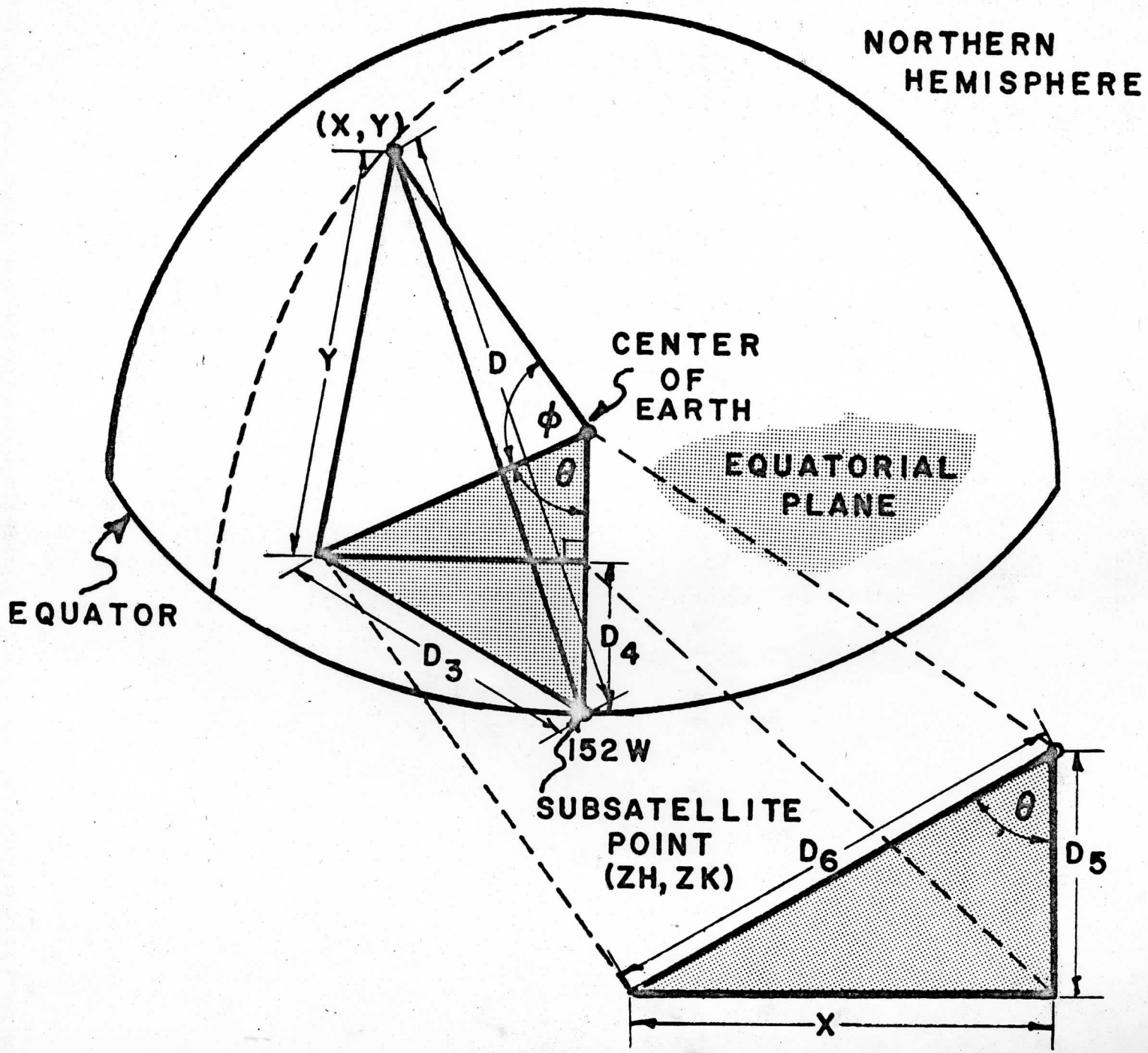
NORTHERN
HEMISPHERE
(X, Y)
Y
D
CENTER
OF
EARTH
φ
θ
EQUATORIAL
PLANE
EQUATOR
D3
D4
152 W
SUBSATELLITE
POINT
(ZH, ZK)
D6
θ
D5
X

FIG 16

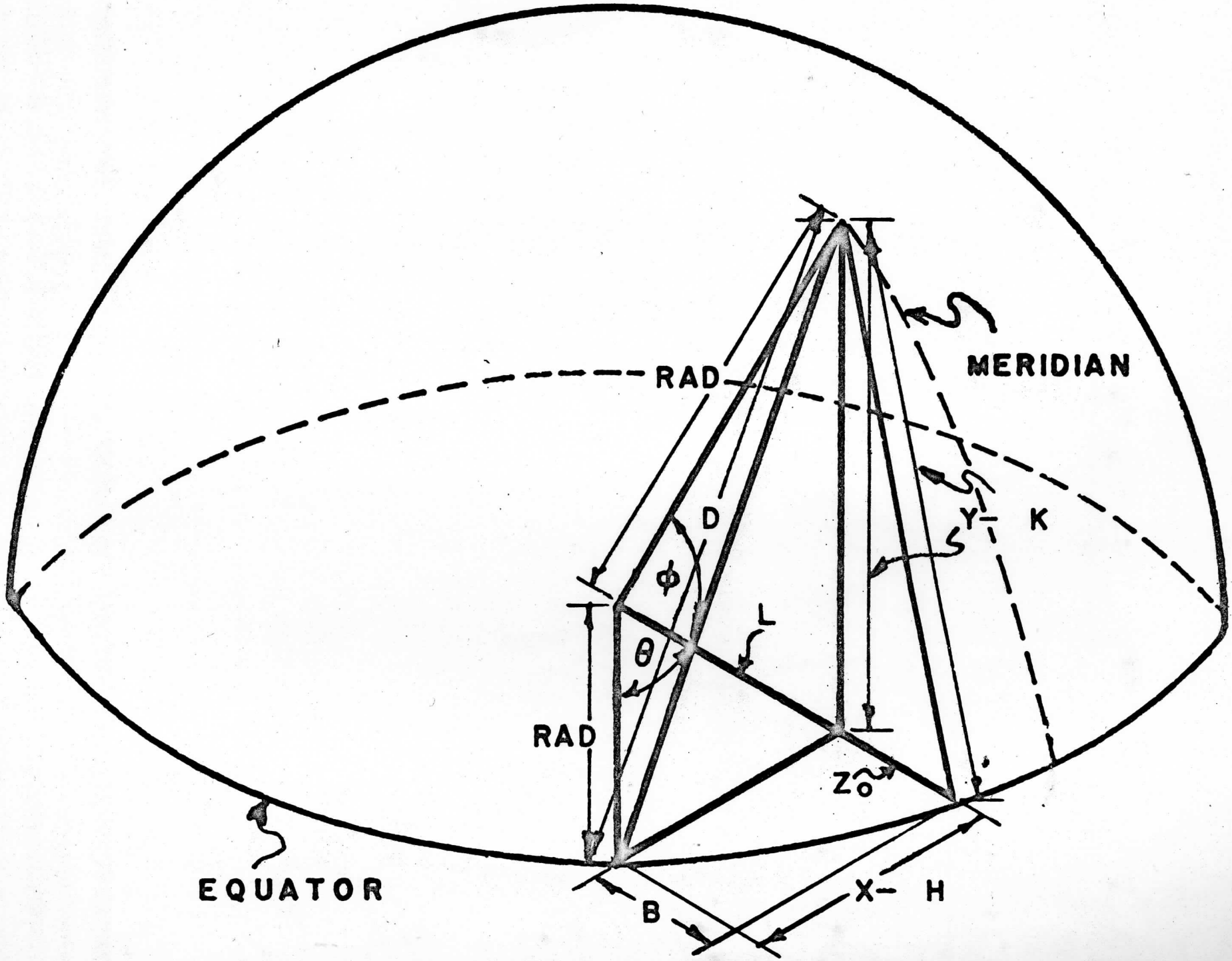

Fig 16a

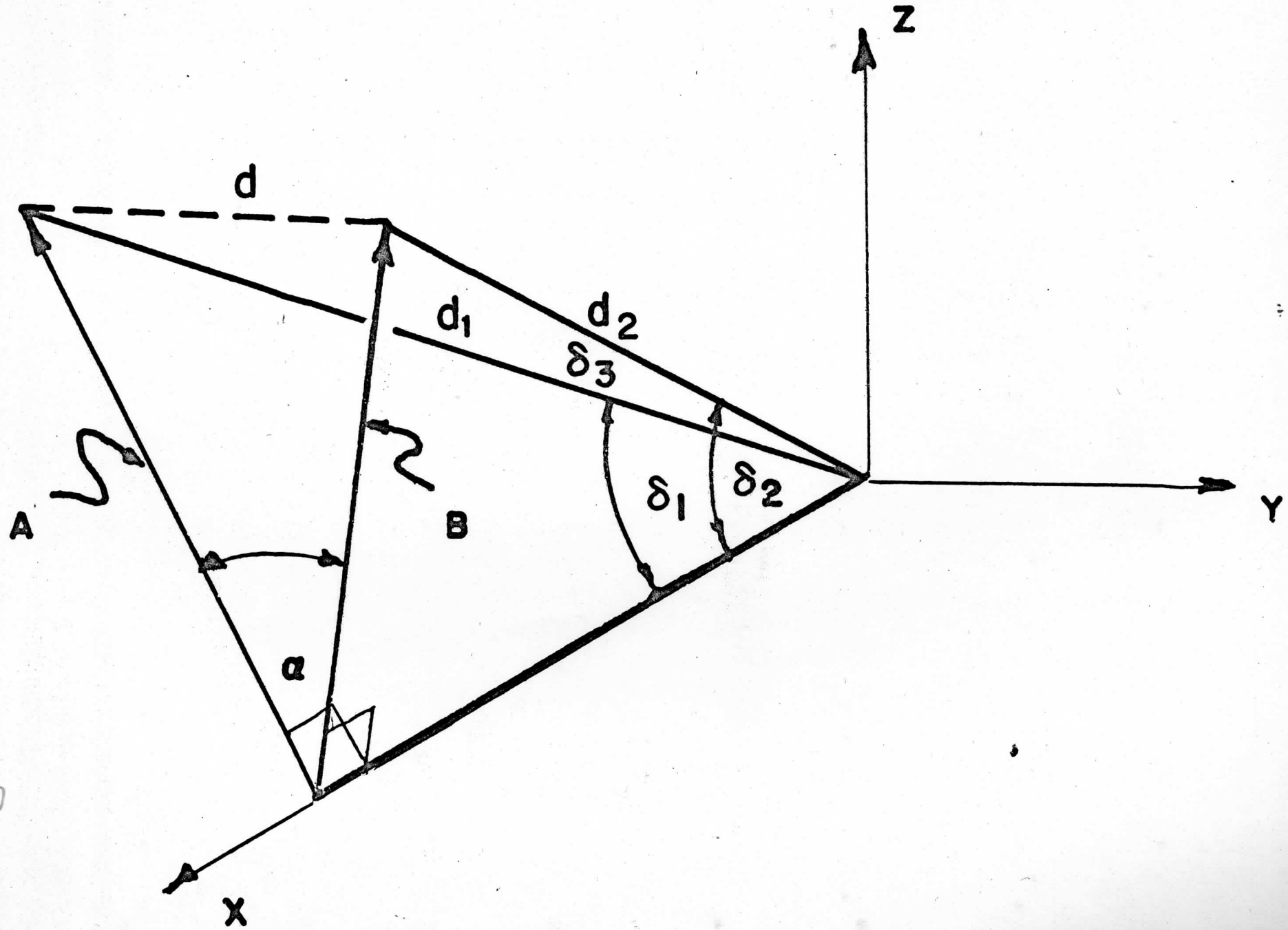
Z
d
d1
d2
δ3
δ1
δ2
A
B
Y
α
X

$d_1 = R \sec \theta$

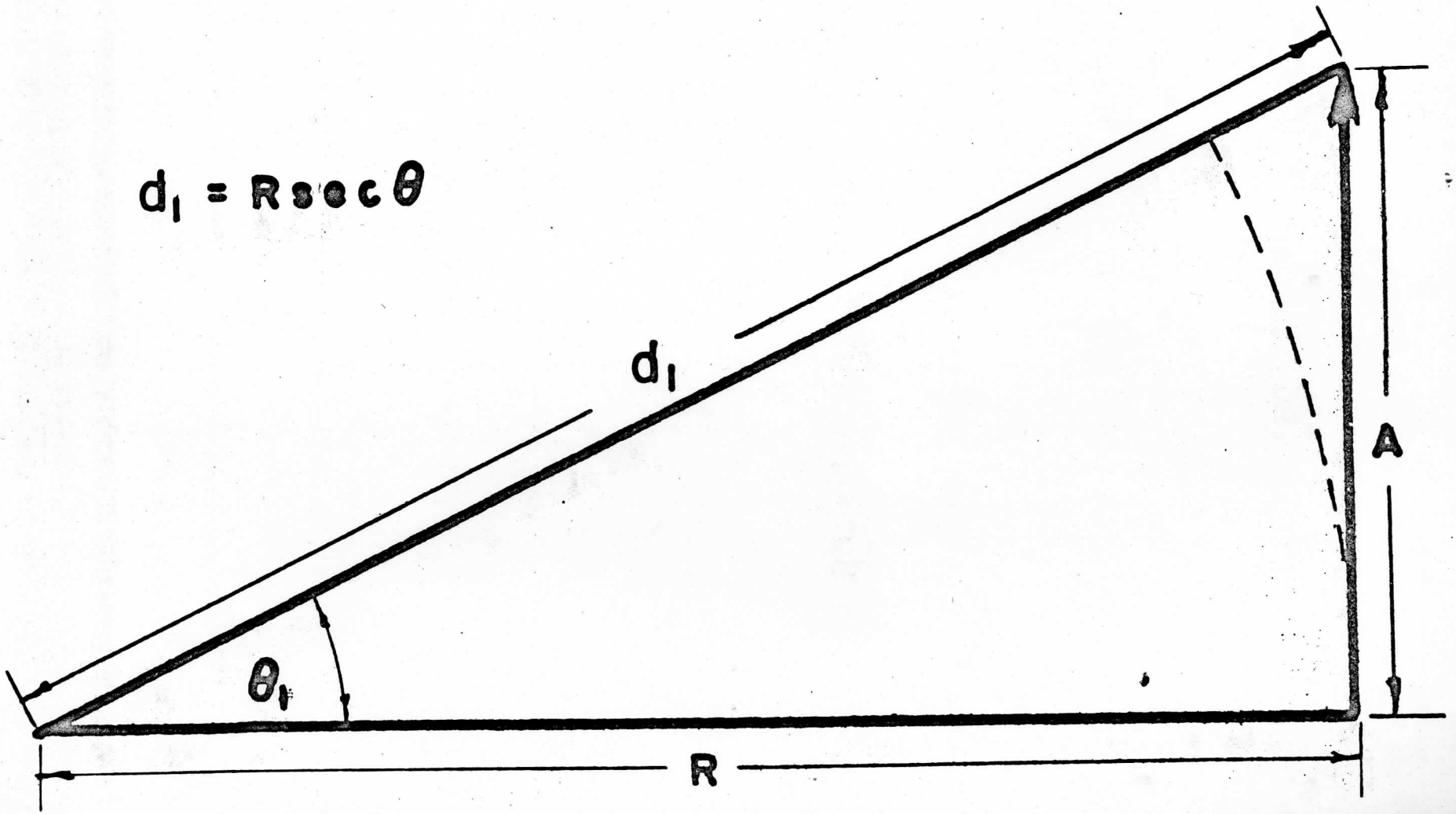

Fig 12a

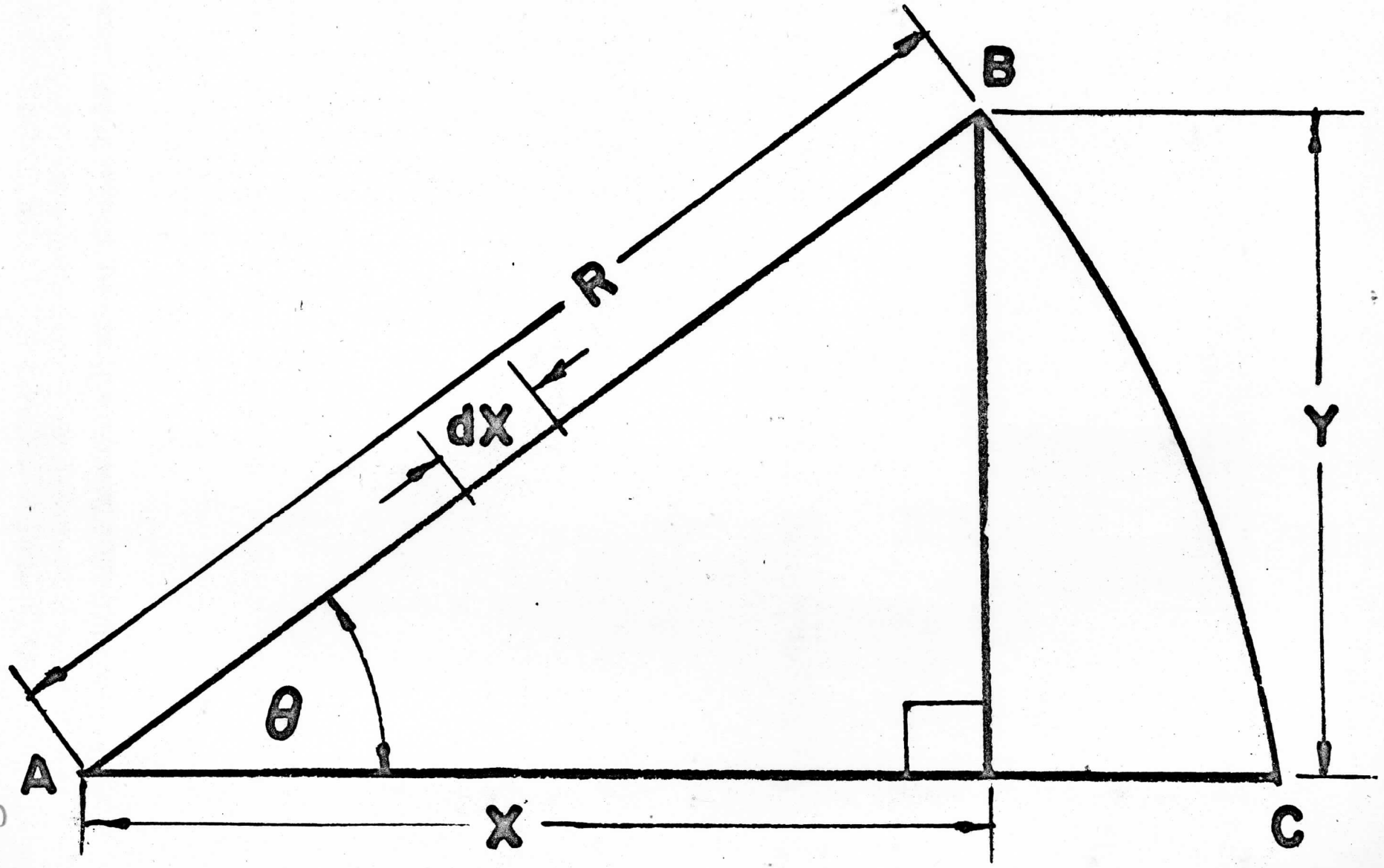

Fig 80

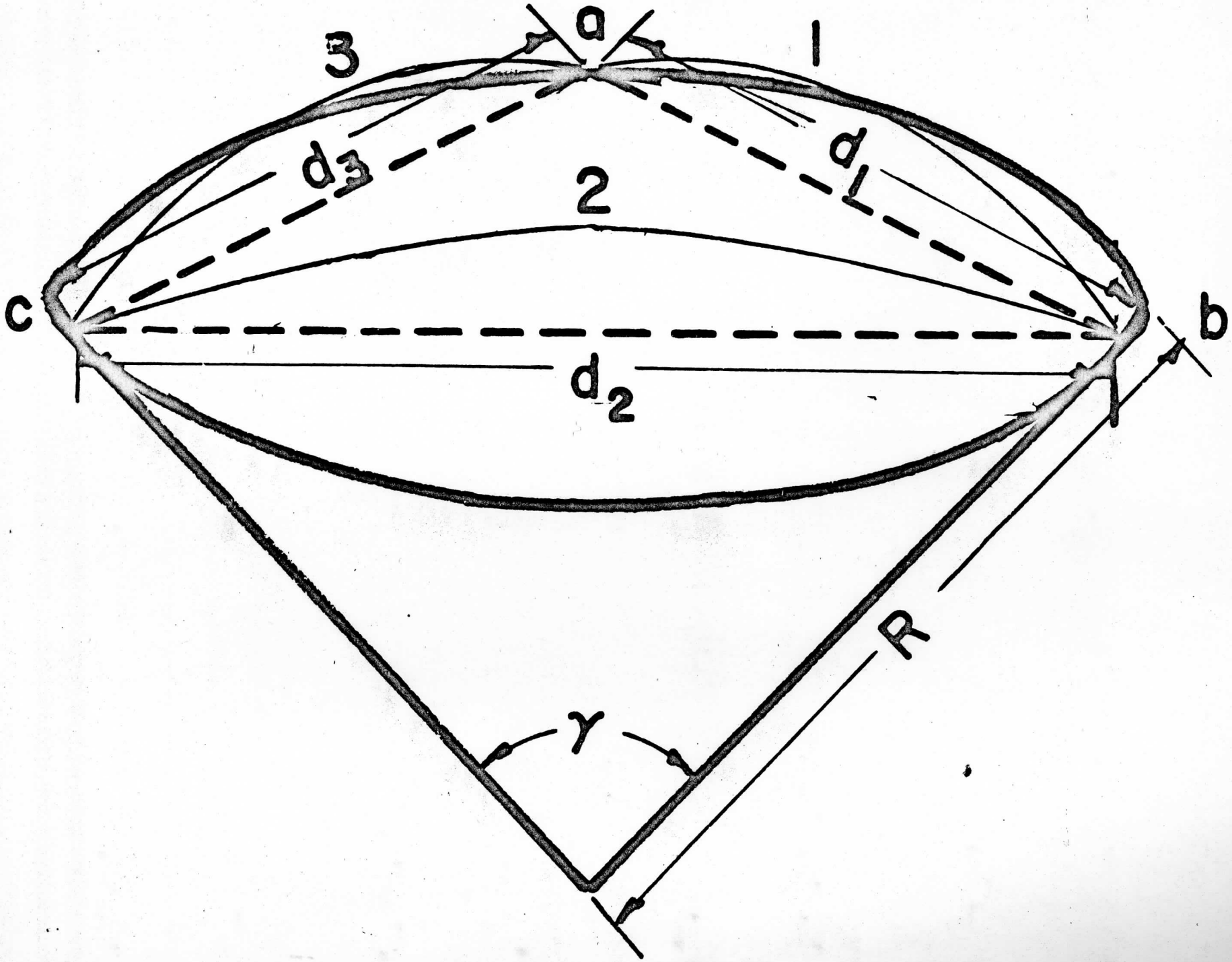

Fig 18a

$\rho = a(\theta \pm k\pi)$

$\rho = -a(\theta \pm k\pi)$

$a = \rho/\theta$

$\rho = -e^{a(\theta \pm k\pi)}$

$\rho = e^{a(\theta \pm k\pi)}$

$a = \ln \rho/\theta$

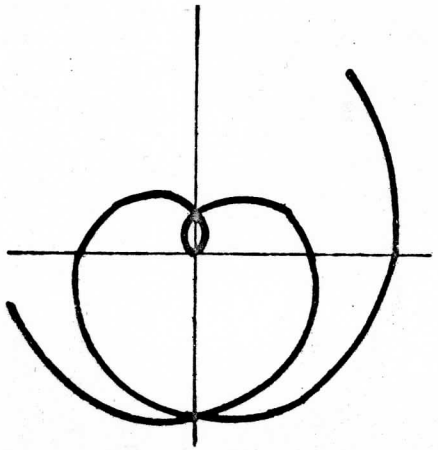

a)

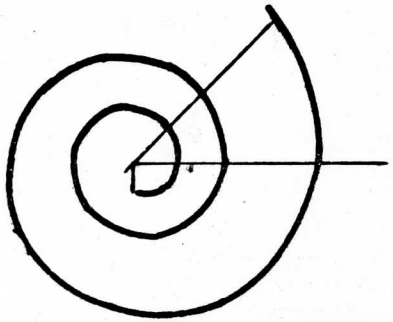

b)

$(\rho - a)^2 = 4ak\theta$

$\rho\theta = a$

$\rho(\theta \pm k\pi) = -a$

$a = k(\rho/k + 2\theta) \pm k(2\rho\theta/k + 2\theta^2)^{1/2}$

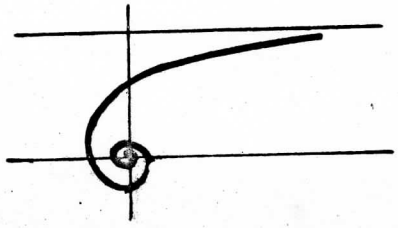

c)

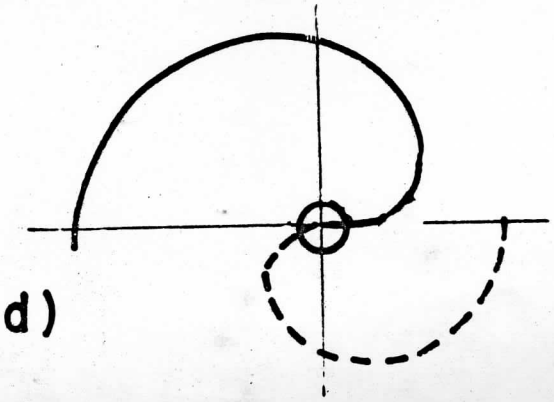

d)

THE UNIVERSITY OF WISCONSIN

DEPARTMENT OF METEOROLOGY

Aug. 9, 1968

Dr. Verner Suomi, Editor
Mr. Kirby Hanson, Editor
1024 Regent Street
Madison, Wisconsin

Dear Sirs:

Enclosed is the revised manuscript of "Some Display and Analysis Techniques for ATS Digital Data Users."

I have made all but one of the changes suggested by the reviewer (his first suggestion would not clarify). His comments on cloud motions not being easily measurable with time sequenced photographs was given our attention yet we don't feel this affects the validity of the techniques explained in the paper. I did not put forward any of the application programs as solutions to meteorological problems; only techniques to help the meteorologist solve problems.

Sincerely,

Eric A. Smith

Eric A. Smith

EAS/pae

original

30

THE INSPACE, ABSOLUTE CALIBRATION OF ATS-1 CLOUD CAMERA

by

Kirby J. Hanson

and

Verner E. Suomi

TABLE OF CONTENTS

		Page
	Definition of Terms	iii
1.	Introduction	1
2.	Theory of Calibration	3
	a. General Development	3
	b. Bidirectional Reflectance of the Moon	9
3.	Calibration of September 1967	12
	a. Description of the Experiment	12
	b. Calibration Constants a, b and c	13
4.	Calibration Equations and Their Application	18
	a. Estimating Total Radiance from Effective Radiance	19
	1. Solar Spectral Distribution	20
	2. Non-solar Spectral Distribution	21
Appendix -	Significant Constants	24
	1. Astronomical Constants	24
	2. ATS-1 and Related Constants	24
	3. Radiation Constants	25

TABLE OF CONTENTS

		Page
	Definition of Terms	iii
1.	Introduction	1
2.	Theory of Calibration	3
	a. General Development	3
	b. Bidirectional Reflectance of the Moon	9
3.	Calibration of September 1967	12
	a. Description of the Experiment	12
	b. Calibration Constants a, b and c	13
4.	Calibration Equations and Their Application	18
	a. Estimating Total Radiance from Effective Radiance	19
	1. Solar Spectral Distribution	20
	2. Non-solar Spectral Distribution	21
5.	Summary	22
	Appendix - Significant Constants	24
	1. Astronomical Constants	24
	2. ATS-1 and Related Constants	24
	3. Radiation Constants	25
	References	28

Definition of Terms

a - Calibration constant [millivolts]

a* - Angular Field of View of ATS-1 camera [m rad.]

A_c - Aperature-area of the ATS-1 camera [cm^2]

A_f - Ratio of area of spot photometer field of view filled by the brightness source to the total area of the photometer field of view [dimensionless]

AU - Earth-sun distance [cm]

b - Calibration constant [sr^{-1}]

B - Luminance associated with radiance (N_r), assuming maximum luminous efficiency of 680 [lumens $watt^{-1}$], Units of B are: [lumens M^{-2} sr^{-1}] or [ft. L.]

B_M - Brightness of the moon, measured by a narrow beam photometer [ft. L]

B_P - Brightness of Kodak White Paper, measured by a narrow beam photometer [ft. L.]

c - Calibration constant [WM^{-2}]

c_1 - Instrument constant, for narrow beam photometer

"camera output" - This term indicates the gain on the camera. It has also been named "wide-band-data-mode" in NASA (1966). It is defined as,

"camera output" #1 = 0 db. gain

"camera output" #2 = 10db. gain

DN - Digitizer value on a scale from 0 to 255. The DN values a proportional to brightness or input power to the camera.

$(DN)_{1,0}$ - Digital value that would result with "nominal gain settings."

F_{α} - Phase angle function of the moon [dimensionless]

"Ground Station Gain" - adjustable gain on the video signal induced within the ground equipment. The various gain factors are given by Pukna, et al., Table _____, in this volume.

H or H_8 - Irradiance of the sun at the earth's mean distance [WM^{-2}]

H' or H_8 - Effective irradiance [WM^{-2}]

m* - Optical air mass [dimensionless]

MV - Millivolt output of the ATS-1 camera [millivolts]

$[MV]_{1,0}$ - Millivolt output that would result with "nominal gain settings" [millivolts]

"Nominal Gain Settings" - arbitrarily defined as the lowest gain settings possible. These are,

"camera output" #1, and

"Ground Station Gain" #0.

N_r - Radiance of the earth and atmosphere [$WM^{-2}\ sr^{-1}$]

N_r' - Effective radiance of the earth and atmosphere [$WM^{-2}\ sr^{-1}$]

$N_{r\lambda}$ - Spectral radiance of the earth and atmosphere [$WM^{-2}\ sr^{-1}\ \mu^{-1}$]

$N_{\odot}$ - Radiance of the sun [$WM^{-2} sr^{-1}$]

$N_{\odot}'$ - Effective radiance of the sun [$WM^{-2}\ sr^{-1}$]

$N_{\odot\lambda}$ - Spectral radiance of the sun $[WM^{-2}sr^{-1}\mu^{-1}]$

$N_{r\odot}$ - Radiance of the earth and atmosphere, but having the same spectral distribution as $N_{\odot\lambda}$ $[WM^{-2}sr^{-1}]$

P_r' - Effective radiant power into the ATS-1 camera aperature [W]

R_λ - Spectral sensitivity of ATS-1 camera [dimensionless]

sr - [Steradian]

V_m - Visual magnitude

α - Phase angle of the moon. That is, the angle made by the sun, moon and "observer." (Note: In determining a value for a, the "observer" is the ATS-1 camera.) [degrees]

γ - Zenith angle of the ATS-1 satellite as determined at the earth's surface and center of ATS-1 field-of-view [degrees]

δ - Zenith angle of the sun, determined at same point as for γ [degrees]

ρ' - Bidirectional reflectance $[sr^{-1}]$

ρ_λ' - Bidirectional spectral reflectance $[sr^{-1}]$

ρ_M' - Bidirectional reflectance of the moon $[sr^{-1}]$

$\rho_{M\lambda}'$ - Bidirectional spectral reflectance of the moon $[sr^{-1}]$

ρ_P' - Bidirectional reflectance of Kodak White Paper $[sr^{-1}]$

$\rho_{P\lambda}'$ - Bidirectional spectral reflectance of Kodak White paper $[sr^{-1}]$

ρ_P - Directional reflectance of Kodak White paper [dimensionless]

$\bar{\rho}'$ - Bidirectional reflectance (of the medium in the field-of-view) which is independent of wavelength over the range of R_λ.

$-\tau_\lambda$ - Spectral transmittance of the earth's atmosphere [dimensionless]

ϕ_1 - Azimuth angle of the sun, at the same point as for $\underline{\gamma}$ [degrees]

ϕ_2 - Azimuth angle of the ATS-1 satellite, at the same point as for $\underline{\gamma}$ [degrees]

ω_c - Solid angle field-of-view of the ATS-1 camera [sr]

$\omega_\odot$ - Solid angle subtended by the sun at the earth's mean distance from it [sr]

$\omega_\odot^*$ - Solid angle subtended by the sun at the moon, during full-moon [sr]

1. INTRODUCTION

In the history of satellite radiometer or photometer experiments on United States spacecraft there have been many attempts to obtain absolute radiation values from the measurements. These have met with varying degrees of success; and, in fact, there is even considerable difference of opinion among scientists on the degree of success of such attempts. The primary difficulty in obtaining absolute values arises from degradation of the satellite sensor, or sensor optics, in space. As a result, a suitable prelaunch calibration is of little value after degradation begins, unless there is an inherent technique for performing the calibration in space.

The cloud camera experiments on ATS-1 and -3 used photomultiplier tubes as detectors. It is well known that photomultipliers tend to be unstable under varying light conditions. Because of this, the tubes were "burned-in" for a number of hours before launch in an attempt to stabalize their sensitivity (Suomi and Parent (1967)). In the future it would be wise to incorporate inspace calibration schemes into the experiment. Two promising methods appear feasible, in addition to the calibration technique which was used for ATS-1 and is the subject of this paper. One method is to monitor the current output of the photocathode when the camera "sees" the sun. This is possible during the equinoxes. A second method of inspace calibration is to periodically view a Cerenkóv Standard Source with the photomultiplier. These sources have previously been used in this way (NASA, 1964). In these sources, quartz or other transparent substance exposed to gamma radiation produces a weak, continuous spectrum from red to ultraviolet. They are reasonable constant and the distribution and intensity of the continuum depends on the

index of refraction of the transparent substance. Quartz is often used because its index of refraction is nearly independent of temperature.

The present paper considers the absolute calibration of the ATS-1 camera. Although neither of the two schemes mentioned above were incorporated, we are able to obtain an absolute calibration on the moon in the following manner. We can observe the moon with ATS-1 for about 2 days out of 14, as the moon traverses the earth's equatorial plane. Thus, the moon may serve as a passive brightness source on which to determine the response of the ATS-1 camera. The main requirement of this technique is to accurately determine the brightness of the lunar target which the ATS-1 camera is viewing. Its brightness can be determined a number of ways. For example, astronomers have measured the brightness-phase function of the moon. They have also measured the lunar reflectance. Both of these determinations could serve as the basis for calibrating the ATS-1 camera. However, the accuracy of such a calibration would depend on the precision

of the astronomer's methods, instrument calibration, and measurement accuracy. These are difficult to reconstruct.

We have, therefore, decided to determine the bidirectional reflectance of the moon relative to a standard MgO_2 reflectance surface. This surface has well known reflectance properties [Richmond (1962) and NBS (1939)]. Our procedure was to first determine the absolute value of bidirectional reflectance for Kodak white paper by comparative measurements with a MgO_2 surface. This was accomplished in an integrating sphere. Second, we determined the absolute value of bidirectional reflectance of the moon (at the time it was viewed by ATS-1) using comparative measurement with the previously "calibrated" Kodak white paper. Thus, the Kodak paper served as a secondary-standard reflectance surface with which to relate the relative lunar reflectance measurement to an absolute reflectance value. The second comparison mentioned above was carried out at Barcraft Laboratory, White Mountain, California in September, 1967 and is discussed in detail in a later section. Such comparisons could be carried out at frequent intervals if there is evidence the ATS-1 photomultiplier is degrading.

This paper is intended to show the theory of the inflight calibration technique; this is given in Section 2. It is also our desire to show the calibration of ATS-1, obtained in September, 1967; this is given in Section 3. In addition, this paper discusses use of equators, based on ATS-1 calibration, for determining the radiance of the earth and

atmosphere, and for determining the bidirectional reflectance within the field of view of the camera. This is given in Section 4.

2. THEORY OF CALIBRATION

An excellent introductory development of the theory is given in the paper by Peekna, et al., in this Volume. The development given here is an extension of that given in their paper. For those readers who are unfamiliar with the notation used here, which is essentially that of Nicodemus (1963 and 1965), we recommend they follow the development of Peekna, et al., before continuing with this paper.

a. General Development

In her paper, Peekna has shown that the effective radiant power (P_r') into the ATS-1 camera aperature due to radiance from an earth target is

$$P_r' = A_c \cdot \omega_c \rho' \cdot H_\delta' \cdot \cos\delta \qquad (1)$$

All of these terms are illustrated in Figure 1, where: A_c and ω_c are the aperature-area and solid-angle-field-of-view of the ATS-1 camera; ρ' is the bidirectional reflectance, that is, the fraction of radiance incident from direction (δ, ϕ_1) which is reflected in direction (γ, ϕ_2); H_δ' is the effective irradiance of the sun at the earth; and δ is the zenith angle of the sun at the center of the intersection of the cone ω_c and the earth.

Another convenient way of expressing the effective power to the

ATS-1 camera is as a function of the sun's radiance, $N_{\odot}$. The radiance and irradiance of the sun are related by the solid angle subtended by the sun at the earth, $\omega_{\odot}$, that is,

$$H' = \omega_{\odot} \cdot N_{\odot}' \tag{2}$$

as a result we may combine (1) and (2) to give,

$$P_r' = A_c \cdot \omega_c \cdot \rho' \cdot \cos\delta \cdot \omega_{\odot} \cdot N_{\odot}' \tag{3}$$

An even more basic form would be to write (3) to include the spectral radiance of the sun, $N_{\odot\lambda}$, and the spectral sensitivity of the ATS-1 camera, R_{λ}. This form is,

$$P_r' = A_c \cdot \omega_c \cdot \rho' \cdot \cos\delta\, \omega_{\odot} \int_0^{\infty} N_{\odot\lambda} \cdot R_{\lambda}\, d\lambda \tag{4}$$

This is probably the most complete form of the effective power input to the camera, and one in which the power input is very clearly specified in terms of:

(1) a "throughput" term for the camera ($A_c \cdot \omega_c$), as defined by Nicodemus (1963). This term includes the camera aperature and solid angle field of view. Physically, it might be thought of as the "geometrical aperature" through which power may pass into the camera - hence, the term "throughput."

(2) the bidirectional reflectance of the earth and atmosphere within the field of view (ρ').

(3) geometry factors for the solar radiance impinging on the atmosphere within the field of view ($\cos\delta \cdot \omega_{\odot}$), and

(4) the integral of solar spectral radiance and spectral sensitivity of the ATS-1 camera. This integral is defined as the "effective" solar radiance. That is, that solar radiance which is sensed by the ATS-1 camera.

Perhaps the final useful form to express the effective radiant power into the camera is simply in terms of the radiance of the earth and atmosphere within the field of view. This form is,

$$P_r' = A_c \omega_c N_r' \tag{5}$$

The effective radiance from the earth and atmosphere N_r' (illustrated in Fig. 1) is defined as

$$N_r' = \rho' \cos\delta \, \omega_\odot \int_0^\infty N_{\odot\lambda} R_\lambda \, d\lambda \tag{6}$$

Thus, it is apparent that (5) follows from combining (4) and (6).

This completes the defininition of the rather general geometric and radiometric quantities required for the calibration. We may now proceed with the equations which are unique to this particular calibration technique.

Peekna et al. (Chapter) have shown that the effective radiant power input to the camera and millivolt output from the camera are linearly related, providing the photomultiplier is not saturated. That is, providing the output is below the "knee" of the response curve, as shown by Peekna's Figure 2 (this volume). Since this is true, we know that millivolt output

(MV) is proportional to the effective power input, P_r'. That is,

$$MV \propto P_r' \tag{7}$$

Therefore, by (5) and (7) we can also write that,

$$MV \propto A_c \omega_c N_r' \tag{8}$$

or,

$$MV \propto A_c \omega_c \rho' \cos\delta \omega_\odot \int_0^\infty N_{\odot\lambda} R_\lambda d\lambda \tag{9}$$

This proportionality is the key to the inflight calibration. We may write equation (9) for some time, t_0, as the denominator in equation (10), and for some later time, t_1, as the numerator.

$$\frac{[MV]_{t_1}}{[MV]_{t_0}} = \frac{[A_c \omega_c \rho' \cos\delta \omega_\odot \int_0^\infty N_{\odot\lambda} R_\lambda d\lambda]_{t_1}}{[A_c \omega_c \rho' \cos\delta \omega_\odot \int_0^\infty N_{\odot\lambda} R_\lambda d\lambda]_{t_0}} \tag{10}$$

Now let the designation t_0 be the time of inflight calibration of the satellite camera. It will be shown later that during the calibration we measure the millivolt output of the camera $[MV]_{t_0}$, when the camera is viewing the moon; using another photometer, we also measure the bi-directional reflectance of the moon, $[\rho']_{t_0}$, at that time. Thus, two terms in the denominator are measured. The remaining terms in the denominator are known, and their values are given in the Appendix A. So we may logically rewrite (10) by treating the denominator terms as constants of the calibration. Let us also drop the subscript t_1 and recognize that the numerator terms in (10) apply to any time after t_0. Thus, equation (10) becomes,

$$MV = \frac{a}{b \cdot c} \cdot \rho' \cdot \cos\delta \cdot \omega_{\odot} \int_0^{\infty} N_{\odot\lambda} \cdot R_{\lambda} \, d\lambda \qquad (11)$$

where:

$$\left.\begin{aligned} a &\equiv [MV]_{t_0} \\ b &\equiv [\rho']_{t_0} \\ c &\equiv [\omega_{\odot} \int_0^{\infty} N_{\odot\lambda} \cdot R_{\lambda} \, d\lambda]_{t_0} \end{aligned}\right\} \qquad (12)$$

Equation (11) is a useful form of the calibration result which now specifies the camera output in MV as a function of the variables, ρ' and $\cos\delta$. The remaining terms on the right hand side of (11) may be treated as constants. Thus, in (11) the camera output depends on the bidirectional reflectance in the camera field of view. This equation is written with ρ' outside the integral and therefore assumes it is independent of λ. However, it could have been written inside the integral, if this is desired in order to treat ρ as spectrally dependent. Equation (11) also assumes the bidirectional reflectance of the moon is independent of λ within the spectral range of the camera (0.45 - 0.65 microns). In actual practice, one would use equation (11) to solve for ρ', given the ATS-1 camera output in MV and the solar zenith angle δ.

Another form of writing this equation is to specify camera output as a function of the earth's radiance. N_r'. By equations (6) and (11), this is,

$$MV = \frac{a}{b \cdot c} \cdot N_r' \qquad (13)$$

Again, in practice, one would use equation (13) to solve for $\underline{N'_r}$, given the ATS-1 camera output in MV. The assumptions going into (13) are that:

1. the bidirectional reflectance of the moon is independent of wavelength within the spectral range of the camera,
2. the bidirectional reflectance of the earth and atmosphere within the field of view is independent of wavelength for the spectral range of the camera, and
3. that we know the effective solar radiance, $N'_{\odot}$, to suitable accuracy.

So equation (11) and (13) are the useful equations for working with ATS-1 digital data in order to obtain absolute radiance values, or bidirectional reflectance values, given the camera output in millivolts and a suitable calibration of the camera. Which equation to use, and how it is used, will depend on the particular application of the researcher.

Now that the general development has been completed, we must go back and look more carefully at one term - the bidirectional reflectance of the moon $[\rho']_{t_0}$, which appeared in equation (11), so we may examine the method by which it is determined. Much of the credibility of this calibration rests on establishing an accurate method for determining this quantity. Therefore a separate section of the theory has been given to this determination.

b. Bidirectional Reflectance of the Moon

In this direction we will show how the bidirectional reflectance of the moon can be determined by comparative measurements with the bidirectional reflectance of a known reflectance surface. Solar radiance is the source of energy in both measurements and the problem is to eliminate the effects of the earth's atmosphere which intervenes.

If we have a narrow beam photometer on the earth's surface whose field of view is filled by a portion of the full moon's disc, then the brightness of the moon measured by the photometer can be given as,

$$B_M = C_1 \omega_\odot^* \int_0^\infty N_{\odot\lambda} \cdot \rho'_{M\lambda} \cdot e^{-\tau_\lambda} \cdot S_\lambda d\lambda \qquad (14)$$

where: C_1 is an instrument constant; $\omega_\odot^*$ is the solid angle subtended by the sun at the moon; $N_{\odot\lambda}$ is the solar radiance; $\rho'_{M\lambda}$ is the spectral bidirectional reflectance of the lunar surface within the field of view; $e^{-\tau\lambda}$ is the spectral transmittance of the earth's atmosphere; and $S\lambda$ is the spectral sensitivity of the photometer.

If the same photometer is used on the earth's surface to measure the brightness of a piece of Kodak white paper held normal to the direct solar beam, then the measured brightness would be given as,

$$B_P = C_1 \cdot \omega_\odot \int_0^\infty N_{\odot\lambda} \cdot \rho'_{P\lambda} \cdot e^{-\tau_\lambda} \cdot S_\lambda d\lambda \qquad (15)$$

Here: the terms common to (14) are as defined there; $\rho'_{P\lambda}$ is the spectral bidirectional reflectance of the paper; and $\omega_\odot$ is the solid angle subtended by the sun at the earth.

Let us assume the bidirectional reflectance of both the moon and paper are not wavelength dependent in the spectral range of the photometer. With this assumption, $\rho'_{M\lambda}$ may be removed from the integral in (14); and $\rho'_{P\lambda}$ may be removed in (15). The remaining integral values are identical, then, in (14) and (15). By taking the ratio of (14) to (15) we obtain,

$$\frac{B_M}{B_P} = \frac{\omega^*_\odot}{\omega_\odot} \cdot \frac{\rho'_M}{\rho'_P} \tag{16}$$

This can be rewritten as,

$$\rho'_M = \rho'_P \cdot \frac{\omega_\odot}{\omega^*_\odot} \cdot \frac{B_M}{B_P} \tag{17}$$

With this result it is apparent that the bidirectional reflectance of the moon, ρ'_M, can be determined from the ratio of only relative brightness measurements of the moon surface and a known reflectance surface; absolute brightness measurements are not required. The omega ratio term corrects for the fact that the moon and earth may not be the same distance from the sun when the measurements are made. Notice also that the attenuation of the earth's atmosphere, cancels from the equation because it appears with both measurements. However, the observations must be made with the same optical air mass and the same meteorological conditions in order for the $e^{-\tau_\lambda}$ terms to be identical and cancel. Thus, equation (17) would serve very well for the photometer described and measurements made at the time of full moon.

We have found it necessary to generalize (17) so that measurements may be made at times other than full moon. We have also found it necessary to generalize (17) so that measurements may be made with a photometer whose field of view is such that the moon fills only a portion of the field of view. This simply means two additional terms are included in (17), so that the more generalized form is,

$$\rho'_M = \rho'_P \cdot \frac{1}{A_f \cdot F_\alpha} \cdot \frac{\omega_\odot}{\omega^*_\odot} \frac{B_M}{B_P} \qquad (18)$$

Here A_f is a ratio of the area of the photometer field of view filled by the brightness source to the total area of the photometer field of view. This is easily determined experimentally. F_α is the lunar phase function which is used by astronomers; a recent discussion is given by Gehrels, et al., (1964). This term, which is defined in the next section, corrects the brightness to its equivalent full moon value.

The calibration work reported in the next section of this paper used a 1.5 degree field of view spot photometer and measurements were not made at full moon. Therefore, equation (18) has been used in the present work in order to determine ρ'_M. This term was then used as the value of the calibration constant b in equation (12). Thus we may make use of the calibration equations (11) or (13) which requires this constant. This is the subject of the following two sections.

3. CALIBRATION OF SEPTEMBER, 1967

a. Description of the Experiment

The purpose of this calibration is to determine numerical values for the constants a and b in equation (12). Where, you will recall

$$a \equiv [MV]_{t_0}$$

$$b \equiv [\rho']_{t_0}$$

and t_0 will be the time of calibration. Now in reality it is usually not possible to determine a and b simultaneously. Yet these two quantitives must be evaluated for the same time, t_0. Since they both depend on the integral brightness of the moon, it is convenient to calculate their equivalent values for full moon using lunar brightness vs. phase angle relation. The relation used in this study is that of Gehrels, et al., (1963), as shown in Fig. 2.

The task of calibration has two parts, the first is to determine a, the camera response in millivolts in viewing the moon. This was carried out by NASA at the Mojave tracking station. The quantitative measurements were digitized and stored on magnetic tape; these tapes were read and evaluated at Wisconsin.

The second portion of the calibration, that of determining b, was conducted at Barcroft Laboratory, White Mountain, California. This is an excellent facility because its altitude (12,470 ft.) is above much of the atmospheric haze. It is located 18 miles NNE of Bishop, California, and is a part of the University of California at Berkeley.

b. Calibration Constants a, b and c

The constant a has been determined from ATS-1 picture 261-7-162755 which was obtained on September 18, 1967. The original data was digitized and recorded on magnetic tape with the following two gain settings:

$$\left.\begin{array}{l}\text{Camera output} = 2\\ \text{Ground Station Gain} = 6\end{array}\right\} \qquad (19)$$

The moon occupied 64 scan lines and a maximum of 202 elements near its equator. A computer display of the moon's disc, using a program described by Smith and Vonder Haar in this Volume, is shown in Fig. 3. The isolines are digital numbers (DN) of 75, 50 and 35; the latter value approximates the lunar limb. Considerable detail is available in the data which is not shown in Figure 3. For example, the average brightness of some scan lines in the lower portion of the moon's disc are near DN's of 160.

There are 10,316 elements on the moon's disc in picture 261-7-162755 and the average DN is 109.74 on a scale of 0-255 DN. The digitizer conversion is given by Parent (1967) as,

$$MV = 1.96076 \cdot DN[\text{Millivolts}] \qquad (20)$$

Thus the measured digital value of 109.74 is equivalent to a camera output of 215.17 [MV]. However this output is for amplifier gain setting indicated in (19), which is much higher than nominal because of the relatively low brightness of the moon.

A more logical way of expressing the numerical value of a is by determining the equivalent output for nominal gain settings. These are,

$$\left.\begin{aligned} \text{Camera output} &= 1 \\ \text{Ground Station gain} &= 0 \end{aligned}\right\} \qquad (21)$$

According to Peekna's table , the amplification for gain setting in (19) is greater than for (21) by a factor of 6.324. Therefore the equivalent millivolt output at nominal gain settings is

$$MV = 215.17/6.324$$

or,

$$MV = 34.02 \text{ [millivolts]} \qquad (22)$$

The final adjustment that must be made to this value is that of determining its equivalent full moon value, so that the camera output as well as input has been normalized to its equivalent at full moon. Using Gehrel's phase angle function (Fig. 2) we find the phase angle of 6.5 degrees requires a factor of 1.192 in order to determine the camera output at full moon. Thus,

$$a = 1.192 \times 34.02$$

$$a = (40.55)_{0,1} \text{ [millivolts]} \qquad (23)$$

This, then, is the camera output at calibration, normalized to its equivalent value at full moon, and nominal gain settings, which are indicated in Eq. 21. To clearly indicate the gain settings are nominal, let us adopt the subscript notation indicated in (23) and continue this through the paper. The reason is, as will be apparent later, any camera

output value must be normalized to this common base if the calibration equations are to be used to infer radiance or bidirectional reflectance.

The constant b is evaluated with Eq. 18 and is based on the comparative measurements at White Mountain and other constants. You will recall that this equation is

$$\rho'_M = \rho'_P \frac{1}{A_f \cdot F_\alpha} \cdot \frac{\omega_\odot}{\omega^*_\odot} \cdot \frac{B_M}{B_P}$$

The five terms on the right hand side of this equation will be evaluated in order.

1. ρ'_P. This term is the bidirectional reflectance of Kodak white paper (Gray-scale card) at a zenith angle of 60 degrees. This angle corresponds to the direction in which B_p has measured. The vaue of this term is,

$$\rho'_P = \frac{0.919 \times \rho_P}{\pi} \tag{24}$$

We have determined the (total) directional reflectance (ρ_P) of Kodak white paper by comparison with M_gO_2 surfaces and found $\rho_P = 0.90$. The factor 0.919 is the non-Lambertian reflectance of this surface at a zenith angle of 60 degrees. Evaluating (24) gives,

$$\rho'_P = 0.2633 \tag{25}$$

2. A_f. This term, previously defined, was evaluated experimentally and found to be 1/8.263. This is in close agreement with the theoretical value of 1/8.466 for the moon (0.5181 degrees) in a 1.5 degree field of

view photometer, we have therefore used

$$A_f = 1/8.263 \qquad [-] \tag{26}$$

3. F_α. This factor is to correct the observed moon bidirectional reflectance at t_0 to its full moon equivalent. It is defined as

$$[V_m]_{t_0} - V_m = -2.512 \log (F_\alpha) \tag{27}$$

where $[V_m]_{t_0}$ is the visual magnitude at its time of calibration and V_m is the visual magnitude at full moon. Therefore, F_α has values between zero and unity.

For the calibration at White Mountain on September 20, 1967, the measurement of ρ'_M at air mass = 1 was obtained at 06086MT. The phase angle (α) at this time was 19.87 degrees. Again using Gehrel's phase angle functioning (Fig. 2) we find that

$$F_\alpha = 0.6096 \qquad [-] \tag{28}$$

4. $\omega_\odot/\omega_\odot^*$ - Since we are comparing the measured brightness of this moon with that of white paper on the earth, we must have the same irradiance onto both of these surfaces if we are to infer reflectance values from measurements of reflected radiance. This omega ratio term corrects the irradiance on the full moon (moon at distance from the sun) to what the irradiance will be at the earth's mean distance from the sun.

Using the distance given in Appendix A, it is easy to show that

$$\frac{\omega_\odot}{\omega_\odot^*} = 0.9948 \qquad [-] \tag{29}$$

5. B_M/B_P - The measurements made at White Mountain on September 20, 1967 are illustrated in Fig. 4. These were obtained with a Model SB, 1.5 degree Spot Photometer of the Photo Research Corporation. The Regulated Brightness Source for this instrument was calibrated by the manufacturer prior to obtaining the White Mountain series of measurements. The Brightness source was subsequently checked and found to be in calibration following the series of measurements. Because the instrument was calibrated, we are giving the measurements in foot Lamberts (ft. L.) in Fig. 4 and in the following equations. However, the reader will recall from the theory that absolute measurements, such as ft. L., are not required for this series of measurements; relative measurements would be sufficient.

If we evaluate the curves in Fig. 4 at an optical air mass equal to 1 ($m^* = 1$), we find

$$B_M = (98.4)_{m^*=1} \quad [\text{ft. L.}]$$

$$B_P = (10,700)_{m^*=1} \quad [\text{ft. L.}]$$

These two measurement values give the ratio,

$$\frac{B_M}{B_P} = 0.9196 \times 10^{-2} \quad [-] \tag{30}$$

This completes evaluation of the five terms in equation (18). Now, if we solve (18) with these particular constants at the time of calibration, t_0, we find the bidirectional reflectance of the full moon is,

Scanner's note:

There are no more pages in this document.